Measurement of the strong-phase difference between D^0 and $\overline{D}^0$ decays to $K^0_S K^+ K^-$ at CLEO-c and a determination of observables related to $\mathcal{CP}$ violation in $B^\pm \to DK^\pm$ decays at LHCb

Christopher M. Thomas

St John's College, University of Oxford and
STFC Rutherford Appleton Laboratory

A thesis submitted for the degree of Doctor of Philosophy
at the University of Oxford

Trinity Term 2011

Dedicated to the memory of Kunal Moorthy.

Measurement of the strong-phase difference between D^0 and $\overline{D}^0$ decays to $K^0_S K^+ K^-$ at CLEO-c and a determination of observables related to $\mathcal{CP}$ violation in $B^\pm \to DK^\pm$ decays at LHCb

Christopher M. Thomas

St John's College, University of Oxford and STFC Rutherford Appleton Laboratory

A thesis submitted for the degree of Doctor of Philosophy at the University of Oxford

Trinity Term 2011

Abstract

A central goal of flavour physics is a precise determination of the elements of the CKM matrix, which quantifies the strength of charged-current weak interactions between quarks. Of particular interest is the angle γ in the '$b-d$' unitarity triangle parameterisation of the CKM matrix. One of the most promising methods to determine γ directly is to measure $\mathcal{CP}$ violation in interfering $B^\pm \to DK^\pm$ decays, where D indicates a coherent superposition of D^0 and $\overline{D}^0$, both of which decay to the same final state. When using this method it is essential to determine the hadronic decay parameters of the D precisely in order to reduce the systematic uncertainties on the measurement of γ. One such parameter is the strong-phase difference between D^0 and $\overline{D}^0$ decays, which must be accurately known across the entire kinematic phase space.

In this thesis we present measurements related to the determination of γ at both the CLEO-c experiment at Cornell University and the LHCb experiment at CERN. Firstly, we describe a model-independent determination of the $D \to K^0_S K^+ K^-$ strong-phase difference using 818 pb^{-1} of quantum-correlated $D^0\overline{D}^0$ data collected by CLEO-c at the $\psi(3770)$ resonance. We reconstruct $D \to K^0_S K^+ K^-$ decays tagged with a variety of final states. By studying these decays we determine the weighted cosine and sine of the strong-phase difference in bins across the Dalitz plane. We run simulations to estimate the impact of these measurements on a determination of γ using $B^\pm \to (K^0_S K^+ K^-)_D K^\pm$ decays. The resulting uncertainty on γ due to the CLEO-c inputs is between 3.2° and 3.9°, depending on how the Dalitz plane is binned. Furthermore, we present a model-independent measurement of the $\mathcal{CP}$ content of the decay $D^0 \to K^0_S K^+ K^-$ in the kinematic region of the $\phi \to K^+K^-$ resonance. The fraction of $\mathcal{CP}$-odd events in this region is 0.76 or higher at the 90% C.L.

We also present an analysis of data recorded by LHCb in 2010, corresponding to an integrated luminosity of 36.5 pb^{-1}. We reconstruct the decays $B^\pm \to (K^\pm\pi^\mp)_D h^\pm$ and $B^\pm \to (K^+K^-)_D h^\pm$, where $h^\pm$ indicates either $K^\pm$ or $\pi^\pm$. Although there are not enough events in this dataset to measure γ, we are able to measure other observables related to $\mathcal{CP}$ violation in the $B^\pm \to Dh^\pm$ system. We measure $\mathcal{B}^{DK}_{\rm Fav}/\mathcal{B}^{D\pi}_{\rm Fav}$, the ratio of the branching fraction of $B^\pm \to (K^\pm\pi^\mp)_D K^\pm$ to that of $B^\pm \to (K^\pm\pi^\mp)_D \pi^\pm$, to be $0.066 \pm 0.005 \pm 0.004$, and $\mathcal{B}^{DK}_{\mathcal{CP}}/\mathcal{B}^{D\pi}_{\mathcal{CP}}$, the ratio of the branching fraction of $B^\pm \to (K^+K^-)_D K^\pm$ to that of $B^\pm \to (K^+K^-)_D \pi^\pm$, to be $0.093 \pm 0.019 \pm 0.005$. We determine several $\mathcal{CP}$ asymmetries: $A^{DK}_{\mathcal{CP}+}$, the $\mathcal{CP}$ asymmetry in $B^\pm \to (K^+K^-)_D K^\pm$ decays, is measured as $0.06 \pm 0.17 \pm 0.07$; $A^{D\pi}_{\mathcal{CP}+}$, the $\mathcal{CP}$ asymmetry in $B^\pm \to (K^+K^-)_D \pi^\pm$ decays, is found to be $0.009 \pm 0.042 \pm 0.011$; and $A^{DK}_{\rm Fav}$, the $\mathcal{CP}$ asymmetry in $B^\pm \to (K^\pm\pi^\mp)_D K^\pm$ decays, is measured as $-0.109 \pm 0.085 \pm 0.019$. Finally we calculate $R_{\mathcal{CP}+}$, the ratio of the branching fraction of $B^\pm \to (K^+K^-)_D K^\pm$ to that of $B^\pm \to (K^\pm\pi^\mp)_D K^\pm$, to be $1.41 \pm 0.31 \pm 0.11$. These results indicate that LHCb is in a strong position to make a world-leading measurement of γ with a larger data sample.

Acknowledgements

There are many people who I wish to thank for helping me to complete this thesis. Firstly, it has been a pleasure to work with my supervisors Stefania Ricciardi and Guy Wilkinson. I have received great guidance, training and support throughout the last four years. Their careful proofreading of my thesis has been absolutely invaluable.

Many thanks to Andrew Powell for providing crucial help on countless occasions and for never being too busy to have a chat. As well as Andrew, I greatly enjoyed working with Paolo Gandini, Philip Hunt and Malcolm John on the LHCb analysis. In particular I spent an enjoyable four years, at both Oxford and CERN, as a contemporary of Philip.

Thanks to Sean Brisbane, Qing He, Jim Libby and Sneha Malde for their very important help and advice on the CLEO-c analysis, and also to Tim Gershon and Jonas Rademacker for useful discussions in the UK CLEO meetings. I wish to thank the BaBar collaboration for providing the $K^0_S K^+ K^-$ strong phase bitmap. I had a great summer in Ithaca which is thanks in no small part to Brian Moziak, Paras Naik, Peter Onyisi, Adam Robichaud and Eric White, as well as the rest of the people I met out there.

While at CERN I worked on the LHCb trigger software and I wish to thank Vava Gligorov, Patrick Spradlin and Mike Williams for all the help they gave me.

I met many great people at CERN and these acknowledgements are too small to contain all of their names! Thanks to all of you for making my stay there very enjoyable.

Thanks to Neville Harnew for leading the Oxford LHCb group so effectively and providing support on several occasions. I also want to thank the Oxford LHCb group as a whole: Mat Charles, Andrea Contu, Rhorry Gauld, Hamish Gordon, Ed Greening, Dan Johnson, Lauren Martin, Andrei Nomerotski, Sophie Redford, Ed Smith, Nick Torr and Philip Xing.

Many thanks to thank Jacopo Nardulli for his excellent help and insight. Thanks to Glenn Patrick and John Morris for leading the RAL LHCb group, and also to the members of that group for providing very useful help on many occasions: Sajan Easo, Raja Nandakumar, Antonis Papanestis and Fergus Wilson.

I gratefully acknowledge the Science and Technology Facilities Council for providing me with the opportunity to study for the past four years and for funding my trips to Cornell and CERN. In addition, thanks to the Oxford physics department, RAL and St John's College for their financial support that enabled me to travel to several conferences and schools.

I wish to thank Katy Morgan for providing me with endless support and encouragement throughout this process, and for having fantastic proofreading skills! I am very lucky to have you in my life. Lastly, thanks to my parents, brother and sister for everything they have done for me over the years. You have inspired me to get to where I am today.

Preface

A precise determination of the CKM angle γ, the $\mathcal{CP}$-violating phase between $b\to u$ and $b\to c$ transitions, is one of the primary objectives of heavy flavour physics in the coming decade. The current uncertainty on γ from direct measurements is 11–14° [1, 2], making it the least well-determined of the three angles of the '$b-d$' unitarity triangle. One of the most promising techniques to determine γ directly is to measure $\mathcal{CP}$ violation in interfering $B^{\pm}\to DK^{\pm}$ decays, in which the D represents a coherent superposition of D^0 and $\overline{D}^0$ mesons[1] which both decay to a common final state. This method is expected to be largely insensitive to new physics because $B^{\pm}\to DK^{\pm}$ decays are mediated solely by tree-level processes. The value of γ obtained using $B^{\pm}\to DK^{\pm}$ decays can therefore be compared to alternative measurements of γ using decays that involve loop diagrams, and a discrepancy between the measurements will be a strong indication that new physics exists. Precise measurements of γ are also important to overconstrain measurements of the unitarity triangle and to test the three-generation quark model.

Measurements of γ can be made by studying $B^{\pm}\to DK^{\pm}$ decays in which the D decays to a variety of final states. For each final state, the parameters that quantify the interference between D^0 and $\overline{D}^0$ decays are a source of systematic uncertainty on γ and must therefore be known precisely. The CLEO-c experiment at Cornell University has collected a sample of quantum-correlated $\psi(3770) \to D^0\overline{D}^0$ decays that can be used for this purpose. The decay parameters of several D final states have been measured at CLEO-c, including $D\to K^{\pm}\pi^{\mp}$ [3, 4], $D\to K^{\pm}\pi^{\mp}\pi^{+}\pi^{-}$ and $D\to K^{\pm}\pi^{\mp}\pi^{0}$ [5], and $D\to K^0_S\pi^{+}\pi^{-}$ [6].

In this thesis we present a model-independent measurement of the strong-phase difference between D^0 and $\overline{D}^0$ decays to $K^0_SK^+K^-$ at CLEO-c [7]. This measurement will be an important input to the measurement of γ in future studies of $B^{\pm} \to (K^0_SK^+K^-)_DK^{\pm}$ decays.

Furthermore, we describe the measurement of parameters related to $\mathcal{CP}$ violation in $B^{\pm}\to Dh^{\pm}$ decays using data recorded in 2010 by the LHCb experiment at CERN. There are not enough events in the dataset to determine γ directly, but the work presented is an intermediate step towards that measurement. The principal work done by the author is in Chapters 3, 4, 5, 7 and 8.

[1] This convention is used throughout this thesis.

In Chapter 1 we present the relevant theoretical background to both analyses. We discuss $\mathcal{CP}$ violation in the quark sector and its parameterisation using the CKM matrix. The formalism associated with Dalitz plots is also outlined. We describe the determination of γ using $B^{\pm}\to DK^{\pm}$ decays in which the D decays to several final states, discussing both the 'ADS/GLW' analysis of D decays to $K^{\pm}\pi^{\mp}$ and $K^{+}K^{-}$ and the binned Dalitz plot analysis of D decays to $K^{0}_{S}K^{+}K^{-}$.

In Chapter 2 we describe the operation and performance of the CLEO-c detector. Chapter 3 details the reconstruction of the $D\to K^{0}_{S}K^{+}K^{-}$ final state in quantum-correlated $D^{0}\overline{D}^{0}$ data recorded at CLEO-c. We describe the selection of events and show their resulting distribution across the $K^{0}_{S}K^{+}K^{-}$ Dalitz plane. The analysis of the selected events is presented in Chapter 4. We detail the choice of Dalitz plane binning, the fit to extract the parameters of interest, and the systematic uncertainties associated with the analysis. Furthermore, we present a determination of the fraction of $\mathcal{CP}$-odd events in the kinematic vicinity of the $\phi \to K^{+}K^{-}$ resonance in $D\to K^{0}_{S}K^{+}K^{-}$ decays. In Chapter 5 we quantify the impact of the $D\to K^{0}_{S}K^{+}K^{-}$ strong-phase difference measurements on a determination of γ using $B^{\pm} \to (K^{0}_{S}K^{+}K^{-})_{D}K^{\pm}$ decays.

In Chapter 6 we present the operation and performance of the LHCb detector. We focus in particular on the PID calibration procedure, which is essential to distinguish $B^{\pm}\to DK^{\pm}$ decays from $B^{\pm}\to D\pi^{\pm}$ decays. The reconstruction of the decays $B^{\pm} \to (K^{\pm}\pi^{\mp})_{D}h^{\pm}$ and $B^{\pm} \to (K^{+}K^{-})_{D}h^{\pm}$, where $h^{\pm}$ is $K^{\pm}$ or $\pi^{\pm}$, is described in Chapter 7. We discuss the event selection procedure and detail the various components used to fit the reconstructed $B^{\pm}$ mass lineshape. In Chapter 8 we present the fit that is used to extract the observables of interest from the data and we list the sources of systematic uncertainty in the analysis.

Contents

Chapter 1

Theoretical background

1.1 Overview of the Standard Model

The Standard Model of particle physics is an extremely successful description of the properties and interactions of elementary particles. It is able to explain a wide variety of observed phenomena and has made many predictions that have been confirmed by experiment.

In the Standard Model there are three generations of spin-1/2 quarks and leptons, which in the weak basis are written:

$$\begin{bmatrix} \nu_e & u \\ e^- & d' \end{bmatrix}, \qquad \begin{bmatrix} \nu_\mu & c \\ \mu^- & s' \end{bmatrix}, \qquad \begin{bmatrix} \nu_\tau & t \\ \tau^- & b' \end{bmatrix} \tag{1.1}$$

with an equivalent structure for antiparticles[1].

Interactions between particles are mediated by spin-1 gauge bosons: the photon for electromagnetic interactions, the $W^\pm$ and Z for electroweak interactions, and gluons for strong interactions. The gauge structure of the Standard Model is $SU(3)_C \otimes SU(2)_L \otimes U(1)_Y$, where C is the colour charge quantum number, L refers to left-handed weak interactions, and Y is the hypercharge quantum number. In addition to the fermions and gauge bosons the Standard Model contains the currently-unobserved Higgs scalar. Particles gain mass via spontaneous symmetry breaking in the Higgs mechanism [8].

In this chapter we will concentrate on $\mathcal{CP}$-violating effects in weak quark interactions. The Standard Model in its entirety is discussed extensively in the literature, e.g. Refs. [9–11].

[1] The relationship between the weak and mass bases is described in Section 1.3.1.

1.2 Discrete symmetries and $\mathcal{CP}$ violation

1.2.1 Discrete symmetries

The concept of symmetry is essential to many branches of physics. Seemingly complex phenomena can often be explained in a simple, elegant way by determining the underlying symmetry of a system. A symmetry is present if a system is invariant under a particular transformation. For example, a perfect sphere exhibits rotational symmetry in all directions. Regardless of how it is rotated it remains indistinguishable from the initial state.

It is important to make a distinction between *continuous* and *discrete* symmetries. A continuous symmetry is one in which a macroscopic transformation of a system can be obtained by repeatedly applying infinitesimal transformations to the system, at each stage preserving the symmetry. This is not possible in a discrete symmetry for which only a finite number of particular configurations can be entered by the system. In this case, the transformation between states must proceed by macroscopic 'flips', rather than passing through a continuum of equivalent states.

The concept of *chirality* is important when considering discrete symmetries. A system is said to be chiral if it is impossible to map it onto its mirror image by any number of translations or rotations. Chirality has an important effect on the structure of the Standard Model; the symmetry group $SU(2)_L$ ensures that only left-handed chiral states participate in the weak interaction.

In quantum-mechanical systems there are three important discrete symmetry transformations: parity ($\mathcal{P}$), charge conjugation ($\mathcal{C}$) and time reversal ($\mathcal{T}$). Extensive discussions on discrete symmetries can be found in Ref. [12].

1.2.1.1 Parity

The parity operator $\mathcal{P}$ inverts the spatial coordinates of a system with respect to the origin. Such a transformation cannot be reproduced by any sequence of rotations or translations. A right-handed chirality state becomes left-handed under the parity transformation, and vice versa. The parity operation is therefore very important for the part of the Standard Model governed by the $SU(2)_L$ group.

The direction of a vector is inverted when it undergoes a parity transformation, whereas the direction of an axial vector remains the same. This is because axial vectors can be written as the cross product of two vectors; for example, angular momentum $\mathbf{L}$ is the cross product of displacement $\mathbf{r}$ and momentum $\mathbf{p}$. Applying the parity operator to an angular momentum vector gives $\mathcal{P}(\mathbf{L}) = \mathcal{P}(\mathbf{r}) \times \mathcal{P}(\mathbf{p}) = -\mathbf{r} \times -\mathbf{p} = \mathbf{L}$. Analogously, quantum-mechanical spin

is unchanged under the parity operation[2].

A generic quantum mechanical state $|\mathbf{p}, s, a\rangle$, where $\mathbf{p}$ is the three-momentum, s is the spin and a labels the charge of the state, is transformed under parity as follows:

$$\mathcal{P}|\mathbf{p}, s, a\rangle = \eta_P|-\mathbf{p}, s, a\rangle, \tag{1.2}$$

where $\eta_P = e^{i\xi_P}$, ξ_P is real and $|\eta_P| = 1$.

The quantity η_P is the *intrinsic* parity of the state. The intrinsic parity of the photon is equal to -1. The relative intrinsic parity of a fermion and its antiparticle is always -1 (independent of the value of η_P), whereas the intrinsic parity of a boson is the same as that of its antiparticle. Pseudoscalar mesons have negative intrinsic parity.

Intrinsic parities are multiplicative. Therefore for two particles p_1 and p_2, the overall parity is equal to $\eta_P^{p_1} \cdot \eta_P^{p_2} \cdot (-1)^L$, where L is the relative orbital angular momentum between the two particles. The parity of a fermion-antifermion state is therefore equal to $(-1)^{L+1}$, and the equivalent for a boson-antiboson state is $(-1)^L$.

Strong and electromagnetic interactions conserve parity, but in weak interactions parity is maximally violated. Whereas left-handed particles e_L^- can participate in the charged-current weak interaction, right-handed particles e_R^- never do.

Parity violation in weak decays was first proposed by Lee and Yang in 1956 [13]. The first evidence of parity violation was found in β decay from polarised ^{60}Co nuclei by Wu *et al.* in 1957 [14].

1.2.1.2 Charge conjugation

The charge conjugation transformation $\mathcal{C}$ reverses the sign of any additive quantum number (e.g. electric charge, baryon number, and strangeness). Kinematic quantities and spin are unaffected by $\mathcal{C}$. The $\mathcal{C}$ transformation applied to the generic state considered above is:

$$\mathcal{C}|\mathbf{p}, s, a\rangle = \eta_C|\mathbf{p}, s, -a\rangle, \tag{1.3}$$

where $\eta_C = e^{i\xi_C}$, ξ_C is real and $|\eta_C| = 1$.

Only neutral particles can be eigenstates of $\mathcal{C}$. As with parity, eigenvalues of $\mathcal{C}$ are multiplicative and $\mathcal{C}$ is maximally violated by weak interactions; $W^\pm$ bosons couple to e_L^- but not its $\mathcal{C}$ conjugate e_L^+.

The $\mathcal{C}$ eigenvalue of the photon is equal to -1. A neutral particle-antiparticle system has $\mathcal{C}$ eigenvalue $\eta_C = (-1)^{L+S}$, where L is the relative orbital angular momentum between the

[2]The parity operator therefore inverts the helicity $(\mathbf{p} \cdot \mathbf{s})$ of a system because the momentum is reversed whereas the spin is unchanged.

particles and S is the total quantum-mechanical spin of the system. This is true for both fermions and bosons.

1.2.1.3 Time reversal

For completeness we consider the time reversal transformation $\mathcal{T}$. This operator changes the direction of motion of a system; its action on the same generic state considered above is:

$$\mathcal{T}|\mathbf{p}, s, a\rangle = \eta_T|-\mathbf{p}, -s, a\rangle, \tag{1.4}$$

where as before $\eta_T = e^{i\xi_T}$, ξ_T is real and $|\eta_T| = 1$.

1.2.1.4 The $\mathcal{CPT}$ theorem

The operator $\mathcal{CPT}$ is the product of the $\mathcal{C}$, $\mathcal{P}$ and $\mathcal{T}$ transformations; the order in which the transformations are applied is irrelevant. The $\mathcal{CPT}$ theorem states that any quantum field theory with a Lorentz invariant, local, Hermitian Hamiltonian is invariant under the $\mathcal{CPT}$ transformation. This holds irrespective of its behaviour under the individual $\mathcal{C}$, $\mathcal{P}$ and $\mathcal{T}$ transformations. This is the only combination of the three transformations that could still be an exact symmetry of nature; all others have been shown to be violated at some level. So far, all observations indicate that $\mathcal{CPT}$ is indeed an exact symmetry.

1.2.2 Introduction to $\mathcal{CP}$ violation

1.2.2.1 The $\mathcal{CP}$ transformation

The product of the $\mathcal{C}$ and $\mathcal{P}$ operators yields the $\mathcal{CP}$ transformation. This transformation converts a particle into its antiparticle and inverts its spatial coordinates with respect to the origin. The action of $\mathcal{CP}$ on the generic quantum state considered above is as follows:

$$\mathcal{CP}|\mathbf{p}, s, a\rangle = \eta_{CP}|-\mathbf{p}, s, -a\rangle, \tag{1.5}$$

where $\eta_{CP} = e^{i\xi_{CP}}$, ξ_{CP} is real and $|\eta_{CP}| = 1$. The spin of the system is unchanged, so $\mathcal{CP}$ transforms left-handed fermions into right-handed antifermions.

$W^{\pm}$ bosons couple to left-handed particles e_L^- and their $\mathcal{CP}$ conjugates, i.e. right-handed antiparticles e_R^+. Initially it was assumed that although $\mathcal{C}$ and $\mathcal{P}$ were violated individually, their product was still an exact symmetry. However, $\mathcal{CP}$ violation was observed in the neutral kaon sector in 1964 [15].

The $\mathcal{CPT}$ theorem implies that if one of the three symmetries is violated then at least one other must be as well. The fact that $\mathcal{CP}$ violation has been observed at a non-zero level

therefore indicates that $\mathcal{T}$ must also be violated, and vice versa.

1.2.2.2 $\mathcal{CP}$ violation in the Standard Model

The presence of $\mathcal{CP}$ violation in the Standard Model is accommodated by the sum of a term and its complex conjugate in the Lagrangian density [10–12]. Consider a Yukawa term:

$$\mathcal{L}_Y = g\bar{\psi}_L\phi\psi_R + g^*\bar{\psi}_R\phi^\dagger\psi_L\,, \tag{1.6}$$

where ψ is a fermion, ϕ is the Higgs field and g is the coupling strength. This expression transforms under $\mathcal{CP}$ to:

$$\mathcal{L}_Y^{CP} = g\bar{\psi}_R\phi^\dagger\psi_L + g^*\bar{\psi}_L\phi\psi_R\,. \tag{1.7}$$

If $g = g^*$ then $\mathcal{L}_Y = \mathcal{L}_Y^{CP}$; if not, there is a relative phase between the two expressions and $\mathcal{CP}$ violation occurs[3]. Such phases are called *weak* phases because in the Standard Model $\mathcal{CP}$ violation can only occur in weak interactions.

1.3 The CKM matrix and the unitarity triangle

1.3.1 Origin of the CKM matrix

In the Standard Model, quarks gain mass through Yukawa interactions with the Higgs field. After spontaneous symmetry breaking, the Lagrangian that describes these interactions can be written as follows:

$$\begin{aligned}\mathcal{L}_Y^q &= -\sum_{i,j=1}^{3}\left(1+\frac{H}{v}\right)\left\{\bar{d}'_{iL}c^d_{ij}\frac{v}{\sqrt{2}}d'_{jR} + \bar{u}'_{iL}c^u_{ij}\frac{v}{\sqrt{2}}u'_{jR}\right\} + \text{h.c.}\\ &= -\left(1+\frac{H}{v}\right)\left\{\bar{\mathbf{d}}'_L\mathrm{M}'_d\mathbf{d}'_R + \bar{\mathbf{u}}'_L\mathrm{M}'_u\mathbf{u}'_R\right\} + \text{h.c.}\end{aligned} \tag{1.8}$$

where i and j label the quark generations, $\mathbf{u}'_{L,R}$ and $\mathbf{d}'_{L,R}$ are vectors in flavour space of up-type and down-type quarks respectively, H is the Higgs field and v is the vacuum expectation value of this field, $\mathbf{c}^{u,d}$ are matrices of coupling constants for up-type and down-type quarks, and M'_d and M'_u are matrices in flavour space, defined as:

$$(\mathrm{M}'_d)_{ij} \equiv c^d_{ij}\frac{v}{\sqrt{2}}, \qquad (\mathrm{M}'_u)_{ij} \equiv c^u_{ij}\frac{v}{\sqrt{2}}. \tag{1.9}$$

The quantities $\mathbf{c}^{u,d}$ can in general be complex, so it is possible for $\mathcal{CP}$ violation to occur in charged-current quark interactions.

[3]Strictly speaking, this is only true if the complex phase cannot be removed by multiplying the entire expression by a complex constant.

Physical quark states are obtained by diagonalising the matrices M'_d and M'_u. The diagonalisation for the down-type quarks proceeds as follows: $\mathrm{M}'_d = \mathbf{S}^\dagger_{dL}\mathrm{M}_d\mathbf{S}_{dR}$ where the $\mathbf{S}$ are unitary matrices and M_d is a diagonal, Hermitian and positive definite matrix equal to $\mathrm{diag}(m_d, m_s, m_b)$. The equivalent for up-type quarks is $\mathrm{M}_u = \mathrm{diag}(m_u, m_c, m_t)$. In general, $\mathbf{S}_u \neq \mathbf{S}_d$.

In charged-current interactions between quarks and $W^\pm$ bosons, the rotation from the weak basis to the mass basis leads to the appearance of the Cabibbo-Kobayashi-Maskawa (CKM) matrix $\mathbf{V}_{\mathrm{CKM}}$ [16, 17] in the Lagrangian density:

$$\mathcal{L}^q_{CC} = -\frac{g}{2\sqrt{2}}\left\{W^\dagger_\mu\left[\sum_{i,j=1}^{3}\bar{u}_i\gamma^\mu(1-\gamma_5)(\mathbf{V}_{\mathrm{CKM}})_{ij}d_j\right] + \mathrm{h.c.}\right\}, \tag{1.10}$$

where g is a coupling constant, W_μ is the $W^\pm$ gauge boson and $\bar{u}$ and d are up-type and down-type quarks respectively. The CKM matrix can be written as follows:

$$\mathbf{V}_{\mathrm{CKM}} \equiv \mathbf{S}_{uL}\mathbf{S}^\dagger_{dL} \equiv \begin{pmatrix} V_{\mathrm{ud}} & V_{\mathrm{us}} & V_{\mathrm{ub}} \\ V_{\mathrm{cd}} & V_{\mathrm{cs}} & V_{\mathrm{cb}} \\ V_{\mathrm{td}} & V_{\mathrm{ts}} & V_{\mathrm{tb}} \end{pmatrix}, \tag{1.11}$$

where element V_{xy} of the matrix expresses the coupling strength in a weak interaction between quarks x and y.

The CKM matrix is unitary, obeying the relation $\mathbf{V}^\dagger_{\mathrm{CKM}}\mathbf{V}_{\mathrm{CKM}} = \mathbb{I}_3$. A generic unitary matrix of dimensions $n \times n$ can be parameterised by $n(n-1)/2$ angles and $n(n+1)/2$ phases. In the case of the CKM matrix, $(2n-1)$ of the phases are irrelevant because they are unphysical and can be redefined arbitrarily; there are therefore $(n-1)(n-2)/2$ remaining. For $n = 3$ generations, there are three angles and one phase. If this phase is non-zero it leads to $\mathcal{CP}$ violation in the Standard Model.

1.3.2 Parameterisation

There are many possible ways to represent the elements of the CKM matrix. A standard parameterisation is [11, 18, 19]:

$$\mathbf{V}_{\mathrm{CKM}} = \begin{pmatrix} c_{12}c_{13} & s_{12}c_{13} & s_{13}e^{-i\delta} \\ -s_{12}c_{23} - c_{12}s_{23}s_{13}e^{i\delta} & c_{12}c_{23} - s_{12}s_{23}s_{13}e^{i\delta} & s_{23}c_{13} \\ s_{12}s_{23} - c_{12}c_{23}s_{13}e^{i\delta} & -c_{12}s_{23} - s_{12}c_{23}s_{13}e^{i\delta} & c_{23}c_{13} \end{pmatrix}, \tag{1.12}$$

where $s_{ij} \equiv \sin(\theta_{ij})$, $c_{ij} \equiv \cos(\theta_{ij})$ and δ is the $\mathcal{CP}$-violating phase. The quantities θ_{ij} are denoted *mixing angles*.

Empirically the following hierarchy is observed: $s_{13} \ll s_{23} \ll s_{12} \ll 1$. This is exploited in the Wolfenstein parameterisation [20] of the CKM matrix which has four parameters: λ (the expansion parameter), A, ρ and η. The following definitions hold to all orders in λ:

$$s_{12} \equiv \lambda, \tag{1.13}$$

$$s_{23} \equiv A\lambda^2, \tag{1.14}$$

$$s_{13}e^{-i\delta} \equiv A\lambda^3(\rho - i\eta). \tag{1.15}$$

A Taylor expansion of the above expressions is used to determine values of c_{12}, c_{13} and c_{23}:

$$c_{12} \equiv \sqrt{1-\lambda^2} = 1 - \frac{1}{2}\lambda^2 - \frac{1}{8}\lambda^4 + \dots\ , \tag{1.16}$$

$$c_{23} \equiv \sqrt{1-A^2\lambda^4} = 1 - \frac{1}{2}A^2\lambda^4 - \frac{1}{8}A^4\lambda^8 + \dots\ , \tag{1.17}$$

$$c_{13} \equiv \sqrt{1-A^2\lambda^6(\rho^2+\eta^2)} = 1 - \frac{1}{2}A^2\lambda^6(\rho^2+\eta^2) - \frac{1}{8}A^4\lambda^{12}(\rho^2+\eta^2)^2 + \dots\ . \tag{1.18}$$

To third order in λ, $\mathbf{V}_{\mathrm{CKM}}$ is:

$$\mathbf{V}_{\mathrm{CKM}} = \begin{pmatrix} 1-\lambda^2/2 & \lambda & A\lambda^3(\rho - i\eta) \\ -\lambda & 1-\lambda^2/2 & A\lambda^2 \\ A\lambda^3(1-\rho-i\eta) & -A\lambda^2 & 1 \end{pmatrix} + \mathcal{O}(\lambda^4). \tag{1.19}$$

In this representation, the condition necessary for $\mathcal{CP}$ violation to occur is for η to be non-zero.

A global fit to extract the moduli of the CKM matrix elements [1] gives:

$$\begin{pmatrix} |V_{\mathrm{ud}}| & |V_{\mathrm{us}}| & |V_{\mathrm{ub}}| \\ |V_{\mathrm{cd}}| & |V_{\mathrm{cs}}| & |V_{\mathrm{cb}}| \\ |V_{\mathrm{td}}| & |V_{\mathrm{ts}}| & |V_{\mathrm{tb}}| \end{pmatrix} = \begin{pmatrix} 0.97425^{+0.00018}_{-0.00018} & 0.22543^{+0.00077}_{-0.00077} & 0.00354^{+0.00016}_{-0.00014} \\ 0.22529^{+0.00077}_{-0.00077} & 0.97342^{+0.00021}_{-0.00019} & 0.04128^{+0.00058}_{-0.00129} \\ 0.00858^{+0.00030}_{-0.00034} & 0.04054^{+0.00057}_{-0.00129} & 0.999141^{+0.000053}_{-0.000024} \end{pmatrix}. \tag{1.20}$$

To determine λ we can use the following equivalence:

$$\lambda = s_{12} = \frac{|V_{\mathrm{us}}|}{\sqrt{|V_{\mathrm{ud}}|^2 + |V_{\mathrm{us}}|^2}} \simeq 0.225 \pm 0.001. \tag{1.21}$$

The fourth power of λ is approximately equal to 0.0026. When investigating $\mathcal{CP}$ violation in the Standard Model it is therefore acceptable to neglect terms in $\mathbf{V}_{\mathrm{CKM}}$ that appear at $\mathcal{O}(\lambda^4)$ and higher, especially since corrections to the imaginary terms usually appear at $\mathcal{O}(\lambda^7)$ and beyond [19].

Finally we define the angle θ_C, introduced by Cabibbo [16] in the context of a two-generation quark mixing model. This angle is defined as $\theta_C = \tan^{-1}(|V_{\mathrm{us}}|/|V_{\mathrm{ud}}|) \simeq 13.0^\circ$.

1.3.3 Unitarity triangle

The fact that the CKM matrix is unitary leads to nine relations between its elements. Three of them sum to 1 and hence express weak universality in the three-generation quark model:

$$V_{\mathrm{ud}}^{*}V_{\mathrm{ud}} + V_{\mathrm{us}}^{*}V_{\mathrm{us}} + V_{\mathrm{ub}}^{*}V_{\mathrm{ub}} = 1, \tag{1.22}$$

$$V_{\mathrm{cd}}^{*}V_{\mathrm{cd}} + V_{\mathrm{cs}}^{*}V_{\mathrm{cs}} + V_{\mathrm{cb}}^{*}V_{\mathrm{cb}} = 1, \tag{1.23}$$

$$V_{\mathrm{td}}^{*}V_{\mathrm{td}} + V_{\mathrm{ts}}^{*}V_{\mathrm{ts}} + V_{\mathrm{tb}}^{*}V_{\mathrm{tb}} = 1. \tag{1.24}$$

The other six relations sum to zero:

$$V_{\mathrm{ud}}^{*}V_{\mathrm{us}} + V_{\mathrm{cd}}^{*}V_{\mathrm{cs}} + V_{\mathrm{td}}^{*}V_{\mathrm{ts}} = 0, \tag{1.25}$$

$$V_{\mathrm{ud}}^{*}V_{\mathrm{ub}} + V_{\mathrm{cd}}^{*}V_{\mathrm{cb}} + V_{\mathrm{td}}^{*}V_{\mathrm{tb}} = 0, \tag{1.26}$$

$$V_{\mathrm{us}}^{*}V_{\mathrm{ud}} + V_{\mathrm{cs}}^{*}V_{\mathrm{cd}} + V_{\mathrm{ts}}^{*}V_{\mathrm{td}} = 0, \tag{1.27}$$

$$V_{\mathrm{us}}^{*}V_{\mathrm{ub}} + V_{\mathrm{cs}}^{*}V_{\mathrm{cb}} + V_{\mathrm{ts}}^{*}V_{\mathrm{tb}} = 0, \tag{1.28}$$

$$V_{\mathrm{ub}}^{*}V_{\mathrm{ud}} + V_{\mathrm{cb}}^{*}V_{\mathrm{cd}} + V_{\mathrm{tb}}^{*}V_{\mathrm{td}} = 0, \tag{1.29}$$

$$V_{\mathrm{ub}}^{*}V_{\mathrm{us}} + V_{\mathrm{cb}}^{*}V_{\mathrm{cs}} + V_{\mathrm{tb}}^{*}V_{\mathrm{ts}} = 0. \tag{1.30}$$

Each of these six relations can be represented as a triangle on the complex plane. Using these relations in conjunction with the Wolfenstein parameterisation we obtain an intuitive geometrical picture of $\mathcal{CP}$ violation. Several of the triangles are almost flat, in which case $\mathcal{CP}$-violating asymmetries occur at a very low level [1] (for example in the neutral kaon sector). The triangle related to the $B_{u,d}$ system is obtained from Equation 1.29 and is often referred to as the '$b-d$' unitarity triangle. The length of each side is of order λ^3 [21], so the angles of the triangle are all large and significant $\mathcal{CP}$-violating asymmetries are possible.

Equation 1.29 is rescaled by dividing by $V_{\mathrm{cb}}^{*}V_{\mathrm{cd}}$:

$$\frac{V_{\mathrm{ub}}^{*}V_{\mathrm{ud}}}{V_{\mathrm{cb}}^{*}V_{\mathrm{cd}}} + 1 + \frac{V_{\mathrm{tb}}^{*}V_{\mathrm{td}}}{V_{\mathrm{cb}}^{*}V_{\mathrm{cd}}} = 0. \tag{1.31}$$

The representation of this triangle on the complex plane is illustrated in Figure 1.1. Its three angles are denoted α, β and γ (these are alternatively called ϕ_2, ϕ_1 and ϕ_3 respectively). The three angles are defined as follows:

$$\alpha \equiv \arg\left(-\frac{V_{\mathrm{tb}}^{*}V_{\mathrm{td}}}{V_{\mathrm{ub}}^{*}V_{\mathrm{ud}}}\right), \qquad \beta \equiv \arg\left(-\frac{V_{\mathrm{cb}}^{*}V_{\mathrm{cd}}}{V_{\mathrm{tb}}^{*}V_{\mathrm{td}}}\right), \qquad \gamma \equiv \arg\left(-\frac{V_{\mathrm{ub}}^{*}V_{\mathrm{ud}}}{V_{\mathrm{cb}}^{*}V_{\mathrm{cd}}}\right). \tag{1.32}$$

The current best fit for the angles and sides of the unitarity triangle by CKMFitter [1] is shown in Figure 1.2.

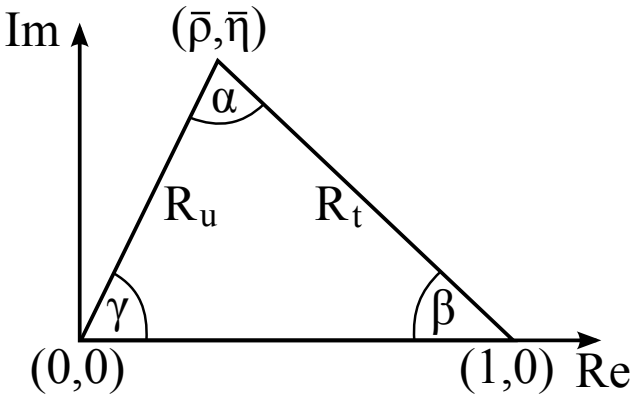

Figure 1.1: The $b-d$ unitarity triangle. The quantities $\bar{\rho}$ and $\bar{\eta}$ are defined in Equation 1.34 and R_u and R_t are defined in Equation 1.35.

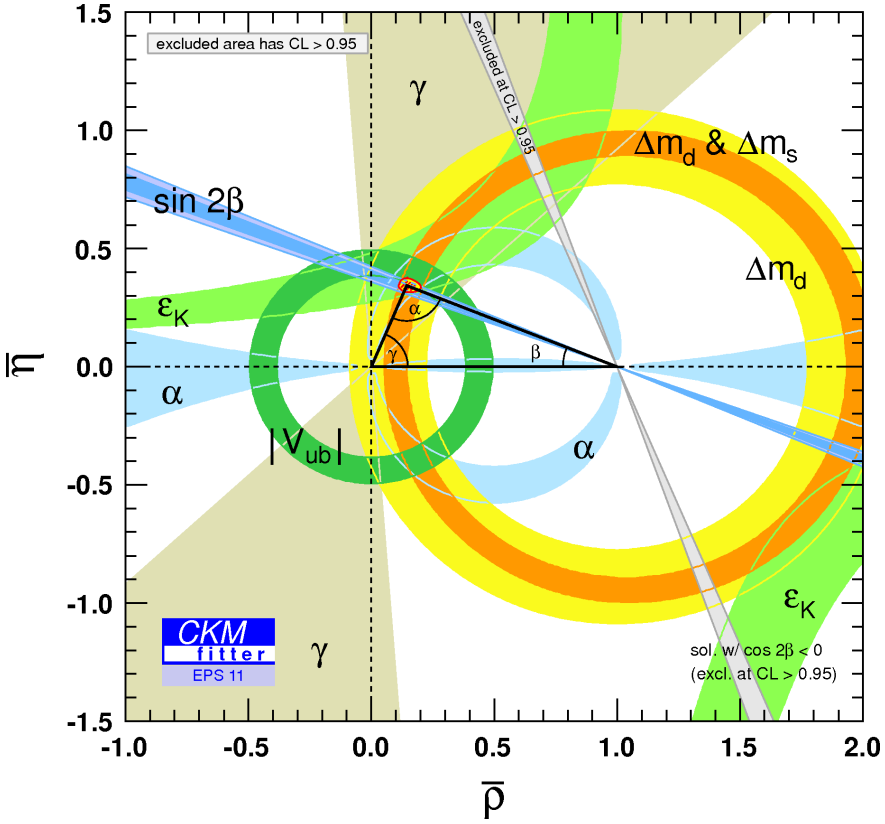

Figure 1.2: The current fit to the unitarity triangle from CKMFitter (shown at EPS 2011). The triangle is shown in black. The red hashed area indicates the 68% C.L. region in which the apex of the triangle could lie.

We can rewrite the expression for γ using the Wolfenstein parameterisation:

$$\begin{aligned}\gamma &= \arg\left(-\frac{c_{12}c_{13}s_{13}e^{i\delta}}{(-s_{12}c_{23}-c_{12}s_{23}s_{13}e^{i\delta})s_{23}c_{13}}\right)\\ &= \arg\left(\frac{\sqrt{1-\lambda^2}A\lambda^3(\rho+i\eta)}{(\lambda\sqrt{1-A^2\lambda^4}+\sqrt{1-\lambda^2}A\lambda^2A\lambda^3(\rho+i\eta))A\lambda^2}\right)\\ &= \arg\left(\frac{\sqrt{1-\lambda^2}(\rho+i\eta)}{\sqrt{1-A^2\lambda^4}+\sqrt{1-\lambda^2}A^2\lambda^4(\rho+i\eta)}\right).\end{aligned} \tag{1.33}$$

We define

$$\bar{\rho} + i\bar{\eta} \equiv \left(\frac{\sqrt{1-\lambda^2}(\rho + i\eta)}{\sqrt{1 - A^2\lambda^4} + \sqrt{1-\lambda^2}A^2\lambda^4(\rho + i\eta)} \right) \tag{1.34}$$

so that $\gamma = \tan^{-1}(\bar{\eta}/\bar{\rho})$. The values of ρ and η differ by about 3% from $\bar{\rho}$ and $\bar{\eta}$ [19].

The sides of the triangle have lengths

$$1, \qquad R_u = \left| \frac{V_{\rm ub}^* V_{\rm ud}}{V_{\rm cb}^* V_{\rm cd}} \right| = \sqrt{\bar{\rho}^2 + \bar{\eta}^2}, \qquad R_t = \left| \frac{V_{\rm tb}^* V_{\rm td}}{V_{\rm cb}^* V_{\rm cd}} \right| = \sqrt{(1-\bar{\rho})^2 + \bar{\eta}^2}. \tag{1.35}$$

As well as the possibility of observing new physics processes, it is important to overconstrain the various angle and length measurements in order validate the unitarity model and test the three-generation hypothesis.

1.3.4 Link between the CKM matrix and $\mathcal{CP}$ violation

Each of the six unitarity triangles has the same area, equal to half the Jarlskog invariant J [22]. The Jarlskog invariant is a phase-independent measure of $\mathcal{CP}$ violation. In terms of the CKM matrix elements,

$$\begin{aligned} J &= |\mathfrak{Im}\{V_{ij} V_{kl} V_{il}^* V_{kj}^*\}| \\ &= c_{12}c_{23}c_{13}^2 s_{12}s_{23}s_{13}\sin(\delta) \qquad (1.36) \\ &= A^2\lambda^6\eta(1 - \lambda^2/2) + \mathcal{O}(\lambda^{10}), \qquad (1.37) \end{aligned}$$

where the expression is the same regardless of which quark flavours are assigned to i, j, k and l. The current fit value of J is $2.96^{+0.18}_{-0.17}$ [1].

As well as a non-zero value of J, two further criteria must be satisfied in order for $\mathcal{CP}$ violation to appear in the quark sector: there must be three or more quark generations, and no two quarks of the same charge can be degenerate in mass. These criteria can be summarised by the following statement:

$$\mathcal{CP} \text{ violation} \Leftrightarrow \mathfrak{Im}\{\det[\mathbf{M}_u, \mathbf{M}_d]\} \neq 0 \tag{1.38}$$

where

$$\mathfrak{Im}\{\det[\mathbf{M}_u, \mathbf{M}_d]\} \propto (m_t^2 - m_c^2)(m_t^2 - m_u^2)(m_c^2 - m_u^2)(m_b^2 - m_s^2)(m_b^2 - m_d^2)(m_s^2 - m_d^2)J. \tag{1.39}$$

1.4 Pseudoscalar meson systems

In this section we examine various properties of charged and neutral pseudoscalar (spin-0) mesons. Both physics analyses presented in this thesis are studies of meson systems.

1.4.1 $\mathcal{CP}$ eigenstates

Neutral pseudoscalar mesons are not $\mathcal{CP}$ eigenstates, but $\mathcal{CP}$ eigenstates can be constructed from overlapping meson-antimeson wavefunctions. For a neutral meson M^0 and its antiparticle $\overline{M}^0$ we adopt the convention:

$$\mathcal{CP}|M^0\rangle = \eta_{CP}|\overline{M}^0\rangle = e^{i\xi_M}|\overline{M}^0\rangle, \qquad \mathcal{CP}|\overline{M}^0\rangle = \eta^*_{CP}|M^0\rangle = e^{-i\xi_M}|M^0\rangle. \tag{1.40}$$

Using the fact that the intrinsic parity of a pseudoscalar meson is -1 and $\mathcal{C}$ and $\mathcal{P}$ are multiplicative, we find $\eta_{CP} = -\eta_C$. Without loss of generality[4] we can set $\eta_{CP} = 1$. We can then define $\mathcal{CP}$ eigenstates as follows:

$$|M_{\mathcal{CP}\pm}\rangle = \frac{1}{\sqrt{2}}(|M^0\rangle \pm |\overline{M}^0\rangle), \tag{1.41}$$

so that

$$\mathcal{CP}|M_{\mathcal{CP}\pm}\rangle = \frac{1}{\sqrt{2}}(|\overline{M}^0\rangle \pm |M^0\rangle) = \pm|M_{\mathcal{CP}\pm}\rangle. \tag{1.42}$$

1.4.2 Correlated pseudoscalar meson pairs

In this section we consider quantum-correlated pairs of pseudoscalar mesons. Mesons are bosons, so given a relative orbital angular momentum L between the mesons the eigenvalues of both $\mathcal{P}$ and $\mathcal{C}$ are equal to $(-1)^L$.

The wavefunction of a correlated pair of pseudoscalar mesons in the centre-of-mass frame of the pair is:

$$|\chi_{\mathcal{CP}\pm}\rangle = \frac{1}{\sqrt{2}}\Big(|M^0\rangle(\mathbf{p})|\overline{M}^0\rangle(-\mathbf{p}) + (-1)^L\overline{M}^0(\mathbf{p})M^0(-\mathbf{p})\Big), \tag{1.43}$$

where $\mathbf{p}$ is the momentum of M^0.

This expression can also be written in terms of the $\mathcal{CP}$ eigenstates introduced in Section 1.4.1:

$$|\chi_{\mathcal{CP}+}\rangle = \frac{1}{\sqrt{2}}\Big(|M_{\mathcal{CP}+}\rangle(\mathbf{p})|M_{\mathcal{CP}+}\rangle(-\mathbf{p}) - |M_{\mathcal{CP}-}\rangle(\mathbf{p})|M_{\mathcal{CP}-}\rangle(-\mathbf{p})\Big), \tag{1.44}$$

$$|\chi_{\mathcal{CP}-}\rangle = \frac{1}{\sqrt{2}}\Big(|M_{\mathcal{CP}-}\rangle(\mathbf{p})|M_{\mathcal{CP}+}\rangle(-\mathbf{p}) - |M_{\mathcal{CP}+}\rangle(\mathbf{p})|M_{\mathcal{CP}-}\rangle(-\mathbf{p})\Big). \tag{1.45}$$

$|\chi_{\mathcal{CP}+}\rangle$ is symmetric and corresponds to the case when L is even; $|\chi_{\mathcal{CP}-}\rangle$ is antisymmetric and corresponds to the case when L is odd. Both of these states have the same $\mathcal{CP}$ eigenvalue, but decay to different $\mathcal{CP}$ states by virtue of their (anti-)correlation. Because the mesons undergo

[4] When this expression is squared to determine the probability, the phases disappear.

coherent flavour oscillations, the $\mathcal{CP}$ of one meson can *always* be deduced by determining the $\mathcal{CP}$ of the other meson, even if they are separated by a spacelike interval.

1.4.2.1 Quantum-correlated $D^0\overline{D}^0$ decays

We consider the particular case of a correlated $D^0\overline{D}^0$ pair, which is most relevant for this thesis. In particular we consider the following reaction at an e^+e^- collider:

$$e^+e^- \to \psi(3770) \to D^0\overline{D}^0. \tag{1.46}$$

The J^{PC} of the $\psi(3770)$ is 1^{--} [11]. At the threshold energy, the $D^0\overline{D}^0$ pair is therefore produced in a $\mathcal{C} = -1$ state because $\mathcal{C}$ is conserved in strong decays[5] [23]. The spin of the $\psi(3770)$ causes the $D^0\overline{D}^0$ pair to be produced in a P-wave ($L = 1$), so $\mathcal{P} = -1$. The $D^0\overline{D}^0$ pair must therefore lie in the antisymmetric state:

$$\begin{aligned} |D^0\overline{D}^0\rangle &= \frac{1}{\sqrt{2}}\left\{D^0(\mathbf{p})\overline{D}^0(-\mathbf{p}) - \overline{D}^0(\mathbf{p})D^0(-\mathbf{p})\right\} \\ &= \frac{1}{\sqrt{2}}\left\{D_{\mathcal{CP}-}(\mathbf{p})D_{\mathcal{CP}+}(-\mathbf{p}) - D_{\mathcal{CP}+}(\mathbf{p})D_{\mathcal{CP}-}(-\mathbf{p})\right\}. \end{aligned} \tag{1.47}$$

If we know the $\mathcal{CP}$ of one of the D mesons produced then the other D must have the opposite $\mathcal{CP}$. This concept forms the basis of the analysis of CLEO-c data as described in Chapters 3 and 4.

1.4.3 Direct $\mathcal{CP}$ violation in charged meson systems

$\mathcal{CP}$ violation in meson systems can be classified according to where any complex phases appear: in decay, in mixing, or in interference between decays and mixing. In this section we focus on $\mathcal{CP}$ violation in decays, also denoted *direct* $\mathcal{CP}$ violation. This is the only type of $\mathcal{CP}$ violation possible in charged meson systems, and has direct relevance to this thesis. Further information on each type of $\mathcal{CP}$ violation in meson systems can be found in Refs. [11, 12]. Henceforth the charged meson is denoted $M^\pm$ and the final state and its $\mathcal{CP}$ conjugate are denoted f and $\bar{f}$ respectively.

Several criteria must be fulfilled for direct $\mathcal{CP}$ violation to be observable. Firstly, M^+ must decay to f via two interfering diagrams (labelled X_1 and X_2). The total decay amplitude is:

$$\mathcal{A}(M^+ \to f) = \mathcal{A}(M^+ \xrightarrow{X_1} f) + \mathcal{A}(M^+ \xrightarrow{X_2} f) = a_1 e^{i\theta_1} + a_2 e^{i\theta_2}, \tag{1.48}$$

where $\theta_{1,2}$ are weak phases[6] and $a_{1,2}$ are the amplitude moduli. The corresponding decay

[5] At higher energies, it is possible to have a $\mathcal{C} = +1$ state if a photon is produced as well.
[6] The concept of weak phases was introduced in Section 1.2.2.2.

rate is:

$$\Gamma(M^+ \to f) = a_1^2 + a_2^2 + 2a_1 a_2 \cos(\theta_1 - \theta_2) = a_1^2 + a_2^2 + 2a_1 a_2 \cos(\delta_W), \tag{1.49}$$

where the weak phase difference $\delta_W \equiv \theta_1 - \theta_2$. If $\theta_1 = \theta_2$, the rate is equal to $a_1^2 + a_2^2 + 2a_1 a_2$ and no information about the phase difference can be obtained.

Considering the $\mathcal{CP}$ transform of the decay, both weak phases are conjugated:

$$\mathcal{A}(M^- \to \bar{f}) = a_1 e^{-i\theta_1} + a_2 e^{-i\theta_2}, \tag{1.50}$$

and the decay rate is:

$$\Gamma(M^- \to \bar{f}) = a_1^2 + a_2^2 + 2a_1 a_2 \cos(-\delta_W) = a_1^2 + a_2^2 + 2a_1 a_2 \cos(\delta_W). \tag{1.51}$$

The decay rates of particles and antiparticles are therefore insensitive to the sign of δ_W. Additional phases must be present if a difference in rate is to be observed; such phases can appear in final-state interactions consisting of contributions from intermediate on-shell states. These phases are denoted *strong* phases because they usually result from strong interactions between various particles and resonances. The crucial property of strong phases is that, unlike weak phases, they are invariant under a $\mathcal{CP}$ transformation.

Denoting the strong phases $\phi_{1,2}$, the amplitude of M^+ decaying to f is:

$$\mathcal{A}(M^+ \to f) = a_1 e^{i(\theta_1 + \phi_1)} + a_2 e^{i(\theta_2 + \phi_2)} \tag{1.52}$$

and the decay rate is:

$$\begin{aligned} \Gamma(M^+ \to f) &= a_1^2 + a_2^2 + 2a_1 a_2 \cos(\theta_1 - \theta_2 + \phi_1 - \phi_2) \\ &= a_1^2 + a_2^2 + 2a_1 a_2 \cos(\delta_W + \delta_S), \end{aligned} \tag{1.53}$$

where $\delta_S \equiv \phi_1 - \phi_2$.

The equivalent amplitude for antiparticles is:

$$\mathcal{A}(M^- \to \bar{f}) = a_1 e^{i(-\theta_1 + \phi_1)} + a_2 e^{i(-\theta_2 + \phi_2)} \tag{1.54}$$

and the rate is:

$$\begin{aligned} \Gamma(M^- \to \bar{f}) &= a_1^2 + a_2^2 + 2a_1 a_2 \cos(-\theta_1 + \theta_2 + \phi_1 - \phi_2) \\ &= a_1^2 + a_2^2 + 2a_1 a_2 \cos(-\delta_W + \delta_S). \end{aligned} \tag{1.55}$$

Unless either δ_W or δ_S are equal to 0, there is now a distinct difference between the two decay rates which enables $\mathcal{CP}$ violation to be detected.

To summarise, for direct $\mathcal{CP}$ violation to be observable a particle must be able to decay via two different interfering diagrams with different weak- and strong-phase differences in each case. $\mathcal{CP}$ violation can then be detected by comparing the decay rates of the particle and its antiparticle. An example of such a system is $B^{\pm}\to DK^{\pm}$ in which the weak-phase difference is γ and the strong-phase difference is δ_B; this is described in detail in Section 1.6.2.

1.5 Dalitz plots

When a particle decays to three or more particles, analysis of the distributions of the Lorentz-invariant final-state kinematic variables yields useful information about the processes involved in the decay. A scatter plot of one such variable against another is called a *Dalitz plot*[7], after studies by Dalitz in 1953 of a kaon decay to three pions [24].

In general, the distribution of events that are produced by a particular decay is influenced by both the kinematics (the four-momenta of the initial- and final-state particles) and the dynamics (any interactions that occur during the decay). To some extent it is possible to separate the two; once the kinematics have been unfolded from the final distribution, any residual effects are due to the dynamics. This separation provides invaluable information about how the decay proceeds.

A commonly used coordinate basis for Dalitz plots is the invariant mass squared of pairs of particles. For particles a and b this quantity is m^2_{ab} and is obtained from the squared sum of the four momenta, i.e. $(P_a + P_b)^2$.

1.5.1 Kinematics

The general Lorentz-invariant expression for the rate of transition from an initial state D (a spin-0 particle of mass M) to a final state f consisting of three particles (labelled a, b and c) is:

$$\begin{aligned} \mathrm{d}\Gamma &= \frac{(2\pi)^4}{2M}|\mathcal{M}|^2 \cdot \left(\prod_{i=a,b,c} \frac{\mathrm{d}^3\mathbf{p}_i}{(2\pi)^3(2E_i)}\right) \cdot \delta^4\left(P_D - \sum_{i=a,b,c} P_i\right) \\ &= \frac{1}{16M(2\pi)^5}|\mathcal{M}|^2 \cdot \left(\prod_{i=a,b,c} \frac{\mathrm{d}^3\mathbf{p}_i}{E_i}\right) \cdot \delta^4\left(P_D - \sum_{i=a,b,c} P_i\right), \end{aligned} \tag{1.56}$$

where P_X, E_X and $\mathbf{p}_X$ are respectively the four-momentum, the energy and the three-momentum of particle X, and $\mathcal{M}$ is the matrix element associated with the transition $D \to f$.

[7]This terminology is formally reserved for the decay of a meson to three pseudoscalar particles.

We consider the system in the rest frame of the decaying particle, so $P_D = (M, \mathbf{0})$. After integration over the three-momentum of particle c, we obtain:

$$\mathrm{d}\Gamma = \frac{1}{16M(2\pi)^5}|\mathcal{M}|^2 \cdot \frac{\mathrm{d}^3\mathbf{p}_a \mathrm{d}^3\mathbf{p}_b}{E_a E_b E_c} \cdot \delta\left(M - \sum_{i=a,b,c} E_i\right). \tag{1.57}$$

The infinitesimal volume elements in momentum space are now re-expressed in spherical polar coordinates. We set the z axis to lie along the direction of motion of a and define the quantity θ as the angle between a and b. The transition rate becomes:

$$\begin{aligned}\mathrm{d}\Gamma &= \frac{1}{16M(2\pi)^5}|\mathcal{M}|^2 \cdot \frac{4\pi|\mathbf{p}_a|^2\mathrm{d}|\mathbf{p}_a|2\pi|\mathbf{p}_b|^2\mathrm{d}|\mathbf{p}_b|\mathrm{d}\cos(\theta)}{E_a E_b E_c} \cdot \delta\left(M - \sum_{i=a,b,c} E_i\right) \\ &= \frac{1}{8M(2\pi)^3}|\mathcal{M}|^2 \cdot \frac{|\mathbf{p}_a|\mathrm{d}|\mathbf{p}_a||\mathbf{p}_b|\mathrm{d}|\mathbf{p}_b||\mathbf{p}_a||\mathbf{p}_b|\mathrm{d}\cos(\theta)}{E_a E_b E_c} \cdot \delta\left(M - \sum_{i=a,b,c} E_i\right).\end{aligned} \tag{1.58}$$

We use the relations $E_a\mathrm{d}E_a = |\mathbf{p}_a|\mathrm{d}|\mathbf{p}_a|$ and $E_b\mathrm{d}E_b = |\mathbf{p}_b|\mathrm{d}|\mathbf{p}_b|$ to obtain:

$$\mathrm{d}\Gamma = \frac{1}{8M(2\pi)^3}|\mathcal{M}|^2 \cdot \frac{\mathrm{d}E_a\mathrm{d}E_b|\mathbf{p}_a||\mathbf{p}_b|\mathrm{d}\cos(\theta)}{E_c} \cdot \delta\left(M - \sum_{i=a,b,c} E_i\right). \tag{1.59}$$

Because $E_c^2 = (\mathbf{p}_a + \mathbf{p}_b)^2 + m_c^2 = |\mathbf{p}_a|^2 + |\mathbf{p}_b|^2 + 2|\mathbf{p}_a||\mathbf{p}_b|\cos(\theta)$, we find $2E_c\mathrm{d}E_c = 2|\mathbf{p}_a||\mathbf{p}_b|\mathrm{d}\cos(\theta)$. This assumes that $\mathbf{p}_a$ and $\mathbf{p}_b$ are fixed, so we must perform the integral over $\mathrm{d}\cos(\theta)$ first, resulting in:

$$\mathrm{d}\Gamma = \frac{1}{8M(2\pi)^3}|\mathcal{M}|^2 \cdot \mathrm{d}E_a\mathrm{d}E_b\mathrm{d}E_c \cdot \delta\left(M - \sum_{i=a,b,c} E_i\right). \tag{1.60}$$

Finally, we perform the integration over $\mathrm{d}E_c$ to obtain:

$$\mathrm{d}\Gamma = \frac{1}{8M(2\pi)^3}|\mathcal{M}|^2\mathrm{d}E_a\mathrm{d}E_b. \tag{1.61}$$

We wish to express the rate in terms of the invariant mass combinations:

$$m_{bc}^2 = (P_D - P_a)^2 = (P_b + P_c)^2 = M^2 + m_a^2 - 2ME_a, \tag{1.62}$$

$$m_{ac}^2 = (P_D - P_b)^2 = (P_a + P_c)^2 = M^2 + m_b^2 - 2ME_b, \tag{1.63}$$

$$m_{ab}^2 = (P_D - P_c)^2 = (P_a + P_b)^2 = M^2 + m_c^2 - 2ME_c, \tag{1.64}$$

where all energies are defined in the rest frame of the decaying particle. We use these

relations to rewrite the rate as:

$$\mathrm{d}\Gamma = \frac{1}{32M^3(2\pi)^3}|\mathcal{M}|^2\,\mathrm{d}(m^2_{bc})\,\mathrm{d}(m^2_{ac}). \tag{1.65}$$

The distribution of events across the (m^2_{bc}, m^2_{ac}) plane is therefore kinematically flat; any structure is provided wholly by the matrix element $\mathcal{M}$. For example, assume particle D decays via a resonance r that subsequently decays into a and b. The decay rate of this process will be significantly enhanced when m^2_{ab} is close to the square of the mass of the resonance. This will form a visibly enhanced band of events on the Dalitz plot.

Figure 1.3 shows an example of a $D\to K^0_S\pi^+\pi^-$ Dalitz plot recorded by the BaBar collaboration [25]. There is significant nonuniformity in the Dalitz plot caused by D decays that proceed via various intermediate resonances, and also by interference between those resonances. Two prominent spin-1 resonances, the $K^*(892)^-$ and $\rho(770)^0$, have been marked by arrows pointing along the squares of their invariant masses. For each resonance there is an enhancement in the event yield that peaks along the invariant mass squared. Due to the non-zero spin of these resonances there are significantly more events at the kinematic limits of the Dalitz plane than in the centre (see Section 1.5.2.1).

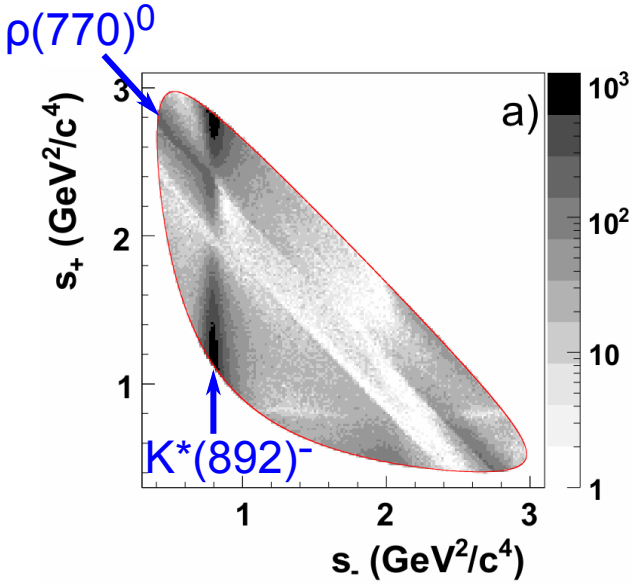

Figure 1.3: Example of a $D\to K^0_S\pi^+\pi^-$ Dalitz plot produced by BaBar [25]. The horizontal axis is the invariant mass squared of the $K^0_S\pi^-$ pair and the vertical axis is the invariant mass squared of the $K^0_S\pi^+$ pair. The colour of each grid element represents the yield of events integrated over that element, as labelled by the axis on the right-hand side of the plot. The kinematic boundary of the Dalitz plot is marked in red. The squared invariant masses of two intermediate resonances, the $K^*(892)^-$ and the $\rho(770)^0$, have been marked. In each case the arrow points along the axis that defines the invariant mass squared of the two daughters: the $K^*(892)^-$ decays to $K^0_S\pi^-$ and the $\rho(770)^0$ decays to $\pi^+\pi^-$.

1.5.2 Dynamics

The matrix element $\mathcal{M}$ describes all of the dynamics in the decay system; most significantly it describes intermediate resonances in the decay process. We consider the decay of a particle D into rc, where r is an intermediate resonance that decays into a and b; all final state particles are taken to be pseudoscalars. In general there could be more than one intermediate resonance. Following Ref. [11], the matrix element can be written as the product of various components:

$$\mathcal{M}(J, L, l, m_{ab}, m_{bc}) = Z(J, L, l, \mathbf{p}_c, \mathbf{p}_a) B_L^{rc}(|\mathbf{p}_c|) B_L^{ab}(|\mathbf{p}_a|) T(m_{ab}) \tag{1.66}$$

where J is total angular momentum of D, L is the relative orbital angular momentum between r and c, and l is the orbital angular momentum between a and b. The quantities $\mathbf{p}_{(a,c)}$ are the three-momenta of (a, c) in the rest frame of r. The function Z encapsulates the angular distribution of the final-state particles. B_L^{rc} and B_L^{ab} are the Blatt-Weisskopf barrier factors for the production of rc and ab, and T is the dynamical function describing r. Below we consider both the Breit-Wigner and Flatté dynamical functions.

1.5.2.1 Angular distribution of events

The value of L influences the angular distribution Z of the decay products [26]. In our example all final state particles are spin-0. If L is zero, the angular distribution of the final state particles is uniform. For L equal to 1 and 2, the angular distributions are respectively

$$(1 + \zeta^2) \cos^2 \theta \qquad \text{and} \qquad \left(\zeta^2 + \frac{3}{2}\right)^2 (\cos^2 \theta - 1/3)^2, \tag{1.67}$$

where θ is the angle between a and c in the rest frame of r and $\sqrt{1 + \zeta^2}$ is a relativistic correction factor equal to E_r/m_{ab}, where $E_r = (m_D^2 + m_{ab}^2 - m_c^2)/2m_D$. The angular distributions of intermediate resonances with non-zero spin lead to visible structures on the Dalitz plane. For example, a spin-1 intermediate resonance has a lobe-like structure with enhancements at the edge of the Dalitz plot and a deficit of events in the centre. Examples of this have been noted in Figure 1.3.

1.5.2.2 Blatt-Weisskopf barrier factor

The momentum q of a decaying particle limits the possible spin states it can enter. The probability of a particle decaying to a high-angular-momentum resonance is relatively small. This is especially true for slow particles with a large effective radius d ('large' is taken to be ~ 1 fm). In order to take this into account, the amplitudes of decays to different spin states

are weighted by the Blatt-Weisskopf barrier factor B_L [27]. These factors for resonances of spin 0, 1 and 2 respectively are:

$$1, \qquad \sqrt{\frac{2z}{1+z}}, \qquad \sqrt{\frac{13z^2}{(z-3)^2+9z}}, \tag{1.68}$$

where $z = (|q|d)^2$.

1.5.2.3 Breit-Wigner function

The functional form of the relativistic Breit-Wigner lineshape [10] is:

$$T(m_{ab}) = \frac{1}{m_0^2 - m_{ab}^2 - im_0\Gamma_{ab}(\mathrm{p}_a)}, \tag{1.69}$$

where m_0 is the pole mass of the resonance. The width $\Gamma_{ab}(\mathrm{p}_a)$ is defined as:

$$\Gamma_{ab}(\mathrm{p}_a) = \Gamma_0 \left(\frac{\mathrm{p}_a}{\mathrm{p}_a^0}\right)^{2J+1} \left(\frac{m_0}{m_{ab}}\right) \left[B_L^{ab}(J, m_{ab})\right]^2, \tag{1.70}$$

where Γ_0 is the natural width of the resonance and p_a^0 is the value of p_a when $m_{ab} = m_0$.

When multiple intermediate resonances are parameterised with Breit-Wigner lineshapes they should be well isolated from each other. Furthermore, each resonance should not be near to the threshold of another decay channel. If either of these criteria is violated then the parameterisation will probably yield a poor description of the decay lineshape and may violate unitarity.

1.5.2.4 Flatté function

The Flatté lineshape [28] can be used to model the situation in which a resonance can decay to an alternative pair of particles that have a threshold close to the peak mass, distorting the usual Breit-Wigner shape. The functional form is:

$$T(m_{ab}) = \frac{1}{m_0^2 - m_{ab}^2 - i(\rho_1 g_1^2 + \rho_2 g_2^2)}, \tag{1.71}$$

where $g_{1,2}$ are coupling constants and $\rho_{1,2}$ are phase space terms. The coupling constants obey the relation $g_1^2 + g_2^2 = m_0\Gamma_0$ where Γ_0 is the natural width of the resonance and m_0 is its pole mass. The phase space terms are expressed as:

$$\rho_{ab} = \sqrt{\left(1 - \left(\frac{m_a - m_b}{m_{ab}}\right)^2\right)\left(1 - \left(\frac{m_a + m_b}{m_{ab}}\right)^2\right)}. \tag{1.72}$$

This model is required for decays of the $a_0(980)^{0,\pm}$ resonance, which can decay to both $\pi\eta$ and $K\overline{K}$ final states. The coupling constants are denoted $g_{\pi\eta}$ and g_{KK}, and the phase space terms are $\rho_{\pi\eta}$ and ρ_{KK}.

1.5.2.5 Isobar model

The total matrix element is usually constructed as the sum of several interfering resonances, each of which is a quasi-two-body contribution. This concept is denoted the *isobar* model. The expression for the total matrix element is:

$$\mathcal{M} = a_0 e^{i\delta_0} + \sum_j a_j e^{i\delta_j} \mathcal{M}_j \,, \tag{1.73}$$

where $a_j e^{i\delta_j}$ are complex weighting coefficients, $\mathcal{M}_j$ are matrix elements associated with the individual resonances, and $a_0 e^{i\delta_0}$ is a possible nonresonant component.

1.6 Determining the CKM angle γ

1.6.1 Introduction

The angle γ is the least precisely determined of the three angles of the $b-d$ unitarity triangle. The most precisely measured angle is β, which can be determined using decays such as $B^0 \to (c\bar{c})K^{(*)0}$; the current value calculated by the CKMFitter collaboration [1] is $(21.15^{+0.90}_{-0.88})^\circ$. The angle α has been measured as $(89.0^{+4.4}_{-4.2})^\circ$ [1] using B decays to $\pi\pi$, $\rho\pi$, $\rho\rho$, etc. In contrast, the value of γ obtained from direct measurements is found to be $(68^{+13}_{-14})^\circ$ by the CKMFitter collaboration [1] and $(74 \pm 11)^\circ$ by the UTFit collaboration [2].

It is particularly interesting to compare the value of γ obtained from analyses of tree-level processes to that obtained from loop-level processes. A discrepancy between the tree- and loop-level measurements will be a strong indication that new physics exists. Figure 1.4 [1] shows the current status of both types of measurement. At present, γ as determined indirectly from loop-level processes is known much more precisely.

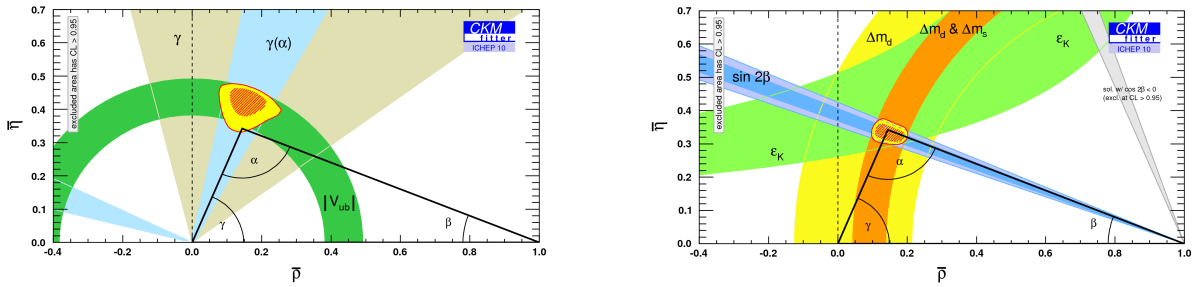

Figure 1.4: Determinations of γ from tree-level (left) and loop-level (right) processes.

1.6.2 Determining γ from $B^{\pm}\to DK^{\pm}$ decays

The analysis of $B^{\pm}$ decays to $DK^{\pm}$ is a highly promising method to determine γ. The concept at the heart of this method is the exploitation of interference between $b \to c$ and $b \to u$ quark transitions. $B^{\pm}\to DK^{\pm}$ decays proceed at tree level, with negligible contributions from loop diagrams. They are therefore largely insensitive to new physics, providing a useful 'standard candle' against which other determinations of γ can be compared. Analyses of this class of decay typically rely on time-integrated quantities, avoiding the complexities inherent in time-dependent analyses. Further information on the program to determine γ at LHCb can be found in Ref. [29].

We consider the decay of B^- mesons to both D^0K^- and $\overline{D}^0K^-$. The former decay involves a $b \to c$ transition, the latter a $b \to u$ transition. Feynman diagrams for the decays are shown in Figure 1.5. For interference to occur it is essential that both D^0 and $\overline{D}^0$ decay to the same final state f.

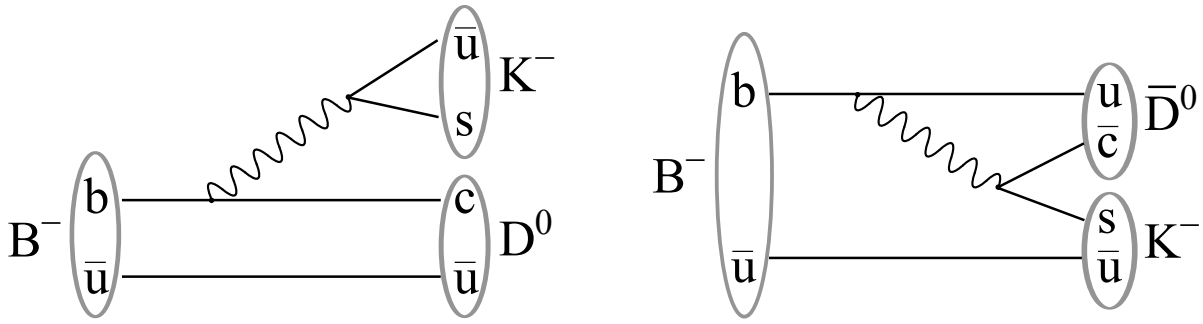

Figure 1.5: Feynman diagrams for the decays $B^-\to D^0K^-$ (left) and $B^-\to\overline{D}^0K^-$ (right).

The amplitude of the favoured $B^-\to D^0K^-$ decay is defined as:

$$\mathcal{A}(B^- \to D^0K^-) \equiv A_B, \tag{1.74}$$

where A_B is a normalisation factor, set to 1. The equivalent amplitude of the suppressed $B^-\to\overline{D}^0K^-$ decay is:

$$\mathcal{A}(B^- \to \overline{D}^0K^-) \equiv A_B r_B e^{i(\delta_B-\gamma)}, \tag{1.75}$$

where r_B is the ratio of the moduli of the suppressed and favoured decay amplitudes and δ_B is the $\mathcal{CP}$-invariant strong-phase difference between the two decays. The $\mathbf{V}_{\rm CKM}$ elements associated with the favoured transition are $V_{\rm cb}^*V_{\rm us}$, and those associated with the suppressed transition are $V_{\rm ub}^*V_{\rm cs}$. The total decay rate of $B^-\to DK^-$ is proportional to the square of the sum of these amplitudes and will therefore involve a term dependent upon γ.

There are two principal factors which determine the value of r_B. The first is the ratio of the moduli of the $\mathbf{V}_{\rm CKM}$ elements associated with the decay vertices: $|V_{\rm ub}^*V_{\rm cs}|/|V_{\rm cb}^*V_{\rm us}| \sim 0.37$. The second is *colour suppression* due to internal W emission in $B^-\to\overline{D}^0K^-$ decays; the

quarks emitted by the W are constrained to have the same colour charge which leads to an additional factor of $\sim 1/3$. The product of these factors gives r_B which is approximately 1/10, in agreement with recent measurements [30–32].

The relative weak phase between the two diagrams is $\arg(V_{\rm ub}^* V_{\rm cs}/V_{\rm cb}^* V_{\rm us})$; in comparison, γ is defined as $\arg(-V_{\rm ub}^* V_{\rm ud}/V_{\rm cb}^* V_{\rm cd})$. Superficially, some of the factors in these expressions are different, but as demonstrated in Section 1.3.2 they are real up to $\mathcal{O}(\lambda^4)$ in the Wolfenstein parameterisation and the phase is therefore unaffected.

The above formalism is identical for B^+ decays except the sign in front of γ is changed; the amplitude of the suppressed $B^+ \to D^0 K^+$ decay is $A_B r_B e^{i(\delta_B+\gamma)}$. The requirements for the observation of direct $\mathcal{CP}$ violation, detailed in Section 1.4.3, have therefore been fulfilled: the $B^\pm$ can decay to the final state f via two diagrams with a relative strong-phase difference δ_B and a relative weak-phase difference γ.

The practicalities of extracting γ are highly dependent upon the D final state. In Section 1.6.2.1 we review projections of the expected sensitivity to γ that LHCb can achieve with different D final states. In Section 1.6.3 we describe the method used when the D decays to a two body $\mathcal{CP}$ eigenstate (e.g. K^+K^-) or a non-$\mathcal{CP}$ eigenstate (e.g. $K^\pm\pi^\mp$). In Section 1.6.4 we describe the method used when the D decays to a multibody state that is its own $\mathcal{CP}$ conjugate (e.g. $K^0_S h^+ h^-$). In all cases, mixing and $\mathcal{CP}$ violation in the D system are ignored; they are both sub-percent effects [33].

The formalism presented below applies to $B^\pm \to DK^\pm$ decays, but it is very similar for $B^\pm \to D\pi^\pm$. The latter decay plays a role in the analysis of LHCb data. $\mathcal{CP}$ violation in this system is suppressed relative to $B^\pm \to DK^\pm$ because it has a smaller value of r_B ($\simeq 0.01$ [21]). Occasionally we must distinguish between the various moduli and phases associated with these two modes; in those instances a superscript indicates the mode in question, for example r_B^{DK} and $r_B^{D\pi}$.

1.6.2.1 LHCb γ sensitivity studies

In this section we present the results of several studies of the sensitivity to γ that can be achieved using 2 fb^{-1} of LHCb data. The studies were all performed prior to the data-taking period using 'toy Monte Carlo' techniques. Each study considered a particular D decay mode or group of similar modes. In each case the projected uncertainty on γ that could be achieved using the decay mode in question was determined. High-sensitivity channels have a low uncertainty on γ and vice versa.

Table 1.1 presents the uncertainty on γ for each decay mode studied. In each study several different values of δ_B were considered, leading to a range of uncertainties. The final study in the table is a 'global' combination of many channels in an extraction of γ. Regarding

$B^\pm \to (K^0_S\pi^+\pi^-)_D K^\pm$ decays, the terms 'model independent' and 'model dependent' are introduced in Section 1.6.3.3.

Decay channel	Sensitivity in 2 fb^{-1} (°)
$B^\pm \to (h^+h^-)_D K^\pm$ [34]	9.9–11.3
$B^0 \to (h^+h^-)_D K^*$ [35]	15–25
$B^\pm \to (K^0_S\pi^+\pi^-)_D K^\pm$ model independent [36]	8.8–12.8
$B^\pm \to (K^0_S\pi^+\pi^-)_D K^\pm$ model dependent [37]	7.3–11.7
Global [38]	3.9–5.1

Table 1.1: Studies of LHCb sensitivity to γ for different decay channels using 2 fb^{-1} of data.

A sensitivity study of $B^\pm \to (K^0_S K^+K^-)_D K^\pm$ at LHCb has not been performed. However, considering the fact that the equivalent $K^0_S\pi^+\pi^-$ mode has good sensitivity, we anticipate that $B^\pm \to (K^0_S K^+K^-)_D K^\pm$ will make a useful contribution to the global determination of γ.

1.6.3 Determining γ from $B^\pm \to (h^+h^-)_D K^\pm$ decays

1.6.3.1 D decays to $\mathcal{CP}$ eigenstates

The first proposal to use $B^\pm \to DK^\pm$ to determine γ was developed by Gronau, London and Wyler in Refs. [39, 40] and is consequently known as the GLW method. In this approach D decays to $\mathcal{CP}$ eigenstates are used; the D must therefore itself be in a $\mathcal{CP}$ eigenstate upon decay, with a wavefunction taking the form of Equation 1.41. The decay of a B^- is thus:

$$B^- \to \frac{1}{\sqrt{2}}\left(D^0 \pm \overline{D}^0\right) K^-. \tag{1.76}$$

The amplitude of this decay is:

$$\mathcal{A}(B^- \to (\mathcal{CP}\pm)_D K^-) = \frac{1}{\sqrt{2}}(1 \pm r_B e^{i(\delta_B - \gamma)}), \tag{1.77}$$

and the decay rate is:

$$\begin{aligned}\Gamma(B^- \to (\mathcal{CP}\pm)_D K^-) &= \frac{1}{2}\left|1 \pm r_B e^{i(\delta_B-\gamma)}\right|^2 \\ &= \frac{1}{2}\left(1 + r_B^2 \pm r_B \mathfrak{Re}\{e^{i(\delta_B-\gamma)}\} \pm r_B \mathfrak{Re}\{e^{-i(\delta_B-\gamma)}\}\right) \\ &= \frac{1}{2}\left(1 + r_B^2 \pm 2r_B\cos(\delta_B - \gamma)\right).\end{aligned} \tag{1.78}$$

For the equivalent B^+ decay, the sign in front of γ is changed to a plus:

$$\Gamma(B^+ \to (\mathcal{CP}\pm)_D K^+) = \frac{1}{2}\left(1 + r_B^2 \pm 2r_B\cos(\delta_B + \gamma)\right). \tag{1.79}$$

1.6.3.2 D decays to non-$\mathcal{CP}$ eigenstates

The possibility of using D decays to non-$\mathcal{CP}$ eigenstates in order to determine γ was first suggested by Atwood, Dunietz and Soni [41, 42]; the procedure is therefore known as the ADS method. Examples of non-$\mathcal{CP}$ final states are $K^{\pm}\pi^{\mp}$, $K^{\pm}\pi^{\mp}\pi^{+}\pi^{-}$ and $K^{\pm}\pi^{\mp}\pi^{0}$. For each of these cases the D can decay to both possible final states with different kaon charges, one of which is doubly-Cabibbo-suppressed (DCS) with respect to the other.

In the case of $D \to K^{\pm}\pi^{\mp}$ the relative amplitude of decays to the two final states is:

$$\frac{\mathcal{A}(D^0 \to K^+\pi^-)}{\mathcal{A}(D^0 \to K^-\pi^+)} = \frac{\mathcal{A}(\overline{D}^0 \to K^-\pi^+)}{\mathcal{A}(\overline{D}^0 \to K^+\pi^-)} \equiv r_D^{K\pi} e^{-i\delta_D^{K\pi}}, \tag{1.80}$$

where $r_D^{K\pi}$ is the ratio of moduli and $\delta_D^{K\pi}$ is the relative strong phase. $r_D^{K\pi}$ has been measured as 0.0575 ± 0.009 [21] and the value of $\delta_D^{K\pi}$ is $(22^{+11+9}_{-12-11})^\circ$ [21]. The Feynman diagrams for the two D^0 decays are shown in Figure 1.6.

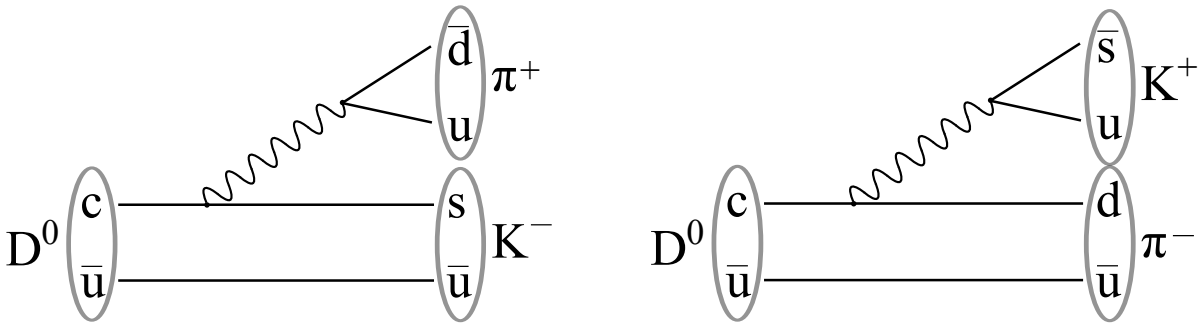

Figure 1.6: Feynman diagrams for the decays $D^0 \to K^-\pi^+$ (left) and $D^0 \to K^+\pi^-$ (right).

In order to determine the $B^{\pm}$ decay rates we must use the fact that the D^0 and $\overline{D}^0$ can decay to the same final state, so there are two possible decay routes in each case. There are then four possible combinations of the charges of the $B^{\pm}$ and the $K^{\pm}$ emitted by the D. The decay rates of each combination are:

$$\Gamma(B^+ \to (K^+\pi^-)_D K^+) = 1 \quad + (r_B r_D^{K\pi})^2 + 2 r_B r_D^{K\pi} \cdot \cos(\delta_B - \delta_D^{K\pi} + \gamma), \tag{1.81}$$

$$\Gamma(B^+ \to (K^-\pi^+)_D K^+) = r_B^2 + (r_D^{K\pi})^2 \quad + 2 r_B r_D^{K\pi} \cdot \cos(\delta_B + \delta_D^{K\pi} + \gamma), \tag{1.82}$$

$$\Gamma(B^- \to (K^+\pi^-)_D K^-) = r_B^2 + (r_D^{K\pi})^2 \quad + 2 r_B r_D^{K\pi} \cdot \cos(\delta_B + \delta_D^{K\pi} - \gamma), \tag{1.83}$$

$$\Gamma(B^- \to (K^-\pi^+)_D K^-) = 1 \quad + (r_B r_D^{K\pi})^2 + 2 r_B r_D^{K\pi} \cdot \cos(\delta_B - \delta_D^{K\pi} - \gamma). \tag{1.84}$$

Even though r_B is small, significant interference between the favoured and suppressed decay modes leads to a good sensitivity to γ. Of particular importance are the decays in which the two final-state kaons have opposite charge, commonly denoted 'wrong-sign' or 'ADS' modes (Equations 1.82 and 1.83). Interference between these diagrams is large compared to the equivalent 'GLW' diagram whose sensitivity to γ is suppressed by the low

value of r_B. The two possible decay routes of B^- to the wrong-sign mode are illustrated in Figure 1.7 along with the relative amplitudes of the suppressed decay at each stage.

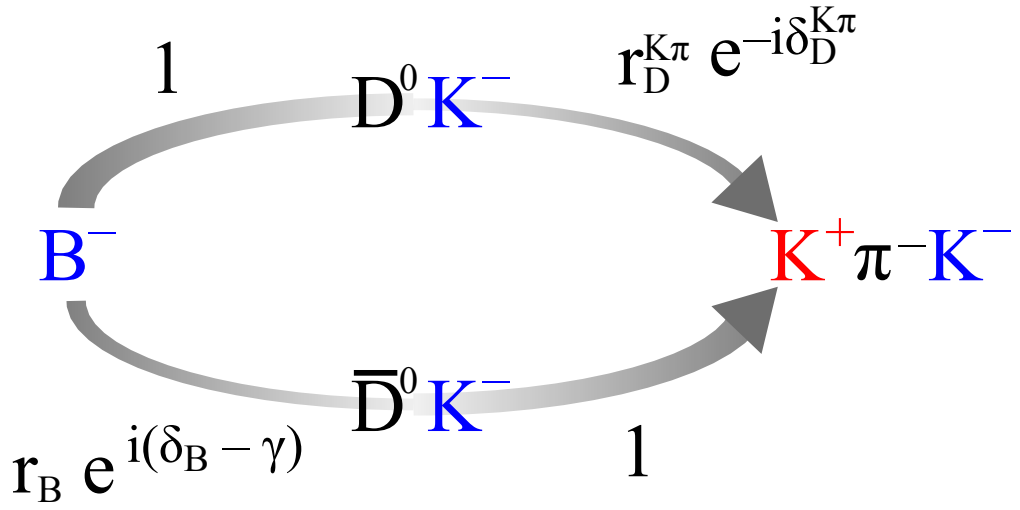

Figure 1.7: Possible routes of wrong-sign $B^- \to (K^+\pi^-)_D K^-$ decays and the relative amplitude of the suppressed decay at each stage. The upper route is $B^- \to D^0(K^+\pi^-)K^-$, with a suppressed D^0 decay; the lower route is $B^- \to \overline{D}^0(K^+\pi^-)K^-$, with a suppressed B^- decay.

1.6.3.3 D decays to non-$\mathcal{CP}$ eigenstates with three or more particles

It is possible to extend the ADS formalism to non-$\mathcal{CP}$ eigenstates consisting of three or more particles. This situation is more complicated than the two-body case because it is possible that there are multiple interfering resonances, so the strong-phase difference between D^0 and $\overline{D}^0$ decays varies over the phase space. In order to account for this effect a new parameter is required, called the *coherence factor* [43].

The coherence factor is defined for D decays to $K^\pm\pi^\mp\pi^0$ as follows:

$$R_{K\pi\pi^0} e^{-i\delta_D^{K\pi\pi^0}} = \frac{\int \mathcal{A}(D^0 \to K^+\pi^-\pi^0)(\mathbf{x})\mathcal{A}(D^0 \to K^-\pi^+\pi^0)(\mathbf{x})\,\mathrm{d}\mathbf{x}}{A_{K^+\pi^-\pi^0} A_{K^-\pi^+\pi^0}}, \tag{1.85}$$

where d$\mathbf{x}$ is an infinitesimal region of multibody phase space and

$$A_{K^\pm\pi^\mp\pi^0} = \sqrt{\int |\mathcal{A}(D^0 \to K^\pm\pi^\mp\pi^0)(\mathbf{x})|^2\,\mathrm{d}(\mathbf{x})}. \tag{1.86}$$

In each case the integral is performed over all phase space.

The coherence factor must lie between zero and one. If it is close to zero, it indicates that there is a lack of coherence between the intermediate resonances, and no single resonance dominates the decay. If it is close to one, it indicates that the resonances are in phase, or that one resonance dominates.

The ADS analysis can therefore be extended to multibody modes with the introduction of just one extra parameter. The coherence factor has been measured for $D \to K^\pm\pi^\mp\pi^+\pi^-$

and $D \to K^{\pm}\pi^{\mp}\pi^0$ at CLEO-c [5].

1.6.3.4 Combination of ADS and GLW methods

When studying $B^{\pm} \to DK^{\pm}$ decays it is necessary to simultaneously determine γ, δ_B, r_B, $r_D^{K\pi}$, $\delta_D^{K\pi}$, and a normalisation factor. With only four decay rates available using the ADS method, additional constraints are required. These can be obtained by determining the rates of decay of $B^{\pm}$ to GLW modes. Furthermore, it is advantageous to use externally-determined values of $r_D^{K\pi}$ and $\delta_D^{K\pi}$, leading to an overconstrained system. Only one normalisation factor is necessary because known D^0 branching fractions can be used to fix the relative yields of individual decay modes once they have been corrected for selection efficiency.

1.6.3.5 ADS/GLW observables

The rates of ADS and GLW decay modes are conventionally measured as asymmetries and ratios:

- The ADS asymmetry:

$$\begin{aligned} A_{\rm ADS} &\equiv \frac{\Gamma(B^- \to (K^+\pi^-)_D K^-) - \Gamma(B^+ \to (K^-\pi^+)_D K^+)}{\Gamma(B^- \to (K^+\pi^-)_D K^-) + \Gamma(B^+ \to (K^-\pi^+)_D K^+)} \\ &= \frac{2 r_B r_D^{K\pi} \sin(\delta_B + \delta_D^{K\pi}) \sin(\gamma)}{r_B^2 + (r_D^{K\pi})^2 + 2 r_B r_D^{K\pi} \cos(\delta_B + \delta_D^{K\pi}) \cos(\gamma)}. \end{aligned} \tag{1.87}$$

- The ratio of decay rates of ADS modes to the decay rates of Cabibbo-favoured modes:

$$\begin{aligned} R_{\rm ADS} &\equiv \frac{\Gamma(B^- \to (K^+\pi^-)_D K^-) + \Gamma(B^+ \to (K^-\pi^+)_D K^+)}{\Gamma(B^- \to D^0 K^-) + \Gamma(B^+ \to \overline{D}^0 K^+)} \\ &= r_B^2 + (r_D^{K\pi})^2 + 2 r_B r_D^{K\pi} \cos(\delta_B + \delta_D^{K\pi}) \cos(\gamma). \end{aligned} \tag{1.88}$$

- The $\mathcal{CP}$ asymmetry in $B^{\pm} \to DK^{\pm}$ and $B^{\pm} \to D\pi^{\pm}$ decays in which the D decays to $\mathcal{CP}\pm$ eigenstates:

$$\begin{aligned} A_{\mathcal{CP}\pm}^{DK} &\equiv \frac{\Gamma(B^- \to (\mathcal{CP}\pm)_D K^-) - \Gamma(B^+ \to (\mathcal{CP}\pm)_D K^+)}{\Gamma(B^- \to (\mathcal{CP}\pm)_D K^-) + \Gamma(B^+ \to (\mathcal{CP}\pm)_D K^+)} \\ &= \frac{\pm 2 r_B^{DK} \sin(\delta_B^{DK}) \sin(\gamma)}{1 + (r_B^{DK})^2 \pm 2 r_B^{DK} \cos(\delta_B^{DK}) \cos(\gamma)}, \end{aligned} \tag{1.89}$$

$$A_{\mathcal{CP}\pm}^{D\pi} = \frac{\pm 2 r_B^{D\pi} \sin(\delta_B^{D\pi}) \sin(\gamma)}{1 + (r_B^{D\pi})^2 \pm 2 r_B^{D\pi} \cos(\delta_B^{D\pi}) \cos(\gamma)}. \tag{1.90}$$

- The ratio of the rate of $B^{\pm} \to DK^{\pm}$ decays in which the D decays to $\mathcal{CP}\pm$ eigenstates

to those in which the D decays to Cabibbo-favoured final states:

$$R_{\mathcal{CP}\pm} \equiv 2\frac{\Gamma(B^- \to (\mathcal{CP}\pm)_D K^-) + \Gamma(B^+ \to (\mathcal{CP}\pm)_D K^+)}{\Gamma(B^- \to D^0 K^-) + \Gamma(B^+ \to \overline{D}^0 K^+)}$$
$$= 1 + (r_B^{DK})^2 \pm 2 r_B^{DK} \cos(\delta_B^{DK}) \cos(\gamma). \tag{1.91}$$

- The asymmetry in $B^\pm \to DK^\pm$ and $B^\pm \to D\pi^\pm$ decays in which the D decays to Cabibbo-favoured final states:

$$A_{\text{Fav}}^{DK} = \frac{\Gamma(B^- \to D^0 K^-) - \Gamma(B^+ \to \overline{D}^0 K^+)}{\Gamma(B^- \to D^0 K^-) + \Gamma(B^+ \to \overline{D}^0 K^+)}, \tag{1.92}$$

$$A_{\text{Fav}}^{D\pi} = \frac{\Gamma(B^- \to D^0 \pi^-) - \Gamma(B^+ \to \overline{D}^0 \pi^+)}{\Gamma(B^- \to D^0 \pi^-) + \Gamma(B^+ \to \overline{D}^0 \pi^+)}. \tag{1.93}$$

  These quantities are expected to be close to zero because the decay rates contain very small $\mathcal{CP}$-violating terms.

- The ratio of branching fractions $\mathcal{B}^{DK}/\mathcal{B}^{D\pi} \equiv \mathcal{B}_{B\to DK}/\mathcal{B}_{B\to D\pi}$ is an important observable. This is expected to be different depending on the D decay mode, so two values are defined: $\mathcal{B}_{\text{Fav}}^{DK}/\mathcal{B}_{\text{Fav}}^{D\pi}$ and $\mathcal{B}_{\mathcal{CP}}^{DK}/\mathcal{B}_{\mathcal{CP}}^{D\pi}$, where Fav refers to Cabibbo-favoured $D \to K^\pm\pi^\mp$ decays and $\mathcal{CP}$ refers to $D \to K^+K^-$ decays.

World averages of these quantities can be found in Refs. [11, 21]. Section 8.2.1 has a short review of the current measurements.

In order to determine $R_{\mathcal{CP}\pm}$ it is advantageous to use the approximation [44]:

$$R_{\mathcal{CP}\pm} \approx R_\pm = \frac{R_{K/\pi}^\pm}{R_{K/\pi}} \tag{1.94}$$

where

$$R_{K/\pi}^\pm \equiv \frac{\Gamma(B^- \to (\mathcal{CP}\pm)_D K^-) + \Gamma(B^+ \to (\mathcal{CP}\pm)_D K^+)}{\Gamma(B^- \to (\mathcal{CP}\pm)_D \pi^-) + \Gamma(B^+ \to (\mathcal{CP}\pm)_D \pi^+)} \tag{1.95}$$

and

$$R_{K/\pi} \equiv \frac{\Gamma(B^- \to (K^-\pi^+)_D K^-) + \Gamma(B^+ \to (K^+\pi^-)_D K^+)}{\Gamma(B^- \to (K^-\pi^+)_D \pi^-) + \Gamma(B^+ \to (K^+\pi^-)_D \pi^+)}. \tag{1.96}$$

The value of $R_\pm$ is therefore:

$$\begin{aligned}
R_\pm &= \frac{\Gamma(B^- \to (\mathcal{CP}\pm)_D K^-) + \Gamma(B^+ \to (\mathcal{CP}\pm)_D K^+)}{\Gamma(B^- \to (\mathcal{CP}\pm)_D \pi^-) + \Gamma(B^+ \to (\mathcal{CP}\pm)_D \pi^+)} \\
&\times \frac{\Gamma(B^- \to (K^-\pi^+)_D \pi^-) + \Gamma(B^+ \to (K^+\pi^-)_D \pi^+)}{\Gamma(B^- \to (K^-\pi^+)_D K^-) + \Gamma(B^+ \to (K^+\pi^-)_D K^+)} \\
&= \frac{1 + (r_B^{DK})^2 \pm 2 r_B^{DK} \cos(\delta_B^{DK}) \cos(\gamma)}{1 + (r_B^{D\pi})^2 \pm 2 r_B^{D\pi} \cos(\delta_B^{D\pi}) \cos(\gamma)} \\
&\times \frac{1 + r_B^{D\pi 2} r_D^2 + 2 r_B^{D\pi} r_D [\cos(\delta_B^{D\pi} - \delta_D) \cos(\gamma)]}{1 + r_B^{DK 2} r_D^2 + 2 r_B^{DK} r_D [\cos(\delta_B^{DK} - \delta_D) \cos(\gamma)]}.
\end{aligned} \tag{1.97}$$

There is a systematic uncertainty associated with making the approximation in Equation 1.94. In order to determine the magnitude of the uncertainty, we define R_c such that $R_\pm \equiv R_{\mathcal{CP}\pm} \times (1 + R_c)$. We have

$$\begin{aligned}
R_\pm &= R_{\mathcal{CP}\pm} \cdot \frac{1}{1 + (r_B^{D\pi})^2 \pm 2 r_B^{D\pi} \cos(\delta_B^{D\pi}) \cos(\gamma)} \\
&\times \frac{1 + r_B^{D\pi 2} r_D^2 + 2 r_B^{D\pi} r_D [\cos(\delta_B^{D\pi} - \delta_D) \cos(\gamma)]}{1 + r_B^{DK 2} r_D^2 + 2 r_B^{DK} r_D [\cos(\delta_B^{DK} - \delta_D) \cos(\gamma)]}.
\end{aligned} \tag{1.98}$$

Setting $r_D = \tan^2(\theta_C)$ and $r_B^{D\pi} = r_B^{DK} \tan^2(\theta_C)$, where θ_C is the Cabibbo angle, we obtain:

$$\begin{aligned}
R_\pm &= R_{\mathcal{CP}\pm} \cdot \frac{1}{1 + (r_B^{DK} \tan^2(\theta_C))^2 \pm 2 (r_B^{DK} \tan^2(\theta_C)) \cos(\delta_B^{D\pi}) \cos(\gamma)} \\
&\times \frac{1 + (r_B^{DK} \tan^2(\theta_C))^2 (\tan^2(\theta_C))^2 + 2 (r_B^{DK} \tan^2(\theta_C)) (\tan^2(\theta_C)) [\cos(\delta_B^{D\pi} - \delta_D) \cos(\gamma)]}{1 + r_B^{DK 2} (\tan^2(\theta_C))^2 + 2 r_B^{DK} (\tan^2(\theta_C)) [\cos(\delta_B^{DK} - \delta_D) \cos(\gamma)]}.
\end{aligned} \tag{1.99}$$

We then neglect terms of $\mathcal{O}(\tan^4(\theta_C))$:

$$\begin{aligned}
R_\pm &\simeq R_{\mathcal{CP}\pm} \cdot \frac{1}{1 \pm 2 (r_B^{DK} \tan^2(\theta_C)) \cos(\delta_B^{D\pi}) \cos\gamma} \cdot \frac{1}{1 + 2 r_B^{DK} (\tan^2(\theta_C)) [\cos(\delta_B^{DK} - \delta_D) \cos\gamma]} \\
&\simeq R_{\mathcal{CP}\pm} \cdot \frac{1}{1 + 2 (r_B^{DK} \tan^2(\theta_C)) [\pm \cos(\delta_B^{D\pi}) \cos(\gamma) + \cos(\delta_B^{DK} - \delta_D) \cos(\gamma)]}.
\end{aligned} \tag{1.100}$$

We assign values to the cosine terms that maximise $|R_c|$:

$$\begin{aligned}
R_\pm &= R_{\mathcal{CP}\pm} \cdot \frac{1}{1 + 2 (r_B^{DK} \tan^2(\theta_C)) [\pm 2]} \\
&= R_{\mathcal{CP}\pm} \cdot \frac{1}{1 \pm 4 r_B^{DK} \tan^2(\theta_C)} \\
&= R_{\mathcal{CP}\pm} \cdot (1 \pm 4 r_B^{DK} \tan^2(\theta_C)).
\end{aligned} \tag{1.101}$$

The value of R_c is therefore $4 r_B^{DK} \tan^2(\theta_C) \simeq 2.2\%$.

1.6.4 Determining γ using $B^{\pm} \to (K^0_{S,L}K^+K^-)_D K^{\pm}$ decays

An alternative to the ADS/GLW method of determining γ is to study $B^{\pm}\to DK^{\pm}$ decays in which the D decays to $K^0_{S,L}h^+h^-$ ($h^{\pm} = K^{\pm}$ or $\pi^{\pm}$) [45, 46]. Such final states are $\mathcal{CP}$ self-conjugate but are not $\mathcal{CP}$ eigenstates; decays to these states can typically proceed via several intermediate resonances of differing $\mathcal{CP}$ eigenvalue. This method was first advocated by Giri, Grossman, Soffer and Zupan [46] and is hence known as the GGSZ method. The formalism detailed below applies in particular to $D\to K^0_{S,L}K^+K^-$ decays; much of it is identical for $K^0_{S,L}\pi^+\pi^-$ but the associated complex decay amplitudes are in general different.

In this approach the distribution of the final state particles across the Dalitz plot is studied. All final and initial state particles are pseudoscalars, so any nonuniform structure in the Dalitz plot is due to the dynamics of the decay (see Section 1.5). We use the basis $(x, y) \equiv (m^2_{K^0_S K^+}, m^2_{K^0_S K^-})$ to describe the location of events on the Dalitz plot.

We define the amplitude of the D^0 decay at the point (x, y):

$$\mathcal{A}(D^0 \to K^0_S K^+ K^-) \equiv A_D(x, y) \equiv a_{xy} e^{i\delta^{D^0}_{xy}}. \tag{1.102}$$

A_D is normalised such that

$$\int |A_D(x, y)|^2 \, \mathrm{d}x \, \mathrm{d}y = 1, \tag{1.103}$$

where the integral is carried out over all of phase space.

Assuming there is no $\mathcal{CP}$ violation or mixing in the $D^0\overline{D}^0$ system:

$$\mathcal{A}(D^0 \to K^0_S K^+ K^-)(x, y) = \mathcal{A}(\overline{D}^0 \to K^0_S K^+ K^-)(y, x). \tag{1.104}$$

An interchange of the Dalitz plane coordinates corresponds to a swap of the two charged hadrons in the final state, equivalent to applying the $\mathcal{CP}$ operator to the decay as a whole.

So far we have considered neutral kaons in the physical basis (K^0_S and K^0_L). It is also important to consider the flavour basis K^0 and $\overline{K}^0$. Feynman diagrams for D^0 decays in this basis are shown in Figure 1.8. Considering $\mathbf{V}_{\mathrm{CKM}}$ vertex factors, the relative amplitude between the two diagrams is $\mathcal{A}(D^0 \to K^0K^+K^-)/\mathcal{A}(D^0 \to \overline{K}^0K^+K^-) = |V_{\mathrm{us}}V_{\mathrm{cd}}|/|V_{\mathrm{ud}}V_{\mathrm{cs}}| \sim 0.054$.

Ignoring the low level of $\mathcal{CP}$ violation in the kaon system, we define:

$$K^0_S \equiv \frac{1}{\sqrt{2}}(K^0 + \overline{K}^0), \qquad K^0_L \equiv \frac{1}{\sqrt{2}}(K^0 - \overline{K}^0). \tag{1.105}$$

We initially focus on $D\to K^0_S K^+K^-$ decays; the analysis of $D\to K^0_L K^+K^-$ decays is discussed in Section 1.6.5.5.

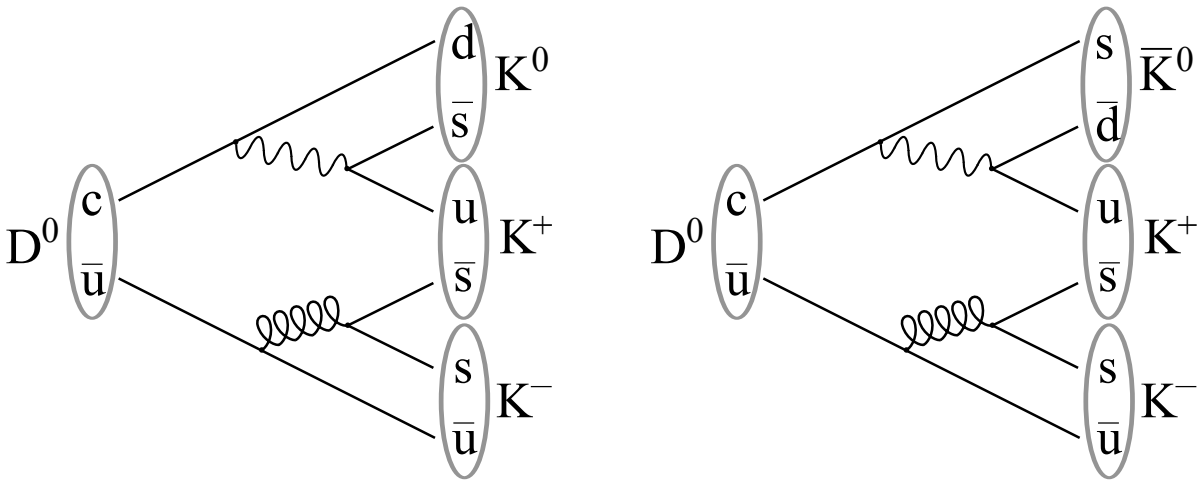

Figure 1.8: Feynman diagrams for the decays $D^0 \to K^0 K^+ K^-$ (left) and $D^0 \to \overline{K}^0 K^+ K^-$ (right).

The amplitude of the decay $B^\pm \to (K^0_S K^+ K^-)_D K^\pm$ as a function of Dalitz plane coordinates is:

$$\begin{aligned}
&\mathcal{A}(B^\pm \to (K^0_S K^+ K^-)_D K^\pm)(x,y) \\
&= \mathcal{A}(B^\pm \to D^0(K^0_S K^+ K^-)K^\pm)(x,y) + \mathcal{A}(B^\pm \to \overline{D}^0(K^0_S K^+ K^-)K^\pm)(x,y) \\
&= A_B \mathcal{P}_D \Big(A_D(x,y) + r_B e^{i(\delta_B \pm \gamma)} A_D(y,x) \Big),
\end{aligned} \tag{1.106}$$

where $\mathcal{P}_D$ is the propagator of the D. The relation given in Equation 1.104 has been used to reverse the coordinates in the second half of the expression.

Using the very accurate narrow width approximation we set $\mathcal{P}_D$ to 1. The reduced partial decay width of the $B^\pm$ decay can thus be written:

$$\begin{aligned}
&\mathrm{d}\widehat{\Gamma}(B^\pm \to (K^0_S K^+ K^-)_D K^\pm) \\
&= \Big(a^2_{xy} + r^2_B a^2_{yx} + 2 r_B a_{xy} a_{yx} \cos((\delta^{D^0}_{xy} - \delta^{D^0}_{yx}) + (-\delta_B \mp \gamma)) \Big)\, \mathrm{d}p \\
&= \Big(a^2_{xy} + r^2_B a^2_{yx} + 2 r_B a_{xy} a_{yx} \{ \cos(\delta^{D^0}_{xy} - \delta^{D^0}_{yx}) \cos(\delta_B \pm \gamma) \\
&\qquad + \sin(\delta^{D^0}_{xy} - \delta^{D^0}_{yx}) \sin(\delta_B \pm \gamma) \} \Big)\, \mathrm{d}p \,,
\end{aligned} \tag{1.107}$$

where $\mathrm{d}p$ represents an infinitesimal region of phase space.

It is therefore possible to determine γ by measuring the rates of $B^\pm \to (K^0_S K^+ K^-)_D K^\pm$ decays in different regions of phase space. To do this it is essential to have a good understanding of the amplitude of the $D \to K^0_S K^+ K^-$ decay; in particular, the strong-phase difference between D^0 and $\overline{D}^0$ decays:

$$\Delta\delta_D(x,y) \equiv \delta^{D^0}_{xy} - \delta^{\bar{D}^0}_{xy} = \delta^{D^0}_{xy} - \delta^{D^0}_{yx} \,. \tag{1.108}$$

Substituting this into Equation 1.107 and considering both B^+ and B^- decays we obtain:

$$\begin{aligned}&\mathrm{d}\widehat{\Gamma}(B^\pm \to (K^0_S K^+ K^-)_D K^\pm) = \\ &\Big(a^2_{xy} + r^2_B a^2_{yx} + 2r_B a_{xy} a_{yx}\{\cos(\Delta\delta_D)\cos(\delta_B \pm \gamma) + \sin(\Delta\delta_D)\sin(\delta_B \pm \gamma)\}\Big)\mathrm{d}p. \qquad (1.109)\end{aligned}$$

Henceforth we use the simplified notation δ_{xy} (δ_{yx}) to denote $\delta^{D^0}_{xy}$ ($\delta^{D^0}_{yx}$).

There are three approaches that can be used to determine γ with $B^\pm \to (K^0_S K^+ K^-)_D K^\pm$ data:

- Determine all $B^\pm$ and D decay parameters from the $B^\pm$ decay sample [46]. This approach requires very high $B^\pm$ decay statistics because the behaviour of the D system across the entire Dalitz plot must be measured.

- Determine the D-decay parameters externally by fitting a model to a high-statistics sample of $D \to K^0_S K^+ K^-$ decays. The extraction of γ from the $B^\pm$ decay sample then becomes significantly more feasible. The fit to determine the D-decay parameters is usually performed on a sample of $D^{*\pm} \to D(K^0_S K^+ K^-)\pi^\pm$ events in which the charge of the pion enables the flavour of the D to be tagged. This approach is taken by BaBar [25, 47, 48] and Belle [31, 49, 50]. The modulus of the decay amplitude across the Dalitz plot can be directly measured, but it is not possible to determine the phase, which must be inferred using model-dependent assumptions. There is therefore an uncertainty associated with the modelling that is both irreducible and hard to quantify. In future analyses, with much more $B^\pm$-decay data than is presently available, this uncertainty will become the dominant source of uncertainty on the measurement of γ.

- Determine the D-decay parameters externally by measuring the strong-phase difference in bins across the Dalitz plane. This is a *model-independent* method that is discussed in detail in Section 1.6.5. The model-related uncertainty associated with the previous method is replaced by an uncertainty related to the size of the $D \to K^0_S K^+ K^-$ dataset; with a large enough sample the uncertainty becomes negligible. A recent study by Belle [32] has used this method for D decays to $K^0_S \pi^+ \pi^-$.

1.6.5 Binned analysis of the $D^0 \to K^0_{S,L} K^+ K^-$ Dalitz plane

Determining γ in $B^\pm \to (K^0_S K^+ K^-)_D K^\pm$ events by binning the $D \to K^0_S K^+ K^-$ Dalitz plane was advocated in Refs. [46,51]. The Dalitz plane is divided into $2\mathcal{N}$ bins, arranged such that they are symmetric about the axis $m^2_{K^0_S K^+} = m^2_{K^0_S K^-}$. The bins below this axis are labelled i ($i = 1 \ldots \mathcal{N}$) and the bins above the axis are labelled $-i$. An example of such a binning is shown in Figure 1.9.

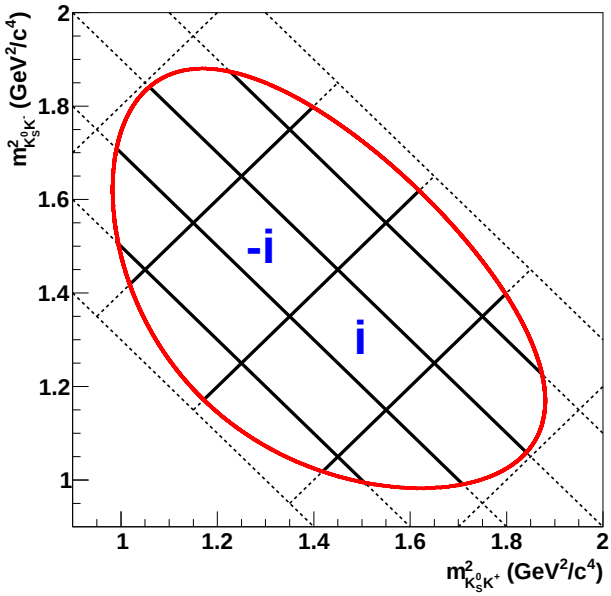

Figure 1.9: An example of a rectangular binning of the $K^0_S K^+ K^-$ Dalitz plane with bins labelled i and $-i$. The red line indicates the boundary of the physically-allowed region.

Any binning may in theory be employed, but some will result in a greater statistical sensitivity than others. The binning that allows for the greatest sensitivity is a division of the Dalitz plane into regions of similar strong-phase difference, as suggested by Bondar and Poluektov [45,52,53]. The bin boundaries are determined using a decay model, but this does not introduce any model-related bias on the value of γ; the only penalty introduced with the use of a binning based on an incorrect model is a reduced statistical sensitivity. A detailed discussion of the choice of binning in the analysis of CLEO-c data is given in Section 4.2.

The analysis proceeds by counting the number of B^+ and B^- events in each bin. Following Equation 1.109, the decay rate of $B^\pm \to DK^\pm$ in the i^{th} bin can be written:

$$\begin{aligned}\Gamma_i^\pm &\equiv \int_{\mathcal{D}_i} \mathrm{d}\Gamma(B^\pm \to (K^0_S K^+ K^-)_D K^\pm) \\ &= \int_{\mathcal{D}_i} \mathrm{d}x\,\mathrm{d}y \Big(a^2_{xy} + r_B^2 a^2_{yx} + 2 r_B a_{xy} a_{yx} \{ \cos(\Delta\delta_D(x,y)) \cos(\delta_B \pm \gamma) \\ &\qquad + \sin(\Delta\delta_D(x,y)) \sin(\delta_B \pm \gamma) \} \Big), \end{aligned} \tag{1.110}$$

where $\mathcal{D}_i$ is the Dalitz plot region covered by bin i. The equivalent decay rate in the $-i^{\text{th}}$ bin is[8]:

$$\begin{aligned}\Gamma_{-i}^\pm = \int_{\mathcal{D}_{-i}} \mathrm{d}x\,\mathrm{d}y \Big(a^2_{yx} + r_B^2 a^2_{xy} + 2 r_B a_{yx} a_{xy} \{ \cos(\Delta\delta_D(x,y)) \cos(\delta_B \pm \gamma) \\ - \sin(\Delta\delta_D(x,y)) \sin(\delta_B \pm \gamma) \} \Big). \end{aligned} \tag{1.111}$$

[8]Note the relative sign difference between the cosine and sine terms for bins i and $-i$.

It is therefore necessary to determine amplitude-weighted values of $\cos(\Delta\delta_D)$ and $\sin(\Delta\delta_D)$ in each bin, denoted c_i and s_i respectively.

We define the population of events in the i^{th} bin as a fraction of the total:

$$T_i \equiv \int_{\mathcal{D}_i} |A_D(x,y)|^2 \,\mathrm{d}x\,\mathrm{d}y = \int_{\mathcal{D}_i} a_{xy}^2 \,\mathrm{d}x\,\mathrm{d}y. \tag{1.112}$$

We are using a normalisation convention such that $\sum_{i=1}^{\mathcal{N}}(T_i + T_{-i}) = 1$. c_i and s_i are expressed as:

$$c_i \equiv \frac{1}{\sqrt{T_i T_{-i}}} \int_{\mathcal{D}_i} a_{xy}a_{yx}\cos(\delta_{xy}-\delta_{yx}) \,\mathrm{d}x\,\mathrm{d}y, \tag{1.113}$$

$$s_i \equiv \frac{1}{\sqrt{T_i T_{-i}}} \int_{\mathcal{D}_i} a_{xy}a_{yx}\sin(\delta_{xy}-\delta_{yx}) \,\mathrm{d}x\,\mathrm{d}y. \tag{1.114}$$

The relationships between the quantities in mirror-image bins are as follows:

$$c_i = c_{-i}, \qquad s_i = -s_{-i}. \tag{1.115}$$

Consequently, only $\mathcal{N}$ of each variable need to be considered in the expressions for decay rates that are derived below. However, T_i is not in general equal to T_{-i}.

The rate of decay of $B^\pm \to (K^0_S K^+ K^-)_D K^\pm$ in the i^{th} bin of the Dalitz plane can be written in terms of c_i, s_i and T_i as:

$$\Gamma_i^\pm = T_i + r_B^2 T_{-i} + 2r_B\sqrt{T_i T_{-i}}[\cos(\delta_B \pm \gamma)c_i + \sin(\delta_B \pm \gamma)s_i]. \tag{1.116}$$

The equivalent decay rate in the $-i^{\text{th}}$ bin is:

$$\Gamma_{-i}^\pm = T_{-i} + r_B^2 T_i + 2r_B\sqrt{T_i T_{-i}}[\cos(\delta_B \pm \gamma)c_i - \sin(\delta_B \pm \gamma)s_i]. \tag{1.117}$$

The quantities T_i and T_{-i} can be measured using an external sample of $D{\to}K^0_S K^+ K^-$ decays. The yield of D decays in the i^{th} bin is:

$$K_i = a_D \int_{\mathcal{D}_i} |A_D(x,y)|^2 \,\mathrm{d}x\,\mathrm{d}y = a_D T_i, \tag{1.118}$$

where a_D is a normalisation factor equal to the total number of $D{\to}K^0_S K^+ K^-$ decays in the charm sample.

The yield of $B^\pm \to (K^0_S K^+ K^-)_D K^\pm$ decays in the i^{th} Dalitz plot bin is then:

$$N_i^\pm = a_B^\pm \, \Gamma_i^\pm \tag{1.119}$$

$$= a_B^\pm (T_i + r_B^2 T_{-i} + 2 r_B \sqrt{T_i T_{-i}} [\cos(\delta_B \pm \gamma) c_i + \sin(\delta_B \pm \gamma) s_i]) \tag{1.120}$$

$$= \frac{a_B^\pm}{a_D} (K_i + r_B^2 K_{-i} + 2 r_B \sqrt{K_i K_{-i}} [\cos(\delta_B \pm \gamma) c_i + \sin(\delta_B \pm \gamma) s_i]), \tag{1.121}$$

where $a_B^\pm$ is a normalisation factor equal to the total number of $B^\pm \to (K^0_S K^+ K^-)_D K^\pm$ events in the $B^\pm$-decay sample. The equivalent yield in the $-i^{\text{th}}$ bin is:

$$N_{-i}^\pm = \frac{a_B^\pm}{a_D} (K_{-i} + r_B^2 K_i + 2 r_B \sqrt{K_i K_{-i}} [\cos(\delta_B \pm \gamma) c_i - \sin(\delta_B \pm \gamma) s_i]). \tag{1.122}$$

A fit to the time-integrated yields on the Dalitz plot using external values of c_i, s_i and K_i then allows γ, r_B and δ_B to be extracted.

1.6.5.1 Use of a quantum-correlated $D^0\overline{D}^0$ dataset

In order to measure c_i and s_i it is essential to use a set of quantum-correlated $D^0\overline{D}^0$ decays. The properties of such a system were introduced in Section 1.4.2.1. The most significant feature is that if the $\mathcal{CP}$ eigenvalue of one D is measured as η_{CP} at a particular instant in time, the $\mathcal{CP}$ of the other is known to be equal to $-\eta_{CP}$ at the same instant. The use of a quantum-correlated dataset enables access to information about the strong phase of the D decay that cannot be determined by studying a flavour-tagged sample.

Events that are relevant to this technique are those in which one D decays to $K^0_S K^+ K^-$ and the other D decays to one of a variety of final states. The $D \to K^0_S K^+ K^-$ decay is denoted the *signal-side* decay and the decay of the other D in the correlated pair is denoted the *opposite-side* decay. The signal-side decay is said to be *tagged* with the opposite-side final state. The opposite-side final states are classified as $\mathcal{CP}$ eigenstates (e.g. K^+K^-), flavour states[9] (e.g. $K^\pm e^\mp \nu_e$) and mixed-$\mathcal{CP}$ states of the form $K^0_{S,L} h^+ h^-$. In an analysis to determine c_i and s_i, at least one of each type of final state must be used. In Section 1.6.5.2 we list the key observables that must be measured in order to determine c_i and s_i.

The total number of $D^0\overline{D}^0$ pairs in the data sample is denoted $N_{D^0\overline{D}^0}$. In terms of experimentally measurable quantities, $N_{D^0\overline{D}^0}$ is equal to:

$$N_{D^0\overline{D}^0} = \sigma_{D^0\overline{D}^0} \times \int \mathcal{L} \, \mathrm{d}t \,, \tag{1.123}$$

where $\sigma_{D^0\overline{D}^0}$ is the cross section of the $\psi(3770) \to D^0\overline{D}^0$ decay and $\int \mathcal{L} \, \mathrm{d}t$ is the total

[9] Fully hadronic 'flavour' final states such as $K^\pm \pi^\mp$ are more accurately termed *pseudo-flavour* states because they cannot be used to determine unambiguously the flavour of the parent D. The correction to the bin yields that must consequently be assigned is described in Section 3.4.3.

integrated luminosity of the data used.

A *single tag* is defined as a D that decays to a particular state, irrespective of the state that the other D decays to. The total single tag yield of the final state X is:

$$S_X = 2N_{D^0\overline{D}^0}\mathcal{B}_X \tag{1.124}$$

where $\mathcal{B}_X$ is the branching fraction of $D \to X$.

A *double tag* is defined as a $D^0\overline{D}^0$ pair, both of which decay to specific final states. The total number of double tags in which one D decays to $K^0_S K^+K^-$ and the other to X is:

$$D_X = 2N_{D^0\overline{D}^0}\mathcal{B}_{K^0_S K^+K^-}\mathcal{B}_X. \tag{1.125}$$

This relation is exact because D-mixing has been neglected. However, it is important to note that the value of $\mathcal{B}_{K^0_S K^+K^-}$ can change depending on the nature of the opposite-side final state. For example, if the opposite side is a $\mathcal{CP}+$ eigenstate the D must decay to $K^0_S K^+K^-$ through the ($\mathcal{CP}-$) $K^0_S\phi$ resonance, and the branching fraction of D decays to $K^0_S\phi$ is not equal to the total branching fraction of D to $K^0_S K^+K^-$.

We note that for the flavour state F:

$$a_D = S_F\mathcal{B}_{K^0_S K^+K^-}. \tag{1.126}$$

The situation in which both D mesons decay to $K^0_S K^+K^-$ is a special case; the indistinguishability of the final states reduces the combinatorics by a factor of 2. The total number of double tags in this case is therefore $D_{K^0_S K^+K^-} = N_{D^0\overline{D}^0}\mathcal{B}_{K^0_S K^+K^-}\mathcal{B}_{K^0_S K^+K^-}$.

The double-tag yield of $K^0_S K^+K^-$ reconstructed against a flavour state F in the i^{th} Dalitz plot bin has previously been defined as K_i (Equation 1.118). This quantity can be expressed in terms of S_F and D_F as:

$$\begin{aligned} K_i &= D_F T_i \\ &= 2N_{D^0\overline{D}^0}\mathcal{B}_{K^0_S K^+K^-}\mathcal{B}_F T_i \\ &= S_F\mathcal{B}_{K^0_S K^+K^-}T_i. \end{aligned} \tag{1.127}$$

Rearranging, we obtain a relation that is used in Section 4.3.2 (e.g. see Equation 4.10):

$$K_i/S_F = \mathcal{B}_{K^0_S K^+K^-}T_i. \tag{1.128}$$

1.6.5.2 Observables of interest

In order to determine c_i and s_i several quantities must be measured using the quantum-correlated $D^0\overline{D}^0$ dataset. For convenience the observables of interest are listed below; detailed derivations can be found in the following sections.

- $M_i^{\pm}$: the yield of events in which $K^0_S K^+ K^-$ has been tagged with $\mathcal{CP}\mp$ eigenstates in the i^{th} bin of the $K^0_S K^+ K^-$ Dalitz plane. This quantity depends upon c_i as follows:

$$M_i^{\pm} \propto K_i \pm 2c_i\sqrt{K_i K_{-i}} + K_{-i}. \tag{1.129}$$

  This relation is derived in Section 1.6.5.3.

- M_{ij}: the yield of events in which $K^0_S K^+ K^-$ has been tagged with final states of the form $K^0_S h^+ h^-$ in the i^{th} bin of the $K^0_S K^+ K^-$ Dalitz plane and the j^{th} bin of the $K^0_S h^+ h^-$ Dalitz plane. This quantity depends upon c_i and s_i as follows:

$$M_{ij} \propto K_i K_{-j} + K_{-i} K_j - 2\sqrt{K_i K_{-j} K_{-i} K_j}(c_i c_j + s_i s_j). \tag{1.130}$$

  This relation is derived in Section 1.6.5.4.

In addition to double-tagged $D\to K^0_S K^+ K^-$ decays it is possible to utilise $D\to K^0_L K^+ K^-$ decays (see Section 1.6.5.5). The expressions for the yields of such decays are similar, but not identical to, those for $D\to K^0_S K^+ K^-$. All primed quantities relate to $K^0_L K^+ K^-$ and are the equivalents of the unprimed values that relate to $K^0_S K^+ K^-$. The following relations are derived in Section 1.6.5.6.

- $M_i^{\pm\prime}$: the yield of events in which $K^0_L K^+ K^-$ has been tagged with $\mathcal{CP}\mp$ eigenstates in the i^{th} bin of the $K^0_L K^+ K^-$ Dalitz plane. This quantity depends upon c'_i as follows:

$$M_i^{\pm\prime} \propto K'_i \mp 2c'_i\sqrt{K'_i K'_{-i}} + K'_{-i}. \tag{1.131}$$

- M'_{ij}: the yield of events in which $K^0_L K^+ K^-$ has been tagged with final states of the form $K^0_S h^+ h^-$ in the i^{th} bin of the $K^0_L K^+ K^-$ Dalitz plane and the j^{th} bin of the $K^0_S h^+ h^-$ Dalitz plane. This quantity depends upon c'_i and s'_i as follows:

$$M'_{ij} \propto K_i K'_{-j} + K_{-i} K'_j + 2\sqrt{K_{-i} K'_{-j} K_{-i} K'_j}(c_i c'_j + s_i s'_j). \tag{1.132}$$

1.6.5.3 Determining c_i from $\mathcal{CP}$-tagged $K^0_S K^+ K^-$ decays

Values of c_i can be determined using events in which one D decays to $K^0_S K^+ K^-$ and the other D decays to a a $\mathcal{CP}$ eigenstate P. Following Equation 1.41, the decay amplitude of a

D in a $\mathcal{CP}$ eigenstate is:

$$A_{\mathcal{CP}\pm}(x,y) \equiv \frac{1}{\sqrt{2}}(A_D(x,y) \pm A_D(y,x)) \tag{1.133}$$

and the partial decay width is:

$$\mathrm{d}\Gamma_{\mathcal{CP}\pm} = \left(\frac{1}{2}(a_{xy}^2 + a_{yx}^2) \pm a_{xy}a_{yx}\cos(\delta_{xy} - \delta_{yx})\right) \mathrm{d}p \ , \tag{1.134}$$

where dp is an infinitesimal region of phase space. The number of events in the i^{th} bin of the $K_S^0K^+K^-$ Dalitz plot when the $K_S^0K^+K^-$ has $\mathcal{CP}$ eigenvalue ±1 is therefore:

$$M_i^{\pm} \equiv a_{\pm}\int_{\mathcal{D}_i} |A_{\mathcal{CP}\pm}(x,y)|^2 \,\mathrm{d}x\,\mathrm{d}y \tag{1.135}$$

$$= \frac{a_{\pm}}{2a_D}(K_i \pm 2c_i\sqrt{K_iK_{-i}} + K_{-i}), \tag{1.136}$$

where $a_{\pm}$ is a normalisation factor such that $\sum_{i=1}^{\mathcal{N}}(M_i^{\pm} + M_{-i}^{\pm})$ is equal to the total number of double-tagged $K_S^0K^+K^-$ against P events.

We must determine $a_{\pm}$ in terms of known quantities. To do this we start with an alternative expression for $M_i^{\pm}$:

$$M_i^{\pm} = S_{\mp}\mathcal{B}^{\pm}_{K_S^0K^+K^-}\frac{\int_{\mathcal{D}_i}|A_{\mathcal{CP}\pm}(x,y)|^2\,\mathrm{d}x\,\mathrm{d}y}{\int|A_{\mathcal{CP}\pm}(x,y)|^2\,\mathrm{d}x\,\mathrm{d}y} \tag{1.137}$$

where $\mathcal{B}^{\pm}_{K_S^0K^+K^-}$ is the branching fraction of the $D\to K_S^0K^+K^-$ decay in a $\mathcal{CP}\pm$ eigenstate and $S_{\mp}$ is the number of single tags for the particular $\mathcal{CP}\mp$ mode against which the $K_S^0K^+K^-$ is reconstructed. Equating 1.136 and 1.137 we find:

$$a_{\pm} = \frac{S_{\mp}\mathcal{B}^{\pm}_{K_S^0K^+K^-}}{\int|A_{\mathcal{CP}\pm}(x,y)|^2\,\mathrm{d}x\,\mathrm{d}y}. \tag{1.138}$$

We use the general relation $\mathcal{B}_X \propto \int|A_X|^2\,\mathrm{d}p$ to write

$$\frac{\mathcal{B}^{\pm}_{K_S^0K^+K^-}}{\mathcal{B}_{K_S^0K^+K^-}} = \frac{\int|A_{\mathcal{CP}\pm}(x,y)|^2\,\mathrm{d}x\,\mathrm{d}y}{\int|A_D(x,y)|^2\,\mathrm{d}x\,\mathrm{d}y} = \int|A_{\mathcal{CP}\pm}(x,y)|^2\,\mathrm{d}x\,\mathrm{d}y. \tag{1.139}$$

Combining Equations 1.138 and 1.139:

$$a_{\pm} = S_{\mp}\mathcal{B}_{K_S^0K^+K^-}. \tag{1.140}$$

Using this relation along with Equation 1.126:

$$\frac{a_{\pm}}{a_D} = \frac{S_{\mp}}{S_F}. \tag{1.141}$$

Substituting this into Equation 1.136:

$$\frac{M_i^{\pm}}{S_{\mp}} = \frac{K_i \pm 2c_i\sqrt{K_i K_{-i}} + K_{-i}}{2S_F}. \tag{1.142}$$

The quantity $M_i^{\pm}$ is one of the key observables listed in Section 1.6.5.2. Measurements of $M_i^{\pm}$ and $K_{(-)i}$ can be used to calculate c_i.

Equation 1.142 is symmetric between bins i and $-i$, so

$$M_i^{\pm} = M_{-i}^{\pm}. \tag{1.143}$$

A practical consequence of this symmetry is that event yields in mirror-image bins can be combined, reducing the number of free parameters if a fit is performed.

1.6.5.4 Determining c_i and s_i using $K^0_S K^+K^-$ decays tagged with $K^0_S h^+h^-$

Decays in which $K^0_S K^+K^-$ is tagged with $K^0_S h^+h^-$ can be used to measure c_i and s_i. It is necessary to consider the quantum-correlated $D^0\overline{D}^0$ system as a whole; in particular, the distributions of events across both Dalitz planes must be determined. Following Equation 1.47, the decay amplitude of this system is:

$$A_{\text{corr}}(x, y, x'y') \equiv \frac{1}{\sqrt{2}}(A_D(x, y)A_D(y', x') - A_D(x', y')A_D(y, x)), \tag{1.144}$$

where (x, y) are the Dalitz plot coordinates associated with the $K^0_S K^+K^-$, and (x', y') are the coordinates associated with the opposite-side $K^0_S h^+h^-$. The partial decay width of the correlated system is:

$$\mathrm{d}\Gamma_{\text{corr}} = \frac{1}{2}\Big(a_{xy}^2 a_{yx}{}'^2 + a_{yx}^2 a_{xy}{}'^2 - 2a_{xy}a_{yx}{}'a_{yx}a_{xy}{}' \cos[(\delta_{xy} - \delta_{yx}) - (\delta_{xy}{}' - \delta_{yx}{}')]\Big)\,\mathrm{d}p\ , \tag{1.145}$$

where $\mathrm{d}p$ is an infinitesimal region of phase space.

The number of events expected in the i^{th} bin of the $K^0_S K^+K^-$ Dalitz plot and the j^{th}

bin of the $K^0_S h^+h^-$ Dalitz plot is:

$$M_{ij} = \frac{1}{2}a_{\rm corr}\int_{\mathcal{D}_i}\int_{\mathcal{D}_j}|A_D(x,y)A_D(y',x') - A_D(x',y')A_D(y,x)|^2\,{\rm d}x\,{\rm d}y\,{\rm d}x'\,{\rm d}y' \tag{1.146}$$

$$= \frac{1}{2}a_{\rm corr}(T_iT_{-j} + T_{-i}T_j - 2\sqrt{T_iT_{-j}T_{-i}T_j}(c_ic_j + s_is_j))$$

$$= \frac{a_{\rm corr}}{2a_D^2}(K_iK_{-j} + K_{-i}K_j - 2\sqrt{K_iK_{-j}K_{-i}K_j}(c_ic_j + s_is_j)), \tag{1.147}$$

where $a_{\rm corr}$ is a normalisation factor such that the quantity

$$\sum_{i=1}^{\mathcal{N}}\sum_{j=1}^{\mathcal{N}}(M_{ij} + M_{-ij} + M_{i-j} + M_{-i-j}) \tag{1.148}$$

is equal to the total number of events in which $K^0_S K^+K^-$ is tagged with $K^0_S h^+h^-$.

In order to determine $a_{\rm corr}/a_D^2$, we define

$$M_{\rm tot} = a_{\rm corr}\int|A_{\rm corr}(x,y,x',y')|^2\,{\rm d}x\,{\rm d}y\,{\rm d}x'\,{\rm d}y' \tag{1.149}$$

$$= N_{D^0\overline{D}^0}\frac{\int|A_{\rm corr}(x,y,x',y')|^2\,{\rm d}x\,{\rm d}y\,{\rm d}x'\,{\rm d}y'}{\int|A_{D^0\overline{D}^0}|^2\,{\rm d}p} \tag{1.150}$$

where $A_{D^0\overline{D}^0}$ is the total amplitude of *all* possible correlated $D^0\overline{D}^0$ decays, normalised such that $\int|A_{D^0\overline{D}^0}|^2\,{\rm d}p = 1$. From these relations we obtain

$$a_{\rm corr} = \frac{N_{D^0\overline{D}^0}}{\int|A_{D^0\overline{D}^0}|^2\,{\rm d}p}. \tag{1.151}$$

Furthermore, we define

$$K_{\rm tot} = a_D\int|A_D(x,y)|^2\,{\rm d}x\,{\rm d}y \tag{1.152}$$

$$= 2N_{D^0\overline{D}^0}\mathcal{B}_F\mathcal{B}_{K^0_SK^+K^-} \tag{1.153}$$

$$= 2N_{D^0\overline{D}^0}\frac{\int|A_F|^2\,{\rm d}p\int|A_D(x,y)|^2\,{\rm d}x\,{\rm d}y}{\int|A_{D^0\overline{D}^0}|^2\,{\rm d}p}, \tag{1.154}$$

where $\mathcal{B}_F$ is the branching fraction of D decays to the flavour state F and A_F is the decay amplitude of the process $D\to F$. To convert branching fractions into integrals of amplitude squared we have again used the general relation $\mathcal{B}_X \propto \int|A_X|^2\,{\rm d}p$. The division by $\int|A_{D^0\overline{D}^0}|^2\,{\rm d}p$ ensures correct normalisation. From these relations we obtain

$$a_D = \frac{2N_{D^0\overline{D}^0}\int|A_F|^2\,{\rm d}p}{\int|A_{D^0\overline{D}^0}|^2\,{\rm d}p}. \tag{1.155}$$

We then use Equations 1.151 and 1.155 to calculate:

$$\frac{a_{corr}}{a_D^2} = \frac{N_{D^0\overline{D}^0}}{\int |A_{D^0\overline{D}^0}|^2 \,\mathrm{d}p} \cdot \frac{[\int |A_{D^0\overline{D}^0}|^2 \,\mathrm{d}p]^2}{4N^2_{D^0\overline{D}^0}[\int |A_f|^2 \,\mathrm{d}p]^2} \tag{1.156}$$

$$= \frac{\int |A_{D^0\overline{D}^0}|^2 \,\mathrm{d}p}{4N_{D^0\overline{D}^0}[\int |A_f|^2 \,\mathrm{d}p]^2}$$

$$= \frac{1}{4N_{D^0\overline{D}^0}\mathcal{B}_F^2}. \tag{1.157}$$

We then substitute this ratio into Equation 1.147 to obtain

$$M_{ij} = \frac{1}{8N_{D^0\overline{D}^0}\mathcal{B}_F^2}(K_iK_{-j} + K_{-i}K_j - 2\sqrt{K_iK_{-j}K_{-i}K_j}(c_ic_j + s_is_j)) \tag{1.158}$$

$$= \frac{N_{D^0\overline{D}^0}}{2S_F^2}(K_iK_{-j} + K_{-i}K_j - 2\sqrt{K_iK_{-j}K_{-i}K_j}(c_ic_j + s_is_j)), \tag{1.159}$$

where we have used Equation 1.124 to equate the branching fraction with the number of single tags. The quantity M_{ij} is one of the key observables listed in Section 1.6.5.2. Measurements of M_{ij} and $K_{(-)i}$ can be used to calculate c_i and s_i.

Equation 1.158 can be used to derive the following identities:

$$M_{ij} = M_{-i-j}, \tag{1.160}$$

$$M_{-ij} = M_{i-j}. \tag{1.161}$$

As with the equivalence between M_i and M_{-i}, an experimental consequence of these relations is that certain bin yields can be combined.

1.6.5.5 Use of $D \to K^0_L K^+ K^-$ decays

In a sample of quantum correlated $D^0\overline{D}^0$ events a significant fraction of D mesons will decay to the final state $K^0_L K^+ K^-$. The analysis of the kinematic distributions of these decays provides greater experimental precision on the values of c_i and s_i when combined with measurements of $D \to K^0_S K^+ K^-$. The formalism describing $D \to K^0_L K^+ K^-$ decays is similar, but not identical, to that describing $D \to K^0_S K^+ K^-$.

To first order, $K^0_L K^+ K^-$ has the opposite $\mathcal{CP}$ to $K^0_S K^+ K^-$ because, neglecting $\mathcal{CP}$ violation, $\mathcal{CP}|K^0_S\rangle = +|K^0_S\rangle$ and $\mathcal{CP}|K^0_L\rangle = -|K^0_L\rangle$. This implies, for example, that the events in which $K^0_L K^+ K^-$ decays against $\mathcal{CP}\pm$ eigenstates will be distributed in a similar manner to events in which $K^0_S K^+ K^-$ decays against $\mathcal{CP}\mp$ eigenstates. The amplitude of the $D^0 \to K^0_S K^+ K^-$ decay can be expressed as:

$$\mathcal{A}(D^0 \to K^0_S K^+ K^-) = \frac{1}{\sqrt{2}}\left\{\mathcal{A}(D^0 \to \overline{K}^0 K^+ K^-) + \mathcal{A}(D^0 \to K^0 K^+ K^-)\right\}, \tag{1.162}$$

and the equivalent for $K^0_L K^+ K^-$ is:

$$\mathcal{A}(D^0 \to K^0_L K^+ K^-) = \frac{1}{\sqrt{2}} \left\{ \mathcal{A}(D^0 \to \overline{K}^0 K^+ K^-) - \mathcal{A}(D^0 \to K^0 K^+ K^-) \right\}. \tag{1.163}$$

The decay $D^0 \to K^0 K^+ K^-$ is doubly-Cabibbo-suppressed relative to the decay $D^0 \to \overline{K}^0 K^+ K^-$ (see Figure 1.8).

The decay amplitude of $D^0 \to K^0_{S,L} K^+ K^-$ can be expressed in terms of the different intermediate resonances through which the decay can occur. Let $a_0^{\pm} K^{\mp}$ represent all charged intermediate resonances and $f_0 K^0$ represent all neutral intermediate resonances. The amplitude of the Cabibbo-favoured D^0 decay expressed in terms of this basis is:

$$\mathcal{A}(D^0 \to \overline{K}^0 K^+ K^-) = \sum_i \alpha_i [a_0^+ K^-]_i + \sum_j \alpha_j [f_0 \overline{K}^0]_j \,, \tag{1.164}$$

and the amplitude of the doubly-Cabibbo-suppressed decay is:

$$\mathcal{A}(D^0 \to K^0 K^+ K^-) = \sum_i \beta_i [a_0^- K^+]_i + \sum_j \beta_j [f_0 K^0]_j \,, \tag{1.165}$$

where the α and β are multiplicative constants. The decay amplitudes of $D^0 \to K^0_S K^+ K^-$ and $D^0 \to K^0_L K^+ K^-$ are respectively:

$$\mathcal{A}(D^0 \to K^0_S K^+ K^-) = \frac{1}{\sqrt{2}} \Big\{ \sum_i \alpha_i [a_0^+ K^-]_i + \beta_i [a_0^- K^+]_i + \sum_j \alpha_j [f_0 \overline{K}^0]_j + \beta_j [f_0 K^0]_j \Big\}, \tag{1.166}$$

$$\mathcal{A}(D^0 \to K^0_L K^+ K^-) = \frac{1}{\sqrt{2}} \Big\{ \sum_i \alpha_i [a_0^+ K^-]_i - \beta_i [a_0^- K^+]_i + \sum_j \alpha_j [f_0 \overline{K}^0]_j - \beta_j [f_0 K^0]_j \Big\}. \tag{1.167}$$

Comparing Equations 1.166 and 1.167, we observe that the amplitude of the Cabibbo-favoured $D^0 \to a_0^+ K^-$ resonance is the same for $K^0_S K^+ K^-$ and $K^0_L K^+ K^-$, but the doubly-Cabibbo-suppressed $D^0 \to a_0^- K^+$ resonance has a relative phase shift of π.

The differences in the amplitudes of the neutral intermediate resonances for $K^0_S K^+ K^-$ and $K^0_L K^+ K^-$ are less straightforward. To proceed further, we consider the relative ampli-

tude between $D^0 \to K^0_S K^+K^-$ and $D^0 \to K^0_L K^+K^-$ decays:

$$\begin{aligned}\frac{\mathcal{A}(D^0 \to K^0_L K^+K^-)}{\mathcal{A}(D^0 \to K^0_S K^+K^-)} &= \frac{\mathcal{A}(D^0 \to \overline{K}^0 K^+K^-) - \mathcal{A}(D^0 \to K^0 K^+K^-)}{\mathcal{A}(D^0 \to \overline{K}^0 K^+K^-) + \mathcal{A}(D^0 \to K^0 K^+K^-)} \qquad (1.168)\\ &= \frac{1 - \mathcal{A}(D^0 \to K^0 K^+K^-)/\mathcal{A}(D^0 \to \overline{K}^0 K^+K^-)}{1 + \mathcal{A}(D^0 \to K^0 K^+K^-)/\mathcal{A}(D^0 \to \overline{K}^0 K^+K^-)} \\ &\simeq 1 - 2\mathcal{A}(D^0 \to K^0 K^+K^-)/\mathcal{A}(D^0 \to \overline{K}^0 K^+K^-) \\ &= 1 - 2r \cdot e^{i\alpha}, \qquad (1.169)\end{aligned}$$

where r and α are real numbers. We multiply the amplitudes of the neutral intermediate resonances for $D^0 \to K^0_S K^+K^-$ by this factor in order to determine the amplitudes of the equivalent neutral intermediate resonances for $D^0 \to K^0_L K^+K^-$. The quantity r is taken to be $\tan^2\theta_C$ and the completely unknown phase α is set to 0. The same quantities are used for all neutral intermediate resonances; further theoretical work would be required to estimate the values more precisely. More information about the relationship between the decay amplitudes of $D^0 \to K^0_S X$ and $D^0 \to K^0_L X$ can be found in Refs. [6, 54–56].

The modified intermediate resonances are used to produce signal Monte Carlo $D \to K^0_L K^+K^-$ decays as described in Section 3.5.1. To compute the systematic uncertainty from the assumptions made about the values of r and α, their values are varied as described in Section 4.5.5.

1.6.5.6 Determining c'_i and s'_i from $\mathcal{CP}$-tagged $K^0_L K^+K^-$ decays

The formalism for $\mathcal{CP}$-tagged $K^0_L K^+K^-$ decays is very similar to that for $\mathcal{CP}$-tagged $K^0_S K^+K^-$; in general, $\pm$ is changed to $\mp$. Henceforth all primed quantities relate to $K^0_L K^+K^-$. Following Equation 1.142, the number of events in the i^{th} bin of a $\mathcal{CP}$-tagged $K^0_L K^+K^-$ sample is:

$$\frac{M^{\pm\prime}_i}{S'_{\mp}} = \frac{K'_i \mp 2c'_i\sqrt{K'_i K'_{-i}} + K'_{-i}}{2S'_F}. \qquad (1.170)$$

The decay amplitude of $K^0_L K^+K^-$ against $K^0_S h^+h^-$ [10] is:

$$\begin{aligned}A_{\text{corr}}(x, y, x', y') &= \frac{1}{\sqrt{2}}(A_D(K^0_S h^+h^-)A_D{}'(K^0_L K^+K^-) - A_D{}'(K^0_L K^+K^-)A_D(K^0_S h^+h^-)) \\ &= -(A_D(x, y)A_D{}'(y', x') + A_D{}'(x', y')A_D(y, x)). \qquad (1.171)\end{aligned}$$

[10] The formalism for $K^0_S K^+K^-$ tagged with $K^0_L \pi^+\pi^-$ is the same as that for $K^0_S K^+K^-$ against $K^0_L K^+K^-$.

The partial decay width of these decays is:

$$\begin{aligned}\mathrm{d}\Gamma_{\mathrm{corr}} = \frac{1}{2}\Big(&a_{xy}^2 {a_{yx}}'^2 + a_{yx}^2 {a_{xy}}'^2 \\ &+ 2a_{xy}{a_{yx}}' a_{yx}{a_{xy}}' \cos[(\delta_{xy} - \delta_{yx}) - (\delta_{xy}' - \delta_{yx}')]\Big)\mathrm{d}p. \end{aligned} \tag{1.172}$$

The number of events expected in the j^{th} bin of the $K^0_L K^+K^-$ Dalitz plot and the i^{th} bin of the $K^0_S h^+h^-$ Dalitz plot is:

$$\begin{aligned} M'_{ij} &= \frac{1}{2}a_{\mathrm{corr}} \int_{\mathcal{D}_i}\int_{\mathcal{D}_j} |A_D(x,y)A'_D(y',x') + A'_D(x',y')A_D(y,x)|^2 \,\mathrm{d}x\,\mathrm{d}y\,\mathrm{d}x'\,\mathrm{d}y' \qquad (1.173)\\ &= \frac{1}{2}a_{\mathrm{corr}}(T_iT'_{-j} + T_{-i}T'_j + 2\sqrt{T_iT'_{-j}T_{-i}T'_j}(c_ic'_j + s_is'_j)) \\ &= \frac{a_{\mathrm{corr}}}{2a_Da'_D}(K_iK'_{-j} + K_{-i}K'_j + 2\sqrt{K_{-i}K'_{-j}K_{-i}K'_j}(c_ic'_j + s_is'_j)) \\ &= \frac{N_{D^0\bar{D}^0}}{2S_FS'_F}(K_iK'_{-j} + K_{-i}K'_j + 2\sqrt{K_{-i}K'_{-j}K_{-i}K'_j}(c_ic'_j + s_is'_j)). \qquad (1.174)\end{aligned}$$

It is evident that analysis of the event distributions of $K^0_L K^+K^-$ against $K^0_S h^+h^-$ enables further information about c_i and s_i to be obtained. The quantities $M_i^{\pm\prime}$ and M'_{ij} are two of the key observables listed in Section 1.6.5.2.

1.6.5.7 $\mathcal{CP}$-odd component under the $K^0_{S,L}\phi$ resonance

The neutral resonance $K^0_S\phi(K^+K^-)$ is a $\mathcal{CP}$-odd eigenstate of spin 1. It is interesting to determine the fraction of $\mathcal{CP}$-odd events that lie near to the peak of this resonance; if this fraction is not equal to one, there are additional components (e.g. an S-wave resonance or a nonresonant decay) contributing to the decay amplitude. This is important information for assessing the purity of the '$\mathcal{CP}-$' assignment when experiments use $K^0_S\phi$ as a $\mathcal{CP}$-odd decay.

Using Equation 1.143 we observe that $M_i^+ + M_i^- = M_{-i}^+ + M_{-i}^-$ for all bins. Furthermore, this sum is proportional to $K_i + K_{-i}$ (see Equation 1.142) which itself is proportional to the total decay rate of $D{\to}K^0_S K^+K^-$ in this bin. We define a bin on the $m^2_{K^+K^-}$ projection that encompasses a narrow region around the nominal value of m^2_ϕ. The number of $\mathcal{CP}$-odd events in this bin is $M_i^- + M_{-i}^-$. The fraction of $\mathcal{CP}$-odd $D^0{\to}K^0_S K^+K^-$ decays in this bin is therefore:

$$\mathcal{F}_- = \frac{M_i^- + M_{-i}^-}{M_i^- + M_{-i}^- + M_i^+ + M_{-i}^+}. \tag{1.175}$$

1.6.5.8 Summary

We now summarise the key measurements that can be made in a binned analysis of the $D{\to}K^0_S K^+K^-$ Dalitz plane. The yield of $K^0_S K^+K^-$ ($K^0_L K^+K^-$) tagged with $\mathcal{CP}$ eigenstates

in each bin can be used to measure c_i (c_i'), as described in Equations 1.142 and 1.170. The yield of $K^0_S K^+ K^-$ tagged with $K^0_S h^+ h^-$ in each bin can be used to measure both c_i and s_i, following Equation 1.158. The yield of $K^0_S K^+ K^-$ tagged with $K^0_L K^+ K^-$ in each bin is sensitive to c_i, s_i, c_i' and s_i' as shown in Equation 1.173. Finally, $\mathcal{CP}$-tagged events can be used to determine the fraction of $\mathcal{CP}$-odd $D^0 \to K^0_S K^+ K^-$ decays in the region near the ϕ resonance as described in Equation 1.175.

Chapter 2

The CLEO-c detector

2.1 Introduction

The CLEO-c detector was located in Cornell University, Ithaca, New York, USA. It was the latest in a series of detectors dating back to the 1970s. Particle collisions were provided by the Cornell Electron Storage Ring (CESR), an electron-positron collider. Earlier versions of the CLEO detector (numbered I, I.5, II, II.5 and III) ran at or near the $\Upsilon(4S)$ resonance and pioneered investigations into several key areas of flavour physics such as the flavour-changing neutral current $b \to s\gamma$ [57, 58]. In 2002, when it became clear that CLEO would not be able to compete with the much higher-luminosity B-factories, the decision was made to lower the beam energy and modify the detector into a configuration dedicated to charm physics. CLEO-c produced an array of impressive results in areas such as CKM metrology, charmonium spectroscopy and precision tests of lattice QCD.

In this chapter we outline the basic operation of CESR and describe the various subdetectors that comprise CLEO-c. The main source of reference on the detector operation and performance is Ref. [59]. Information on CLEO-III, which shared many common features with CLEO-c, can be found in Refs. [60, 61].

2.2 CESR

Particles were accelerated to the desired energy in three machines: a linear accelerator (LINAC), a synchrotron and the storage ring CESR. The circumference of CESR was 768 m. The three stages of acceleration are shown schematically in Figure 2.1.

The 30 m long LINAC produced electrons with a 120 kV electron gun. The electrons were accelerated up to 300 MeV using low-frequency RF cavities. A tungsten target could be inserted into the beam; electrons incident upon this target produced showers consisting

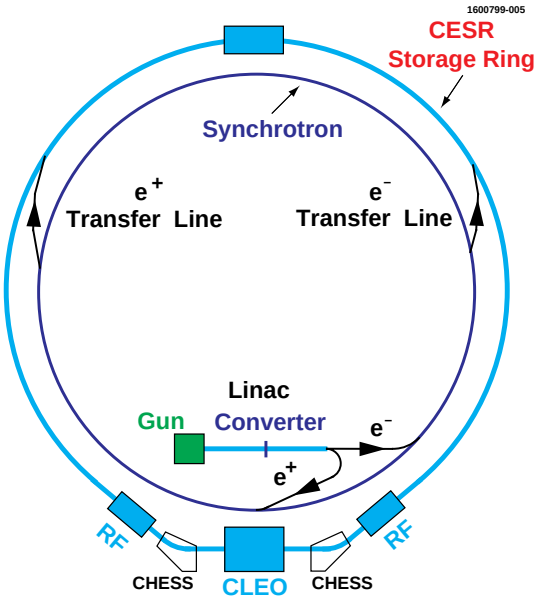

Figure 2.1: A schematic of CESR showing the constituent accelerators and the location of the CLEO detector.

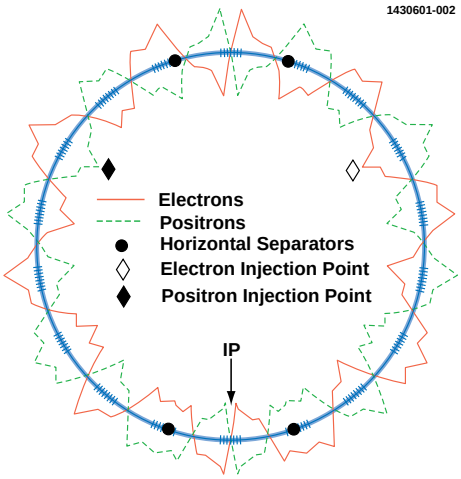

Figure 2.2: A schematic of CESR showing exaggerated pretzel orbits.

of a variety of particles including positrons. The positrons were captured and accelerated to 160 MeV. Two transfer lines were used to pass the electrons and positrons of specific momenta into the synchrotron.

The purpose of the synchrotron was to increase the energy of the particles from LINAC to CESR energies. Fully accelerated particles were injected from the synchrotron into CESR using fast kicker magnets. Both the synchrotron and CESR contained dipole magnets to control the beam direction, quadrupoles for focusing and defocusing the beam, and sextupoles to correct for chromatic effects.

Particles injected into CESR were grouped in bunches approximately 1 cm long. The bunches were further grouped in *trains*. Each train consisted of between three and five bunches separated by 14 ns. There were usually eight or nine trains in the ring, each separated by about 240 ns. Bunches collided at the interaction point (IP). To avoid undesired collisions at other locations around the ring the bunches were arranged in *pretzel* orbits. Electrostatic separators were placed close to the interaction point and imparted horizontal kicks in opposite directions for electrons and positrons. Figure 2.2 shows an exaggerated schematic of pretzel orbits.

Even when the bunches were arranged in pretzel orbits, collisions could have occurred at the point of the ring opposite the IP. Additional electrostatic separators were therefore placed near that point to deflect the beams in opposite vertical directions.

The collider was initially designed to run at a centre-of-mass energy between 9 and 16 GeV to enable it to reach the heavy Υ resonances. In this regime, *radiation damping* ensured the emittance of the beam remained low. Radiation damping occurs when energy

lost via synchrotron radiation reduces the transverse momentum of the beam. The lost energy is replaced using superconducting RF cavities. When the focus of the experiment was shifted to charm studies, with a centre-of-mass energy of approximately 4 GeV, the radiation damping became less effective because the intensity of synchrotron radiation has an E^4 dependence. Therefore additional radiation was induced with 12 *wiggler* magnets, which had alternating vertical magnetic fields and caused the beam particles to oscillate horizontally. The energy spread of particles in the beam was approximately 1.5 MeV which corresponds to a spread in centre-of-mass energy of approximately 2.1 MeV.

The instantaneous luminosity achieved by CESR in the CLEO-c era was $\mathcal{O}(10^{31})$ cm^{-2} s^{-1}.

2.3 CLEO-c

CLEO-c was a symmetric detector covering approximately 93% of the solid angle. Its subdetectors were designed to measure kinematic properties of detected particles and distinguish between different particle species. Figure 2.3 shows a cutaway view of the detector with the subdetectors labelled, and Figure 2.4 shows a vertical section of one quadrant of the detector. In the following sections we outline features of each subdetector and additionally describe the trigger and data acquisition (DAQ) systems.

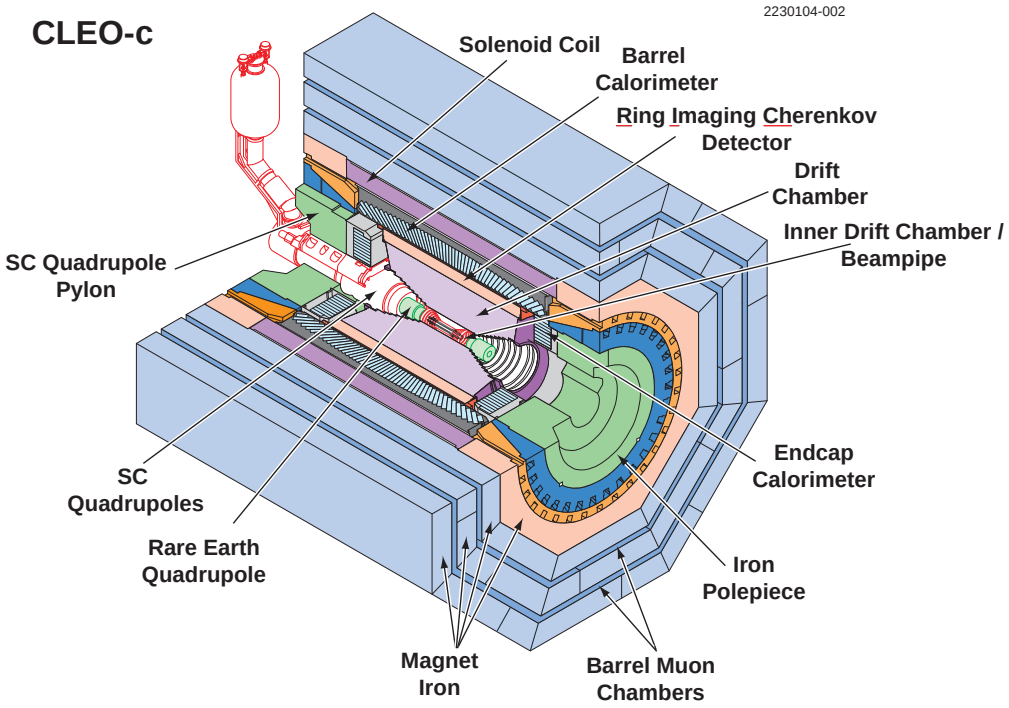

Figure 2.3: A cutaway view of the CLEO-c detector with components labelled.

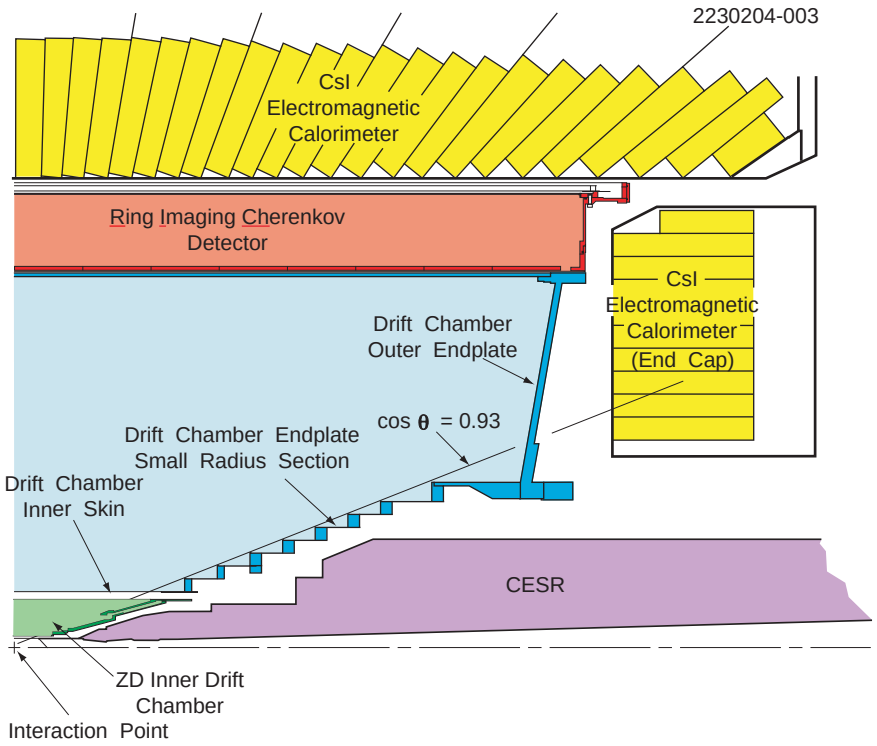

Figure 2.4: A vertical section of one quadrant of the CLEO-c detector.

2.3.1 Coordinate system

Two coordinate systems can be used to describe the positions of objects within CLEO-c. The first is a right-handed Cartesian coordinate system in which the z axis points along the direction of motion of positrons in the ring, the y axis points vertically upwards, and the x axis points outwards from centre of the ring. The second is a spherical coordinate system with the same z direction as the Cartesian system. The polar angle θ is 0° along $+z$ and 180° along $-z$, and the azimuthal angle ϕ is 0° along $+x$ and 90° along $+y$.

2.3.2 Tracking systems

The tracking systems in CLEO-c were designed to determine the trajectories and energy losses of incident charged particles. Two concentric cylindrical tracking systems were used in CLEO-c: the ZD (inner Drift chamber) and DR (outer DRift chamber) [62, 63]. In total, the tracking systems covered about 93% of 4π. The ZD was the inner of the two and replaced the silicon vertex detector that had been used in CLEO III. Both were located in a 1 Tesla magnetic field generated by a superconducting solenoid. Charged particles' trajectories were consequently curved in the $x - y$ plane. The ZD and DR both contained a 60%:40% mix of helium and propane.

The sensory equipment used in both tracking detectors was divided into approximately square *cells*. Each cell consisted of a *sense wire* surrounded by eight parallel *field wires*.

In the ZD the cell side was 10 mm, whereas it was 14 mm in the DR. The sense wires were constructed from gold-plated tungsten and had a radius of 20 µm; the field wires were constructed from gold-plated aluminium and had a radius of 110 µm. The potential difference between the sense wire and the field wires was 2.1 kV in the ZD and 1.9 kV in the DR.

The ZD covered the region 4.1–11.7 cm from the beamline and consisted of 300 sense wires in six layers. The layers were arranged approximately parallel to the z axis but were offset by a stereo angle (12–15°) in order to measure the trajectory of particles along the z direction. The inner three layers had an opposite stereo angle to the outer three layers. The momentum resolution of the ZD, σ_p/p, was about 0.4% for charged particles at normal incidence. The ZD was the most effective of all the subdetectors at detecting low-momentum particles.

The DR covered the region 13.2–82.0 cm from the beamline and consisted of 9796 sense wires. The DR was divided into two sections. The inner *axial* section consisted of 16 layers of sense wires parallel to the z axis and the outer *stereo* section consisted of 31 layers of sense wires that were offset from the z axis by stereo angles (1.2–1.7°). The layers in the stereo section were organised into eight *superlayers* consisting of four layers each, except the outer superlayer that contained three. The stereo angle of the layers in each superlayer was the same, and the angles alternated between the superlayers. The outer radial wall of the DR was lined with segmented cathode pads. These helped to constrain the track parameters further and hence improve the spatial resolution in the z direction.

The overall positional resolution of the tracking detectors was about 100 µm. The momentum resolution σ_p/p was about 0.6% for 1 GeV/c tracks that traversed every layer of the ZD and DR.

2.3.2.1 Particle detection

The trajectory of charged particles that passed through the tracking systems could be determined by searching for signals deposited in the sense wires. The charged particles caused the gas in the drift chamber to ionise, liberating electrons that drifted towards a sense wire due to the electric and magnetic fields present in the chamber. The strong electric field near the anode caused the electrons to ionise the gas further, creating an avalanche with an amplified signal that could be detected. The time at which the avalanche occurred was determined and, along with information about bunch crossing times from the detector, could be used to calculate the time taken for the initial electron to reach the sense wire. The nominal time for an electron to reach the sense wire as a function of its position in the cell was known, so the distance of closest approach of the parent particle to the sense wire could be determined. Information from all cells that recorded an avalanche could be used to determine the

trajectory of the charged particle. A Kalman filter [64] was used to determine the best-fit trajectory of the particle, accounting for energy loss.

2.3.2.2 Particle identification

The tracking stations could be used to aid particle identification by determining the energy loss per unit length, $\mathrm{d}E/\mathrm{d}x$, of a charged particle in the gas. The $\mathrm{d}E/\mathrm{d}x$ of an incident particle was determined by measuring the pulse height of the avalanche created by the particle. The Bethe equation [11] was used to convert the $\mathrm{d}E/\mathrm{d}x$ to an estimated velocity. When combined with a measurement of the particle momentum ($|\mathbf{p}|$) this enabled a determination of the mass of the particle.

The distribution of events on the ($|\mathbf{p}|$, $\mathrm{d}E/\mathrm{d}x$) plane for difference particle species is shown in Figure 2.5. Given a track with particular $|\mathbf{p}|$ and $\mathrm{d}E/\mathrm{d}x$, the number of standard

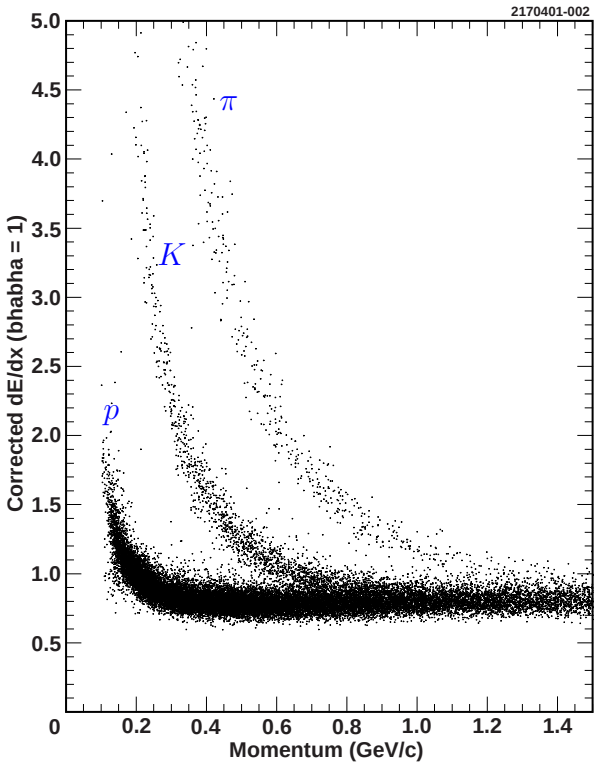

Figure 2.5: ($|\mathbf{p}|$, $\mathrm{d}E/\mathrm{d}x$) plane for various particle species (p, K and π). The $\mathrm{d}E/\mathrm{d}x$ scale has been normalised such that it is 1 for electrons and positrons from Bhabha events.

deviations (ρ) between the measured values and the values expected for each potential particle species could be computed. The relative likelihood between two species A and B is encapsulated as a $\Delta\chi^2$ term:

$$\Delta\chi^2_{\mathrm{d}E/\mathrm{d}x} = \rho_A^2 - \rho_B^2 \tag{2.1}$$

where a value of $\Delta\chi^2_{\mathrm{d}E/\mathrm{d}x}$ less than zero favours hypothesis A. This method was only effective to identify particles with momenta $\lesssim 700$ MeV/c; above that there was not sufficient discriminating power between different species.

2.3.3 Ring imaging Cherenkov (RICH) detector

CLEO-c was equipped with a Ring Imaging CHerenkov (RICH) detector [65]. The basic operating principle of a RICH is that a charged particle travelling faster than the speed of light in a medium emits a cone of Cherenkov light. The Cherenkov light is incident upon photosensitive material and is detected as a ring of hits. The opening angle of the Cherenkov light (θ_{Ch}) is dependent upon the velocity of the particle (v) and the refractive index of the medium (n):

$$\cos(\theta_{\mathrm{Ch}}) = \frac{c}{nv} \tag{2.2}$$

$$= \frac{1}{n}\sqrt{1+\left(\frac{mc}{|\mathbf{p}|}\right)^2}, \tag{2.3}$$

where m and $\mathbf{p}$ are respectively the mass and momentum of the particle. The maximum Cherenkov angle is thus equal to $1/n$. The velocity of the particle can be inferred from the radius of the ring. This can be combined with a momentum measurement to determine the most likely particle species.

The RICH was located outside the DR and covered about 83% of the total solid angle. A schematic of the RICH is shown in Figure 2.6.

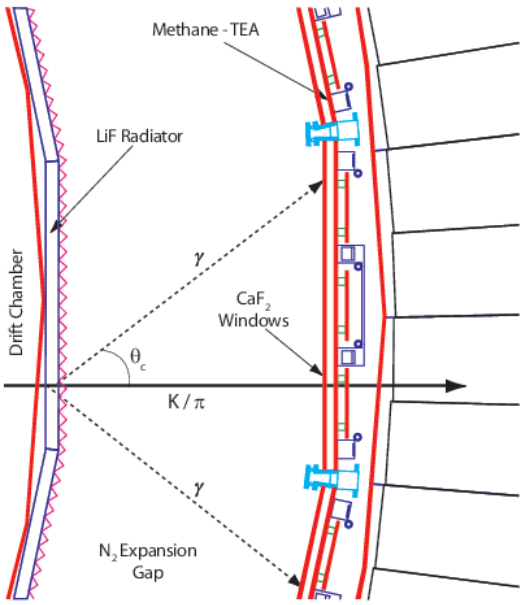

Figure 2.6: A cross section of the CLEO-c RICH detector. The solid black arrow shows the path of a charged particle and the dashed arrows are emitted Cherenkov light.

The inner surface of the RICH was covered with 1 cm thick LiF crystals with a refractive index of 1.5, so the maximum opening angle of the light cone was 48°. The crystals close to the interaction region were produced with a 'sawtooth' pattern at their surfaces. As illus-

trated in Figure 2.7, this reduced the possibility of total internal reflection that could occur when charged particles were incident approximately normal to the surface of the crystal. It was not necessary to use the sawtooth pattern further away from the interaction point because total internal reflection was less likely to occur.

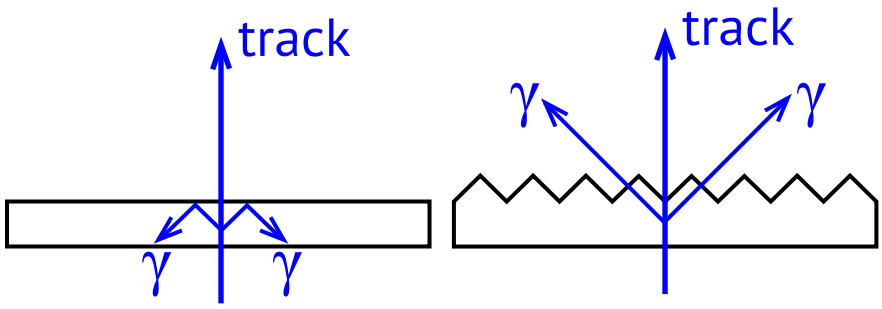

Figure 2.7: The effect of the sawtooth pattern on LiF crystals in the RICH. The left-hand diagram shows a track normally incident on a flat crystal, for which the Cherenkov light is totally internally reflected. The right-hand diagram shows the same situation for a crystal with a sawtooth surface. Total internal reflection no longer occurs.

Photons generated in the crystals then passed through an approximately 16 cm N_2 expansion gap that ensured the cone of Cherenkov light would be large enough to be measurable. The photons then passed through a CaF_2 window into a region containing a gaseous mixture of methane and triethylamine (TEA). The photoelectrons produced by the ionisation of this gas were amplified in a multiwire proportional chamber and the resulting charge was detected by 7.5 mm $\times$ 8 mm cathode pads. A two-dimensional image of the resulting avalanches could be inspected to locate Cherenkov rings.

The likelihood that a ring was produced by a particular particle species was determined by considering the Cherenkov photons that were positioned within five standard deviations of the expected ring size for that species. The structure of the RICH detector led to ambiguities in the possible optical paths taken by the photons. Each possible optical path was weighted by the probability P_{opt}, calculated by determining the path length and taking the refractive indices of the gases into account. The likelihood was then constructed as follows:

$$\mathcal{L}_h = \prod_{j=1}^{n_\gamma} \left\{ P_{\text{bkg}} + \sum_{\text{opt}} P_{\text{opt}}^j \cdot P_{\text{sig}} \left(\theta_\gamma^{\text{opt},j} | \theta_{\text{exp}}^h, \sigma_\theta^{\text{opt},j} \right) \right\}, \tag{2.4}$$

where h is the hypothesised particle species, n_γ is the number of Cherenkov photons considered, P_{bkg} is the background probability, P_{sig} is the signal probability, θ_{exp}^h is the expected Cherenkov angle for species h, $\theta_\gamma^{\text{opt},j}$ is the observed angle for photon j given optical path 'opt' and $\sigma_\theta^{\text{opt},j}$ is the uncertainty on this quantity. The resulting likelihood $\mathcal{L}$ was converted to an effective $\chi^2 = -2\ln(\mathcal{L})$. The difference between likelihoods for pairs of species was

used to evaluate the most likely species. Again considering species A and B:

$$\Delta\chi^2_{RICH} = -2\ln(\mathcal{L}_A) + 2\ln(\mathcal{L}_B) \tag{2.5}$$

where species A is favoured if $\Delta\chi^2_{RICH}$ is less than zero. Relative likelihoods between different particle species as a function of momentum are shown in Figure 2.8.

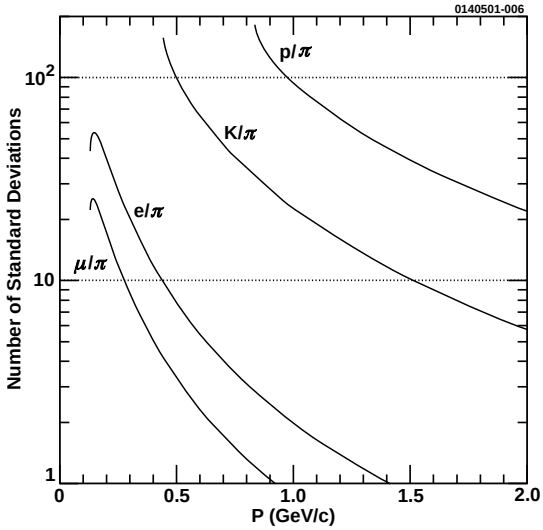

Figure 2.8: Separation in terms of the number of standard deviations between various particle hypotheses as a function of momentum that could be achieved by the CLEO-c RICH detector.

The RICH achieved 87% kaon ID efficiency with a 0.2% pion fake rate at $p = 0.9$ GeV/c. The PID performance of the RICH was complementary to that of the tracking systems. The RICH performance was degraded in the low-momentum regime, in which good dE/dx separation could be achieved, and vice versa. An overall $\Delta\chi^2$ term could be constructed using both RICH and dE/dx information:

$$\Delta\chi^2_{total} = \Delta\chi^2_{\mathrm{d}E/\mathrm{d}x} + \Delta\chi^2_{RICH} \tag{2.6}$$

$$= \rho^2_A - \rho^2_B - 2\ln(\mathcal{L}_A) + 2\ln(\mathcal{L}_B). \tag{2.7}$$

In the studies presented later the charged particle momenta typically lie in the range 0.1–1.0 GeV/c. Kaons and pions can thus be accurately distinguished using information from both the dE/dx and RICH systems.

2.3.4 Crystal calorimeter

The crystal calorimeter [66] was designed to measure the energy of electromagnetic showers. It consisted of 7800 scintillating crystals and covered about 93% of 4π. The crystals were composed of CsI doped with 0.1% thallium and were 5 cm × 5 cm × 30 cm in size. The crystals were located in the central barrel region and also in two endcaps, as shown in

Figure 2.4. The crystals in the barrel were aligned such that the long axis pointed towards a point slightly displaced from the interaction region. This reduced the chances of particles travelling in a gap between the crystals and hence being missed. The crystals in the endcap were all aligned with the z axis.

Four photodiodes were located at the end of each crystal in order to detect scintillation light. The Molière radius[1] of CsI is 3.8 cm, so most of the energy deposited by a shower in a crystal was deposited either in that crystal or its immediate neighbours.

Both photons and electrons produced relatively narrow deposits of energy in the calorimeter. Photon candidates were detected as deposits of energy that were not associated with a track. Two closely-spaced energy deposits were a signal of a π^0 or η decay to $\gamma\gamma$.

Hadronic interactions in the calorimeter material could produce secondary particles that travelled a significant distance before depositing energy. These *splitoff* shower candidates were isolated from reconstructed tracks and formed a significant background to photon signals.

In addition, photon conversions in the RICH resulted in false signals in the calorimeter. In Section 3.2.3.2 we describe how we reconstruct π^0 candidates taking splitoff showers into account.

The energy resolution of showers in regions of the barrel and endcaps was $\sigma_E/E \sim 5\%$ at $E = 100$ MeV.

2.3.5 Muon chambers

The CLEO-c detector contained chambers designed to detect muons. The chambers consisted of anode wires interleaved with layers of iron that were designed to stop other particles from penetrating. The chambers covered about 85% of 4π. The muon chambers were designed when CESR was running at higher energies than those used in CLEO-c. Muons produced at CLEO-c energies usually had insufficient momentum to penetrate the muon chambers, so the analysis presented in this thesis does not use any information from the muon chambers.

2.3.6 Trigger and data acquisition

The trigger system at CLEO-c was designed to select decays of interest while rejecting backgrounds. The trigger also provided timing information that was used in the reconstruction. The collision rate at CLEO-c was on average 80 Hz, so the trigger could easily accept almost all events, rejecting only backgrounds such as interactions between the beam and the beampipe. Events accepted by the trigger were stored by the data acquisition (DAQ) software.

[1]The Molière radius of a material characterises the lateral width of an electromagnetic cascade [67].

In order to ensure short processing times, events were not fully reconstructed in the trigger; the only information used was recorded by the DR and calorimeter. There were thus two main stages denoted the 'tracking' and 'calorimeter' triggers. Information from each trigger was used to determine the presence of showers and tracks in the event. If these objects matched a particular set of conditions, the event was accepted and stored unless the DAQ was in the process of writing a previous event.

The tracking trigger consisted of two components. One searched for tracks in the axial region of the DR and the other searched for tracks in the stereo region. The principle for both triggers was the same: search for particular hit patterns that could be generated by tracks that had a transverse momentum greater than 133 MeV/c (axial) or 167 MeV/c (stereo) and an impact parameter with respect to the interaction point less than 5 mm.

The calorimeter trigger determined the location and magnitude of energy deposits. Individual deposits could span multiple crystals, and the energy of a deposit in one particular cell may have been smaller than the threshold energy required to keep the event, so it was imperative that the software examined all of the deposits in neighbouring cells. The trigger therefore examined 8×8 blocks of crystals denoted *tiles*. A particular tile shared 4×4 blocks of crystals at each corner with its neighbouring tiles, so a signal in a particular crystal was detected in four tiles. The typical diameter of a signal was ~ 5 cells. An illustrative example of an energy deposition is shown in Figure 2.9.

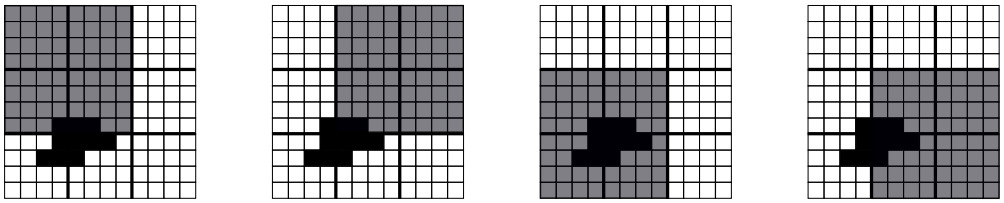

Figure 2.9: An energy deposition (solid black) in calorimeter tiles. The small squares are individual crystals; a tile (shown in grey) is composed of 8×8 block of crystals. Four overlapping tiles are considered; the signal is present in each of them.

Three minimum energy thresholds were used to decide whether or not to store a decay candidate. In the barrel the thresholds were 150, 500 and 1000 MeV, and in the endcap they were 150, 500 and 750 MeV.

In order to decide whether or not to keep an event, the trigger software determined whether or not the event met certain criteria. There were several different sets of criteria used, denoted *lines*, listed in Table 2.1. An event was stored if it passed one or more lines. In addition to searching for specific signals, there was a random trigger that arbitrarily accepted events at a rate of 1 kHz.

Bhabha scattering ($e^+e^- \to e^+e^-$) has a precisely determined cross-section and can be used to calculate the collider luminosity. A trigger line was designed to select events in which

Bhabha scattering left energy deposits in the calorimeter barrel. The acceptance rate of this line was approximately 20 Hz, used as a reference point for the other lines.

Name	Definition	Prescale	Relative rate
Hadronic	$(N_{\text{axial}} > 1)$ and $(N_{\text{CB}}^{\text{low}} > 0)$	1	0.41
μ-pair	Two back-to-back stereo tracks	1	1.40
Barrel Bhabha	Back to back high-E showers in CB	1	1.00
Endcap Bhabha	Back to back high-E showers in CE	1/8	0.23
Electron + track	$(N_{\text{axial}} > 0)$ and $(N_{\text{CB}}^{\text{med}} > 0)$	1	1.48
τ/Radiative	$(N_{\text{stereo}} > 1)$ and $(N_{\text{CB}}^{\text{low}} > 0)$	1	2.00
Two Track	$N_{\text{axial}} > 1$	1/10	0.69
Random	Random 1 kHz source	1/1000	0.05

Table 2.1: Trigger lines used in CLEO-c. The rate of each line is shown relative to the barrel Bhabha line. The quantity N indicates the number of showers or tracks required for the event to be accepted by a line. 'Stereo' and 'axial' refer to where charged particles were detected in the DR. 'CB' is the calorimeter barrel and 'CE' is the calorimeter endcap. 'Low', 'med' and 'high' refer to the energy thresholds for event acceptance in the calorimeter. The prescale of a line is the fraction of events considered by the line; the remainder are automatically rejected.

An event passing the trigger was sent to the DAQ. This DAQ took approximately 30 µs to record the event information and recorded events at 500 Hz. A typical event size was 25 kB and the data transfer bandwidth was 6 MB/s. The average dead time was 3%.

2.3.7 Reconstruction software

Events recorded by the DAQ were fully reconstructed using software known as Pass2. This software constructed and stored track and shower objects for further analysis, and determined $\mathrm{d}E/\mathrm{d}x$ and RICH PID information. It also determined calibration constants for each event.

2.4 Data collected

CLEO-c ran at several energies in the charmonium regime. A total of (818 ± 8) pb^{-1} of data were collected at a centre-of-mass energy of 3.77 GeV and (586 ± 6) pb^{-1} were recorded at a centre-of-mass energy of 4.17 GeV. The data collected at 3.77 GeV, consisting of $\psi(3770)$ decays to $D^0\overline{D}^0$ pairs, were used in the analysis described in this thesis. The cross section of $\psi(3770) \to D^0\overline{D}^0$ decays is equal to $(3.66 \pm 0.06 \pm 0.03)$ nb [68].

Ten sets of data were recorded at 3.77 GeV, numbered 31–33, 35–37 and 43–46. The integrated luminosity of each dataset is given in Table 2.2.

Dataset	$\int \mathcal{L}\,\mathrm{d}t$ (pb^{-1})	Dataset	$\int \mathcal{L}\,\mathrm{d}t$ (pb^{-1})
31	19.104	37	109.437
32	30.498	43	116.648
33	6.184	44	174.288
35	47.704	45	108.264
36	68.612	46	137.373

Table 2.2: The integrated luminosity of each dataset used in the study.

2.5 Monte Carlo data

Many samples of Monte Carlo ('MC') simulated data were produced at CLEO-c. Such samples are essential to determine event selection efficiencies and also to identify various sources of background.

The EvtGen [69] package was used to simulate e^+e^- collisions and the resulting propagation and decay of the products. The final state particles were then passed into the GEANT [70, 71] package. This simulates the passage of particles through the detector including material interactions, noise and bremsstrahlung. Random trigger information taken from collected data was merged with these events in order to increase the realism of the simulated events. Different calibration constants were used to generate MC samples in order to be representative of the total dataset.

The simulated detector responses were recorded in the format used to save real events obtained from the DAQ. Monte Carlo truth information was also stored in order to enable the determination of the origin of particular final state particles and showers. The saved events were run through Pass2 just as with real data.

In the analysis presented in this thesis we use many samples of 'signal' Monte Carlo, each containing only one simulated $D^0\overline{D}^0$ decay. Such samples are useful to determine the selection efficiency of the final states reconstructed in data. The generation of the signal MC samples is discussed in Section 3.5.1. We also use a 'generic' Monte Carlo sample produced centrally by CLEO-c that contains many different D decays (see Section 2.5.1).

2.5.1 Generic Monte Carlo sample

We use a sample of generic Monte Carlo data to estimate background yields and tune selection criteria. The generic sample contains both $D^0\overline{D}^0$ and D^+D^- events generated at the $\psi(3770)$ resonance. Each D decays to a final state with a probability equal to its measured branching fraction. The integrated luminosities of each Monte Carlo dataset are larger than those of the data; for datasets 31–33 and 35–37 (for brevity referred to as datasets 31–37), the integrated luminosity is ~ 30 times higher, and for datasets 43–46 the ratio is ~ 20.

The generic Monte Carlo sample was generated without simulating quantum correlations in the $D^0\overline{D}^0$ system. The population of events in certain regions of the $D\to K^0_{S,L}K^+K^-$ Dalitz plot will therefore be incorrectly enhanced or reduced compared to what would be seen in reality. The effect is especially pronounced for $\mathcal{CP}$-tagged $K^0_SK^+K^-$ decays. In order to mitigate this, events in the generic Monte Carlo sample are removed until the remaining sample has a kinematic distribution approximately equivalent to that expected in quantum-correlated data.

Furthermore, the intermediate resonances of the $D\to K^0_{S,L}K^+K^-$ decays were not simulated in the generic Monte Carlo, so events are generated uniformly over phase space rather than reflecting the resonant structure of the D decay. If we use the generic MC sample to determine background yields across the Dalitz plane they will therefore be inaccurate. Section 3.6.4 describes how this problem is averted.

2.5.1.1 Scaling yields in generic MC to yields in data

As described in Section 3.6 we use the generic Monte Carlo sample to estimate the prevalence of certain types of background in the data. In order to do this we scale the quantity of background reconstructed in the generic MC by the factor $f_{D^0\bar{D}^0}$:

$$f_{D^0\bar{D}^0} \equiv \frac{\int \mathcal{L}_{\text{data}}\,\mathrm{d}t}{\int \mathcal{L}_{\text{MC}}\,\mathrm{d}t} \times f_Q\,, \tag{2.8}$$

where f_Q is an extra factor that is necessary because of the removal of events during the process that mimics quantum correlations. The values of f_Q are 1/0.504 and 1/0.507 for datasets 31–37 and 43–46 respectively. The relation in Equation 2.8 is used for the sample of Monte Carlo that has been generated based on datasets 43–46. This is a 20× integrated luminosity sample so the MC-data scaling ratio is

$$f^{43-46}_{D^0\bar{D}^0} = \frac{1}{20} \times f^{43-46}_{Q} = \frac{1}{20} \times \frac{1}{0.507} = 0.0986. \tag{2.9}$$

However, for datasets 31–37 the Monte Carlo was generated with incorrect assumptions about the cross section and the ratio of $D^0\overline{D}^0$ pairs to D^+D^- pairs produced. In order to correct this, the number of $D\overline{D}$ pairs[2] in an external reference sample is used to calibrate the scaling. The integrated luminosity of datasets 31–37 is 0.2936 fb^{-1}, so the integrated luminosity of the Monte Carlo sample is 0.2936 fb^{-1} × 30 = 8.808 fb^{-1}. The cross section of the interaction $e^+e^- \to \psi(3770) \to D\overline{D}$ is 5.84 nb, resulting in a total of 51.44×10^6 $D\overline{D}$ pairs in the MC. The ratio of $D^0\overline{D}^0$ decays to D^+D^- generated in the Monte Carlo sample is 57.14 : 42.86. The number of $D^0\overline{D}^0$ pairs expected in the Monte Carlo is therefore

[2]In this instance $D\overline{D}$ indicates $D^0\overline{D}^0$ or D^+D^-.

29.39×10^6. The number of $D^0\overline{D}^0$ pairs counted in datasets 31–37 is $(1.031 \pm 0.015) \times 10^6$ [68]. As a result, the scaling factor between data and Monte Carlo is:

$$f_{D^0\bar{D}^0}^{31-37} = \frac{N_{D^0\bar{D}^0}^{\text{data}}}{N_{D^0\bar{D}^0}^{\text{MC}}} \times f_Q^{31-37} \tag{2.10}$$

$$= \frac{1.031 \times 10^6}{29.39 \times 10^6} \times \frac{1}{0.504}$$

$$= 0.0696. \tag{2.11}$$

Chapter 3

Reconstruction of $D \to K^0_{S,L} K^+ K^-$ decays at CLEO-c

3.1 Introduction

In this chapter we describe the reconstruction of $D \to K^0_{S,L} K^+ K^-$ decays using the 818 pb^{-1} of quantum-correlated $\psi(3770)$ data collected by CLEO-c. We reconstruct D decays to $K^0_{S,L} K^+ K^-$ that have been tagged[1] with many different final states, including the $\mathcal{CP}$ eigenstates that are central to the analysis. We must reconstruct the decay products of both the D^0 and the $\overline{D}^0$ in the event in order to obtain the largest possible amount of information. It is possible to reconstruct specific final states of both decaying D mesons with a high degree of confidence because the e^+e^- collisions lead to a relatively clean detector environment. Furthermore, the decay of the $\psi(3770)$ to $D^0\overline{D}^0$ occurs close to threshold, so there are no fragmentation particles.

The selection of fully-reconstructed events is described in Section 3.2.2. Because of the clean environment it is also possible to reconstruct D decays to final states in which one particle was not directly detected. To do this, the total four momentum of the detected particles is determined; when this is combined with the (known) beam energy, the four momentum and hence invariant mass of the missing particle can be deduced. Final states containing both K^0_L and ν_e are reconstructed using this method, described in detail in Section 3.2.3.

[1]The concept of tagging was introduced in Section 1.6.5.1. We further recall that the $D \to K^0_{S,L} K^+ K^-$ decay is defined as the 'signal-side' decay and the decay of the other D in the correlated pair is the 'opposite-side' decay.

3.2 Event selection

We apply various selection criteria ('cuts') to the data in order to remove background events while retaining sufficient quantities of signal. We cut on kinematic and geometrical quantities as well as the quality of particle reconstruction.

There are several stages to the reconstruction. The selected data have been centrally *skimmed* (preselected); the skim is a loose set of selection criteria designed to reduce the dataset to a manageable level. The skim also reconstructs many commonly-used final states, enabling the user to easily select all such decays in the dataset and combine them as appropriate. The final selection stage involves applying additional cuts in order to further separate signal from background.

The branching fraction of $D \to K^0_S K^+ K^-$ is approximately 6 times smaller than that of $D \to K^0_S \pi^+ \pi^-$, on which a very similar study has been performed [6, 7]. In order to select as many events as possible, we consider more opposite-side final states than in the $K^0_S \pi^+ \pi^-$ analysis.

3.2.1 Event preselection

CLEO-c software is used to initially select particles and combine them into composite final states. A large number of such final states have been defined in the software, including all of the fully-reconstructed decays considered in this analysis. During the initial reconstruction, standardised selection cuts are applied to the particles and their combinations. The CLEO-c software selects the following final state particles: $K^\pm$, $\pi^\pm$, π^0, η, η' and K^0_S. Additionally, the software reconstructs the parent D mesons. We now outline the default selection criteria used in the skimming procedure.

3.2.1.1 $K^\pm$, $\pi^\pm$

Charged kaon and pion tracks are required to lie in the momentum range 0.05–2.0 GeV/c. Cuts are applied to the impact parameter of the track, defined as the distance of closest approach of the track to the interaction point. The impact parameter cuts are designed to ensure that signal tracks emanate from the interaction point and to reject random combinatoric backgrounds. Two impact parameters are evaluated: z_0 in the z-direction and d_b in the $x - y$ plane. By default, $|d_b|$ must be less than 0.005 m and $|z_0|$ must be less than 0.05 m. The χ^2 of the track fit must be less than 100,000. The track must lie in the region $|\cos(\theta)| < 0.93$, where θ is the angle between the track and the beam axis. Finally, the track hit fraction $f_{\rm hit}$ must be at least 0.5. The hit fraction is defined as the number of hits recorded in the tracker divided by the number that should have been recorded given the

momentum and trajectory of the track.

We also use PID information to distinguish between charged pions and kaons. We require that the $\mathrm{d}E/\mathrm{d}x$ of a particular track is at most 3σ away from the $\mathrm{d}E/\mathrm{d}x$ expected for the hypothesised species, given the track momentum. Information from the RICH is also used if several criteria are fulfilled: $|\cos(\theta)| \leq 0.83$, $|\mathbf{p}| \geq 700$ MeV/c, both $\pi^{\pm}$ and $K^{\pm}$ hypotheses have been analysed, and there are at least three detected Cherenkov photons. If these criteria are all fulfilled, a combined log likelihood difference ($\Delta \log \mathcal{L}$) term is constructed from the $\mathrm{d}E/\mathrm{d}x$ and RICH information. Following Equation 2.6, the $\Delta \log \mathcal{L}$ for the kaon and pion hypotheses is:

$$\Delta \log \mathcal{L} \equiv \rho_{\pi}^2 - \rho_K^2 - 2 \log \mathcal{L}_{\pi} + 2 \log \mathcal{L}_K. \tag{3.1}$$

If this quantity is less (greater) than zero, the track is identified as a pion (kaon).

3.2.1.2 π^0, η

Neutral π^0 and η candidates are reconstructed by searching for their characteristic decay to a diphoton final state. The reconstructed invariant mass of the candidate must lie between 0 and 1,000 MeV/c^2. Furthermore, the magnitude of the pull mass m_p of the candidate must be less than 3. For π^0 candidates, the pull mass is defined as:

$$m_p \equiv \frac{|m_{\pi} - m_0|}{\sigma_m}, \tag{3.2}$$

where m_{π} is the measured π^0 mass, m_0 is the nominal π^0 mass and σ_m is the uncertainty on the measured mass. An equivalent cut is placed on η candidates, with the nominal mass changed appropriately. The χ^2 of the mass-constrained fit of the photons to the neutral candidate must be less than 10,000.

3.2.1.3 K_S^0

K_S^0 candidates are reconstructed by combining two oppositely-charged pions[2]. The invariant mass of the combination must lie within ± 30 MeV of the nominal K_S^0 mass. Furthermore, the χ^2 of the K_S^0 vertex fit must be less than 1,000.

3.2.1.4 η'

η' candidates are reconstructed by combining two oppositely-charged pions and an η that itself has been reconstructed from a diphoton pair. All η' candidates are required to lie within ± 10 MeV/c^2 of the nominal η' mass.

[2]The track quality and PID cuts listed in Section 3.2.1.1 are not applied to these pions.

3.2.1.5 *D*

D mesons are reconstructed by combining all of the relevant final-state particles. In order to ensure that the D has been correctly reconstructed, cuts are placed on two kinematic quantities. The first is the energy difference:

$$\Delta E \equiv E_D - E_{\text{beam}}\,, \tag{3.3}$$

where E_D is the reconstructed energy of the D candidate and E_{beam} is the beam energy. For correctly-reconstructed signal events ΔE is expected to equal zero. In the preselection we require $|\Delta E| < 0.1$ GeV.

A cut is also placed on the beam-constrained mass m_{bc} of the D:

$$m_{\text{bc}} \equiv \sqrt{E_{\text{beam}}^2/c^4 - \mathbf{p}_D^2/c^2}\,, \tag{3.4}$$

where p_D is the summed three-momentum of the final state daughters. In the preselection m_{bc} must be greater than 1.83 GeV/c^2.

3.2.1.6 Modification to standard preselection cuts

In order to select as many signal events as possible we relax some of the preselection criteria when selecting the $D \to K^0_S K^+ K^-$ final state. The modified critera are described below; for all other reconstructed final states we retain the default preselection cuts.

We loosen the impact parameter cuts that are applied to charged kaon candidates. Examining the impact parameter distribution in generic Monte Carlo data it is clear that more events can be gained with minimal extra background retention. We loosen the cut on $|d_b|$ from 0.005 m to 0.02 m and we loosen the cut on $|z_0|$ from 0.05 m to 0.2 m.

A significant number of $K^0_S K^+ K^-$ events are removed by the default cut of 0.5 on the hit fraction f_{hit} of charged kaons. Figure 3.1 shows the hit fraction for both signal and background events in a sample of generic Monte Carlo in which $K^0_S K^+ K^-$ has been tagged with $K^\pm \pi^\mp \pi^0$. It is clear that a non-negligible fraction of signal events are removed by this cut, so we loosen it from 0.5 to 0.0. Almost no extra background is retained.

In order to verify that these changes have been effective, we record the number of signal (S) and background (B) events selected in a sample of generic Monte Carlo and from those numbers determine the significance metric $S/\sqrt{S+B}$. We examine several high-statistics flavour-tagged samples of both $K^0_S K^+ K^-$ and $K^0_L K^+ K^-$. The results are presented in Table 3.1. For all final states, loosening the charged kaon cuts increases the significance.

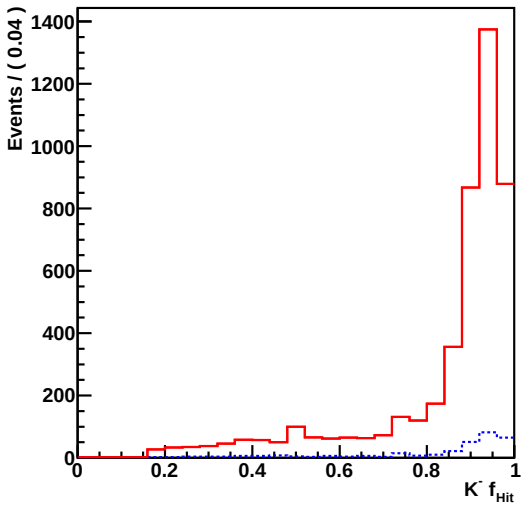

Figure 3.1: The value of $f_{\rm hit}$ for the negatively-charged kaon in decays of $K^0_S K^+ K^-$ tagged with $K^\pm\pi^\mp\pi^0$ in generic Monte Carlo data. Signal events are in solid red and background events are in dotted blue.

Final state	Signal yield		Background yield		$S/\sqrt{(S+B)}$	
	Loose	Default	Loose	Default	Loose	Default
$K^0_S K^+ K^-$ against $K^\pm\pi^\mp$	1852	1564	24	21	42.8	39.3
$K^0_S K^+ K^-$ against $K^\pm\pi^\mp\pi^0$	3974	3322	71	57	62.5	57.1
$K^0_S K^+ K^-$ against $K^\pm\pi^\mp\pi^+\pi^-$	2880	2416	59	50	53.1	48.7
$K^0_L K^+ K^-$ against $K^\pm\pi^\mp$	3512	3004	447	387	55.8	51.6
$K^0_L K^+ K^-$ against $K^\pm\pi^\mp\pi^0$	7518	6476	1283	1140	80.1	74.2
$K^0_L K^+ K^-$ against $K^\pm\pi^\mp\pi^+\pi^-$	3958	3402	651	568	58.3	54.0

Table 3.1: Effect of looser charged kaon cuts on the signal significance in generic Monte Carlo data.

3.2.2 Selection of fully-reconstructed events

After the preselection, we apply additional cuts to provide even greater separation between signal and background. In this section we describe the cuts applied to each final state particle in a fully-reconstructed decay.

3.2.2.1 Final selection of π^0 and η

We place an additional requirement on the electromagnetic showers associated with π^0 and η candidates. The energy deposited by each shower in the 3×3 grid of calorimeter cells centred on the shower must be equal to at least 99% of the energy deposited in the 5×5 grid of cells centred on the shower. This ensures that the showers are well-isolated.

Additionally, we require that the invariant mass cut of selected η candidates lies between 0.506 and 0.590 GeV/c^2. This reduces the large backgrounds due to splitoff showers (see Section 2.3.4) and $\pi^0 \to \gamma\gamma$ decays.

3.2.2.2 Selection of events containing K^0_S

We require that each K^0_S candidate lies within a mass window of 7.5 MeV/c^2 about the nominal K^0_S mass. In addition, we apply a cut on the three dimensional flight significance of the K^0_S, defined as the separation of the K^0_S decay vertex from the interaction region divided by the uncertainty assigned to the K^0_S flight distance. For all final states containing a K^0_S *except* $K^0_S K^+K^-$, we require that the minimum value of this quantity is 2.0. For the $K^0_S K^+K^-$ final state, the cut value is reduced to 0.5 based on the distribution in generic Monte Carlo data, shown in Figure 3.2. The flight significance of signal events is peaked around 0.5 because the relatively large invariant mass of the charged kaon pair results in less available momentum for the K^0_S, hence it flies less far. Out of all final states considered in this analysis, this property is unique to $K^0_S K^+K^-$.

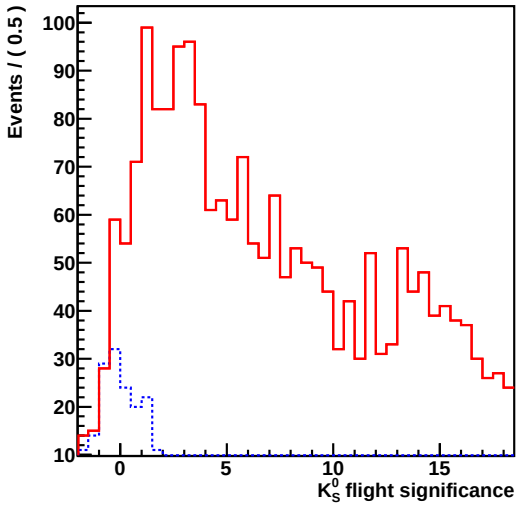

Figure 3.2: The K^0_S flight difference in decays of $K^0_S K^+K^-$ tagged with $K^\pm\pi^\mp\pi^0$ in generic Monte Carlo data. Signal events are in red and background in blue.

In order to determine whether this cut is useful, we determine the signal significance $S/\sqrt{S+B}$ in Monte Carlo for cuts on the flight significance of 0.5 and 2.0 for $K^0_S K^+K^-$ events tagged with different final states. The results are shown in Table 3.2; in each case, there is a slight improvement in the significance.

Final state	Signal yield		Background yield		$S/\sqrt{(S+B)}$	
	Loose	Default	Loose	Default	Loose	Default
$K^0_S K^+K^-$ against $K^\pm\pi^\mp$	1852	1706	24	7	42.8	41.2
$K^0_S K^+K^-$ against $K^\pm\pi^\mp\pi^0$	3974	3754	71	36	62.5	61.0
$K^0_S K^+K^-$ against $K^\pm\pi^\mp\pi^+\pi^-$	2880	2741	59	27	53.1	52.1

Table 3.2: Effect of looser K^0_S flight significance on the signal significance in generic Monte Carlo.

3.2.2.3 Selection of composite objects

Short-lived particles that are detected by reconstructing their daughters are known as *composite* particles[3]. In this analysis there are several such particles: the ω and η, which are reconstructed decaying to $\pi^+\pi^-\pi^0$, and the η', which is reconstructed decaying to $\pi^+\pi^-\eta$. In order to select composite particles we require each daughter to pass the relevant selection criteria detailed above. We fit the vertex using the FitEvt package [72] and ensure that the χ^2 of the fit is positive. Finally we apply an invariant mass cut to the composite particle. This greatly reduces the background from random combinations of objects that fake daughter candidates.

The invariant mass cut applied to the ω is $0.762 < m_\omega < 0.802$ GeV/c^2 and the cut applied to the η' is $0.950 < m_{\eta'} < 0.964$ GeV/c^2. The mass cut applied to the η was detailed in Section 3.2.2.1.

3.2.3 Selection of events containing missing particles

Several final states contain final state particles that are 'missing', either because they decay outside the CLEO-c detector, or do not interact at all (e.g. neutrinos). The excellent detector hermiticity makes it feasible to reconstruct such particles.

In the analysis described in this thesis the yields of all final states of a particular $\mathcal{CP}$ are summed. The inclusion of $\mathcal{CP}$- and flavour-tagged decays containing missing particles is very important; it significantly enhances the event yields and hence results in greater statistical precision on the final results.

There are two classes of event that contain missing particles: events containing a neutrino and events containing a K^0_L. Reconstruction of both types of event proceeds along broadly similar lines; the key point is that the missing four-momentum in the event is determined. We do not consider events containing more than one missing particle.

3.2.3.1 Selection of events containing a neutrino

To events in which $K^0_S K^+ K^-$ is tagged with $K^\pm e^\mp \nu_e$, we fully reconstruct the $K^0_S K^+ K^-$ candidate and require that both a kaon and an electron/positron of opposite charge to the kaon have been reconstructed in the remainder of the event. We then determine the quantity $U_{\rm miss}$, where

$$U_{\rm miss} \equiv E_{\rm miss} - c|\mathbf{p}_{\rm miss}| \tag{3.5}$$

where $E_{\rm miss}$ and $\mathbf{p}_{\rm miss}$ are respectively the missing energy and the magnitude of the missing three-momentum in the event. We determine those quantities using the four-momenta of the

[3]The K^0_S, π^0 and $\eta(\gamma\gamma)$ fall into this category but are considered separately.

fully-reconstructed particles and knowledge of the beam energy. For a correctly-identified event U_{miss} will be equal to zero. The potential background arising from fully-reconstructed hadronic events in which a charged hadron is mistaken for an electron or positron is not considered but is anticipated to be very low.

3.2.3.2 Selection of events containing K_L^0

We select several different final states containing a K_L^0: either $K_S^0 K^+ K^-$ tagged with a final state containing a K_L^0, or $K_L^0 K^+ K^-$ tagged with a fully-reconstructed state. As described in Section 1.6.5.5, information from reconstructed $K_L^0 K^+ K^-$ events can be used to constrain the extracted c_i and s_i further.

The underlying method is the same for both cases; the total four-momentum of the fully-reconstructed particles in the event is determined and the square of the missing invariant mass, m^2_{miss}, is then calculated:

$$m^2_{\text{miss}} \equiv E^2_{\text{miss}}/c^4 - \mathbf{p}^2_{\text{miss}}/c^2. \tag{3.6}$$

The squared missing mass is used to discriminate between signal and background. For correctly-reconstructed events m^2_{miss} will peak at the square of the mass of the K_L^0 ($\sim 0.25\ \text{GeV}/c^2$), so we select events based on a cut centred on this value. The use of different discriminating variables for events containing K_L^0 and ν_e is a convention.

We cannot use the CLEO-c software to automatically select final states containing K_L^0. We therefore manually reconstruct final states using the lists of tracks and showers that were collated for each event by the Pass2 software. We place the same requirements on charged and neutral particles that were outlined in Section 3.2.2; in addition, there are several other reconstruction techniques that significantly reduce the level of background selected.

In order to veto backgrounds to final states containing K_L^0 mesons, we only accept events in which the expected number of each type of final-state particle has been reconstructed. For example, when reconstructing $K_L^0 K^+ K^-$ we require two charged kaon-like tracks, no charged pion-like tracks and no neutral particles, and when reconstructing $K_L^0 \omega(\pi^+\pi^-\pi^0)$ we require two charged pion-like tracks, no charged kaon-like tracks and one π^0.

We apply a cut on calorimeter showers that are not directly associated with the final state under study. Each unassociated shower can be classified according to two variables: the energy of the shower E_s and the angle θ between that shower and the inferred missing momentum in the event. We use a two-dimensional cut on the $E_s - \cos(\theta)$ plane to classify each shower according to its position on the plane. We reject events in which at least one shower is classified as failing.

We observe that a very large proportion of signal events lie in the region $\cos(\theta) \geq 0.98$.

This is because a shower that is almost entirely aligned with the inferred K_L^0 momentum is more likely to be associated with that K_L^0. We therefore accept any event in this region. We apply a further cut, parameterised as follows:

$$E_s < \alpha - \frac{1}{\beta(\cos(\theta) - 0.98001)} \tag{3.7}$$

where α and β are mode-dependent. For each final state, the values of α and β are chosen to maximise the signal significance $S/\sqrt{S+B}$ on a sample of generic MC. The values obtained for each final state are presented in Table 3.3.

Final state	α (GeV)	β
$K_L^0\pi^0$	0.31	85000
$K_L^0\eta$	0.27	50000
$K_L^0\omega$	0.37	100000
$K_L^0\eta(\pi^+\pi^-\pi^0)$	0.37	100000
$K_L^0\pi^0\pi^0$	0.20	100000
$K_L^0\pi^+\pi^-$	0.25	100000
$K_L^0K^+K^-$	0.32	100000

Table 3.3: The values of the shower cut quantities α and β used for each final state.

Figure 3.3 shows the $E_s - \cos(\theta)$ plane for $K_L^0\pi^0$ and $K_L^0\eta$ and Figure 3.4 shows the $E_s - \cos(\theta)$ plane for $K_L^0K^+K^-$ and $K_L^0\pi^+\pi^-$.

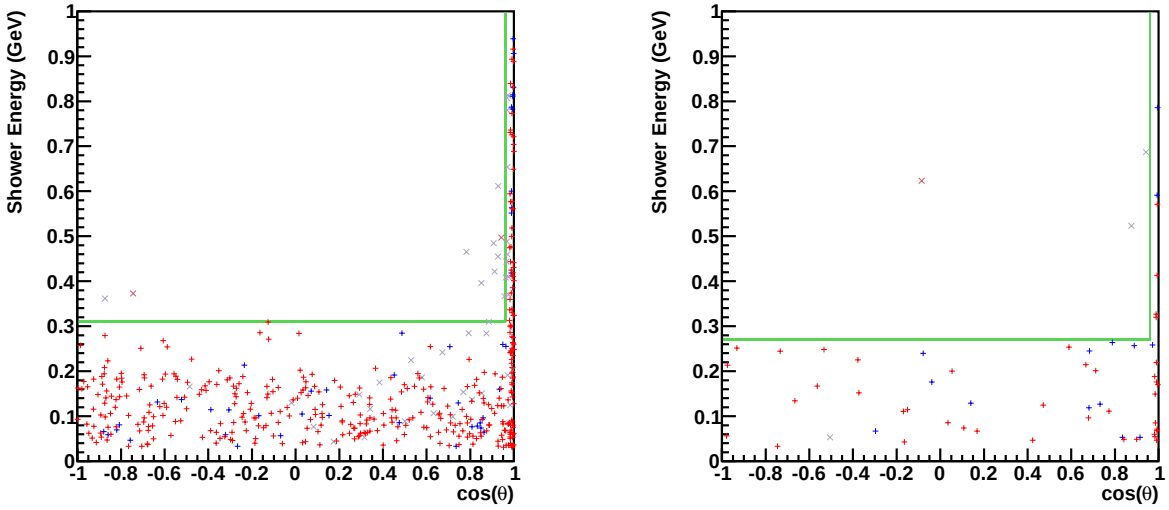

Figure 3.3: $E_s - \cos(\theta)$ plane for $K_L^0\pi^0$ (left) and $K_L^0\eta(\gamma\gamma)$ (right). The green line indicates the location of the cut on the plane; showers to the upper left of this line fail the cut. The red (blue) vertical crosses are signal (background) Monte Carlo events whose showers all pass the cut; the red (grey) diagonal crosses are signal (background) events that contain one or more failing shower.

We apply momentum cuts to π^0 and η candidates in order to reduce backgrounds further. The momentum cuts vary depending on the mode reconstructed:

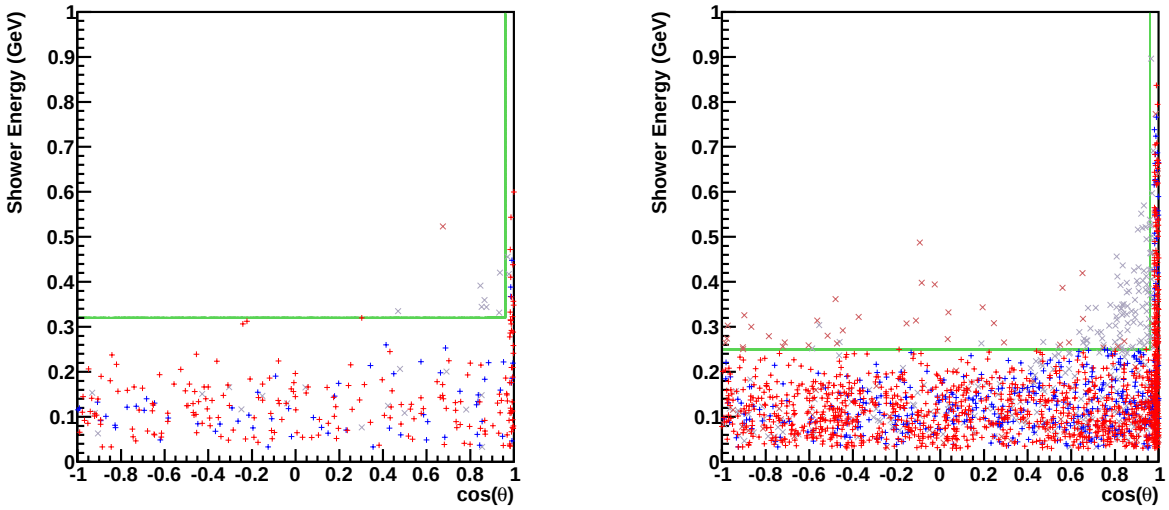

Figure 3.4: $E_s - \cos(\theta)$ plane for $K^0_L K^+ K^-$ (left) and $K^0_L \pi^+ \pi^-$ (right). The symbols indicate the same as in Figure 3.3.

- $K^0_L \pi^0$: the momentum of the π^0 is constrained to lie within $0.75 - 1.00$ GeV/c;
- $K^0_L \eta(\gamma\gamma)$: the momentum of the η is constrained to lie within $0.60 - 1.00$ GeV/c;
- $K^0_L \omega(\pi^+\pi^-\pi^0)$, $K^0_L \eta(\pi^+\pi^-\pi^0)$, $K^0_L \eta'(\pi^+\pi^-\eta)$: the momentum of the π^0/η emitted in the decay of the resonance is constrained to lie within $0.20 - 0.60$ GeV/c;
- $K^0_L \pi^0 \pi^0$: the momentum of each π^0 is constrained to lie within $0.5 - 0.8$ GeV/c.

When reconstructing $K^0_L K^+ K^-$ events we observe a large $K^\pm e^\mp \nu_e$ background at low values of $m^2_{\rm miss}$. In order to reduce the size of this background we determine whether either of the charged tracks is identified as an electron by the CLEO-c software. If so, we reject the event.

3.2.3.3 Selection of neutral particles in K^0_L final states

Neutral particles (π^0 and η) are intrinsically more challenging to reconstruct than charged particles. Their presence must be inferred by detecting two daughter photons (ignoring for the moment decays of η to $\pi^+\pi^-\pi^0$) which are reconstructed as calorimeter showers.

As an example, we consider a final state containing a K^0_L and one or more π^0; a similar procedure occurs for final states containing η. The signal-side $K^0_S K^+ K^-$ decay has been fully reconstructed. We determine a list of the reconstructed π^0 candidates in the event and also a list of the calorimeter showers that are not directly associated with the $K^0_S K^+ K^-$. A diagram showing an example of the selection procedure is shown in Figure 3.5. Stages 1–4 of the diagram are described below.

At stage 1, a list of π^0 candidates is created by looping over all π^0 candidates present in the event and admitting any candidate that passes the following criteria:

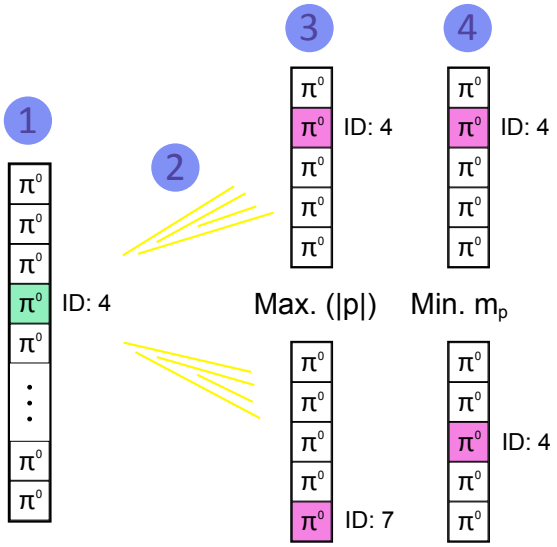

Figure 3.5: A diagram of the selection procedure for π^0 candidates. Stages 1–4 are explained in the main text.

- Both calorimeter showers associated with this π^0 are present in the list of showers not associated with the signal-side $K^0_S K^+ K^-$.
- The magnitude of the π^0 pull mass, defined in Section 3.2.1.2, is less than 3.
- The π^0 momentum is greater than 0.2 GeV/c. This cut removes a large background consisting of low-momentum π^0 candidates.

Each π^0 in this list is examined in turn. Each has a numerical identifier assigned by the CLEO-c software; the example in Figure 3.5 has an identifier of 4 (chosen randomly for illustration).

At stage 2, the high- and low-energy showers of the π^0 under study (for clarity denoted the 'initial' π^0) are examined. Two further lists of π^0 candidates are created, one for each shower (the lists are consequently denoted the 'high-energy' and 'low-energy' lists). All π^0 candidates in the list created at stage 1 are studied, excepting the initial π^0. If a π^0 candidate is associated to the high- (low-) energy shower it is added to the high- (low-) energy list.

At stage 3, the identifiers of the π^0 mesons with the highest momenta in the high-energy and low-energy lists are determined. In Figure 3.5 the identifiers are respectively 4 and 7.

At stage 4, the identifier of the π^0 with the lowest pull mass in the high-energy list is determined; again, its identifier is 4. The identifier of the π^0 with the lowest pull mass in the low-energy list is also 4 in this example.

Four π^0 identifiers have therefore been determined. If at least three out of four of these identifiers are equal to the identifier of the initial π^0, the initial π^0 is added to the list of 'unique' π^0 candidates. In the example given in Figure 3.5, three of the four π^0 identifiers are 4, which corresponds to the identifier of the initial π^0. The initial π^0 is therefore classed as a 'unique' π^0. Requiring all four identifiers to be the same is too stringent; there are

sometimes occurrences in which another π^0 fits one or more of the four criteria better than the original. However, the requirement of at least three is sufficiently robust to discount most of these cases. The total number of unique π^0 and η candidates is recorded.

3.2.4 Selection of D candidates

After reconstructing the final state particles we apply selection criteria to the reconstructed D candidates in the event. We select events that lie in a mode-dependent range of the energy difference ΔE. The cut values for each final state are shown in Table 3.4.

Mode	Minimum ΔE (GeV)	Maximum ΔE (GeV)
K^+K^-	-0.020	0.020
$\pi^+\pi^-$	-0.030	0.030
$K^\pm\pi^\mp$	-0.0294	0.0294
$K^\pm\pi^\mp\pi^0$	-0.030	0.030
$K^\pm\pi^\mp\pi^+\pi^-$	-0.020	0.020
$K^\pm e^\mp\nu_e$	-0.020	0.020
$K^0_S\pi^0$	-0.071	0.045
$K^0_S\eta$	-0.055	0.035
$K^0_S\omega$	-0.025	0.025
$K^0_S\eta'$	-0.030	0.020
$K^0_S\pi^0\pi^0$	-0.055	0.045
$K^0_S\pi^+\pi^-$	-0.020	0.020
$K^0_SK^+K^-$	-0.015	0.015

Table 3.4: ΔE selection criteria for D candidates decaying to different final states.

3.2.5 Multiple candidate selection

Reconstructed events occasionally contain more than one candidate D. We must choose only one of these candidates so we use a discriminating variable to select between them. When both the signal- and opposite-side final states have been reconstructed, we choose the candidate with the smallest value of the following figure of merit:

$$\delta_F \equiv \left| \frac{m_{\rm bc}(S) + m_{\rm bc}(O)}{2} - m_{D^0} \right| \tag{3.8}$$

where $m_{\rm bc}(S)$ and $m_{\rm bc}(O)$ are the beam-constrained masses of the signal-side and opposite-side final states respectively and m_{D^0} is the PDG[4] [11] D^0 mass.

For situations in which one final state contains a missing particle, a different figure of merit is minimised:

$$\delta_P \equiv |m_{\rm bc}(S) - m_{D^0}| \tag{3.9}$$

[4]Particle Data Group.

where $m_{\rm bc}(S)$ is the $m_{\rm bc}$ of the candidate that does not contain the missing particle.

3.2.6 Determining event yields

The final stage of the reconstruction procedure is to determine the yields of selected events. The method to do this is different for fully- and partially-reconstructed decays, but the overall concept is similar. A *signal region* is defined as a particular range or ranges of a discriminating variable. Events that lie in the signal region are used to calculate the parameters of interest.

Even when all the selection cuts have been applied, there are inevitably background events in the remaining sample. We therefore define *sidebands* which are used to perform a data-driven estimate of the level of background present in the signal region. To avoid cross-feed from the signal region into the sidebands (and vice versa) we ensure the sidebands are well separated from the signal region.

For each type of final state we define a space on which the signal region and sidebands are located. For fully-reconstructed final states we utilise the scatter plot of the $m_{\rm bc}$ of one reconstructed D against the $m_{\rm bc}$ of the other D, known as the $m_{\rm bc}$ *plane*. For final states containing ν_e we use the projection of $U_{\rm miss}$, and for final states containing K^0_L we use the projection of $m^2_{\rm miss}$.

3.2.6.1 Signal region and sidebands for fully-reconstructed decays

For fully-reconstructed decays, we define a signal region (labelled S) and four sidebands (A, B, C and D) on the $m_{\rm bc}$ plane. Sidebands A and B are useful to determine the quantity of backgrounds for which one D has been correctly identified (hence whose $m_{\rm bc} \simeq m_{D^0}$) and the other has been misidentified. Sideband C is primarily useful for determining the level of continuum events and sideband D is useful to determine pure combinatoric events. In sidebands C and D, requirements are placed on the quantity $\delta m_{\rm bc} \equiv |m_{\rm bc}(D_1) - m_{\rm bc}(D_2)|$, where the two D-mesons are denoted D_1 and D_2. The region boundaries are summarised in Table 3.5 and illustrated in Figure 3.6.

Region	$m_{\rm bc}$ (D_1)(GeV/c^2)		$m_{\rm bc}$ (D_2)(GeV/c^2)		$\delta m_{\rm bc}$ (GeV/c^2)
	Min.	Max.	Min.	Max.	
S	1.860	1.870	1.860	1.870	—
A	1.830	1.855	1.860	1.870	—
B	1.860	1.870	1.830	1.855	—
C	1.830	1.855	1.830	1.855	≤ 0.0035
D	1.830	1.855	1.830	1.855	≥ 0.0055

Table 3.5: Sideband and signal region definitions for $K^0_S K^+ K^-$ against fully-reconstructed final states.

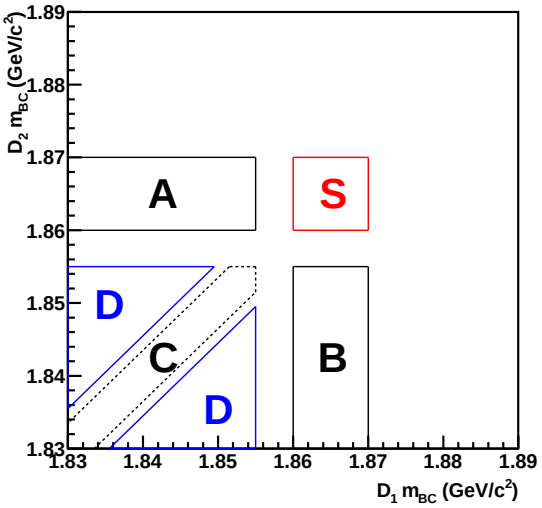

Figure 3.6: Signal region (S) and sidebands (A–D) on the $m_{\rm bc}$ plane.

3.2.6.2 Signal region and sidebands for partially-reconstructed decays

For final states in which the presence of a K^0_L is inferred by the missing mass technique, we define a signal region on the $m^2_{\rm miss}$ plane that is centred on $m^2_{K^0_L} \sim 0.25$ GeV/c^2. We also define sidebands at low and high values of $m^2_{\rm miss}$. The extent of the signal region and sidebands varies for each mode, and is determined by studying Monte Carlo data. Final states containing more charged tracks are typically easier to reconstruct and hence have a narrower signal region[5]. When determining the range of each sideband we aim for as large an extent as possible in order to enhance statistical precision. Occasionally there are large peaks from specific decay modes that are well-isolated from the signal region. If included in the background estimation, these peaks would result in an unrepresentative yield. The sidebands are therefore truncated in order to ensure that this type of peak is not included. The signal region and sideband definitions for each final state are listed in Table 3.6. We have included the signal region and sidebands for $K^0_S K^+ K^-$ against $K^\pm e^\mp \nu_e$; in this case, the regions are defined on the projection of $U_{\rm miss}$ instead of $m^2_{\rm miss}$.

3.3 Selection results

3.3.1 Yields

Table 3.7 lists the yields of $K^0_{S,L} K^+ K^-$ tagged with each opposite-side final state. Background subtraction and efficiency correction have not been applied. The low level of $\mathcal{CP}$ violation in the neutral kaon system is neglected when determining the $\mathcal{CP}$ eigenvalue of final states containing K^0_S and K^0_L.

[5]The only exception is $K^0_L \pi^0 \pi^0$, for which a narrow signal region is clearly visible in Monte Carlo data. We choose to use this region in order to minimise possible background contamination.

Final state	Low sideband (GeV/c^2)		Signal region (GeV/c^2)		High sideband (GeV/c^2)	
	Minimum	Maximum	Minimum	Maximum	Minimum	Maximum
$K^0_L\pi^0$	-0.1	0.1	0.1	0.5	0.6	1.0
$K^0_L\eta$	0.0	0.1	0.15	0.35	0.4	1.2
$K^0_L\omega$	0.0	0.1	0.15	0.35	0.4	1.2
$K^0_L\eta'$	0.0	0.1	0.15	0.35	0.4	1.2
$K^0_L\pi^0\pi^0$	0.0	0.15	0.2	0.3	0.4	0.6
$K^0_L\pi^+\pi^-$	0.1	0.15	0.2	0.3	0.35	0.5
$K^0_LK^+K^-$	0.05	0.2	0.2	0.3	0.35	0.5
$K^\pm e^\mp\nu_e$	-0.3	-0.05	-0.05	0.05	0.05	0.3

Table 3.6: Signal region and sidebands for partially-reconstructed final states. The regions are defined on the m^2_{miss} projection for all final states containing a K^0_L and on the U_{miss} projection for $K^\pm e^\mp\nu_e$.

Final state category	Opposite-side final state	Yield	
		$K^0_SK^+K^-$	$K^0_LK^+K^-$
Flavour	$K^\pm\pi^\mp$	168	302
	$K^\pm\pi^\mp\pi^0$	330	585
	$K^\pm\pi^\mp\pi^+\pi^-$	248	287
	$K^\pm e^\mp\nu_e$	100	
$\mathcal{CP}$ even	K^+K^-	12	32
	$\pi^+\pi^-$	4	13
	$K^0_S\pi^0\pi^0$	7	14
	$K^0_L\pi^0$	17	
	$K^0_L\eta(\gamma\gamma)$	4	
	$K^0_L\eta(\pi^+\pi^-\pi^0)$	1	
	$K^0_L\omega$	4	
	$K^0_L\eta'$	1	
$\mathcal{CP}$ odd	$K^0_S\pi^0$	18	43
	$K^0_S\eta(\gamma\gamma)$	4	6
	$K^0_S\eta(\pi^+\pi^-\pi^0)$	2	1
	$K^0_S\omega$	14	10
	$K^0_S\eta'$	3	4
	$K^0_L\pi^0\pi^0$	5	
Mixed $\mathcal{CP}$	$K^0_S\pi^+\pi^-$	56	126
	$K^0_L\pi^+\pi^-$	140	
	$K^0_SK^+K^-$	4	9

Table 3.7: Yields of $K^0_{S,L}K^+K^-$ selected against each final state. The yields are shown prior to background subtraction and efficiency correction.

3.3.2 Distribution of events on the m_{bc} plane

The distribution of events on the m_{bc} plane and also on the m_{bc} projection of the signal-side decay is shown for $\mathcal{CP}+$ final states (Figure 3.7), $\mathcal{CP}-$ final states (Figure 3.8), flavour final states (Figure 3.10) and $K^0_Sh^+h^-$ final states (Figure 3.9). In all cases the majority of events

are contained within region the signal region S, marked with a red square.

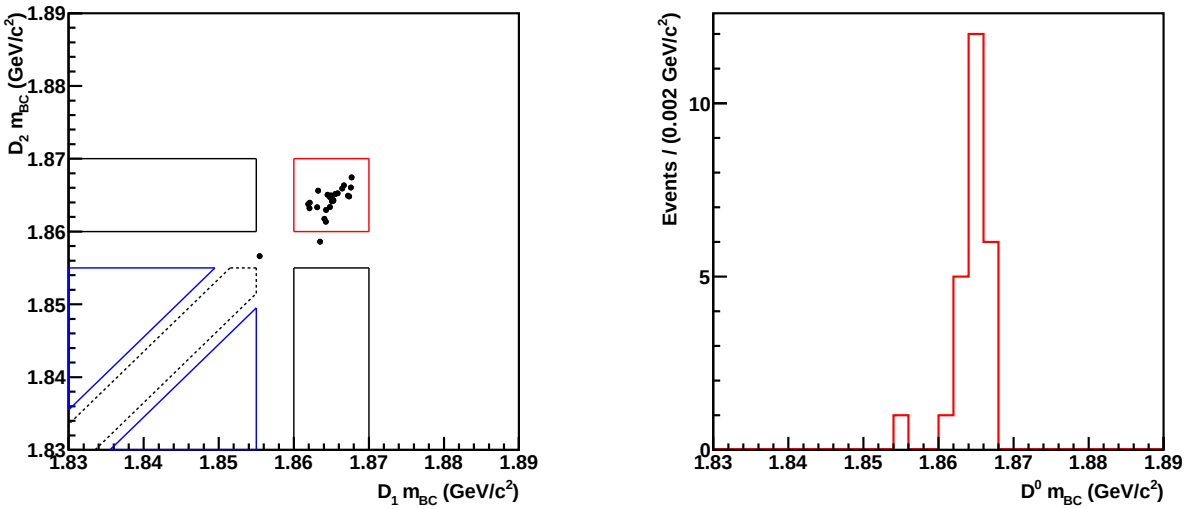

Figure 3.7: $m_{\rm bc}$ plane (left) and $m_{\rm bc}$ projection (right) for $K^0_S K^+ K^-$ tagged with $\mathcal{CP}+$ final states.

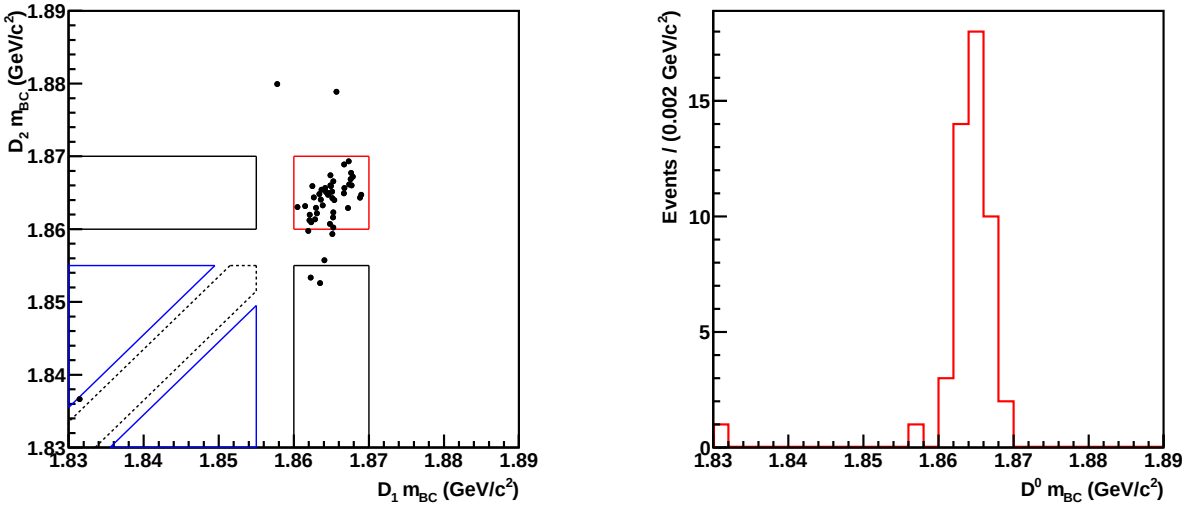

Figure 3.8: $m_{\rm bc}$ plane (left) and $m_{\rm bc}$ projection (right) of $K^0_S K^+ K^-$ tagged with $\mathcal{CP}-$ final states.

3.3.3 Distribution of events on the $m^2_{\rm miss}$ projection

Figures 3.11–3.13 show $m^2_{\rm miss}$ projections for events grouped by final state category. The estimated background is shown along with the data. This background is estimated using a combination of data and Monte Carlo in the signal region and sidebands. This procedure is described in detail in Section 3.6. Good agreement is observed between the yields of data and estimated background in the sidebands.

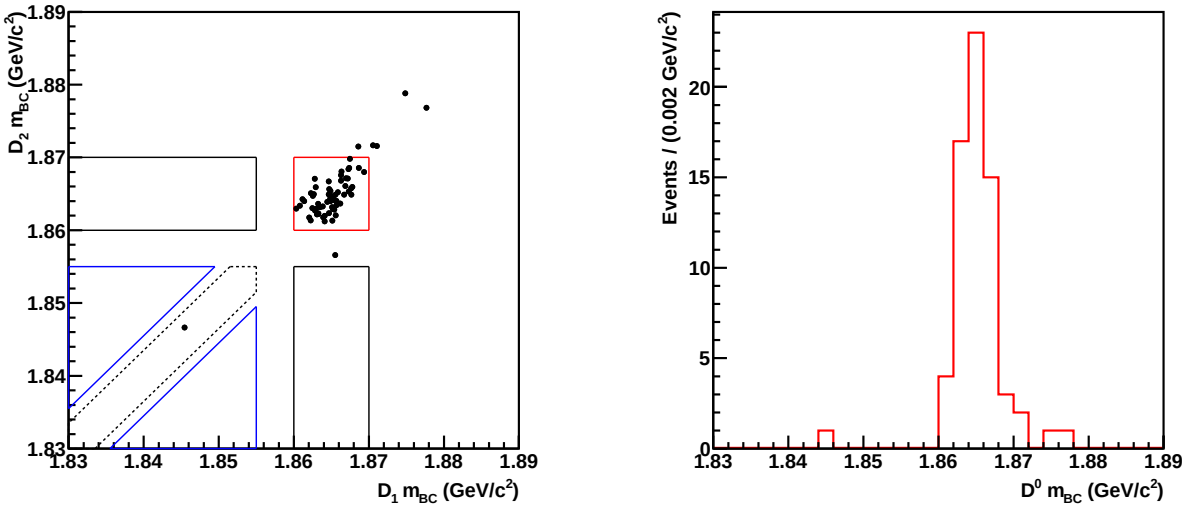

Figure 3.9: $m_{\rm bc}$ plane (left) and $m_{\rm bc}$ projection (right) of $K^0_S K^+ K^-$ tagged with $K^0_S h^+ h^-$ final states.

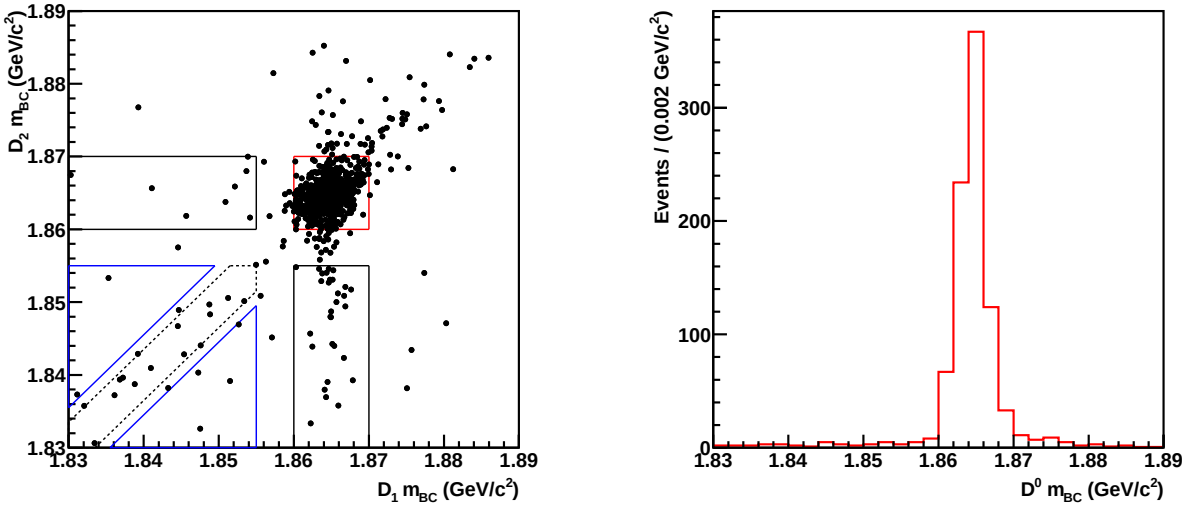

Figure 3.10: $m_{\rm bc}$ plane (left) and $m_{\rm bc}$ projection (right) of $K^0_S K^+ K^-$ tagged with flavour final states.

3.3.4 Distribution of events on the $U_{\rm miss}$ projection

Figure 3.14 shows the distribution of $U_{\rm miss}$ in $K^0_S K^+ K^-$ against $K^\pm e^\mp \nu_e$ data. The estimated background, almost negligible, is shown along with the data.

3.4 Determination of yields across the Dalitz plane

The analysis presented in Chapter 4 uses event yields in bins across the Dalitz plane to determine the parameters of interest. A detailed discussion of how the Dalitz plane is binned can be found in that chapter, but in this section we describe how the bin yields are determined.

Boundaries of bins on the Dalitz plane are defined in the coordinate basis $(m^2_{K^0_S h^+}, m^2_{K^0_S h^-})$

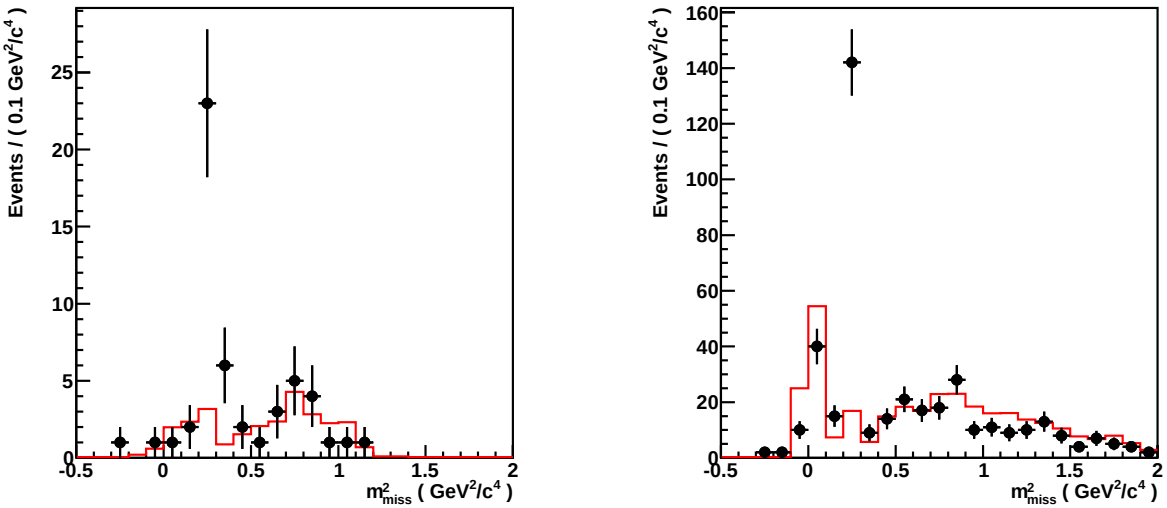

Figure 3.11: Missing mass distribution of $K^0_S K^+ K^-$ tagged with $\mathcal{CP}\pm$ final states containing a K^0_L (left) and with $K^0_L \pi^+ \pi^-$ (right). The black points are the data and the red line is the estimated background.

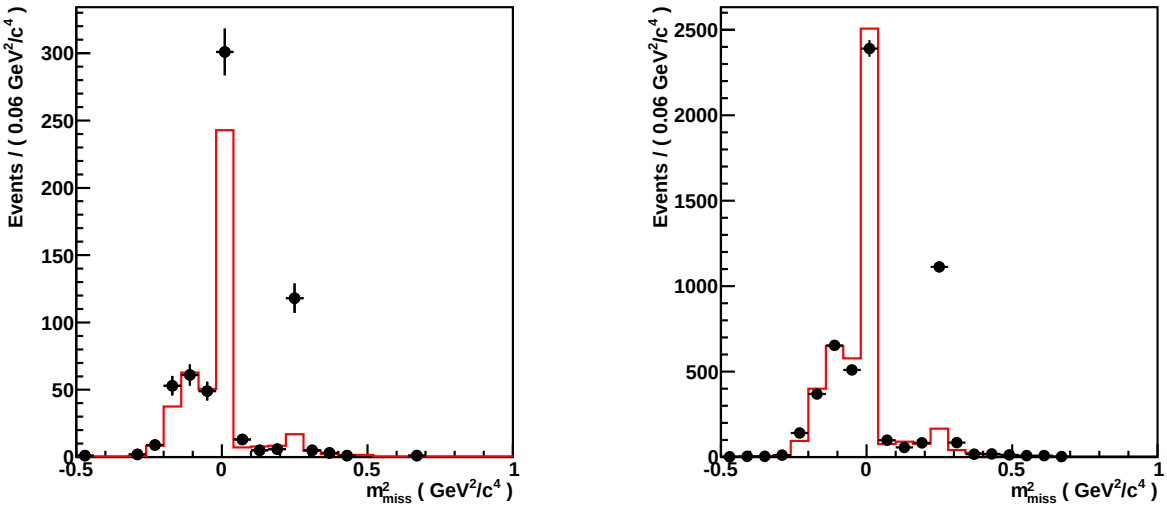

Figure 3.12: Missing mass distribution of $K^0_L K^+ K^-$ tagged with $\mathcal{CP}\pm$ final states (left) and flavour final states (right). The black points are the data and the red line is the estimated background.

so we must determine these quantities for each event in order to determine which bin it is assigned to. The same procedure is used for both $K^0_{S,L} K^+ K^-$ and $K^0_{S,L} \pi^+ \pi^-$ final states, collectively denoted $K^0_{S,L} h^+ h^-$. For events in which $K^0_{S,L} K^+ K^-$ is tagged with $K^0_{S,L} h^+ h^-$ we determine the position of the event on both associated Dalitz planes.

3.4.1 Kinematic fitting of $K^0_{S,L} h^+ h^-$ final states

We use a kinematic fit to constrain the four-momenta of the particles in the $K^0_{S,L} h^+ h^-$ final state. This enables the position of the event on the Dalitz plane to be determined more accurately. Two or more reconstructed particles can be constrained to emanate from a best-fit origin vertex; alternatively, their four-momenta can be constrained such that the parent

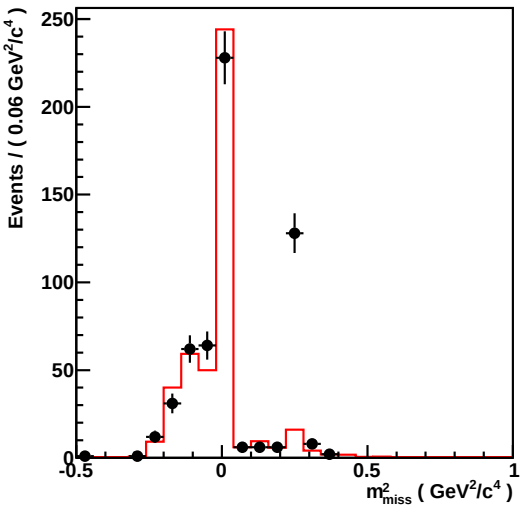

Figure 3.13: Missing mass distribution of $K^0_L K^+ K^-$ tagged with $K^0_S h^+ h^-$. The black points are the data and the red line is the estimated background.

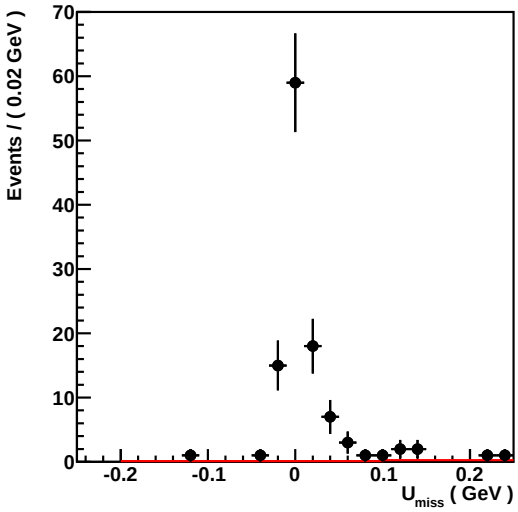

Figure 3.14: $U_{\rm miss}$ distribution for events in which $K^0_S K^+ K^-$ is tagged with $K^\pm e^\mp \nu_e$. The points are data and the red line is the estimated background.

particle has a particular invariant mass. We use the FitEvt [72] package to perform the fits using the method of least squares. In order to ensure accurate convergence, the fit is performed iteratively. Furthermore, information about the position of the beamspot and the crossing angle between the beams is included.

Seven parameters are considered in the fits: the three spatial coordinates of the parent particle and each component of its four-momentum. The covariance matrix associated with the fit therefore has dimensions 7×7.

3.4.1.1 $K^0_S h^+ h^-$ fit

A reconstructed $K^0_S h^+ h^-$ final state consists of two charged hadrons and a K^0_S which has two charged pion daughters. The first stage of the fit is to constrain the two K^0_S daughter pions to the nominal K^0_S mass. If the fit is successful (indicated by a positive χ^2), the K^0_S and the two charged hadrons are then combined in a further fit to the nominal D mass. If the χ^2 of this fit is greater than zero, the fit values of the $(m^2_{K^0_S h^+}, m^2_{K^0_S h^-})$ coordinates are used to determine the location of the event on the Dalitz plane. If the fit fails, the default values of $(m^2_{K^0_S h^+}, m^2_{K^0_S h^-})$ returned by CLEO-c are taken. Occasionally this results in events lying outside of the physical region, an effect which must be corrected for as described in Section 3.4.2.

3.4.1.2 $K^0_L h^+ h^-$ fit

Kinematically constraining $K^0_L h^+ h^-$ final states is more complicated than for $K^0_S h^+ h^-$ because the K^0_L is not directly reconstructed. As much kinematic information as possible is

used in the fit. As described in Section 3.2.3.2, the position and 4-momentum of the K^0_L are inferred from the properties of the other particles and the beam energy.

The opposite-side final state is fit to the nominal D mass and the resulting four-momentum of the mother particle is determined. If this fit fails (indicated by a negative fit χ^2), the default information provided by the CLEO-c software is used.

The two signal-side charged hadrons are constrained to emanate from a common vertex. Again, if this fit fails the default kinematic information provided by the CLEO-c software is used.

Information about the opposite-side final state and di-hadron vertex is then combined with the beamspot momentum and the covariance matrices to determine the missing four-momentum in the event. A K^0_L object with associated position and four-momentum is constructed. The invariant mass of the K^0_L is changed to the nominal value by rescaling its energy while retaining the overall three-momentum.

The K^0_L is then combined with the di-hadron vertex in a mass-fit to the D^0. The fit usually succeeds; if it is unsuccessful, the three momentum of the K^0_L is manually adjusted to minimise the residual between the reconstructed D mass and the nominal value. These quantities are then used to determine the location of the event on the Dalitz plot.

The fit fails in about 1–3% of cases depending on the decay mode. If the fitting procedure fails, we change the values of $m^2_{K^0_{S,L}h^+}$ and $m^2_{K^0_{S,L}h^-}$ by an equal amount such that their invariant mass combination is equal to the nominal D mass.

3.4.1.3 Effect on reconstructed *D* resolution

The effectiveness of the D mass fit can be evaluated using signal Monte Carlo data. We consider the differences between generator- and reconstruction-level kinematic variables both with and without the fit. We study the three invariant masses $m^2_{K^0_{S,L}K^+}$, $m^2_{K^0_{S,L}K^-}$ and $m^2_{K^+K^-}$. A double Gaussian function is fit to the invariant mass distributions using the RooFit package [73]. The form of the double Gaussian is:

$$f \cdot \frac{1}{\sqrt{2\pi\sigma_1^2}} \exp\left\{-\frac{(m-\mu)^2}{2\sigma_1^2}\right\} + (1-f) \cdot \frac{1}{\sqrt{2\pi\sigma_2^2}} \exp\left\{-\frac{(m-\mu)^2}{2\sigma_2^2}\right\} \tag{3.10}$$

where μ is the mean common to both Gaussians, σ_1 and σ_2 are the widths and f is the fraction of one of the Gaussians. The width of the narrower Gaussian is recorded for various representative final states in Table 3.8.

In general, the mass fit results in a narrower width for both $K^0_S K^+K^-$ and $K^0_L K^+K^-$. Plots of the residuals for $K^0_S K^+K^-$ against K^+K^- are shown in Figures 3.15 and 3.16. The equivalent plots for $K^0_L K^+K^-$ against K^+K^- are shown in Figures 3.17 and 3.18. In the majority of cases the number of events in the non-Gaussian tails is reduced.

Final states	Narrow Gaussian width (GeV^2/c^4)					
	$m^2_{K^0_S K^+}\times 10^3$		$m^2_{K^0_S K^-}\times 10^3$		$m^2_{K^+K^-}\times 10^3$	
	With fit	Without fit	With fit	Without fit	With fit	Without fit
$K^0_S K^+K^-$ against K^+K^-	0.92 ± 0.07	2.10 ± 0.49	0.86 ± 0.04	2.31 ± 0.54	0.89 ± 0.04	1.09 ± 0.09
$K^0_S K^+K^-$ against $K^0_S\pi^0$	0.92 ± 0.09	2.21 ± 0.49	0.64 ± 0.30	0.91 ± 0.28	0.79 ± 0.07	1.03 ± 0.10
$K^0_S K^+K^-$ against $K^\pm\pi^\mp$	0.86 ± 0.09	1.42 ± 0.43	1.03 ± 0.06	1.02 ± 0.36	0.71 ± 0.04	0.95 ± 0.07
$K^0_L K^+K^-$ against K^+K^-	1.61 ± 0.16	1.46 ± 0.23	1.38 ± 0.15	0.96 ± 0.14	0.82 ± 0.06	0.99 ± 0.06
$K^0_L K^+K^-$ against $K^0_S\pi^0$	1.24 ± 0.19	1.51 ± 0.41	1.18 ± 0.13	1.53 ± 0.35	0.91 ± 0.09	1.07 ± 0.08
$K^0_L K^+K^-$ against $K^\pm\pi^\mp$	1.13 ± 0.24	1.35 ± 0.25	1.16 ± 0.12	1.40 ± 0.18	0.91 ± 0.06	1.02 ± 0.05

Table 3.8: The width of the 'narrow' Gaussian of a double Gaussian fitted to the difference between the generator- and reconstruction-level $K^0_{S,L}K^+K^-$ invariant masses in MC.

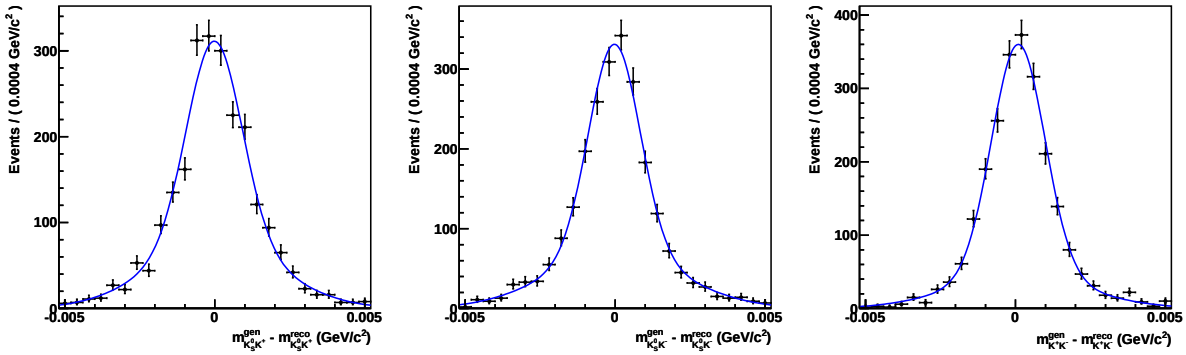

Figure 3.15: Difference between generator- and reconstruction-level $m^2_{K^0_S K^+}$ (left), $m^2_{K^0_S K^-}$ (centre) and $m^2_{K^+K^-}$ (right) in $K^0_S K^+K^-$ against K^+K^- signal Monte Carlo in which a mass fit has been performed.

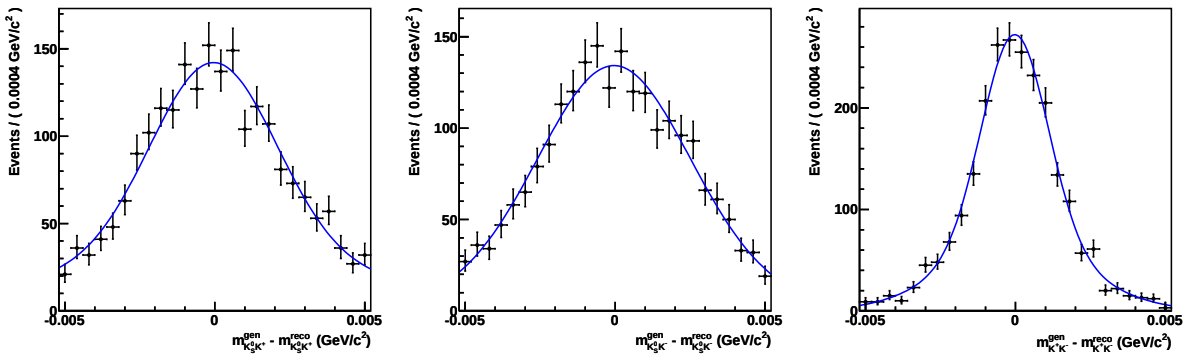

Figure 3.16: Difference between generator- and reconstruction-level $m^2_{K^0_S K^+}$ (left), $m^2_{K^0_S K^-}$ (centre) and $m^2_{K^+K^-}$ (right) in $K^0_S K^+K^-$ against K^+K^- signal Monte Carlo without a mass fit.

3.4.2 Bin assignment

The kinematic variables of a reconstructed event are used to determine which Dalitz plane bin it lies in.

Occasionally an event is reconstructed outside the physical region. A vector from this point to the Dalitz plane boundary is determined such that the vector is perpendicular to the tangent to the boundary at the point of intersection between the vector and the boundary. There is one unique vector that satisfies this condition, denoted the *vector of*

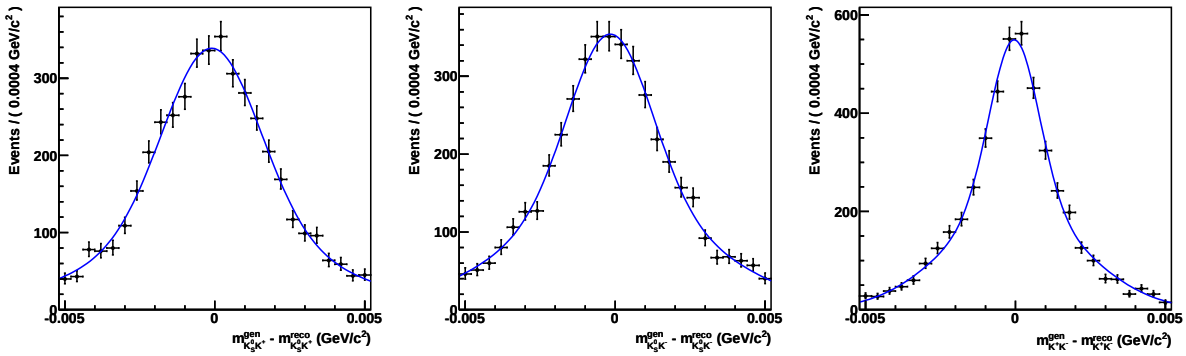

Figure 3.17: Difference between generator- and reconstruction-level $m^2_{K^0_L K^+}$ (left), $m^2_{K^0_L K^-}$ (centre) and $m^2_{K^+K^-}$ (right) in $K^0_L K^+ K^-$ against K^+K^- signal Monte Carlo in which a mass fit has been performed.

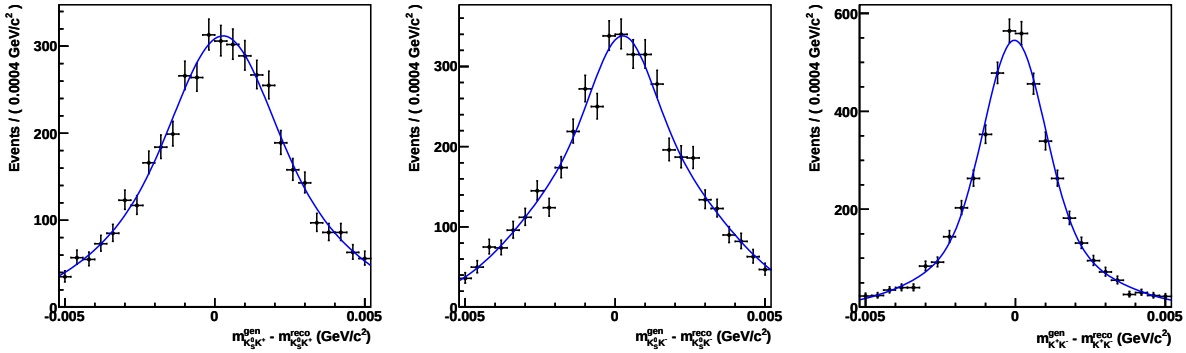

Figure 3.18: Difference between generator- and reconstruction-level $m^2_{K^0_L K^+}$ (left), $m^2_{K^0_L K^-}$ (centre) and $m^2_{K^+K^-}$ (right) in $K^0_L K^+ K^-$ against K^+K^- signal Monte Carlo without a mass fit.

closest approach. Figure 3.19 shows a diagram of this vector. To determine the vector of closest approach, a numerical approximation is used instead of an analytic calculation. Points along the kinematic boundary are sampled at very close intervals. The vector from each sampled point to the original data point is determined, and the vector with the minimum magnitude is designated the vector of closest approach.

The fraction of events moved inside the physical limit is 3% for data and 4% for reconstructed signal Monte Carlo. The movement of points for data and MC is shown in Figure 3.20. We can be confident that the bins assigned by this method are correct due to the simple structure of the binning at the Dalitz plot boundary (see Section 4.2).

Figure 3.21 shows the distribution of distances by which points are moved to the boundary of the plot for reconstructed data and MC. The mean and RMS values are $(0.007, 0.010)$ GeV$^2/c^4$ for data and $(0.007, 0.010)$ GeV$^2/c^4$ for MC. This is a rare case in which the behaviours of data and Monte Carlo on reconstruction can be directly compared, and it indicates that they are well-matched.

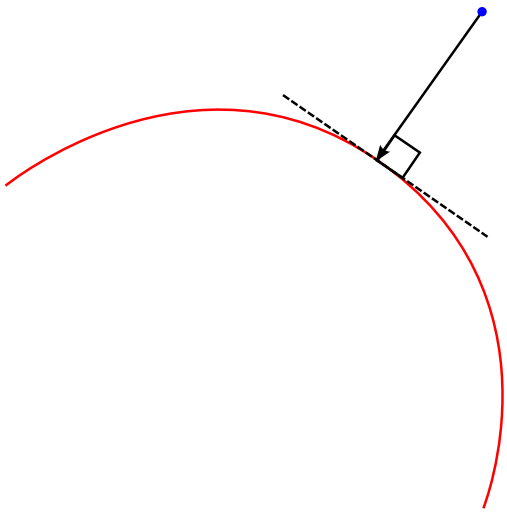

Figure 3.19: A diagram of the vector of closest approach to the Dalitz plane boundary. The blue point is the event to be moved, the arrow is the vector of closest approach, the red line is the boundary, and the dotted line is the tangent to the boundary at the intersection of the vector and boundary.

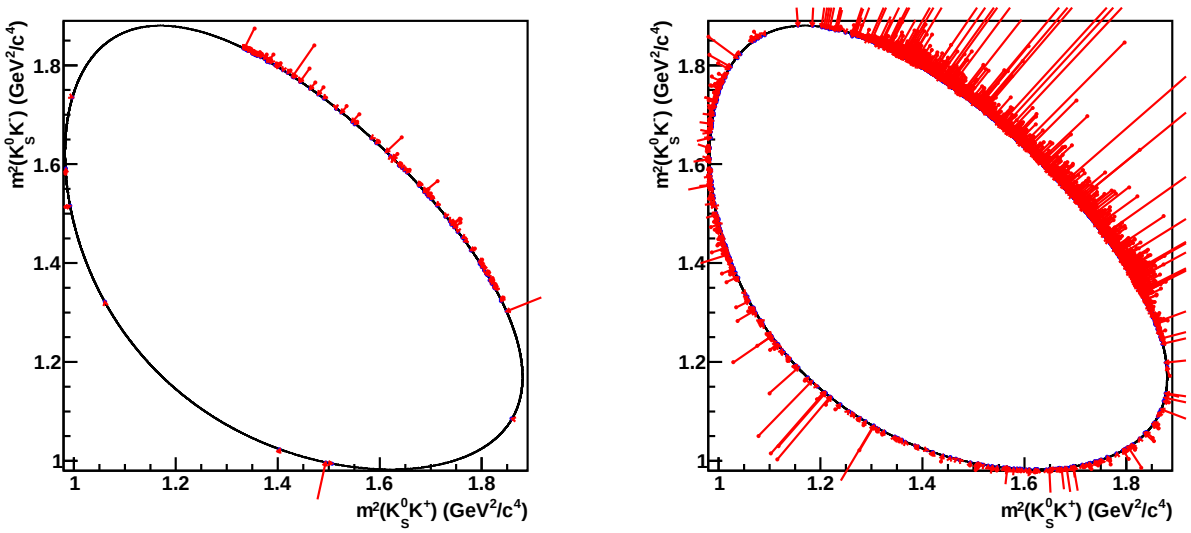

Figure 3.20: The movement of unphysical points onto the Dalitz plot boundary for reconstructed data (left) and signal Monte Carlo (right). Red points show the initial location and blue shows the final location; the red arrow indicates the movement of individual points. The black line is the physical boundary.

3.4.3 Correction to hadronic flavour yields

The most abundant decays considered in the analysis are those in which the opposite-side D decays to a flavour state. Three of the flavour states are fully hadronic final states ($K^{\pm}\pi^{\mp}$, $K^{\pm}\pi^{\mp}\pi^0$ and $K^{\pm}\pi^{\mp}\pi^{+}\pi^{-}$) and one is semileptonic ($K^{\pm}e^{\mp}\nu_e$).

The semileptonic flavour state $K^{\pm}e^{\mp}\nu_e$ enables an unambiguous determination of the flavour of the parent D. If the kaon is negatively charged we know that the parent particle is a D^0, and if the kaon is positively charged the parent is a $\overline{D}^0$. Due to the fact that the $D^0\overline{D}^0$ system is anticorrelated, the parent of the $K^0_S K^+ K^-$ final state must be a D^0 if the

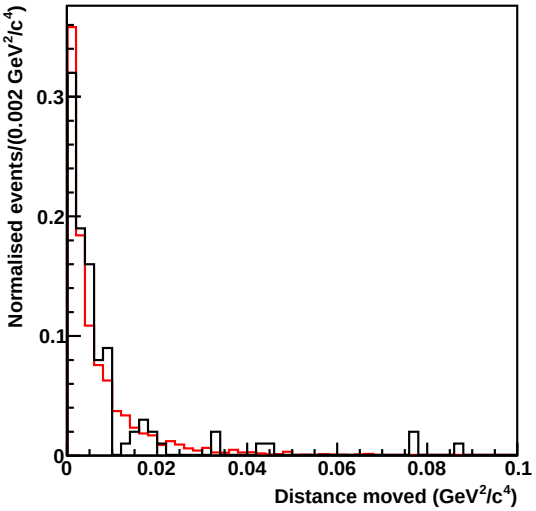

Figure 3.21: The distance moved by an initially unphysical point to the edge of the Dalitz plane boundary. The black line is data and the red line is reconstructed signal Monte Carlo.

parent of the $K^{\pm}e^{\mp}\nu_e$ is a $\overline{D}^0$, and vice versa. This information can be used to assign a particular event to a Dalitz plane bin. If the parent of the $K^0_S K^+ K^-$ is a $\overline{D}^0$, its coordinates on the Dalitz plane are swapped before determining the event location.

In contrast, the flavour of the parent D for a fully hadronic final state is inherently uncertain. In this case, the D can decay to both a Cabibbo-favoured (CF) final state and a doubly-Cabibbo-suppressed (DCS) final state which is the charge conjugate of the CF state. The charge of the kaon cannot be used to determine the flavour of the parent D unambiguously because a DCS decay will be interpreted as a CF decay of the opposite flavour. In this case the event will be misassigned to the mirror image of its true location, leading to biases in the Dalitz plane bin yields.

In order to mitigate this effect we apply a correction to the yields of events tagged with hadronic final states. For each hadronic final state F, we multiply the yield in each bin $\mathcal{D}_i$ by the factor:

$$f_F^{DCS} = \frac{\int_{\mathcal{D}_i} |\mathcal{A}(D^0 \to K^0_S K^+ K^-)(x,y)|^2 \,\mathrm{d}x\,\mathrm{d}y}{\int_{\mathcal{D}_i} |\mathcal{A}(D^0 \to K^0_S K^+ K^-)(x,y) + R_F r_D^F e^{i\delta_D^F} \mathcal{A}(\overline{D}^0 \to K^0_S K^+ K^-)(x,y)|^2 \,\mathrm{d}x\,\mathrm{d}y}, \tag{3.11}$$

where r_D^F is the ratio of moduli of suppressed and favoured decays, δ_D^F is the relative strong phase, and R_F is the coherence factor (see Section 1.6.3.3).

We use an amplitude model developed by BaBar [25] to determine $\mathcal{A}(D \to K^0_S K^+ K^-)$. The model is described in detail in Section 3.5.1. Values of r_D^F are determined using PDG [11] branching fractions. Values of δ_D^F are taken from [21] in the case of $K^{\pm}\pi^{\mp}$ and from the relevant analyses of $K^{\pm}\pi^{\mp}\pi^0$ and $K^{\pm}\pi^{\mp}\pi^+\pi^-$ [5]. The values of each parameter for each final state are listed in Table 3.9.

The corrections to the bin-by-bin yields of hadronic flavour decays are tabulated for two,

Final state F	$r_D^F(\%)$	$\delta_D^F(^\circ)$	R_F
$K^\pm\pi^\mp$	0.580 ± 0.008	202 ± 10	1
$K^\pm\pi^\mp\pi^0$	0.48 ± 0.02	227 ± 17	0.84 ± 0.07
$K^\pm\pi^\mp\pi^+\pi^-$	0.57 ± 0.02	114 ± 26	0.33 ± 0.26

Table 3.9: Quantities used to determine correction factors to pseudo-flavour yields. These quantities have been taken from Refs. [11, 21].

three and four Dalitz plane bins[6] in Tables 3.10–3.12.

Final state	Bin 1	Bin 2	Bin −1	Bin −2
$K^0_S K^+K^-$ against $K^\pm\pi^\mp$	0.995	1.006	0.995	1.003
$K^0_S K^+K^-$ against $K^\pm\pi^\mp\pi^0$	1.001	0.997	1.003	0.999
$K^0_S K^+K^-$ against $K^\pm\pi^\mp\pi^+\pi^-$	1.004	1.000	1.000	0.997
$K^0_L K^+K^-$ against $K^\pm\pi^\mp$	0.995	1.006	0.994	1.003
$K^0_L K^+K^-$ against $K^\pm\pi^\mp\pi^0$	1.001	0.997	1.003	0.999
$K^0_L K^+K^-$ against $K^\pm\pi^\mp\pi^+\pi^-$	1.004	1.001	1.000	0.997

Table 3.10: Corrections to pseudo-flavour yields: two bins.

Final state	Bin 1	Bin 2	Bin 3	Bin −1	Bin −2	Bin −3
$K^0_S K^+K^-$ against $K^\pm\pi^\mp$	0.995	1.006	0.997	0.995	1.003	1.001
$K^0_S K^+K^-$ against $K^\pm\pi^\mp\pi^0$	1.002	0.997	1.003	1.003	0.999	0.999
$K^0_S K^+K^-$ against $K^\pm\pi^\mp\pi^+\pi^-$	1.004	1.001	0.994	1.000	0.997	1.002
$K^0_L K^+K^-$ against $K^\pm\pi^\mp$	0.995	1.006	1.006	0.994	1.003	1.003
$K^0_L K^+K^-$ against $K^\pm\pi^\mp\pi^0$	1.002	0.997	0.997	1.003	1.000	0.999
$K^0_L K^+K^-$ against $K^\pm\pi^\mp\pi^+\pi^-$	1.004	1.001	0.999	1.001	0.997	0.998

Table 3.11: Corrections to pseudo-flavour yields: three bins.

Final state	Bin 1	Bin 2	Bin 3	Bin 4	Bin −1	Bin −2	Bin −3	Bin −4
$K^0_S K^+K^-$ against $K^\pm\pi^\mp$	0.994	1.002	1.007	0.991	0.994	0.999	1.004	1.000
$K^0_S K^+K^-$ against $K^\pm\pi^\mp\pi^0$	1.002	0.998	0.996	1.008	1.003	1.002	0.999	0.999
$K^0_S K^+K^-$ against $K^\pm\pi^\mp\pi^+\pi^-$	1.004	1.003	1.000	0.991	1.001	0.997	0.997	1.002
$K^0_L K^+K^-$ against $K^\pm\pi^\mp$	0.995	1.001	1.007	1.011	0.994	0.998	1.004	1.002
$K^0_L K^+K^-$ against $K^\pm\pi^\mp\pi^0$	1.002	0.999	0.996	0.994	1.003	1.002	0.999	0.999
$K^0_L K^+K^-$ against $K^\pm\pi^\mp\pi^+\pi^-$	1.003	1.003	1.000	1.000	1.001	0.997	0.997	0.999

Table 3.12: Corrections for pseudo-flavour yields: four bins.

3.4.4 Bin yield summation

After each event has been assigned to a Dalitz plane bin, the yield in each bin is determined. Depending on the type of final state, one of the following counters is incremented:

[6]The division of the Dalitz plane into bins is described in detail in Section 4.2.

- M_i: The number of $\mathcal{CP}$-tagged $K^0_{S,L}K^+K^-$ events in the i^{th} bin. Yields of $\mathcal{CP}$-tagged events are often relatively low. In order to increase the statistical precision on the values of M_i we combine the yields of all $\mathcal{CP}+$ final states, and do the same for all $\mathcal{CP}-$ final states.

- K_i: The number of flavour-tagged $K^0_{S,L}K^+K^-$ events in the i^{th} bin. These are all abundant decay modes so are treated separately.

- M_{ij}: The number of events in the i^{th} bin of the $K^0_{S,L}K^+K^-$ Dalitz plot and the j^{th} bin of the $K^0_{S,L}h^+h^-$ Dalitz plot. These are all treated separately.

For each type of opposite-side final state it is possible to sum the yields in bins that depend upon the same observables and are therefore expected to be equal. This will reduce the relative statistical uncertainty in each bin and also reduce the number of parameters in the fit to extract the observables. We use the relations in Equations 1.143, 1.160 and 1.161:

$$M_i = M_{-i}, \qquad M_{ij} = M_{-i-j}, \qquad M_{-ij} = M_{i-j}. \tag{3.12}$$

For $K^0_{S,L}K^+K^-$ tagged with $\mathcal{CP}$ final states, the yields in bins i and $-i$ can be summed. For $K^0_SK^+K^-$ against $K^0_{S,L}h^+h^-$, two sets of bin yields can be summed: (i,j) and $(-i,-j)$, and $(-i,j)$ and $(i,-j)$.

3.4.5 Dalitz plane data distributions

The Dalitz plane distributions and $m^2_{h^+h^-}$ projections in data are shown for $K^0_SK^+K^-$ tagged with $\mathcal{CP}$ even eigenstates (Figure 3.22), $K^0_SK^+K^-$ tagged with $\mathcal{CP}$ odd eigenstates (Figure 3.23), $K^0_SK^+K^-$ tagged with flavour states (Figure 3.24), $K^0_LK^+K^-$ tagged with $\mathcal{CP}$ even eigenstates (Figure 3.25), $K^0_LK^+K^-$ tagged with $\mathcal{CP}$ odd eigenstates (Figure 3.26), $K^0_LK^+K^-$ tagged with flavour states (Figure 3.27) and $K^0_{S,L}K^+K^-$ tagged with $K^0_{S,L}h^+h^-$ (Figures 3.28–3.37). The final states have been grouped according to the value of $\mathcal{CP}$ in order to highlight the evident differences between the distributions of these groups.

The $m^2_{K^+K^-}$ projection of $K^0_SK^+K^-$ against $\mathcal{CP}+$ eigenstates has a prominent peak centred on $m^2_\phi = 1.04\ \text{GeV}^2/c^4$. This reflects the quantum-correlated nature of the $D^0\overline{D}^0$ system. The fact that the opposite-side state is $\mathcal{CP}+$ ensures that the signal-side decay proceeds via a $\mathcal{CP}-$ resonance, the dominant resonance in this case being $K^0_S\phi$. The $\phi \to K^+K^-$ resonance has a narrow width, resulting in the strong peak seen in the $m^2_{K^+K^-}$ projection. In contrast, the $m^2_{K^+K^-}$ projection of $K^0_SK^+K^-$ against $\mathcal{CP}-$ eigenstates lacks a strong ϕ peak. The $K^0_SK^+K^-$ system is in a $\mathcal{CP}+$ state and does not decay through the $K^0_S\phi$ resonance.

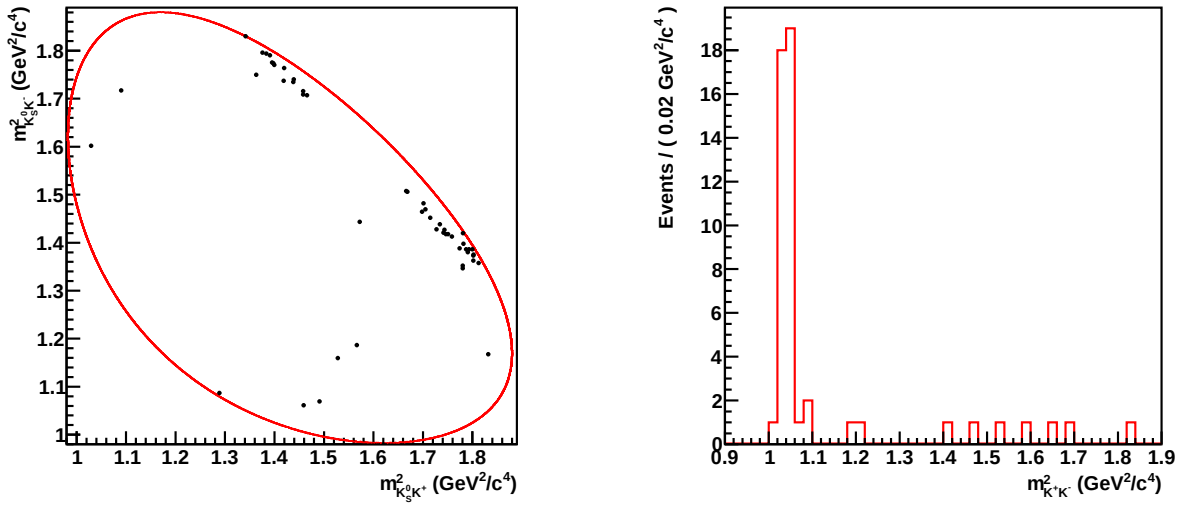

Figure 3.22: Dalitz plane distribution (left) and $m^2_{K^+K^-}$ projection (right) for $K^0_S K^+ K^-$ tagged with $\mathcal{CP}+$ eigenstates.

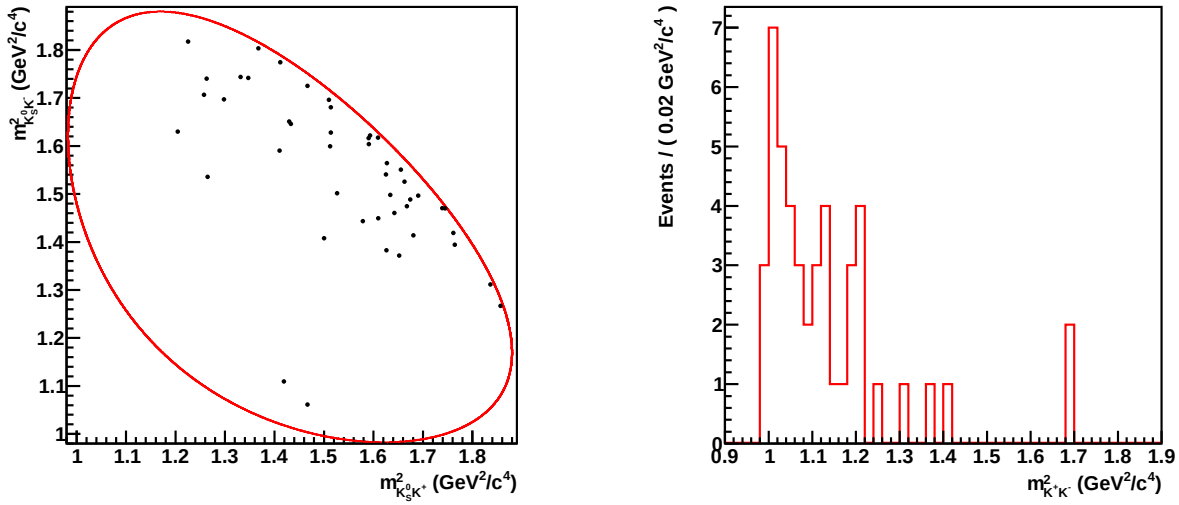

Figure 3.23: Dalitz plane distribution (left) and $m^2_{K^+K^-}$ projection (right) for $K^0_S K^+ K^-$ tagged with $\mathcal{CP}-$ eigenstates.

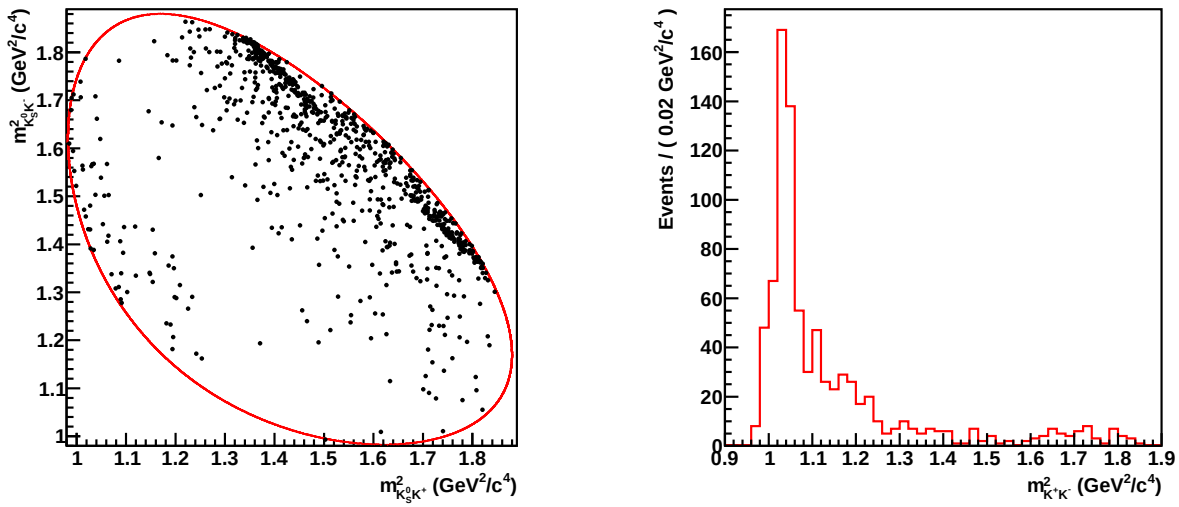

Figure 3.24: Dalitz plane distribution (left) and $m^2_{K^+K^-}$ projection (right) for $K^0_S K^+ K^-$ tagged with flavour states.

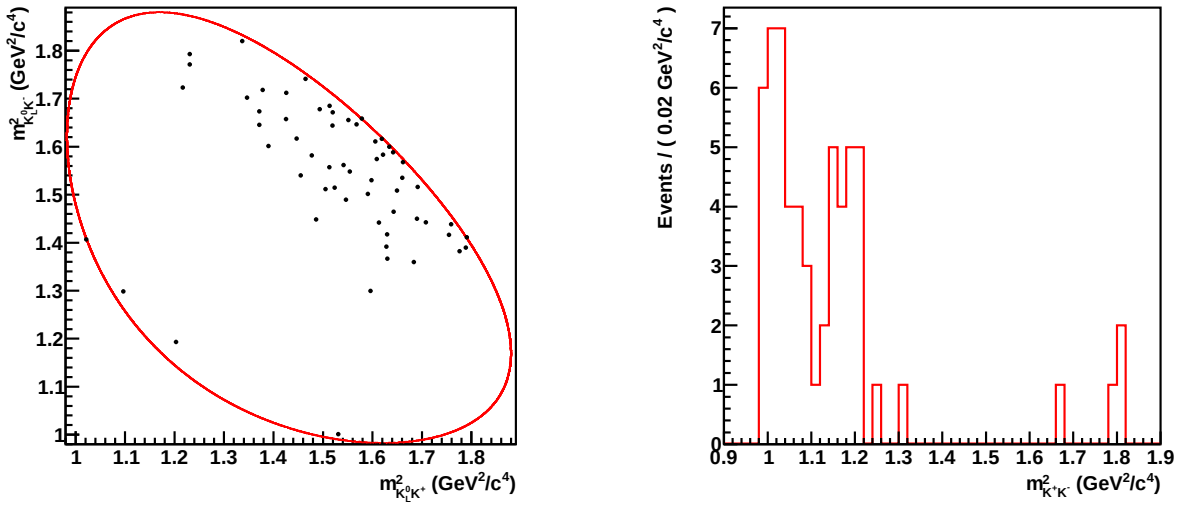

Figure 3.25: Dalitz plane distribution (left) and $m^2_{K^+K^-}$ projection (right) for $K^0_L K^+ K^-$ tagged with $\mathcal{CP}+$ eigenstates.

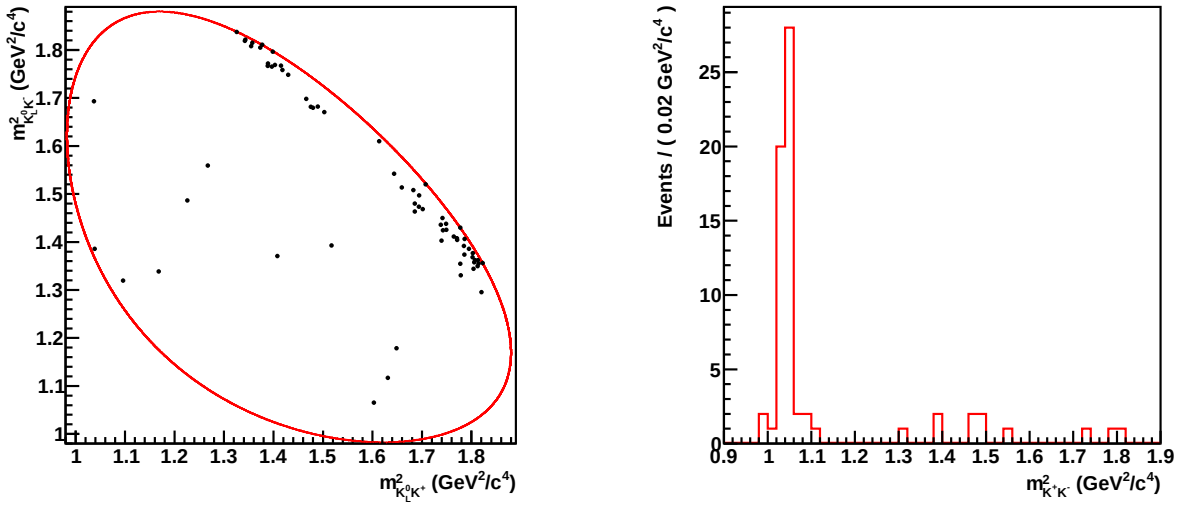

Figure 3.26: Dalitz plane distribution (left) and $m^2_{K^+K^-}$ projection (right) for $K^0_L K^+ K^-$ tagged with $\mathcal{CP}-$ eigenstates.

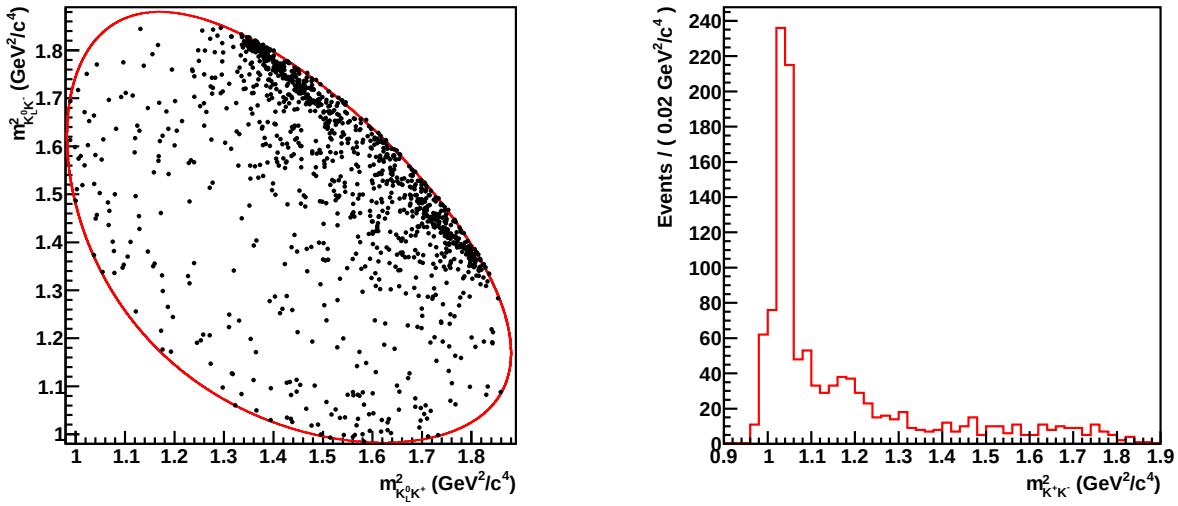

Figure 3.27: Dalitz plane distribution (left) and $m^2_{K^+K^-}$ projection (right) for $K^0_L K^+ K^-$ tagged with flavour states.

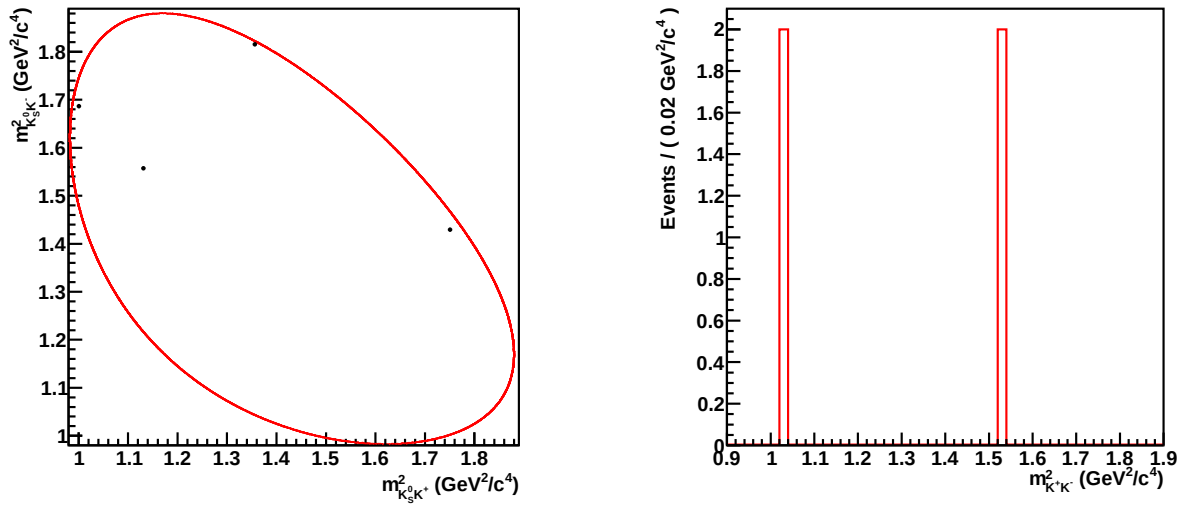

Figure 3.28: Dalitz plane distribution (left) and $m^2_{K^+K^-}$ projection (right) for $K^0_S K^+ K^-$ tagged with $K^0_S K^+ K^-$, signal side.

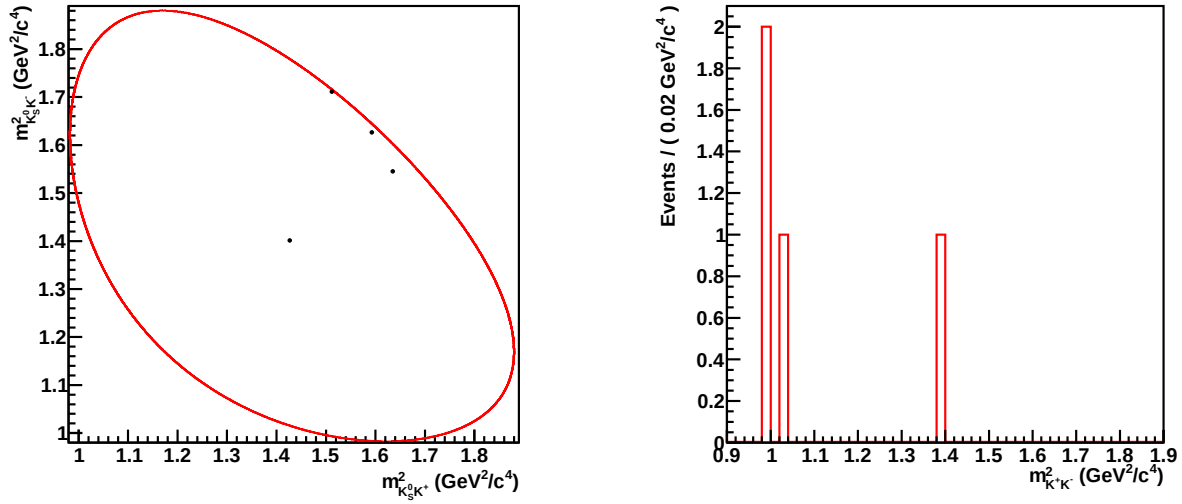

Figure 3.29: Dalitz plane distribution (left) and $m^2_{K^+K^-}$ projection (right) for $K^0_S K^+ K^-$ tagged with $K^0_S K^+ K^-$, opposite side.

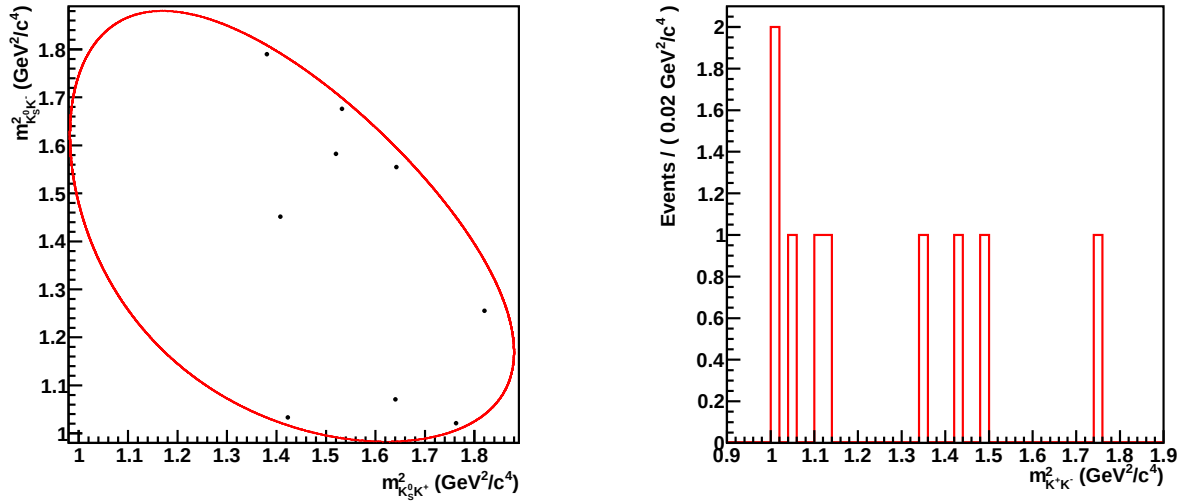

Figure 3.30: Dalitz plane distribution (left) and $m^2_{K^+K^-}$ projection (right) for $K^0_S K^+ K^-$ tagged with $K^0_L K^+ K^-$, signal side.

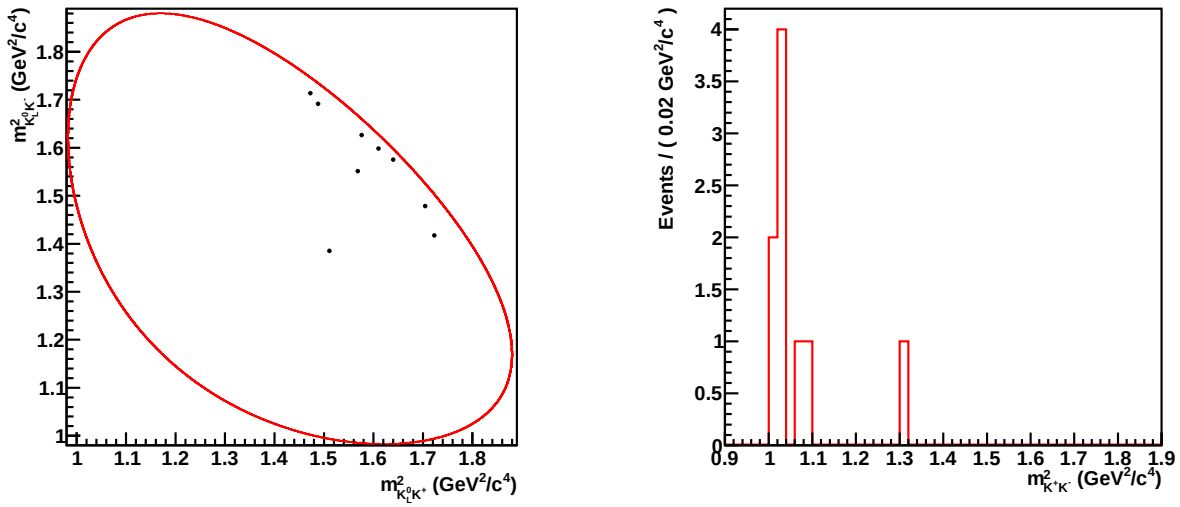

Figure 3.31: Dalitz plane distribution (left) and $m^2_{K^+K^-}$ projection (right) for $K^0_S K^+ K^-$ tagged with $K^0_L K^+ K^-$, opposite side.

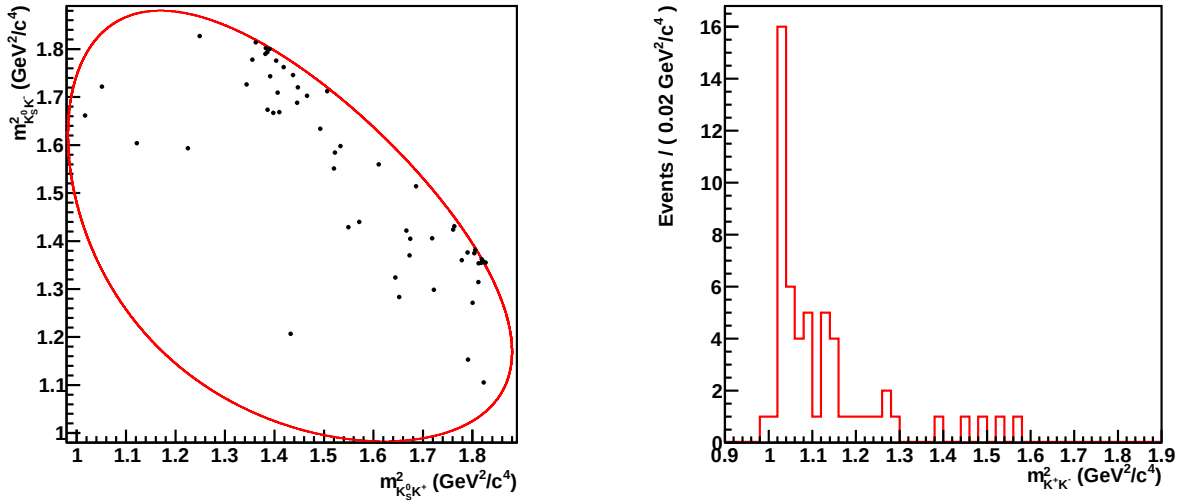

Figure 3.32: Dalitz plane distribution (left) and $m^2_{K^+K^-}$ projection (right) for $K^0_S K^+ K^-$ tagged with $K^0_S \pi^+ \pi^-$, signal side.

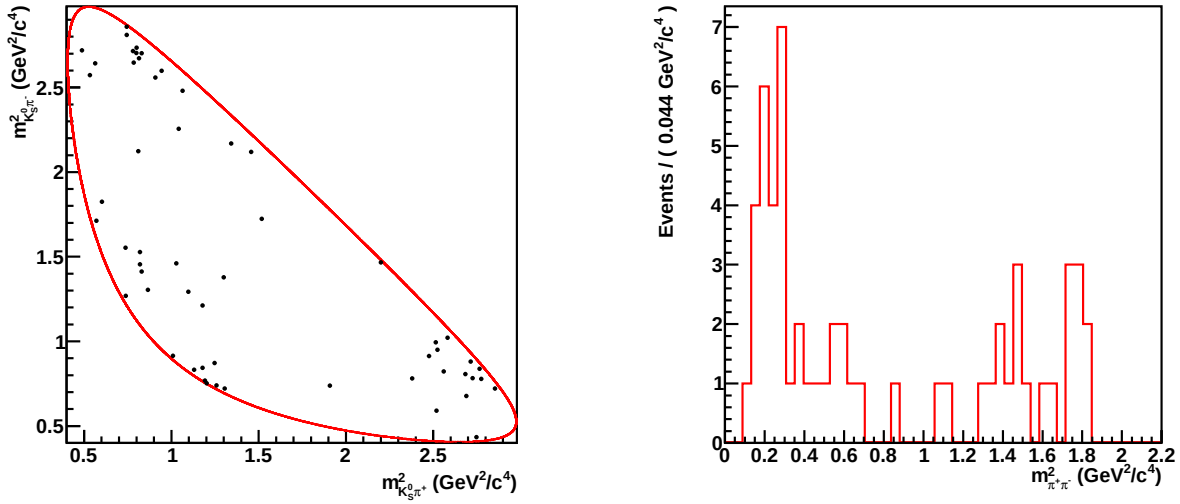

Figure 3.33: Dalitz plane distribution (left) and $m^2_{\pi^+\pi^-}$ projection (right) for $K^0_S K^+ K^-$ tagged with $K^0_S \pi^+ \pi^-$, opposite side.

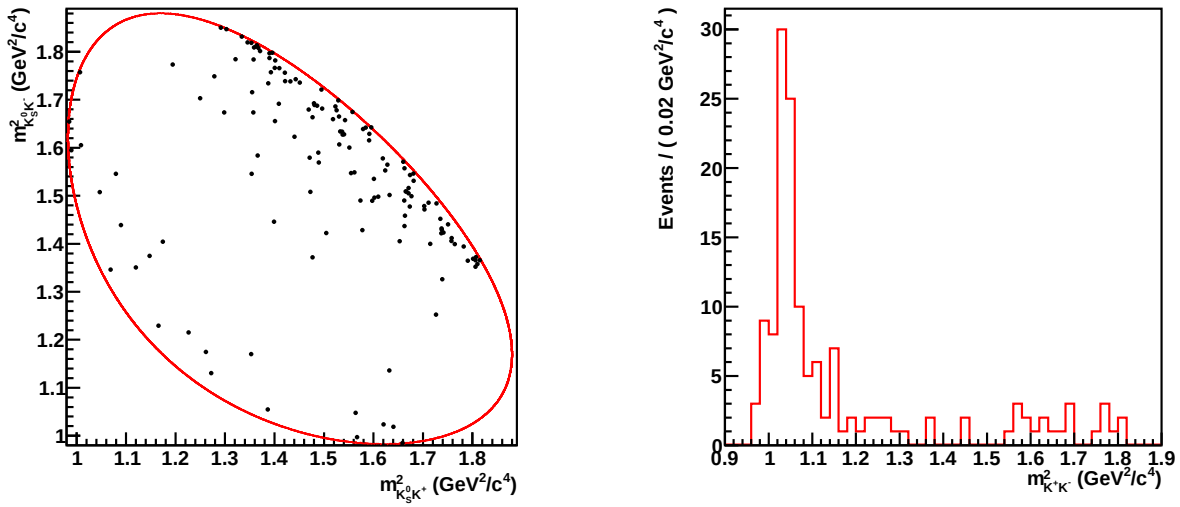

Figure 3.34: Dalitz plane distribution (left) and $m^2_{K^+K^-}$ projection (right) for $K^0_S K^+ K^-$ tagged with $K^0_L \pi^+ \pi^-$, signal side.

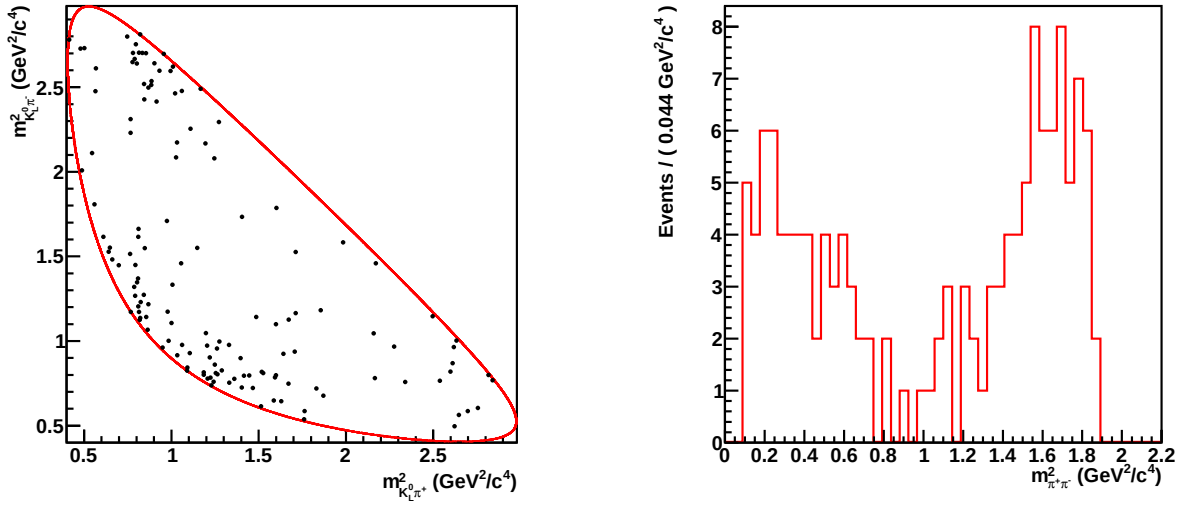

Figure 3.35: Dalitz plane distribution (left) and $m^2_{\pi^+\pi^-}$ projection (right) for $K^0_S K^+ K^-$ tagged with $K^0_L \pi^+ \pi^-$, opposite side.

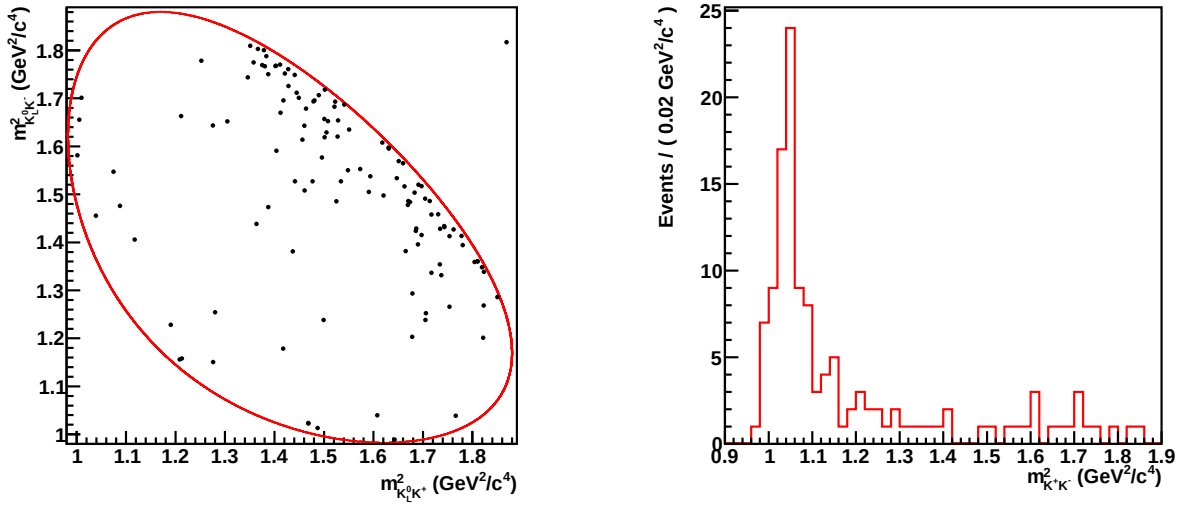

Figure 3.36: Dalitz plane distribution (left) and $m^2_{K^+K^-}$ projection (right) for $K^0_L K^+ K^-$ tagged with $K^0_S \pi^+ \pi^-$, signal side.

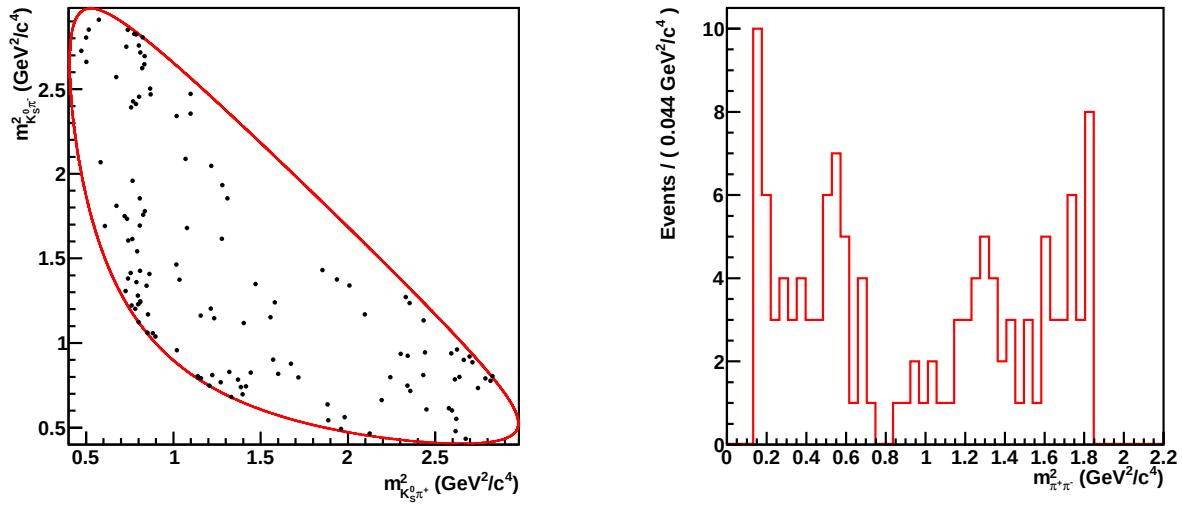

Figure 3.37: Dalitz plane distribution (left) and $m^2_{\pi^+\pi^-}$ projection (right) for $K^0_L K^+ K^-$ tagged with $K^0_S\pi^+\pi^-$, opposite side.

The $m^2_{K^+K^-}$ projections for $K^0_S K^+ K^-$ against flavour and mixed-$\mathcal{CP}$ states contain both $\mathcal{CP}+$ and $\mathcal{CP}-$ components, so the $K^0_S\phi$ resonance is present but not as pronounced. The $m^2_{K^+K^-}$ projection of $K^0_L K^+ K^-$ against $\mathcal{CP}-$ eigenstates has a similar shape to that of $K^0_S K^+ K^-$ against $\mathcal{CP}+$ eigenstates. This is because K^0_L has the opposite $\mathcal{CP}$ to K^0_S, so the $K^0_L\phi$ resonance is $\mathcal{CP}+$.

3.5 Studies of signal Monte Carlo

Samples of Monte Carlo data are generated for each $D^0\overline{D}^0$ mode under study. Each sample contains 40,000 events. We use these samples to determine the selection efficiency of the reconstruction procedure. Section 2.5.1 contains information about the software used to generate the samples.

3.5.1 Amplitude model

In order to generate realistic $D\to K^0_{S,L}K^+K^-$ decays we use an amplitude model determined by the BaBar collaboration [25]. The $D\to K^0_S K^+ K^-$ model consists of eight intermediate resonances whose moduli and phases are listed in Table 3.13. The $D\to K^0_L K^+ K^-$ model consists of eight similar resonances that have been modified following the procedure in Section 1.6.5.5. The moduli and phases of the resonances are quoted relative to the modulus and phase of $K^0_S a_0(980)^0$, which are fixed to 1 and 0 respectively.

The $a_0(980)^{0,\pm}$ resonance is modelled with the Flatté parameterisation (see Section 1.5.2.4). The coupling parameters g_{KK} and $g_{\eta\pi}$ are 0.550 ± 0.010 GeV/c^2 and 0.324 ± 0.015 GeV/c^2 respectively [25]. All other resonances are modelled with a relativistic

Resonance	$K^0_S K^+ K^-$		$K^0_L K^+ K^-$	
	Modulus	Phase (°)	Modulus	Phase (°)
$K^0_S a_0(980)^0$	1.000	0	0.889	0
$K^0_S \phi$	0.227	−56.2	0.202	−56.2
$K^0_S f_0(1370)$	0.040	−2	0.036	−2
$K^0_S f_2(1270)$	0.261	−9	0.232	−9
$K^0_S a_0(1450)^0$	0.650	−95	0.578	−95
$K^- a_0(980)^+$	0.562	179	0.562	179
$K^- a_0(1450)^+$	0.840	97	0.840	97
$K^+ a_0(980)^-$	0.118	138	0.118	318

Table 3.13: The moduli and phases of the intermediate resonances of $D \to K^0_{S,L} K^+ K^-$ decays.

Breit-Wigner lineshape (see Section 1.5.2.3).

The BaBar collaboration has also provided a high-resolution *bitmap* containing information about the amplitude and phase of $D \to K^0_S K^+ K^-$ decays at each point across the Dalitz plane. The bitmap extends over the entire kinematic region in the ($m^2_{K^0_S K^+}$, $m^2_{K^0_S K^-}$) plane and is divided into 500 × 500 grid elements. The bitmap is used to determine the Dalitz plane bin boundaries as described in Section 4.2.

The intermediate resonances of $K^0_{S,L}\pi^+\pi^-$ decays are simulated using the model from Ref. [47].

$K^0_{S,L} K^+ K^-$ decays are produced in the appropriate $\mathcal{CP}$ or flavour state by including quantum correlations in the $D^0\overline{D}^0$ system. For $\mathcal{CP}+$ $(-)$ states the correlation of the $K^0_{S,L} K^+ K^-$ with the opposite-side tag is simulated by using the (anti)symmetric wavefunction (following Section 1.4.1):

$$A_{\mathcal{CP}\pm}(x,y) = \frac{1}{\sqrt{2}}(A_D(x,y) \pm A_D(y,x)). \tag{3.13}$$

To simulate $K^0_{S,L} K^+ K^-$ against $K^0_{S,L} h^+ h^-$ decays, in which both D mesons decay through intermediate resonances, a fully (anti)correlated decay amplitude is used. The wavefunction for $K^0_S K^+ K^-$ against $K^0_S h^+ h^-$ is (following Section 1.4.2):

$$A^{K^0_S h^+ h^-}_{K^0_S h^+ h^-}(x,y,x',y') = \frac{1}{\sqrt{2}}(A_D(x,y)A_{D'}(y',x') - A_{D'}(x',y')A_D(y,x)), \tag{3.14}$$

where the primed symbols refer to the opposite-side $K^0_S h^+ h^-$. To simulate $K^0_S K^+ K^-$ tagged against $K^0_L h^+ h^-$, the sum of the two terms is used instead of the difference:

$$A^{K^0_L h^+ h^-}_{K^0_S h^+ h^-}(x,y,x',y') = \frac{1}{\sqrt{2}}(A_D(x,y)A_{D'}(y',x') + A_{D'}(x',y')A_D(y,x)), \tag{3.15}$$

where the decay amplitudes A_D and $A_{D'}$ are in general different.

3.5.2 Efficiency determination

The signal Monte Carlo samples are used to determine the selection efficiency for each reconstructed decay mode. The cuts used to select signal Monte Carlo for a particular final state are the same as those used to select the data. We determine the global selection efficiency, defined as the total number of events that pass the selection cuts divided by the total number of initial events. We also determine the selection efficiency in each bin of the Dalitz plane:

$$\varepsilon_i \equiv n_i^{\rm sel}/n_i^{\rm gen}, \tag{3.16}$$

where $n_i^{\rm sel}$ and $n_i^{\rm gen}$ are respectively the number of events selected and generated in the $i^{\rm th}$ Dalitz plane bin. Global selection efficiencies for each final state are listed in Section 3.5.6.

3.5.3 Signal Monte Carlo Dalitz plane distribution

Some example generator- and reconstruction-level Dalitz plots of signal Monte Carlo decays are shown in Figures 3.38–3.40. The simulation represents well the most obvious features seen in the data, such as the prominent band of events centred on m_ϕ^2.

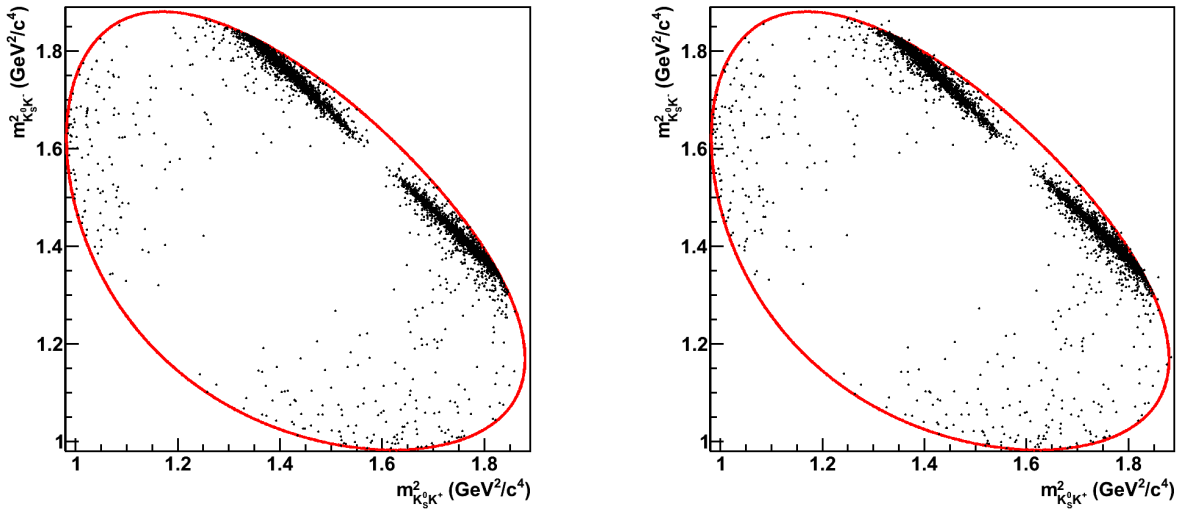

Figure 3.38: Generator-level (left) and reconstruction-level (right) events for $K^0_S K^+ K^-$ against K^+K^-.

3.5.4 Detector resolution effects

The finite CLEO-c detector resolution induces an uncertainty on the kinematics of reconstructed events and can therefore change the distribution of events on the Dalitz plane. It is important to determine the magnitude of this effect, in particular to determine the migration of events between Dalitz plane bins. To calculate how far events typically move on

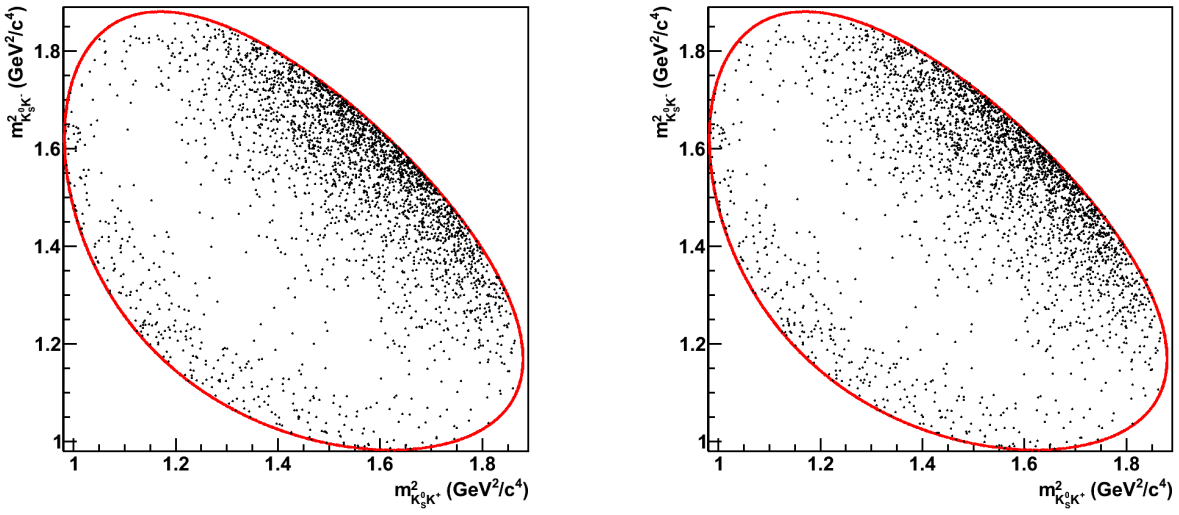

Figure 3.39: Generator-level (left) and reconstruction-level (right) events for $K^0_S K^+ K^-$ against $K^0_S \pi^0$.

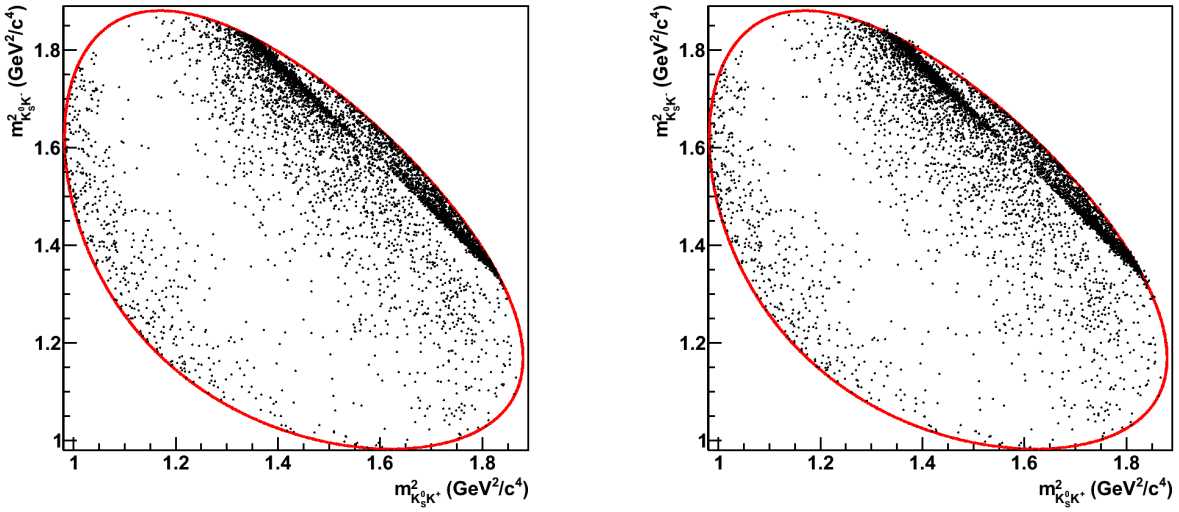

Figure 3.40: Generator-level (left) and reconstruction-level (right) events for $K^0_S K^+ K^-$ against $K^\pm \pi^\mp$.

reconstruction we determine the generator- and reconstruction-level values of $m^2_{K^0_S K^+}$ and $m^2_{K^0_S K^-}$ in signal Monte Carlo. The distance moved by an event on the Dalitz plane is:

$$\Delta r \equiv \sqrt{([m^2_{K^0_S K^+}]^{\rm gen} - [m^2_{K^0_S K^+}]^{\rm reco})^2 + ([m^2_{K^0_S K^-}]^{\rm gen} - [m^2_{K^0_S K^-}]^{\rm reco})^2}, \qquad (3.17)$$

where the superscripts 'gen' and 'reco' indicate the generator- and reconstruction-level values, respectively.

Distributions of Δr are determined for several signal MC samples. Empirically it is observed that in each case a Landau [11, 74, 75] function fits the distribution of Δr well. The most probable value (MPV) and width ($\sigma_{\Delta r}$) of this function are determined for a representative sample of final states and listed in Table 3.14. The quantities both with and without the D-mass fit, discussed in Section 3.4.1, are listed.

Final state	MPV (GeV^2/c^4) $\times 10^3$		$\sigma_{\Delta r}$ (GeV^2/c^4) $\times 10^3$	
	With fit	Without fit	With fit	Without fit
$K^0_S K^+ K^-$ against $K^+ K^-$	1.97	5.64	0.89	2.32
$K^0_S K^+ K^-$ against $K^0_S \pi^0$	2.31	5.11	1.06	2.13
$K^0_S K^+ K^-$ against $K^\pm \pi^\mp$	2.05	5.51	0.92	2.36
$K^0_L K^+ K^-$ against $K^+ K^-$	4.72	5.58	1.99	2.40
$K^0_L K^+ K^-$ against $K^0_S \pi^0$	4.16	6.02	1.85	2.85
$K^0_L K^+ K^-$ against $K^\pm \pi^\mp$	4.59	5.52	2.06	2.27

Table 3.14: The most probable value and width of a Landau distribution fitted to the distribution of distances that events move on reconstruction, in signal Monte Carlo, for various final states.

The D-mass fit reduces the MPV significantly. A lower MPV implies that events are reconstructed closer to their 'true' locations, which provides further justification for the use of the mass fit. The MPV for $K^0_L K^+ K^-$ is larger than that for $K^0_S K^+ K^-$, reflecting the fact that the reconstruction of $K^0_L K^+ K^-$ events is inherently more uncertain.

Figures 3.41 and 3.42 show the Δr distributions and 2D scatterplots of the distance moved on the Dalitz plane for two illustrative final states.

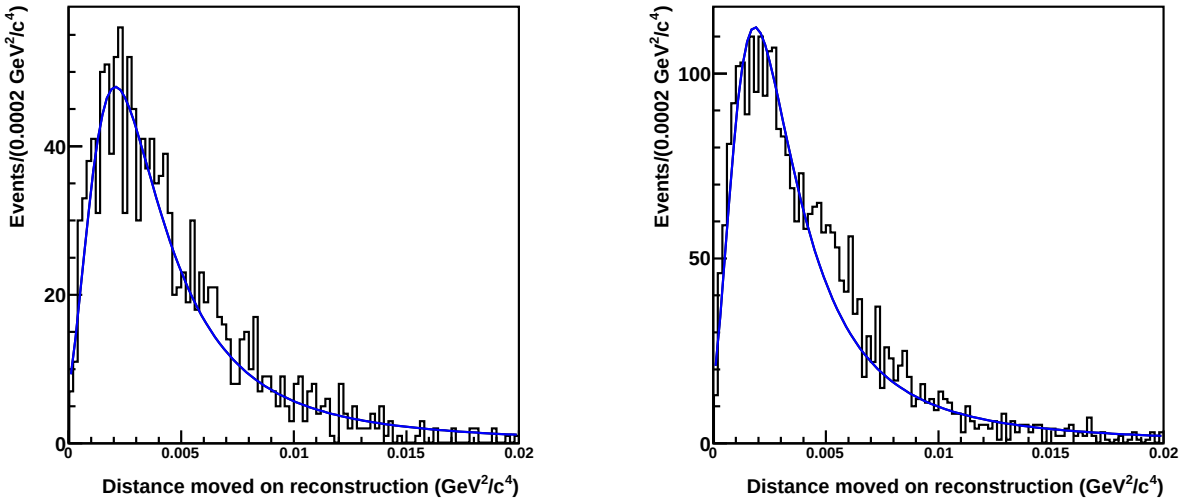

Figure 3.41: Distribution of Δr for $K^0_S K^+ K^-$ against $K^0_S \pi^0$ (left) and $K^0_S K^+ K^-$ against $K^\pm \pi^\mp$ (right) signal Monte Carlo. A D-mass fit has been performed on the reconstructed events. A Landau distribution fit to the events is shown in blue.

3.5.5 Bin-to-bin migration

3.5.5.1 Motivation

We have observed that the finite detector resolution causes events to move on the Dalitz plane after reconstruction. This will occasionally cause an event to be reconstructed in the wrong Dalitz plane bin. This is undesirable because an accurate determination of the yields in each bin is critical to determine the parameters of interest precisely. The effect is

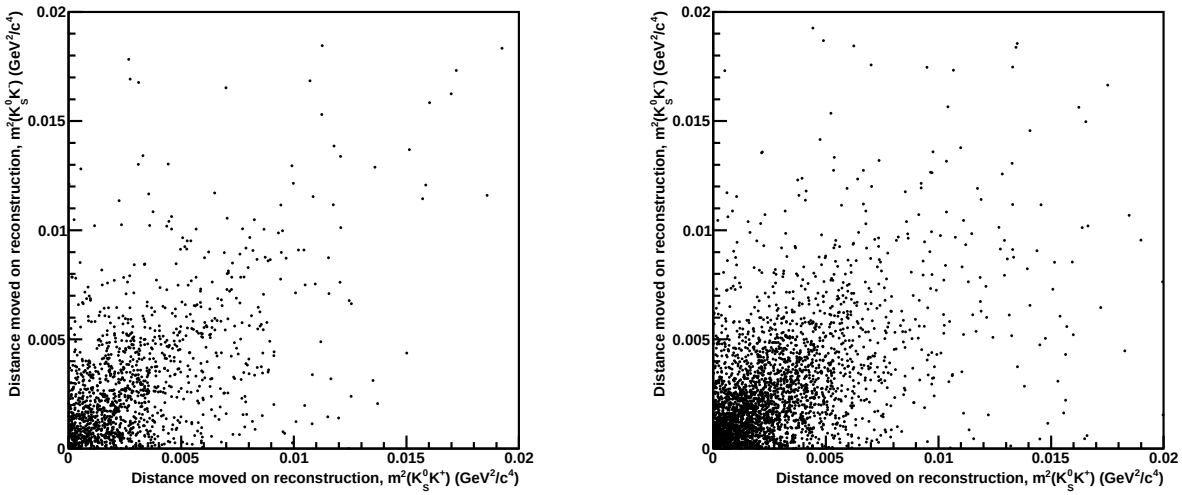

Figure 3.42: Distribution of distances moved on the Dalitz plane for $K^0_S K^+ K^-$ against $K^0_S \pi^0$ (left) and $K^0_S K^+ K^-$ against $K^\pm \pi^\mp$ (right) signal Monte Carlo. A D-mass fit has been performed on the reconstructed events.

particularly pronounced for $K^0_L K^+ K^-$ decays because events move further on average than for $K^0_S K^+ K^-$.

The movement between any pair of bins is usually approximately balanced. However, for one situation ($K^0_L K^+ K^-$ against $\mathcal{CP}-$ states), there is a very high density of events in the bin that covers the $\phi \to K^+ K^-$ resonance compared with the surrounding areas of the Dalitz space, and a consequent net movement of events out of this bin. Approximately 5% of events migrate out of this bin for $K^0_S K^+ K^-$ events and 10–25% for $K^0_L K^+ K^-$.

To counteract the migration of events in Monte Carlo data, the reconstructed decays are traced back to their generator-level positions and the population of each bin is recounted. Selection efficiencies are then calculated using these numbers.

3.5.5.2 Quantifying the migration

The level of bin-to-bin migration is quantified using signal Monte Carlo. It is assumed that the reconstruction of $\mathcal{CP}$ and flavour-tagged $K^0_{S,L} K^+ K^-$ events is independent of the opposite-side final state, within a particular $\mathcal{CP}$-classification of final states (e.g. $K^0_S K^+ K^-$ against $\mathcal{CP}+$). Then, in order to simplify the analysis, one state out of each group is chosen to be representative of all other states in that group. The states used are: $K^0_S K^+ K^-$ against $K^+ K^-$ ($\mathcal{CP}+$), $K^0_S K^+ K^-$ against $K^0_S \pi^0$ ($\mathcal{CP}-$), $K^0_S K^+ K^-$ against $K^\pm \pi^\mp$ (flavour), $K^0_L K^+ K^-$ against $K^+ K^-$ ($\mathcal{CP}+$), $K^0_L K^+ K^-$ against $K^0_S \pi^0$ ($\mathcal{CP}-$) and $K^0_L K^+ K^-$ against $K^\pm \pi^\mp$ (flavour). All $K^0_{S,L} K^+ K^-$ against $K^0_{S,L} h^+ h^-$ decays are considered separately, leading to a total of 11 categories.

The migration of signal Monte Carlo events for each of the flavour and $\mathcal{CP}$ states is shown in Figures 3.43–3.45. Particularly for the $K^0_L K^+ K^-$ cases, some events move a very large

distance. These are sufficiently rare that they can be ignored.

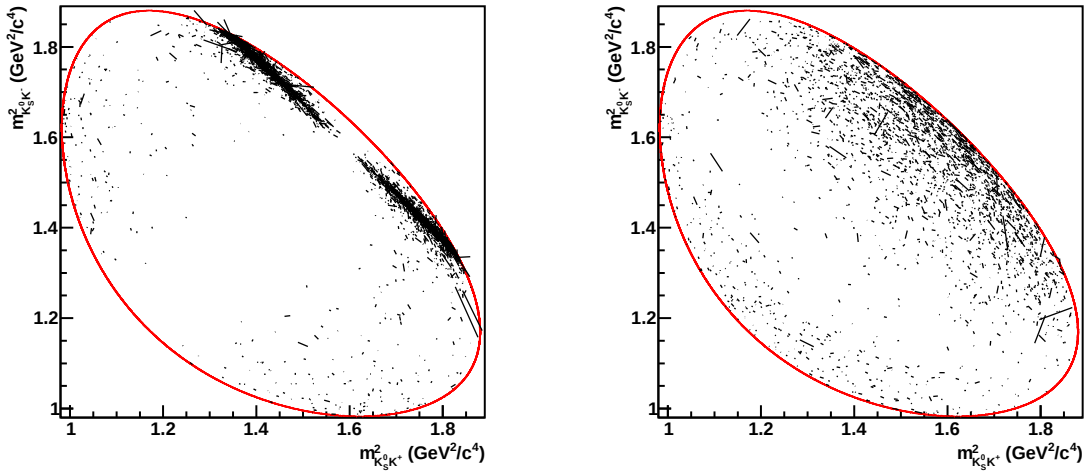

Figure 3.43: Migration of signal Monte Carlo events on reconstruction for $K^0_S K^+ K^-$ against $K^+ K^-$ (left) and $K^0_S K^+ K^-$ against $K^0_S \pi^0$ (right). The black lines show the movement of individual points and the red line is the kinematic limit.

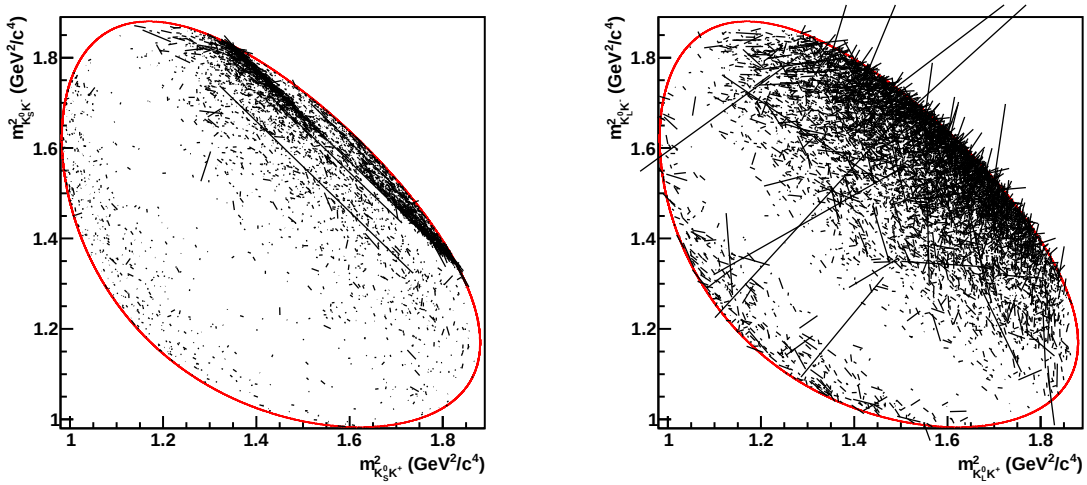

Figure 3.44: Migration of signal Monte Carlo events on reconstruction for $K^0_S K^+ K^-$ against $K^\pm \pi^\mp$ (left) and $K^0_L K^+ K^-$ against $K^\pm \pi^\mp$ (right). The black lines show the movement of individual points and the red line is the kinematic limit.

3.5.5.3 Method

When studying data it is not possible to determine the kinematic locations of events prior to reconstruction. Events in data must therefore be assumed to move on reconstruction in the same way as those in signal Monte Carlo. The yields in data are adjusted to mimic the migration observed in MC. Estimated background yields do not have to be treated in the same way due to how they are calculated (see Section 3.6.4). However, the data may contain background events that migrate differently to signal. The treatment of such events as signal will induce inaccuracies in the adjusted yields. The magnitude of this effect is expected to be small due to the high purity of most reconstructed final states and the relatively simple

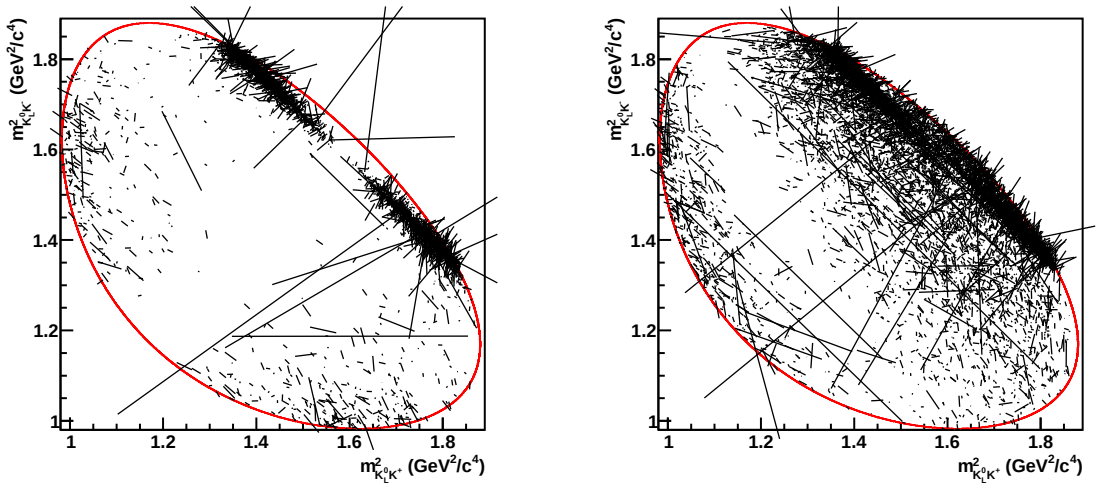

Figure 3.45: Migration of signal Monte Carlo events on reconstruction for $K^0_L K^+ K^-$ against $K^0_S \pi^0$ (left) and $K^0_L K^+ K^-$ against $K^\pm \pi^\mp$ (right). The black lines show the movement of individual points and the red line is the kinematic limit.

Dalitz plane binning that is employed (see Section 4.2). Furthermore, we incorporate a conservative systematic uncertainty related to the distribution of background events across the Dalitz plane (see Section 4.5.3).

Considering yields in data, we wish to transform between $\mathbf{D}^F$, the vector of yields measured in each bin, to $\mathbf{D}^I$, the vector of initial (unknown) yields in each bin. These vectors are $2\mathcal{N}$-dimensional because bins above and below the line $y = x$ are treated separately. For clarity, we denote the number of the i^{th} bin above the line, which by default is $-i$, to be $i + \mathcal{N}$.

To transform $\mathbf{D}^I$ into $\mathbf{D}^F$ we construct a $2\mathcal{N} \times 2\mathcal{N}$ *migration matrix* $\mathbf{U}$ such that:

$$\mathbf{D}^F = \mathbf{U}\mathbf{D}^I. \tag{3.18}$$

We can write the above expression in terms of individual elements of the vectors and matrices. Considering the movement of events from bin j into bin i:

$$\mathbf{D}^F_i = \sum_{j=1}^{2\mathcal{N}} \mathbf{U}_{i,j}\mathbf{D}^I_j. \tag{3.19}$$

The matrix element $\mathbf{U}_{i,j}$ is therefore equal to $u_{j,i}$, the number of events that move from bin j into bin i, divided by the total number of events that are initially in bin j:

$$\mathbf{U}_{i,j} \equiv \frac{u_{j,i}}{\sum_{k=1}^{2\mathcal{N}} u_{j,k}}. \tag{3.20}$$

The quantities $u_{j,i}$ must be determined using samples of signal MC. After determining $\mathbf{U}$,

we calculate $\mathbf{D}^I$ by inverting Equation 3.18:

$$\mathbf{D}^I = \mathbf{U}^{-1}\mathbf{D}^F. \tag{3.21}$$

Equation 3.22 shows the migration matrix for $K^0_L K^+K^-$ against $K^0_S\pi^0$, for a division of the Dalitz plane into three bins:

$$\begin{pmatrix} 0.862 & 0.118 & 0.005 & 0.004 & 0.000 & 0.000 \\ 0.113 & 0.881 & 0.005 & 0.000 & 0.000 & 0.000 \\ 0.015 & 0.001 & 0.989 & 0.000 & 0.000 & 0.000 \\ 0.010 & 0.001 & 0.000 & 0.852 & 0.106 & 0.000 \\ 0.000 & 0.000 & 0.000 & 0.139 & 0.894 & 0.010 \\ 0.000 & 0.000 & 0.000 & 0.004 & 0.001 & 0.990 \end{pmatrix}. \tag{3.22}$$

Further examples of migration matrices for different binnings are given in Section A.1. All of the migration matrices that are used in this analysis are invertible. This procedure induces systematic uncertainties on the parameters of interest which are quantified in Section 4.5.2.

3.5.5.4 Treatment of $K^0_{S,L}K^+K^-$ against $K^0_{S,L}h^+h^-$

Bin-to-bin migration is especially important for $K^0_{S,L}K^+K^-$ selected against $K^0_{S,L}h^+h^-$; the location of each event on both Dalitz planes must be taken into account simultaneously. There are four bin numbers to take into account: initial signal-side (i), initial opposite-side (j), final signal-side (k) and final opposite-side (l). Rather than use a 4-dimensional tensor, the initial and final numbers are converted into a unique index. Defining the number of bins on the opposite side as $\mathcal{N}_{\bar{D}^0}$, the signal-side index is

$$p = 2\mathcal{N}_{\bar{D}^0} \cdot i + j, \tag{3.23}$$

and the opposite-side index is

$$q = 2\mathcal{N}_{\bar{D}^0} \cdot k + l. \tag{3.24}$$

The migration matrix is then constructed as before using the values $u_{p,q}$ that have been measured in MC. For $K^0_S K^+K^-$ selected against $K^0_{S,L}K^+K^-$, the migration matrix dimensions are $4\mathcal{N}^2 \times 4\mathcal{N}^2$, and for $K^0_{S,L}K^+K^-$ selected against $K^0_{S,L}\pi^+\pi^-$ the dimensions are $32\mathcal{N} \times 32\mathcal{N}$.

3.5.5.5 Correction for negative yields

A few bins contain negative yields after the migration procedure has been applied. This usually occurs for bins in which no events are reconstructed in data. If there is a net migration of events out of such a bin in the reconstructed MC, the migrated yield in data will become negative. This is undesirable because negative bin yields are unphysical. In addition, the fit to extract the observables (see Section 4.3) may fail if the yield is used as a Poisson mean.

All negative bin yields are therefore changed to zero. The yields of the remaining 'positive' bins are redistributed so that the total number of events remains constant. The redistribution is designed to ensure the yields in the positive bins remain proportional to each other. We define r as the total number of events to be redistributed. Considering a bin of yield n, after redistribution the bin yield becomes $n \cdot (1 - r/n_{tot})$, where n_{tot} is the total number of events in the bins with positive yields.

Only a few bin yields must be altered in this manner. Table 3.15 shows the total of the negative yields in two, three and four bins compared to the yield in data. There are

Final state	Total of negative bins			Number of events in data
	$\mathcal{N} = 2$	3	4	
$K^0_S K^+ K^-$ against $\mathcal{CP}+$	−0.731	−0.418	−1.528	50
$K^0_S K^+ K^-$ against $\mathcal{CP}-$	−0.281	−0.266	−0.664	46
$K^0_S K^+ K^-$ against flavour	0.000	0.000	−0.049	846
$K^0_L K^+ K^-$ against $\mathcal{CP}+$	−0.588	−0.617	−1.210	59
$K^0_L K^+ K^-$ against $\mathcal{CP}-$	−0.408	−0.268	−3.742	64
$K^0_L K^+ K^-$ against flavour	0.000	0.000	0.000	1174
$K^0_S K^+ K^-$ against $K^0_L K^+ K^-$	−0.950	−0.910	−2.290	9
$K^0_S K^+ K^-$ against $K^0_S \pi^+ \pi^-$	−2.280	−2.000	−5.650	56
$K^0_S K^+ K^-$ against $K^0_L \pi^+ \pi^-$	−2.310	−5.740	−8.840	140
$K^0_L K^+ K^-$ against $K^0_S \pi^+ \pi^-$	−3.440	−4.200	−19.30	126

Table 3.15: The total of the negative bins for different final states.

almost no negative bins for the flavour-tagged decays because the large quantity of events reconstructed in each case ensures that each bin is well-populated. In contrast, decays tagged with mixed-$\mathcal{CP}$ events have a significant number of bins with zero events, which results in a proportionally large number of negative bins after the migration procedure. The most significant case is $K^0_L K^+ K^-$ against $K^0_S \pi^+ \pi^-$ with four Dalitz plane bins; the yield in the negative bins is over 10% of the total yield. There are 128 bins[7] for 126 events so it is unsurprising that many bins are empty.

[7]For the purposes of migration, bins above and below the line $y = x$ on the Dalitz plane are considered separately. In this case the $K^0_L K^+ K^-$ Dalitz plane is therefore divided into eight bins and the $K^0_S \pi^+ \pi^-$ Dalitz plane is divided into 16 bins, leading to a total of 128.

3.5.6 Global selection efficiencies

The global selection efficiency for each reconstructed final state is displayed in Table 3.16. The uncertainties reflect the size of the Monte Carlo data samples.

Final state category	Opposite-side final state	Efficiency (%)	
		$K^0_S K^+ K^-$	$K^0_L K^+ K^-$
Flavour	$K^\pm\pi^\mp$	14.6 ± 0.2	25.2 ± 0.3
	$K^\pm\pi^\mp\pi^0$	8.5 ± 0.2	14.3 ± 0.2
	$K^\pm\pi^\mp\pi^+\pi^-$	10.8 ± 0.2	15.9 ± 0.2
	$K^\pm e^\mp \nu_e$	11.9 ± 0.2	
$\mathcal{CP}$ even	K^+K^-	12.2 ± 0.2	23.7 ± 0.3
	$\pi^+\pi^-$	15.1 ± 0.2	29.4 ± 0.3
	$K^0_S\pi^0\pi^0$	2.8 ± 0.1	5.9 ± 0.1
	$K^0_L\pi^0$	8.0 ± 0.1	
	$K^0_L\eta(\gamma\gamma)$	7.9 ± 0.1	
	$K^0_L\eta(\pi^+\pi^-\pi^0)$	1.6 ± 0.1	
	$K^0_L\omega$	3.1 ± 0.1	
	$K^0_L\eta'(\pi^+\pi^-\eta)$	1.7 ± 0.1	
$\mathcal{CP}$ odd	$K^0_S\pi^0$	7.1 ± 0.1	10.6 ± 0.2
	$K^0_S\eta(\gamma\gamma)$	6.5 ± 0.1	9.7 ± 0.2
	$K^0_S\eta(\pi^+\pi^-\pi^0)$	4.4 ± 0.1	6.8 ± 0.1
	$K^0_S\omega$	3.4 ± 0.1	5.0 ± 0.1
	$K^0_S\eta'(\pi^+\pi^-\eta)$	1.4 ± 0.1	2.0 ± 0.1
	$K^0_L\pi^0\pi^0$	0.51 ± 0.04	
Mixed $\mathcal{CP}$	$K^0_S\pi^+\pi^-$	7.9 ± 0.1	13.0 ± 0.2
	$K^0_L\pi^+\pi^-$	14.0 ± 0.2	
	$K^0_S K^+ K^-$	4.9 ± 0.1	7.0 ± 0.1

Table 3.16: Selection efficiency for the different $K^0_{S,L}K^+K^-$ modes.

3.5.7 Kaon momentum spectrum

Using both signal Monte Carlo and data we determine the momentum spectrum of each of the reconstructed particles in the $K^0_S K^+ K^-$ final state. In both cases we use $K^0_S K^+ K^-$ selected against $K^\pm\pi^\mp$.

Figure 3.46 shows a comparison between the momentum spectra in MC and data. The mean and RMS of these distributions are listed in Table 3.17. At low momentum, dis-

Data type	$p_{K^0_S}$ (GeV/c^2)	p_{K^+} (GeV/c^2)	p_{K^-} (GeV/c^2)
Model generator-level MC	0.493 ± 0.103	0.307 ± 0.117	0.308 ± 0.117
Model reconstruction-level MC	0.478 ± 0.104	0.320 ± 0.109	0.322 ± 0.108
Data	0.471 ± 0.099	0.344 ± 0.106	0.309 ± 0.104

Table 3.17: Average momenta for each particle in the $K^0_S K^+ K^-$ decay, for various datatypes.

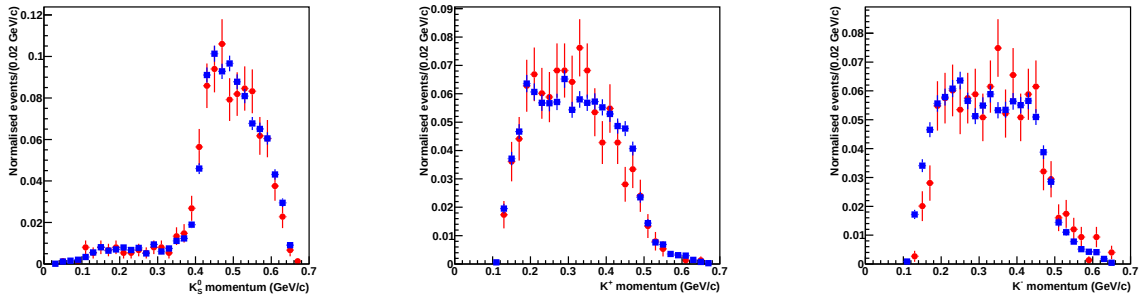

Figure 3.46: Momentum spectra for data (red circles) and signal Monte Carlo (blue squares). The spectra shown are for the K^0_S (left), K^+ (middle) and K^- (right).

crepancies are observed between the spectra in data and Monte Carlo. In Section 4.5.9 we describe the evaluation of a systematic uncertainty related to this effect. These discrepancies occur for the $K^0_S K^+ K^-$ final state because of the looser cuts employed to select these events. For all other final states containing kaons the standard selections are used and no difference is seen.

3.6 Background studies

3.6.1 Introduction

It is very important to estimate the level of background in each sample of data that we use in the analysis. We consider two types of background: *flat* and *peaking*.

Flat backgrounds are distributed across the signal region and sidebands without any significant peaking structures. The quantity of flat background in the signal region can be estimated using the sideband populations in data. An example of a flat background is the semileptonic background to $K^0_S K^+ K^-$ tagged with $K^+ K^-$. In this situation a $K^\pm e^\mp \nu_e$ final state can be misreconstructed as $K^+ K^-$ if the electron is misidentified as a kaon and the neutrino is (inevitably) not reconstructed. The resulting $m_{\rm bc}$ calculated for the opposite-side D candidate can take a spectrum of values depending on the kinematics of the $K^\pm e^\mp \nu_e$ system. In contrast, the $K^0_S K^+ K^-$ system is correctly reconstructed so the signal-side $m_{\rm bc}$ values are all located close to the nominal D^0 mass.

Peaking backgrounds are those that lie predominantly in the signal region. They often have the same final-state particle content as the signal decay. For example, the nonresonant decay $D \to K^+ K^- \pi^+ \pi^-$ is a peaking background to $D \to K^0_S K^+ K^-$. Such backgrounds cannot be reliably distinguished from genuine signal events in the data. The amount of peaking background must therefore be estimated by scaling the yield found in MC by the ratio of integrated luminosities (see Section 2.5.1.1).

For each reconstructed decay mode the estimated quantities of peaking and flat back-

ground in the signal region are denoted B_P and B_F respectively. For $\mathcal{CP}$-tagged events, a combined background estimate is made (separately for $\mathcal{CP}+$ and $\mathcal{CP}-$). Often the yields for individual $\mathcal{CP}$ eigenstates are very low and hence have large uncertainties, so the background estimate is very sensitive to fluctuations. Summing the yields reduces this sensitivity and therefore the background yields are more accurately estimated. This approach is consistent with the combination of $\mathcal{CP}$-tagged events in the data (see Section 3.4.4).

3.6.2 Fully-reconstructed events

For fully-reconstructed events, the yield of flat background in the signal region is estimated by measuring data yields in the sidebands on the $m_{\rm bc}$ plane. The boundaries of the sidebands have been defined in Section 3.2.6.1. The sideband yields are extrapolated into the signal region as follows:

$$B_F = \frac{a_S}{a_D} n_D + \sum_{i=A,B,C} \frac{a_S}{a_i} \left(n_i - \frac{a_i}{a_D} n_D \right), \tag{3.25}$$

where a_x is the area of sideband x ($x = A, B, C, D$), n_x is the flat background yield in sideband x, a_S is the area of the signal region and n_S is the number of events in the signal region. This formulation ensures there is no double counting of events. The distributions of data across the $m_{\rm bc}$ plane have been presented in Section 3.4.5. The yields of data in each region are summarised in Table 3.18.

Final state	S	A	B	C	D
$K^0_S K^+ K^-$ against $K^+ K^-$	12	0	0	0	0
$K^0_S K^+ K^-$ against $\pi^+ \pi^-$	4	0	0	0	0
$K^0_S K^+ K^-$ against $K^0_S \pi^0 \pi^0$	7	0	0	0	0
$K^0_S K^+ K^-$ against $K^0_S \pi^0$	18	2	0	0	0
$K^0_S K^+ K^-$ against $K^0_S \eta(\gamma\gamma)$	4	0	0	0	0
$K^0_S K^+ K^-$ against $K^0_S \omega(\pi^+\pi^-\pi^0)$	14	0	0	0	0
$K^0_S K^+ K^-$ against $K^0_S \eta(\pi^+\pi^-\pi^0)$	2	0	0	0	0
$K^0_S K^+ K^-$ against $K^0_S \eta'(\pi^+\pi^-\eta)$	3	0	0	0	0
$K^0_S K^+ K^-$ against $K^\pm \pi^\mp$	168	0	1	2	1
$K^0_S K^+ K^-$ against $K^\pm \pi^\mp \pi^0$	330	17	0	5	1
$K^0_S K^+ K^-$ against $K^\pm \pi^\mp \pi^+ \pi^-$	250	11	6	7	2
$K^0_S K^+ K^-$ against $K^0_S K^+ K^-$	4	0	0	0	0
$K^0_S K^+ K^-$ against $K^0_S \pi^+ \pi^-$	56	0	0	1	0

Table 3.18: Data yields in the signal region S and sidebands (A, B, C, D) for $K^0_S K^+ K^-$ against fully-reconstructed final states.

The estimated signal region yield of peaking background is:

$$B_P = m_P^{31-37} \times f_{D^0\bar{D}^0}^{31-37} + m_P^{43-46} \times f_{D^0\bar{D}^0}^{43-46}, \tag{3.26}$$

where $f_{D^0\bar{D}^0}^{31-37}$ and $f_{D^0\bar{D}^0}^{43-46}$ are the integrated luminosity ratios between Monte Carlo and data

for datasets 31–37 and 43–46 (defined in Section 2.5) and m_P^{31-37} and m_P^{43-46} are the MC peaking background yields in these datasets. It is assumed that the branching fractions of the peaking background decays are correctly represented in the generic Monte Carlo samples; the systematic uncertainty related to this assumption is evaluated in Section 4.5.3.

The backgrounds to $K_S^0K^+K^-$ selected against fully-reconstructed final states are in general very low. The largest background contribution is usually the $K^+K^-\pi^+\pi^-$ peaking background in which the two pions combine to fake the $K_S^0K^+K^-$ final state. The yield of this background is approximately 3.2% of the signal yield. The ratio of flat background to signal is less than 7.3% for all decay modes.

Figures 3.47–3.52 show the Monte Carlo background distribution across the $m_{\rm bc}$ plane for fully-reconstructed final states. The backgrounds are colour-coded and listed on the plots[8]. The Monte Carlo signal and background yields are summarised in Table 3.19.

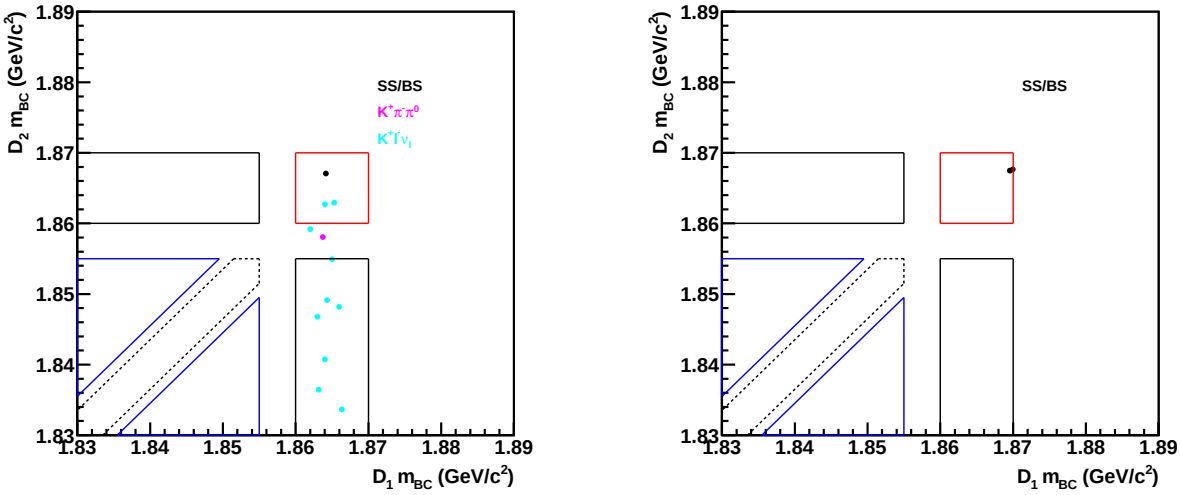

Figure 3.47: Background distribution across the $m_{\rm bc}$ plane for $K_S^0K^+K^-$ against K^+K^- (left) and $K_S^0K^+K^-$ against $\pi^+\pi^-$ (right).

3.6.3 Events containing a missing particle

For events containing a missing particle we do not use the $m_{\rm bc}$ plane to estimate the level of background. For final states containing a K_L^0 we use the $m^2_{\rm miss}$ projection, and for states containing a neutrino we use the $U_{\rm miss}$ projection. In contrast to the procedure used for fully-reconstructed final states, Monte Carlo data are used to estimate the yield of both peaking and flat backgrounds. The sideband backgrounds are rarely 'flat', so we estimate the background using the ratios between MC yields in the sidebands and signal region. There is a systematic uncertainty associated with this procedure that is evaluated in Section 4.5.3.

[8]Acronyms are defined in Table B.1.

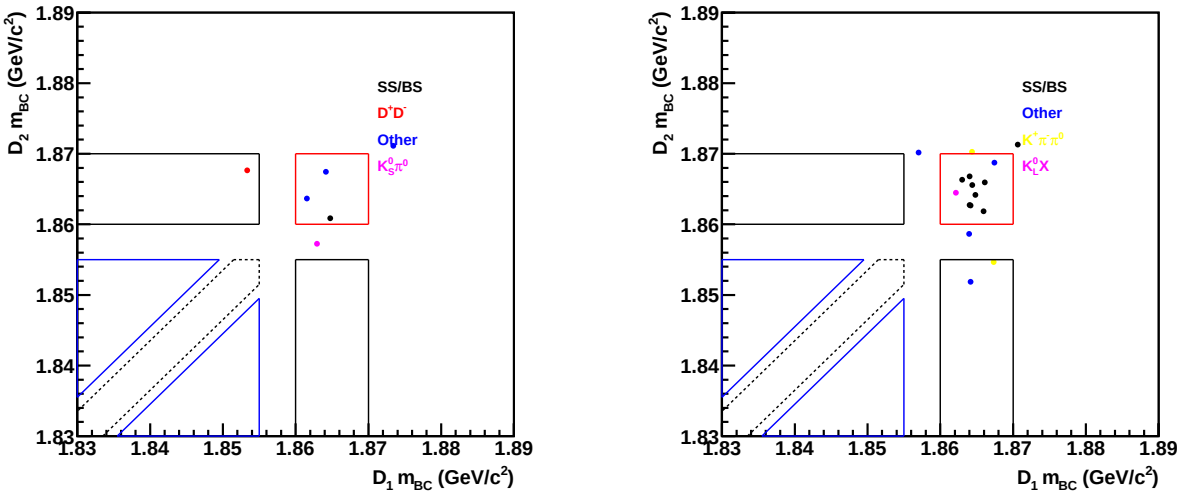

Figure 3.48: Background distribution across the $m_{\rm bc}$ plane for $K^0_S K^+ K^-$ against $K^0_S \pi^0 \pi^0$ (left) and $K^0_S K^+ K^-$ against $K^0_S \pi^0$ (right).

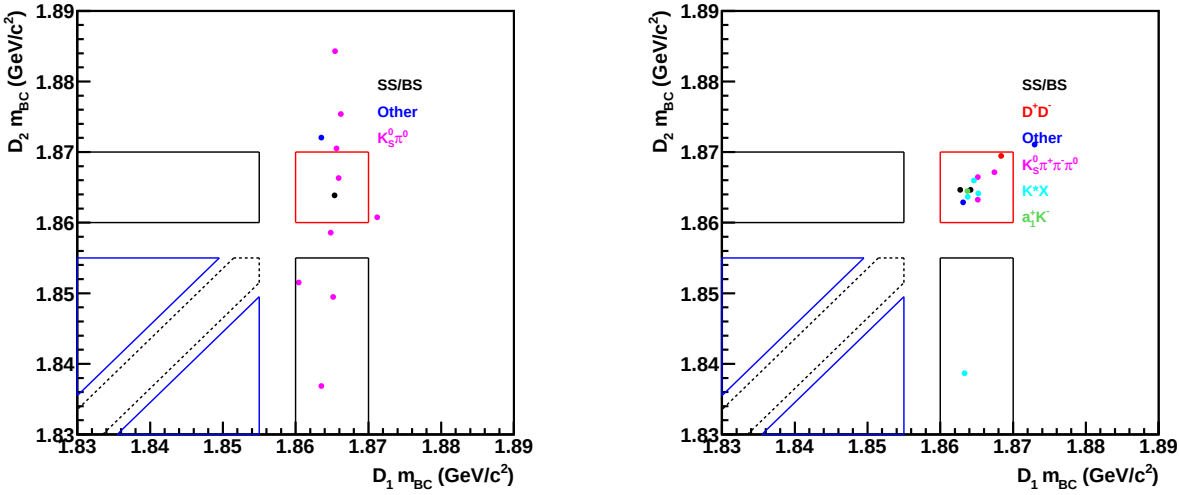

Figure 3.49: Background distribution across the $m_{\rm bc}$ plane for $K^0_S K^+ K^-$ against $K^0_S \eta(\gamma\gamma)$ (left) and $K^0_S K^+ K^-$ against $K^0_S \omega(\pi^+\pi^-\pi^0)$ (right).

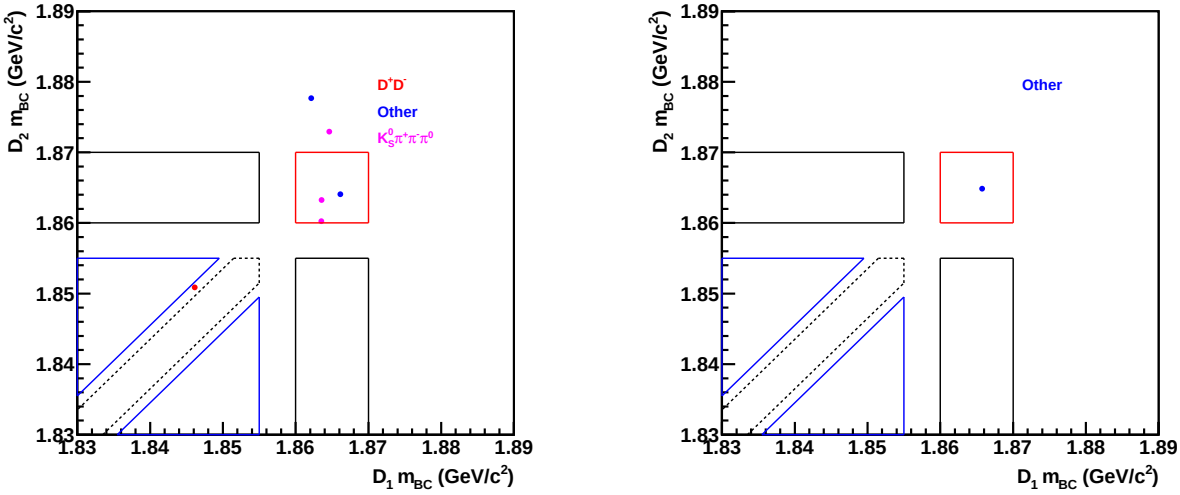

Figure 3.50: Background distribution across the $m_{\rm bc}$ plane for $K^0_S K^+ K^-$ against $K^0_S \eta(\pi^+\pi^-\pi^0)$ (left) and $K^0_S K^+ K^-$ against $K^0_S K^+ K^-$ (right).

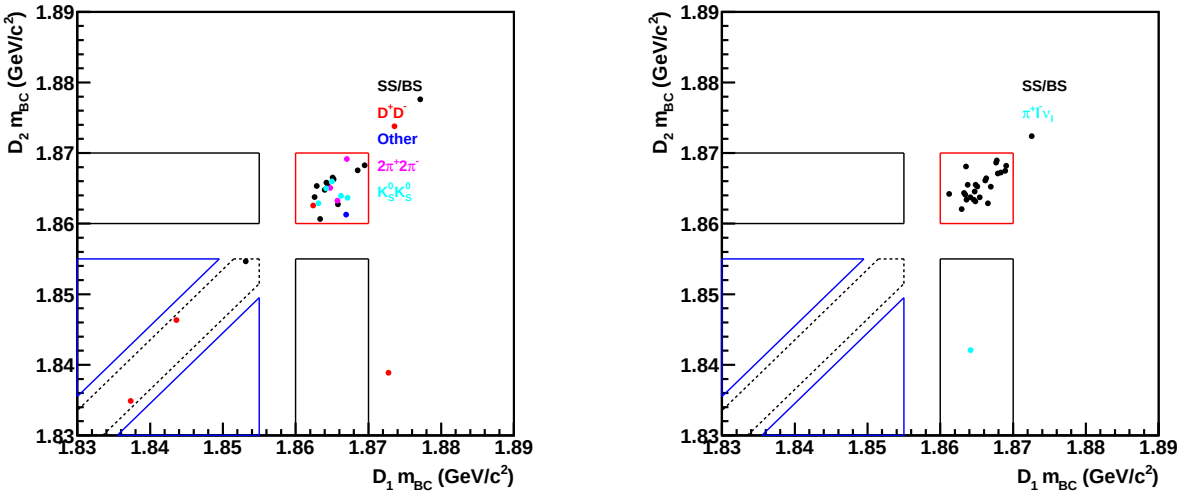

Figure 3.51: Background distribution across the $m_{\rm bc}$ plane for $K^0_S K^+ K^-$ against $K^0_S \pi^+ \pi^-$ (left) and $K^0_S K^+ K^-$ against $K^\pm \pi^\mp$ (right).

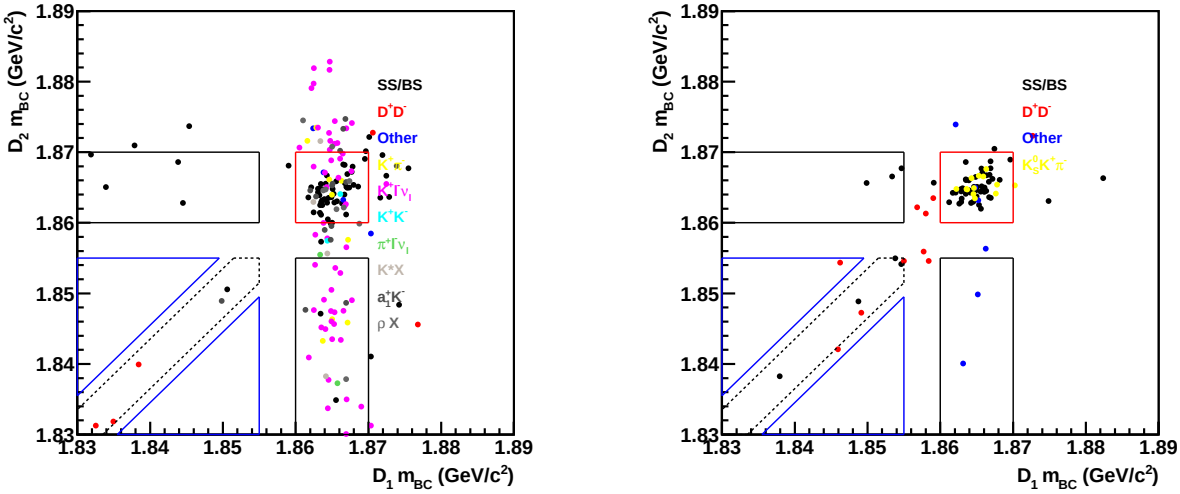

Figure 3.52: Background distribution across the $m_{\rm bc}$ plane for $K^0_S K^+ K^-$ against $K^\pm \pi^\mp \pi^0$ (left) and $K^0_S K^+ K^-$ against $K^\pm \pi^\mp \pi^+ \pi^-$ (right).

For final states with a missing particle there are significant backgrounds due to particle misidentifications and decays containing extra particles that were missed in the reconstruction. This is a particular problem for neutral particles reconstructed using calorimeter showers; for example, the $K^0_L \pi^0 \pi^0$ final state could be reconstructed as $K^0_L \pi^0$ if one of the π^0 was missed.

We aim to determine the *true* quantities of background in the signal region using the known yields of data and MC. The backgrounds are divided into three categories depending on their principal location on the $m^2_{\rm miss}$ or $U_{\rm miss}$ projection: peaking predominantly in the signal region (denoted P), predominantly in the low sideband (denoted L), and predominantly in the high sideband (denoted H). All quantities of interest are defined in Table 3.20.

Final state	S		A		B		C		D	
	S	B (B_P)	S	B	S	B	S	B	S	B
$K^0_S K^+ K^-$ against K^+K^-	273	3 (1)	0	7	1	0	0	0	0	0
$K^0_S K^+ K^-$ against $\pi^+\pi^-$	121	2 (2)	0	0	0	0	0	0	0	0
$K^0_S K^+ K^-$ against $K^0_S\pi^0\pi^0$	135	3 (1)	2	0	1	1	0	0	0	0
$K^0_S K^+ K^-$ against $K^0_S\pi^0$	116	10 (8)	0	2	0	0	0	0	0	0
$K^0_S K^+ K^-$ against $K^0_S\eta(\gamma\gamma)$	24	2 (1)	0	3	0	0	0	0	0	0
$K^0_S K^+ K^-$ against $K^0_S\omega(\pi^+\pi^-\pi^0)$	69	11 (2)	0	1	1	0	0	0	0	0
$K^0_S K^+ K^-$ against $K^0_S\eta(\pi^+\pi^-\pi^0)$	9	3 (0)	0	0	0	0	0	0	0	0
$K^0_S K^+ K^-$ against $K^0_S\eta'(\pi^+\pi^-\eta)$	10	0 (0)	0	0	0	0	0	0	0	0
$K^0_S K^+ K^-$ against $K^0_S K^+K^-$	45	1 (1)	0	0	1	0	0	0	0	0
$K^0_S K^+ K^-$ against $K^0_S\pi^+\pi^-$	643	21 (11)	1	0	3	0	0	3	0	0
$K^0_S K^+ K^-$ against $K^\pm\pi^\mp$	1852	24 (24)	1	1	15	0	0	0	0	0
$K^0_S K^+ K^-$ against $K^\pm\pi^\mp\pi^0$	3974	71 (44)	120	32	9	4	0	5	1	0
$K^0_S K^+ K^-$ against $K^\pm\pi^\mp\pi^+\pi^-$	2880	59 (45)	7	2	7	3	0	5	1	1

Table 3.19: Generic Monte Carlo signal and background yields in the signal region (S) and sidebands (A, B, C, D) for $K^0_S K^+ K^-$ against fully-reconstructed final states. S represents the signal MC count, B is background, and B_P is the yield of peaking background in the signal region.

Type of data	Low sideband	Signal region	High sideband
MC signal	m_{S1}	m_{S2}	m_{S3}
MC background (L)	m_{L1}	m_{L2}	m_{L3}
MC background (H)	m_{H1}	m_{H2}	m_{H3}
MC background (P)	m_{P1}	m_{P2}	m_{P3}
Data	D_1	D_2	D_3
True signal	T_{S1}	T_{S2}	T_{S3}
True background (L)	T_{L1}	T_{L2}	T_{L3}
True background (H)	T_{H1}	T_{H2}	T_{H3}
True background (P)	T_{P1}	T_{P2}	T_{P3}

Table 3.20: Definitions of quantities used in the background estimation for partially-reconstructed final states.

The true amount of peaking background in region i is equal to:

$$T_{Pi} = m_{Pi}^{31-37} \times f_{D^0\overline{D}^0}^{31-37} + m_{Pi}^{43-46} \times f_{D^0\overline{D}^0}^{43-46}, \tag{3.27}$$

where m_{Pi}^{31-37} and m_{Pi}^{43-46} are the peaking background yields in datasets 31–37 and 43–46 respectively.

The following is true for sideband i:

$$D_i = T_{Si} + T_{Li} + T_{Hi} + T_{Pi} \tag{3.28}$$

$$\implies (D_i - T_{Pi}) = T_{Si} + T_{Li} + T_{Hi}. \tag{3.29}$$

We assume that the ratio $T_{Si} : T_{Li} : T_{Hi}$ is the same as $m_{Si} : m_{Li} : m_{Hi}$. By definition, m_{Li}

will predominantly lie in the low sideband, i.e. it will predominantly consist of background of the type m_{L1}. Similarly, the majority of m_{Hi} will be m_{H3} and the majority of m_{Si} will be m_{S2}.

Our goal is to determine the true quantity of signal and each type of background in the signal region, i.e. T_{S2}, T_{L2}, T_{H2} and T_{P2}. Equation 3.29 must therefore be expressed in terms of only these variables. The equivalence between the ratios of data and Monte Carlo described above can be used. In order to avoid division by zero, we rewrite the T_{xi} as $T_{yi} \cdot (m_{xi}/m_{yi})$ where the subscript y is the dominant region for datatype x:

$$(D_1 - T_{P1}) = T_{S2}\frac{m_{S1}}{m_{S2}} + T_{L1}\frac{m_{L1}}{m_{L1}} + T_{H3}\frac{m_{H1}}{m_{H3}}, \tag{3.30}$$

$$(D_2 - T_{P2}) = T_{S2}\frac{m_{S2}}{m_{S2}} + T_{L1}\frac{m_{L2}}{m_{L1}} + T_{H3}\frac{m_{H2}}{m_{H3}}, \tag{3.31}$$

$$(D_3 - T_{P3}) = T_{S2}\frac{m_{S3}}{m_{S2}} + T_{L1}\frac{m_{L3}}{m_{L1}} + T_{H3}\frac{m_{H3}}{m_{H3}}. \tag{3.32}$$

The quantities in the signal region can be determined as follows. We define a matrix of ratios of MC yields:

$$\mathbf{A} \equiv \begin{pmatrix} m_{S1}/m_{S2} & 1 & m_{H1}/m_{H3} \\ 1 & m_{L2}/m_{L1} & m_{H2}/m_{H3} \\ m_{S3}/m_{S2} & m_{L3}/m_{L1} & 1 \end{pmatrix}. \tag{3.33}$$

We also define $\mathbf{b}$, a vector of data yields with the estimated peaking background subtracted, and $\mathbf{x}$, a vector of true quantities which is to be evaluated:

$$\mathbf{b} \equiv \begin{pmatrix} D_1 - T_{P1} \\ D_2 - T_{P2} \\ D_3 - T_{P3} \end{pmatrix}, \qquad \mathbf{x} \equiv \begin{pmatrix} T_{S2} \\ T_{L1} \\ T_{H3} \end{pmatrix}. \tag{3.34}$$

The quantities are related as follows:

$$\mathbf{b} = \mathbf{A}\mathbf{x} \qquad \Longrightarrow \qquad \mathbf{x} = \mathbf{A}^{-1}\mathbf{b}. \tag{3.35}$$

We therefore have:

$$T_{S2} = \mathbf{x}_0, \tag{3.36}$$

$$T_{L2} = \mathbf{x}_1 \times m_{L2}/m_{L1}, \tag{3.37}$$

$$T_{H2} = \mathbf{x}_2 \times m_{H2}/m_{H3}. \tag{3.38}$$

The final flat and peaking background yields are:

$$B_F = T_{L2} + T_{H2}, \tag{3.39}$$

$$B_P = T_{P2}. \tag{3.40}$$

The backgrounds for $K^0_S K^+ K^-$ against final states containing a K^0_L ('$K^0_L X$') usually peak in the high or low sidebands. There are three main types of background to $K^0_L K^+ K^-$:

- $K^0_S K^+ K^-$ events that are misreconstructed as $K^0_L K^+ K^-$. These are the largest contribution because the three final state particles are identical in quark content, and hence have similar kinematics, to those of $K^0_L K^+ K^-$. They consequently peak directly underneath the signal peak on the $m^2_{\rm miss}$ plane. The K^0_S decays either to $\pi^+\pi^-$ or $\pi^0\pi^0$, both of which are missed by the reconstruction technique. The vast majority decay to $\pi^0\pi^0$, which is expected because it is comparatively more difficult to reconstruct a neutral particle than a charged one. For $K^0_L K^+ K^-$ against $K^\pm\pi^\mp$, $K^\pm\pi^\mp\pi^0$ and $K^\pm\pi^\mp\pi^+\pi^-$, the fraction that decay to $\pi^+\pi^-$ is 1.6%, 1.0% and 2.1% respectively. This is much lower than the measured branching fraction of $K^0_S \to \pi^+\pi^-$ decays, 69.2% [11].

- Well-isolated peaks such as $K^\pm e^\mp \nu_e$ and $K^\pm\pi^\mp$. These do not impinge on the signal region or the sidebands.

- $K^+K^-\pi^0\pi^0$ decays for which both π^0 daughters are not reconstructed. This background lies in both the signal region and low mass sideband because a spectrum of $m^2_{\rm miss}$ values can be obtained depending on the kinematics of the final state. The combined invariant mass of the four particles is often close to that expected for $K^0_L K^+ K^-$. This background is not flatly distributed across the signal region and low mass sideband, so to avoid a biased background estimate it is treated as peaking.

Figures 3.53–3.62 show the Monte Carlo background distributions across the $m^2_{\rm miss}$ projection for each final state containing K^0_L. In each case the L, S and H regions have been indicated at the top of the plot. The backgrounds are colour-coded and are shown stacked on top of each other[9]. The signal distribution is drawn with a thick black line; it has not been stacked with the backgrounds.

Figure 3.63 shows the background distribution on the $U_{\rm miss}$ projection for $K^0_S K^+ K^-$ against $K^\pm e^\mp \nu_e$ Monte Carlo. The backgrounds are shown stacked in colour and the signal is the thick black line.

The data and background yields for $K^0_S K^+ K^-$ against $K^0_L X$ states are summarised in Table 3.21.

[9] Acronyms are defined in Table B.2.

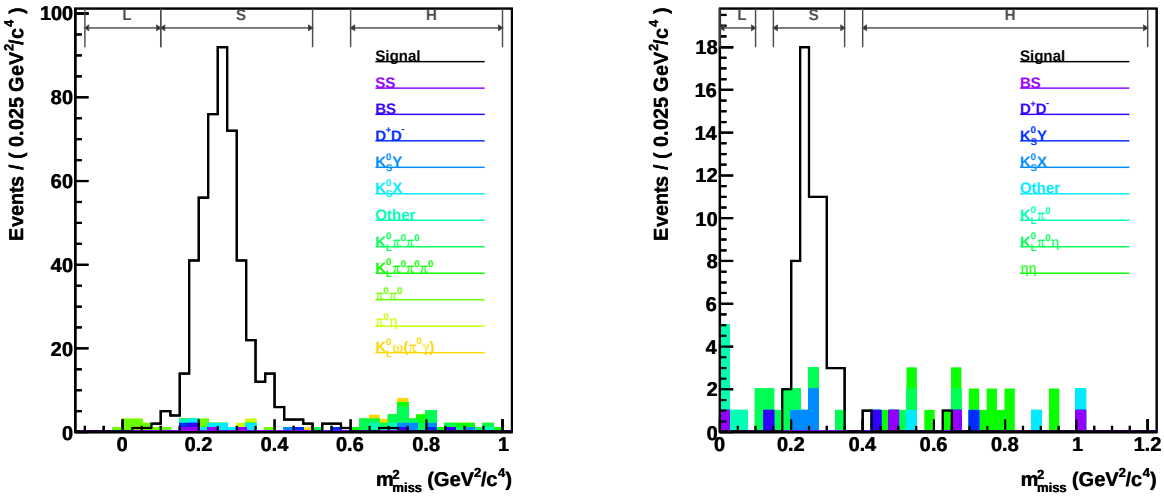

Figure 3.53: m^2_{miss} distribution for $K^0_S K^+ K^-$ against $K^0_L \pi^0$ (left) and $K^0_S K^+ K^-$ against $K^0_L \eta(\gamma\gamma)$ (right).

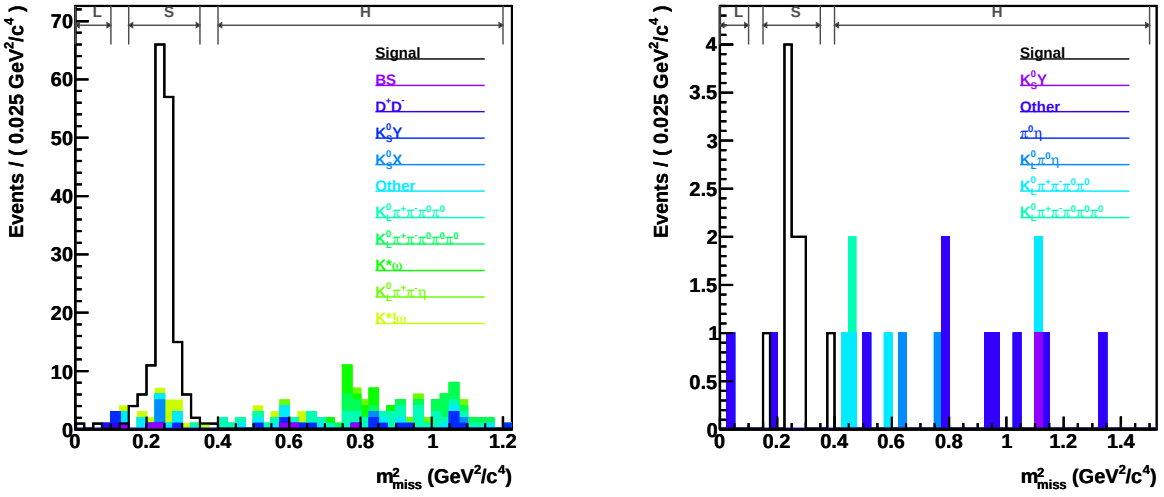

Figure 3.54: m^2_{miss} distribution for $K^0_S K^+ K^-$ against $K^0_L \omega(\pi^+\pi^-\pi^0)$ (left) and $K^0_S K^+ K^-$ against $K^0_L \eta(\pi^+\pi^-\pi^0)$ (right).

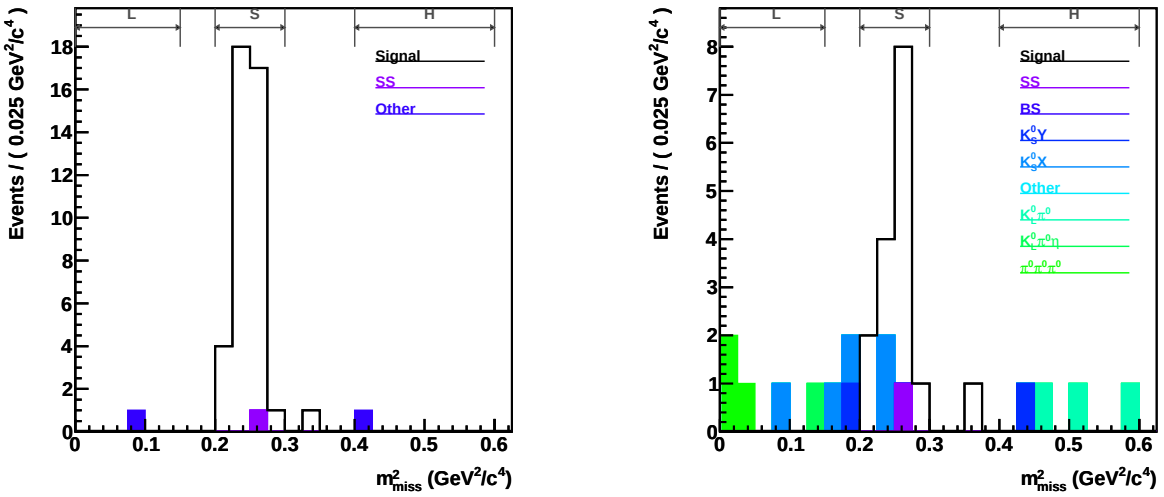

Figure 3.55: m^2_{miss} distribution for $K^0_S K^+ K^-$ against $K^0_L \eta'(\pi^+\pi^-\eta)$ (left) and $K^0_S K^+ K^-$ against $K^0_L \pi^0\pi^0$ (right).

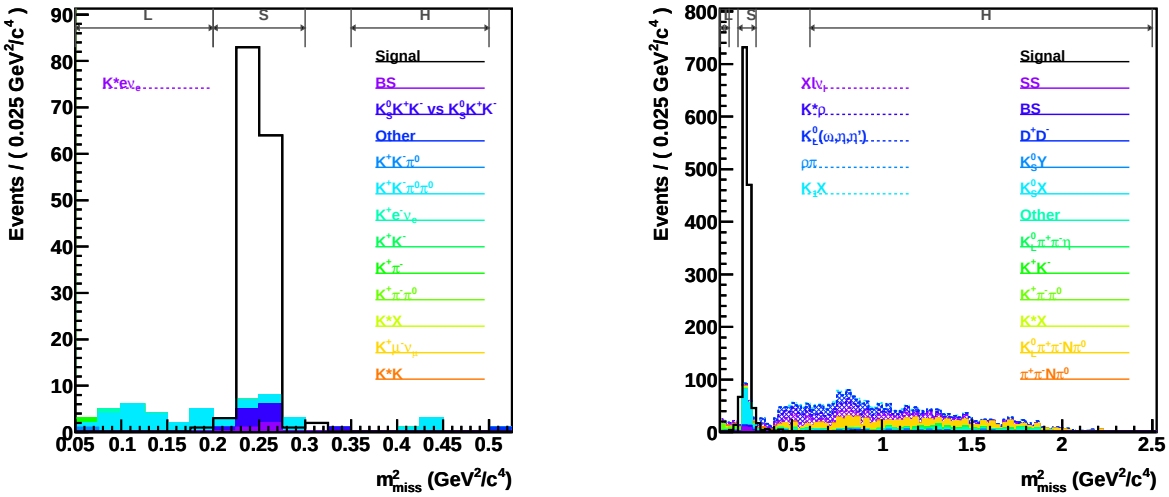

Figure 3.56: m^2_{miss} distribution for $K^0_S K^+ K^-$ against $K^0_L K^+ K^-$ (left) and $K^0_S K^+ K^-$ against $K^0_L \pi^+ \pi^-$ (right).

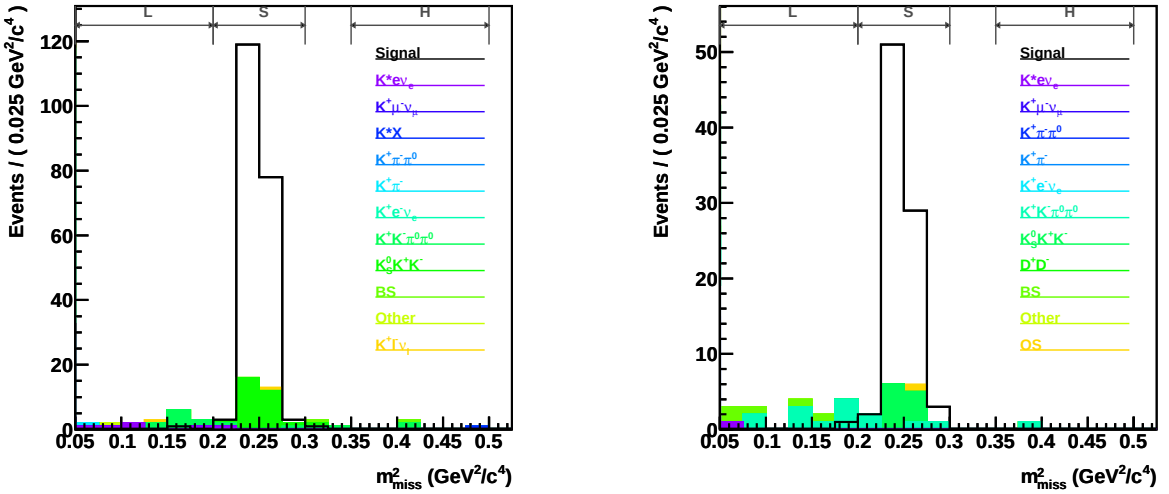

Figure 3.57: m^2_{miss} distribution for $K^0_L K^+ K^-$ against $K^+ K^-$ (left) and $K^0_L K^+ K^-$ against $\pi^+ \pi^-$ (right).

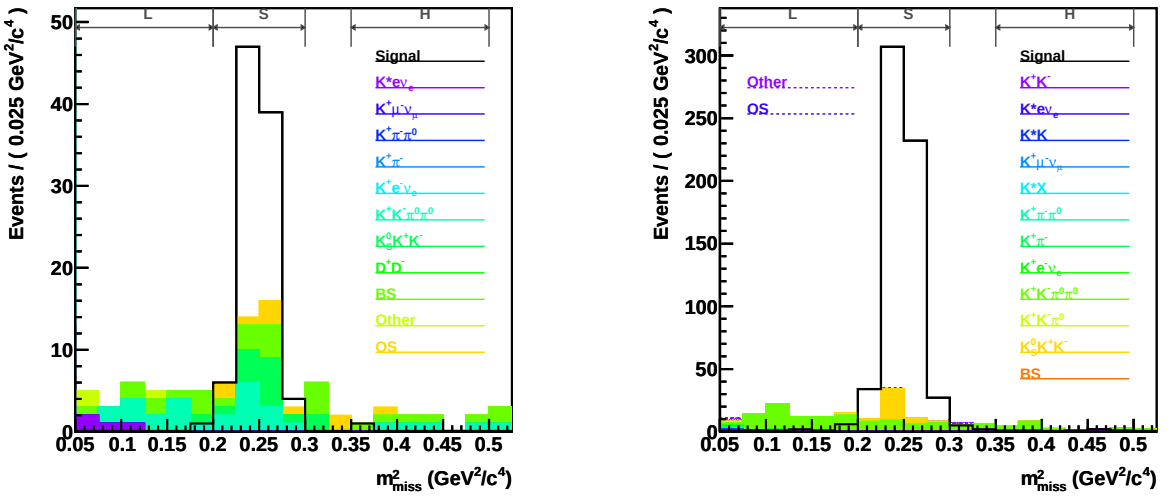

Figure 3.58: m^2_{miss} distribution for $K^0_L K^+ K^-$ against $K^0_S \pi^0 \pi^0$ (left) and $K^0_L K^+ K^-$ against $K^0_S \pi^0$ (right).

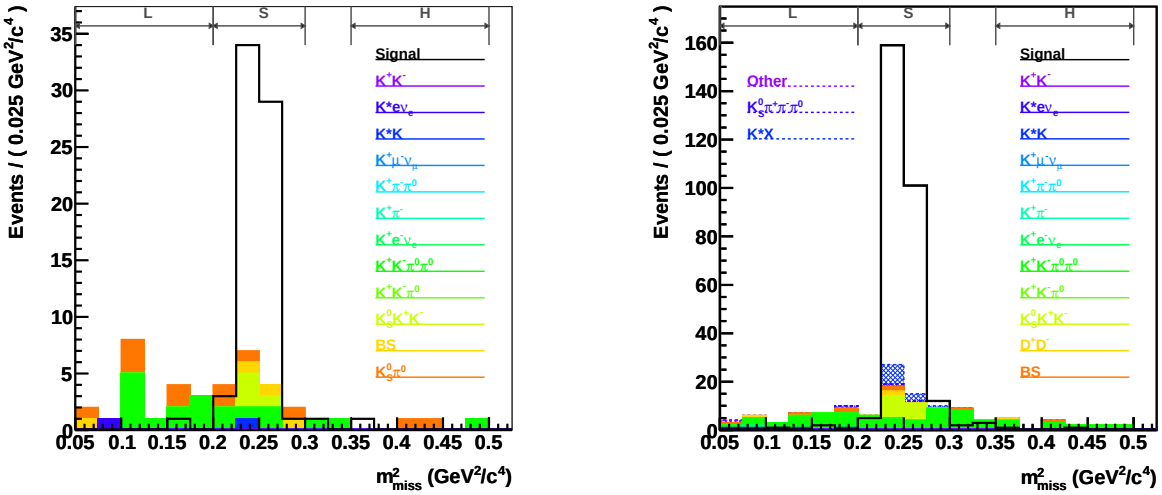

Figure 3.59: m^2_{miss} distribution for $K^0_L K^+K^-$ against $K^0_S\eta(\gamma\gamma)$ (left) and $K^0_L K^+K^-$ against $K^0_S\omega(\pi^+\pi^-\pi^0)$ (right).

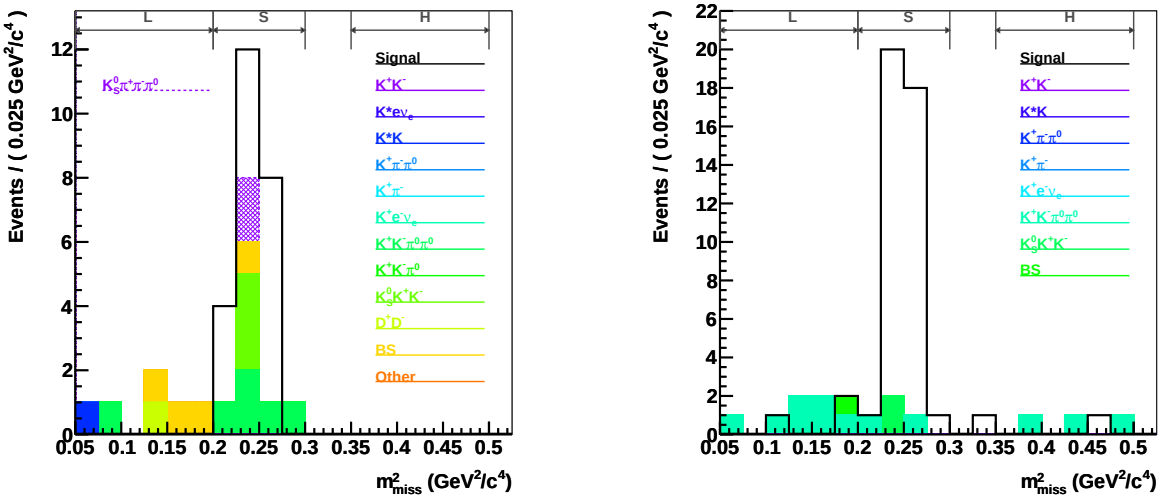

Figure 3.60: m^2_{miss} distribution for $K^0_L K^+K^-$ against $K^0_S\eta(\pi^+\pi^-\pi^0)$ (left) and $K^0_L K^+K^-$ against $K^0_S\eta'(\pi^+\pi^-\eta)$ (right).

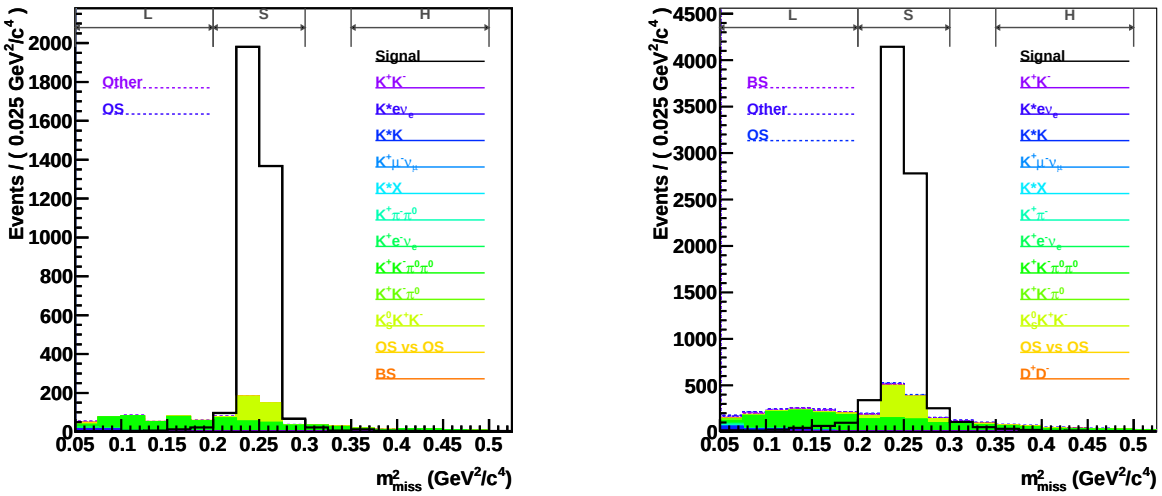

Figure 3.61: m^2_{miss} distribution for $K^0_L K^+K^-$ against $K^\pm\pi^\mp$ (left) and $K^0_L K^+K^-$ against $K^\pm\pi^\mp\pi^0$ (right).

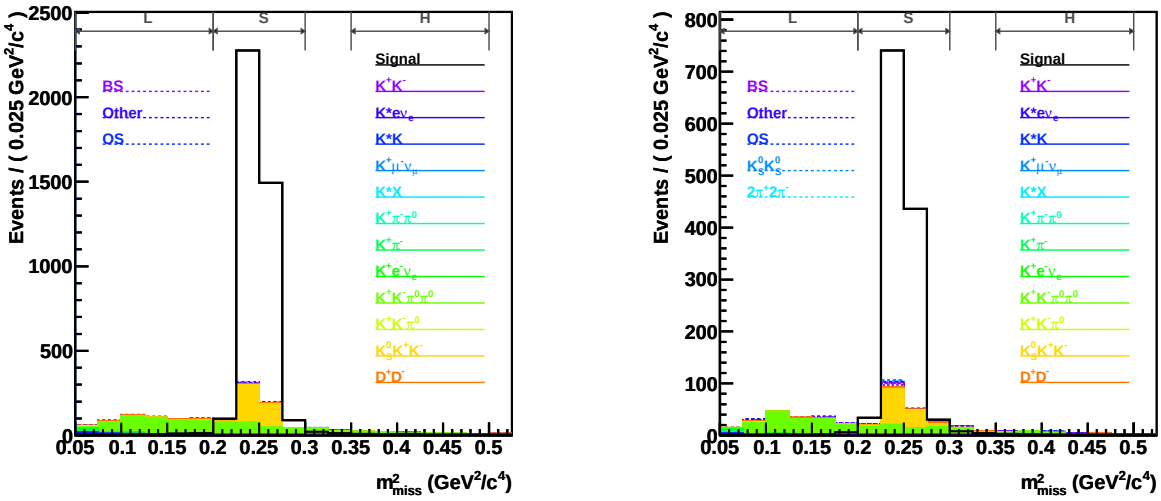

Figure 3.62: m^2_{miss} distribution for $K^0_L K^+ K^-$ against $K^\pm \pi^\mp \pi^+ \pi^-$ (left) and $K^0_L K^+ K^-$ against $K^0_S \pi^+ \pi^-$ (right).

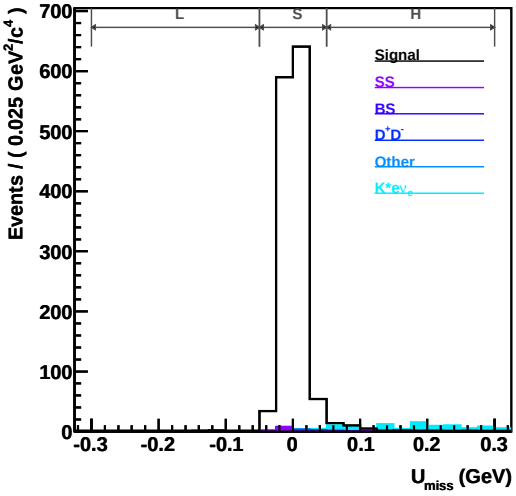

Figure 3.63: U_{miss} distribution for $K^0_S K^+ K^-$ against $K^\pm e^\mp \nu_e$.

The data and background yields for $K^0_L K^+ K^-$ against all final states and $K^0_S K^+ K^-$ against $K^\pm e^\mp \nu_e$ are summarised in Table 3.22.

3.6.4 $K^0_{S,L} K^+ K^-$ background distribution across the Dalitz plane

We are considering event yields in bins across the Dalitz plane so it is important to determine the estimated yield of both flat and peaking backgrounds in each bin. Some backgrounds are expected to be distributed evenly across the Dalitz plane ('phase-space'), and others are expected to be distributed according to the $K^0_S K^+ K^-$ resonant model ('resonant').

We consider the following phase-space backgrounds:

- Signal-side background to $K^0_S K^+ K^-$,

Opposite-side final state	Quantity	Yield Low	Signal	High
$K^0_L\pi^0$	D_k	1	17	6
	m_{sk}	4	463	2
	m_{pk}	0	8	1
	m_{lk}	10	4	0
	m_{hk}	0	12	45
$K^0_L\eta(\gamma\gamma)$	D_k	0	4	5
	m_{sk}	0	56	2
	m_{pk}	0	4	0
	m_{lk}	0	0	0
	m_{hk}	7	6	25
$K^0_L\omega(\pi^+\pi^-\pi^0)$	D_k	0	4	4
	m_{sk}	2	167	0
	m_{pk}	0	4	2
	m_{lk}	0	0	0
	m_{hk}	1	20	111
$K^0_L\eta(\pi^+\pi^-\pi^0)$	D_k	0	1	2
	m_{sk}	0	9	0
	m_{pk}	0	0	0
	m_{lk}	0	0	0
	m_{hk}	1	1	16

Opposite-side final state	Quantity	Yield Low	Signal	High
$K^0_L\eta'(\pi^+\pi^-\eta)$	D_k	0	1	0
	m_{sk}	0	40	0
	m_{pk}	0	0	0
	m_{lk}	0	0	0
	m_{hk}	1	1	1
$K^0_L\pi^0\pi^0$	D_k	1	5	0
	m_{sk}	0	15	0
	m_{pk}	1	2	0
	m_{lk}	0	0	0
	m_{hk}	4	1	4
$K^0_L K^+K^-$	D_k	1	10	0
	m_{sk}	1	151	0
	m_{pk}	0	0	0
	m_{lk}	22	9	4
	m_{hk}	3	12	0
$K^0_L\pi^+\pi^-$	D_k	8	142	148
	m_{sk}	1	1315	6
	m_{pk}	0	113	4
	m_{lk}	17	11	6
	m_{hk}	27	72	2103

Table 3.21: Data and MC yields for $K^0_S K^+K^-$ against final states containing $K^0_L X$.

Opposite-side final state	Quantity	Yield Low	Signal	High
K^+K^-	D_k	2	32	1
	m_{sk}	1	203	0
	m_{pk}	0	30	0
	m_{lk}	10	2	2
	m_{hk}	8	2	2
$\pi^+\pi^-$	D_k	3	13	2
	m_{sk}	1	85	0
	m_{pk}	0	10	0
	m_{lk}	10	4	1
	m_{hk}	6	1	0
$K^0_S\pi^0\pi^0$	D_k	4	14	0
	m_{sk}	1	96	1
	m_{pk}	2	24	0
	m_{lk}	24	24	8
	m_{hk}	32	30	12
$K^0_S\pi^0$	D_k	4	46	0
	m_{sk}	11	600	6
	m_{pk}	1	33	0
	m_{lk}	71	30	19
	m_{hk}	14	1	1
$K^0_S\eta(\gamma\gamma)$	D_k	1	6	1
	m_{sk}	1	67	1
	m_{pk}	0	4	0
	m_{lk}	11	5	1
	m_{hk}	8	8	2
$K^0_S\omega(\pi^+\pi^-\pi^0)$	D_k	3	10	0
	m_{sk}	3	277	2
	m_{pk}	1	30	0
	m_{lk}	24	24	13
	m_{hk}	12	4	2

Opposite-side final state	Quantity	Yield Low	Signal	High
$K^0_S\eta(\pi^+\pi^-\pi^0)$	D_k	0	1	0
	m_{sk}	0	24	0
	m_{pk}	0	3	0
	m_{lk}	1	5	0
	m_{hk}	5	3	0
$K^0_S\eta'(\pi^+\pi^-\eta)$	D_k	1	4	0
	m_{sk}	3	40	1
	m_{pk}	0	2	0
	m_{lk}	7	2	3
	m_{hk}	1	0	0
$K^\pm\pi^\mp$	D_k	22	308	2
	m_{sk}	49	3512	27
	m_{pk}	3	237	2
	m_{lk}	297	194	67
	m_{hk}	103	16	6
$K^\pm\pi^\mp\pi^0$	D_k	128	595	34
	m_{sk}	253	7518	84
	m_{pk}	47	666	22
	m_{lk}	890	490	227
	m_{hk}	414	127	49
$K^\pm\pi^\mp\pi^+\pi^-$	D_k	27	294	6
	m_{sk}	37	3958	25
	m_{pk}	3	364	1
	m_{lk}	434	237	81
	m_{hk}	147	50	23
$K^0_S\pi^+\pi^-$	D_k	12	126	2
	m_{sk}	10	1241	7
	m_{pk}	0	116	2
	m_{lk}	144	67	23
	m_{hk}	43	27	13
$K^\pm e^\mp\nu_e$	D_k	2	100	13
	m_{sk}	7	1319	34
	m_{pk}	0	12	1
	m_{lk}	0	0	0
	m_{hk}	7	5	16

Table 3.22: Data and MC yields for $K^0_L K^+K^-$ against all final states and $K^0_S K^+K^-$ against $K^\pm e^\mp\nu_e$.

- Signal-side background to $K^0_L K^+ K^-$ *except* $K^0_S K^+ K^-$.

The following backgrounds are assumed to be resonant:

- $K^0_{S,L} K^+ K^-$ against opposite-side background,
- $K^0_S K^+ K^-$ background to $K^0_L K^+ K^-$.

We consider similar backgrounds to $K^0_{S,L}\pi^+\pi^-$ decays.

We use a signal MC sample of $K^0_{S,L} K^+ K^-$ tagged with $K^\pm\pi^\mp$ to estimate the bin-by-bin yield of resonant backgrounds, and estimate the bin-by-bin yield of phase-space backgrounds using the relative areas of the Dalitz plane bins. Table 3.23 lists the quantities used to estimate the distribution of both types of background across the Dalitz plane. These quantities

Background type	Raw numbers		Scaled numbers	
	Resonant	Phase space	Resonant	Phase space
Flat	n_{FR}	n_{FP}	B_{FR}	B_{FP}
Peaking	n_{PR}	n_{PP}	B_{PR}	B_{PP}

Table 3.23: Definitions of quantities used in estimating the background distribution across the Dalitz plane.

are related as follows:

$$B_{FR} = B_F \frac{n_{FR}}{n_{FR} + n_{FP}}, \qquad B_{FP} = B_F \frac{n_{FP}}{n_{FR} + n_{FP}}, \tag{3.41}$$

$$B_{PR} = B_P \frac{n_{PR}}{n_{PR} + n_{PP}}, \qquad B_{PP} = B_P \frac{n_{PP}}{n_{PR} + n_{PP}}. \tag{3.42}$$

We define p_i to be the $K^0_{S,L} K^+ K^-$ against $K^\pm\pi^\mp$ Monte Carlo population of the i^{th} bin and a_i to be the area of the i^{th} bin. The totals of these quantities are defined as p_T and a_T respectively. The quantities of flat and peaking backgrounds in the i^{th} bin are then:

$$B^i_F = B_{FP} \times \frac{a_i}{a_T} + B_{FR} \times \frac{p_i}{p_T}, \tag{3.43}$$

$$B^i_P = B_{PP} \times \frac{a_i}{a_T} + B_{PR} \times \frac{p_i}{p_T}. \tag{3.44}$$

There is a systematic uncertainty associated with these assumptions that we evaluate in Section 4.5.3.

The same procedure is used to estimate the backgrounds for $K^0_{S,L} K^+ K^-$ against $K^0_{S,L} h^+ h^-$. As before, the correlations between points on the two Dalitz plots must be considered. The appropriate signal Monte Carlo sample is used to estimate the proportion of resonant background in each bin. The estimated background in the i^{th} bin of the

$K^0_{S,L}K^+K^-$ Dalitz plot and the j^{th} bin of the $K^0_{S,L}h^+h^-$ Dalitz plot is:

$$B_F^{ij} = B_{FR} \times \frac{a_i a_j}{a_T} + B_{FP} \times \frac{p_{ij}}{p_T}, \tag{3.45}$$

$$B_P^{ij} = B_{PR} \times \frac{a_i a_j}{a_T} + B_{PP} \times \frac{p_{ij}}{p_T}, \tag{3.46}$$

where p_{ij} is the quantity of $K^0_{S,L}K^+K^-$ against $K^\pm\pi^\mp$ signal Monte Carlo in these bins.

The normalised bin areas on the $K^0_SK^+K^-$ and $K^0_S\pi^+\pi^-$ Dalitz planes are listed in Tables A.1 and A.2 respectively. The normalised yields of $K^0_{S,L}K^+K^-$ tagged with $K^\pm\pi^\mp$ in MC are shown in Tables A.3–A.5.

3.6.5 Background yield uncertainty

The uncertainties on the estimated background yields are determined by varying each input used to determine the yields: the sideband data yields for fully-reconstructed events, and various quantities in the Monte Carlo data. The inputs are varied according to a Poisson distribution, taking the initial value as the mean. The new values of each background yield are then determined. This is repeated 1000 times in order to build up a distribution of values. The standard deviation of the distribution is taken to be the uncertainty in each case. Figure 3.64 shows the flat, peaking and total background distributions for $K^0_SK^+K^-$ against $\mathcal{CP}+$ eigenstates.

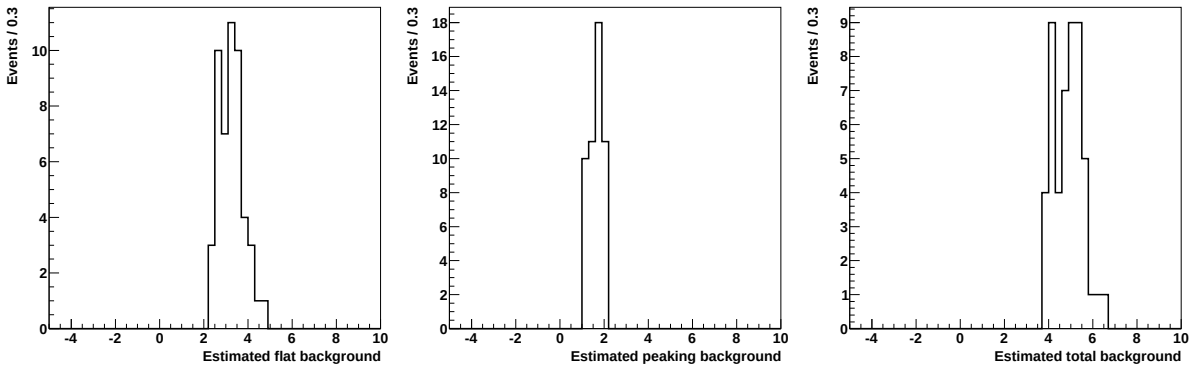

Figure 3.64: Flat (left), peaking (middle) and total (left) background distributions after smearing for $K^0_SK^+K^-$ against $\mathcal{CP}+$ eigenstates.

3.6.6 Background yields

Table 3.24 shows the estimated flat, peaking and total background for each mode considered. The uncertainties quoted are those determined as described in Section 3.6.5.

For fully-reconstructed final states, the estimated level of flat background is usually larger than the peaking background. In contrast, the peaking background is dominant

Final state	Flat	Peaking	Total
$K^0_S K^+ K^-$ against $\mathcal{CP}+$	3.3 ± 1.1	1.6 ± 0.4	4.9 ± 1.2
$K^0_S K^+ K^-$ against $\mathcal{CP}-$	0.8 ± 0.6	1.1 ± 0.3	1.9 ± 0.6
$K^0_S K^+ K^-$ against $K^\pm\pi^\mp$	0.0 ± 0.0	1.9 ± 0.4	1.9 ± 0.4
$K^0_S K^+ K^-$ against $K^\pm\pi^\mp\pi^0$	9.3 ± 2.2	3.4 ± 0.5	12.8 ± 2.3
$K^0_S K^+ K^-$ against $K^\pm\pi^\mp\pi^+\pi^-$	10.0 ± 2.5	3.5 ± 0.5	13.5 ± 2.6
$K^0_S K^+ K^-$ against $K^\pm e^\mp \nu_e$	3.3 ± 1.9	1.0 ± 0.3	4.3 ± 2.0
$K^0_L K^+ K^-$ against $\mathcal{CP}+$	6.2 ± 6.5	5.3 ± 0.7	11.6 ± 6.5
$K^0_L K^+ K^-$ against $\mathcal{CP}-$	2.6 ± 2.6	6.5 ± 0.8	9.1 ± 2.9
$K^0_L K^+ K^-$ against $K^\pm\pi^\mp$	-1.4 ± 6.1	20.8 ± 1.3	19.4 ± 6.2
$K^0_L K^+ K^-$ against $K^\pm\pi^\mp\pi^0$	58.0 ± 12.0	58.3 ± 2.3	116.2 ± 12.2
$K^0_L K^+ K^-$ against $K^\pm\pi^\mp\pi^+\pi^-$	11.9 ± 19.7	31.9 ± 1.6	43.8 ± 19.2
$K^0_S K^+ K^-$ against $K^0_S K^+ K^-$	0.0 ± 0.0	0.0 ± 0.0	0.0 ± 0.0
$K^0_S K^+ K^-$ against $K^0_L K^+ K^-$	3.8 ± 4.8	0.0 ± 0.0	3.8 ± 4.8
$K^0_S K^+ K^-$ against $K^0_S\pi^+\pi^-$	0.2 ± 0.6	0.2 ± 0.3	0.4 ± 0.7
$K^0_S K^+ K^-$ against $K^0_L\pi^+\pi^-$	8.9 ± 3.0	9.7 ± 0.9	18.5 ± 3.1
$K^0_L K^+ K^-$ against $K^0_S\pi^+\pi^-$	4.5 ± 3.9	10.2 ± 1.0	14.7 ± 4.4

Table 3.24: Summary of flat, peaking and total background yield estimates for each final state.

for partially-reconstructed final states. The $K^0_L K^+ K^-$ against $K^\pm\pi^\mp$ flat background is predicted to be negative, but easily covers zero within its uncertainty. This could be because the corresponding peaking background has been overestimated.

3.7 Conclusions

In this chapter we have described the reconstruction of 818 pb^{-1} of $\psi(3770) \to D^0\overline{D}^0$ data collected by CLEO-c. We have reconstructed $K^0_{S,L} K^+ K^-$ decays tagged with $\mathcal{CP}$ eigenstates, flavour states and mixed-$\mathcal{CP}$ eigenstates. The yields of these decays have been determined in bins across the Dalitz plane and will be used in a fit to extract the observables of interest. We have used samples of Monte Carlo data to determine the selection efficiencies and estimate the background yields across the Dalitz plane, both of which are crucial inputs to the fit. The fit to the reconstructed data is the subject of the next chapter.

Chapter 4

Determination of the strong-phase difference between D^0 and $\overline{D}^0$ decays to $K^0_S K^+ K^-$

4.1 Introduction

This chapter describes the procedure used to determine the strong-phase difference $\Delta\delta_D$ between D^0 and $\overline{D}^0$ decays to $K^0_S K^+ K^-$ in bins across the Dalitz plane. We use CLEO-c data that have been selected and reconstructed as described in Chapter 3.

In Section 4.2 we describe the choice of Dalitz plane binning. Section 4.3 contains a description of the fit used to determine the parameters of interest. Results and systematic uncertainties are presented in Sections 4.4–4.6. Lastly, Section 4.7 describes the determination of the $\mathcal{CP}$ content of $D \to K^0_S K^+ K^-$ decays in the region of the $\phi \to K^+ K^-$ resonance.

4.2 Dalitz plane binning

The goal of the binned analysis of the $K^0_S K^+ K^-$ Dalitz plane is to determine the amplitude-weighted cosine and sine of the strong-phase difference in each bin, denoted c_i and s_i respectively. The formalism related to this procedure has been introduced in Section 1.6.5. When binning the Dalitz plane we must consider both the expected statistical sensitivity to γ and the size of the dataset available.

In Refs. [45, 52, 53] it has been shown that the best statistical sensitivity to γ can be obtained by dividing the Dalitz plane into bins of similar strong-phase difference. In order to follow this prescription we must therefore use a model of $D \to K^0_S K^+ K^-$ decays that has been determined elsewhere. We employ the high-resolution bitmap of $D \to K^0_S K^+ K^-$

amplitudes provided by BaBar [25] to parameterise the $D \to K^0_S K^+ K^-$ decay at each point across the Dalitz plane. Both the decay model and the bitmap have been described in detail in Section 3.5.1. Figure 4.1 shows the Dalitz plane divided into 24 equal strong-phase difference bins, using the bitmap to determine the modulus and phase of the decay amplitude at each point.

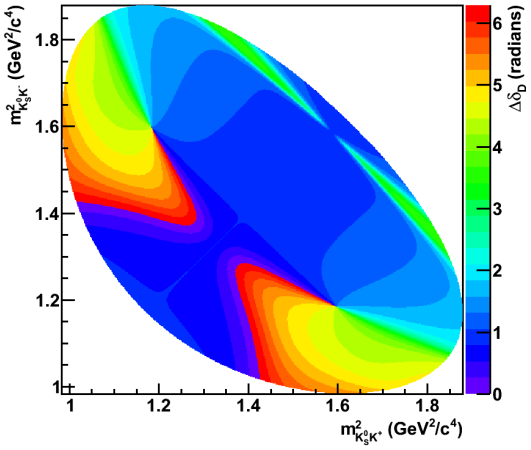

Figure 4.1: The $K^0_S K^+ K^-$ Dalitz plane binned in 24 regions of equal strong-phase difference ($\Delta\delta_D$). Each coloured region denotes a range of strong-phase difference; the white region is outside the physical limit.

Dividing the plane into a large number of bins provides increased sensitivity to γ because it more closely approximates the unbinned situation, which has the highest sensitivity [45,53]. On the other hand, a larger number of bins limits the statistical precision on c_i and s_i due to the small size of the CLEO-c dataset. With this tension in mind we consider divisions of the Dalitz plane into two, three and four equal $\Delta\delta_D$ bins. Configurations with five or more bins suffer from a lack of data and the fit to extract the parameters fails to converge. By considering a variety of binnings we provide flexibility for future analyses aiming to extract γ, in which the choice of binning might depend on the sample size available.

Each point on the Dalitz plane is assigned a bin number based on the value of $\Delta\delta_D$ at that point. The plane is divided into equally-spaced $\Delta\delta_D$ bins such that bin 1 is centred on 0 radians. Bin k encompasses the range $[(2k-3)\pi/\mathcal{N}, (2k-1)\pi/\mathcal{N}]$ radians. The strong-phase difference is constrained to lie in the range $[0, 2\pi]$ so bin 1 wraps around and covers two ranges: $[0, \pi/\mathcal{N}]$ and $[(2-1/\mathcal{N})\pi, 2\pi]$.

The binnings obtained using the above definitions are shown in Figures 4.2 and 4.3. In each case, there is a narrow bin located at low values of $m^2_{K^+K^-}$, close to the kinematic boundary. This bin encompasses the $K^0_S\phi$ resonance and typically contains a large number of events (see Section 3.4.5). Additionally, there are *lobes* at high values of $m^2_{K^+K^-}$ that are sparsely populated.

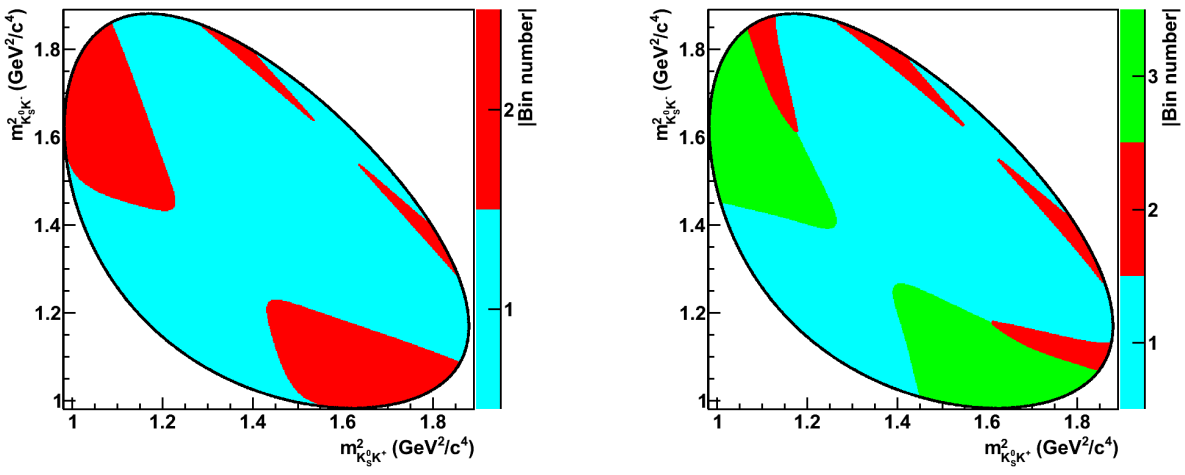

Figure 4.2: Division of the $K^0_S K^+ K^-$ Dalitz plane into two bins (left) and three bins (right), equally spaced in strong-phase difference.

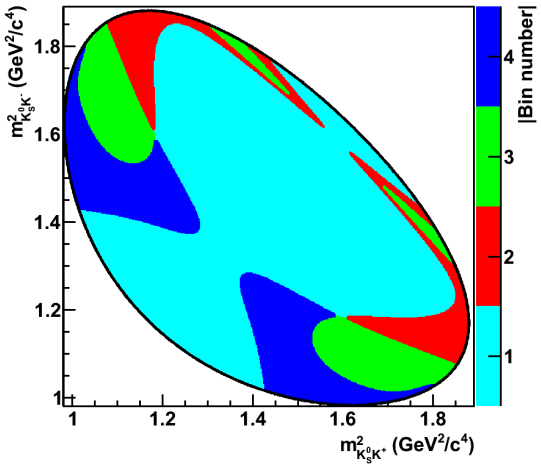

Figure 4.3: Division of the $K^0_S K^+ K^-$ Dalitz plane into four bins, equally spaced in strong-phase difference.

4.3 Fit to extract observables

4.3.1 Method outline

After dividing the Dalitz plane into bins we determine the yields of reconstructed events in each bin, as described in Section 3.4. Values of $c_i(')$ and $s_i(')$ can then be determined from these yields. Each of the cosine and sine terms is a free parameter in the fit, so there are $4\mathcal{N}$ free parameters in total.

The yield of $K^0_S K^+ K^-$ tagged with $\mathcal{CP}\mp$ eigenstates, $M^{\pm}_i$, depends upon c_i as follows (Equation 1.142):

$$\frac{M^{\pm}_i}{S_{\mp}} = \frac{K_i \pm 2c_i\sqrt{K_i K_{-i}} + K_{-i}}{2S_F}, \tag{4.1}$$

where $S_{\mp}$ is the quantity of $\mathcal{CP}\mp$ single tags, K_i (K_{-i}) is the number of flavour-tagged $K^0_S K^+K^-$ in bin i ($-i$) and S_F is the quantity of flavour single tags. Similarly, the yield of $K^0_L K^+K^-$ tagged with $\mathcal{CP}\mp$ eigenstates, $M_i^{\pm\prime}$ depends upon c_i' (Equation 1.170):

$$\frac{M_i^{\pm\prime}}{S'_{\mp}} = \frac{K'_i \mp 2c'_i\sqrt{K'_iK'_{-i}} + K'_{-i}}{2S'_F}. \tag{4.2}$$

The yield of $K^0_S K^+K^-$ tagged with $K^0_S h^+h^-$ in bin i of the $K^0_S K^+K^-$ Dalitz plane and bin j of the $K^0_S h^+h^-$ Dalitz plane, M_{ij}, depends upon both c_i and s_i and is given by (Equation 1.158):

$$M_{ij} = \frac{N_{D^0\overline{D}^0}}{2S_F^2}(K_iK_{-j} + K_{-i}K_j - 2\sqrt{K_iK_{-j}K_{-i}K_j}(c_ic_j + s_is_j)), \tag{4.3}$$

where $N_{D^0\overline{D}^0}$ is total the number of $D^0\overline{D}^0$ pairs in the dataset. The equivalent for $K^0_S K^+K^-$ tagged with $K^0_L h^+h^-$ (and $K^0_L K^+K^-$ tagged with $K^0_S \pi^+\pi^-$) depends on c_i, s_i, c'_i and s'_i and is equal to (Equation 1.173):

$$M'_{ij} = \frac{N_{D^0\overline{D}^0}}{2S_FS'_F}(K_iK'_{-j} + K_{-i}K'_j + 2\sqrt{K_{-i}K'_{-j}K_{-i}K'_j}(c_ic'_j + s_is'_j)). \tag{4.4}$$

We use a maximum likelihood fit to simultaneously determine all of the $(c,s)_i(')$ parameters using the yields described above. Using the Minuit minimisation package [76], the measured yields in each bin are compared to their expected values, which depend upon $(c,s)_i(')$. The fit procedure determines the values of $(c,s)_i(')$ that minimise the following log likelihood expression:

$$\begin{aligned}
-2\log\mathcal{L} = &-2\sum_i \log P(M_i^{\pm}, \langle M_i^{\pm}\rangle)_{K^0_S K^+K^-,\ \mathcal{CP}} \\
&-2\sum_i \log P(M_i^{\pm}, \langle M_i^{\pm}\rangle)_{K^0_L K^+K^-,\ \mathcal{CP}} \\
&-2\sum_{i,j} \log P(M_{ij}, \langle M_{ij}\rangle)_{K^0_S K^+K^-,\ K^0_S K^+K^-} \\
&-2\sum_{i,j} \log P(M_{ij}, \langle M_{ij}\rangle)_{K^0_S K^+K^-,\ K^0_L K^+K^-} \\
&-2\sum_{i,j} \log P(M_{ij}, \langle M_{ij}\rangle)_{K^0_S K^+K^-,\ K^0_S \pi^+\pi^-} \\
&-2\sum_{i,j} \log P(M_{ij}, \langle M_{ij}\rangle)_{K^0_S K^+K^-,\ K^0_L \pi^+\pi^-} \\
&-2\sum_{i,j} \log P(M_{ij}, \langle M_{ij}\rangle)_{K^0_L K^+K^-,\ K^0_S \pi^+\pi^-} \\
&+\chi^2,
\end{aligned} \tag{4.5}$$

where $\langle X \rangle$ is the expected value of the yield X, the subscripts indicate the signal- and opposite-side decays for each component, and $P(X, \langle X \rangle)$ is the Poisson probability of obtaining X events given a mean of $\langle X \rangle$:

$$P(X, \langle X \rangle) \equiv \frac{\langle X \rangle^X e^{-\langle X \rangle}}{X!}. \tag{4.6}$$

The terms are normalised such that the expected quantity in each bin is compared to the raw number of events. The background yield is added to the expected number of events rather than subtracted from the measured quantity. Section 4.3.2 contains further detail about the normalisation and the treatment of background yields. The χ^2 term is explained in detail in Section 4.3.4.

4.3.2 Yield normalisation

The yields used in the fit must be correctly normalised in order to ensure proper convergence. In this section we describe how this normalisation is achieved and how the expected yield of each final state is determined. We assume that all yields have been appropriately corrected for bin-to-bin migration (Section 3.5.5) and that the yields of fully hadronic flavour states have been multiplied by the factors to correct for the presence of DCS decays (Section 3.4.3). Henceforth the symbol $\mathcal{B}_X$ indicates the branching fraction of $D^0 \to X$.

We distinguish between efficiency-corrected yields, indicated with a superscript c, and uncorrected (i.e. raw) yields, indicated with a superscript u. For $\mathcal{CP}$-tagged events the two quantities are related as follows:

$$M_i^c = M_i^u / \varepsilon_i, \tag{4.7}$$

where ε_i is the selection efficiency in the i^{th} bin. The selection efficiency is determined using Monte Carlo data as detailed in Section 3.5.2.

There is a similar relation for $K^0_{S,L}K^+K^-$ against $K^0_{S,L}h^+h^-$. In this case, we determine the yield of events in the i^{th} bin of the $K^0_{S,L}K^+K^-$ Dalitz plane and the j^{th} bin of the $K^0_{S,L}h^+h^-$ Dalitz plane:

$$M_{ij}^c = M_{ij}^u / \varepsilon_{ij}. \tag{4.8}$$

We consider a situation in which one sample of $K^0_S K^+K^-$ is tagged with a $\mathcal{CP}$ eigenstate P and another sample of $K^0_S K^+K^-$ is tagged with a flavour state F. The efficiency-corrected yield in bin i of $K^0_S K^+K^-$ tagged with P (F) is denoted M_i^c (K_i^c). The equation relating these yields becomes:

$$\frac{M_i^c}{S_P} = \frac{K_i^c \pm 2c_i\sqrt{K_i^c K_{-i}^c} + K_{-i}^c}{2S_F}, \tag{4.9}$$

where S_P and S_F are respectively the total number of $D \to P$ and $D \to F$ single tags in the

event, both of which have been efficiency-corrected.

We now determine the number of *expected* $\mathcal{CP}$-tagged events using Equation 4.9. Rearranging the expression and substituting we obtain:

$$\begin{aligned}\langle M_i^c \rangle &= \frac{S_P}{2} \cdot \frac{K_i^c \pm 2c_i\sqrt{K_i^c K_{-i}^c} + K_{-i}^c}{S_F} \\ &= N_{D^0\bar{D}^0}\mathcal{B}_P \frac{K_i^c \pm 2c_i\sqrt{K_i^c K_{-i}^c} + K_{-i}^c}{S_F} \\ &= N_{D^0\bar{D}^0}\mathcal{B}_P\mathcal{B}_{K_S^0K^+K^-}(T_i \pm 2c_i\sqrt{T_iT_{-i}} + T_{-i})\end{aligned} \tag{4.10}$$

where we have used Equations 1.124 and 1.128. The use of branching fractions here and elsewhere induces a systematic uncertainty that is evaluated in Section 4.5.7.

We finally multiply both sides by the selection efficiency of P:

$$\langle M_i^u \rangle = \varepsilon_i \cdot N_{D^0\bar{D}^0}\mathcal{B}_P\mathcal{B}_{K_S^0K^+K^-}(T_i \pm 2c_i\sqrt{T_iT_{-i}} + T_{-i}). \tag{4.11}$$

This formulation for the expected number of $\mathcal{CP}$-tagged events ensures that the statistical uncertainty returned by the fitting software is representative of the raw number of events selected. In addition, from a practical standpoint it avoids the possibility of division by zero if the selection efficiency in a particular bin is zero. This could occur if the bin is not populated in the Monte Carlo simulation. Even though a large number of events were generated for each final state, this is possible because the distribution of events across the Dalitz plane is not flat.

When multiple flavour states have been reconstructed, the normalised yield T_i is replaced by $\widehat{T}_i$, the weighted average over all flavour-tagged yields. The weight used for each flavour state is its PDG [11] branching fraction. This ensures that the more imprecise values of T_i, obtained for less populous flavour states, are relatively insignificant in the determination of $\widehat{T}_i$. The expression for $\widehat{T}_i$ is:

$$\widehat{T}_i = \frac{\sum_{k=1}^{n_F}\mathcal{B}_{F_k}T_i^{F_k}}{\sum_{k=1}^{n_F}\mathcal{B}_{F_k}}, \tag{4.12}$$

where F_k are the flavour states and n_F is total the number of flavour states (four for $K_S^0K^+K^-$, three for $K_L^0K^+K^-$). The expression for the expected quantity of $\mathcal{CP}$-tagged events using weighted flavour-tagged yields is:

$$\langle M_i^u \rangle = \varepsilon_i \cdot N_{D^0\bar{D}^0}\mathcal{B}_P\mathcal{B}_{K_S^0K^+K^-}(\widehat{T}_i \pm 2c_i\sqrt{\widehat{T}_i\widehat{T}_{-i}} + \widehat{T}_{-i}). \tag{4.13}$$

The bin-by-bin yields of $\mathcal{CP}$-tagged $K_{S,L}^0K^+K^-$ are summed according to whether they are in a $\mathcal{CP}\pm$ state, analogously to the treatment of the background (see Section 3.6), and this sum is used as a single term in the fit. This reduces the number of free parameters in

the fit and hence lowers the relative statistical uncertainty.

When considering $K^0_{S,L}K^+K^-$ tagged with $K^0_{S,L}h^+h^-$ we have the following expression for the expected yield in bins (i,j):

$$\langle M^c_{ij}\rangle = \frac{N_{D^0\bar{D}^0}}{2S_F S'_F}(K^c_i K'^c_{-j} + K^c_{-i}K'^c_j + 2\sqrt{K^c_i K'^c_{-j}K^c_{-i}K'^c_j}(c_i c'_j + s_i s'_j)). \tag{4.14}$$

For $K^0_S K^+K^-$ against $K^0_S K^+K^-$ this expression must be divided by two to avoid double counting (see Section 1.6.5.1). Substituting in the relevant expressions and rearranging we obtain:

$$\begin{aligned}\langle M^c_{ij}\rangle &= \frac{N_{D^0\bar{D}^0}}{2S_F S'_F}(K^c_i K'^c_{-j} + K^c_{-i}K'^c_j + 2\sqrt{K^c_i K'^c_{-j}K^c_{-i}K'^c_j}(c_i c'_j + s_i s'_j)) \\ &= \frac{1}{2}N_{D^0\bar{D}^0}\mathcal{B}_{K^0_{S,L}K^+K^-}\mathcal{B}_{K^0_{S,L}h^+h^-}(T_i T'_{-j} + T_{-i}T'_j + 2\sqrt{T_i T'_{-j}T_{-i}T'_j}(c_i c'_j + s_i s'_j)).\end{aligned} \tag{4.15}$$

As before, we can transparently substitute T_i with the weighted average $\widehat{T}_i$:

$$\langle M^u_{ij}\rangle = \varepsilon_{ij}\cdot\frac{1}{2}N_{D^0\bar{D}^0}\mathcal{B}_{K^0_{S,L}K^+K^-}\mathcal{B}_{K^0_{S,L}h^+h^-}(\widehat{T}_i\widehat{T}'_{-j} + \widehat{T}_{-i}\widehat{T}'_j + 2\sqrt{\widehat{T}_i\widehat{T}'_{-j}\widehat{T}_{-i}\widehat{T}'_j}(c_i c'_j + s_i s'_j)). \tag{4.16}$$

Rather than subtracting backgrounds from the raw data yields in the fit, we add the background to the expected quantity to obtain the Poisson mean. These two approaches are equivalent because the expected quantity has been calculated assuming zero background. This prevents the yield in the fit from becoming negative after background subtraction.

4.3.3 $K^0_S\pi^+\pi^-$-related quantities

The expression for the expected yield of $K^0_{S,L}K^+K^-$ events tagged with $K^0_{S,L}\pi^+\pi^-$ takes the form of Equation 4.4 and is in part dependent upon the values of $c_i(')$, $s_i(')$ and $\widehat{T}_{(-)i}$ in the $D\to K^0_{S,L}\pi^+\pi^-$ system. Rather than leaving these quantities floating in the fit, we use values that have been determined by an external analysis [7]. The number of free parameters in the fit is thus significantly reduced, especially because the $K^0_S\pi^+\pi^-$ Dalitz plane is divided into eight bins. This reduction is essential to ensure the fit converges properly.

The $K^0_S\pi^+\pi^-$ Dalitz plane is divided into eight equally-spaced bins of similar strong-phase difference. The $D\to K^0_S\pi^+\pi^-$ decay model used to determine the strong-phase difference has been determined in Ref. [48]. Values of $(c,s)_i$ and $(c,s)'_i$ for $D\to K^0_{S,L}\pi^+\pi^-$ decays are shown in Table 4.1 and values of $\widehat{T}_{(-)i}$ and $\widehat{T}'_{(-)i}$ are shown in Table 4.2.

The central values of the $K^0_{S,L}\pi^+\pi^-$ parameters are used in the fit. The use of external quantities introduces systematic uncertainties which are evaluated as described in Section 4.5.6.

Bin i	c_i	s_i	c'_i	s'_i
1	$0.655 \pm 0.036 \pm 0.042$	$-0.025 \pm 0.098 \pm 0.043$	$0.768 \pm 0.038 \pm 0.051$	$-0.079 \pm 0.095 \pm 0.108$
2	$0.511 \pm 0.068 \pm 0.063$	$0.141 \pm 0.183 \pm 0.066$	$0.679 \pm 0.067 \pm 0.090$	$0.080 \pm 0.183 \pm 0.196$
3	$0.024 \pm 0.140 \pm 0.080$	$1.111 \pm 0.131 \pm 0.044$	$0.278 \pm 0.106 \pm 0.112$	$1.090 \pm 0.106 \pm 0.119$
4	$-0.569 \pm 0.118 \pm 0.098$	$0.328 \pm 0.202 \pm 0.072$	$-0.446 \pm 0.116 \pm 0.128$	$0.455 \pm 0.219 \pm 0.235$
5	$-0.903 \pm 0.045 \pm 0.042$	$-0.181 \pm 0.131 \pm 0.026$	$0.824 \pm 0.051 \pm 0.056$	$-0.194 \pm 0.136 \pm 0.140$
6	$-0.616 \pm 0.103 \pm 0.072$	$-0.520 \pm 0.196 \pm 0.059$	$-0.240 \pm 0.116 \pm 0.123$	$-0.557 \pm 0.201 \pm 0.211$
7	$0.100 \pm 0.106 \pm 0.124$	$-1.129 \pm 0.120 \pm 0.096$	$0.480 \pm 0.106 \pm 0.113$	$-0.975 \pm 0.104 \pm 0.141$
8	$0.422 \pm 0.069 \pm 0.075$	$-0.350 \pm 0.151 \pm 0.045$	$0.708 \pm 0.066 \pm 0.083$	$-0.285 \pm 0.150 \pm 0.158$

Table 4.1: Values of $(c, s)_i(')$ for $K^0_{S,L}\pi^+\pi^-$ decays in eight strong-phase difference bins. The values have been taken from Ref. [7].

Bin i	$\widehat{T}_i$	$\widehat{T}_{-i}$	$\widehat{T}'_i$	$\widehat{T}'_{-i}$
1	0.090 ± 0.004	0.026 ± 0.002	0.086 ± 0.003	0.029 ± 0.005
2	0.144 ± 0.005	0.005 ± 0.001	0.132 ± 0.003	0.013 ± 0.002
3	0.147 ± 0.005	0.003 ± 0.001	0.143 ± 0.004	0.010 ± 0.002
4	0.099 ± 0.004	0.059 ± 0.003	0.107 ± 0.004	0.071 ± 0.017
5	0.057 ± 0.003	0.033 ± 0.002	0.049 ± 0.002	0.040 ± 0.008
6	0.075 ± 0.004	0.005 ± 0.001	0.064 ± 0.003	0.011 ± 0.002
7	0.109 ± 0.004	0.055 ± 0.003	0.104 ± 0.003	0.062 ± 0.010
8	0.022 ± 0.002	0.069 ± 0.003	0.020 ± 0.002	0.060 ± 0.014

Table 4.2: Values of $\widehat{T}_{(-)i}$ and $\widehat{T}'_{(-)i}$ for $K^0_{S,L}\pi^+\pi^-$ decays in eight strong-phase difference bins. The values have been taken from Ref. [7].

4.3.4 χ^2 constraint term

The χ^2 term in Equation 4.5 is a constraint on the difference between the strong phase information in $K^0_S K^+K^-$ and $K^0_L K^+K^-$ decays:

$$\chi^2 = \sum_i \left(\frac{c'_i - c_i - \Delta c_i}{\delta \Delta c_i} \right)^2 + \sum_i \left(\frac{s'_i - s_i - \Delta s_i}{\delta \Delta s_i} \right)^2, \tag{4.17}$$

where $\Delta(c, s)_i$ is the model-predicted difference between $(c, s)'_i$ and $(c, s)_i$ and $\delta\Delta(c, s)_i$ is the uncertainty on this value. The addition of the χ^2 term to the log likelihood expression improves the precision on the results, while introducing a small model dependence which is quantified using a systematic study. In Section 4.4.2.1 we show that the use of this term does not introduce a significant bias in the central values returned by the fit.

We determine the predicted values of $(c, s)_i(')$ using the BaBar parameterisation of the strong-phase difference [25], whose intermediate resonances are listed in Section 3.5.1. In order to determine the decay amplitude at each point on the Dalitz plane we model the resonances explicitly instead of using the bitmap to look up the value. We do this because a model of the $K^0_L K^+K^-$ resonant structure is also required and a bitmap does not exist for that case.

The $K^0_L K^+K^-$ model is obtained by modifying the intermediate resonances of the $K^0_S K^+K^-$ model. As described in Section 1.6.5.5, the phase of the $D^0 \to K^+ a_0(980)^-$ res-

onance is shifted by π radians and the complex amplitude of each neutral resonance is multiplied by $(1 - 2re^{i\alpha})$, where $r = \tan^2(\theta_C)$ and $\alpha = 0$ (see Equation 1.168).

Predicted values of $c_i(')$ and $s_i(')$ are shown in Tables 4.3–4.5.

i	c_i	s_i	c'_i	s'_i
1	0.742	0.275	0.768	0.286
2	−0.679	0.318	−0.680	0.397

Table 4.3: Predicted $c_i(')$ and $s_i(')$ for two bins.

i	c_i	s_i	c'_i	s'_i
1	0.801	0.268	0.827	0.269
2	−0.657	0.411	−0.593	0.435
3	−0.043	−0.661	−0.680	0.126

Table 4.4: Predicted $c_i(')$ and $s_i(')$ for three bins.

i	c_i	s_i	c'_i	s'_i
1	0.845	0.239	0.864	0.242
2	−0.028	0.531	0.095	0.512
3	−0.804	0.332	−0.779	0.382
4	0.232	−0.738	−0.718	0.262

Table 4.5: Predicted $c_i(')$ and $s_i(')$ for four bins.

There are two sources of uncertainty on the $\Delta(c, s)_i$ parameters. The first has its origin in the uncertainties on the amplitudes and phases in the BaBar parameterisation. These quantities are smeared using the covariance matrix between the real and imaginary parts of the eight resonances. We use the following method to perform the smearing, taking multivariate correlations into account. We determine $\mathbf{X}$, a vector of smeared amplitudes and phases of each intermediate resonance, using the equation:

$$\mathbf{X} = \boldsymbol{\mu} + \mathbf{AZ} \tag{4.18}$$

where $\mathbf{Z}$ is a random vector of quantities drawn from a Gaussian distribution with zero mean and unit width, μ is a vector of the central values of the BaBar parameters, and $\mathbf{A}$ is the Cholesky decomposition of the covariance matrix of the BaBar parameters. This is done 1000 times; each time, the values of Δc_i and Δs_i are recorded. The standard deviations of the distributions are calculated in order to obtain the uncertainties, $[\delta\Delta(c, s)_i]^{res}$. The distributions of events on the (c_i,s_i) plane is shown in Figure 4.4. The black circle indicates the locus $c_i^2 + s_i^2 = 1$; this is for illustration only and is not a constraint in the fit. This is true for all plots of this type.

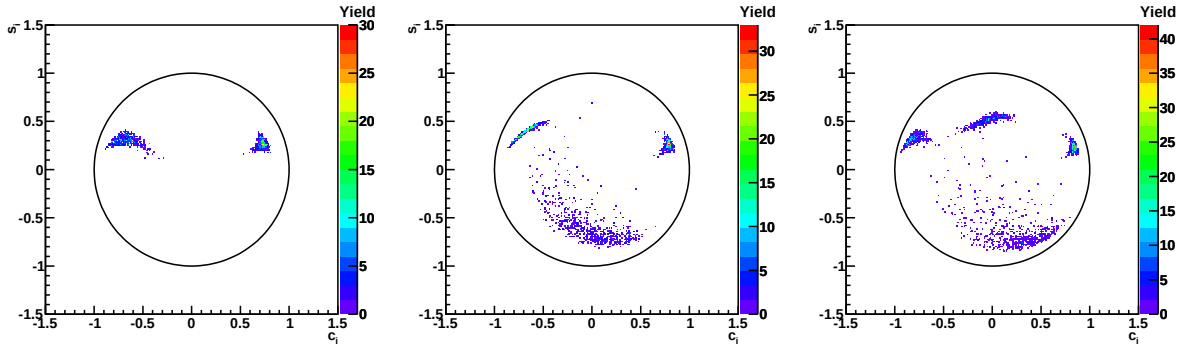

Figure 4.4: Distribution of events on the (c_i,s_i) plane after smearing of BaBar parameters: two bins (left), three bins (middle) and four bins (right).

The second source of uncertainty on $\Delta(c,s)_i$ is due to the imperfect knowledge of the values of the parameters r and α. The uncertainty on r is conservatively estimated to be approximately half of its initial value, i.e. 0.025. A value of r is obtained by randomly drawing it from a Gaussian distribution that is centred on its initial value and with a width equal to 0.025. We have no information about the value of α so we take it to be uniformly distributed in the range $(0, 2\pi)$ and draw a random value. New values of $\Delta(c,s)_i$ are determined using these values and recorded. This is repeated 1000 times. The standard deviations of the resulting distributions of $\Delta(c,s)_i$ are used to estimate the uncertainties, $[\delta\Delta(c,s)_i]^{DCS}$. The distributions of events on the (c'_i,s'_i) plane is shown in Figure 4.5. We do not show the (c_i,s_i) plane because r and α only enter in the expressions for the $K^0_L K^+ K^-$ amplitude.

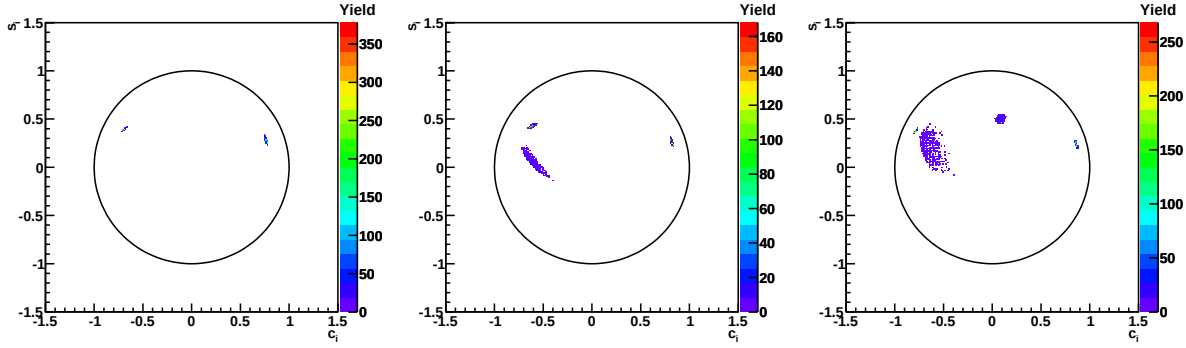

Figure 4.5: Distribution of events on the (c'_i,s'_i) plane after smearing of r and α: two bins (left), three bins (middle) and four bins (right).

The total uncertainty, $\delta\Delta(c,s)_i$, is obtained by adding $[\delta\Delta(c,s)_i]^{res}$ and $[\delta\Delta(c,s)_i]^{DCS}$ in quadrature. Results are presented in Tables 4.6–4.8.

One feature observed for the three and four bin cases is the relatively large values of $\Delta(c,s)_i$ in the highest-numbered bin, which corresponds to the lobes on the Dalitz plot. The model has a very low amplitude in this region and contains a neutral resonance, the $a_0(1450)^0$, so small differences between the $K^0_S K^+ K^-$ and $K^0_L K^+ K^-$ models are proportionally more significant.

i	$\Delta c_i \pm \delta\Delta c_i$	$\Delta s_i \pm \delta\Delta s_i$
1	0.026 ± 0.017	0.011 ± 0.023
2	-0.001 ± 0.036	0.079 ± 0.021

Table 4.6: Model-predicted $\Delta(c,s)_i$ and the associated $\delta\Delta(c,s)_i$ for two bins.

i	$\Delta c_i \pm \delta\Delta c_i$	$\Delta s_i \pm \delta\Delta s_i$
1	0.026 ± 0.014	0.001 ± 0.023
2	0.064 ± 0.019	0.024 ± 0.010
3	-0.637 ± 0.311	0.787 ± 0.161

Table 4.7: Model-predicted $\Delta(c,s)_i$ and the associated $\delta\Delta(c,s)_i$ for three bins.

i	$\Delta c_i \pm \delta\Delta c_i$	$\Delta s_i \pm \delta\Delta s_i$
1	0.019 ± 0.011	0.003 ± 0.021
2	0.123 ± 0.029	-0.019 ± 0.022
3	0.025 ± 0.019	0.050 ± 0.015
4	-0.950 ± 0.355	1.000 ± 0.254

Table 4.8: Model-predicted $\Delta(c,s)_i$ and the associated $\delta\Delta(c,s)_i$ for four bins.

4.4 Results

In this section we present the results obtained from the fit to CLEO-c data.

4.4.1 Flavour-tagged yields

Table 4.9 shows the weighted average of the normalised flavour-tagged yields in each bin of the Dalitz plane, for each of the binnings considered. Both the measured and predicted quantities are listed. The uncertainty on the measured quantities incorporates both the statistical uncertainty and the systematic uncertainty related to the uncertainties on the branching fractions used to determine the weighted average. The uncertainty on the predicted quantities is obtained by smearing the amplitude model parameters (using the same method detailed in Section 4.3.4) many times and building up a distribution from which an uncertainty is determined.

In all cases we see reasonable agreement between the measured and predicted quantities except for $\widehat{T}_{-1}$, for which the discrepancy is greater than three sigma for all binnings. This could be due to either a statistical fluctuation or an inaccurate description of the amplitude by the model in that region. In order to determine how significant this discrepancy is, we re-run the fit using the predicted values of $\widehat{T}_{(-)i}$ in place of the measured values. The resulting parameters are only very slightly different to those obtained using the measured values. We conclude that the discrepancy does not have a significant effect.

$\mathcal{N}$	Bin i	$\widehat{T}_i$ (%)		$\widehat{T}_{-i}$ (%)	
		Measured	Predicted	Measured	Predicted
2	1	23.9 ± 1.6	22.5 ± 4.2	35.5 ± 1.9	28.6 ± 1.1
	2	17.3 ± 1.5	21.1 ± 1.2	23.3 ± 1.7	27.8 ± 4.1
3	1	22.0 ± 1.5	19.8 ± 3.8	33.0 ± 1.7	25.6 ± 1.0
	2	18.1 ± 1.4	22.7 ± 1.4	22.8 ± 1.6	26.1 ± 5.3
	3	1.2 ± 0.4	1.4 ± 0.7	3.0 ± 0.6	3.8 ± 1.6
4	1	20.0 ± 1.5	18.3 ± 3.3	30.5 ± 1.7	23.0 ± 1.1
	2	7.2 ± 1.1	8.5 ± 1.0	7.6 ± 1.3	8.6 ± 1.3
	3	13.3 ± 1.4	16.3 ± 1.3	17.7 ± 1.4	21.3 ± 4.0
	4	0.8 ± 0.4	0.5 ± 0.4	2.8 ± 0.6	3.5 ± 1.3

Table 4.9: Weighted average $\widehat{T}_{(-)i}$ for the different binnings considered in this analysis.

4.4.2 Strong phase difference parameters

The fit values of c_i, s_i, c_i' and s_i' are listed in Table 4.10. The uncertainty shown is the quadrature sum of the statistical uncertainty and the uncertainty associated with the χ^2 constraint in the fit. Correlation matrices for the statistical uncertainties are listed in Section A.3. Section 4.5 describes how the systematic uncertainties are evaluated and the final results are shown in Section 4.6.

$\mathcal{N}$	Bin i	c_i	s_i	c_i'	s_i'
2	1	0.818 ± 0.107	0.445 ± 0.215	0.839 ± 0.108	0.445 ± 0.216
	2	-0.746 ± 0.083	0.229 ± 0.220	-0.775 ± 0.085	0.298 ± 0.220
3	1	0.793 ± 0.063	0.431 ± 0.222	0.814 ± 0.063	0.422 ± 0.222
	2	-0.566 ± 0.092	0.413 ± 0.234	-0.529 ± 0.092	0.426 ± 0.234
	3	-0.096 ± 0.329	-0.461 ± 0.432	-0.583 ± 0.349	0.241 ± 0.456
4	1	0.858 ± 0.059	0.309 ± 0.248	0.874 ± 0.059	0.303 ± 0.248
	2	0.176 ± 0.223	0.992 ± 0.473	0.270 ± 0.225	0.965 ± 0.473
	3	-0.819 ± 0.095	0.307 ± 0.267	-0.810 ± 0.096	0.346 ± 0.268
	4	0.376 ± 0.329	-0.133 ± 0.659	-0.317 ± 0.408	0.770 ± 0.696

Table 4.10: The measured values of c_i, s_i, c_i' and s_i' for each Dalitz plane binning. The uncertainty is statistical, including the uncertainty associated with the $\Delta(c,s)_i$ constraints.

4.4.2.1 χ^2 contribution to log likelihood

For each fit we determine the size of the χ^2 term in the log likelihood expression (Equation 4.5), which for brevity is denoted $\chi^2_{\log\mathcal{L}}$. The individual $\chi^2_{\log\mathcal{L}}$ in each bin and the total in all bins are listed in Table 4.11. The table also shows the value of $-2\log\mathcal{L}$ for comparison. There are no large contributions from any of the individual terms; the largest is 0.392. The

$\mathcal{N}$	Bin i	$\chi^2_{\log\mathcal{L}}$			$-2\log\mathcal{L}$
		c_i	s_i	Total	
2	1	0.039	0.004		
	2	0.261	0.007	0.311	−1242
3	1	0.041	0.002		
	2	0.053	0.000		
	3	0.021	0.345	0.463	−924
4	1	0.027	0.001		
	2	0.003	0.000		
	3	0.058	0.000		
	4	0.153	0.392	0.634	−672

Table 4.11: χ^2 contribution to log likelihood term in each bin, the total χ^2 in all bins, and the value of $-2\log\mathcal{L}$.

addition of the χ^2 term therefore does not bias the extracted parameters away from the values that are initially selected by the fit.

4.5 Systematic uncertainties

Potential sources of systematic bias are introduced at several stages in the analysis. In this section we describe the procedure used to determine the impact of each systematic effect on the final results, list the sources of uncertainty, and provide the magnitude of the uncertainty induced for each one.

4.5.1 Strategy

To calculate the systematic uncertainties on $(c,s)_i$ one of two possible methods is used. The method used most often is to vary the quantities that are relevant to the source of uncertainty in question, taking correlations into account, and then redetermine the $(c,s)_i$. This is performed many times to build up distributions of the $(c,s)_i$ coefficients, enabling the associated covariance matrix to be calculated. We determine the standard deviation of the distribution of each $(c,s)_i$ coefficient and also the Pearson correlation coefficient [75] between all pairs of $(c,s)_i$. The distribution of smeared points on the (c_i,s_i) plane is shown for each systematic uncertainty that is evaluated with this approach unless the effect is negligible.

An alternative approach is to vary the relevant quantity by '1σ' and re-evaluate the $(c,s)_i$ coefficients obtained from the fit. The systematic uncertainty is taken to be the difference between the central values obtained in this case and those obtained in the default case. When the correlation between the uncertainties is unknown, the correlation matrix is conservatively assumed to have all off-diagonal elements equal to 0.5. This approach is used to quantify the

uncertainty due to the multiple candidate selection (see Section 4.5.11) and the assumptions made in the fit (Section 4.5.12).

4.5.2 Bin-to-bin migration

As detailed in Section 3.5.4, the finite detector resolution causes events to move on the Dalitz plane after reconstruction. If the effect is different for Monte Carlo and data, the selection efficiencies and migration matrices that are used to correct the yields in data will produce unrepresentative results.

The detector resolution is quantified in both data and Monte Carlo by using the prominent ϕ resonance that appears on the $m^2_{K^+K^-}$ projection. The relevant $\mathcal{CP}$-tagged data are used in order to obtain a sample free of contamination from other resonances; this is possible because $K^0_S\phi$ is the only $\mathcal{CP}-$ resonance present in the $K^0_SK^+K^-$ resonant model, and likewise $K^0_L\phi$ is the only $\mathcal{CP}+$ resonance for $K^0_LK^+K^-$. The most significant migration occurs in this region so it is very useful to quantify the resolution there.

Values of $m_{K^+K^-}$ are obtained by taking the square root of the calculated values of $m^2_{K^+K^-}$. A Voigt function[1] is fit to the $m_{K^+K^-}$ distribution in the range $(0.99, 1.05)$ GeV/c^2. The Breit-Wigner pole mass and width are fixed to the PDG [11] values of 1.019 GeV/c^2 and 4.26 MeV/c^2 respectively. The Gaussian width is left floating and extracted using the RooFit package [73]. The widths obtained from fits to data ($\sigma^m_{\rm data}$) and Monte Carlo ($\sigma^m_{\rm MC}$) are presented in Table 4.12. The superscript m indicates these are the resolutions on $m_{K^+K^-}$ as opposed to $m^2_{K^+K^-}$. Figures 4.6 and 4.7 show fits to $K^0_{S,L}K^+K^-$ data and Monte Carlo.

Final state	Width $\times 10^3$ (GeV/c^2)	
	$\sigma^m_{\rm data}$	$\sigma^m_{\rm MC}$
$K^0_SK^+K^-$ against $\mathcal{CP}+$	4.64 ± 0.85	4.74 ± 0.06
$K^0_LK^+K^-$ against $\mathcal{CP}-$	4.95 ± 0.83	4.81 ± 0.08

Table 4.12: Extracted $K^0_{S,L}\phi$-peak Gaussian widths (and associated uncertainties) for $\mathcal{CP}$-tagged data and Monte Carlo.

In both cases the resolution of the Monte Carlo is compatible with that of the data. This corroborates the conclusion of the investigation into the distance moved by data and MC onto the edge of the Dalitz plot (see Section 3.4.2).

We make a conservative estimate of the effect of the difference between data and MC, considering the case where the resolution found in MC underestimates that in data. The conservative data resolution $\sigma^m_{\rm data+}$ is defined as the central value fluctuated upwards by '1σ'.

[1] A Voigt function is the convolution of a Breit-Wigner with a Gaussian.

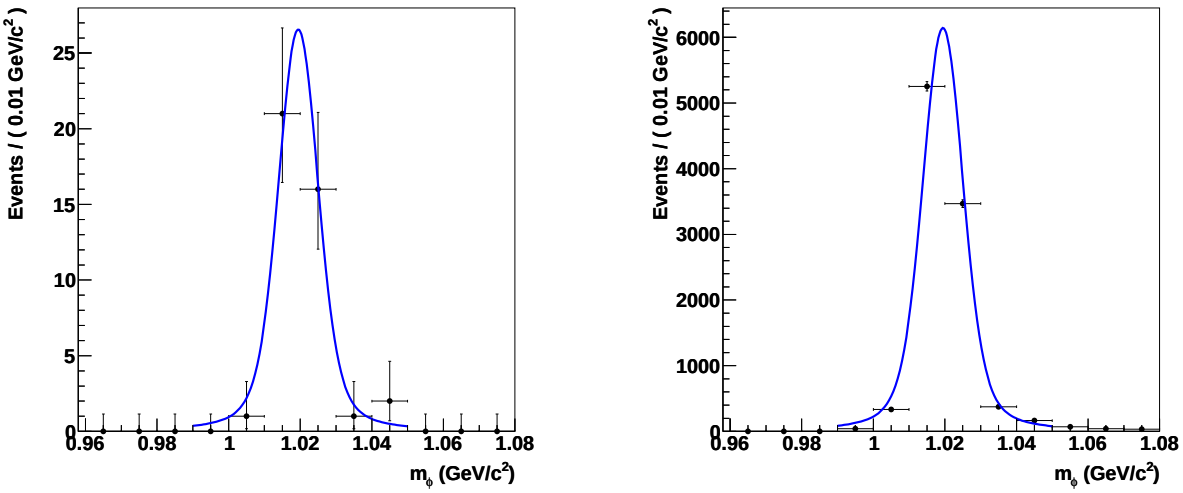

Figure 4.6: A Voigt fit to $K^0_S K^+ K^-$ tagged with $\mathcal{CP}+$ data (left) and MC (right).

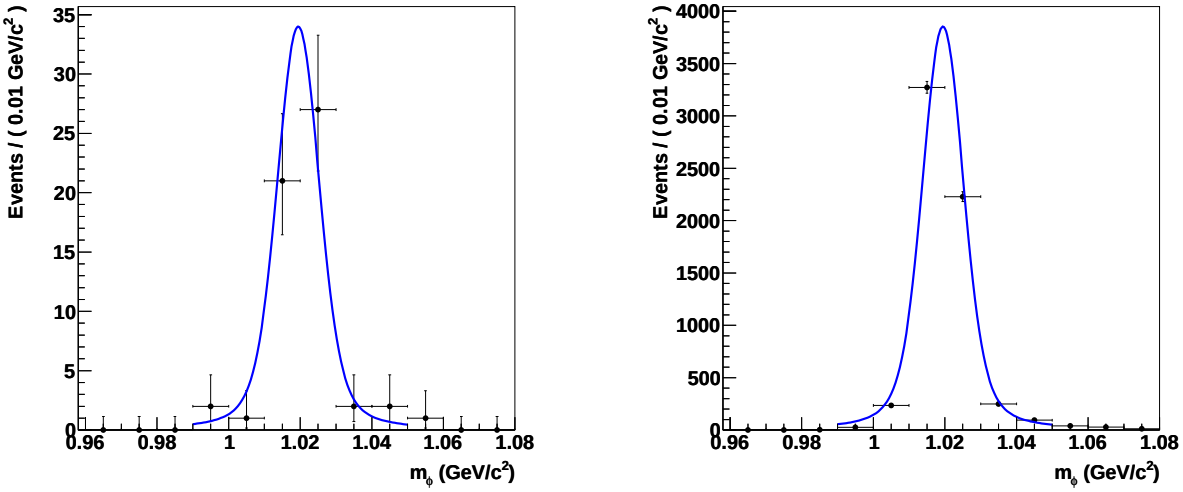

Figure 4.7: A Voigt fit to $K^0_L K^+ K^-$ tagged with $\mathcal{CP}+$ data (left) and MC (right).

The distribution of Monte Carlo events is then 'corrected' by smearing the events' locations on the $(m^2_{K^0_S K^+}, m^2_{K^0_S K^-})$ plane. The smearing function is a Gaussian whose width, $\sigma^{m^2}_{\rm corr}$, is the quadrature difference between the conservative data resolution and the Monte Carlo resolution:

$$\sigma^{m^2}_{\rm corr} = \sqrt{(\sigma^{m^2}_{\rm data+})^2 - (\sigma^{m^2}_{\rm MC})^2}. \tag{4.19}$$

The superscript indicates the smearing is now to be performed in m^2 space. To convert between m and m^2, we use the relation:

$$\sigma^{m^2} = 2m\sigma^m. \tag{4.20}$$

Therefore

$$\sigma^{m^2}_{\rm corr} = 2m\sqrt{(\sigma^{m}_{\rm data+})^2 - (\sigma^{m}_{\rm MC})^2}. \tag{4.21}$$

The fit is centred on m_ϕ so this used as the value of m. Consequently $\sigma^{m^2}_{\text{corr}}$ is (0.006 ± 0.003) GeV$^2/c^4$ for $K^0_S K^+K^-$ and (0.007 ± 0.003) GeV$^2/c^4$ for $K^0_L K^+K^-$.

The Monte Carlo events are simultaneously smeared along vectors in the $m^2_{K^0_S K^+}$ and $m^2_{K^0_S K^-}$ directions. The calculated width is in terms of $m^2_{K^+K^-}$, so the smearing width for each direction on the Dalitz plane is taken to be $\sigma^{m^2}_{\text{corr}}/\sqrt{2}$. This evaluates to (0.004 ± 0.002) GeV$^2/c^4$ for $K^0_S K^+K^-$ and (0.005 ± 0.002) GeV$^2/c^4$ for $K^0_L K^+K^-$. The smearing width is chosen to be 0.004 GeV$^2/c^4$. This estimate is conservative for $K^0_S K^+K^-$ and approximately correct for $K^0_L K^+K^-$ when compared to the most probable value of the distance moved by $K^0_L K^+K^-$ events during reconstruction (see Section 3.5.4).

Each reconstructed event in Monte Carlo data is smeared by assuming its position follows a Gaussian distribution with width 0.004 GeV$^2/c^4$. The fit is then rerun and new values of $(c, s)_i$ are recorded. This procedure is repeated many times in order to obtain a distribution of extracted $(c, s)_i$. The standard deviations of these distributions are taken to be the uncertainty on $(c, s)_i$. In addition we evaluate the Pearson correlation coefficient between each pair of $(c, s)_i$.

Figure 4.8 shows the distribution of events on the (c_i, s_i) plane after Monte Carlo smearing.

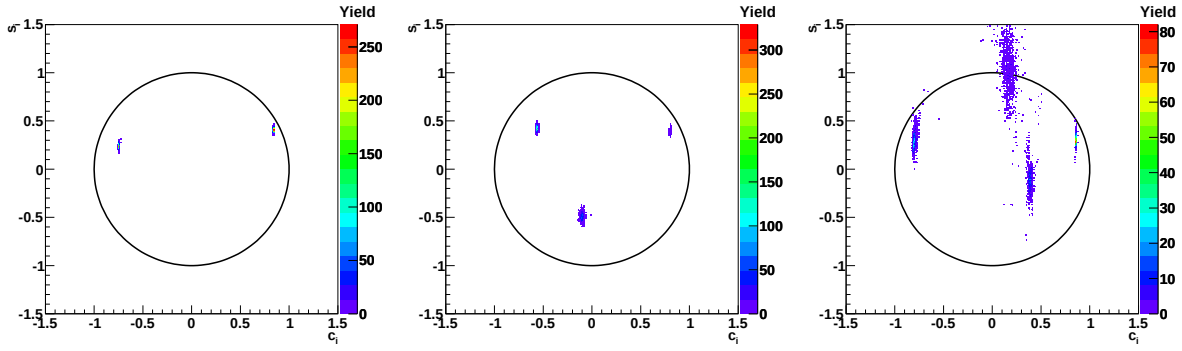

Figure 4.8: Events on the (c_i, s_i) plane with Monte Carlo smearing: two bins (left), three bins (middle), four bins (right).

4.5.2.1 m_ϕ resolution without a D^0 mass fit

A further test of the efficacy of the kinematic constraint of the $K^0_{S,L} K^+K^-$ final state to the D^0 mass (Section 3.4.1) can be performed by repeating the determination of the m_ϕ resolution using events that have *not* been subject to a D^0 mass fit. Exactly the same procedure is used as above. The widths for data (σ^m_{data}) and Monte Carlo (σ^m_{MC}) are presented in Table 4.13.

For three out of four of the cases, the width is slightly degraded when the mass fit is not used. For $K^0_S K^+K^-$ against $\mathcal{CP}+$ eigenstates, the resolution improves from $(4.64 \pm 0.85) \times 10^{-3}$ GeV$/c^2$ to $(4.47 \pm 0.76) \times 10^{-3}$ GeV$/c^2$. This change is well within the statistical

Final state	Width $\times 10^3$ (GeV/c^2)	
	σ^m_{data}	σ^m_{MC}
$K^0_S K^+ K^-$ against $\mathcal{CP}+$	4.47 ± 0.76	4.78 ± 0.05
$K^0_L K^+ K^-$ against $\mathcal{CP}-$	4.99 ± 0.83	4.82 ± 0.08

Table 4.13: Extracted $K^0_{S,L}\phi$-peak Gaussian widths (and associated uncertainties) for $\mathcal{CP}$-tagged data and Monte Carlo with no D^0 mass fit.

uncertainty.

Fits to $K^0_{S,L}K^+K^-$ data and Monte Carlo are shown in Figures 4.9 and 4.10.

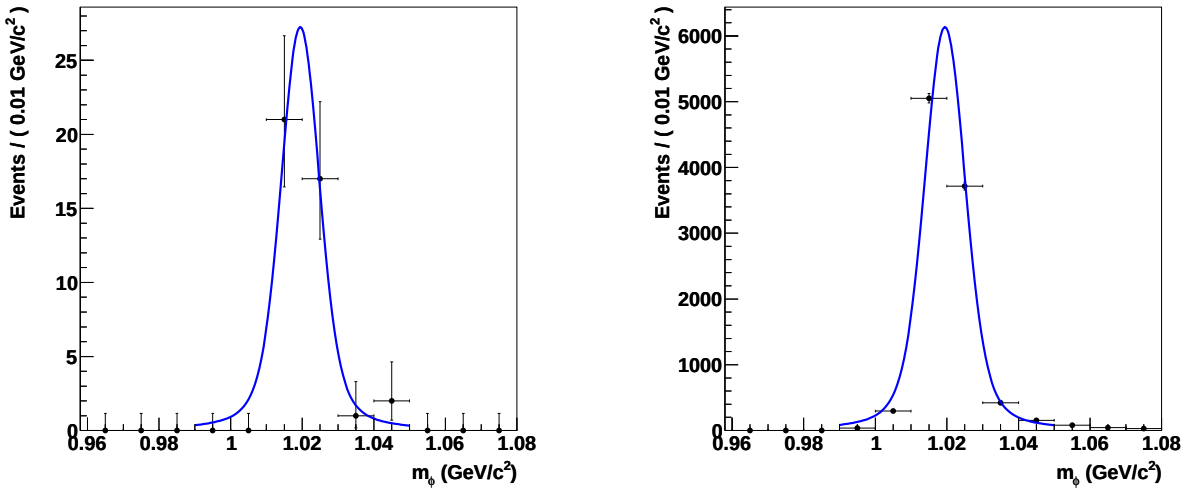

Figure 4.9: A Voigt fit to $K^0_S K^+ K^-$ tagged with $\mathcal{CP}+$ data (left) and MC (right) with no D^0 mass fit.

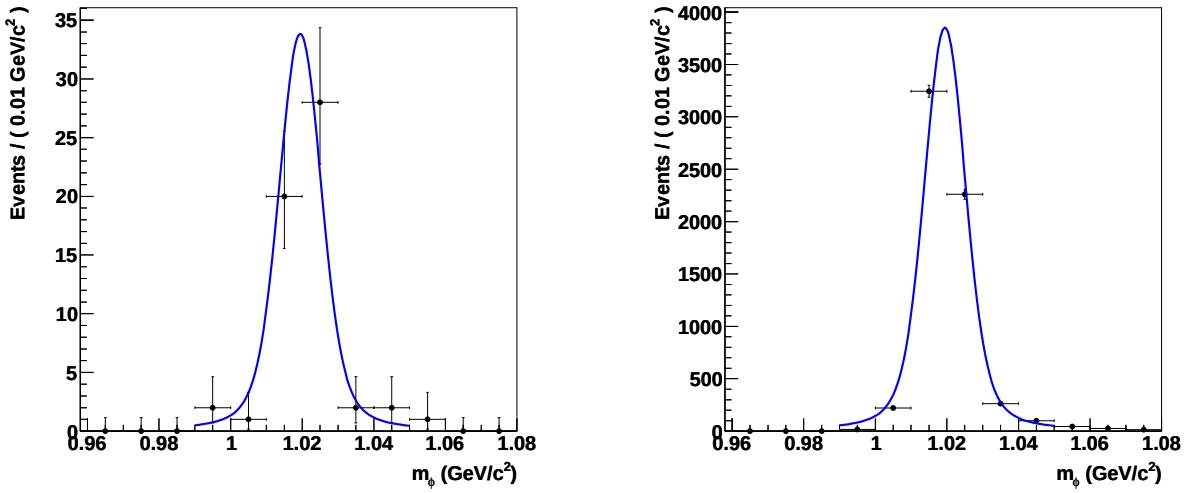

Figure 4.10: A Voigt fit to $K^0_L K^+ K^-$ tagged with $\mathcal{CP}+$ data (left) and MC (right) with no D^0 mass fit.

4.5.2.2 Negative bin correction

In Section 3.5.5.5 we described the procedure used to correct negative bin yields caused by the migration. This procedure causes a shift in the extracted values of c_i and s_i. The shift, along with the statistical uncertainty for comparison, is presented in Tables 4.14–4.16. The shift is always easily covered by the statistical uncertainty. We do not assign an additional systematic uncertainty to this effect.

Quantity	Shift in central value	Statistical uncertainty
c_1	0.007	0.067
c_2	−0.017	0.085
s_1	0.000	0.215
s_2	−0.001	0.220

Table 4.14: The shift in central values of c_i and s_i caused by the correction for negative bin yields, for two equal $\Delta\delta_D$ bins.

Quantity	Shift in central value	Statistical uncertainty
c_1	0.004	0.067
c_2	−0.010	0.093
c_3	−0.013	0.330
s_1	0.000	0.222
s_2	−0.000	0.234
s_3	0.002	0.432

Table 4.15: The shift in central values of c_i and s_i caused by the correction for negative bin yields, for three equal $\Delta\delta_D$ bins.

Quantity	Shift in central value	Statistical uncertainty
c_1	−0.009	0.061
c_2	0.155	0.211
c_3	−0.019	0.082
c_4	−0.009	0.330
s_1	0.001	0.248
s_2	0.004	0.473
s_3	−0.006	0.267
s_4	−0.001	0.659

Table 4.16: The shift in central values of c_i and s_i caused by the correction for negative bin yields, for four equal $\Delta\delta_D$ bins.

4.5.3 Background yields

When determining the expected background yield we use several quantities obtained from Monte Carlo data (Section 3.6). To evaluate the systematic uncertainty associated with this

approach we smear each of these quantities, assuming they follow Poisson statistics. In each case, the mean of the Poisson distribution is taken to be the reconstructed yield.

For fully-reconstructed final states we estimate the level of peaking background in the signal region by scaling the quantity of such events in the Monte Carlo. We therefore smear the yield of each decay mode classified as peaking.

For final states containing a missing particle we use Monte Carlo to determine the yields of signal, backgrounds that predominantly peak in the signal region, and backgrounds that predominantly peak in the sidebands. The level of background is estimated using the yields of each of these types in the signal region and the sidebands, so they are all smeared when determining the systematic uncertainty. The level of background in events with a missing particle is typically higher than for fully-reconstructed events, so the corresponding systematic uncertainties are larger.

We do not smear all background yields simultaneously. Instead, we classify each decay mode for which we are determining the background systematic as either fully-reconstructed or partially-reconstructed and either flavour or non-flavour, leading to a total of four categories. The background yields for each category are smeared independently and the fit is rerun. This procedure is repeated many times for each category and the resulting distributions of $(c, s)_i$ are used to determine the systematic uncertainties.

The scatter of events on the (c_i,s_i) plane is very low for all types of background except partially-reconstructed non-flavour decays. Figure 4.11 shows the distribution of events on the (c_i,s_i) plane after smearing of background yields in that case.

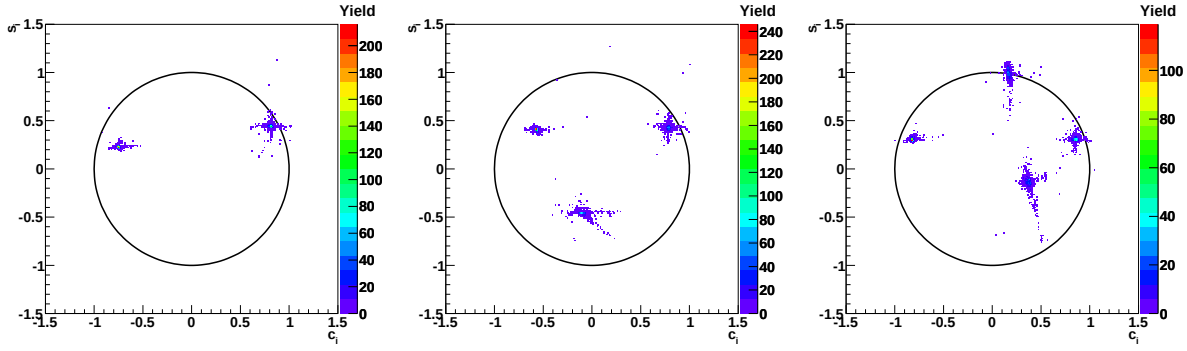

Figure 4.11: Events on the (c_i,s_i) plane with partially-reconstructed non-flavour state background smearing: two bins (left), three bins (middle) and four bins (right).

Our assumptions about the distribution of backgrounds across the Dalitz plane also result in a systematic uncertainty. As described in Section 3.6.4, backgrounds are classified as either 'phase-space' or 'resonant'. By default, the two types of background are assumed be in the same proportion as in Monte Carlo. We define the fractions of the total background yield as $f_{\rm PS}$ and $f_{\rm res}$ for phase-space and resonant backgrounds respectively, so $0 \leq f_{\rm PS} \leq 1$ and $f_{\rm res} \equiv 1 - f_{\rm PS}$. To determine the systematic uncertainty, $f_{\rm PS}$ is taken to be a random number

uniformly distributed between 0 and 1 and the corresponding $f_{\rm res}$ is calculated. Bin-by-bin background yields are then determined and the fit coefficients are extracted.

Figure 4.12 shows the distribution of events on the (c_i,s_i) plane after smearing of the phase-space/resonant background ratios.

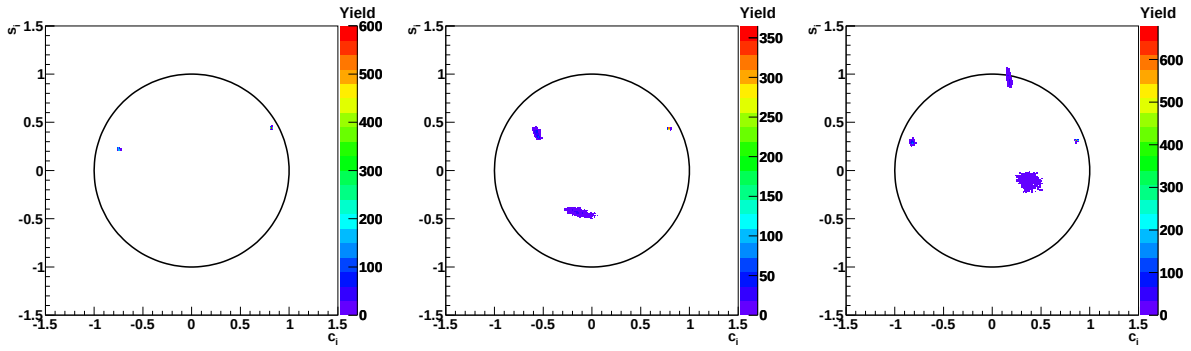

Figure 4.12: Events on the (c_i,s_i) plane with phase-space/resonant background smearing: two bins (left), three bins (middle) and four bins (right).

We assign an additional systematic uncertainty related to the scaling of flat backgrounds from the sidebands into the signal region for fully-reconstructed decays. These backgrounds almost always arise when the opposite side has been incorrectly reconstructed, so the events lie in sideband A (see Figure 3.6). It is possible that such backgrounds are not truly 'flat' but rather exhibit a non-zero gradient or some other structure. To evaluate the uncertainty related to this possibility we multiply the ratio of the area of sideband A to the area of the signal region by a number drawn from a uniform distribution between 0.5 and 2. The ratio of areas is then used to determine the new quantity of flat backgrounds in the signal region. We rerun the fit and determine the new central values of c_i and s_i. This procedure is repeated many times in order to build up a distribution of events on the (c_i, s_i) plane. The variation of the scaling factor between 0.5 and 2 is somewhat arbitrary but the size of the effect is small enough that this is a reasonable range to use.

The scatter of events on the (c_i, s_i) plane is very low for this systematic uncertainty so we do not show it.

A final contribution to the systematic uncertainty associated with background estimation is the fact that the yield of each peaking background is estimated by scaling its population in generic Monte Carlo by its PDG [11] branching fraction (see Sections 3.6.2 and 3.6.3). The branching fraction is fixed in the decay model used to create the Monte Carlo, but it has an associated uncertainty.

As an example, consider a background (denoted X) that mimics the opposite-side of a $K^0_S K^+ K^-$ decay. The number of such events present in the Monte Carlo, after efficiency-

correction, is approximately:

$$N_X = 2 f_{D^0\bar{D}^0} N_{D^0\bar{D}^0} \mathcal{B}_{K^0_S K^+ K^-} \mathcal{B}_X \tag{4.22}$$

where $f_{D^0\bar{D}^0}$ is the integrated luminosity ratio between the data and the Monte Carlo (see Section 2.5.1.1).

Each branching fraction is smeared according to a Gaussian distribution using the central value and uncertainty from the PDG, yielding the quantity $\mathcal{B}'_X$. The yield of this type of event becomes:

$$N'_X = 2 f_{D^0\bar{D}^0} N_{D^0\bar{D}^0} \mathcal{B}_{K^0_S K^+ K^-} \mathcal{B}'_X. \tag{4.23}$$

The initial number of peaking background of events, m_X, is multiplied by the ratio of N'_X to N_X to give the new estimated quantity:

$$m'_X = m_X \frac{N'_X}{N_X} = m_X \frac{\mathcal{B}'_X}{\mathcal{B}_X}. \tag{4.24}$$

A value of m'_X is obtained for each peaking background and new values of $(c, s)_i$ are extracted from the fit. This procedure is repeated many times.

Figure 4.13 shows the distribution of events on the (c_i,s_i) plane after smearing the PDG branching fractions of the peaking backgrounds.

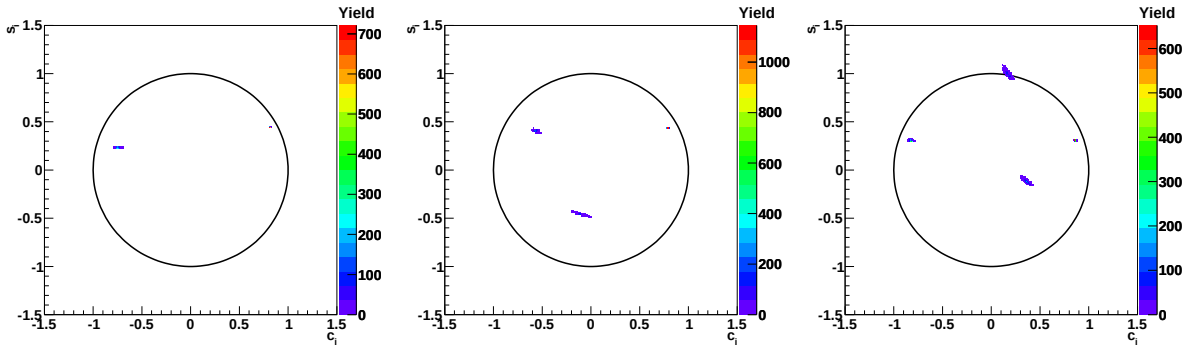

Figure 4.13: Events on the (c_i,s_i) plane with peaking background branching fraction smearing: two bins (left), three bins (middle), four bins (right).

4.5.4 Flavour-tagged $K^0_{S,L}K^+K^-$ yields

Yields of flavour-tagged $K^0_{S,L}K^+K^-$ events are assumed to be constants in the fit; their uncertainties are not considered when determining the statistical uncertainty on $(c, s)_i$. To evaluate an uncertainty related to the finite size of these samples, each raw yield is Poisson-smeared. The weighted, normalised quantities $\widehat{T}_{(-)i}(')$ (see Section 4.3.2) are recalculated, keeping the PDG branching fractions at their central values, and the fit is repeated. This

procedure is performed many times and the uncertainties on $c_i(')$ and $s_i(')$ are determined.

Figure 4.14 shows the distribution of events on the (c_i,s_i) plane after flavour-tagged $K^0_{S,L}K^+K^-$ yield smearing.

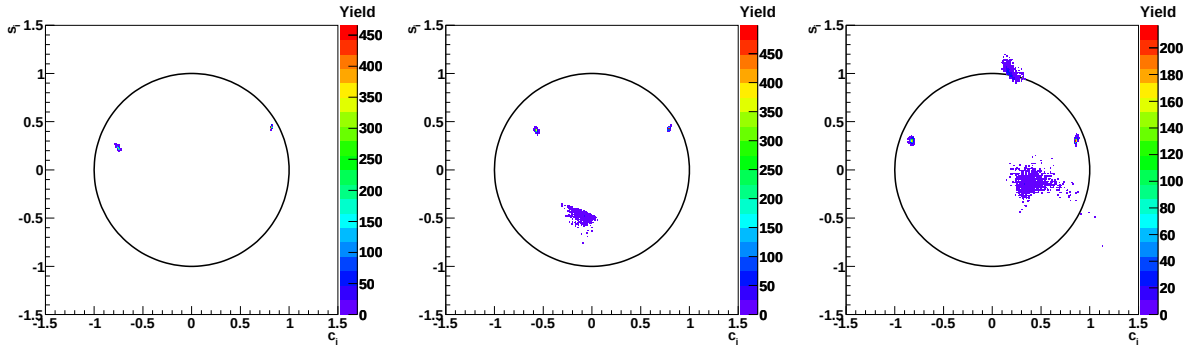

Figure 4.14: Events on the (c_i,s_i) plane with flavour-tagged $K^0_{S,L}K^+K^-$ yield smearing: two bins (left), three bins (middle), four bins (right).

4.5.5 Correction to $K^0_{S,L}K^+K^-$ flavour-tagged yields

As described in Section 3.4.3 we apply correction factors to the yields of $K^0_{S,L}K^+K^-$ tagged with fully hadronic final states. This is necessary because of the expected contamination from DCS decays, causing events to be placed in the wrong bin. The correction factors have their own associated uncertainties which are obtained by using the same smearing procedure that was used to determine $\delta\Delta(c,s)_i$. Each correction factor is smeared by its uncertainties and the corrected flavour-tagged yields are redetermined before calculating $\widehat{T}_{(-)i}(')$ and fitting for (c_i,s_i).

The scatter of events on the (c_i,s_i) plane is very low for this systematic uncertainty so we do not show it.

4.5.6 $K^0_{S,L}\pi^+\pi^-$ inputs

As described in Section 4.3.3, the fit procedure relies on external input from the analysis of $K^0_{S,L}\pi^+\pi^-$ decays, specifically the normalised flavour-tagged yields and the values of $(c,s)_i(')$ for the equal $\Delta\delta_D$ binning of the $K^0_S\pi^+\pi^-$ Dalitz plane. In the fit, all of these quantities are set to their central values and kept constant. In order to determine the systematic uncertainty associated with the $K^0_S\pi^+\pi^-$ inputs, the quantities are smeared by their reported uncertainties, taking correlations into account, and the fit is performed again. When smearing correlated quantities we use the method that is described in Section 4.3.4.

The scatter of events on the (c_i,s_i) plane is very low for the flavour-tagged $K^0_{S,L}\pi^+\pi^-$ yield smearing so we do not show it.

Figure 4.15 shows the distribution after $K^0_{S,L}\pi^+\pi^-$ $(c,s)_i(')$ smearing.

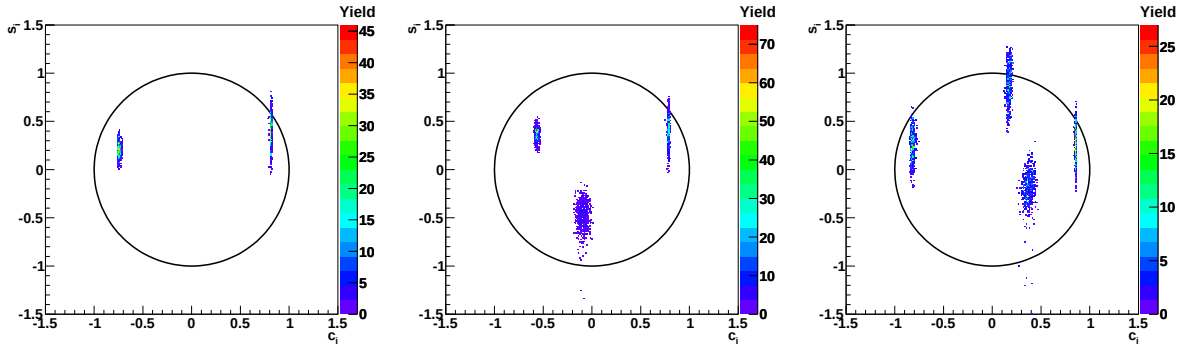

Figure 4.15: Events on the (c_i,s_i) plane with $K^0_{S,L}\pi^+\pi^-$ coefficient smearing: two bins (left), three bins (middle), four bins (right).

4.5.7 Numerical quantities

We use several numerical quantities to ensure that the raw yields obtained in data are appropriately normalised[2]: the PDG branching fractions of each mode under study and $N_{D^0\overline{D}^0}$. Each quantity used in the fit is varied by assuming it follows a Gaussian distribution with a width equal to its reported uncertainty and then drawing numbers randomly from that distribution. The quantities used to determine $N_{D^0\overline{D}^0}$ (see Equation 1.123) are separately smeared before they are multiplied together. The fit is performed many times to build up a distribution of events on the (c_i,s_i) plane.

For each of the numerical quantities considered, the scatter of events on the (c_i,s_i) plane is very low after this procedure so we do not show any of them.

4.5.8 Data and Monte Carlo reconstruction and ID efficiencies

Previous CLEO-c investigations have established that reconstruction and particle identification efficiencies differ between Monte Carlo and data. The differences, always small, vary depending on the particular final state particle. We therefore apply a correction to each reconstruction efficiency used in the analysis on a particle-by-particle basis. There is an uncertainty associated with each correction; the corrections and uncertainties for each final state particle are listed in Table 4.17. In order to determine the systematic uncertainty associated with these corrections, each correction is varied randomly by its uncertainty assuming it is drawn from a Gaussian distribution and the selection efficiencies are recalculated before the fit is repeated. This is performed many times.

The scatter of events on the (c_i,s_i) plane is very low for the efficiency smearing so we do not show it.

[2]The selection efficiencies determined from Monte Carlo data are also used to normalise the yields; the systematic uncertainties associated with this are discussed in Sections 4.5.2, 4.5.8 and 4.5.10.

Final-state particle	Correction factor	Uncertainty
$K^{\pm}$	1.000	0.006
$\pi^{\pm}$	1.000	0.003
π^0	0.940	0.013
η	0.944	0.040
K^0_S	1.000	0.009
K^0_L	1.000	0.030
$e^{\pm}$	1.000	0.006

Table 4.17: Correction factors between data and Monte Carlo for each final state particle that is used in the analysis.

4.5.9 Kaon momentum-dependent systematic

There is a momentum-dependent systematic uncertainty associated with charged kaon reconstruction. In Section 3.5.7 we showed the momentum spectra of the K^0_S, K^+ and K^- produced by D decays in both data and Monte Carlo. Differences between these spectra can be observed at low momentum. To account for this we apply a correction factor to the selection efficiency. The correction factor changes depending on the particle momentum; we use bins in momentum of width 100 MeV/c to classify particles. We determine the average correction factor for a particular final state by weighting each individual factor according to the population of events in the momentum bins. The systematic uncertainty associated with this procedure is determined by varying each correction factor by its reported uncertainty and recomputing the average.

The scatter of events on the (c_i,s_i) plane is very low for the kaon momentum-dependent systematic so we do not show it.

4.5.10 Signal Monte Carlo statistics

Even though large quantities of signal Monte Carlo data were generated for efficiency and migration studies, there is a non-negligible statistical uncertainty associated with the quantities reconstructed in each bin. In order to quantify this we smear the yields in each bin, assuming they are drawn from a Poisson distribution with the mean equal to the initial value. We then redetermine the migration matrices, calculate the migrated yields of data, and rerun the fit. This is performed many times.

Figure 4.16 shows the distribution of events on the (c_i,s_i) plane after smearing the signal Monte Carlo yields.

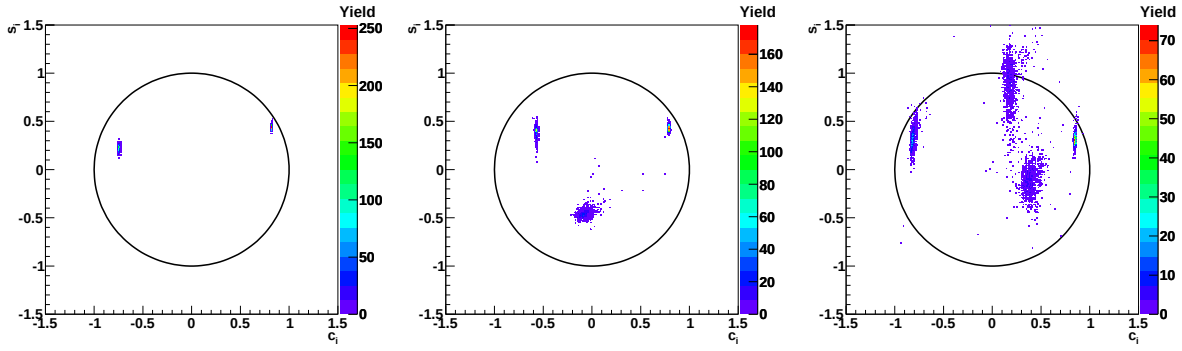

Figure 4.16: Events on the (c_i,s_i) plane with signal Monte Carlo yield smearing: two bins (left), three bins (middle), four bins (right).

4.5.11 Multiple candidate selection

Selected events occasionally have more than one reconstructed D candidate. By default, the candidate with the beam-constrained mass closest to m_{D^0} is selected (Section 3.2.5). It is possible that this method introduces a bias in the parameters of interest. An alternative criterion is to select the candidate with the smallest value of the energy difference ΔE, defined in Equation 3.3. We investigate the use of this criterion and assign any difference in the extracted parameters as a systematic uncertainty.

Most final states are reconstructed with a candidate/event ratio close to 1. Table 4.18 shows the candidate/event ratio for each selected final state, and the overall average. The numbers shown are for all events selected, not just those in the signal region. The decay mode with the largest candidate/event ratio is $K^0_S K^+ K^-$ selected against $K^\pm\pi^\mp\pi^0$.

The most significant effect of using the alternative candidate selection is on the distribution of events across the Dalitz plane. In order to determine the systematic uncertainty, the change in this distribution observed for $K^0_S K^+ K^-$ against $K^\pm\pi^\mp\pi^0$ is extrapolated to the distributions of events for the remaining final states. In order to do this, a technique very similar to the migration matrix method (see Section 3.5.5) is used. Instead of using generator- and reconstruction- level signal Monte Carlo populations, we determine the '$m_{\rm bc}$' and 'ΔE' populations in each bin (the names refer to the method used to select candidates). The $m_{\rm bc}$ population is treated as the generator-level population in the migration formalism and the ΔE population is treated as the reconstruction-level. The matrices obtained are shown in Tables 4.19–4.21. The distribution across the Dalitz plane for each final state is then migrated using these populations. For $K^0_{S,L} K^+ K^-$ against $K^0_{S,L} h^+ h^-$, only the signal-side populations are changed. The shift in the central value of coefficients is determined and the difference from the defaults is taken to be the uncertainty. This method is conservative considering that most final states have a candidate/event ratio close to 1.

The scatter of events on the (c_i,s_i) plane is very low for the multiple candidate selection

Final state	Candidates/Event	
	$K^0_S K^+ K^-$	$K^0_L K^+ K^-$
K^+K^-	1.00 ± 0.41	1.03 ± 0.13
$\pi^+\pi^-$	1.25 ± 0.84	1.00 ± 0.18
$K^0_S\pi^0\pi^0$	1.22 ± 0.55	1.12 ± 0.18
$K^0_L\pi^0$	1.07 ± 0.23	
$K^0_L\eta(\gamma\gamma)$	1.06 ± 0.36	
$K^0_L\omega(\pi^+\pi^-\pi^0)$	1.06 ± 0.25	
$K^0_L\eta(\pi^+\pi^-\pi^0)$	1.09 ± 0.46	
$K^0_L\eta'(\pi^+\pi^-\eta)$	1.00 ± 1.41	
$K^0_S\pi^0$	1.05 ± 0.32	1.00 ± 0.09
$K^0_S\eta(\gamma\gamma)$	1.00 ± 0.50	1.11 ± 0.23
$K^0_S\omega(\pi^+\pi^-\pi^0)$	1.00 ± 0.38	1.00 ± 0.15
$K^0_S\eta(\pi^+\pi^-\pi^0)$	1.00 ± 0.82	1.00 ± 0.41
$K^0_S\eta'(\pi^+\pi^-\eta)$	1.00 ± 0.82	1.00 ± 0.41
$K^0_L\pi^0\pi^0$	1.22 ± 0.55	
$K^\pm\pi^\mp$	1.02 ± 0.11	1.00 ± 0.04
$K^\pm\pi^\mp\pi^0$	1.34 ± 0.09	1.09 ± 0.03
$K^\pm\pi^\mp\pi^+\pi^-$	1.14 ± 0.09	1.00 ± 0.03
$K^\pm e^\mp\nu_e$	1.05 ± 0.14	
$K^0_S K^+ K^-$	1.25 ± 0.84	
$K^0_L K^+ K^-$	1.03 ± 0.18	
$K^0_S\pi^+\pi^-$	1.03 ± 0.24	1.01 ± 0.06
$K^0_L\pi^+\pi^-$	1.00 ± 0.06	
Total	1.05 ± 0.02	

Table 4.18: The candidate/event ratio for each reconstructed decay mode.

i	1	2	-1	-2
1	1.000	0.011	0.000	0.000
2	0.000	0.979	0.000	0.000
-1	0.000	0.010	1.000	0.010
-2	0.000	0.000	0.000	0.990

Table 4.19: Matrix describing the bin-to-bin migration associated with the two methods of selecting multiple candidates in an event for two bins.

i	1	2	3	-1	-2	-3
1	1.000	0.008	0.000	0.000	0.000	0.000
2	0.000	0.981	0.000	0.000	0.000	0.000
3	0.000	0.002	1.000	0.000	0.000	0.000
-1	0.000	0.009	0.000	1.000	0.006	0.000
-2	0.000	0.000	0.000	0.000	0.988	0.000
-3	0.000	0.000	0.000	0.000	0.006	1.000

Table 4.20: Matrix describing the bin-to-bin migration associated with the two methods of selecting multiple candidates in an event for three bins.

i	1	2	3	4	−1	−2	−3	−4
1	1.000	0.002	0.005	0.000	0.000	0.000	0.000	0.000
2	0.000	0.998	0.000	0.000	0.000	0.000	0.000	0.000
3	0.000	0.000	0.979	0.000	0.000	0.000	0.000	0.000
4	0.000	0.000	0.002	1.000	0.000	0.000	0.000	0.000
−1	0.000	0.000	0.014	0.000	1.000	0.000	0.005	0.000
−2	0.000	0.000	0.000	0.000	0.000	1.000	0.012	0.000
−3	0.000	0.000	0.000	0.000	0.000	0.000	0.973	0.000
−4	0.000	0.000	0.000	0.000	0.000	0.000	0.010	1.000

Table 4.21: Matrix describing the bin-to-bin migration associated with the two methods of selecting multiple candidates in an event for four bins.

systematic so we do not show it.

4.5.12 Fit assumptions

A consistency check of the fit procedure can be performed by using signal Monte Carlo in place of the data. We expect to extract values of c_i and s_i close to the model-predicted values, because the model was used to produce the signal Monte Carlo in the first place. Throughout the following, all backgrounds are set to zero and all efficiencies to 100%.

The yield of each final state can be arbitrarily fixed as long as the scaling between the number of single and double tags is consistent. For simplicity, the branching fractions of most states are set to zero. The branching fractions of certain representative states (e.g. $K^0_S K^+ K^-$ against $\mathcal{CP}+$) are set to 1. The total number of single tags S^X_T is determined using the formula:

$$S^X_T = 2N_{D^0\overline{D}^0}\mathcal{B}_X, \tag{4.25}$$

and the total number of double tags D^X_T is determined using the formula:

$$D^X_T = 2N_{D^0\overline{D}^0}\mathcal{B}_{K^0_S K^+K^-}\mathcal{B}_X. \tag{4.26}$$

The signal Monte Carlo samples are necessary to determine the relative populations in each bin. For a total of m_T signal Monte Carlo events, and the population of bin i equal to m_i, the number of double-tagged events in each bin is therefore:

$$D^X_i = D^X_T \frac{m_i}{m_T}. \tag{4.27}$$

Using this method, the number of $K^0_S K^+ K^-$ against $K^0_{S,L} K^+ K^-$ events is easily large enough to constrain the s_i, so it is not necessary to use $K^0_{S,L} K^+ K^-$ against $K^0_{S,L}\pi^+\pi^-$ events. This is beneficial because it removes the dependence on the $K^0_{S,L}\pi^+\pi^-$ flavour-tagged yields and strong phase coefficients.

The statistical uncertainty on the fit results is evaluated by fluctuating the signal Monte Carlo yield in each bin. The yield is assumed to follow a Poisson distribution with the mean equal to the yield before normalisation (i.e. the m_i in the above text). The $(c, s)_i$ are extracted and a distribution is built up by smearing many times. The width on this distribution is taken to be the associated statistical uncertainty.

Results for two, three and four bins are presented in Tables 4.22–4.24. The uncertainties quoted are those for the statistical uncertainty on the signal MC. The Monte Carlo was produced with an older $D^0 \to K^0_S K^+ K^-$ decay model so the predicted quantities are different from those listed in Tables 4.3–4.5.

Quantity	Fit result	Predicted
c_1	0.757 ± 0.002	0.764
c_2	-0.643 ± 0.003	-0.634
s_1	0.255 ± 0.010	0.261
s_2	0.307 ± 0.012	0.317

Table 4.22: Fit results using signal MC in the fit, compared with the model-predicted values, for two bins.

Quantity	Fit result	Predicted
c_1	0.810 ± 0.002	0.818
c_2	-0.639 ± 0.003	-0.640
c_3	0.334 ± 0.014	0.347
s_1	0.239 ± 0.009	0.252
s_2	0.407 ± 0.009	0.410
s_3	-0.641 ± 0.040	-0.684

Table 4.23: Fit results using signal MC in the fit, compared with the model-predicted values, for three bins.

Quantity	Fit result	Predicted
c_1	0.853 ± 0.002	0.859
c_2	0.001 ± 0.006	0.010
c_3	-0.777 ± 0.003	-0.769
c_4	0.543 ± 0.022	0.515
s_1	0.217 ± 0.010	0.225
s_2	0.519 ± 0.020	0.510
s_3	0.332 ± 0.011	0.327
s_4	-0.677 ± 0.059	-0.684

Table 4.24: Fit results using signal MC in the fit, compared with the model-predicted values, for four bins.

In some cases, especially for the c_i, there are significant biases (approximately 3–4 times the uncertainty due to MC statistics) between the predicted and obtained quantities. This

is caused by the granularity of the bitmap and the fact that quantum correlations are not taken into account when computing double tag branching fractions. The absolute value of the difference is small and is taken to be the systematic uncertainty due to assumptions made in the fit procedure.

4.5.13 $K^0_L K^+ K^-$ model uncertainty

The use of the χ^2 term in the fit (see Section 4.3.4) causes both the statistical uncertainty and the uncertainty on $\Delta(c,s)_i$ to contribute to the uncertainty reported by the fit software. In order to determine the magnitude of each of these contributions, the fit is repeated but the values of c'_i and s'_i are not floated independently in the fit. Instead, the differences $(c'_i - c_i)$ and $(s'_i - s_i)$ are constrained to the values predicted by the $D \to K^0_S K^+ K^-$ decay model. The fit results and statistical uncertainties for the constrained fit are shown in Table 4.25.

$\mathcal{N}$	Bin i	c_i	s_i
2	1	0.815 ± 0.057	0.444 ± 0.215
	2	-0.751 ± 0.085	0.228 ± 0.220
3	1	0.790 ± 0.063	0.430 ± 0.222
	2	-0.568 ± 0.096	0.405 ± 0.235
	3	-0.064 ± 0.304	-0.462 ± 0.430
4	1	0.856 ± 0.057	0.308 ± 0.248
	2	0.176 ± 0.199	0.992 ± 0.473
	3	-0.821 ± 0.086	0.304 ± 0.268
	4	0.417 ± 0.306	-0.133 ± 0.658

Table 4.25: Central values and statistical uncertainties for fits in which the differences $(c'_i - c_i)$ and $(s'_i - s_i)$ are set to their model-predicted values.

For each Dalitz plane binning we determine the uncertainty related to the $K^0_L K^+ K^-$ model by subtracting the covariance matrix of constrained fit parameters from the covariance matrix of default fit parameters. We find that the resulting covariance matrices contain unphysical negative diagonal elements. This is caused by the central values of c_i and s_i changing in the two fits, as well as the fact that the fit parameters do not behave in a Gaussian manner when they are close to the boundary of the physical region. Consequently we present the covariance matrix that contains the combined statistical and $K^0_L K^+ K^-$ model contributions. We estimate the magnitude of the uncertainties associated with the $K^0_L K^+ K^-$ model and set any negative entries to zero. These uncertainties are always small compared to both the statistical uncertainty and the dominant systematic uncertainties.

4.5.14 Results

Summaries of the systematic uncertainties on $(c, s)_i$ for two, three and four bins are presented in Tables 4.26–4.28. The tables include the statistical and $K^0_L K^+ K^-$ model uncertainties and the total uncertainty, obtained by adding the individual uncertainties in quadrature. We have combined some of the systematic uncertainties described in the previous sections:

- The parameterisation of backgrounds to fully-reconstructed events;
- The parameterisation of backgrounds to partially-reconstructed events;
- (Pseudo-)flavour statistics for $K^0_S K^+ K^-$ and $K^0_S \pi^+ \pi^-$;
- The 'mode-to-mode normalisation systematic' is a combination of the uncertainties on $N_{D^0\bar{D}^0}$, the PDG branching fractions, differences in reconstruction between data and MC, and the kaon momentum dependent efficiency correction.

Uncertainty	c_1	c_2	s_1	s_2
(Pseudo-)flavour statistics	0.004	0.009	0.013	0.012
Momentum resolution	0.002	0.004	0.017	0.021
Mode-to-mode normalisation	0.004	0.007	0.001	0.001
Multiple-candidate selection	0.007	0.009	0.006	0.010
DCS correction	0.001	0.001	0.002	0.001
$K^0_{S,L}\pi^+\pi^-$ strong phase parameters	0.005	0.011	0.131	0.067
Fitter assumptions	0.003	0.005	0.001	0.001
MC statistics	0.003	0.006	0.020	0.029
Backgrounds to fully-reconstructed events	0.001	0.005	0.001	0.001
Backgrounds to partially-reconstructed events	0.034	0.024	0.049	0.018
Background Dalitz space distribution	0.006	0.007	0.005	0.006
Assumed background $\mathcal{B}$	0.004	0.014	0.001	0.002
Total systematic	0.037	0.036	0.143	0.079
Statistical plus $K^0_L K^+ K^-$ model	0.107	0.083	0.215	0.220
$K^0_L K^+ K^-$ model alone	0.091	0.000	0.007	0.010
Total	0.113	0.090	0.258	0.234

Table 4.26: Summary of statistical and systematic uncertainties on $(c, s)_i$ for two bins.

Summaries of the systematic uncertainties on $(c, s)'_i$ for two, three and four bins are presented in Tables 4.29–4.31.

Covariance matrices for the statistical and systematic uncertainties are presented in Tables A.6–A.11.

4.5.15 Summary of systematic uncertainties

The statistical uncertainties dominate the measurements. The most significant sources of systematic uncertainty are the momentum resolution, the background estimation for partially-

Uncertainty	c_1	c_2	c_3	s_1	s_2	s_3
(Pseudo-)flavour statistics	0.005	0.007	0.055	0.015	0.013	0.039
Momentum resolution	0.002	0.004	0.012	0.018	0.025	0.032
Mode-to-mode normalisation	0.004	0.008	0.017	0.001	0.010	0.004
Multiple-candidate selection	0.004	0.003	0.015	0.004	0.008	0.002
DCS correction	0.001	0.001	0.003	0.002	0.005	0.002
$K^0_{S,L}\pi^+\pi^-$ strong phase parameters	0.006	0.011	0.036	0.132	0.063	0.135
Fitter assumptions	0.008	0.001	0.013	0.013	0.003	0.043
MC statistics	0.005	0.007	0.057	0.024	0.051	0.048
Backgrounds to fully-reconstructed events	0.001	0.005	0.006	0.000	0.010	0.003
Backgrounds to partially-reconstructed events	0.034	0.020	0.061	0.038	0.015	0.071
Background Dalitz space distribution	0.006	0.015	0.062	0.005	0.029	0.022
Assumed background $\mathcal{B}$	0.004	0.014	0.032	0.001	0.007	0.009
Total systematic	0.038	0.035	0.131	0.142	0.094	0.175
Statistical plus $K^0_L K^+K^-$ model	0.063	0.092	0.329	0.222	0.234	0.432
$K^0_L K^+K^-$ model alone	0.000	0.000	0.136	0.007	0.000	0.039
Total	0.073	0.098	0.354	0.264	0.252	0.466

Table 4.27: Summary of statistical and systematic uncertainties on $(c, s)_i$ for three bins.

Uncertainty	c_1	c_2	c_3	c_4	s_1	s_2	s_3	s_4
(Pseudo-)flavour statistics	0.006	0.032	0.010	0.112	0.019	0.046	0.018	0.100
Momentum resolution	0.003	0.045	0.015	0.023	0.044	0.220	0.088	0.147
Mode-to-mode normalisation	0.001	0.008	0.004	0.009	0.000	0.009	0.003	0.009
Multiple-candidate selection	0.002	0.012	0.005	0.030	0.004	0.018	0.003	0.012
DCS correction	0.001	0.001	0.001	0.003	0.002	0.002	0.001	0.003
$K^0_{S,L}\pi^+\pi^-$ strong phase parameters	0.005	0.015	0.014	0.035	0.157	0.177	0.138	0.195
Fitter assumptions	0.006	0.009	0.008	0.028	0.008	0.009	0.005	0.007
MC statistics	0.007	0.058	0.021	0.060	0.063	0.267	0.112	0.141
Backgrounds to fully-reconstructed events	0.001	0.004	0.005	0.006	0.001	0.001	0.003	0.008
Backgrounds to partially-reconstructed events	0.030	0.027	0.026	0.045	0.034	0.075	0.016	0.114
Background Dalitz space distribution	0.006	0.011	0.010	0.047	0.004	0.048	0.015	0.038
Assumed background $\mathcal{B}$	0.004	0.019	0.011	0.021	0.002	0.024	0.005	0.017
Total systematic	0.034	0.091	0.045	0.157	0.180	0.403	0.201	0.323
Statistical plus $K^0_L K^+K^-$ model	0.059	0.223	0.095	0.329	0.248	0.473	0.267	0.659
$K^0_L K^+K^-$ model alone	0.016	0.106	0.041	0.102	0.000	0.009	0.000	0.033
Total	0.068	0.241	0.105	0.364	0.306	0.621	0.334	0.734

Table 4.28: Summary of statistical and systematic uncertainties on $(c, s)_i$ for four bins.

reconstructed final states, uncertainty on the flavour-tagged $K^0_{S,L}K^+K^-$ yields, the $K^0_S\pi^+\pi^-$ strong phase coefficients and the assumptions made in the fit.

4.6 Final results including systematics

Tables 4.32 and 4.33 show the final results with the statistical and systematic uncertainties. These results are shown on the (c_i,s_i) plane, together with the model-predicted quantities, in Figures 4.17 and 4.18.

The combination of bins 1 and 2 (3 and 4) on the four-binned Dalitz plane covers approximately the same range of strong phase difference as bin 1 (2) on the two-binned Dalitz

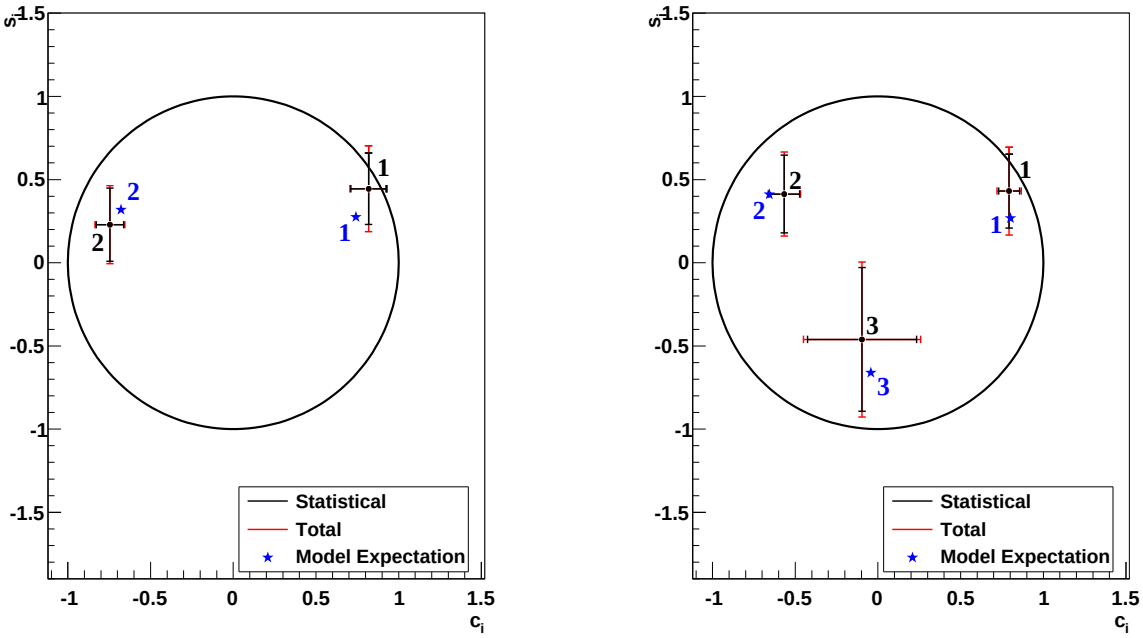

Figure 4.17: The values of $(c, s)_i$ obtained for division of the Dalitz plane into two bins (left) and three bins (right). The black points are the central values, the black error bars indicate the magnitude of the statistical uncertainty, and the red error bars indicate the magnitude of the statistical and systematic uncertainties added in quadrature. The blue stars indicate the values predicted by the model that was used to determine the Dalitz plane binning.

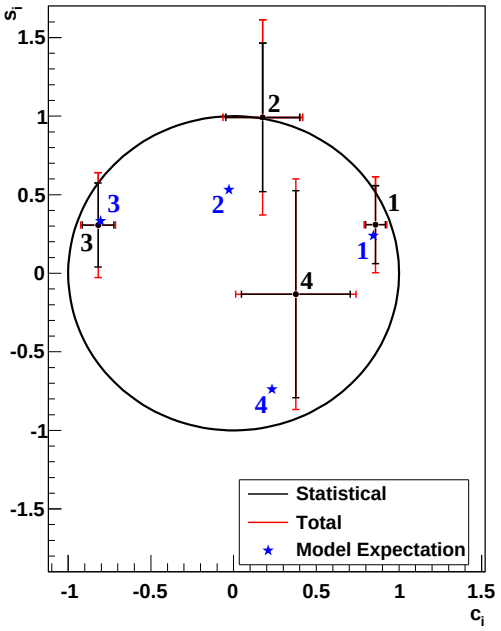

Figure 4.18: The values of $(c, s)_i$ obtained for division of the Dalitz plane into four bins. The black points are the central values, the black error bars indicate the magnitude of the statistical uncertainty, and the red error bars indicate the magnitude of the statistical and systematic uncertainties added in quadrature. The blue stars indicate the values predicted by the model that was used to determine the Dalitz plane binning.

Uncertainty	c'_1	c'_2	s'_1	s'_2
(Pseudo-)flavour statistics	0.004	0.008	0.013	0.012
Momentum resolution	0.002	0.003	0.017	0.021
Mode-to-mode normalisation	0.004	0.007	0.001	0.001
Multiple-candidate selection	0.004	0.004	0.001	0.001
DCS correction	0.001	0.001	0.002	0.001
$K^0_{S,L}\pi^+\pi^-$ strong phase parameters	0.005	0.010	0.131	0.067
Fitter assumptions	0.063	0.058	0.046	0.050
MC statistics	0.003	0.006	0.020	0.029
Backgrounds to fully-reconstructed events	0.001	0.005	0.001	0.001
Backgrounds to partially-reconstructed events	0.036	0.026	0.050	0.018
Background Dalitz space distribution	0.006	0.007	0.004	0.006
Assumed background $\mathcal{B}$	0.004	0.014	0.001	0.002
Total systematic	0.073	0.068	0.150	0.093
Statistical plus $K^0_L K^+K^-$ model	0.108	0.085	0.216	0.220
Total	0.131	0.109	0.263	0.239

Table 4.29: Summary of statistical and systematic uncertainties on $(c, s)'_i$ for two bins.

Uncertainty	c'_1	c'_2	c'_3	s'_1	s'_2	s'_3
(Pseudo-)flavour statistics	0.005	0.007	0.053	0.015	0.013	0.039
Momentum resolution	0.002	0.004	0.012	0.018	0.025	0.032
Mode-to-mode normalisation	0.004	0.008	0.024	0.001	0.010	0.005
Multiple-candidate selection	0.003	0.003	0.009	0.004	0.009	0.003
DCS correction	0.001	0.001	0.003	0.002	0.005	0.002
$K^0_{S,L}\pi^+\pi^-$ strong phase parameters	0.006	0.011	0.056	0.132	0.063	0.139
Fitter assumptions	0.052	0.062	0.125	0.017	0.029	0.044
MC statistics	0.005	0.007	0.051	0.024	0.051	0.048
Backgrounds to fully-reconstructed events	0.001	0.005	0.004	0.000	0.010	0.003
Backgrounds to partially-reconstructed events	0.035	0.021	0.096	0.039	0.015	0.077
Background Dalitz space distribution	0.006	0.015	0.058	0.005	0.029	0.022
Assumed background $\mathcal{B}$	0.004	0.014	0.035	0.001	0.007	0.010
Total systematic	0.064	0.071	0.197	0.143	0.098	0.181
Statistical plus $K^0_L K^+K^-$ model	0.063	0.092	0.349	0.222	0.234	0.456
Total	0.090	0.116	0.401	0.264	0.254	0.490

Table 4.30: Summary of statistical and systematic uncertainties on $(c, s)'_i$ for three bins.

plane. Consequently the weighted mean of c_1 and c_2 (c_3 and c_4) in the four-binned case should be approximately equal to c_1 (c_2) in the two-binned case. The same is true for all equivalent pairs of s_i. Table 4.34 shows the weighted means of $(c, s)_i$ in each adjacent pair of bins on the four-binned Dalitz plane and the equivalent $(c, s)_i$ on the two-binned Dalitz plane. The quantities all agree well within their uncertainties.

We evaluate the compatibility between the fit values of $(c, s)_i$ and the predicted values by evaluating the fit χ^2, defined as:

$$\chi^2 = (\mathbf{P} - \mathbf{P}^{\text{model}})^T \mathbf{V}^{-1} (\mathbf{P} - \mathbf{P}^{\text{model}}) \,, \tag{4.28}$$

Uncertainty	c'_1	c'_2	c'_3	c'_4	s'_1	s'_2	s'_3	s'_4
(Pseudo-)flavour statistics	0.006	0.032	0.009	0.096	0.019	0.046	0.018	0.102
Momentum resolution	0.003	0.045	0.015	0.023	0.045	0.220	0.088	0.147
Mode-to-mode normalisation	0.003	0.012	0.005	0.022	0.000	0.009	0.003	0.010
Multiple-candidate selection	0.002	0.012	0.006	0.033	0.004	0.018	0.003	0.012
DCS correction	0.001	0.001	0.001	0.003	0.002	0.002	0.001	0.003
$K^0_{S,L}\pi^+\pi^-$ strong phase parameters	0.005	0.014	0.013	0.061	0.157	0.177	0.138	0.200
Fitter assumptions	0.043	0.132	0.040	0.097	0.016	0.051	0.035	0.085
MC statistics	0.007	0.059	0.022	0.067	0.063	0.267	0.112	0.143
Backgrounds to fully-reconstructed events	0.001	0.004	0.005	0.005	0.001	0.001	0.003	0.008
Backgrounds to partially-reconstructed events	0.031	0.028	0.026	0.091	0.035	0.075	0.017	0.140
Background Dalitz space distribution	0.006	0.011	0.011	0.048	0.003	0.048	0.015	0.043
Assumed background $\mathcal{B}$	0.004	0.019	0.011	0.028	0.002	0.024	0.005	0.018
Total systematic	0.055	0.160	0.060	0.201	0.180	0.406	0.204	0.350
Statistical plus $K^0_L K^+K^-$ model	0.059	0.225	0.096	0.408	0.248	0.473	0.268	0.696
Total	0.080	0.276	0.113	0.455	0.307	0.623	0.337	0.779

Table 4.31: Summary of statistical and systematic uncertainties on $(c,s)'_i$ for four bins.

$\mathcal{N}$	Bin i	c_i	s_i
2	1	$0.818 \pm 0.107 \pm 0.037$	$0.445 \pm 0.215 \pm 0.143$
	2	$-0.746 \pm 0.083 \pm 0.036$	$0.229 \pm 0.220 \pm 0.079$
3	1	$0.793 \pm 0.063 \pm 0.038$	$0.431 \pm 0.222 \pm 0.142$
	2	$-0.566 \pm 0.092 \pm 0.035$	$0.413 \pm 0.234 \pm 0.094$
	3	$-0.096 \pm 0.329 \pm 0.131$	$-0.461 \pm 0.432 \pm 0.175$
4	1	$0.858 \pm 0.059 \pm 0.034$	$0.309 \pm 0.248 \pm 0.180$
	2	$0.176 \pm 0.223 \pm 0.091$	$0.992 \pm 0.473 \pm 0.403$
	3	$-0.819 \pm 0.095 \pm 0.045$	$0.307 \pm 0.267 \pm 0.201$
	4	$0.376 \pm 0.329 \pm 0.157$	$-0.133 \pm 0.659 \pm 0.323$

Table 4.32: The measured values of c_i and s_i for each Dalitz plane binning. The first uncertainty is statistical, including the uncertainty associated with the $\Delta(c,s)_i$ constraints, and the second uncertainty is systematic.

where $\mathbf{P}$ is a vector of the measured values of $(c,s)_i$, $\mathbf{P}^{\text{model}}$ is a vector of the predicted values of $(c,s)_i$, and $\mathbf{V}$ is the sum of the statistical and systematic covariance matrices associated with the measurements. The results along with the associated probabilities are shown in Table 4.35. In all cases, the results obtained are in good agreement with those predicted by the model.

4.7 $\mathcal{CP}$-odd fraction in the ϕ bin

As described in Section 1.6.5.7, it is interesting to determine the $\mathcal{CP}$ content of events that lie in the region of the $D\to K^0_S\phi$ resonance on the $D\to K^0_S K^+K^-$ Dalitz plane. To do this we define a bin i that is centred on m^2_ϕ and satisfies the following requirement:

$$\Delta m^2_{K^+K^-} \equiv |m^2_{K^+K^-} - m^2_\phi| < \delta_M, \tag{4.29}$$

$\mathcal{N}$	Bin i	c_i'	s_i'
2	1	$0.839 \pm 0.108 \pm 0.073$	$0.445 \pm 0.216 \pm 0.150$
	2	$-0.775 \pm 0.085 \pm 0.068$	$0.298 \pm 0.220 \pm 0.093$
3	1	$0.814 \pm 0.063 \pm 0.064$	$0.422 \pm 0.222 \pm 0.143$
	2	$-0.529 \pm 0.092 \pm 0.071$	$0.426 \pm 0.234 \pm 0.098$
	3	$-0.583 \pm 0.349 \pm 0.197$	$0.241 \pm 0.456 \pm 0.181$
4	1	$0.874 \pm 0.059 \pm 0.055$	$0.303 \pm 0.248 \pm 0.180$
	2	$0.270 \pm 0.225 \pm 0.160$	$0.965 \pm 0.473 \pm 0.406$
	3	$-0.810 \pm 0.096 \pm 0.060$	$0.346 \pm 0.268 \pm 0.204$
	4	$-0.317 \pm 0.408 \pm 0.201$	$0.770 \pm 0.696 \pm 0.350$

Table 4.33: The measured values of c_i' and s_i' for each Dalitz plane binning. The first uncertainty is statistical, including the uncertainty associated with the $\Delta(c,s)_i$ constraints, and the second uncertainty is systematic.

Quantities for $\mathcal{N}=4$	Weighted mean	Quantity for $\mathcal{N}=2$
c_1, c_2	0.808 ± 0.065	$c_1 = 0.818 \pm 0.113$
c_3, c_4	-0.727 ± 0.101	$c_2 = -0.746 \pm 0.090$
s_1, s_2	0.442 ± 0.274	$s_1 = 0.445 \pm 0.258$
s_3, s_4	0.232 ± 0.304	$s_2 = 0.229 \pm 0.234$

Table 4.34: Weighted means of c_i and s_i in pairs of adjacent bins on the four-binned Dalitz plane. These quantities are compared to the equivalent values on the two-binned Dalitz plane.

$\mathcal{N}$	χ^2/DOF	Probability
2	1.7/4	79%
3	1.4/6	96%
4	2.2/8	98%

Table 4.35: Values of χ^2/DOF and the corresponding probability obtained by comparing the measured values of c_i and s_i with those predicted by the model.

where δ_M is half of the bin width. The requirement defines a diagonal band across the Dalitz plane; the bin distribution for $\delta_M = 0.018$ GeV$^2/c^4$ is shown in Figure 4.19. Unlike in the analysis to determine c_i and s_i, the bin extends across the entirety of the Dalitz plane rather than being divided into $+i$ and $-i$.

The fraction of $\mathcal{CP}$ odd events is then determined using M_i^+ and M_i^-, the yields of $\mathcal{CP}+$ and $\mathcal{CP}-$ events bin i:

$$\mathcal{F}_- = \frac{M_i^-}{M_i^- + M_i^+}. \tag{4.30}$$

We determine the value of $M_i^\pm$ for each $\mathcal{CP}$ eigenstate by correcting the yield in data for bin-to-bin migration, subtracting the background, and dividing by the selection efficiency ε_i. We do not make an individual estimate of the level of background for each $\mathcal{CP}$ eigenstate, instead making one estimate for $\mathcal{CP}\pm$ eigenstates as a whole. We therefore scale this estimate

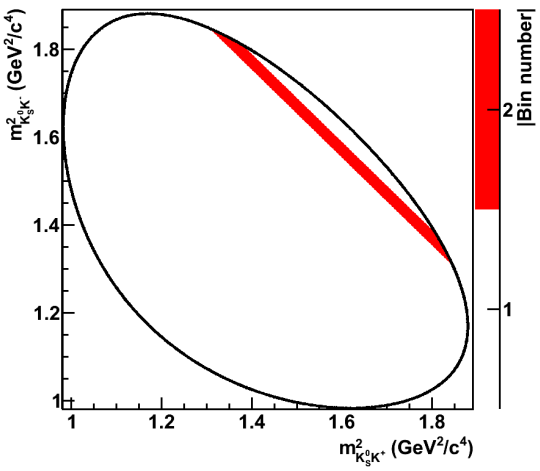

Figure 4.19: Binning of the $K^0_S K^+ K^-$ Dalitz plane with a bin centred on m^2_ϕ such that the half-width of the diagonal bin is 0.018 GeV$^2/c^4$.

by the relevant branching fraction of the $\mathcal{CP}$ eigenstate in question. There is a systematic uncertainty associated with this procedure.

Four values of δ_M are considered in this study. Values of $\mathcal{F}_-$ for in each of these regions are presented in Table 4.36. By considering different bin widths, we enable future experiments that use these results to select the version most appropriate for the detector resolution.

δ_M (GeV$^2/c^4$)	$\mathcal{F}_-$	$\mathcal{F}'_+$	$\Delta\mathcal{F}$	$\widehat{\mathcal{F}}_-$
0.006	$1.09 \pm 0.09 \pm 0.09$	$0.98 \pm 0.09 \pm 0.02$	-0.02 ± 0.04	$1.03 \pm 0.07 \pm 0.04$
0.010	$1.13 \pm 0.08 \pm 0.08$	$0.98 \pm 0.07 \pm 0.02$	-0.02 ± 0.04	$1.05 \pm 0.06 \pm 0.04$
0.014	$0.73 \pm 0.27 \pm 0.04$	$0.90 \pm 0.09 \pm 0.02$	-0.02 ± 0.05	$0.90 \pm 0.10 \pm 0.02$
0.018	$0.75 \pm 0.22 \pm 0.04$	$0.90 \pm 0.08 \pm 0.02$	-0.03 ± 0.06	$0.90 \pm 0.09 \pm 0.02$

Table 4.36: The measured values of $\mathcal{F}_-$ ($\mathcal{F}_+$) for $D^0 \to K^0_S K^+ K^-$ ($D^0 \to K^0_L K^+ K^-$) decays for each diagonal bin half-width δ_M. The predicted value of $\Delta\mathcal{F}$ and the weighted average value of $\mathcal{F}_-$ for $D^0 \to K^0_S K^+ K^-$ and $D^0 \to K^0_L K^+ K^-$ are also shown. The first uncertainty is statistical and the second is systematic.

We evaluate both the statistical and systematic uncertainties associated with the measurement of $\mathcal{F}_-$. To do this we use the same technique that is used to determine the systematic uncertainties associated with c_i and s_i (see Section 4.5). The quantities related to the source of uncertainty in question are smeared many times, and each time $\mathcal{F}_-$ is recomputed and recorded. The width of the resulting distribution of $\mathcal{F}_-$ is taken to be the uncertainty due to this contribution. The $\mathcal{F}_-$ distribution is often asymmetric, so we determine both an upper and lower width and then conservatively take the larger of the two widths to be the uncertainty.

The statistical uncertainty is evaluated by varying the raw yields of each $\mathcal{CP}$ eigenstate in each bin, assuming they are drawn from a Poisson distribution with the mean equal to the initial value.

Some of the systematic uncertainties considered in Section 4.5 are not relevant to this measurement. We consider the following sources of systematic uncertainty: the parameterisation of the background to $\mathcal{CP}$ eigenstates (including the assumptions made about the background distribution across the Dalitz plane and the uncertainties on the relevant branching fractions), the differences in reconstruction between data and Monte Carlo, the migration of events on the Dalitz plane, the Monte Carlo statistical uncertainty, and the branching fractions used to normalise yields. Table 4.37 list the magnitude of each uncertainty for all four binnings that have been considered.

		$\mathcal{F}_-$				$\mathcal{F}'_+$			
Source of uncertainty	$\delta_M(\,\mathrm{GeV}^2/c^4) =$	0.006	0.010	0.014	0.018	0.006	0.010	0.014	0.018
Momentum resolution		0.03	0.02	0.01	0.01	0.00	0.00	0.00	0.00
Mode-to-mode normalisation		0.01	0.01	0.02	0.02	0.00	0.00	0.01	0.01
MC statistics		0.06	0.04	0.02	0.02	0.01	0.00	0.00	0.00
Backgrounds to fully-reconstructed events		0.00	0.00	0.00	0.00	0.00	0.00	0.00	0.00
Backgrounds to partially-reconstructed events		0.03	0.04	0.01	0.01	0.01	0.01	0.01	0.01
Background Dalitz space distribution		0.05	0.06	0.02	0.02	0.02	0.02	0.01	0.02
Assumed background $\mathcal{B}$		0.00	0.00	0.00	0.00	0.00	0.00	0.00	0.00
Quadrature sum of systematics		0.09	0.08	0.04	0.04	0.02	0.02	0.02	0.02
Statistical uncertainty		0.09	0.08	0.27	0.22	0.09	0.07	0.09	0.08
Total uncertainty		0.13	0.12	0.27	0.22	0.09	0.08	0.10	0.09

Table 4.37: Sources of systematic and statistical uncertainty on $\mathcal{F}_-$ and $\mathcal{F}'_+$ for each bin width δ_M.

In order to improve the precision on this measurement we also analyse $\mathcal{CP}$-tagged $D^0 \to K^0_L K^+ K^-$ events. We calculate $\mathcal{F}'_+$, the fraction of $\mathcal{CP}+$ events under the $K^0_L\phi$ resonance. The central value and statistical and systematic uncertainties are evaluated using the same method as for $\mathcal{F}_-$; the systematic uncertainties associated with $\mathcal{F}_-$ and $\mathcal{F}'_+$ are largely uncorrelated. The values of $\mathcal{F}'_+$ for each value of δ_M are presented in Table 4.36 and the systematic uncertainties are presented in Table 4.37.

We expect differences between $\mathcal{F}_-$ and $\mathcal{F}'_+$ due to the slightly different decay amplitudes of the decays of $D^0 \to K^0_S K^+ K^-$ and $D^0 \to K^0_L K^+ K^-$; this is analogous to the differences between $(c,s)_i$ and $(c,s)'_i$. In order to account for this we determine the difference predicted by the model, denoted $\Delta\mathcal{F}$:

$$\Delta\mathcal{F} \equiv \mathcal{F}'_+ - \mathcal{F}_-. \tag{4.31}$$

This quantity has an associated uncertainty $\delta\Delta\mathcal{F}$. These two quantities are analogous to $\Delta(c,s)_i$ and $\delta\Delta(c,s)_i$ and are evaluated using a similar method. Their values are presented in Table 4.36.

For each value of δ_M we determine $\widehat{\mathcal{F}}_-$, the weighted average of $(\mathcal{F}'_+ - \Delta\mathcal{F})$ and $\mathcal{F}_-$. The uncertainty on each quantity used in the weighted average is the quadrature sum of the statistical and systematic uncertainties. These values and associated uncertainties are presented in Table 4.36.

All values of $\widehat{\mathcal{F}}_-$ are compatible with one, corresponding to an absence of any contamination from states that are not $\mathcal{CP}$-odd. In general the value of $\widehat{\mathcal{F}}_-$ increases as the mass window becomes narrower. Two of the values are greater than one because the background subtraction for individual final states sometimes results in negative quantities.

We determine a lower limit on $\widehat{\mathcal{F}}_-$ at the 90% confidence level. To do this, we define a Gaussian distribution with a central value μ equal to the weighted average and a width σ equal to the weighted uncertainty. We then determine the value of $\widehat{\mathcal{F}}_-$ that encompasses 90% of the Gaussian distribution in the physical region. Denoting this value $\mathcal{F}_{90}$ and the Gaussian distribution $\mathcal{G}(\widehat{\mathcal{F}}_-;\mu,\sigma)$, we determine $\mathcal{F}_{90}$ such that:

$$\frac{\int_{\mathcal{F}_{90}}^{1}\mathcal{G}(\widehat{\mathcal{F}}_-;\mu,\sigma)}{\int_{0}^{1}\mathcal{G}(\widehat{\mathcal{F}}_-;\mu,\sigma)} = 0.9. \tag{4.32}$$

We obtain values of $\mathcal{F}_{90}$ of 0.89, 0.91, 0.76 and 0.77 for values of δ_M of 0.006, 0.010, 0.014 and 0.018 GeV^2/c^4 respectively.

Future experimental studies will be able to use these results when evaluating a systematic uncertainty associated with the $\mathcal{CP}$ content of the $D\to K^0_S\phi$ region. Advantageously, parameterisation of this region with a decay model can be avoided.

4.8 Conclusions

We have determined the strong-phase difference between D^0 and $\overline{D}^0$ decays to $K^0_SK^+K^-$ for three different configurations of Dalitz plane binnings. The results have been presented in Tables 4.32 and 4.33. The measurements are statistically dominated and are in general good agreement with model predictions. Chapter 5 contains a study of the projected impact of these results on a measurement of γ using $B^\pm\to(K^0_SK^+K^-)_DK^\pm$ decays.

In addition, we have determined the fraction of $\mathcal{CP}$-odd events in the region of the $D\to K^0_S\phi$ resonance. In all regions considered, this fraction is at least 0.76 at 90% C.L.

Chapter 5

Impact of CLEO-c results on a measurement of γ

5.1 Introduction

Our measurements of c_i and s_i using $D \to K^0_S K^+ K^-$ decays can be used as inputs to a model-independent analysis to determine γ with $B^\pm \to (K^0_S K^+ K^-)_D K^\pm$ decays. The uncertainties on the values of c_i and s_i will induce an additional uncertainty on the final value of γ, on top of the usual statistical and systematic uncertainties. However, there is no uncertainty related to the parameterisation of the $D \to K^0_S K^+ K^-$ decay model, which is a drawback in alternative measurements.

A 'toy Monte Carlo' study to quantify the magnitude of the uncertainty on γ due to the uncertainties on c_i and s_i is described in Section 5.2. Section 5.3 contains a determination of the relative statistical sensitivity of the model-independent binned and model-dependent unbinned methods. A recent study of $B^\pm \to (K^0_S \pi^+ \pi^-)_D K^\pm$ events by Belle has used a model-independent binned approach to determine γ and is briefly discussed in Section 5.4, along with prospects for the future.

5.2 Toy Monte Carlo study

We use a toy Monte Carlo simulation of $B^\pm \to (K^0_S K^+ K^-)_D K^\pm$ events to determine how the precision of the $(c, s)_i$ measurements impacts on the uncertainty on γ in the model-independent approach. As shown in Equation 1.120, the number of $B^\pm$ events in the i^{th} bin (N_i) depends on c_i, s_i, $T_{(-)i}$, r_B, δ_B, γ, and a normalisation factor. We set the values of r_B, δ_B and γ to 0.1, 130°, and 60° respectively; these quantities are guided by current measurements [1, 2]. We use the experimentally-measured central values of c_i, s_i and $T_{(-)i}$.

The yield in each bin is calculated following Equation 1.120; the yields are normalised such that there are five million events in total, enough to ensure that the statistical uncertainty on the number of events has minimal contribution to the resulting uncertainty on γ. The bin yields are then fluctuated according to a Poisson distribution in order to reflect the expected natural variation. The yield of events in the i^{th} bin obtained using this method is denoted by N_i^I.

The values of c_i and s_i are smeared assuming that they are drawn from Gaussian distributions, taking the correlations between each pair of variables into account. The best-fit values of γ, r_B and δ_B are determined by minimising a χ^2 term:

$$\chi^2 = \sum_i \frac{(N_i^F - N_i^I)^2}{N_i^I} \tag{5.1}$$

where N_i^F is the yield in each bin calculated using the smeared values of $(c, s)_i$.

This procedure is repeated 5000 times, on each iteration using new values of c_i and s_i. The resulting distributions of γ are shown in Figure 5.1, the distributions of δ_B are shown in Figure 5.2 and the distributions of r_B are shown in Figure 5.3.

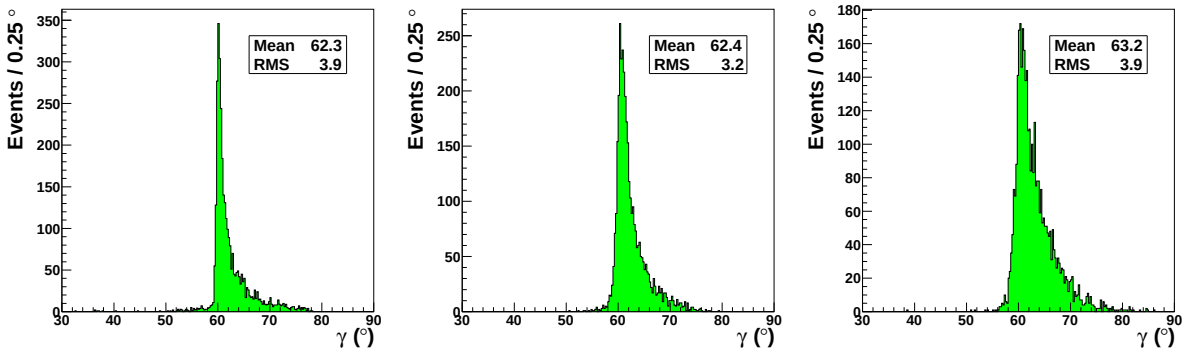

Figure 5.1: Distribution of γ in a toy MC study for two bins (left), three bins (middle), four bins (right).

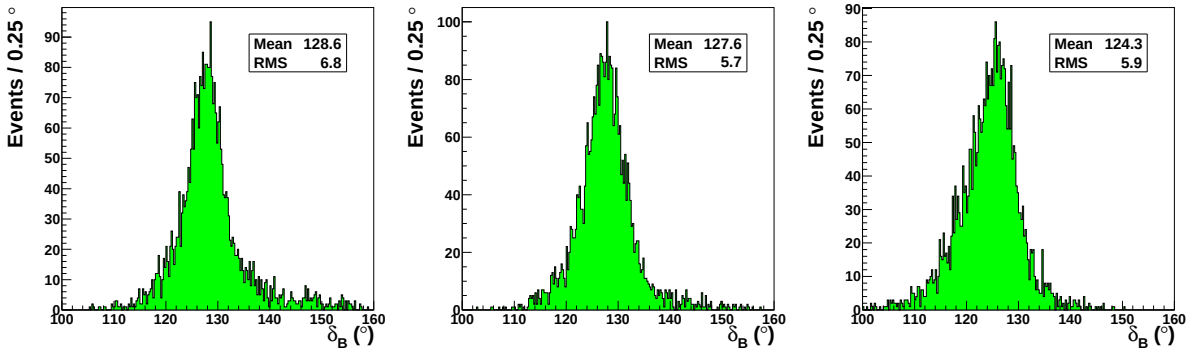

Figure 5.2: Distribution of δ_B in a toy MC study for two bins (left), three bins (middle), four bins (right).

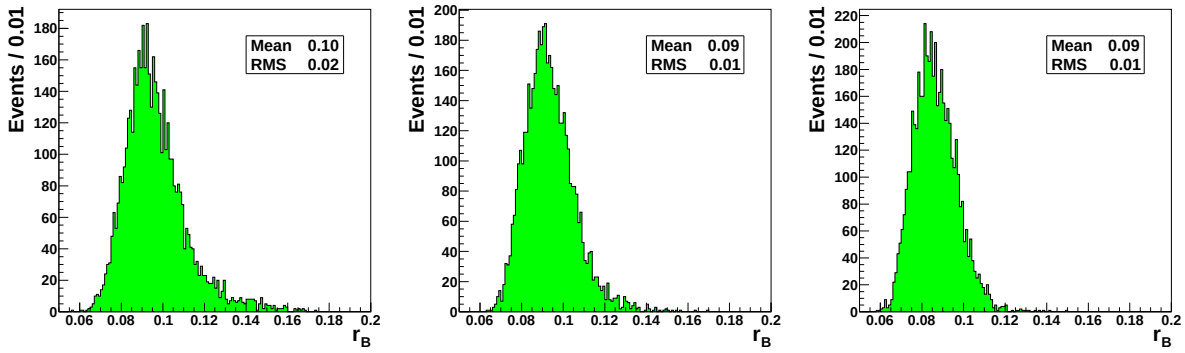

Figure 5.3: Distribution of r_B in a toy MC study for two bins (left), three bins (middle), four bins (right).

The uncertainty on γ is estimated by determining the standard deviation of the distribution of γ. The uncertainty is found to be 3.9°, 3.2°, and 3.9° for two, three and four bins respectively. The lack of improvement in the sensitivity for a larger number of bins is due to the fact that the sample of $D^0 \to K^0_S K^+ K^-$ decays in the CLEO-c data is statistically limited. Furthermore, the dominant resonances in the $D \to K^0_S K^+ K^-$ decay (i.e. $K^0_S \phi$ and $K^0_S a_0(980)^0$) are located close to the $m^2_{K^+K^-}$ kinematic limit and are encompassed by the same pair of bins each time, so adding more bins does not significantly change the yields in these bins.

Small biases of $\mathcal{O}(1°)$ are observed on the central value of γ. This is caused by events in which $(c, s)_i$ lie outside the physical region, i.e. $c_i^2 + s_i^2 > 1$. Even if the smeared values were constrained to lie in the physical region, biases would still be observed because the truncated distributions would not be Gaussian. To corroborate this assertion we observe that the biases disappear if the uncertainties on c_i and s_i are set to zero.

5.3 Comparison of binned and unbinned methods

Dividing the Dalitz plot into bins results in a loss of information and will therefore influence the statistical precision on the measurement of γ. We assume that the unbinned case, corresponding to an infinite number of infinitesimally small bins, has the maximum statistical sensitivity. In order to quantify how much statistical sensitivity is lost by binning, we firstly define the 'Cartesian' basis:

$$\mathcal{X}_\pm \equiv r_B \cos(\delta_B \pm \gamma), \qquad \mathcal{Y}_\pm \equiv r_B \sin(\delta_B \pm \gamma). \tag{5.2}$$

The sensitivity to γ can be quantified as the change in the yield of $B^\pm \to DK^\pm$ events with respect to a change in $\mathcal{X}_\pm$ or $\mathcal{Y}_\pm$. If a change in $\mathcal{X}_\pm$ or $\mathcal{Y}_\pm$ leads to negligible change in the event yield, this indicates that there is little sensitivity to γ; conversely, if the change in

yield is large this indicates high sensitivity to γ. The change in yield with respect to $\mathcal{X}_\pm$ and $\mathcal{Y}_\pm$ is expressed as a multiple of the standard deviation of the number of events[1]. We define $\mathcal{Q}$ [53] as the ratio between the sensitivity to γ in the binned case and the sensitivity in the unbinned case.

We express the $B^\pm \to DK^\pm$ decay amplitude (Equation 1.106) in terms of $\mathcal{X}_\pm$ and $\mathcal{Y}_\pm$:

$$A_B^\pm(x,y) = A_D(x,y) + (\mathcal{X}_\pm + i\mathcal{Y}_\pm)A_D(y,x) \tag{5.3}$$

which, when squared, equals:

$$\begin{aligned}
&|A_B^\pm(x,y)|^2 \\
&= a_{xy}^2 + (\mathcal{X}_\pm^2 + \mathcal{Y}_\pm^2)a_{yx}^2 + a_{xy}a_{yx}\mathfrak{Re}\{(\mathcal{X}_\pm + i\mathcal{Y}_\pm)e^{i(-\delta_{xy}+\delta_{yx})} + (\mathcal{X}_\pm - i\mathcal{Y}_\pm)e^{i(\delta_{xy}-\delta_{yx})}\} \\
&= a_{xy}^2 + (\mathcal{X}_\pm^2 + \mathcal{Y}_\pm^2)a_{yx}^2 + 2a_{xy}a_{yx}(\mathcal{X}_\pm \cos(\Delta\delta_D) + \mathcal{Y}_\pm \sin(\Delta\delta_D)).
\end{aligned} \tag{5.4}$$

The decay rate in the i^{th} bin is defined as:

$$\Gamma_i^\pm = \int_i |A_B^\pm(x,y)|^2 \,\mathrm{d}x\,\mathrm{d}y. \tag{5.5}$$

Following Ref. [53] square of the ratio between the binned and unbinned sensitivities is:

$$\mathcal{Q}^2 = \frac{\sum_i \left[\left(\frac{1}{\sqrt{\Gamma_i^\pm}} \cdot \frac{\mathrm{d}\Gamma_i^\pm}{\mathrm{d}\mathcal{X}_\pm}\right)^2 + \left(\frac{1}{\sqrt{\Gamma_i^\pm}} \cdot \frac{\mathrm{d}\Gamma_i^\pm}{\mathrm{d}\mathcal{Y}_\pm}\right)^2\right]}{\int \left[\left(\frac{1}{\sqrt{|A_B^\pm(x,y)|^2}} \cdot \frac{\mathrm{d}|A_B^\pm(x,y)|^2}{\mathrm{d}\mathcal{X}_\pm}\right)^2 + \left(\frac{1}{\sqrt{|A_B^\pm(x,y)|^2}} \cdot \frac{\mathrm{d}|A_B^\pm(x,y)|^2}{\mathrm{d}\mathcal{Y}_\pm}\right)^2\right] \mathrm{d}x\,\mathrm{d}y}. \tag{5.6}$$

It has been determined [45] that the sensitivity to γ is largely independent of the values of $\mathcal{X}_\pm$ and $\mathcal{Y}_\pm$. Most of the uncertainty on γ relates to the small value of r_B and is only weakly dependent upon the values of γ and δ_B. Both $\mathcal{X}_\pm$ and $\mathcal{Y}_\pm$ are therefore set to zero.

We now determine $\mathcal{Q}^2$ when $\mathcal{X}_\pm = \mathcal{Y}_\pm = 0$, starting from Equation 5.4. We find:

$$\left[\frac{1}{\sqrt{|A_B^\pm(x,y)|^2}} \cdot \frac{\mathrm{d}|A_B^\pm(x,y)|^2}{\mathrm{d}\mathcal{X}_\pm}\right]_{\substack{\mathcal{X}_\pm=0 \\ \mathcal{Y}_\pm=0}} = \frac{1}{a_{xy}} \cdot 2a_{xy}a_{yx}\cos(\Delta\delta_D), \tag{5.7}$$

$$\left[\frac{1}{\sqrt{|A_B^\pm(x,y)|^2}} \cdot \frac{\mathrm{d}|A_B^\pm(x,y)|^2}{\mathrm{d}\mathcal{Y}_\pm}\right]_{\substack{\mathcal{X}_\pm=0 \\ \mathcal{Y}_\pm=0}} = \frac{1}{a_{xy}} \cdot 2a_{xy}a_{yx}\sin(\Delta\delta_D). \tag{5.8}$$

[1] We assume the event yields follow Poisson statistics.

Therefore the denominator of Equation 5.6 when $\mathcal{X}_\pm = \mathcal{Y}_\pm = 0$ is equal to:

$$\begin{aligned}
&\int \left[\frac{1}{\sqrt{|A_B^\pm(x,y)|^2}} \cdot \frac{\mathrm{d}|A_B^\pm(x,y)|^2}{\mathrm{d}\mathcal{X}_\pm}\right]^2_{\substack{\mathcal{X}_\pm=0\\ \mathcal{Y}_\pm=0}} + \left[\frac{1}{\sqrt{|A_B^\pm(x,y)|^2}} \cdot \frac{\mathrm{d}|A_B^\pm(x,y)|^2}{\mathrm{d}\mathcal{Y}_\pm}\right]^2_{\substack{\mathcal{X}_\pm=0\\ \mathcal{Y}_\pm=0}} \mathrm{d}x\,\mathrm{d}y \\
&= \int 4a_{yx}^2[\cos^2(\Delta\delta_D) + \sin^2(\Delta\delta_D)]\,\mathrm{d}x\,\mathrm{d}y \\
&= 4\int a_{yx}^2\,\mathrm{d}x\,\mathrm{d}y = 4. \qquad (5.9)
\end{aligned}$$

The equivalent quantities in the binned case are:

$$\left[\frac{1}{\sqrt{\Gamma_i^\pm}} \cdot \frac{\mathrm{d}\Gamma_i^\pm}{\mathrm{d}\mathcal{X}_\pm}\right]_{\substack{\mathcal{X}_\pm=0\\ \mathcal{Y}_\pm=0}} = \frac{2\int_{\mathcal{D}_i} a_{xy}a_{yx}\cos(\Delta\delta_D)\,\mathrm{d}x\,\mathrm{d}y}{\sqrt{\int_{\mathcal{D}_i} a_{xy}^2\,\mathrm{d}x\,\mathrm{d}y}}, \qquad (5.10)$$

$$\left[\frac{1}{\sqrt{\Gamma_i^\pm}} \cdot \frac{\mathrm{d}\Gamma_i^\pm}{\mathrm{d}\mathcal{Y}_\pm}\right]_{\substack{\mathcal{X}_\pm=0\\ \mathcal{Y}_\pm=0}} = \frac{2\int_{\mathcal{D}_i} a_{xy}a_{yx}\sin(\Delta\delta_D)\,\mathrm{d}x\,\mathrm{d}y}{\sqrt{\int_{\mathcal{D}_i} a_{xy}^2\,\mathrm{d}x\,\mathrm{d}y}}. \qquad (5.11)$$

Therefore the numerator of Equation 5.6 when $\mathcal{X}_\pm = \mathcal{Y}_\pm = 0$ is equal to:

$$\begin{aligned}
&\sum_i \left[\left(\frac{1}{\sqrt{\Gamma_i^\pm}} \cdot \frac{\mathrm{d}\Gamma_i^\pm}{\mathrm{d}\mathcal{X}_\pm}\right)^2 + \left(\frac{1}{\sqrt{\Gamma_i^\pm}} \cdot \frac{\mathrm{d}\Gamma_i^\pm}{\mathrm{d}\mathcal{Y}_\pm}\right)^2\right]_{\substack{\mathcal{X}_\pm=0\\ \mathcal{Y}_\pm=0}} \\
&= \sum_i \left[\left(\frac{2\int_{\mathcal{D}_i} a_{xy}a_{yx}\cos(\Delta\delta_D)\,\mathrm{d}x\,\mathrm{d}y}{\sqrt{\int_{\mathcal{D}_i} a_{xy}^2\,\mathrm{d}x\,\mathrm{d}y}}\right)^2 + \left(\frac{2\int_{\mathcal{D}_i} a_{xy}a_{yx}\sin(\Delta\delta_D)\,\mathrm{d}x\,\mathrm{d}y}{\sqrt{\int_{\mathcal{D}_i} a_{xy}^2\,\mathrm{d}x\,\mathrm{d}y}}\right)^2\right] \\
&= 4\sum_i \left[\frac{\left(\int_{\mathcal{D}_i} a_{xy}a_{yx}\cos(\Delta\delta_D)\,\mathrm{d}x\,\mathrm{d}y\right)^2 + \left(\int_{\mathcal{D}_i} a_{xy}a_{yx}\sin(\Delta\delta_D)\,\mathrm{d}x\,\mathrm{d}y\right)^2}{\int_{\mathcal{D}_i} a_{xy}^2\,\mathrm{d}x\,\mathrm{d}y}\right] \\
&= 4\sum_i \left[(c_i^2 + s_i^2)\int_{\mathcal{D}_i} a_{yx}^2\,\mathrm{d}x\,\mathrm{d}y\right]. \qquad (5.12)
\end{aligned}$$

In the last step we use the relations in Equations 1.112 and 1.113.

Therefore the expression for $\mathcal{Q}^2$ when $\mathcal{X}_\pm = \mathcal{Y}_\pm = 0$ is:

$$\mathcal{Q}^2|_{\mathcal{X}_\pm=\mathcal{Y}_\pm=0} = \frac{a_B^\pm \sum_i \left[(c_i^2 + s_i^2)\int_{\mathcal{D}_i} a_{xy}^2\,\mathrm{d}x\,\mathrm{d}y\right]}{a_B^\pm} = \frac{\sum_i (c_i^2 + s_i^2)N_i^\pm}{\sum_i N_i^\pm} \qquad (5.13)$$

where $N_i^\pm$ is the number of $B^\pm \to DK^\pm$ events in the i^{th} bin when r_B is equal to zero. This expression is much simpler than Equation 5.6 and is henceforth used to determine $\mathcal{Q}$. Large values of $\mathcal{Q}$ are obtained when the Dalitz plane is binned in regions of similar $D^0\overline{D}^0$ strong-phase difference; however, such $\mathcal{Q}$ values are not necessarily the maximum that could possibly be achieved.

In order to determine the uncertainty on $\mathcal{Q}$, we re-employ the toy experiments that were used to determine the sensitivity to γ. The values of $\mathcal{Q}$ obtained from each toy are recorded in a histogram. The resulting distributions of $\mathcal{Q}$ for two, three and four bins is shown in Figure 5.4.

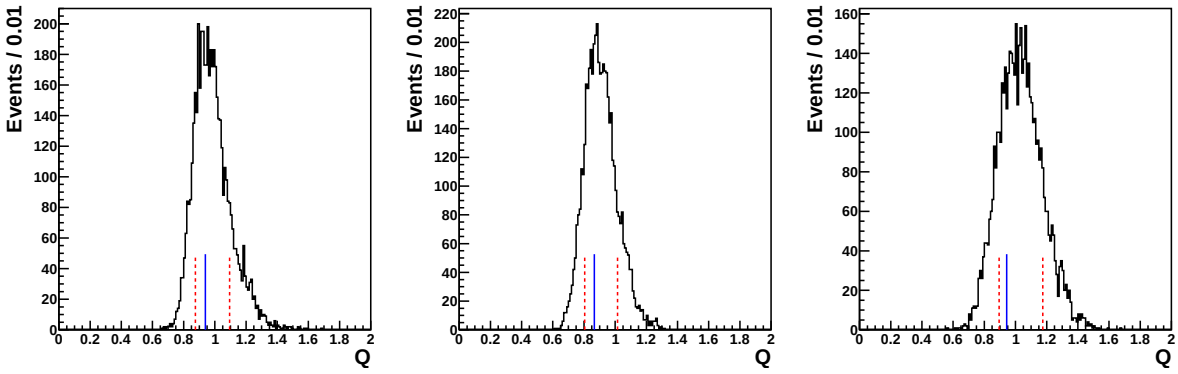

Figure 5.4: Values of $\mathcal{Q}$ obtained in a toy Monte Carlo study for two bins (left), three bins (middle), four bins (right). In each plot the blue line marks the value obtained from the measured values of c_i and s_i. The upper and lower '1σ' bounds are marked as red dashed lines.

In order to quantify the uncertainty on $\mathcal{Q}$, we determine $\mathcal{Q}_L$, and $\mathcal{Q}_H$ such that:

$$\int_0^{\mathcal{Q}_L} \mathcal{Q}\,\mathrm{d}\mathcal{Q} = 0.159, \qquad \int_0^{\mathcal{Q}_H} \mathcal{Q}\,\mathrm{d}\mathcal{Q} = 0.841, \tag{5.14}$$

aiming for '1σ' coverage. The upper and lower uncertainties that we quote are equal to $\mathcal{Q}_H - \mathcal{Q}_C$ and $\mathcal{Q}_C - \mathcal{Q}_L$ respectively, where $\mathcal{Q}_C$ is the value of $\mathcal{Q}$ obtained using the measured values of c_i and s_i.

Table 5.1 lists the values of $\mathcal{Q}$ obtained for each binning. For comparison, the values of $\mathcal{Q}$ calculated using the $D \to K^0_S K^+ K^-$ model-predicted values of c_i, s_i and T_i are also given.

$\mathcal{N}$	$\mathcal{Q}$ (measured)	$\mathcal{Q}$ (predicted)
2	$0.94^{+0.16}_{-0.06}$	0.77
3	$0.87^{+0.14}_{-0.06}$	0.80
4	$0.94^{+0.21}_{-0.06}$	0.82

Table 5.1: Values of $\mathcal{Q}$ obtained using the measured values of c_i and s_i, and also the predicted values of $\mathcal{Q}$, for two, three and four bins.

For all binnings, the value of $\mathcal{Q}$ is close to one. We therefore conclude that the binned method to determine γ will not suffer significant statistical degradation compared to the unbinned approach. The measured values of $\mathcal{Q}$ are in reasonable agreement with the predicted values, with the exception of two bins for which there is a difference of approximately three standard deviations.

5.4 Experimental results from Belle and future prospects

A recent study of $B^\pm \to (K^0_S\pi^+\pi^-)_D K^\pm$ decays by Belle [32] utilised the model-independent approach to determine γ. The values of c_i and s_i were taken from Ref. [7]. A total of 711 fb^{-1} of data, corresponding to 772M $B\overline{B}$ pairs, were analysed. The following results were obtained:

$$\gamma = (77.3^{+15.1}_{-14.9} \pm 4.2 \pm 4.3)^\circ, \tag{5.15}$$

$$r_B = 0.145 \pm 0.030 \pm 0.011 \pm 0.011, \tag{5.16}$$

$$\delta_B = (129.9 \pm 15.0 \pm 3.9 \pm 4.7)^\circ. \tag{5.17}$$

The first uncertainty is statistical, the second systematic, and the third is the uncertainty due to the CLEO-c statistics. The uncertainty on γ is dominated by the limited statistics of the $B^\pm \to DK^\pm$ dataset. The systematic uncertainty and the uncertainty from the CLEO-c statistics are approximately equal.

We compare this result with the result obtained by Belle using a model-*dependent* analysis [31]:

$$\gamma = (78.4^{+10.8}_{-11.6} \pm 3.6 \pm 8.9)^\circ \tag{5.18}$$

where the first uncertainty is statistical, the second is systematic and the third is related to the parameterisation of the $D \to K^0_S\pi^+\pi^-$ decay model. The statistical uncertainty is smaller in the model-dependent analysis because $B^\pm \to D^* K^\pm$ decays were studied in addition to $B^\pm \to DK^\pm$, whereas only $B^\pm \to DK^\pm$ decays were studied in the model-independent analysis. Furthermore, a degradation in the statistical precision is expected in the binned method relative to the unbinned method. We can neglect these considerations when comparing the uncertainties related to the model and the use of CLEO-c data because both uncertainties are largely independent of the size of the B-decay dataset. The uncertainty related to CLEO-c statistics is significantly smaller than the model-related uncertainty which is a strong vindication of the model-independent method.

Measurements of $(c, s)_i$ by BES-III [77] for both $D \to K^0_S K^+ K^-$ and $D \to K^0_S\pi^+\pi^-$ are expected to reduce the uncertainty resulting from the $D^0 \to K^0_S h^+ h^-$ statistics to sub-degree precision. We anticipate that future B-physics experiments will study $B^\pm \to (K^0_S h^+ h^-)_D K^\pm$ decays with significantly larger datasets than those currently available. The statistical and systematic uncertainties on γ should then be reduced to $\mathcal{O}(1^\circ)$.

Chapter 6

The LHCb detector

6.1 Introduction

The Large Hadron Collider (LHC) is a particle accelerator located at the European Organisation for Nuclear Research (CERN) in Switzerland. It is the highest-energy collider in the world, with a maximum centre-of-mass energy equal to 14 TeV. The LHC is designed to store, accelerate and collide two beams of protons or lead ions[1]. The goals of the LHC include searching for new physics at the TeV scale, determining whether the standard model Higgs boson exists, high-precision flavour physics and studying the properties of the quark-gluon plasma.

LHCb[2] is one of four large experiments located on the LHC ring. LHCb is a spectrometer built primarily to study decays of charm and beauty hadrons and search for new physics in such decays.

LHCb has already made significant progress in the flavour physics arena; for example, stringent bounds have been placed on the branching fraction of the decay $B_s \to \mu\mu$ [78], and previously unobserved b-hadron decays (such as $B_s \to J/\psi f_0(980)^0$ [79]) have been detected. Studies have also been performed of soft QCD, charm and electroweak physics.

In this chapter we describe the LHC and the instrumentation and operation of LHCb. The main sources of reference are Refs. [80,81] as well as various subdetector technical design reports.

6.2 LHC

The LHC is located in an approximately circular tunnel of length 26.7 km. The tunnel, originally built to house the LEP accelerator, is about 100 m underground and crosses the

[1] In this thesis we will concentrate solely on proton-proton collisions.
[2] The b stands for beauty.

border between Switzerland and France. The LHC is divided into eight segments, each of which consists of a long straight section, a bending arc and an interaction point. The interaction points are numbered 1–8 moving clockwise around the ring. The four large particle detectors at the LHC are ATLAS (point 1), ALICE (point 2), CMS (point 5) and LHCb (point 8).

Protons circulate around the LHC in two beams travelling in opposite directions. Because all of the colliding particles have the same charge, it is necessary to contain them in two rings and control their trajectories with magnets of opposite polarity. The beams of protons are directed so that particle collisions occur only at the interaction points of the four experiments. A total of 1232 dipole magnets are used to steer and accelerate beams in the LHC; a further 392 quadrupole magnets are used to focus the beams. Each magnet is constructed from niobium-titanium and is maintained at a temperature below 2 K using superfluid helium. The strength of the magnets can be altered as necessary; the maximum magnetic flux density experienced by the beams is 8.33 T.

Protons are generated in the linear accelerator (LINAC 2) at an energy of 50 MeV and transferred to the proton synchrotron booster (PSB) in which they are accelerated to 1.4 GeV. The protons are then transferred to the proton synchrotron (PS), accelerated to 25 GeV, and passed to the super proton synchrotron (SPS) in which they are accelerated to 450 GeV. After this has occurred the protons are transferred to the LHC rings via two transfer lines and accelerated to the full collision energy. A schematic of the accelerator chain and the two beams in the LHC is shown in Figure 6.1. The LHC is filled with protons a few times per day; each fill is assigned a unique number.

The design instantaneous luminosity of the LHC is 10^{34} cm^{-2} s^{-1}. The beam can store a maximum of 1.1×10^{11} protons. The protons are grouped in bunches, of which there can be at most 2808 per beam; the maximum number that collide at LHCb is 2622. The LHC is designed such that bunches can collide every 25 ns, although it is possible to run with longer gaps between collisions, as has been done so far. The beams of protons have a revolution frequency of 11.245 kHz.

The LHC has been operational since late 2009[3]. Due to safety considerations the centre-of-mass energy has been set to 450 GeV in 2009 and 7 TeV in 2010–2011, instead of the full 14 TeV. It is envisaged to run at 7 TeV until the end of 2012, at which point there will be a long shutdown to prepare the machine for running at full energy. Operation will then resume in 2014.

[3]The LHC ran for ten days in 2008 but a serious malfunction led to a delay of one year while various components were repaired.

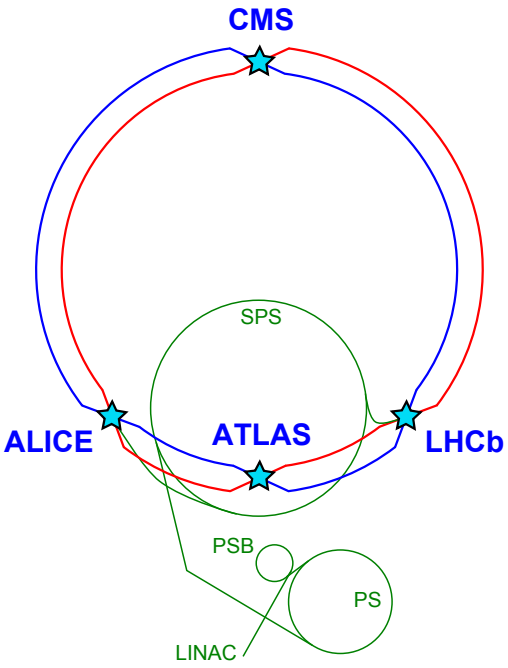

Figure 6.1: A schematic of the LHC and the accelerators that deliver protons to it (not to scale). The green paths show the progression of protons through the LINAC, the PSB, the PS, the SPS and the transfer lines to the LHC. The red and blue lines show exaggerated paths of protons around the LHC ring; protons in the red path travel in the opposite direction to those in the blue path. The blue stars mark the four interaction regions at which detectors are located.

6.3 LHCb

6.3.1 Design considerations

A large quantity of beauty and charm hadrons are produced in every collision at the LHC. Due to the high centre-of-mass energy all species of b-hadrons can be created. The production cross section of $b\bar{b}$ events at 7 TeV has been measured by LHCb to be $(284 \pm 20 \pm 49)$ µb at 7 TeV [82]; the cross section at 14 TeV is estimated to be about twice this value. The cross section of charmed hadrons is larger still; LHCb has measured the open charm cross section to be (6.10 ± 0.93) mb at 7 TeV [83]. LHCb has been specifically designed to exploit the abundance of heavy flavour decays at the LHC, both in terms of the detector geometry and the design of each subdetector.

Pairs of $b\bar{b}$ quarks are produced from p-p collisions by several processes, the most significant in this case being gluon-gluon fusion[4]. The high centre-of-mass energy usually leads to a large momentum asymmetry between the two partons from which the gluons are produced. In the lab frame this results in a large boost of the $b\bar{b}$ pair in the direction of the high-momentum gluon, so the hadrons are produced in a narrow cone at high rapidity. A Pythia simulation of the angular distribution of such events is shown in Figure 6.2. In order

[4]Other processes include flavour excitation and gluon splitting.

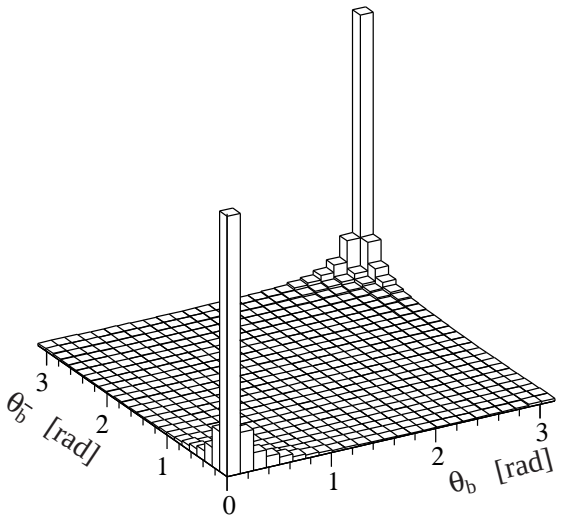

Figure 6.2: A Pythia simulation of the angular distribution of $b\bar{b}$ pairs produced from gluon-gluon fusion at the LHC. There is a strong correlation between the direction of the two b-hadrons, and they are nearly always produced at high rapidity.

to exploit this feature LHCb is instrumented in the forward region. The angular acceptance of LHCb lies from ± 10 mrad to ± 300 (250) mrad in the horizontal (vertical) plane. This corresponds to a pseudorapidity coverage of $1.6 < \eta < 4.9$.

Several characteristics of b-hadron decays have guided the design of LHCb. The average momentum of a b-hadron produced by the LHC is 80 GeV/c, so b-hadrons usually travel a significant distance ($\mathcal{O}(10$ mm$)$) before decaying. A decay vertex that is displaced from the interaction point is therefore a distinctive signature of B-decays. Furthermore, if the b-hadron decays to a c-hadron, the latter will also travel a non-negligible distance before decaying and leave another displaced vertex that can be identified.

Excellent proper time resolution is required in order to resolve B-meson oscillations. It is important to accurately measure particles' 4-momenta and hence invariant mass, which is a very useful variable to discriminate between signal and background. Furthermore, LHCb must be able to determine the identity of final-state particles; there are often background states that are topologically equivalent to the signal, with similar invariant mass, that can only be distinguished using particle ID (PID) information. Lastly, there must be an efficient, highly discriminatory trigger capable of adapting to different running conditions.

The layout of the detector and the various subdetectors is shown in Figure 6.3. The subdetectors of LHCb comprise the VErtex LOcator (VELO), the tracking stations (TT and T1–T3), the Ring Imaging CHerenkov detectors (RICH), the Electromagnetic and Hadronic CALorimeters (ECAL and HCAL), the PreShower detector (PS), the Scintillating Pad Detector (SPD), and the muon chambers (M1–M5). These are described in the following sections, as well as the electronics and software used to control the detector and to read out data. Further information about the design of LHCb can be found in Refs. [84, 85].

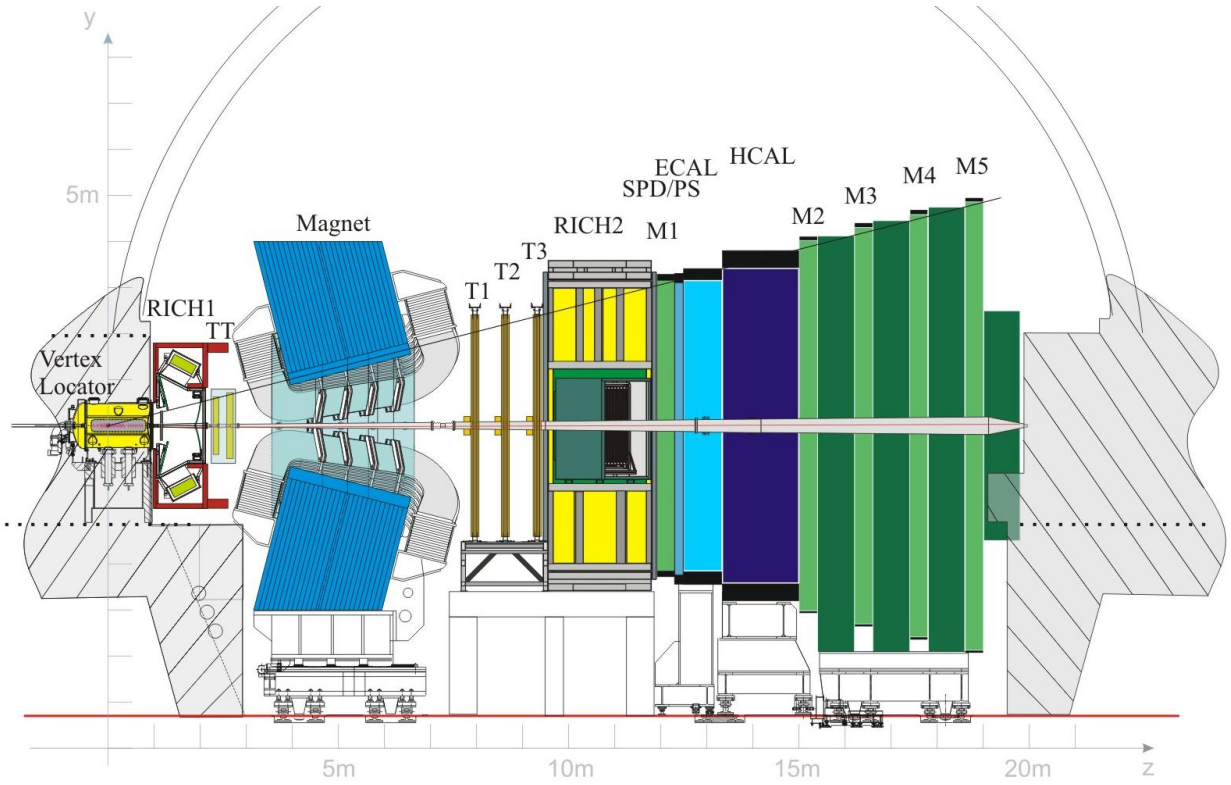

Figure 6.3: Side view of LHCb with subdetectors labelled.

6.3.2 Luminosity

The design luminosity of LHCb is 2×10^{32} cm^{-2} s^{-1} [84], two orders of magnitude lower than the nominal LHC luminosity. This value was chosen because at LHCb it is desirable to have $\mathcal{O}(1)$ p-p interactions per bunch crossing. Furthermore, the hardware-based Level-0 hadron trigger (Section 6.3.11.1) would saturate at much higher luminosities. As of July 2011, the typical luminosity at LHCb is 3–3.5$\times 10^{32}$ cm^{-2} s^{-1}, higher than the design value. This has been possible because of the excellent detector performance. Running at this luminosity and a centre-of-mass energy of 7 TeV will produce approximately 10^{12} $b\bar{b}$ pairs in a nominal year of 10^7 seconds.

The instantaneous luminosity at LHCb can be controlled by varying the displacement of the beams in the interaction region. A technique called *luminosity levelling* is used to maintain constant luminosity over a fill of protons and reduce the pileup at the start of the fill. In this procedure, the beams are deflected vertically so the area of overlap can be increased or decreased as necessary. An example of luminosity levelling in practice is shown in Figure 6.4.

The average number of visible[5] p-p interactions per bunch crossing is denoted μ. μ is

[5] A visible interaction produces at least two charged particles, both of which have sufficient hits in the VELO and tracking stations T1–T3 to allow them to be reconstructible.

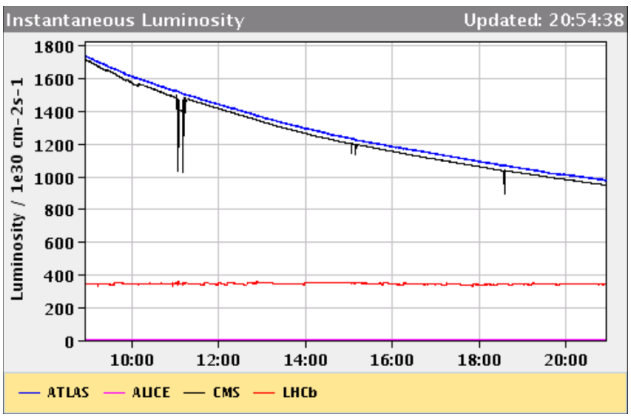

Figure 6.4: Luminosity levelling at LHCb. The red line is the instantaneous luminosity at LHCb; the blue and black lines are the instantaneous luminosities recorded by ATLAS and CMS respectively. The instantaneous luminosity of LHCb is approximately constant over the fill, whereas the instantaneous luminosities of ATLAS and CMS decrease over time.

related to various beam parameters as follows:

$$\mu = \frac{\mathcal{L}\sigma_i f_v}{n_b \nu_r}, \tag{6.1}$$

where $\mathcal{L}$ is the instantaneous luminosity, σ_i is the total inelastic cross section, f_v is the fraction of p-p interactions that are visible, n_b is the total number of bunches in the beam and ν_r is the revolution frequency of the beam. Figure 6.5 shows the number of p-p interactions as a function of the instantaneous luminosity; we have set σ_i to 80 mb and f_v to 1. In the

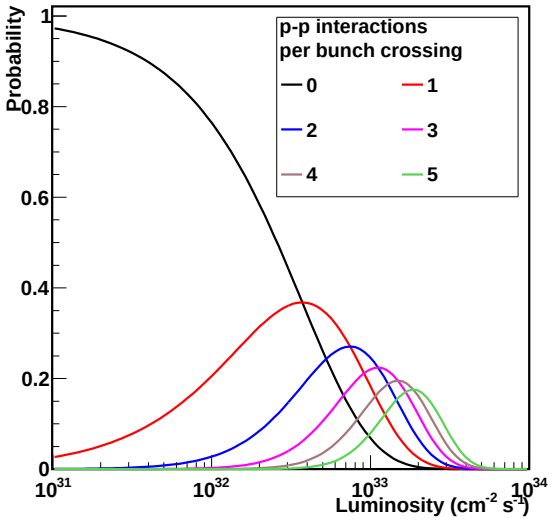

Figure 6.5: Probability of obtaining between 0 and 5 p-p interactions in a bunch crossing as a function of instantaneous luminosity.

current running conditions μ is equal to 1.5–2, higher than the design value. A consequence of this is that the subdetectors have been running at the limit of occupancy, and are ageing at about double the expected speed. However the fact that the instantaneous luminosity is also higher than design compensates for these drawbacks.

6.3.3 Coordinate system

A right handed Cartesian coordinate system is used to describe the location of objects in LHCb. The z axis is defined to point along the clockwise[6] beam direction, the y axis points vertically upwards, and the x axis points outwards from the centre of the ring. The only exception to this is the VELO in which a cylindrical geometry (r, ϕ, z) is used. In both cases, $z = 0$ is at the nominal interaction point of LHCb.

If object A is *downstream* of object B it indicates that the z-coordinate of A is greater than that of B; the opposite is true if A is *upstream* of B.

6.3.4 Vertex locator (VELO)

The purpose of the VELO [86] is to precisely measure the trajectories of charged tracks emanating from the interaction region. The VELO has sufficient spatial resolution to locate the characteristic displaced decay vertices of b- and c-hadrons and also determine charged particles' impact parameters with high precision.

The VELO detects tracks using silicon microstrip technology. The microstrips are grouped in approximately semicircular modules that are perpendicular to the beamline. The VELO is divided into two halves, with 21 modules in each half. Each VELO half can be moved in and out of the detector acceptance according to the status of the LHC beam. When the beam is stable, it has an envelope of approximately 100 µm; the VELO modules are then positioned close to the beamline (about 8 mm) in order to be able to locate the decay products of highly-boosted b-hadrons. During injection the LHC beam envelope increases significantly, so the VELO halves are retracted by approximately 3 cm for safety. The halves are moved back when the beams are stable. When fully closed, the two halves of the VELO overlap in order to ensure as full coverage as possible of the azimuthal acceptance and to aid module alignment.

The VELO modules are located both upstream and downstream of the interaction region because the uncertainty on the z-position of the interaction point is about 5 cm. In order to ensure that charged particles are minimally impeded before reaching the microstrips, the VELO is maintained in a vacuum. The temperature of the modules is kept between -10°C and 0°C. A schematic of the VELO is shown in Figure 6.6.

The VELO modules are arranged in a cylindrical geometry, which permits rapid reconstruction of tracks and vertices. Each module consists of two adjacent sets of silicon sensors, denoted the R and ϕ sensors. The R sensors are concentric arcs that determine the radial position of tracks. The ϕ sensors are straight strips that are used to determine the azimuthal position of tracks; these sensors are alternately skewed in a 'dog leg' design to provide greater

[6] When looking down at the LHC.

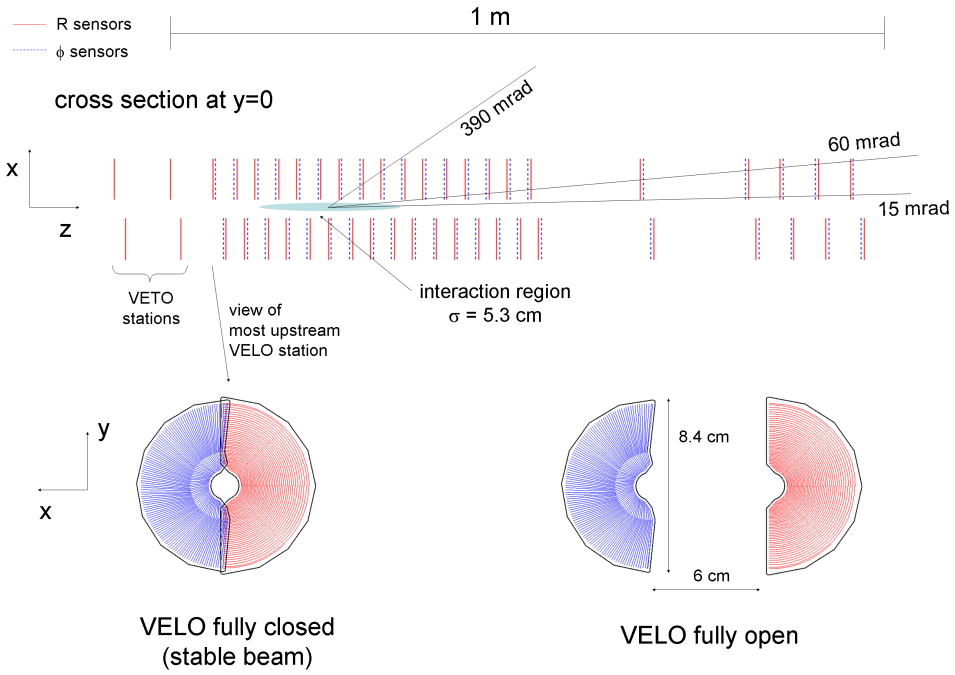

Figure 6.6: The cross section of the VELO in the (x, z) plane with the detector in the fully closed position. In addition there is a view of a module in both the open and closed positions.

precision. The z coordinate of a track is determined using accurate knowledge of the location of each module through which the track passes.

The R and ϕ sensors are ~ 300 µm thick with strip lengths that vary from 4–34 mm (R) and 6–25 mm (ϕ). The pitch of strips in the inner region is approximately half of the pitch of strips in the outer region. There are 2048 readout channels per sensor.

The VELO is contained in a thin aluminium box, the inner face of which is composed of corrugated RF (radio frequency) foils. The foils prevent RF pickup by the LHC beams and also ensure that gas from the detectors does not enter the LHC vacuum.

6.3.4.1 Pileup system

LHCb has a pileup system composed of four VELO R sensors located upstream of the interaction region. The sensors are arranged in two planes perpendicular to the beam line as shown in Figure 6.6 (labelled 'VETO stations'). The pileup system is used to determine the position of any potential primary vertices along the beam line[7], and determine the multiplicity of tracks pointing in the negative z direction. The pileup system is used in the Level-0 trigger as described in Section 6.3.11.1.

[7]The original purpose of the pileup system was to veto events with more than one primary vertex, but this feature is not used.

6.3.4.2 Performance

Figure 6.7 shows the spatial resolution of the VELO in the x direction as a function of the number of tracks in a p-p interaction, and the impact parameter resolution in the x direction as a function of $1/\mathbf{p}_{\mathrm{T}}$, where $\mathbf{p}_{\mathrm{T}}$ is the transverse momentum of each track. Both plots show a comparison between Monte Carlo and 2011 collision data. The best spatial resolution

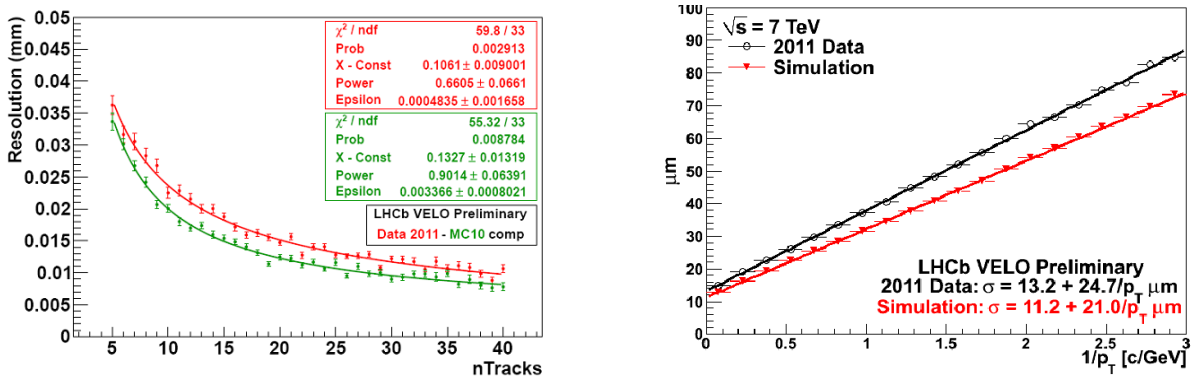

Figure 6.7: Spatial resolution of the VELO in the x direction as a function of the number of tracks in a p-p interaction (left) and impact parameter resolution in the x direction as a function of the reciprocal of the track transverse momentum (right).

achieved by the VELO is ~ 13 µm in the x and y directions and ~ 70 µm in the z-direction. In both cases, the resolution in collision data is $\sim 18\%$ worse than that in Monte Carlo; this effect is thought to be due to multiple scattering that has been incorrectly modelled.

6.3.5 Magnet

LHCb uses a water-cooled dipole magnet [87] to deflect the trajectories of charged tracks in the horizontal direction. The magnitude of the deflection can be used to determine the momentum of a track. The magnet is located between the TT and T1 and covers the full detector acceptance. It measures 11 m × 8 m × 5 m and weighs 1600 tons. There are two field polarities denoted *up* and *down*.

It is important to have as much bending as possible between the VELO and the TT in order to aid track reconstruction. Conversely, the magnetic field inside the RICH and VELO must be as low as possible because straight tracks are desirable in those subdetectors. The RICH and VELO are located outside the nominal field region, but can still be affected by the fringe field. These subdetectors are therefore shielded from the field using metal boxes.

The integrated magnetic field is 0.116 Tm upstream of the magnet and 3.62 Tm downstream of the TT.

6.3.6 Tracking stations

There are four planar tracking stations in LHCb: the Tracker Turicensis (TT), located upstream of the magnet, and stations T1–T3, located downstream of the magnet. The TT is composed entirely of silicon microstrips, whereas T1–T3 are a combination of silicon in the inner regions (Inner Tracker, IT [88]) and straw tubes in the outer regions (Outer Tracker, OT [89]). The silicon only covers about 2% of the total area, but because of the large forward boost in $b\bar{b}$ production 20% of the charged particles pass through it. The impact parameter resolution of high-$\mathbf{p}_{\mathrm{T}}$ tracks in the tracking stations is 14 µm.

6.3.6.1 Tracker Turicensis (TT)

The TT covers the full LHCb acceptance. It is approximately 150 cm wide and 130 cm high and is maintained at a temperature below 5°C. The pitch of the silicon microstrips in the TT is about 200 µm and they are 500 µm thick and up to 38 cm in length. In total there are 143360 strips and the active area of the TT is 8.4 m^2.

The TT comprises four detection layers arranged in a x-u-v-x layout, such that the strips in the x layers are vertical and the strips in layers u and v are rotated by $-5°$ and $+5°$ respectively. The xu layers are separated from the vx layers by 27 cm. This geometry enables the transverse component of the trajectory of a track to be determined more precisely.

Data from the TT are used to reconstruct long-lived neutral particles (e.g. K_S^0) that decay to charged tracks outside the VELO, and low momentum tracks that are diverted out of the acceptance before they reach T1–T3.

6.3.6.2 Inner tracker (IT)

Each tracking station has an IT module at its centre. Each module is approximately 120 cm wide and 40 cm high and cross-shaped; the boundary is chosen such that the occupancy of the outer tracker is no larger than 10% at nominal luminosity. The IT has the same x-u-v-x geometry as the TT. In total there are 129024 readout strips of either 11 or 22 cm in length, with a total active area of 4.0 m^2.

6.3.6.3 Outer tracker (OT)

The OT is an array of gas-tight drift tube modules. Each module is composed of two staggered layers of 64 tubes. The OT covers the full outer detector acceptance and has a total active area of 29.0 m^2. As with the IT, the OT has an x-u-v-x geometry.

The inner diameter of the drift tubes is 4.9 mm, and each tube contains a mixture of 70% argon and 30% CO_2. These conditions ensure that the time taken to cross an individual

tube is less than 50 ns.

In order to determine the trajectories of incident charged tracks, the drift times of the ionisation clusters produced by the tracks are measured and correlated with the beam crossing signal. This is similar to the approach used at CLEO-c, as described in Section 2.3.2.

6.3.7 Particle ID

Good particle identification (PID) is very important at LHCb; when performing an analysis it is often necessary to discriminate between several topologically and kinematically similar final states. Of particular importance to the analysis described in this thesis is the ability to distinguish $B^{\pm}\to DK^{\pm}$ from $B^{\pm}\to D\pi^{\pm}$ decays. PID information at LHCb is provided by the RICH detectors (Section 6.3.8), the calorimeters (Section 6.3.9) and the muon detectors (Section 6.3.10).

In order to determine the most probable species of a particle, the likelihood $\mathcal{L}$ of each possible species is computed separately for each subdetector. The likelihood expressions for electrons, muons and charged hadrons (h) are respectively [85]:

$$\mathcal{L}_e = \mathcal{L}_e^{\mathrm{RICH}} \cdot \mathcal{L}_e^{\mathrm{CALO}} \cdot \mathcal{L}_{\mathrm{non}-\mu}^{\mathrm{MUON}}, \tag{6.2}$$

$$\mathcal{L}_\mu = \mathcal{L}_\mu^{\mathrm{RICH}} \cdot \mathcal{L}_{\mathrm{non}-e}^{\mathrm{CALO}} \cdot \mathcal{L}_\mu^{\mathrm{MUON}}, \tag{6.3}$$

$$\mathcal{L}_h = \mathcal{L}_h^{\mathrm{RICH}} \cdot \mathcal{L}_h^{\mathrm{CALO}} \cdot \mathcal{L}_h^{\mathrm{MUON}}, \tag{6.4}$$

where the superscript indicates the contribution from the relevant subdetector.

In order to distinguish between two species, the difference between the logarithm of the two likelihoods is computed. For example, the difference in log likelihood between kaon and pion hypotheses is:

$$\Delta \log \mathcal{L}(K-\pi) \equiv \log \mathcal{L}_K - \log \mathcal{L}_\pi. \tag{6.5}$$

A positive value indicates the particle is more likely to be a kaon than a pion and vice versa.

6.3.8 Ring imaging Cherenkov (RICH) detectors

The RICH detectors [90] at LHCb are primarily used to identify hadronic final state particles. It is important to be able to discriminate between particle species over a wide momentum spectrum (1–100 GeV/c). To enable this there are two RICH detectors, denoted RICH 1 and RICH 2, that cover different momentum ranges.

As outlined in Section 2.3.3, RICH detectors locate rings of Cherenkov radiation emitted by particles passing through a medium at superluminal speeds. The radius of the ring enables the Cherenkov angle θ_{Ch} to be determined. The value of θ_{Ch} is combined with a

measurement of the momentum and the most probable mass of the particle is deduced.

RICH 1 is located upstream of the dipole magnet and covers the entire detector acceptance. It uses both aerogel and gaseous C_4F_{10} as radiators. RICH 1 is designed to identify particles in the momentum range 1–60 GeV/c.

RICH 2 is downstream of the magnet and is located between T3 and M1 (see Figure 6.3). It is designed to identify particles in the momentum range 15–100 GeV/c. The radiator used in RICH 2 is CF_4. The angular acceptance of RICH 2 is between ±15 mrad and ±120 mrad in the $x-z$ plane and between ±15 mrad and ±100 mrad in the $x-y$ plane.

In both RICH 1 and RICH 2, Cherenkov light is focused onto photon detectors using a combination of spherical and flat mirrors. The photon detectors are placed outside the detector acceptance in order to reduce the material in this region. There are two planes of photon detectors in each RICH; in RICH 1 the planes are separated vertically and in RICH 2 the planes are separated horizontally in the x direction.

For light with a wavelength of 400 nm, the LHCb aerogel has a refractive index of 1.03, C_4F_{10} has a refractive index of 1.0014 and CF_4 has a refractive index of 1.0005. The expected Cherenkov angle as a function of particle momentum for the three radiators is shown in Figure 6.8.

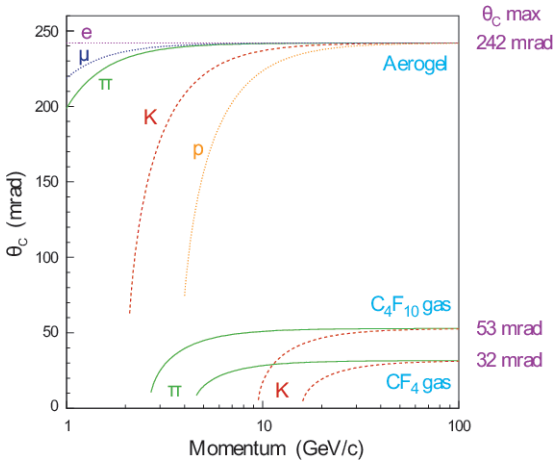

Figure 6.8: Cherenkov angle as a function of momentum for the three radiators used in the RICH detectors.

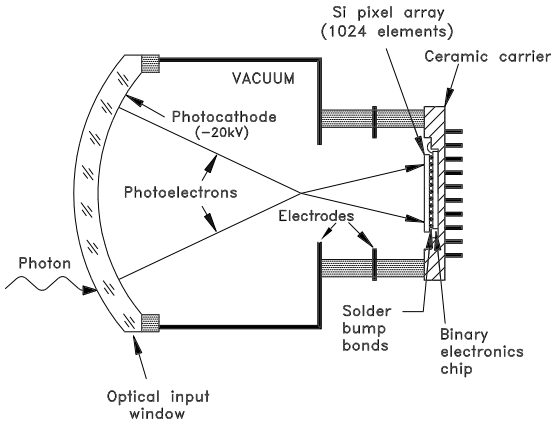

Figure 6.9: A schematic of an HPD.

6.3.8.1 Hybrid Photo Detectors

Cherenkov photons emitted in the RICH detectors are detected using Hybrid Photo Detectors (HPDs). A schematic of an HPD is shown in Figure 6.9. Each HPD has a spherical quartz entrance window of thickness 7 mm and inner radius of curvature 55 mm. When a Cherenkov photon is incident on the photocathode of an HPD, a photoelectron is released and is accelerated by a potential difference of 16–18 kV onto a silicon pixel detector consisting

of a 32×32 square of pixels, each of which measures 500 µm by 500 µm

The HPDs in RICH 1 are located in the upstream fringe field of the dipole magnet which is approximately 60 mT. The magnetic flux density within the HPDs must be significantly reduced for them to work at full efficiency so they are contained in an iron shielding box and individually surrounded by mu-metal cylinders. The flux density inside each HPD is thus approximately 2.4 mT. The HPDs are arranged in hexagonally close packed planes, with their centres separated by 89.5 mm. In RICH 1 there are 7×14 HPDs in each plane and in RICH 2 there are 9×16.

6.3.8.2 RICH 1

A schematic of RICH 1 with various components labelled is shown in Figure 6.10.

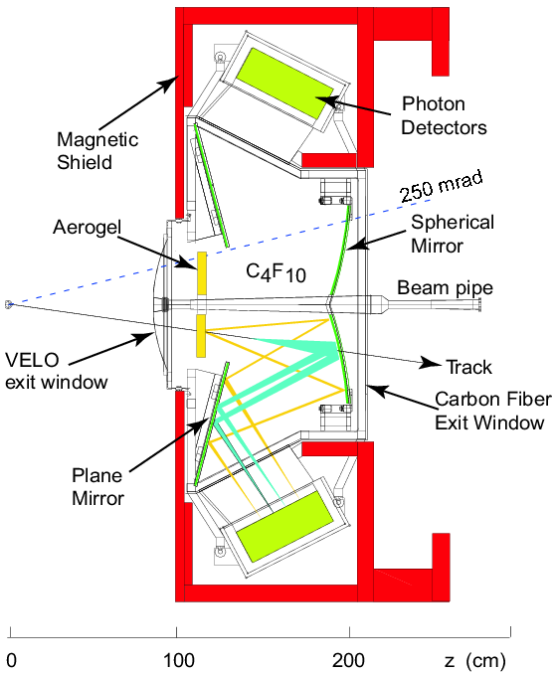

Figure 6.10: Schematic of RICH 1 with components labelled.

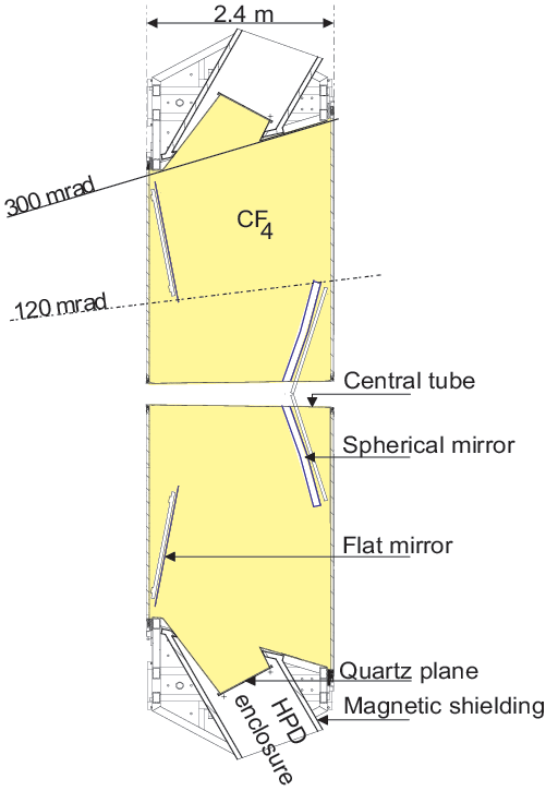

Figure 6.11: Schematic of RICH 2 with components labelled.

The aerogel radiator is located at the entrance to RICH 1 and is divided into tiles measuring $20 \times 20 \times 5.1$ cm. Aerogel can provide discrimination between pions and kaons for momenta up to about 10 GeV/c.

The C_4F_{10} is held at ambient temperature and a pressure of $\lesssim 50$ Pa at the top of the subdetector. The gas is prevented from escaping by an 8 mm thick quartz window coated with magnesium fluoride in order to reduce its reflectivity and enable more photons to reach the HPDs. The gas volume covers about 95 cm in the z direction. C_4F_{10} can provide discrimination between pions and kaons for momenta up to about 60 GeV/c.

Cherenkov photons produced in RICH 1 are initially reflected by tilted spherical mirrors with radius of curvature ~ 2.7 m, and then are further reflected by flat mirrors onto the HPDs. Both types of mirror are grouped into quadrants, with two above the beam line and two below. The mirrors are made of carbon fibre and coated with Al, SiO_2 and HfO_2.

6.3.8.3 RICH 2

A schematic of RICH 2 with various components labelled is shown in Figure 6.11. As in RICH 1, spherical and planar mirrors are used to reflect Cherenkov light onto HPDs that lie outside the detector acceptance. The spherical mirrors have a radius of curvature of ~ 8.6 m. The mirrors are composed of a Simax glass substrate coated with Al, SiO_2 and HfO_2. The gas volume in RICH 2 covers 2.4 m in the z direction and is separated from the HPDs with the same type of quartz window used in RICH 1.

6.3.8.4 RICH pattern recognition

Rings of Cherenkov light are reconstructed using pattern recognition algorithms [90]. The rings are slightly distorted when they reach the HPDs due to the reflection from the spherical mirrors. Rather than fitting the rings, each HPD hit is used to determine the Cherenkov angle with respect to each reconstructed track. Two approaches are used to determine the most likely species of the tracks: a fast 'local' method, which examines the tracks individually, and a slower 'global' method that considers all tracks in both RICH detectors.

In the local method a log likelihood term is constructed as follows:

$$\log \mathcal{L} \propto \sum_{i=1}^{n_{\text{hits}}} \log \left(1 + \frac{1}{\sqrt{2\pi}\sigma_\theta} \exp \left[-\frac{(\theta_i - \theta_x)^2}{2\sigma_\theta^2} \right] \right), \tag{6.6}$$

where n_{hits} is the number of HPD hits, θ_i is the reconstructed emission angle of the i^{th} hit, θ_x is the expected emission angle of photons from the track given a particle hypothesis x, and σ_θ is the angular resolution. The expression is normalised such that $\log \mathcal{L}$ is equal to the number of hits expected for the particular track hypothesis. The number of hits expected for each hypothesis is compared to the number reconstructed, and the hypothesis that provides the best compatibility between these numbers is selected.

The global pattern recognition algorithm is more accurate than the local algorithm, but is about five times slower. The global algorithm can account for hits from other tracks, which are the main background to the local method. A global likelihood term is constructed that compares the number of photoelectrons reconstructed in each HPD pixel with the number

expected from the reconstructed tracks and known sources of background:

$$\log \mathcal{L} = -\sum_{j=1}^{n_{\text{tracks}}} \mu_j + \sum_{i=1}^{n_{\text{pixels}}} n_i \log \left(\sum_{j=1}^{n_{\text{tracks}}} a_{ij} + b_j \right), \tag{6.7}$$

where n_{tracks} is the number of reconstructed tracks, n_{pixels} is the number of HPD pixels, a_{ij} is the expected number of detected photoelectrons from track j in pixel i for a given hypothesis, $\mu_j \equiv \sum_i^{n_{\text{pixels}}} a_{ij}$ is the expectation for the total number of detected photoelectrons from track j, n_i is the number of photoelectrons in pixel i, and b_i is the expected background in pixel i as estimated from the hit multiplicity in adjacent tracking stations. The hypotheses for all tracks are changed in an iterative procedure until $\log \mathcal{L}$ is maximised.

6.3.8.5 Performance

The ability of the RICH detectors to distinguish kaons from pions has been measured using *calibration* samples of data selected solely using kinematic information. One example of such a sample is $D^{*\pm} \to D(K^{\pm}\pi^{\mp})\pi^{\pm}$ decays. Figure 6.12 shows the kaon identification efficiency and the pion misidentification fraction on this sample for various illustrative $\Delta \log \mathcal{L}(K-\pi)$ criteria. Further information about the PID calibration procedure is given in Section 7.7.

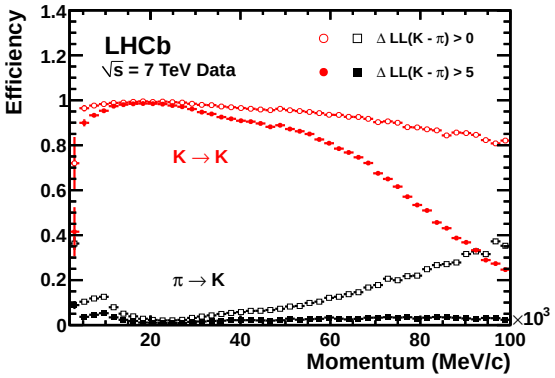

Figure 6.12: Kaon identification efficiency (red) and pion misidentification fraction (black) on collision data. The efficiencies for two different $\Delta \log \mathcal{L}(K-\pi)$ cuts are shown: > 0 (open shapes) and > 5 (filled shapes).

6.3.9 Calorimeters

LHCb has both an electromagnetic and hadronic calorimeter [91], denoted ECAL and HCAL respectively, that are used to determine the energy of various final state particles and aid in particle identification. In particular, the ECAL plays a vital role in locating electrons and photons and measuring their energy. Data from the calorimeters are used in triggering, as detailed in Section 6.3.11.1.

There are two additional detectors that are used to reject the large backgrounds to signal electrons and photons: the preshower detector (PS) and the scintillating pad detector (SPD). The PS is used to remove significant quantities of charged pions and the SPD is used to reject backgrounds of π^0 mesons and high-energy photons.

The calorimeters are located between M1 and M2; the ECAL is located upstream of the HCAL and the PS and SPD are upstream of the ECAL.

Particles incident on the calorimeters emit scintillation light that is transferred to photomultiplier tubes (PMTs) via Wavelength-Shifting (WLS) fibres. In the PS and SPD the light from the fibres is read out with multianode PMTs (MaPMTs), whereas in the ECAL and HCAL the fibre bunches are connected to individual PMTs.

In order to determine the identity of a particle, the barycentre of the energy deposit in the calorimeter is determined. This is matched to a candidate track whose momentum is used to deduce the mass of the particle and hence its identity.

All of the components of the calorimeter are laterally segmented. The density of the segmentation varies with the distance from the beam because the particle occupancies vary by about two orders of magnitude across the surface of the subdetector. The PS, SPD and ECAL are segmented in units of side length 40.4 mm, 60.6 mm and 121.1 mm; the HCAL is segmented in units of 131.3 mm and 262.2 mm.

6.3.9.1 Preshower detector (PS) and scintillating pad detector (SPD)

The SPD/PS structure is a 15 mm lead converter sandwiched between two planes, each of which is tiled with scintillator pads. The active area of the SPD/PS is 44.6 m^2.

Each photocathode in the MaPMT contains 64 pixels, each of which is connected to an output channel. In order to reduce the magnetic field on the MaPMTs they are surrounded by mu-metal cylinders.

6.3.9.2 Electronic calorimeter (ECAL)

The ECAL is arranged in alternating layers of a sampling scintillator made from 4 mm thick polystyrene tiles and a 2 mm thick lead absorber. There are 66 layers in total comprising about 25 electromagnetic radiation lengths; this ensures that showers from high energy electrons and photons are fully contained within the ECAL. The ECAL has the same outer acceptance as the tracking stations, and the inner radius is $\sim \pm 25$ mrad in both the $x - z$ and $x - y$ planes.

6.3.9.3 Hadronic calorimeter (HCAL)

The HCAL is a sampling calorimeter consisting of a sequence of 1 cm long iron absorbers and scintillating tiles that are arranged such that the 'long' side is parallel to the z axis. The sampling component is three tiles deep. The dimensions of the HCAL are 8.4 m $\times$ 6.8 m $\times$ 1.65 m. The depth of the HCAL corresponds to 5.6 hadronic interaction lengths; spatial limitations prevent it from being extended further.

6.3.9.4 Performance

The energy resolution of the calorimeters has been determined using test beam data. The ECAL energy resolution is parameterised as $\sigma_E/E = (9.4 \pm 0.2)\%/\sqrt{E} \oplus (0.83 \pm 0.02)\%$ and the HCAL energy resolution is parameterised as $\sigma_E/E = (69 \pm 5)\%/\sqrt{E} \oplus (9 \pm 2)\%$, where in both cases the particle energy E is in GeV.

Figure 6.13 shows a plot of the diphoton mass distribution in collision data as measured by the ECAL. A clear $\pi^0 \to \gamma\gamma$ signal is observed with a mass resolution of approximately 7.2 MeV/c^2.

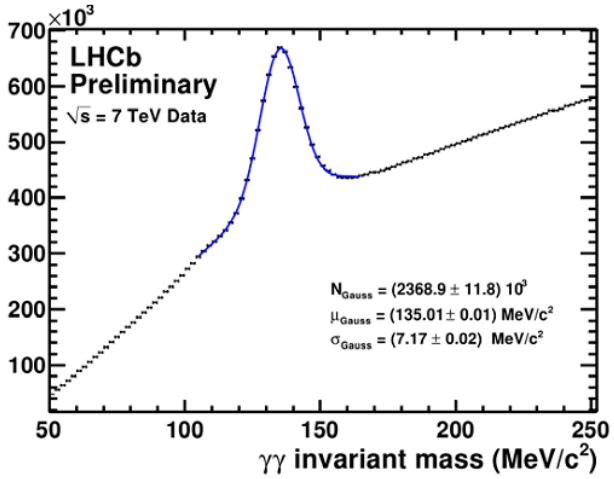

Figure 6.13: ECAL detection of $\pi^0 \to \gamma\gamma$ decays in collision data.

6.3.10 Muon chambers

There are five muon detectors (M1–M5) [92–94] along the beam axis. As well as playing a key role in muon identification, data from the muon stations are used in triggering as detailed in Section 6.3.11.1.

M1 is located between RICH 2 and the calorimeters. Its primary purpose is to obtain a more accurate estimate of the transverse momentum of charged tracks. The remaining muon stations are all downstream of the calorimeters and are interleaved with 80 cm thick iron absorbers, designed to stop hadronic background particles. In total the absorbers account

for about 20 radiation lengths. The angular acceptance of the muon stations is ±20 mrad to ±306 mrad in the $x-z$ plane and ±16 mrad to ±258 mrad in the $x-y$ plane. The total active area of the chambers is 435 m^2.

Each muon station is divided into rectangular *logical pads*. The spatial resolution of the pads is more precise the closer they are to the beam line. The spatial resolution of M1–M3 is particularly high in the bending plane, which enables the trajectories and momenta of muons to be located with high accuracy. The main function of M4 and M5 is to identify muons, rather than determine their kinematic properties, so the spatial resolution is less precise.

The muon chambers are almost entirely instrumented with multi-wire proportional chambers (MWPCs); the only exception to this is the central region of M1 for which gas electron multipliers (GEMs) are used because they are more suited to high radiation flux and age less quickly.

The wires in the MWPCs are 20–30 cm in length and have a 2 mm spacing. The wires are placed symmetrically in 5 mm gas gaps; there are two gaps in M1 and four in M2–M5. The gas consists of a mixture of argon, CO_2 and CF_4 in the ratio 40%:55%:5%. In order to improve the efficiency of the detector, a logical OR is taken of the results obtained by the readout electrodes in each adjacent gap pair. The time resolution of the MWPCs is ~ 5 ns.

There are 12 GEM chambers, each of which contains two superimposed triple-GEM detectors. The GEMs are read out with anode pads and the result for each chamber is a logical OR of the two GEM detectors in that chamber. The gas inside the GEM chambers consists of argon, CO_2 and CF_4 in the ratio 45%:15%:40%.

In order to identify muons, well-reconstructed tracks with momentum ≥ 3 GeV/c are extrapolated into the muon stations and matched to hits in the relevant areas of interest.

6.3.11 Trigger

The trigger at LHCb [95] has been designed to reduce the 10 MHz frequency of visible interactions to a rate that is more feasible in terms of data taking and storage (2–3 kHz). The trigger has been optimised to select decays of interest to physics analyses and reject any backgrounds.

There are two main stages of the trigger: the hardware-based Level-0 (L0) trigger, which reduces the event rate to about 1 MHz, and the software-based High Level Trigger (HLT) which performs the rest of the reduction in rate. Both stages have been designed to exploit common features of b-hadron decays: the fact that b-hadrons usually decay a significant distance from the p-p interaction vertex, and that they are relatively massive and hence decay to particles with high transverse momentum ($\mathbf{p}_T$) and transverse energy (E_T). Events that pass all stages of the trigger are written to offline storage, as described in Section 6.3.12.

6.3.11.1 Level 0 (L0) trigger

The L0 trigger comprises a suite of custom made electronics. It is synchronised with the 40 MHz bunch crossings and operates at a fixed latency[8] of 4 µs, independent of the detector occupancy. The L0 trigger receives information from the calorimeters, the muon chambers, and the pileup stations.

The calorimeter system locates candidate electrons, photons, π^0 mesons and hadrons. To identify candidates, the total E_{T} in 2×2 clusters of cells is determined; clustering the cells ensures that the energy deposited by a particle is not missed because it spilled into a neighbouring cell. The species of the particle that deposited energy in the cluster is determined by using information from the SPD, PS, ECAL and HCAL. For each species, the candidate with the highest E_{T} is recorded. Minimum E_{T} thresholds are defined for each species in order to reject background events.

In order to find muon candidates, the trigger algorithm searches for *towers* in the logical pads. A tower consists of a hit in each muon station, such that the hits form a straight line pointing towards the interaction region. The $\mathbf{p}_{\mathrm{T}}$ of each candidate is determined using its position in the first two muon stations; the uncertainty on the $\mathbf{p}_{\mathrm{T}}$ obtained using this method is about 20%. The two muon candidates with the highest $\mathbf{p}_{\mathrm{T}}$ in each quadrant are recorded.

The number of p-p interactions in the pileup stations is recorded. The information from the calorimeter, muon and pileup systems is collated in the Level-0 Decision Unit (L0DU). In total there are 19420 channels from the calorimeter system, 25920 channels from the muon stations, and 2048 from the pileup system. For each bunch crossing, the L0DU makes a decision whether or not to keep the event. It is possible to implement simple logic in the L0DU, e.g. taking an OR of decisions, and prescaling certain event types.

In each bunch crossing some global event variables are calculated. Firstly, the total energy in all of the HCAL cells is calculated. A lower limit is imposed on this quantity in order to ensure that only crossings with visible interactions are selected. Secondly, the multiplicity of charged particles in the event is determined from the number of hits in the SPD. This can be used to veto events in which there are an excessive number of tracks in order to improve the average processing time per event.

The decision of the L0DU is transmitted to the readout supervisor, which is the interface between the LHCb trigger system and the readout electronics. The readout supervisor is able to impose global restrictions on the rate in order to ensure buffer overflows do not occur. It also ensures that the trigger decisions are synchronised with the LHC clock.

[8]Latency is defined as the time that passes between a p-p interaction and a L0 trigger decision being received by the front-end electronics.

6.3.11.2 High level trigger (HLT)

The software-based High Level Trigger (HLT) is designed to refine the decisions made at L0 in order to reduce significantly the rate of events that are written to storage. A much larger quantity of event information is used to do this compared to L0; to some extent, the selection criteria used in the HLT are looser versions of those used in offline selections. The HLT is a `c++` application that is run on a set of approximately 1350 multiprocessor systems called the Event Filter Farm (EFF). In total about 20000 copies of the HLT run in parallel, asynchronously with the LHC clock. The HLT software is designed such that it can flexibly adapt to different running conditions and physics goals. It consists of both inclusive and exclusive trigger algorithms.

The HLT is split into two sub-levels denoted HLT1 and HLT2. HLT1 employs relatively simple selection criteria based on common features shared by many types of b- and c-hadronic decay. HLT2 uses relatively sophisticated algorithms to identify decays of interest. At both HLT1 and HLT2 there are several algorithms, denoted *lines*, that run in parallel. Each line, or group of lines, is designed to select particular signatures of the physics decays of interest. We will outline the function of the lines most relevant to this thesis: the *1-track* lines at HLT1 and the *topological* lines at HLT2.

The HLT1 1-track trigger [96] is designed using the principle that the majority of b-hadrons that decay in LHCb will leave a track in the detector with high momentum, high $\mathbf{p}_{\mathrm{T}}$, good quality of reconstruction (indicated by a low fit χ^2), and a high impact parameter with respect to the primary vertex. The trigger therefore accepts events that contain such a track. This is a highly inclusive, efficient and fast trigger.

The aim of the HLT2 topological trigger [97] is to reconstruct all possible combinations of two, three and four tracks in an event with various selection cuts applied to select likely b-hadron decay candidates. This trigger is able to select decays of interest efficiently while rejecting backgrounds and ensuring the resulting kinematic distributions are unbiased.

6.3.11.3 Trigger configuration key (TCK)

The particular combination of trigger algorithms (at both L0 and HLT) that is active during a data taking period is encoded in a quantity called the Trigger Configuration Key (TCK). A TCK contains information about the trigger lines that are active, the values of parameters used in the lines, and any pre- or post-scales that may be applied. During data taking, the EFF is configured with a particular TCK. It is possible to change TCK mid-fill without significant downtime.

Each TCK is an eight-digit hexadecimal number, e.g. `0x002e002a`. The rightmost four digits encode the L0 configuration and the leftmost four digits encode the HLT configuration.

6.3.11.4 Performance

The LHCb trigger has performed well in 2010 despite the higher than forseen pileup. At L0, about 400 kHz bandwidth is allocated to the hadronic trigger, the same to the muon trigger and the remainder to the electromagnetic triggers. The typical output rate of the HLT has been 3 kHz, compared to the design rate of 2 kHz. About 1 kHz each are devoted to b decays to leptons, b to hadrons, and charm decays. The average HLT execution time is $\mathcal{O}(20)$ ms per event.

6.3.12 Data acquisition

Events selected by the trigger are sent to storage by the data acquisition (DAQ) systems [98]. There are approximately 350 DAQ interface modules designed to ensure events are correctly synchronised, to perform zero suppression, and to buffer data.

The first stage of the DAQ comprises the front-end electronics that are located on each subdetector. These electronics amplify and shape the detector response. The signals from each subdetector are then stored in 4 µs deep pipeline buffers. If an event is accepted by the L0, the data are transferred from the buffers to a derandomiser. The derandomiser ensures that the rate of readout to the DAQ interface is nearly constant, and that closely-spaced triggers are handled efficiently. The derandomiser is able to hold data from up to 16 events at a time. Data are sent from the derandomiser to TELL1 (Trigger Electronics and Level 1) boards. The TELL1 boards are standardised for all subdetectors, except for the RICH that uses a customised board called the UKL1. The TELL1 boards perform functions such as zero suppression and ensuring that the data are formatted appropriately. Events are then sent to storage.

There are several subsystems that are used to broadcast messages to various LHCb components. The Trigger, Timing and Control (TTC) system transmits clock and synchronisation signals to all front-end and DAQ interface modules. The Timing and Fast Control (TFC) system controls data readout between the front end electronics and the online processing farm. The TFC system consists of a network able to distribute commands, a trigger throttle (that halts execution of the trigger if there is an excess of data in the system) and the readout supervisor that was described in Section 6.3.11.1. The Experimental Control System (ECS) is used to control the operation of the entire detector as well as monitor various quantities such as voltages, temperatures, pressures, gas flows, operation of the electronics and DAQ.

6.3.13 Data storage

6.3.13.1 Distributed computing

All experiments at the LHC use a distributed computing model to store and process data. Computing centres are located worldwide and connected to the Grid [99] infrastructure. The computing centres are divided into a hierarchy of tiers based on their capabilities and expected roles. At the top of the hierarchy is CERN, whose computing centre is denoted Tier-0. Data from CERN are transferred to Tier-1 sites; LHCb uses six Tier-1 sites to store data (CNAF, GridKA, IN2P3, NIKHEF, PIC and RAL). Below this in the hierarchy are many Tier-2 sites, usually universities, that are able to access data and run jobs on the Grid. It is possible to download data to a local site, but full datasets are often prohibitively large. However the distributed model ensures that this is not a barrier to running analyses.

Reconstruction of data is performed at both Tier-0 and Tier-1 centres. Tier-1 centres are used to run analysis tasks that are sent to the Grid from lower tiers. Monte Carlo simulation of events is performed at Tiers 0, 1 and 2.

LHCb uses the DIRAC (Distributed Infrastructure with Remote Agent Control) [100] project to interface with the Grid. The software Ganga (Gaudi-Athena Grid Alliance) [101] is used to configure jobs, submit them to the Grid and monitor them while they are running. Ganga is designed to be as transparent as possible to the user.

6.3.13.2 Stripping

All raw data selected for storage are initially written to disk at CERN. The data are reconstructed to determine various parameters such as the locations of subdetector hits. These quantities are written to a file known as a Data Summary Tape (DST).

Initially, only information that is absolutely necessary for event reconstruction is written, and the output file is called a reduced DST (rDST). It is possible to later reprocess the data with updated calibration and alignment constants. The rDSTs are produced by loosely selecting events in a procedure known as *stripping*. The four-momenta of all particles in an event, including composite particles, are determined along with the location of any primary or secondary vertices. There are a variety of stripping algorithms, denoted *lines*, that are designed to select different final states using this information. Any events that pass the stripping selection criteria are fully reconstructed and written to a DST with all of the event information. These DSTs are then distributed to Tier 1 sites and are accessible to the user.

In late 2010 the average raw event size was 65 kB, and the average size of an event in a full DST was 123 kB. Approximately 10-15% of the events recorded were stripped.

6.3.14 Software

A large proportion of the software used to process data taken by LHCb is based on the Gaudi framework [102]. Gaudi provides a set of algorithms that are able to perform common tasks.

6.3.14.1 Gauss

Event simulations are performed by the Gauss package [103]. There are two principal stages to the operation of Gauss. The first stage is to simulate the generation of particles from p-p interactions and model the particles' subsequent decays. Particles are generated using Pythia [104], and b- and c-hadron decays are modelled with EvtGen [69] and BcVegPy [105]. Radiative decays are simulated with PHOTOS [106].

The next stage is to model the passage of particles through the detector using GEANT4 [70, 71]. A variety of effects are modelled, such as multiple scattering, bremsstrahlung, Cherenkov radiation and decay in flight. Whenever a particle enters or leaves a subdetector a 'hit' is recorded. MC truth information is stored about particles (including intermediate resonances), production and decay vertices, and hits.

6.3.14.2 Boole

The Boole package [107] is the final stage of the LHCb detector simulation. It is used to digitise the response of the detector to particles using the MC detector hits created by Gauss. Further hits from spillover events and the LHC background are also incorporated. Knowledge about detector resolution and subdetector imperfections are used to ensure a realistic response. Data produced by Boole are in exactly the same format as that used to record real data. The associated MC particles are also added to the output.

6.3.14.3 Brunel

The Brunel package [108] is used to reconstruct events, either using real data from the LHCb DAQ or the output of Boole. Tasks performed by Brunel include track finding and fitting, neutral particle reconstruction, location of energy deposits in the calorimeter and location of Cherenkov rings in the RICH. When run over Monte Carlo data Brunel also associates reconstructed tracks with particles. Brunel uses a database of detector alignment constants in order to improve the quality of reconstruction. Files are output in the DST format.

6.3.14.4 DaVinci

The DaVinci package [109] is used to perform the final 'offline' selection of both real and simulated LHCb data that have been processed by Brunel. DaVinci contains a set of tools for

common analysis tasks such as applying selection cuts to events, fitting decay vertices and making composite objects. It is able to access Monte Carlo truth information if necessary.

The output of DaVinci is usually in a format that can be analysed by the ROOT framework [110]. DaVinci is used to strip data as described in Section 6.3.13.2.

6.3.14.5 Moore

The HLT is configured and operated with the Moore package [111], which is run online in the EFF with a desired TCK. It is possible to re-run Moore on Monte Carlo data in order to determine the performance of the trigger using different TCKs.

6.4 Data collected

A total of 36.5 pb^{-1} of data were collected by LHCb in 2010. The analysis described in this thesis is performed on these data. As of September 2011, a total of ~ 850 pb^{-1} of data have been collected.

6.5 Monte Carlo data

Dedicated samples of Monte Carlo data have been centrally produced by LHCb using Gauss. Both signal Monte Carlo, consisting of one specific decay, and background samples containing a variety of decays are available. Each sample usually contains at least 10^5 events; the largest background samples contain about 10^7. The MC samples are produced such that all final state particles lie in the detector acceptance.

In this thesis we use MC data that were produced towards the end of 2010, simulating the running conditions of that period. The data were simulated with a μ of 2.5, for both magnet polarities, and with a 7 TeV centre-of-mass energy.

Chapter 7

Reconstruction of $B^{\pm} \to (h^{\pm}h^{\mp})_D h^{\pm}$ decays at LHCb

7.1 Introduction

In this chapter we describe the reconstruction of the decays $B^{\pm} \to (K^+K^-)_D h^{\pm}$ and $B^{\pm} \to (K^{\pm}\pi^{\mp})_D h^{\pm}$ ($h = \pi$ or K, $D = D^0$ or $\overline{D}^0$) using the 36.5 pb^{-1} of data collected by LHCb in 2010. Henceforth, the $h^{\pm}$ that is emitted by the $B^{\pm}$ is denoted the *bachelor* particle. In Section 7.2 we list the criteria used to select events. Studies of the trigger performance and the various sources of background are described in Sections 7.3 and 7.5 respectively. The lineshapes that are used to fit the $B^{\pm}$ mass distribution are described in Section 7.6. Finally, the calibration of the PID performance is presented in Section 7.7.

The author wishes to acknowledge Paolo Gandini, Philip Hunt, Malcolm John and Andrew Powell who performed some of the work presented in both this chapter and Chapter 8.

7.2 Event selection

We isolate the decays of interest by applying a variety of selection criteria ('cuts') to the data. The data are initially stripped (as introduced in Section 6.3.13.2), and then cut further using criteria that have been optimised to locate the particular decays of interest.

7.2.1 Definitions

We define several variables that are used to discriminate between signal and background events.

- IP χ^2: The χ^2 of the reconstructed impact parameter[1] (IP) between a particle and the 'best' primary vertex[2].
- sIP χ^2: The minimum value of the IP χ^2 between a particle and each reconstructed primary vertex in the event.
- FD χ^2: The χ^2 of the reconstructed distance between the best primary vertex and the decay vertex of a particle.
- D max(DOCA): The maximum distance of closest approach of the D daughters to the D decay vertex.
- Vertex χ^2/DOF: The χ^2 of the fit to the decay vertex of a reconstructed particle divided by the number of degrees of freedom.
- Track χ^2/DOF: The χ^2 of the fit of a reconstructed track divided by the number of degrees of freedom.
- DIRA: The cosine of the angle between the reconstructed momentum of a particle and its reconstructed flight direction.
- Δm_X: The difference between the reconstructed mass of particle X and its nominal (PDG) mass.

7.2.2 Stripping selections

We use data that have been selected by the stripping line `B2DXWithD2hh`. This is an inclusive line that reconstructs and selects $B^{\pm}\to Dh^{\pm}$ decays in which the D decays to all two-body combinations of kaons or pions. The selection cuts used in the line are listed in Table 7.1. Table 7.2 lists the efficiency of the stripping line on Monte Carlo samples of different decay channels. The efficiency is defined as the number of events that are accepted by the line divided by the total number of events in the initial sample[3]. The main source of inefficiency is the reconstruction procedure.

We also use the output of the stripping line `B2DXWithD2hhWS`. The cuts applied in this line are identical to the cuts used in `B2DXWithD2hh`, but the two reconstructed D daughters have the same charge. This is an unphysical situation that can only occur if the final state particles have not come from genuine signal events but are instead random tracks. The data selected by this stripping line are useful to determine the level of combinatoric background as

[1]The IP χ^2 is approximately equal to $(\mathrm{IP}/\sigma_{\mathrm{IP}})^2$, where σ_{IP} is the uncertainty on the IP.

[2]The best primary vertex is the primary vertex that has the smallest impact parameter χ^2 with respect to the particle in question.

[3]In MC samples all signal final state particles are constrained to lie within the detector acceptance.

Variable	Stripping cut
$\lvert\Delta m_{B^\pm}\rvert$	< 500 MeV/c^2
$B^\pm$ IP χ^2	< 25
$B^\pm$ lifetime	> 0.2 ps
$B^\pm$ DIRA	> 0.9998
$B^\pm$ vertex χ^2/DOF	< 12
Bachelor $\lvert\mathbf{p}\rvert$	> 5 GeV/c
Bachelor $\mathbf{p}_\mathrm{T}$	> 500 MeV/c
Bachelor sIP χ^2	> 16
Bachelor track χ^2/DOF	< 5

Variable	Stripping cut
$\lvert\Delta m_{D^0}\rvert$	< 100 MeV/c^2
D $\mathbf{p}_\mathrm{T}$	> 1 GeV/c
D FD χ^2	> 36
D max(DOCA)	< 1.5 mm
D DIRA	> 0.9
D vertex χ^2/DOF	< 12
D daughter track χ^2/DOF	< 5
max(D daughter sIP χ^2)	> 40
D daughter $\mathbf{p}_\mathrm{T}$	> 250 MeV/c
D daughter $\lvert\mathbf{p}\rvert$	> 2 GeV/c
D daughter sIP χ^2	> 4

Table 7.1: Summary of the selection cuts applied in the stripping line `B2DXWithD2hh`.

D decay	Stripping efficiency (%)	
	$B^\pm \to DK^\pm$	$B^\pm \to D\pi^\pm$
$D \to K^\pm\pi^\mp$	17.00 ± 0.03	17.16 ± 0.03
$D \to K^+K^-$	16.52 ± 0.06	16.79 ± 0.06

Table 7.2: Efficiencies of the stripping line `B2DXWithD2hh` on Monte Carlo data samples.

detailed in Section 7.5.1. In order to save disk space only one in five events in this stripping line are saved.

7.2.3 Final selection

Additional cuts are applied to the stripped data in order to reduce the background level further while retaining signal decays. The cuts have been optimised in order to maximise the significance $S/\sqrt{S+B}$, where S (B) is the yield of signal (background) events in the signal region. The optimisation procedure recursively changes the order in which the selection criteria are applied in order to avoid reaching local maxima in $S/\sqrt{S+B}$. The signal region used in the optimisation covers -40 MeV/c^2 $< \Delta m_{D^0} <$ $+30$ MeV/c^2 and -80 MeV/c^2 $< \Delta m_{B^\pm} <$ $+70$ MeV/c^2.

Signal events are taken from a sample of truth-matched MC $B^\pm \to (K^\pm\pi^\mp\pi^+\pi^-)_D K^\pm$ decays[4] and background events are taken from collision data in the D-mass sidebands. The sidebands are defined such that $|\Delta m_{B^\pm}| < 500$ MeV/c^2 and either -98 MeV/c^2 $< \Delta m_{D^0} <$ -60 MeV/c^2 or $+40$ MeV/c^2 $< \Delta m_{D^0} <$ $+98$ MeV/c^2. To obtain the final results we use events in the region $|\Delta m_{B^\pm}| < 50$ MeV/c^2, $|\Delta m_{D^0}| < 25$ MeV/c^2.

The optimised cuts are listed in Section 7.2.6.

[4]When the optimisation was developed, this was the only MC sample available. The cuts used to select $D \to K^\pm\pi^\mp\pi^+\pi^-$ events have been adapted appropriately to select $D \to K^+K^-$ and $D \to K^\pm\pi^\mp$ events.

7.2.4 Charmonium veto

The LHCb trigger selects a significant quantity of events containing muons. It is possible that such events, particularly dimuon pairs from charmonium decays, can fake the signal we are searching for. In order to determine how frequently this occurs, we examine all possible pairs of 'muon-like' tracks of opposite charge in each event. Muon-like tracks are flagged as such by the muon stations. Each track is assigned the PDG [11] muon mass and its energy is recalculated using the relation $E^2 = \mathbf{p}^2c^2 + m^2c^4$. The invariant mass of the pair is then determined. The resulting invariant mass distribution in $B^\pm \to (K^\pm\pi^\mp)_D\pi^\pm$ data is shown in Figure 7.1. Significant quantities of events lie near the PDG J/ψ and ψ(2S) masses, indicating that there is contamination from charmonium decays to dimuons.

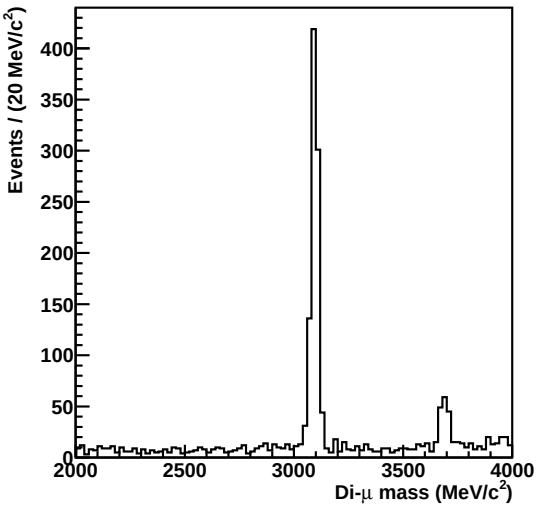

Figure 7.1: Invariant mass of pairs of muon-like tracks, both of which have been assigned a muon mass, in stripped $B^\pm \to (K^\pm\pi^\mp)_D\pi^\pm$ data.

We therefore veto any event containing a pair of muon-like tracks whose invariant mass (as calculated above) lies within 55 MeV/c^2 of either the nominal J/ψ mass or the nominal ψ(2S) mass. We test this veto on a simulated sample of $B^\pm \to J/\psi K^\pm$ decays that have been reconstructed as $B^\pm \to (K^\pm\pi^\mp)_D\pi^\pm$ and find that all events are rejected. Conversely, the veto retains 99.9% of simulated $B^\pm \to (K^\pm\pi^\mp)_D\pi^\pm$ decays.

7.2.5 Use of PID cuts

It is essential to use information about the PID of the bachelor in order to isolate $B^\pm \to DK^\pm$ decays from the much larger quantity of $B^\pm \to D\pi^\pm$ decays. To do this we cut on the bachelor $\Delta\log\mathcal{L}(K-\pi)$, defined in Equation 6.5. A relatively pure sample of $B^\pm \to DK^\pm$ can be obtained by only retaining events in which the bachelor $\Delta\log\mathcal{L}(K-\pi)$ is greater than some large value, indicating that it is very likely that the bachelor is a kaon. On the other hand, an excessively tight $\Delta\log\mathcal{L}(K-\pi)$ cut will result in a loss of statistical precision.

Cut name	Cut efficiency (%)			
	$B^\pm \to (K^\pm\pi^\mp)_D K^\pm$		$B^\pm \to (K^+K^-)_D K^\pm$	
	Signal	Background	Signal	Background
D daughter K $\Delta\log\mathcal{L}(K-\pi) > 0$	96.29 ± 0.04	42.18 ± 0.10	93.36 ± 0.09	16.49 ± 0.07
D daughter $\mathbf{p}_\mathrm{T} > 330$ MeV/c	93.05 ± 0.05	32.79 ± 0.10	90.46 ± 0.10	12.79 ± 0.06
D daughter sIP $\chi^2 > 21$	83.12 ± 0.08	11.14 ± 0.07	79.50 ± 0.14	5.71 ± 0.04
$B^\pm$ IP $\chi^2 < 9$	79.95 ± 0.08	6.38 ± 0.05	76.51 ± 0.15	3.45 ± 0.03
Bachelor K sIP $\chi^2 > 28$	77.39 ± 0.08	5.16 ± 0.05	74.12 ± 0.15	2.89 ± 0.03
D DOCA < 0.3 mm	77.30 ± 0.09	5.06 ± 0.05	74.05 ± 0.15	2.86 ± 0.03
$B^\pm$ DOCA < 0.1 mm	76.59 ± 0.09	4.59 ± 0.04	73.39 ± 0.16	2.65 ± 0.03
$B^\pm$ FD $\chi^2 > 76$	76.48 ± 0.09	4.53 ± 0.04	73.29 ± 0.16	2.62 ± 0.03
D FD $\chi^2 > 252$	71.78 ± 0.09	3.16 ± 0.04	67.74 ± 0.16	2.04 ± 0.03
$B^\pm$ DIRA > 0.99995	68.26 ± 0.09	2.69 ± 0.03	64.66 ± 0.17	1.83 ± 0.02
D DIRA > 0.992	66.44 ± 0.10	2.54 ± 0.03	62.84 ± 0.17	1.77 ± 0.02
D vertex χ^2/DOF < 6	64.03 ± 0.10	2.29 ± 0.03	60.57 ± 0.17	1.64 ± 0.02
J/ψ veto	64.03 ± 0.10	2.16 ± 0.03	60.57 ± 0.17	1.63 ± 0.02
$\psi(2S)$ veto	64.03 ± 0.10	2.14 ± 0.03	60.57 ± 0.17	1.63 ± 0.02
Bachelor K $\mathbf{p}_\mathrm{T} < 10$ GeV/c	62.47 ± 0.10	2.09 ± 0.03	59.03 ± 0.17	1.57 ± 0.02
Bachelor K $\lvert\mathbf{p}\rvert < 100$ GeV/c	57.58 ± 0.10	1.89 ± 0.03	54.63 ± 0.18	1.37 ± 0.02
D mass window ± 25 MeV/c^2	56.12 ± 0.10	N/A	53.73 ± 0.18	N/A
$B^\pm$ mass window ± 50 MeV/c^2	55.37 ± 0.10	0.25 ± 0.01	53.00 ± 0.18	0.14 ± 0.01

Table 7.3: Cut efficiencies for truth-matched MC signal and data D-mass sidebands.

A bachelor $\Delta\log\mathcal{L}(K-\pi)$ cut is not applied at this stage; in Section 8.3.5 we present additional studies to determine the optimal cut value. We do however apply a cut of $\Delta\log\mathcal{L}(K-\pi) > 0$ to any D daughters which are reconstructed as kaons, in order to remove a large pion background.

A calibration procedure is used to determine the percentage of both kaons and pions that are retained by a particular cut on the bachelor $\Delta\log\mathcal{L}(K-\pi)$. This is described in Section 7.7.

7.2.6 Selection results

Table 7.3 lists the efficiency of each selection cut on the signal and D-mass sideband background samples. The stripping cuts have already been applied to both samples. The efficiency of a particular cut is defined as the fraction of candidates that pass that cut and all previous cuts in the table. Over half of the signal events are retained, whereas over 99% of the background events are removed.

7.3 Trigger studies

In this section we evaluate the performance of the trigger hardware and software on the decays of interest to this analysis. We emulate the trigger operation by running the LHCb trigger software (Moore) on a sample of Monte Carlo data and determine which trigger lines predominantly accept events. We aim to test the trigger configurations that were actually

used when recording data, so we study the performance on some representative TCKs[5]. We use offline-selected MC samples of $B^{\pm} \to (K^{\pm}\pi^{\mp})_D h^{\pm}$ decays with approximately 10,000 events per sample.

The final states under study are all fully hadronic. It is therefore useful to focus on the performance of the trigger lines designed to select such states: the L0 hadron trigger, the HLT1 1-track trigger, and the HLT2 topological trigger. We also determine the combined selection efficiency of all lines that are designed to select events containing interesting physics[6]; this includes lines designed to select events containing charm hadrons and leptons.

Of the events selected by the trigger at each stage, we determine:

- The fraction of events in which the reconstructed $B^{\pm}$-decay candidate fired the trigger, denoted Trigger On Signal (TOS).
- The fraction of events in which something other than the reconstructed $B^{\pm}$-decay candidate fired the trigger, denoted Trigger Independent of Signal (TIS).
- The fraction of events that fired the trigger but are neither TIS nor TOS, denoted Trigger On Both (TOB)[7].

It is possible for an event to be simultaneously TOS and TIS if the trigger was fired by both the $B^{\pm}$-decay and other objects in the event. Henceforth we count such events solely as TOS.

7.3.1 Trigger efficiencies

We calculate the selection efficiency of each trigger stage using the TCK `0x002e002a`, which was used to take a significant quantity of data in 2010. In this configuration, a decay candidate will pass the L0 hadronic line if it has a transverse energy in the calorimeter greater than 3.6 GeV. Events are vetoed if the track multiplicity in the SPD is greater than 900, which ensures the average time the trigger takes to process events remains low. The standard 1-track and topological triggers are operational in the HLT[8].

The trigger efficiency is defined as the number of events that pass each trigger stage divided by the total number of events in the sample. For an event to be processed by HLT1 it must have passed one of the L0 physics triggers, and for an event to be processed by HLT2 it must have passed one of the HLT1 physics triggers.

[5] TCKs (Trigger Configuration Keys) were introduced in Section 6.3.11.3.

[6] Some trigger lines are designed for detector monitoring and calibration instead of physics.

[7] In TOB events, the trigger is fired by a combination of some (but not all) of the particles in the $B^{\pm}$-decay final state and some other tracks in the event.

[8] Detailed descriptions of these trigger lines can be found in Refs. [96] and [97].

The trigger efficiencies are listed in Table 7.4. As well as the efficiency of the total sample, efficiencies for purely B^+ and B^- decays are shown. The TOS, TIS and TOB columns show the fractions of events in each category at each stage.

Trigger	B type	$B^{\pm}\to DK^{\pm}$				$B^{\pm}\to D\pi^{\pm}$			
		Efficiency (%)	TOS (%)	TIS (%)	TOB (%)	Efficiency (%)	TOS (%)	TIS (%)	TOB (%)
L0 physics	All $B^{\pm}$	51.8 ± 0.8	74.8 ± 1.0	25.2 ± 1.0	0.0 ± 0.0	53.4 ± 0.8	72.4 ± 1.0	27.6 ± 1.0	0.0 ± 0.0
	B^+	51.2 ± 1.2	75.0 ± 1.4	25.0 ± 1.4	0.0 ± 0.0	52.9 ± 1.1	70.7 ± 1.4	29.3 ± 1.4	0.0 ± 0.0
	B^-	52.5 ± 1.2	74.6 ± 1.4	25.4 ± 1.4	0.0 ± 0.0	53.9 ± 1.2	74.4 ± 1.4	25.6 ± 1.4	0.0 ± 0.0
L0 hadron	All $B^{\pm}$	45.2 ± 0.8	84.8 ± 0.9	15.2 ± 0.9	0.0 ± 0.0	47.3 ± 0.8	80.4 ± 1.0	19.6 ± 1.0	0.0 ± 0.0
	B^+	44.6 ± 1.1	85.3 ± 1.2	14.7 ± 1.2	0.0 ± 0.0	46.8 ± 1.1	78.6 ± 1.4	21.4 ± 1.4	0.0 ± 0.0
	B^-	45.9 ± 1.2	84.2 ± 1.3	15.8 ± 1.3	0.0 ± 0.0	47.7 ± 1.2	82.2 ± 1.3	17.8 ± 1.3	0.0 ± 0.0
HLT1 Physics	All $B^{\pm}$	41.9 ± 0.8	97.3 ± 0.4	2.2 ± 0.4	0.5 ± 0.2	43.1 ± 0.8	96.9 ± 0.4	2.9 ± 0.4	0.3 ± 0.1
	B^+	40.5 ± 1.1	97.5 ± 0.6	2.0 ± 0.5	0.5 ± 0.3	42.7 ± 1.1	96.6 ± 0.6	3.1 ± 0.6	0.4 ± 0.2
	B^-	43.3 ± 1.2	97.2 ± 0.6	2.4 ± 0.5	0.4 ± 0.2	43.4 ± 1.2	97.2 ± 0.6	2.7 ± 0.6	0.1 ± 0.1
HLT1 1Track	All $B^{\pm}$	41.7 ± 0.8	97.8 ± 0.4	2.0 ± 0.4	0.3 ± 0.1	42.7 ± 0.8	97.6 ± 0.4	2.3 ± 0.4	0.1 ± 0.1
	B^+	40.4 ± 1.1	97.9 ± 0.5	1.8 ± 0.5	0.3 ± 0.2	42.4 ± 1.1	97.3 ± 0.6	2.5 ± 0.5	0.2 ± 0.2
	B^-	43.0 ± 1.2	97.7 ± 0.5	2.1 ± 0.5	0.3 ± 0.2	43.1 ± 1.2	97.9 ± 0.5	2.1 ± 0.5	0.0 ± 0.0
HLT2 Physics	All $B^{\pm}$	36.8 ± 0.8	97.9 ± 0.4	1.0 ± 0.3	1.2 ± 0.3	37.8 ± 0.8	97.8 ± 0.4	1.2 ± 0.3	1.0 ± 0.3
	B^+	35.8 ± 1.1	97.8 ± 0.6	1.0 ± 0.4	1.2 ± 0.4	37.1 ± 1.1	98.2 ± 0.5	1.1 ± 0.4	0.7 ± 0.3
	B^-	37.8 ± 1.1	98.0 ± 0.5	0.9 ± 0.4	1.2 ± 0.4	38.4 ± 1.2	97.5 ± 0.6	1.2 ± 0.4	1.3 ± 0.4
HLT2 Topo	All $B^{\pm}$	34.5 ± 0.8	98.0 ± 0.4	0.6 ± 0.2	1.4 ± 0.3	35.3 ± 0.8	98.1 ± 0.4	0.3 ± 0.2	1.6 ± 0.3
	B^+	33.4 ± 1.1	97.6 ± 0.6	0.8 ± 0.4	1.6 ± 0.5	35.0 ± 1.1	98.4 ± 0.5	0.1 ± 0.1	1.5 ± 0.5
	B^-	35.6 ± 1.1	98.4 ± 0.5	0.3 ± 0.2	1.2 ± 0.4	35.5 ± 1.1	97.9 ± 0.6	0.5 ± 0.3	1.6 ± 0.5

Table 7.4: Selection efficiency at various trigger stages on an offline-selected sample of MC $B^{\pm} \to (K^{\pm}\pi^{\mp})_D h^{\pm}$ decays. The TCK used is `0x002e002a`.

We find that events selected by the HLT hadronic lines comprise nearly all of the physics decisions and the L0 hadron line contributes about 80% of the L0 physics decision. The selection efficiency for $B^{\pm}\to D\pi^{\pm}$ decays is in general different to the efficiency for $B^{\pm}\to DK^{\pm}$ due to the slightly different kinematics of the two decays; this is relevant when determining the ratio $\mathcal{B}^{DK}/\mathcal{B}^{D\pi}$ and is discussed in Section 8.4.1. There is no significant difference between B^+ and B^- efficiencies. Most of the events are TOS, particularly at HLT level.

7.3.2 Choice of triggers

We decide to use all events accepted by the trigger, regardless of the TCK used to take the data and the particular lines that fired. The low level of background means we can be reasonably confident that the majority of events are the signal we wish to reconstruct.

At HLT level the difference between taking just the hadronic lines and taking all lines is minimal. On the other hand, the difference at L0 is more pronounced. It is therefore possible that taking all triggers leads to a bias in the final distribution of events. The systematic uncertainty associated with our choice is evaluated in Section 8.4.5.

7.4 $B^{\pm}$ mass distribution

We use the reconstructed $B^{\pm}$ mass as a discriminating variable to separate signal from background. The distribution of offline-selected events reconstructed as $B^{\pm}\to D\pi^{\pm}$ and

$B^{\pm}\to DK^{\pm}$ is shown in Figure 7.2.

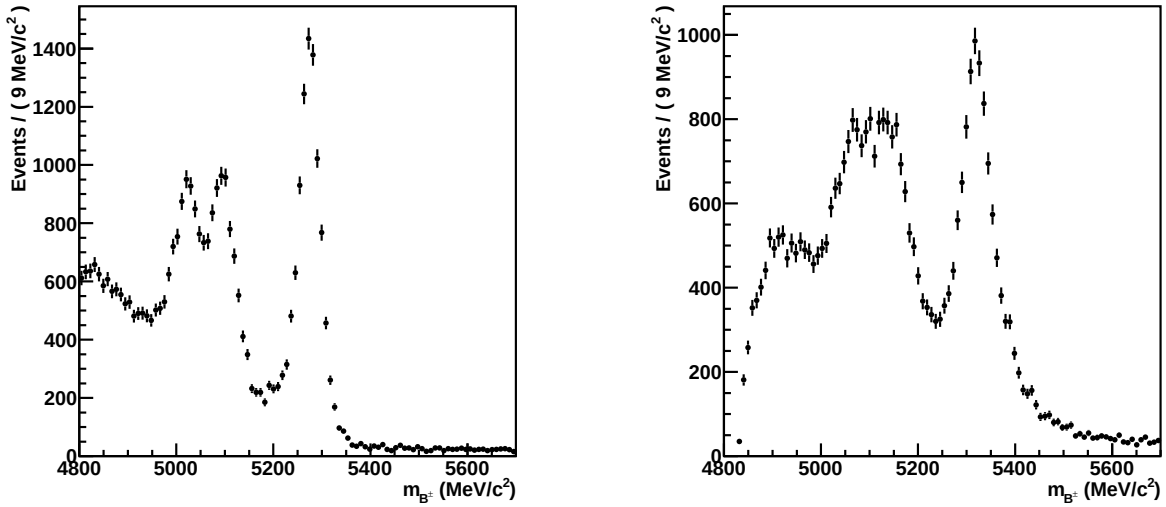

Figure 7.2: $B^{\pm}$ mass distribution in collision data reconstructed as $B^{\pm} \to (K^{\pm}\pi^{\mp})_D\pi^{\pm}$ (left) and $B^{\pm} \to (K^{\pm}\pi^{\mp})_D K^{\pm}$ (right).

A good description of the $B^{\pm}$-decay lineshape is essential to ensure the measured yields and extracted physical parameters are accurate. In Sections 7.5 and 7.6 we describe the components of this shape.

7.5 Background studies

The offline selection cuts have been optimised to reject backgrounds, but even after they are applied a significant quantity of background events remain in the dataset. In order to isolate the signal decays it is important to quantify and parameterise the various types of background that are present. In this section we consider all types of background *except* events in which the bachelor is misidentified (K as π or vice versa); such events are discussed in Section 7.6.

7.5.1 Combinatoric background

The combinatoric background, consisting of events in which random combinations of charged tracks are reconstructed as signal decays, is expected to be essentially smooth across the $B^{\pm}$ mass spectrum. We use offline-selected events from the stripping line `B2DXWithD2hhWS`, containing unphysical charge combinations of D daughter tracks, to determine the shape of this background. Figure 7.3 shows the combinatoric background scaled by a factor of 5 (to account for the prescale of 0.2), and superimposed on offline-selected events from the stripping line `B2DXWithD2hh`. It is evident that this background comprises almost all of the events in the high-mass sideband.

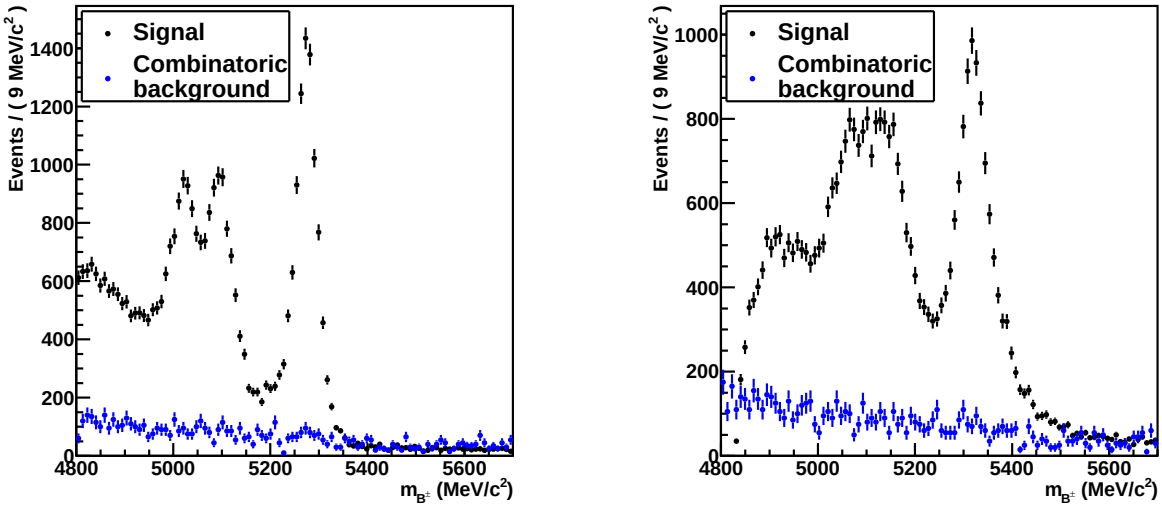

Figure 7.3: Rescaled $B^\pm$ mass distribution of events selected by the `B2DXWithD2hhWS` stripping line (blue points). The black points are events selected by the `B2DXWithD2hh` stripping line. The left plot shows events reconstructed as $B^\pm \to D\pi^\pm$ and the right plot shows events reconstructed as $B^\pm \to DK^\pm$.

We parameterise the shape of this background with a linear Chebychev polynomial [112]. A fit of this function to the data is shown in Figure 7.4. The fit parameter is (-0.62 ± 0.04) MeV/c^2.

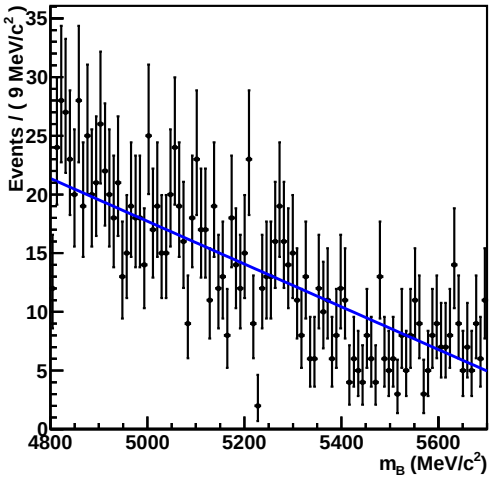

Figure 7.4: Fit of a linear Chebychev polynomial to events selected by the `B2DXWithD2hhWS` stripping line.

7.5.2 Low-mass background

Decays with a similar topology to the signal, but in which one or more particles are not reconstructed, are a significant source of background. Because some 4-momentum in the event is not accounted for in the reconstruction, these events predominantly lie at low $B^\pm$ mass.

We investigate several such decay modes that can be categorised according to the type of particle that is missed: events in which a π^0 is missed ($B^\pm \to D^{*0}(D^0\pi^0)h^\pm$, $B^\pm \to D^0\rho^\pm(\pi^\pm\pi^0)$, $B^\pm \to D^0K^{*\pm}(K^\pm\pi^0)$), events in which a γ is missed ($B^\pm \to D^{*0}(D^0\gamma)h^\pm$) and events in which a $\pi^\pm$ is missed ($B^0 \to D^{*\mp}(D^0\pi^\mp)h^\pm$, $B^0 \to D^0\rho^0(\pi^\pm\pi^\mp)$, $B^0 \to D^0K^{*0}(K^\pm\pi^\mp)$). We do not consider events in which more than one particle is missed because the resulting $B^\pm$ mass usually lies outside the range considered in the analysis.

Using Pythia and EvtGen we have generated private Monte Carlo samples of each decay, comprising 20,000 events each. In order to simulate detector resolution we convolve the resulting $B^\pm$ mass distributions with a Gaussian distribution of width 19.5 MeV/c^2, approximately the width of the $B^\pm \to D\pi^\pm$ signal peak in data. The events are then offline-reconstructed as both $B^\pm \to D\pi^\pm$ and $B^\pm \to DK^\pm$ using the cuts described in Section 7.2.6. Finally, the events are placed in a $B^\pm$ mass histogram.

We combine the reconstructed decay modes into a 'cocktail'. The $B^\pm$ mass histograms of the modes are summed, each histogram being weighted as follows:

$$\mathcal{B} \cdot \varepsilon_{\text{acc}} \cdot \varepsilon_{\text{trig}} \cdot \varepsilon_{\text{sel}} \cdot \varepsilon_{\text{PID}}, \tag{7.1}$$

where $\mathcal{B}$ is the PDG branching fraction of the mode, ε_{acc} is the fraction of events that lie within the LHCb acceptance, $\varepsilon_{\text{trig}}$ is the fraction of signal MC events passing the trigger, ε_{sel} is the fraction of events passing the offline selection in signal MC, and ε_{PID} is the fraction of events passing the bachelor PID cut. The PID efficiency is determined as described in Section 7.7.

The $B^\pm$ mass distributions of the weighted low-mass background cocktails is shown in Figure 7.5. The double peak structure is due to events in which $B^\pm$ daughters have non-zero

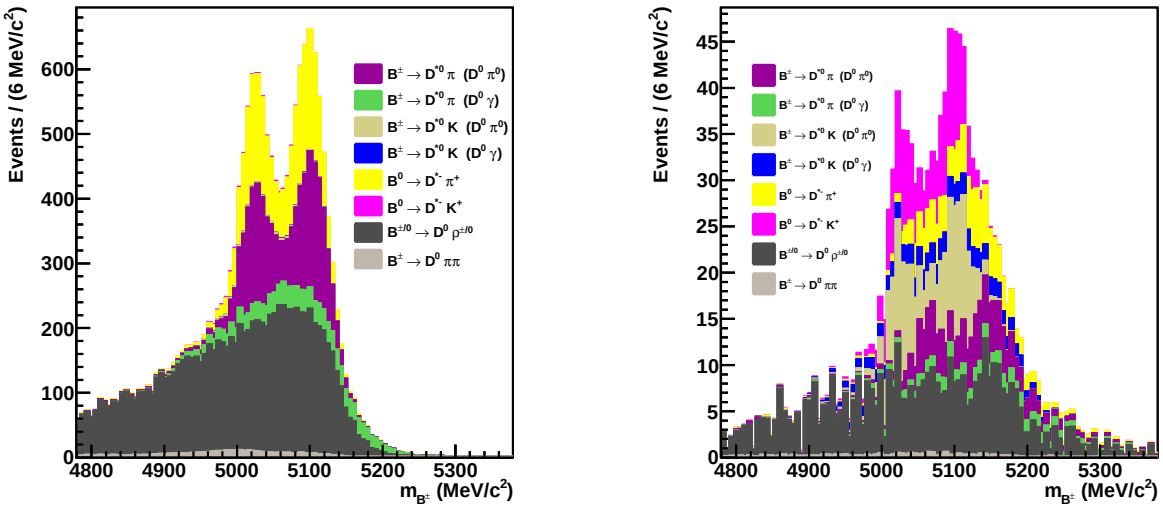

Figure 7.5: Simulated low-mass background for $B^\pm \to D\pi^\pm$ with a bachelor $\Delta\log\mathcal{L}(K-\pi)$ cut of < 4 (left) and $B^\pm \to DK^\pm$ with a bachelor $\Delta\log\mathcal{L}(K-\pi)$ cut of > 4 (right).

spin, e.g. $B^{\pm}\to D^{*}K^{\pm}$.

We use a KEYS[9] PDF[10] [113] to parameterise the sum of the histograms. A separate parameterisation is used for both $B^{\pm}\to DK^{\pm}$ and $B^{\pm}\to D\pi^{\pm}$, for each bachelor PID cut.

7.5.3 Semileptonic background

Another source of background is semileptonic $B^{\pm}$ decays which are misidentified as signal. The most prevalent decay of this type is $B^{\pm}\to D\mu^{\pm}\nu_{\mu}$ in which the muon is misidentified as a pion and the neutrino is not reconstructed. Figure 7.6 shows the distribution of events passing the baseline $B^{\pm}\to D\pi^{\pm}$ selection in data for which the bachelor has also been identified as a muon by the muon stations. We observe a rapidly rising low-mass shape which is probably caused by semileptonic $B^{\pm}$ decays. The tail of a Gaussian distribution is used to parameterise the shape of these events. There is also a small peak, centred on the $B^{\pm}$ mass, caused by events in which a genuine bachelor pion has been misidentified as a muon ('punch-through'). This is parameterised with another Gaussian distribution when fitting the tail, but is not included in the final fit to extract the observables. The Gaussian that parameterises the

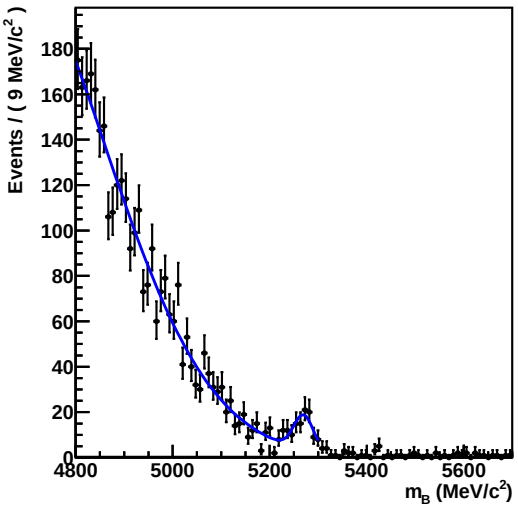

Figure 7.6: Fit of a Gaussian distribution to $B^{\pm}\to D\pi^{\pm}$ selected events in which the bachelor has also been identified as a muon. There is a small peak due to punch-through events that is parameterised with another Gaussian distribution.

semileptonic events has mean (4650 ± 50) MeV/c^2 and width (220 ± 20) MeV/c^2.

7.5.4 Charmless background

Charmless non resonant decays ($B^{\pm}\to h^{\pm}h^{+}h^{-}$) form another possible background to $B^{\pm}\to Dh^{\pm}$ decays, although several selection cuts significantly reduce the level of this background, e.g. D mass, D flight distance and $B^{\pm}$ vertex χ^2.

[9]Kernel Estimation of Your Shapes.
[10]Probability density function.

We find that the only significant contributions are from charmless decays that mimic $B^{\pm} \to (K^{+}K^{-})_{D}h^{\pm}$ final states. We determine the contribution of these backgrounds in a separate fit to data. This is described further in Section 8.3.

7.6 Signal and misID lineshapes

In this section we describe two lineshapes: firstly, the lineshape used to model signal $B^{\pm}\to Dh^{\pm}$ decays, and secondly, the lineshape used to parameterise decays in which the D and its daughters are correctly reconstructed but the bachelor is misidentified. Henceforth these lineshapes are respectively referred to as the *signal* and *misID* lineshapes.

Figure 7.7 shows the $B^{\pm}$ mass distribution of offline-selected events in $B^{\pm} \to (K^{\pm}\pi^{\mp})_{D}\pi^{\pm}$ Monte Carlo data[11]. The figures also shows the $B^{\pm}$ mass distribution for events in which the true bachelor pion has been misidentified as a kaon.

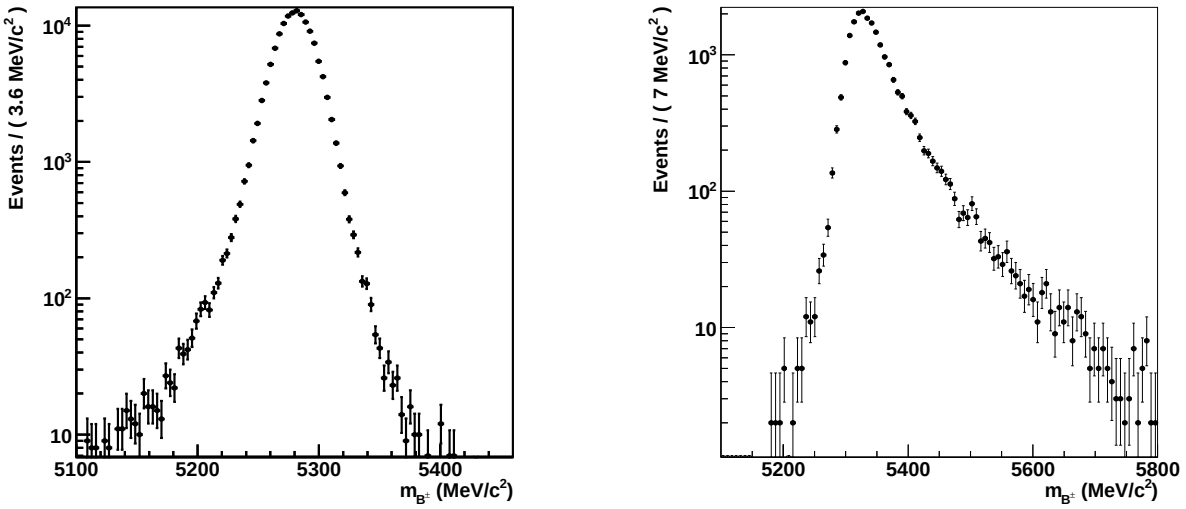

Figure 7.7: $B^{\pm}$ mass distribution in $B^{\pm} \to (K^{\pm}\pi^{\mp})_{D}\pi^{\pm}$ MC for events in which the bachelor has been correctly identified as a pion (left) and misidentified as a kaon (right).

The signal lineshape is parameterised as a detector resolution function convolved with a delta function centred on the $B^{\pm}$ mass[12].

The signal mass distribution exhibits tails at both high and low $B^{\pm}$ mass. The high-mass tail is caused by detector effects such as multiple scattering. The low-mass tail is caused by a combination of detector effects and decays in which photons are radiated but not reconstructed, causing some 4-momentum in the event to be lost.

The misID $B^{\pm}$ mass lineshape is influenced by both the detector resolution and the underlying kinematics. When the bachelor particle is assigned an incorrect mass, the resulting reconstructed $B^{\pm}$ mass can take a spectrum of values. A large tail appears in the misID

[11]The distribution in collision data has been shown in Figure 7.2.
[12]The phrases 'signal lineshape' and 'detector resolution function' are therefore interchangeable.

distribution; when the bachelor is assigned a mass that is higher than its true mass, the tail extends into the high $B^{\pm}$ mass region, and vice versa.

An initial determination of the misID lineshape using MC is described in Section 7.6.1. The signal lineshape is described in Section 7.6.2. Finally, Section 7.6.3 describes the second iteration of the misID lineshape determination using data.

7.6.1 MisID lineshape parameterisation using MC

Monte Carlo truth information is used to examine the influence of the underlying kinematics on the misID lineshape. The parameterisation of the kinematics can then be convolved with the detector resolution function in order to produce the overall misID lineshape.

To obtain a sample of misidentified events we use truth-matched $B^{\pm}\to D\pi^{\pm}$ MC. The bachelor mass is set to the PDG kaon mass and the $B^{\pm}$ mass is then computed from the 4-momenta of all final state particles in the event. Figure 7.8 shows the correlation between the reconstructed misID $B^{\pm}$ mass and the truth-level misID $B^{\pm}$ mass. There is a spike in the true

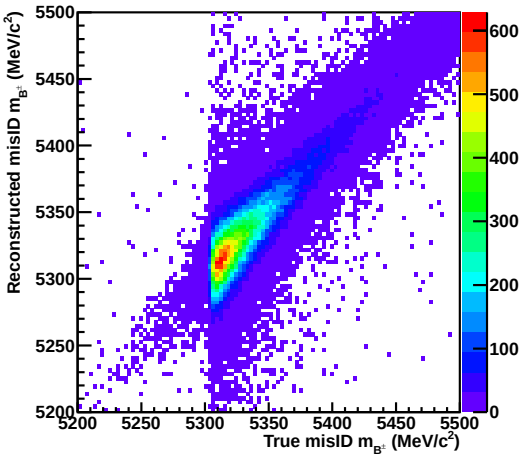

Figure 7.8: Scatter plot of the reconstructed misID $B^{\pm}$ mass against the truth-level misID $B^{\pm}$ mass in Monte Carlo $B^{\pm} \to (K^{\pm}\pi^{\mp})_D\pi^{\pm}$ events.

misID $B^{\pm}$ mass around 5310 MeV/c^2 which is broadened on reconstruction. A small number of events have a true misID $B^{\pm}$ mass below the kinematic threshold ($\sim$ 5300 MeV/c^2). These events have been ignored in the studies presented in this section.

A 'Novosibirsk' [114] function is used to parameterise the truth-level misID $B^{\pm}$ mass distribution. The form of the Novosibirsk function is:

$$\mathcal{N}(m) \equiv A \exp\left(-\frac{1}{2}\left\{\ln^2\left[1+\frac{\sinh(\tau\sqrt{\ln 4})}{\sigma\tau\sqrt{\ln 4}}\tau(m-m_0)\right]/\tau^2+\tau^2\right\}\right), \qquad (7.2)$$

where m_0 is the peak position, σ is the width of the distribution, τ is a tail parameter and A is a normalisation constant. The fit of the Novosibirsk function to MC converges

fully over a range of different bachelor $\Delta\log\mathcal{L}(K-\pi)$ cuts. Figure 7.9 shows a fit of the Novosibirsk function to the misID $B^{\pm}$ distribution in MC with both no PID cut applied and a $\Delta\log\mathcal{L}(K-\pi)$ cut of >8 applied to the bachelor. In the latter case, the fit is relatively poor in the highly-populated bins. As this is the first iteration of the misID lineshape determination, the deviation is not significant.

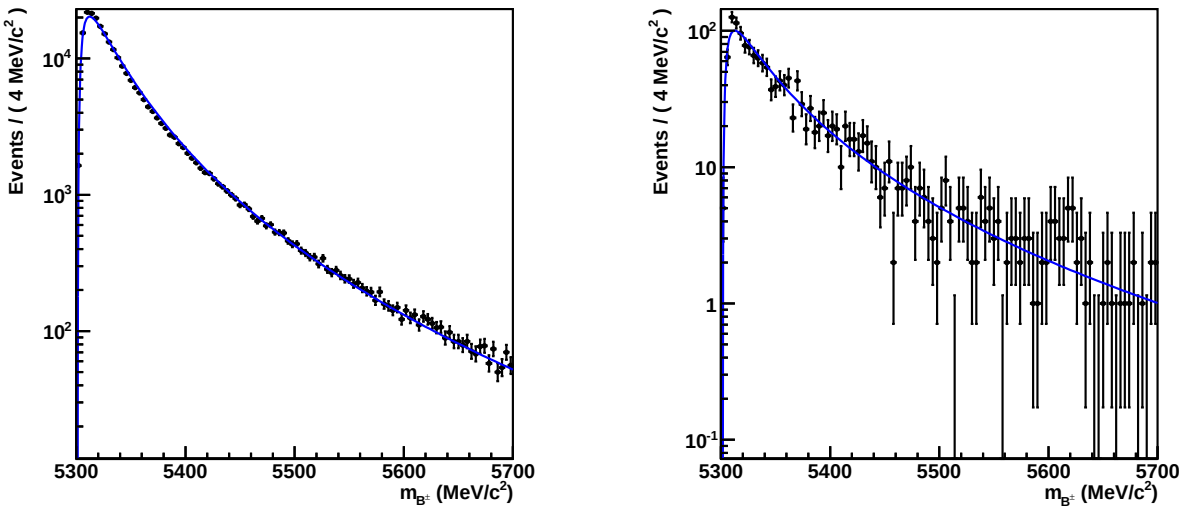

Figure 7.9: Fits of a Novosibirsk function to $B^{\pm}\to(K^{\pm}\pi^{\mp})_D\pi^{\pm}$ MC in which the bachelor pion has been misidentified as a kaon. The left plot shows the fit with no PID cuts and the right plot shows the fit with a bachelor $\Delta\log\mathcal{L}(K-\pi)$ cut of >8.

The Novosibirsk fit parameters obtained for a range of bachelor PID cuts are listed in Table 7.5. In true $B^{\pm}\to D\pi^{\pm}$ data, tighter $\Delta\log\mathcal{L}(K-\pi)$ cuts will leave only badly-

Parameter	Bachelor $\Delta\log\mathcal{L}(K-\pi)>$						
	no cut	0	2	4	6	8	10
m_0(MeV/c^2)	5311	5306	5307	5308	5311	5318	5335
σ(MeV/c^2)	12.5	5.2	7.4	11.1	16.9	29.3	39.3
τ	1.12	1.22	1.34	1.41	1.42	1.29	0.87

Table 7.5: Novosibirsk parameters obtained by fitting to $B^{\pm}\to D\pi^{\pm}$ MC in which the bachelor pion has been misidentified as a kaon.

reconstructed events, so the $B^{\pm}$ mass distribution will consequently be broader due to greater uncertainty on the kinematics. This is reflected by the fact that σ increases with $\Delta\log\mathcal{L}(K-\pi)$ cut.

7.6.2 Signal lineshape parameterisation

We determine the parameterisation of the signal lineshape by fitting lineshapes to $B^{\pm}\to(K^{\pm}\pi^{\mp})_D\pi^{\pm}$ collision data and MC. The sample is made as pure as possible by requiring

the bachelor $\Delta \log \mathcal{L}(K-\pi) < -2$. This ensures that there is minimal contamination from $B^{\pm} \to DK^{\pm}$ decays.

We consider several candidate PDFs to model the detector resolution function: a Gaussian distribution, a Crystal Ball distribution, the sum of two Gaussian distributions with a common mean and different widths, the sum of a Gaussian distribution and a Crystal Ball distribution with a common mean and different widths, the sum of two Crystal Ball distributions with a common mean and width, and a 'Cruijff' PDF.

The Crystal Ball PDF [115] is a Gaussian distribution with a power-law tail. This PDF is usually used to model mass distributions accounting for radiative decays. The functional form of the Crystal Ball PDF is:

$$\mathcal{C}(m) \equiv \begin{cases} \exp\left(-\frac{1}{2}t^2\right) & (t \geq -|\alpha|) \\ \frac{A}{(B-t)^n} & (t < -|\alpha|) \end{cases} \tag{7.3}$$

where $t \equiv \alpha/|\alpha| \cdot (m-m_0)/\sigma$, σ is the width of the distribution, α defines where the power law tail begins, m_0 is the peak mass, $A \equiv (n/|\alpha|)^n \cdot \exp\left(-\frac{1}{2}|\alpha|^2\right)$, $B \equiv (n/|\alpha| - |\alpha|)$ and n is the power law exponent.

The Cruijff PDF $\mathcal{J}(m)$ is a Gaussian distribution with a modified tail component:

$$\mathcal{J}(m) \equiv \exp\left\{-\frac{(m-m_0)^2}{2\sigma^2 + \alpha(m-m_0)^2}\right\}, \qquad \text{where } \alpha = \begin{cases} \alpha_L & m \leq m_0 \\ \alpha_R & m > m_0, \end{cases} \tag{7.4}$$

σ is the width of the distribution, α_L and α_R are tail parameters and m_0 is the peak mass.

Figures 7.10–7.11 show fits of some of the candidate models to MC. For each fit we have included a plot of the pull r_i in each bin, defined as $r_i \equiv (\nu_i - n_i)/\sqrt{n_i}$. Figures 7.12–7.13 show fits of some of the candidate models to data.

It is essential that the signal PDF fits the data well and converges over different fit ranges and background distributions. The PDF must not contain too many free parameters which may result in non-convergence of the fit. It is also desirable to be able to determine all of the PDF parameters by fitting to data, rather than fitting first to MC and then fixing the parameters when fitting to data.

We use the Pearson χ^2 test statistic [75, 116] to determine the goodness of fit of each PDF. For binned data, the statistic is defined as:

$$\chi^2 \equiv \sum_{i=1}^{\mathcal{N}_b} \frac{(n_i - \nu_i)^2}{\nu_i}, \tag{7.5}$$

where $\mathcal{N}_b$ is the number of bins, n_i is the measured yield in the i^{th} bin and ν_i is the expected

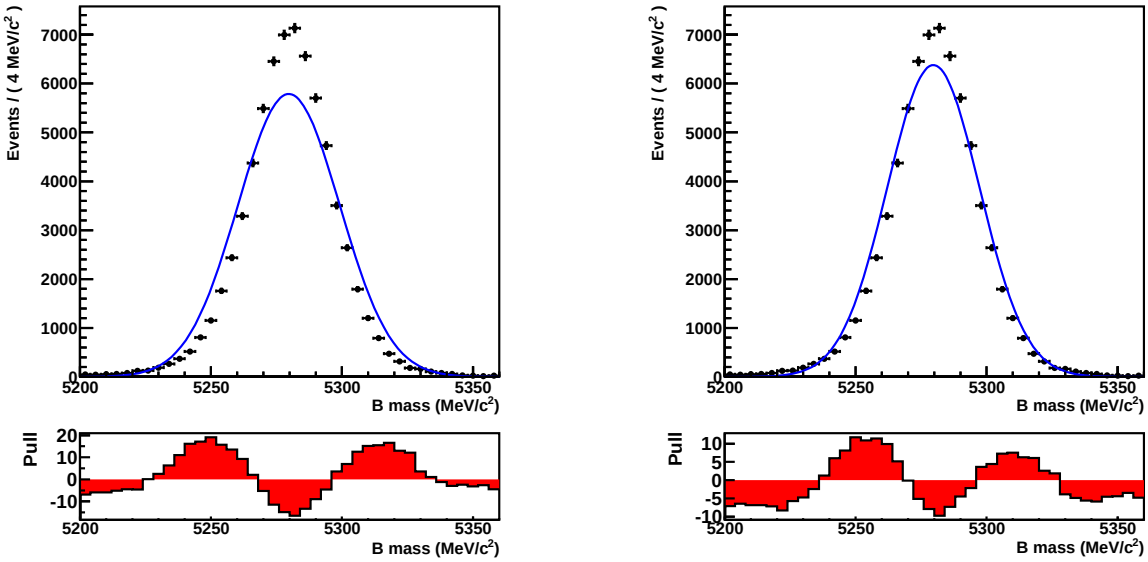

Figure 7.10: Fit of a Gaussian distribution (left) and the sum of two Gaussian distributions (right) to $B^{\pm}\to D\pi^{\pm}$ MC. The data points are black and the fit function is the blue curve. The pull values in each bin are shown below the main plot.

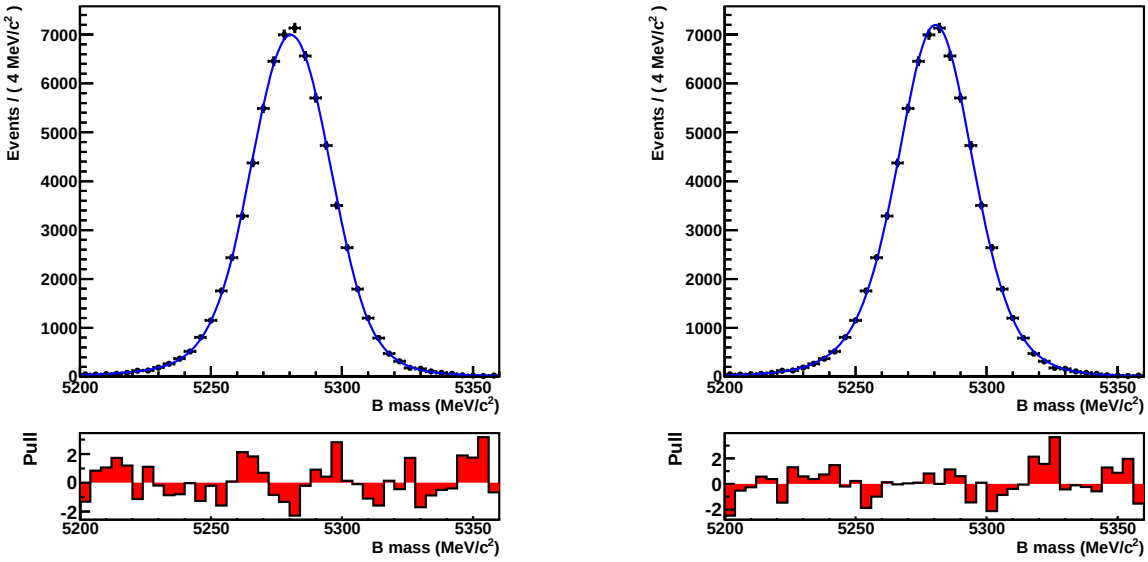

Figure 7.11: Fit of the sum of two Crystal Ball distributions (left) and a Cruijff function (right) to $B^{\pm}\to D\pi^{\pm}$ MC. The data points are black and the fit function is the blue curve. The pull values in each bin are shown below the main plot.

yield in that bin using the fit model. For $\mathcal{N}_p$ free parameters the number of degrees of freedom is $\mathcal{N}_d \equiv \mathcal{N}_b - \mathcal{N}_p - 1$. For each model considered, the p-value is obtained from the calculated χ^2.

When determining the Pearson χ^2 test statistic we use the same binning for each function. We concentrate on the central region which contains the vast majority of events, using 40 bins in the range 5200 MeV/c^2 $< m_{B^{\pm}} <$ 5360 MeV/c^2. If the expected frequency in a bin is less than five, we discard the contribution from that bin and reduce the number of

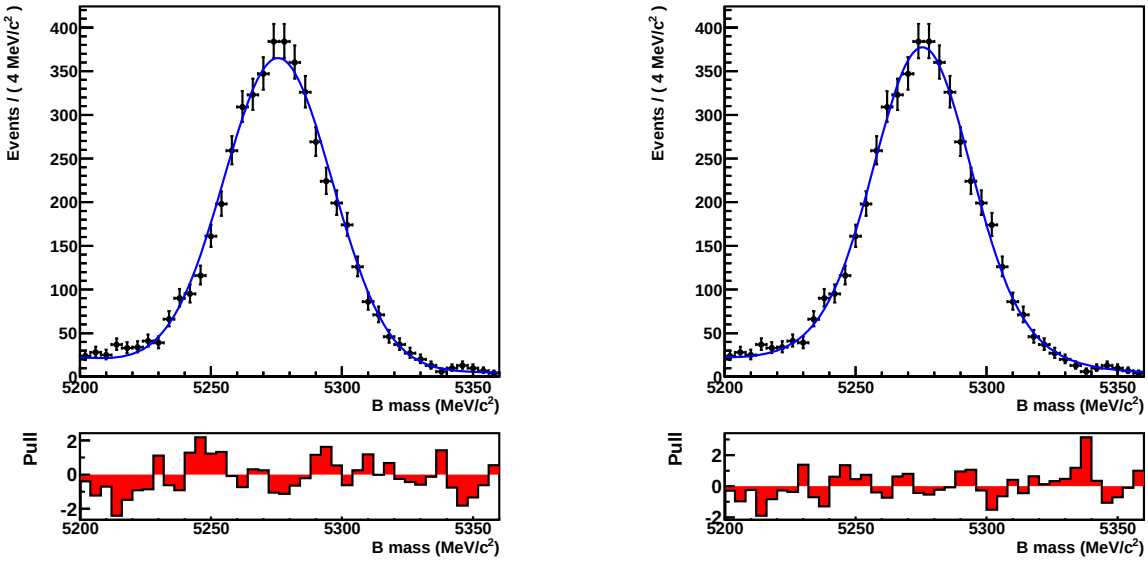

Figure 7.12: Fit of a Gaussian distribution (left) and the sum of two Gaussian distributions (right) to $B^{\pm}\to D\pi^{\pm}$ data. The data points are black and the fit function is the blue curve. The pull values in each bin are shown below the main plot.

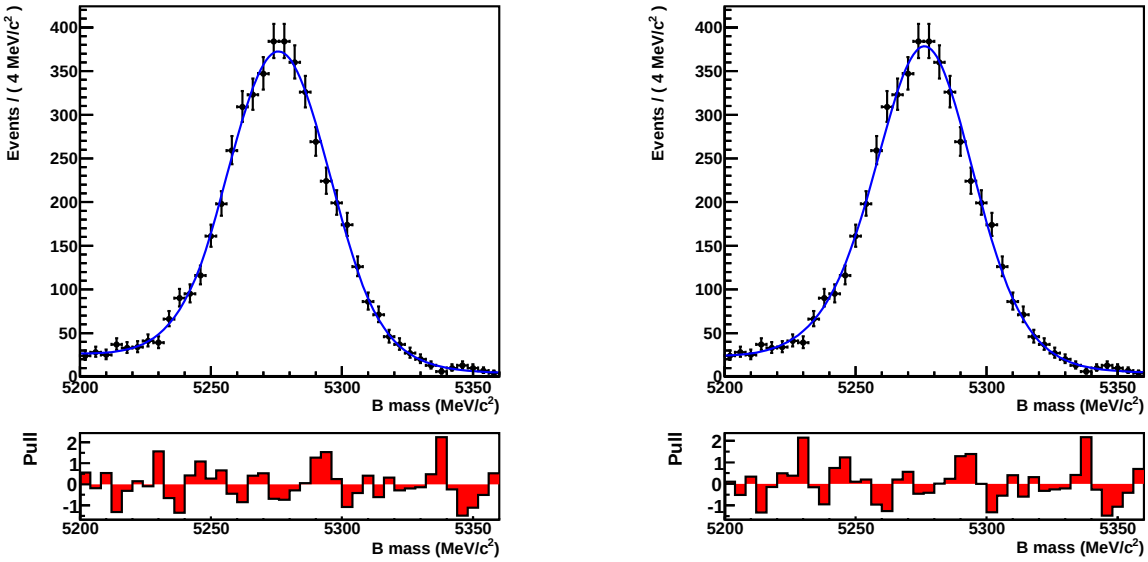

Figure 7.13: Fit of the sum of two Crystal Ball distributions (left) and a Cruijff function (right) to $B^{\pm}\to D\pi^{\pm}$ data. The data points are black and the fit function is the blue curve. The pull values in each bin are shown below the main plot.

degrees of freedom by 1. We include both signal and background components (described in Section 7.5) in the fit. The shape of each background component is fixed but the yields are allowed to float. Table 7.6 lists the Pearson χ^2 and corresponding p-value for fits of each model considered.

The p-values from the fits to data are unable to rule any of the PDFs out as a suitable model at a significance level of 5%. Considering the other criteria outlined above (stability over different fit ranges, relatively few free parameters, etc.), we decide to use the Cruijff

PDF	Pearson χ^2	$\mathcal{N}_d$	p-value
Gaussian	50.8	37	0.065
Crystal Ball	30.9	35	0.665
Double Gaussian	40.9	35	0.226
Gaussian + Crystal Ball	30.9	33	0.571
Double Crystal Ball	26.9	32	0.724
Cruijff	28.1	35	0.791

Table 7.6: χ^2 and p-values of different candidate lineshapes that have been fit to data.

PDF to parameterise the signal lineshape. PDFs involving the Crystal Ball distribution often suffer from convergence problems if the tail parameters are allowed to float. The tail shapes must therefore be fixed using a separate fit to MC, which is undesirable. By visual inspection, the Cruijff seems to provide one of the best fits to the data and MC; additionally the pulls in each bin are consistently low which is not true for many of the other PDFs considered.

Table 7.7 shows the Cruijff PDF fit parameters for $B^\pm \to (K^\pm\pi^\mp)_D h^\pm$ data and Monte Carlo with various $\Delta\log\mathcal{L}(K-\pi)$ cuts on the bachelor particle. The parameters have been defined in Equation 7.4.

Bachelor $\Delta\log\mathcal{L}(K-\pi)$ cut	α_L	α_R	m_0 (MeV/c^2)	σ (MeV/c^2)
		$B^\pm\to D\pi^\pm$ MC		
no cut	0.1217 ± 0.0009	0.0961 ± 0.0011	5280.56 ± 0.05	14.11 ± 0.04
< 0	0.1210 ± 0.0010	0.0941 ± 0.0012	5280.55 ± 0.05	14.06 ± 0.04
< 2	0.1212 ± 0.0010	0.0947 ± 0.0012	5280.56 ± 0.05	14.09 ± 0.04
< 4	0.1212 ± 0.0009	0.0954 ± 0.0011	5280.55 ± 0.05	14.10 ± 0.04
< 6	0.1214 ± 0.0009	0.0955 ± 0.0011	5280.55 ± 0.05	14.10 ± 0.04
< 8	0.1215 ± 0.0009	0.0956 ± 0.0011	5280.56 ± 0.05	14.11 ± 0.04
		$B^\pm\to DK^\pm$ MC		
no cut	0.1110 ± 0.0010	0.0923 ± 0.0012	5280.72 ± 0.05	13.80 ± 0.04
> 0	0.1102 ± 0.0010	0.0912 ± 0.0012	5280.72 ± 0.05	13.78 ± 0.04
> 2	0.1098 ± 0.0010	0.0909 ± 0.0012	5280.72 ± 0.05	13.73 ± 0.04
> 4	0.1097 ± 0.0011	0.0903 ± 0.0012	5280.73 ± 0.05	13.67 ± 0.04
> 6	0.1091 ± 0.0011	0.0896 ± 0.0013	5280.73 ± 0.05	13.62 ± 0.04
> 8	0.1095 ± 0.0011	0.0892 ± 0.0013	5280.74 ± 0.05	13.55 ± 0.04
		$B^\pm\to D\pi^\pm$ data		
no cut	0.148 ± 0.023	0.081 ± 0.013	5275.8 ± 0.4	19.03 ± 0.42
< -2	0.054 ± 0.028	0.077 ± 0.013	5275.8 ± 0.4	19.11 ± 0.47

Table 7.7: Cruijff PDF fit parameters for fits to $B^\pm \to (K^\pm\pi^\mp)_D h^\pm$ data and Monte Carlo with various bachelor PID cuts.

In fits to MC, m_0 is approximately equal to the PDG $B^\pm$ mass, whereas on data it is a few MeV/c^2 lower. This is because the alignment and magnetic field map used in 2010 caused a shift in the mass scale. As the PID cut is tightened, the width of the $B^\pm\to DK^\pm$ distribution decreases; this reflects the fact that with tighter cuts a purer signal sample is

retained. The values of α_L and α_R exhibit some variation with PID cuts. In general, a tighter PID cut causes a decrease in both quantities, indicating that the non-Gaussian tails are being suppressed. The tail parameters for $B^{\pm}\to D\pi^{\pm}$ and $B^{\pm}\to DK^{\pm}$ are different, which must be accounted for in the final fit.

7.6.3 MisID lineshape parameterisation using data

In Section 7.6.1 we used a Novosibirsk function to parameterise the underlying kinematics of $B^{\pm}$ decays in which the bachelor is misidentified. This function can be convolved with the Cruijff PDF to obtain a complete misID lineshape. However, while this is good for a first approximation, a shape derived from data is preferable. We use an iterative approach to determine such a shape.

We perform a fit to the $B^{\pm}$ mass distribution in $B^{\pm}\to D\pi^{\pm}$ data without applying a bachelor $\Delta\log\mathcal{L}(K-\pi)$ cut[13]. As well as the signal and background PDFs, we now include a misidentification component consisting of a Cruijff PDF convolved with a Novosibirsk function. The Cruijff parameters are floating and are common to both the signal and misID shapes. The Novosibirsk parameters are fixed to the values determined by fitting to MC. We also constrain the ratio between the misID yield and the signal yield to be 7.6%, the world-average value of $\mathcal{B}^{DK}/\mathcal{B}^{D\pi}$. The fit to data is shown in Figure 7.14.

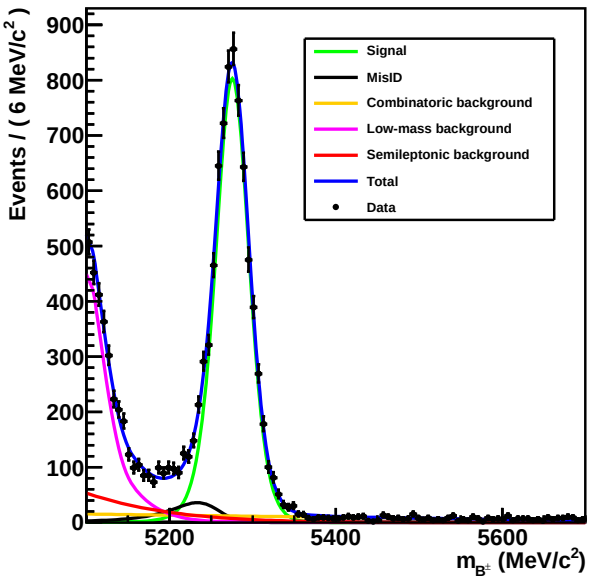

Figure 7.14: Fit to $B^{\pm}\to(K^{\pm}\pi^{\mp})_D\pi^{\pm}$ data. The black points are data and the blue curve shows the overall PDF used in the fit. The green curve is the signal component (modelled with a Cruijff PDF) and the black curve is the misID component (modelled with the convolution of the same Cruijff and a Novosibirsk PDF). The red curve is the semileptonic background component, the orange curve is the combinatoric background, and the purple curve is the low-mass background.

[13]In the following discussion we therefore do not need to consider the PID efficiency.

We then weight the fitted dataset. Given the signal PDF $\mathcal{S}(m_{B^\pm})$ and the total PDF $\mathcal{T}(m_{B^\pm})$, the weight for an event of mass $m_{B^\pm}$ is equal to $\mathcal{S}(m_{B^\pm})/\mathcal{T}(m_{B^\pm})$. By construction the weight lies between 0 and 1. We reassign the mass of the bachelor from $m_{\pi^\pm}$ to $m_{K^\pm}$ in each event and determine the resulting weighted misID $B^\pm$ mass spectrum. The mass distributions of weighted and unweighted events, for both a correctly identified and a misidentified bachelor, are shown in Figure 7.15.

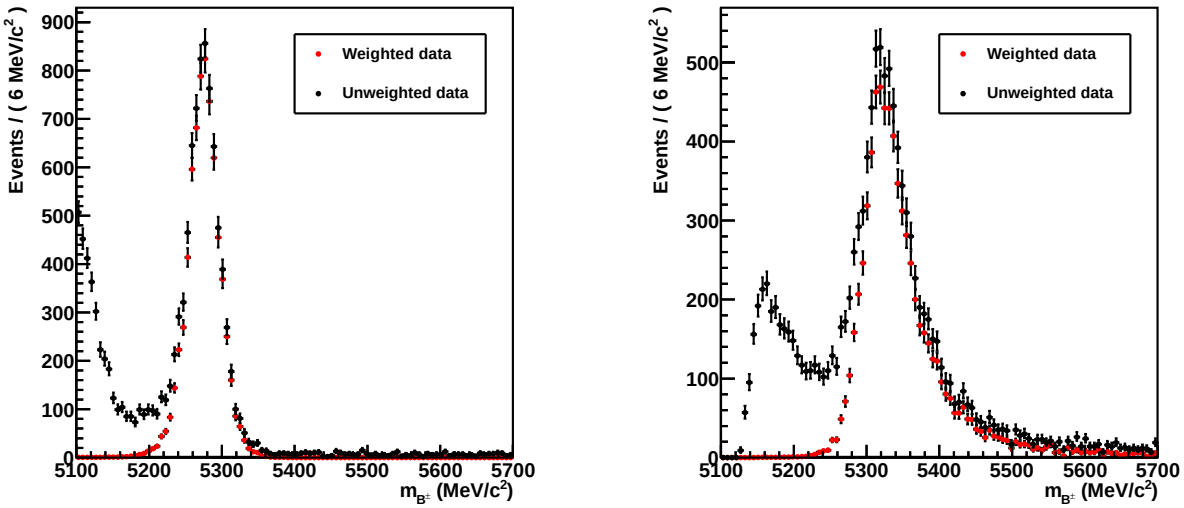

Figure 7.15: Weighted (red) and unweighted (black) $B^\pm$-mass distributions for $B^\pm \to (K^\pm\pi^\mp)_D\pi^\pm$ data in which the bachelor has been correctly identified as a pion (left) and misidentified as a kaon (right). The weighting procedure is detailed in the text.

We parameterise the shape of the weighted misidentified events with just one function, as opposed to convolving a resolution function with the Novosibirsk lineshape. We find that a Double Crystal Ball (DCB) distribution is an excellent description of this shape and is robust for a variety of bachelor PID cuts. The DCB is the same as a Crystal Ball distribution (Equation 7.3) but with one upper and one lower power law tail. There are consequently six free parameters: the mean m_0, the width σ, and the two sets of tail parameters $n_{\text{hi,lo}}$ and $\alpha_{\text{hi,lo}}$. We do not list the parameters here because, as described below, the final values are obtained by iterating this procedure. The DCB fit to misidentified $B^\pm \to (K^\pm\pi^\mp)_D\pi^\pm$ data both with and without a bachelor PID cut is shown in Figure 7.16.

7.6.3.1 Scaling the misID shape

We have determined the DCB parameters for events in which the bachelor pion is misidentified as a kaon (the *high-mass* misID shape), and we wish to know the equivalent parameters for the opposite situation (the *low-mass* misID shape). It is unfeasible to use a data-driven approach to determine the low-mass parameters because the number of $B^\pm \to DK^\pm$ events is small. We therefore determine these parameters by scaling the high-mass parameters found in data by the ratio of low-mass to high-mass parameters in MC. For each fit parameter x

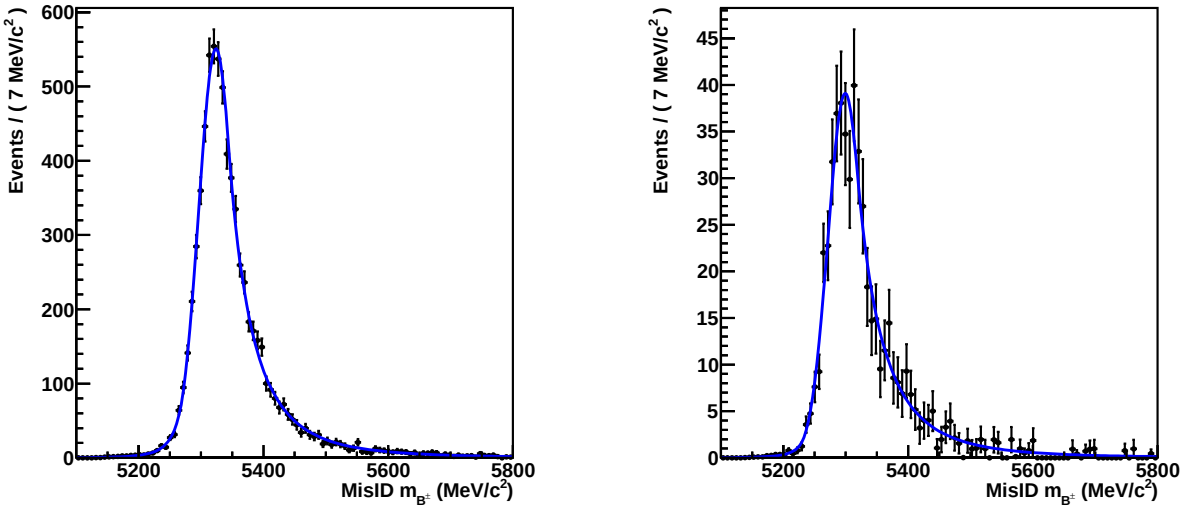

Figure 7.16: Fits of a Double Crystal Ball function to data in which the bachelor has been misidentified and weighting has been applied, for $B^\pm \to (K^\pm\pi^\mp)_D\pi^\pm$ data. The left plot shows the fit without a bachelor PID cut and the right plot shows the fit with a bachelor $\Delta\log\mathcal{L}(K-\pi)$ cut > 4.

we determine the low-mass value as follows:

$$x_{\rm lo}^{\rm data} = x_{\rm hi}^{\rm data} \cdot \frac{x_{\rm lo}^{\rm MC}}{x_{\rm hi}^{\rm MC}} \tag{7.6}$$

where the superscript indicates the data type and the subscript indicates high or low mass.

This procedure is followed for all parameters except the mean mass, for which the values obtained in MC and data behave differently. We scale the high-mass DCB mean as follows:

$$m_D^{\rm data,lo} = m_C^{\rm data,lo} - (m_C^{\rm MC,lo} - m_D^{\rm MC,lo}) \cdot \frac{(m_D^{\rm data,hi} - m_C^{\rm data,hi})}{(m_D^{\rm MC,hi} - m_C^{\rm MC,hi})} \tag{7.7}$$

where m_D is the DCB mean, m_C is the Cruijff mean and the superscript indicates the datatype. We do not show the scaled values here because they are redetermined after an iteration as described below.

7.6.3.2 Iterating on the misID lineshape

We now determine the final parameterisation of the misID lineshape. We use the low-mass DCB as the misID component in a new fit to $B^\pm\to D\pi^\pm$ data, shown in Figure 7.17. The same backgrounds are included in the fit and the ratio between the misID and signal yields is set to 7.6%. The fit is similar, but not identical, to the one in which a Cruijff convolved with a Novosibirsk is used to model the misID shape (Figure 7.14).

The weighting procedure described above is used again. As before, the bachelor mass is reassigned and new DCB parameters are determined. The DCB parameters for different D final states are listed in Tables 7.8–7.9. Within uncertainties, the values of $\alpha_{\rm lo,hi}$ and $n_{\rm lo,hi}$

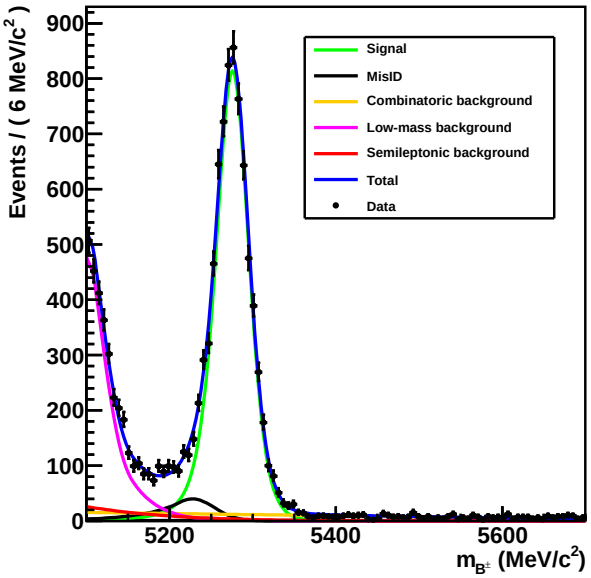

Figure 7.17: Fit to $B^\pm \to (K^\pm\pi^\mp)_D\pi^\pm$ data. The black points are data and the blue curve shows the overall PDF used in the fit. The green curve is the signal component (modelled with a Cruijff PDF) and the black curve is the misID component (modelled with a Double Crystal Ball PDF). The red curve is the semileptonic background component, the orange curve is the combinatoric background, and the purple curve is the low-mass background.

Bachelor $\Delta\log\mathcal{L}(K-\pi)$ cut	$\alpha_{\rm lo}$	$\alpha_{\rm hi}$	$n_{\rm lo}$	$n_{\rm hi}$	m_0 (MeV/c^2)	σ (MeV/c^2)
no cut	1.91 ± 0.12	-0.743 ± 0.036	4.2 ± 1.1	3.81 ± 0.31	5323.8 ± 0.7	27.5 ± 0.7
> 0	2.03 ± 0.32	-0.929 ± 0.111	4.7 ± 6.1	2.91 ± 0.55	5308.4 ± 1.7	29.0 ± 1.5
> 2	2.33 ± 0.57	-0.749 ± 0.062	2.8 ± 6.5	3.93 ± 0.86	5303.4 ± 1.7	28.3 ± 1.3
> 4	2.35 ± 0.55	-0.690 ± 0.123	2.7 ± 6.5	3.82 ± 1.18	5299.2 ± 2.9	27.6 ± 2.2
> 6	1.75 ± 0.57	-0.468 ± 0.109	6.6 ± 5.7	5.17 ± 2.05	5288.3 ± 3.9	20.6 ± 3.7
> 8	1.55 ± 0.69	-0.461 ± 0.124	8.9 ± 6.4	4.35 ± 1.82	5284.0 ± 3.3	17.6 ± 2.7

Table 7.8: Double Crystal Ball parameters obtained from fits to weighted $B^\pm \to (K^\pm\pi^\mp)_D\pi^\pm$ data in which the bachelor pion has been misidentified as a kaon.

Bachelor $\Delta\log\mathcal{L}(K-\pi)$ cut	$\alpha_{\rm lo}$	$\alpha_{\rm hi}$	$n_{\rm lo}$	$n_{\rm hi}$	m_0 (MeV/c^2)	σ (MeV/c^2)
no cut	1.82 ± 0.21	-0.809 ± 0.125	2.0 ± 5.0	2.22 ± 0.42	5321.2 ± 2.2	27.4 ± 2.2
> 0	1.50 ± 0.79	-0.922 ± 0.252	2.8 ± 1.5	1.15 ± 0.33	5299.8 ± 3.9	22.6 ± 4.1
> 2	1.59 ± 0.74	-0.876 ± 0.294	2.8 ± 4.5	1.20 ± 0.43	5297.6 ± 5.1	25.2 ± 5.2
> 4	1.58 ± 0.96	-1.100 ± 0.257	3.4 ± 4.0	0.93 ± 0.31	5296.6 ± 3.7	23.5 ± 3.6
> 6	1.86 ± 0.29	-1.231 ± 0.311	2.0 ± 4.8	0.79 ± 0.32	5297.1 ± 4.6	24.8 ± 4.4
> 8	1.50 ± 0.90	-0.725 ± 0.292	2.0 ± 6.6	1.03 ± 0.31	5283.5 ± 4.4	12.6 ± 4.1

Table 7.9: Double Crystal Ball parameters obtained from fits to weighted $B^\pm \to (K^+K^-)_D\pi^\pm$ data in which the bachelor pion has been misidentified as a kaon.

do not change significantly with the bachelor PID cut. As the PID cut value increases, m_0 decreases towards the nominal $B^\pm$ mass. σ stays approximately constant until very high cut values are reached, at which point it decreases. The fit values for different D final states are approximately equal, excepting m_0 which differs significantly between modes. This is because the D is reconstructed before the $B^\pm$; the D kinematics are determined by the particular final state and this leads to different constraints on the reconstructed $B^\pm$ kinematics. As before, these shapes are scaled using ratios in Monte Carlo in order to obtain the equivalent

low-mass shapes. The values of the parameters for the low-mass DCB shape are shown in Table 7.10.

D decay mode	$\alpha_{\rm lo}$	$\alpha_{\rm hi}$	$n_{\rm lo}$	$n_{\rm hi}$	m_0 (MeV/c^2)	σ (MeV/c^2)
$K^\pm\pi^\mp$	0.606	−2.78	9.47	5.07	5227.6	26.3
K^+K^-	0.567	−2.38	6.93	85.2	5231.5	23.7

Table 7.10: Low-mass Double Crystal Ball parameters obtained by scaling their high-mass equivalents according to MC.

7.7 PID Calibration

7.7.1 Concept

As mentioned in Section 7.2.5, we apply a PID cut to the bachelor in $B^\pm\to Dh^\pm$ decays in order to distinguish $B^\pm\to DK^\pm$ from $B^\pm\to D\pi^\pm$. In order to determine the efficiency of such a cut on both kaons and pions we use an independent high statistics *calibration* sample of $D^{*\pm}\to D(K^\pm\pi^\mp)\pi^\pm$ events[14]. Purely kinematic cuts are applied to the data in order to isolate separate samples of kaons and pions.

It is important to ensure that each calibration sample has similar kinematic properties to the signal decay under study (denoted the *reference* sample). We therefore reweight each calibration sample such that it resembles the reference sample as much as possible. To do this, we identify variables that are thought to be representative of the sample as whole; for $B^\pm\to Dh^\pm$ decays, we use the bachelor $|\mathbf{p}|$, the bachelor η and the number of tracks in each event, $n_{\rm tracks}$.

Each calibration sample is reweighted such that its distribution in these variables matches the distribution in the reference sample as closely as possible. We then expect that the resulting $\Delta\log\mathcal{L}(K-\pi)$ distributions of the calibration samples will match the $\Delta\log\mathcal{L}(K-\pi)$ distributions of the reference samples and can be used to infer the efficiencies of the PID cuts applied. Imperfections in this procedure are accounted for using a systematic uncertainty as detailed in Section 8.4.2.

7.7.2 Samples for PID calibration

Reference samples of signal data are produced for the PID calibration procedure. Different D final states have different kinematic spectra, so we make a separate reference sample for each one. To ensure the reference samples are as pure as possible we use the sPlot [118, 119] technique to isolate the signal component.

[14] For a detailed description of the procedure see Ref. [117].

The sPlot technique can be used to distinguish signal events from a sample that contains several types of background. An extended maximum likelihood fit is performed to determine the yield of each of the types of event, using one or more discriminating variables to do so (in this case, $B^{\pm}$ mass). The covariance matrix of the fit is used to calculate an 'sWeight' for each event in the sample[15]. The distribution of separate 'control' variables in the signal and background samples can be inferred from the sWeighted dataset (in this analysis, the control variables are the bachelor $\Delta\log\mathcal{L}(K-\pi)$, $|\mathbf{p}|$, η and n_{tracks}). The sWeighted distributions of the control variables in the signal sample will be nominally free of background events, without the need for any further selection criteria. Because sWeights are calculated from the fit covariance matrix they can be negative.

Figures 7.18 and 7.19 show the sWeighted bachelor $\Delta\log\mathcal{L}(K-\pi)$ distributions for each final state considered.

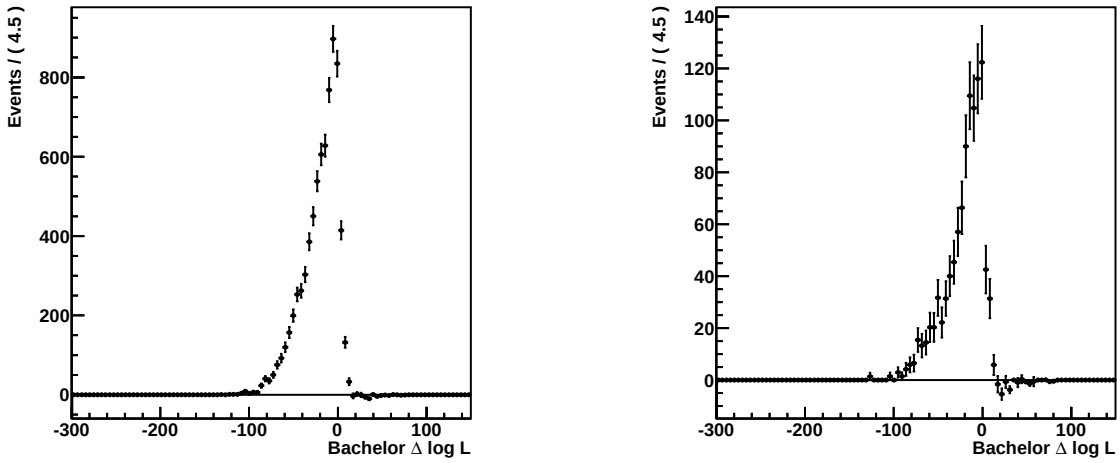

Figure 7.18: sWeighted bachelor $\Delta\log\mathcal{L}(K-\pi)$ distribution for $B^{\pm}\to(K^{\pm}\pi^{\mp})_D\pi^{\pm}$ (left) and $B^{\pm}\to(K^{+}K^{-})_D\pi^{\pm}$ (right) data.

The sWeighted bachelor $\Delta\log\mathcal{L}(K-\pi)$ for $B^{\pm}\to DK^{\pm}$ decays lies predominantly in the range $\Delta\log\mathcal{L}(K-\pi)>0$, as expected for kaons. The opposite is true for the sWeighted $\Delta\log\mathcal{L}(K-\pi)$ in $B^{\pm}\to D\pi^{\pm}$ decays, which lies mostly in the range $\Delta\log\mathcal{L}(K-\pi)<0$. In both cases, this indicates that the sPlot procedure has isolated a relatively pure sample of signal events from the dataset.

7.7.3 Calibration on data

Each sWeighted reference sample is divided into 18 bins of bachelor $|\mathbf{p}|$, 4 bins of bachelor η and 4 bins of n_{track}. The number of events in each bin of each reference sample is then determined. The calibration samples of kaons and pions are binned in the same fashion

[15]The expression to calculate sWeights can be found in Refs. [118,119].

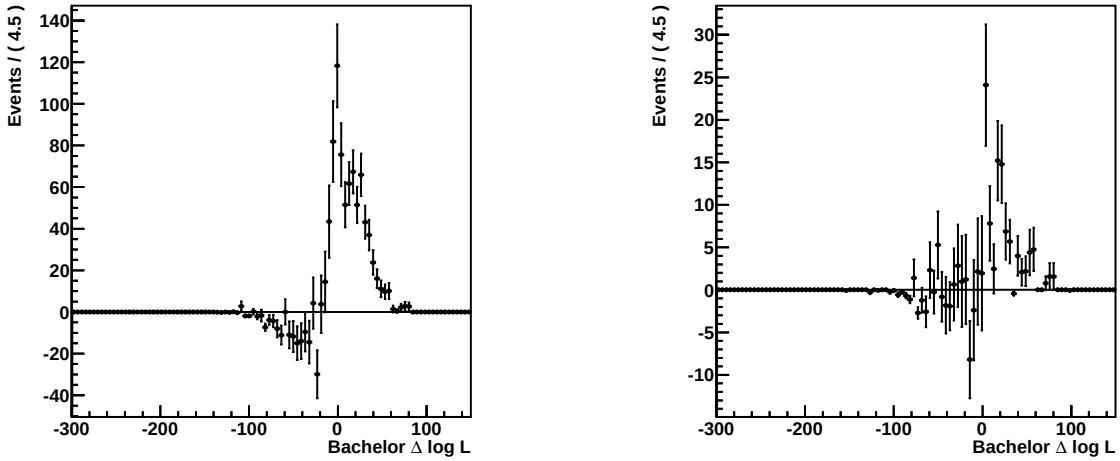

Figure 7.19: sWeighted bachelor $\Delta\log\mathcal{L}(K-\pi)$ distribution for $B^{\pm}\to(K^{\pm}\pi^{\mp})_D K^{\pm}$ (left) and $B^{\pm}\to(K^{+}K^{-})_D K^{\pm}$ (right) data.

and weighted accordingly. The resulting $\Delta\log\mathcal{L}(K-\pi)$ distributions in the reference and weighted calibration samples are shown in Fig. 7.20.

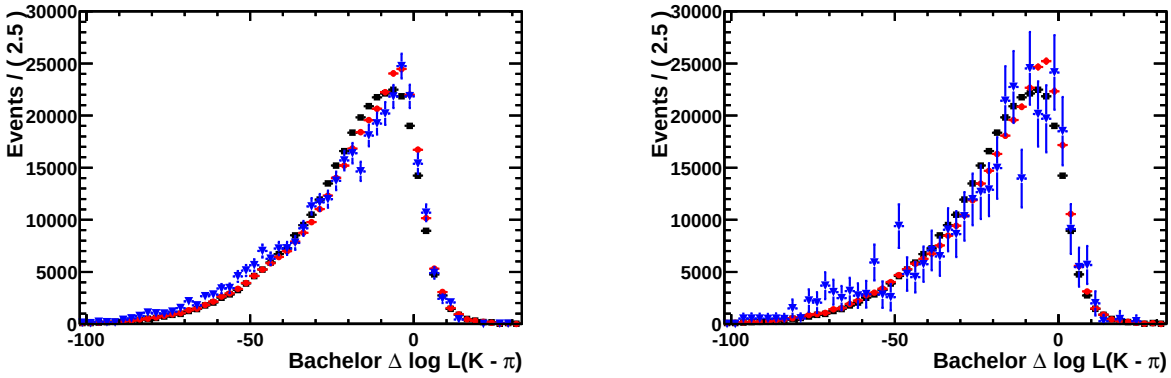

Figure 7.20: Comparison of the $\Delta\log\mathcal{L}(K-\pi)$ distributions for bachelor π^- signal tracks from sPlot fits to $B^{\pm}\to D\pi^{\pm}$ data (▼) against π^- calibration tracks before calibration (■) and after calibration (●). The left plot shows the comparison for $B^{\pm}\to(K^{\pm}\pi^{\mp})_D\pi^{\pm}$ and the right plot shows the comparison for $B^{\pm}\to(K^{+}K^{-})_D\pi^{\pm}$.

The reweighting procedure using the sPlot technique has a significant impact on the bachelor $\Delta\log\mathcal{L}(K-\pi)$ distribution of the calibration samples. The $\Delta\log\mathcal{L}(K-\pi)$ distribution of the weighted calibration sample matches that of the data sample much more closely than the raw calibration sample. We can therefore be confident that the efficiencies determined from the weighted calibration sample match those in the data. A systematic uncertainty is assigned to the differences that remain between the two distributions, as discussed in Section 8.4.2.

The efficiency of a particular $\Delta\log\mathcal{L}(K-\pi)$ cut is determined by applying the cut to the weighted calibration samples and determining the fraction of events that remain. Figure 7.21 shows the resulting kaon misID fraction and pion ID efficiency in the calibration sample of pions. Figure 7.22 shows the resulting pion misID fraction and kaon ID efficiency in the

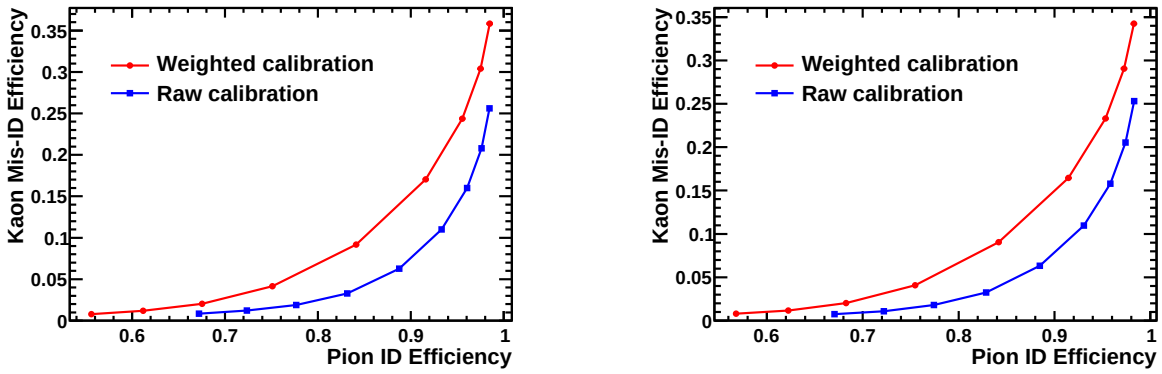

Figure 7.21: Kaon misidentification fraction against pion identification efficiency for positive tracks (left) and negative tracks (right) for the raw (■) and weighted (●) calibration track samples. The following PID requirements have been imposed: $\Delta\log\mathcal{L}(K-\pi) < [\pm 8.0, \pm 6.0, \pm 4.0, \pm 2.0, 0.0]$.

calibration sample of kaons.

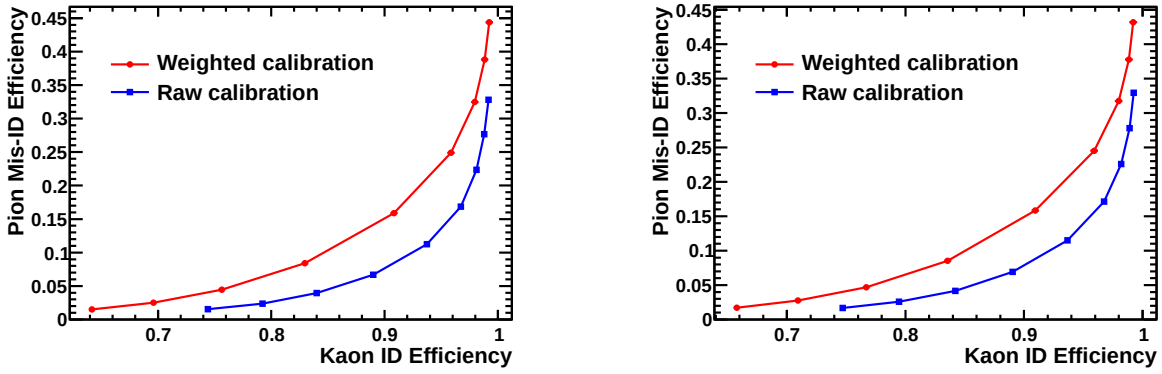

Figure 7.22: Pion misidentification fraction against kaon identification efficiency for positive tracks (left) and negative tracks (right) for the raw (■) and weighted (●) calibration track samples. The following PID requirements have been imposed: $\Delta\log\mathcal{L}(K-\pi) > [\pm 8.0, \pm 6.0, \pm 4.0, \pm 2.0, 0.0]$.

The data shown in Figure 6.12 indicate that the ability of the RICH detectors to distinguish between kaons and pions degrades at higher track momenta. Because the momentum spectrum of the bachelor track in $B^{\pm}\to Dh^{\pm}$ decays is harder than those of the calibration tracks in the prompt D^* sample, the efficiency for selecting the signal track for a particular bachelor $\Delta\log\mathcal{L}(K-\pi)$ cut is lower than the corresponding efficiency for the calibration tracks. When the calibration sample is reweighted its PID performance therefore degrades with respect to its raw performance.

Table 7.11 shows the kaon ID efficiency for both track charges and D final states. As the bachelor $\Delta\log\mathcal{L}(K-\pi)$ cut gets tighter, fewer kaons are retained in the sample, but the efficiency remains relatively high.

Table 7.12 shows the pion ID efficiency for both track charges and D final states. As the bachelor $\Delta\log\mathcal{L}(K-\pi)$ cut gets tighter, significantly more pions are removed from the

	$D \to K^{\pm}\pi^{\mp}$				$D \to K^{+}K^{-}$			
$\Delta \log \mathcal{L}(K-\pi) >$	ε_{K^+}	$\sigma(\varepsilon_{K^+})$	ε_{K^-}	$\sigma(\varepsilon_{K^-})$	ε_{K^+}	$\sigma(\varepsilon_{K^+})$	ε_{K^-}	$\sigma(\varepsilon_{K^-})$
−8.0	0.9918	0.0002	0.9918	0.0002	0.9922	0.0002	0.9920	0.0002
−6.0	0.9877	0.0002	0.9880	0.0002	0.9882	0.0002	0.9881	0.0003
−4.0	0.9800	0.0003	0.9803	0.0003	0.9807	0.0003	0.9800	0.0003
−2.0	0.9660	0.0004	0.9658	0.0004	0.9667	0.0004	0.9652	0.0005
0.0	0.9411	0.0005	0.9405	0.0005	0.9415	0.0006	0.9392	0.0006
2.0	0.9035	0.0006	0.9035	0.0007	0.9036	0.0008	0.9025	0.0008
4.0	0.8560	0.0008	0.8577	0.0008	0.8551	0.0009	0.8553	0.0009
6.0	0.8058	0.0009	0.8074	0.0009	0.8033	0.0010	0.8030	0.0011
8.0	0.7539	0.0010	0.7564	0.0010	0.7496	0.0011	0.7503	0.0012

Table 7.11: Positive and negative kaon efficiencies.

	$D \to K^{\pm}\pi^{\mp}$				$D \to K^{+}K^{-}$			
$\Delta \log \mathcal{L}(K-\pi) <$	ε_{π^+}	$\sigma(\varepsilon_{\pi^+})$	ε_{π^-}	$\sigma(\varepsilon_{\pi^-})$	ε_{π^+}	$\sigma(\varepsilon_{\pi^+})$	ε_{π^-}	$\sigma(\varepsilon_{\pi^-})$
−8.0	0.6683	0.0010	0.6652	0.0010	0.6616	0.0012	0.6566	0.0012
−6.0	0.7239	0.0010	0.7207	0.0009	0.7178	0.0012	0.7134	0.0011
−4.0	0.7813	0.0009	0.7778	0.0009	0.7771	0.0011	0.7724	0.0010
−2.0	0.8374	0.0008	0.8343	0.0008	0.8351	0.0010	0.8303	0.0009
0.0	0.8887	0.0007	0.8853	0.0007	0.8871	0.0008	0.8822	0.0008
2.0	0.9301	0.0005	0.9265	0.0005	0.9286	0.0007	0.9245	0.0006
4.0	0.9575	0.0004	0.9542	0.0004	0.9571	0.0005	0.9534	0.0005
6.0	0.9745	0.0003	0.9716	0.0003	0.9746	0.0004	0.9714	0.0004
8.0	0.9837	0.0002	0.9821	0.0002	0.9840	0.0003	0.9823	0.0003

Table 7.12: Positive and negative pion efficiencies.

sample; only 2% of pions remain for a $\Delta \log \mathcal{L}(K-\pi)$ cut > 8 compared to 75% of kaons.

7.8 Conclusions

In this chapter we have presented the reconstruction of 36.5 pb^{-1} of data collected by LHCb in 2010. We have described the trigger performance and PID calibration. Furthermore, we have developed signal and background lineshapes that will be used in a fit to extract the observables of interest, which is the subject of the next chapter.

Chapter 8

Measurement of observables related to $\mathcal{CP}$ violation in $B^{\pm} \to (h^{\pm}h^{\mp})_D h^{\pm}$ decays

8.1 Introduction

This chapter describes the measurement of observables related to $\mathcal{CP}$ violation using $B^{\pm} \to (K^{\pm}\pi^{\mp})_D h^{\pm}$ and $B^{\pm} \to (K^{+}K^{-})_D h^{\pm}$ decays reconstructed in LHCb data as described in Chapter 7. In Section 8.2 we describe the observables under study and give a short review of current measurements. In Section 8.3 we describe the fit that is used to extract the observables. We discuss systematic uncertainties related to the extraction in Section 8.4 and present the final results in Section 8.5.

8.2 Observables of interest

8.2.1 Physics observables

The physics observables that we wish to measure have been described in Section 1.6.3.5. For convenience we list them here, and where possible we review measurements that have been made at other high energy physics experiments.

- $A^{DK}_{\mathcal{CP}+}$, $A^{D\pi}_{\mathcal{CP}+}$: the asymmetry in D decays to $\mathcal{CP}+$ eigenstates for $B^{\pm}\to DK^{\pm}$ and $B^{\pm}\to D\pi^{\pm}$ respectively[1]. $A^{DK}_{\mathcal{CP}+}$ is defined in Equation 1.89 and $A^{D\pi}_{\mathcal{CP}+}$ is defined in Equation 1.90. The world average measurement of $A^{DK}_{\mathcal{CP}+}$ is 0.24 ± 0.06 [21] with the

[1] We do not measure $A_{\mathcal{CP}-}$ because we do not reconstruct any $D\to\mathcal{CP}-$ final states. Such states are difficult to reconstruct at LHCb because they contain neutral particles, e.g. K^0_S or π^0.

single most precise measurement made by BaBar: $0.25 \pm 0.06 \pm 0.02$ [44].

- $A_{\rm Fav}^{DK}$, $A_{\rm Fav}^{D\pi}$: the asymmetry in D decays to Cabibbo-favoured final states for $B^{\pm}\to DK^{\pm}$ and $B^{\pm}\to D\pi^{\pm}$ respectively. $A_{\rm Fav}^{DK}$ is defined in Equation 1.92 and $A_{\rm Fav}^{D\pi}$ is defined in Equation 1.93. These observables are expected to be close to zero because the decay rates contain very small $\mathcal{CP}$-violating terms.

- $R_{\mathcal{CP}+}$: the ratio of the rate of $B^{\pm}\to DK^{\pm}$ decays in which the D decays to $\mathcal{CP}+$ eigenstates to the rate of $B^{\pm}\to DK^{\pm}$ decays in which the D decays to Cabibbo-favoured final states. We do not measure $R_{\mathcal{CP}+}$ directly but instead assume that it is equal to R_+, defined in Equation 1.97. There is a systematic uncertainty associated with this assumption. The world average measurement of $R_{\mathcal{CP}+}$ is 1.18 ± 0.08 [21] and the single most precise measurement has again been made by BaBar: $1.18 \pm 0.09 \pm 0.05$ [44].

- $\mathcal{B}_{\rm Fav}^{DK}/\mathcal{B}_{\rm Fav}^{D\pi}$, $\mathcal{B}_{\mathcal{CP}}^{DK}/\mathcal{B}_{\mathcal{CP}}^{D\pi}$: the ratio of the branching fraction of $B^{\pm}\to DK^{\pm}$ to the branching fraction of $B^{\pm}\to D\pi^{\pm}$ for D decays to Cabibbo-favoured final states and $\mathcal{CP}$ eigenstates respectively. The world average values of $\mathcal{B}_{\rm Fav}^{DK}/\mathcal{B}_{\rm Fav}^{D\pi}$ and $\mathcal{B}_{\mathcal{CP}}^{DK}/\mathcal{B}_{\mathcal{CP}}^{D\pi}$ are $(7.6 \pm 0.6)\%$ and $(8.6 \pm 0.9)\%$ respectively [11].

- The ADS asymmetry ($A_{\rm ADS}$) and the ADS ratio ($R_{\rm ADS}$), defined in Equations 1.87 and 1.88 respectively, cannot be measured with the small 2010 LHCb dataset.

8.2.2 Asymmetries

Any difference between the number of reconstructed B^+ and B^- decays is caused by an asymmetry or combination of asymmetries. There are a number of possible sources of asymmetry in addition to those caused by $\mathcal{CP}$ violation that have been described above. We consider two possible definitions of asymmetry:

$$A = \frac{N_{B^-} - N_{B^+}}{N_{B^-} + N_{B^+}} \qquad \text{and} \qquad a = \frac{N_{B^-}}{N_{B^+}}. \tag{8.1}$$

The former definition is often used to express physics asymmetries (e.g. $A_{\mathcal{CP}+}$ and $A_{\rm Fav}$), but the latter 'fractional' definition is more convenient for combining several asymmetries from different sources. The two expressions are related as follows:

$$A = \frac{a-1}{a+1}, \qquad a = \frac{1+A}{1-A}. \tag{8.2}$$

We consider the following asymmetries:

- $A_{\rm prod}$: the asymmetry of $B\overline{B}$ production in hadronisation. This is a significant issue at the LHC because it is a proton-proton collider. There are therefore more u than $\bar{u}$

valence quarks in the initial state, and more B^+ than B^- will be produced. We assume that this asymmetry is common to all reconstructed decay modes.

- $A^K_{\rm det}$, $A^\pi_{\rm det}$: the asymmetry of detection of positive and negative kaons and pions respectively. It is possible that positive and negative particles have different interaction lengths in the detector material, leading to different detection efficiencies. We assume that the strong interactions of positive and negative pions in normal matter are identical and therefore set $A^\pi_{\rm det}$ to zero (so $a^\pi_{\rm det}$ is equal to 1).

- $A_{\rm LR}$: Difference in detection asymmetry between the left (L) and right (R) sides of the detector. We cannot determine this asymmetry unless the data are split by magnet polarity. We therefore assume that $A_{\rm LR}$ is equal to zero and do not consider it further.

A difference in the final number of reconstructed B^+ and B^- decays is caused by any initial disparity in the production, or any $\mathcal{CP}$ violation in the decays, or any differences in detecting the final state particles. Therefore the relevant fractional asymmetry is the product of three asymmetries as follows:

$$\frac{N(B^-)}{N(B^+)} = a_{\rm prod}\cdot a_{\rm phys}\cdot a^{\rm FS}_{\rm det}, \tag{8.3}$$

where $a_{\rm phys}$ is the physics asymmetry, either $a_{\mathcal{CP}}$ or $a_{\rm Fav}$, and $a^{\rm FS}_{\rm det}$ is the combined detection asymmetry of all final state particles. The combined detection asymmetry is determined by multiplying together the detection asymmetries associated with all B^- daughters that are negatively-charged and dividing by the detection asymmetries associated with all B^- daughters that are positively-charged. $a^{\rm FS}_{\rm det}$ is in general different for different $B^\pm$ and D final states. For example, in the decay $B^-\to(K^-\pi^+)_DK^-$ there are two negative kaons and one positive pion in the final state, so the overall detection asymmetry is equal to $(a^K_{\rm det})^2/a^\pi_{\rm det}$.

We now relate the number of observed B^+ and B^- decays to the total number of decays and the various asymmetries, considering $B^\pm\to(K^\pm\pi^\mp)_DK^\pm$ as an example. We define $N^{B^\pm\to DK^\pm}_{D\to K^\pm\pi^\mp}$ as the total number of events observed. This quantity is the sum of $N^{B^+\to DK^+}_{D\to K^+\pi^-}$, the number of B^+ decays, and $N^{B^-\to DK^-}_{D\to K^-\pi^+}$, the number of B^- decays. The ratio of negative to positive decays is:

$$\frac{N^{B^-\to DK^-}_{D\to K^-\pi^+}}{N^{B^+\to DK^+}_{D\to K^+\pi^-}} = a_{\rm prod}\cdot a^{DK}_{\rm Fav}\cdot(a^K_{\rm det})^2/a^\pi_{\rm det}. \tag{8.4}$$

Rearranging this, we find:

$$N^{B^+\to DK^+}_{D\to K^+\pi^-} = \frac{N^{B^\pm\to DK^\pm}_{D\to K^\pm\pi^\mp}}{1+a_{\rm prod}\cdot a^{DK}_{\rm Fav}\cdot(a^K_{\rm det})^2/a^\pi_{\rm det}}, \tag{8.5}$$

$$N^{B^-\to DK^-}_{D\to K^-\pi^+} = \frac{N^{B^\pm\to DK^\pm}_{D\to K^\pm\pi^\mp}}{1+a^\pi_{\rm det}/(a_{\rm prod}\cdot a^{DK}_{\rm Fav}\cdot(a^K_{\rm det})^2)}. \tag{8.6}$$

The equivalent relations for the other decay modes that we reconstruct are:

$$
\begin{aligned}
N^{B^+\to D\pi^+}_{D\to K^+\pi^-} &= \frac{N^{B^\pm\to D\pi^\pm}_{D\to K^\pm\pi^\mp}}{1+a_{\rm prod}\cdot a^{D\pi}_{\rm Fav}\cdot a^{K}_{\rm det}}, & N^{B^-\to D\pi^-}_{D\to K^-\pi^+} &= \frac{N^{B^\pm\to D\pi^\pm}_{D\to K^\pm\pi^\mp}}{1+1/(a_{\rm prod}\cdot a^{D\pi}_{\rm Fav}\cdot a^{K}_{\rm det})},\\
N^{B^+\to D\pi^+}_{D\to K^+K^-} &= \frac{N^{B^\pm\to D\pi^\pm}_{D\to K^+K^-}}{1+a_{\rm prod}\cdot a^{D\pi}_{\mathcal{CP}}\cdot a^{\pi}_{\rm det}}, & N^{B^-\to D\pi^-}_{D\to K^+K^-} &= \frac{N^{B^\pm\to D\pi^\pm}_{D\to K^+K^-}}{1+1/(a_{\rm prod}\cdot a^{D\pi}_{\mathcal{CP}}\cdot a^{\pi}_{\rm det})},\\
N^{B^+\to DK^+}_{D\to K^+K^-} &= \frac{N^{B^\pm\to DK^\pm}_{D\to K^+K^-}}{1+a_{\rm prod}\cdot a^{DK}_{\mathcal{CP}}\cdot a^{K}_{\rm det}}, & N^{B^-\to DK^-}_{D\to K^+K^-} &= \frac{N^{B^\pm\to DK^\pm}_{D\to K^+K^-}}{1+1/(a_{\rm prod}\cdot a^{DK}_{\mathcal{CP}}\cdot a^{K}_{\rm det})}.
\end{aligned}
\tag{8.7}
$$

As mentioned above, the pion detection asymmetry $a^{\pi}_{\rm det}$ is assumed to be 1. In addition, $A^{D\pi}_{\rm Fav}$ is expected to be less than 10^{-3} [21] so it is fixed to zero.

8.3 Fit to extract observables

The parameters of interest are extracted in an unbinned extended maximum likelihood fit using the RooFit [73] package. In this section we describe the operation of the fit and list the central values and statistical uncertainties obtained for each parameter. Henceforth this fit is referred to as the 'final fit'.

8.3.1 Fit operation

The basic principle of the final fit is to model the $B^\pm$ mass lineshape in reconstructed $B^\pm\to Dh^\pm$ data by combining the PDFs developed in Sections 7.5 and 7.6. The yields of each PDF are determined, and the signal yield in particular is used to calculate the relevant ratios and asymmetries. In order to ensure the greatest possible statistical precision, all D final states are fit simultaneously.

The data are divided into *slices* based on how they have been reconstructed. Each event in the data sample is reconstructed as either $B^\pm\to DK^\pm$ or $B^\pm\to D\pi^\pm$; in order to decide which, a cut is placed on the $\Delta\log\mathcal{L}(K-\pi)$ (defined in Section 6.3.7) of the reconstructed bachelor. The events that pass the cut are collected in the *pass* slice and reconstructed as $B^\pm\to DK^\pm$; those that are rejected are collected in the *fail* slice and reconstructed as $B^\pm\to D\pi^\pm$. In order to be able to measure charge asymmetries, the pass and fail slices are divided further by the charge of the $B^\pm$, resulting in four slices for each D decay mode. The fit is performed simultaneously in each slice of each mode considered.

We now describe the shapes used in the $B^\pm$ mass fit. In all cases, the shapes used are the same for B^+ and B^-.

In the pass slice, a Cruijff PDF is used to model $B^\pm\to DK^\pm$ signal decays and a Double Crystal Ball (DCB) PDF is used to model $B^\pm\to D\pi^\pm$ decays in which the bachelor is misidentified as a kaon. The opposite occurs in the fail slice, in which a Cruijff PDF is used

to model $B^{\pm}\to D\pi^{\pm}$ signal decays and a DCB is used to model $B^{\pm}\to DK^{\pm}$ decays in which the bachelor is misidentified as a pion. The Cruijff fit parameters in the fail slice are all allowed to float, but this is not possible in the pass slice because there are not enough events to constrain the parameters. The values used in the pass slice are therefore the values obtained in the fail slice scaled by the relevant quantities obtained from fits to MC. This procedure induces a systematic uncertainty that is discussed in Section 8.4.3.4. The DCB parameters in both slices are fixed to values taken from a lookup table. The table has been populated by fitting to weighted data in which the bachelor has been misidentified (see Section 7.6.3). The systematic uncertainty associated with this approach is described in Section 8.4.3.2.

The total yield of $B^{\pm}\to D\pi^{\pm}$ events is a free parameter for each D-decay mode. Of these events, the proportion that pass the bachelor $\Delta\log\mathcal{L}(K-\pi)$ cut is fixed by the pion efficiency determined in the PID calibration procedure (see Section 7.7). The total $B^{\pm}\to DK^{\pm}$ yield is set to a floating fraction of the total $B^{\pm}\to D\pi^{\pm}$ yield, and the number of $B^{\pm}\to DK^{\pm}$ events that pass the $\Delta\log\mathcal{L}(K-\pi)$ cut is fixed by the kaon efficiency obtained from PID calibration.

The combinatoric background is parameterised with a linear Chebychev polynomial (see Section 7.5.1) whose parameter has been fixed from a fit to data in which the reconstructed D daughters both have the same charge. The same shape is used in all of the slices, but the yield of the background can vary independently in each slice.

The low-mass background is a KEYS PDF parameterisation of the weighted background modes described in Section 7.5.2. The same shape is used for each D decay mode, but different shapes are used for the pass and fail slices. The yield of these shapes can vary independently in each slice of each mode.

The semileptonic background is parameterised as the tail of a Gaussian distribution (see Section 7.5.3). Different Gaussian means are used for the pass and fail slices: 4750 MeV/c^2 and 4650 MeV/c^2 respectively. The Gaussian width is fixed to a common value of 300 MeV/c^2. The yield of this component is defined as a floating fraction of the low-mass background yield. This fraction must be identical for all slices across all modes considered.

8.3.2 Multiple candidate selection

It is possible that more than one signal $B^{\pm}$ candidate is reconstructed in an event, especially in conditions of high pileup. In order to account for this we consider separately all $B^{\pm}$ decay candidates whose decay vertices are separated by 2 mm or more. If there are two or more candidates within 2 mm of each other, only one is accepted in the following procedure.

We assign a D decay mode to each $B^{\pm}$ candidate in the event. Only one D decay mode

is assigned per $B^{\pm}$ candidate in order to avoid double counting. We choose the D-decay candidate with the smallest $B^{\pm}$ vertex fit χ^2. At this stage, if there are two or more $B^{\pm}$ candidates within 2 mm of each other, all but one is rejected based on this metric. If the $B^{\pm}$ vertex fit χ^2 is identical between two D decay modes, we choose the candidate whose reconstructed D mass is closest to the PDG value. Approximately 3% of the reconstructed $B^{\pm}\to D\pi^{\pm}$ events contain multiple candidates.

In order to ensure that this method of candidate selection is unbiased, we evaluate the effect of using an alternative procedure on the central values returned by the final fit. In the alternative procedure we always take the 'first' candidate in each event, as labelled in the fit code. The central values obtained from the final fit using this criterion are recorded. We then repeat this procedure but always take the 'second' candidate in each event. For each fit parameter, the largest difference between the two sets of central values and the default central values is about 10–25% of the statistical uncertainty. We conclude that no significant bias is introduced by this procedure.

8.3.3 Charmless background

It is necessary to account for a background of charmless $B^{\pm}\to h^{\pm}h^{+}h^{-}$ decays (see Section 7.5.4). In order to determine the size of this background we perform a secondary fit in a low-D-mass sideband. In this fit we include all lineshapes described above except for the parameterisation of the low-$B^{\pm}$-mass background, which is irrelevant in this context because it always contains a true D. The shape of each of these components is fixed to its equivalent in the final fit. An additional shape is required to parameterise the charmless component; in each slice we use the shape that parameterises $B^{\pm}\to D\pi^{\pm}$ decays (a DCB in the pass slice and a Cruijff PDF in the fail slice).

In the sideband fit all physics asymmetries are set to zero, and the relative size of each charmless contribution is required to be proportional to its PDG branching fraction. The yield of events in the sideband is scaled by the ratio of the areas of the sideband and the signal region, then subtracted from the main signal yield.

The only non-negligible charmless contribution to the total shape occurs for charmless decays that mimic $B^{\pm} \to (K^{+}K^{-})_{D}h^{\pm}$. The result of the fit to the D mass sideband for these decays is shown in Figure 8.1.

8.3.4 Fit results

Figures 8.2 and 8.3 show the results of the final fit for $B^{\pm} \to (K^{\pm}\pi^{\mp})_{D}h^{\pm}$ and $B^{\pm} \to (K^{+}K^{-})_{D}h^{\pm}$ respectively. A bachelor $\Delta\log\mathcal{L}(K-\pi)$ cut of 4 has been used to categorise events into the pass and fail slices.

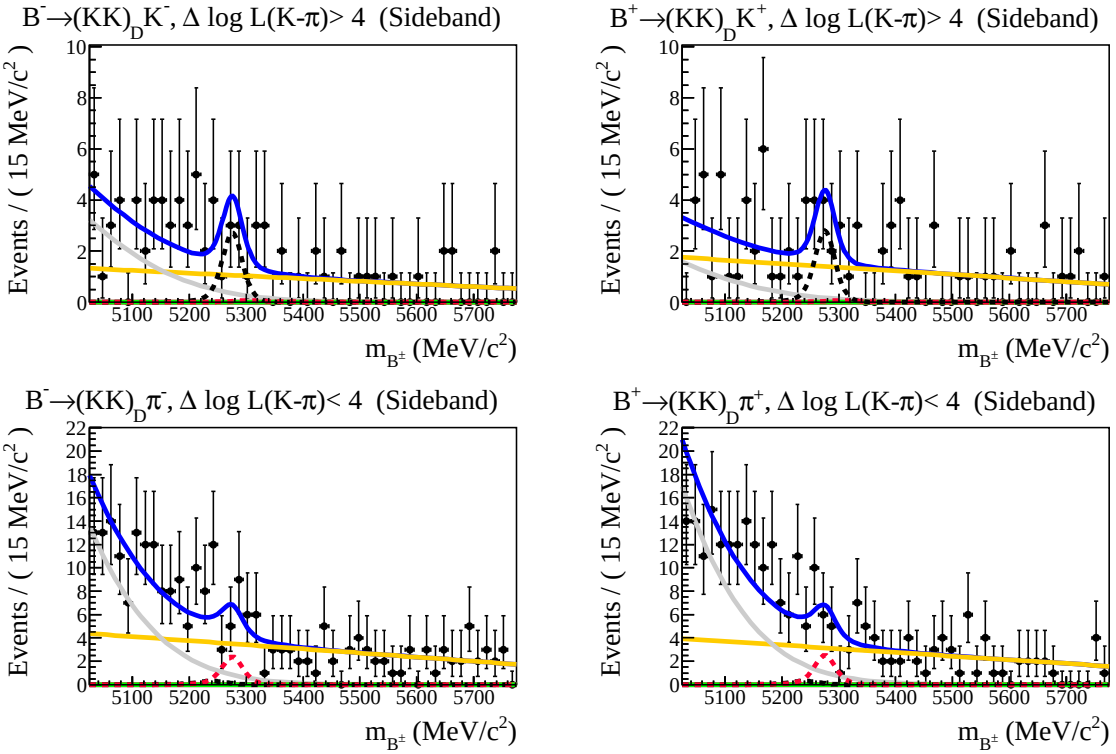

Figure 8.1: Fit in the D-mass sideband for $B^{\pm} \to (K^+K^-)_D h^{\pm}$ events with a bachelor $\Delta \log \mathcal{L}(K-\pi)$ cut of 4. The top row shows fits to the pass slice and the bottom row shows fits to the fail slice. The left column shows B^- decays and the right column shows B^+ decays. The black dotted curve shows events reconstructed as $B^{\pm} \to DK^{\pm}$ and the green curve shows events reconstructed as $B^{\pm} \to D\pi^{\pm}$. The grey curve is the semileptonic background and the orange line is the combinatoric background. The dashed pink curve is the charmless component.

The central values and statistical uncertainties of the ratios and asymmetries of interest are presented in Table 8.1 for five different bachelor $\Delta \log \mathcal{L}(K-\pi)$ cuts. Systematic uncertainties and correction factors are discussed in Section 8.4.

PID cut	Quantity	$A_{\mathcal{CP}+}^{DK}$	$A_{\mathcal{CP}+}^{D\pi}$	A_{Fav}^{DK}	A_{det}^{K}	$\mathcal{B}_{\mathrm{Fav}}^{DK}/\mathcal{B}_{\mathrm{Fav}}^{D\pi}$	$\mathcal{B}_{\mathcal{CP}}^{DK}/\mathcal{B}_{\mathcal{CP}}^{D\pi}$
0	Central value	−0.01	0.016	−0.126	0.027	0.068	0.095
	Statistical uncertainty	0.18	0.042	0.079	0.021	0.005	0.019
2	Central value	0.04	0.014	−0.149	0.028	0.068	0.088
	Statistical uncertainty	0.18	0.042	0.075	0.021	0.005	0.018
4	Central value	0.06	0.009	−0.109	0.024	0.068	0.095
	Statistical uncertainty	0.17	0.042	0.073	0.021	0.005	0.017
6	Central value	−0.05	0.015	−0.085	0.023	0.070	0.090
	Statistical uncertainty	0.17	0.042	0.071	0.021	0.005	0.017
8	Central value	−0.06	0.015	−0.065	0.022	0.074	0.085
	Statistical uncertainty	0.18	0.041	0.068	0.021	0.005	0.017

Table 8.1: Central values and statistical uncertainties of each observable for different bachelor PID cuts.

As the PID cut is changed, the central values of each observable vary; this variation is usually over a range that is smaller than the magnitude of the statistical uncertainty.

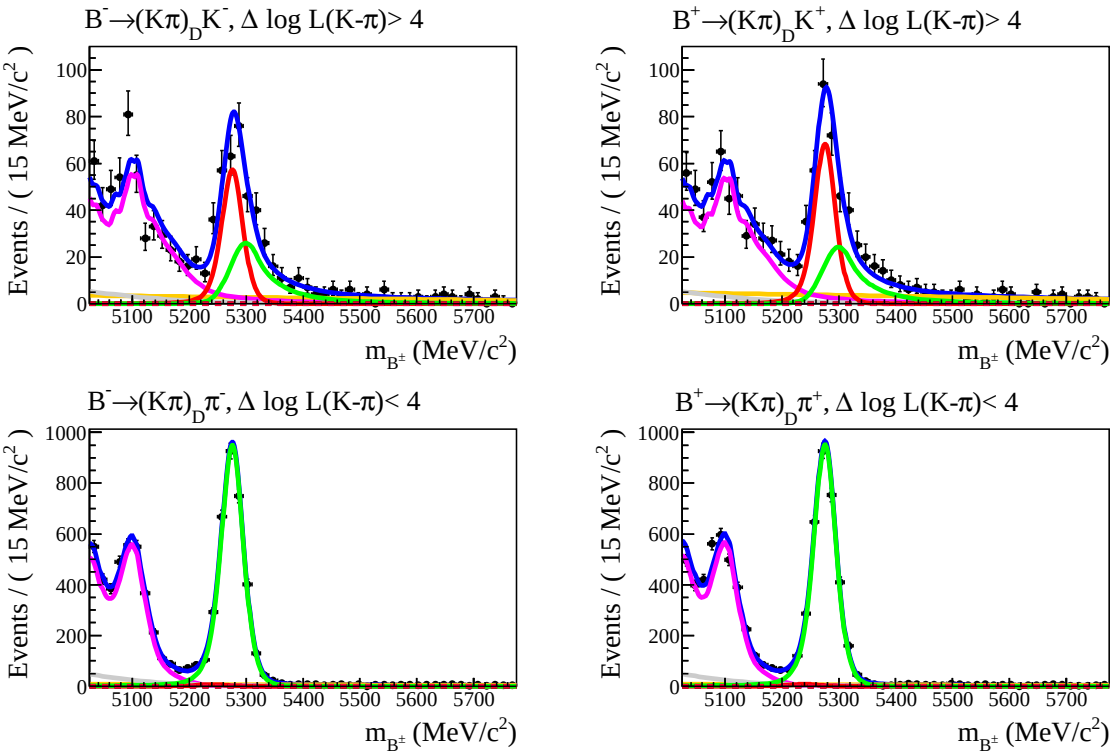

Figure 8.2: Final fit to $B^{\pm} \to (K^{\pm}\pi^{\mp})_D h^{\pm}$ events with a bachelor $\Delta \log \mathcal{L}(K-\pi)$ cut of 4. The top row shows fits to the pass slice and the bottom row shows fits to the fail slice. The left column shows B^- decays and the right column shows B^+ decays. The red curve shows events reconstructed as $B^{\pm}\to DK^{\pm}$ and the green curve shows events reconstructed as $B^{\pm}\to D\pi^{\pm}$. The magenta curve shows the low-mass background, the orange curve shows the combinatoric background and the grey curve shows the semileptonic background. The dotted red curve is a (negligible) contribution from the charmless background.

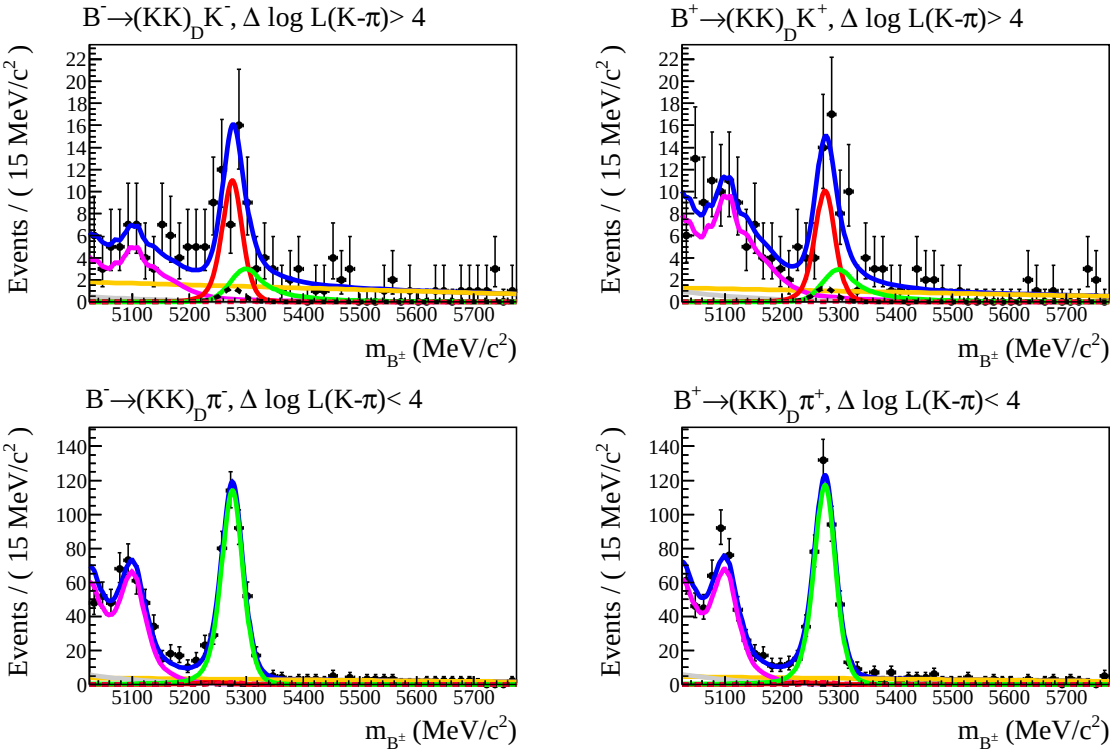

Figure 8.3: Final fit to $B^{\pm} \to (K^{+}K^{-})_D h^{\pm}$ events with a bachelor $\Delta \log \mathcal{L}(K-\pi)$ cut of 4. The figure partitions and curve colours represent the same as in Figure 8.2.

There are no particularly strong correlations between the $\Delta\log\mathcal{L}(K-\pi)$ cut used and the fit observables.

8.3.5 Choice of bachelor $\Delta\log\mathcal{L}(K-\pi)$ cut

Our choice of the cut on the bachelor $\Delta\log\mathcal{L}(K-\pi)$ is guided by toy Monte Carlo studies. We aim to achieve a balance between two competing effects. A looser PID cut places more $B^{\pm}\to D\pi^{\pm}$ events into the pass slice, which increases the difficulty of resolving the $B^{\pm}\to DK^{\pm}$ signal. On the other hand, a tighter PID cut places more $B^{\pm}\to DK^{\pm}$ events into the fail slice where they will be swamped by the background and provide no useful information.

We consider $\Delta\log\mathcal{L}(K-\pi)$ cuts of 0, 2, 4, 6 and 8, running 500 toy fits for each cut. For each cut we use the PID efficiencies that were obtained from the calibration procedure (see Section 7.7). Each toy fit is set up such that the total yield is equal to the total found in data. The observables of interest are then randomly generated and the yields in each slice are computed. The yields in each slice are then smeared, assuming they are drawn from a Poisson distribution with mean equal to the initial quantity, and the fit is performed. For each toy we record the initial and final values of each fit parameter as well as the fit uncertainty.

In order to choose a PID cut we examine the distributions of the fit uncertainties on both $\mathcal{B}^{DK}_{\rm Fav}/\mathcal{B}^{D\pi}_{\rm Fav}$ and $\mathcal{B}^{DK}_{\mathcal{CP}}/\mathcal{B}^{D\pi}_{\mathcal{CP}}$. For each PID cut we fit a Gaussian PDF to the distribution of the 500 uncertainties. Figure 8.4 shows the mean and width of the Gaussian distributions.

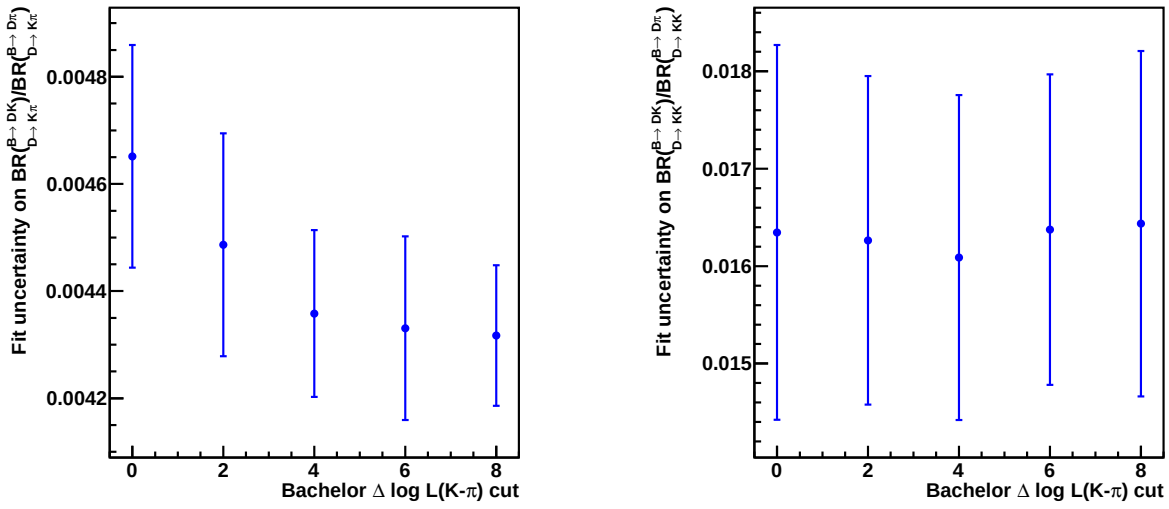

Figure 8.4: The distribution of fit uncertainties obtained by toy MC studies, for $\mathcal{B}^{DK}_{\rm Fav}/\mathcal{B}^{D\pi}_{\rm Fav}$ (left) and $\mathcal{B}^{DK}_{\mathcal{CP}}/\mathcal{B}^{D\pi}_{\mathcal{CP}}$ (right) against bachelor $\Delta\log\mathcal{L}(K-\pi)$ cut. The central value and error bar are respectively the mean and width of a Gaussian fit to the distribution of uncertainties.

There is a shallow minimum in the distribution of mean uncertainties on $\mathcal{B}^{DK}_{\mathcal{CP}}/\mathcal{B}^{D\pi}_{\mathcal{CP}}$ at a PID cut of 4. In contrast, the smallest mean uncertainty on $\mathcal{B}^{DK}_{\rm Fav}/\mathcal{B}^{D\pi}_{\rm Fav}$ is obtained for a

PID cut of 8. Following the analysis in Ref. [120], which studies a larger quantity of data, we decide to use a $\Delta \log \mathcal{L}(K-\pi)$ cut of 4.

8.3.6 Fit bias

In order to determine whether there are any biases in the fit, we run a further 3000 toy Monte Carlo studies with a bachelor $\Delta \log \mathcal{L}(K-\pi)$ cut of 4. For each fit observable we determine the pull of its resulting distribution. The pull of the observable x is defined as $(x_I - x_F)/\sigma_x$, where x_I is the initial value of x, x_F is the fit value of x and σ_x is the fit uncertainty.

We fit a Gaussian PDF to each of the pull distributions, excluding the lineshape parameters. Table 8.2 lists the mean m_p and width w_p of each distribution along with their uncertainties σ_{m_p} and σ_{w_p}. Each pull is distributed around zero and has no significant bias.

Quantity	$m_p \pm \sigma_{m_p}$	$w_p \pm \sigma_{w_p}$	Fit uncertainty correction
$\mathcal{B}^{DK}_{\rm Fav}/\mathcal{B}^{D\pi}_{\rm Fav}$	-0.033 ± 0.019	1.071 ± 0.014	7%
$\mathcal{B}^{DK}_{\mathcal{CP}}/\mathcal{B}^{D\pi}_{\mathcal{CP}}$	-0.060 ± 0.021	1.125 ± 0.015	13%
$A^{DK}_{\mathcal{CP}+}$	0.012 ± 0.019	1.039 ± 0.015	
$A^{D\pi}_{\mathcal{CP}+}$	-0.037 ± 0.021	1.036 ± 0.016	
$A^{DK}_{\rm Fav}$	0.002 ± 0.023	1.157 ± 0.018	16%
$\mathrm{N}(B^\pm \to (K^+K^-)_D\pi^\pm)$	-0.005 ± 0.020	1.078 ± 0.015	
$\mathrm{N}(B^\pm \to (K^\pm\pi^\mp)_D\pi^\pm)$	-0.008 ± 0.020	1.056 ± 0.015	
$A^K_{\rm det}$	-0.006 ± 0.013	0.661 ± 0.011	
$A_{\rm prod}$	0.006 ± 0.014	0.702 ± 0.011	

Table 8.2: Pull mean m_p and width w_p for variables that are floating in the fit, excluding the lineshape parameters. The fit uncertainty correction is assigned to physics observables whose statistical uncertainty may be underestimated.

The pull widths are all slightly larger than one (excluding $A^K_{\rm det}$ and $A_{\rm prod}$ which are discussed below), suggesting that the fit software may underestimate the uncertainty from purely statistical fluctuations in the dataset. For each fit variable, a correction to the uncertainty is applied if $|w_p - 1|/\sigma_{w_p} > 3$, again excepting $A^K_{\rm det}$ and $A_{\rm prod}$.

Figure 8.5 shows the correlations between various fit variables in the toy studies. The variables are uncorrelated, apart from $A_{\rm prod}$ and $A^K_{\rm det}$ which exhibit reasonably high correlation. Rather than fitting both $A_{\rm prod}$ and $A^K_{\rm det}$ simultaneously, we apply a Gaussian constraint to $A_{\rm prod}$. During the final fit procedure, $A_{\rm prod}$ is varied around a preassigned central value, assuming it is drawn from a Gaussian distribution. The fit parameters returned exhibit more spread than they would if the central value of $A_{\rm prod}$ were fixed, and the statistical uncertainty on each parameter is therefore slightly larger. We set $A_{\rm prod}$ to $-0.024 \pm 0.013 \pm 0.010$ which is the value measured in an LHCb analysis of $B^0 \to h^+h^-$ decays [121].

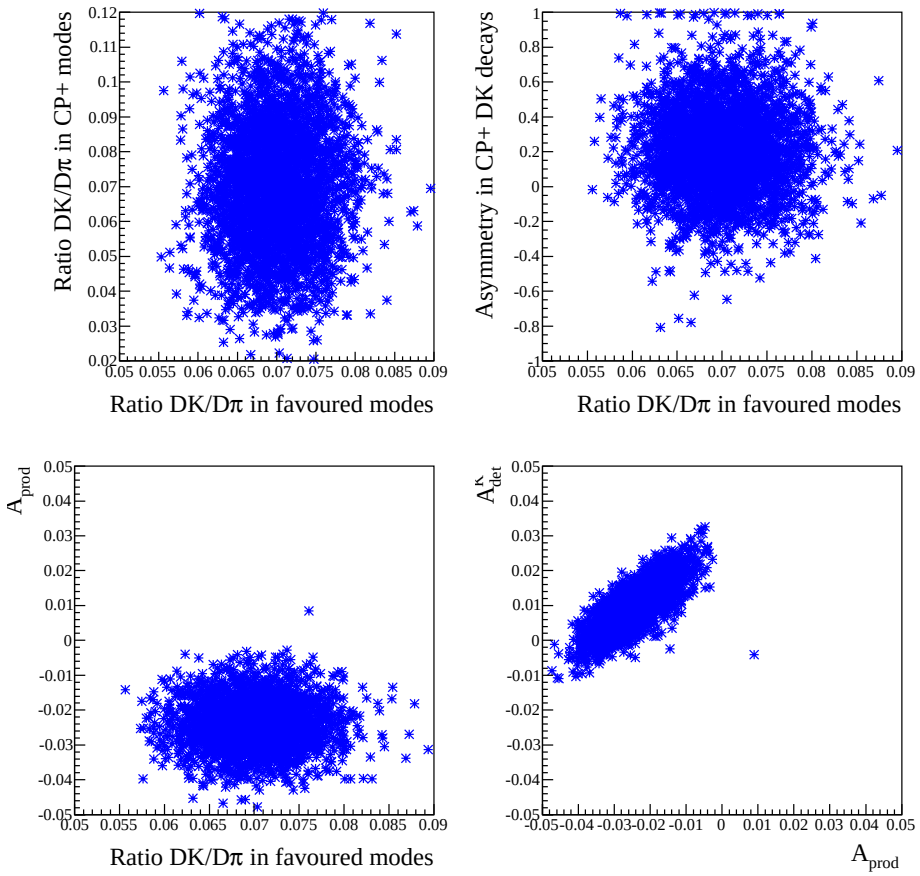

Figure 8.5: Variable correlations from toy studies with a bachelor $\Delta\log\mathcal{L}(K-\pi)$ cut of 4. There is a strong correlation between $A_{\rm prod}$ and $A^K_{\rm det}$.

To obtain the final result for a $\Delta\log\mathcal{L}(K-\pi)$ cut of 4 we correct the uncertainties on the values in Table 8.1 by the factors listed in Table 8.2. The final results are listed in Table 8.3.

Quantity	$A^{DK}_{\mathcal{CP}+}$	$A^{D\pi}_{\mathcal{CP}+}$	$A^{DK}_{\rm Fav}$	$A^{K}_{\rm det}$	$\mathcal{B}^{DK}_{\rm Fav}/\mathcal{B}^{D\pi}_{\rm Fav}$	$\mathcal{B}^{DK}_{\mathcal{CP}}/\mathcal{B}^{D\pi}_{\mathcal{CP}}$
Central value	0.06	0.009	−0.109	0.024	0.068	0.095
Corrected statistical uncertainty	0.17	0.042	0.085	0.021	0.005	0.019

Table 8.3: Central values and statistical uncertainties for a bachelor $\Delta\log\mathcal{L}(K-\pi)$ cut of 4. The uncertainties have been scaled by factors suggested by toy Monte Carlo studies.

8.4 Systematic uncertainties

In this section we discuss the systematic biases and uncertainties on the fit results. We report the magnitude of each uncertainty for each systematic effect.

8.4.1 Uncertainties on the ratio $\mathcal{B}^{DK}/\mathcal{B}^{D\pi}$

There are several sources of uncertainty related to the ratio of branching fractions $\mathcal{B}^{DK}/\mathcal{B}^{D\pi}$. The decay topology and kinematics of $B^{\pm}\to DK^{\pm}$ and $B^{\pm}\to D\pi^{\pm}$ are similar, but not identical. Furthermore, the detector response to kaons and pions is slightly different. In general, the ratio of the number of reconstructed events of each decay ($N_{DK}/N_{D\pi}$) will not be equal to the ratio of branching fractions. The two quantities are related as follows:

$$\frac{N_{DK}}{N_{D\pi}} = \frac{\mathcal{B}^{DK}}{\mathcal{B}^{D\pi}} \cdot \frac{\varepsilon^{DK}_{\rm acc}}{\varepsilon^{D\pi}_{\rm acc}} \cdot \frac{\varepsilon^{DK}_{\rm sel}}{\varepsilon^{D\pi}_{\rm sel}} \cdot \frac{\varepsilon^{DK}_{\rm trig}}{\varepsilon^{D\pi}_{\rm trig}}, \tag{8.8}$$

where $\varepsilon_{\rm acc}$ is the efficiency of detector acceptance[2], $\varepsilon_{\rm sel}$ is the combined efficiency of reconstruction, stripping and offline selections, and $\varepsilon_{\rm trig}$ is the total trigger efficiency.

Using LHCb Monte Carlo we calculate a correction factor equal to the product of the $DK/D\pi$ efficiency ratios. The ratio of branching fractions extracted from the fit is divided by this quantity. The uncertainty on each correction factor, related to the size of the MC samples used, is propagated through as a systematic uncertainty on the final result. The correction factors for each D decay mode are listed in Table 8.4. We do not apply a PID cut to the bachelor.

Detector acceptance (%)		Correction factor $\varepsilon^{DK}_{\rm acc}/\varepsilon^{D\pi}_{\rm acc}$
$B^{\pm}\to(K^{\pm}\pi^{\mp})_D K^{\pm}$	16.33 ± 0.02	
$B^{\pm}\to(K^{\pm}\pi^{\mp})_D \pi^{\pm}$	15.95 ± 0.02	1.024 ± 0.002
$B^{\pm}\to(K^{+}K^{-})_D K^{\pm}$	17.13 ± 0.03	
$B^{\pm}\to(K^{+}K^{-})_D \pi^{\pm}$	16.71 ± 0.03	1.025 ± 0.003
Selection efficiency (%)		Correction factor $\varepsilon^{DK}_{\rm sel}/\varepsilon^{D\pi}_{\rm sel}$
$B^{\pm}\to(K^{\pm}\pi^{\mp})_D K^{\pm}$	9.17 ± 0.03	
$B^{\pm}\to(K^{\pm}\pi^{\mp})_D \pi^{\pm}$	9.25 ± 0.03	0.991 ± 0.004
$B^{\pm}\to(K^{+}K^{-})_D K^{\pm}$	8.79 ± 0.04	
$B^{\pm}\to(K^{+}K^{-})_D \pi^{\pm}$	8.95 ± 0.04	0.982 ± 0.007
Trigger efficiency (%)		Correction factor $\varepsilon^{DK}_{\rm trig}/\varepsilon^{D\pi}_{\rm trig}$
$B^{\pm}\to(K^{\pm}\pi^{\mp})_D K^{\pm}$	38.95 ± 0.40	
$B^{\pm}\to(K^{\pm}\pi^{\mp})_D \pi^{\pm}$	38.48 ± 0.40	1.012 ± 0.015
$B^{\pm}\to(K^{+}K^{-})_D K^{\pm}$	39.53 ± 0.40	
$B^{\pm}\to(K^{+}K^{-})_D \pi^{\pm}$	39.17 ± 0.40	1.009 ± 0.015

Table 8.4: Summary of correction factors on the ratios $\mathcal{B}^{DK}_{\rm Fav}/\mathcal{B}^{D\pi}_{\rm Fav}$ and $\mathcal{B}^{DK}_{\mathcal{CP}}/\mathcal{B}^{D\pi}_{\mathcal{CP}}$.

[2]This efficiency is determined during the central production of Monte Carlo at LHCb.

8.4.2 PID calibration

The PID calibration procedure is used to determine the efficiencies of pion and kaon identification (see Section 7.7). In this procedure we assume that the $\Delta\log\mathcal{L}(K-\pi)$ distribution of both the signal and calibration samples is solely dependent upon the three variables that were used to bin the samples, namely $|\mathbf{p}|$, η and n_{tracks}. This assumption only holds approximately, so the weighting procedure does not in general result in perfect correspondence between the $\Delta\log\mathcal{L}(K-\pi)$ distributions of the two samples. The consequently imperfect knowledge of the PID efficiencies results in a systematic uncertainty on the fit observables.

In order to determine the magnitude of the systematic uncertainty we perform the weighting procedure on samples of $B^{\pm}\to Dh^{\pm}$ MC. Because we can access the MC truth information, we can determine how well the actual PID efficiencies are reproduced by the calibration procedure. This correspondence (or lack thereof) can then be translated to the PID efficiencies in data.

We define the PID asymmetry:

$$A_{\text{PID}} \equiv \frac{\varepsilon_{\text{sig}} - \varepsilon_{\text{cal}}}{\varepsilon_{\text{sig}} + \varepsilon_{\text{cal}}} \tag{8.9}$$

where ε_{sig} and ε_{cal} are the PID efficiencies on the signal and calibration samples respectively for a given $\Delta\log\mathcal{L}(K-\pi)$ cut. We also define the residual efficiency $\varepsilon_{\text{sig}} - \varepsilon_{\text{cal}}$.

Assuming that A_{PID} is the same in data and MC, the residual efficiency in data can be expressed as:

$$(\varepsilon_{\text{sig}} - \varepsilon_{\text{cal}})_{\text{data}} = (\varepsilon_{\text{sig}} + \varepsilon_{\text{cal}})_{\text{data}} \times \left(\frac{\varepsilon_{\text{sig}} - \varepsilon_{\text{cal}}}{\varepsilon_{\text{sig}} + \varepsilon_{\text{cal}}}\right)_{\text{MC}}. \tag{8.10}$$

We assume that $(\varepsilon_{\text{sig}} + \varepsilon_{\text{cal}})_{\text{data}} \approx 2 \times \varepsilon_{\text{cal}}|_{\text{data}}$, so the residual efficiency in data is equal to:

$$(\varepsilon_{\text{sig}} - \varepsilon_{\text{cal}})_{\text{data}} = 2 \times \varepsilon_{\text{cal}}|_{\text{data}} \times \left(\frac{\varepsilon_{\text{sig}} - \varepsilon_{\text{cal}}}{\varepsilon_{\text{sig}} + \varepsilon_{\text{cal}}}\right)_{\text{MC}}. \tag{8.11}$$

The right hand side of the above equation can be calculated using entirely known parameters.

We determine the residual efficiency in data for a range of bachelor $\Delta\log\mathcal{L}(K-\pi)$ cuts. It is likely that the PID asymmetries in data and MC do not match due to mismodelling of detector imperfections. We therefore determine the residuals over a relatively large range of cuts: from -10 to $+20$ in steps of 2. The choice of range is motivated by the fact that the mean $\Delta\log\mathcal{L}(K-\pi)$ values in data and MC differ by approximately 10. We therefore conservatively examine a range of $\Delta\log\mathcal{L}(K-\pi)$ equal to ~ 10 either side of the core range (0–8) that is considered in the analysis.

Figures 8.6 and 8.7 show the residual efficiencies in data for bachelor pions and kaons respectively.

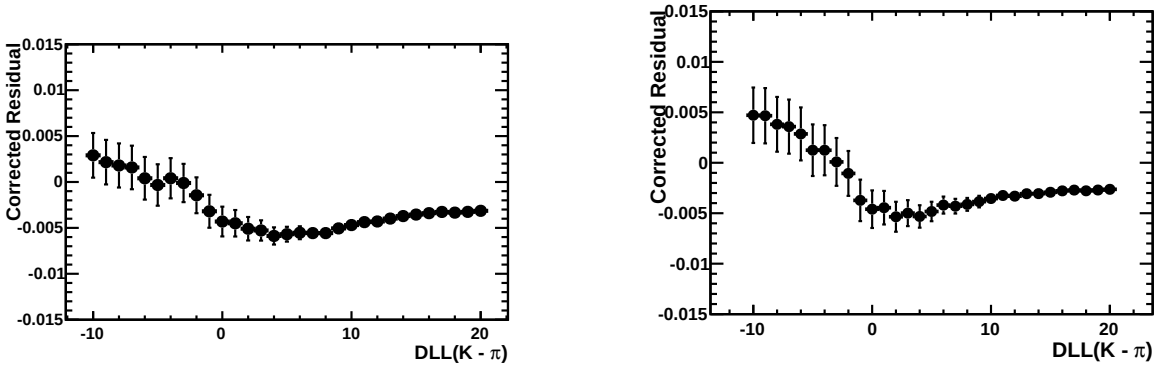

Figure 8.6: Estimates of the residual $\varepsilon_{\rm sig} - \varepsilon_{\rm cal}$ in data for $\Delta\log\mathcal{L}(K-\pi) < -10, -8, ..., 18, 20$. The left plot shows $B^{\pm} \to (K^{\pm}\pi^{\mp})_D\pi^{\pm}$, the right plot shows $B^{\pm} \to (K^{+}K^{-})_D\pi^{\pm}$. The calibration MC has been weighted according to the corresponding signal MC in each case.

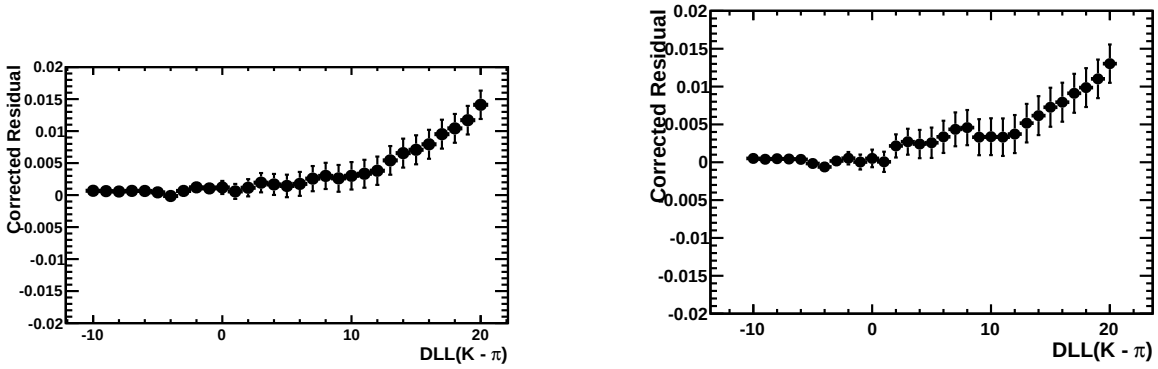

Figure 8.7: Estimates of the residual $\varepsilon_{\rm sig} - \varepsilon_{\rm cal}$ in data for $\Delta\log\mathcal{L}(K-\pi) > -10, -8, ..., 18, 20$. The left plot shows $B^{\pm} \to (K^{\pm}\pi^{\mp})_D K^{\pm}$, the right plot shows $B^{\pm} \to (K^{+}K^{-})_D K^{\pm}$. The calibration MC has been weighted according to the corresponding signal MC in each case.

In order to assign a systematic uncertainty, we conservatively take the largest residual across the entire range of $\Delta\log\mathcal{L}(K-\pi)$ cuts, equal to 0.5% and 1.5% for pions and kaons respectively. We then vary the PID efficiency by this uncertainty, assuming it is drawn from a Gaussian distribution, and rerun the final fit. This is repeated many times in order to build up a distribution for each observable in the final fit. The standard deviation of each distribution is computed and assigned as the systematic uncertainty on that observable.

8.4.3 Lineshape parameterisation

In this section we describe the systematic uncertainties related to the various lineshapes used in the final fit.

8.4.3.1 Signal lineshape

The $B^{\pm}\to D\pi^{\pm}$ signal lineshape is modelled with a Cruijff PDF. All of the Cruijff parameters are floating in the fit, so the uncertainty returned by the fit is the statistical uncertainty added in quadrature with the signal lineshape uncertainty. In order to isolate the latter con-

tribution, we rerun the fit but fix the lineshape parameters. The signal lineshape uncertainty is then the quadrature difference between the default uncertainty and the uncertainty with the parameters fixed. This uncertainty is always negligible.

8.4.3.2 MisID lineshape

The misID lineshape is modelled by a Double Crystal Ball (DCB) PDF that has been determined from a fit to a weighted sample of data in which the bachelor has been misidentified. We use a two-stage process to determine the systematic uncertainty associated with the misID lineshape parameters.

Firstly, we determine the covariance matrix associated with the DCB parameters. We do this using a method that reflects the size of the data sample. The $B^{\pm}$-mass distribution is binned, and then the yield in each bin is varied assuming it is drawn from a Poisson distribution with a mean equal to the initial value. The DCB is then fit to this smeared distribution and the parameters are recorded. This procedure is repeated many times, building up a distribution of the DCB parameters. The covariance matrix of the parameters can then be determined from the distributions. During this procedure we keep the parameters that describe the left-hand tail ($n_{\rm lo}$ and $\alpha_{\rm lo}$) constant. This is a low-statistics region and the parameters often have large variations that destabilise the fit. For example, $n_{\rm lo}$ can vary between 10 and 100 with a very minor change in shape. These two parameters are fixed at their initial central values.

The second stage is to use the covariance matrix of DCB parameters to alter the lookup table of DCB parameters used in the fit. The vector of final parameters, $\mathbf{x}$, is obtained as follows:

$$\mathbf{x} = \boldsymbol{\mu} + \mathbf{A}\mathbf{z} \tag{8.12}$$

where μ is a vector of the central values of the parameters, $\mathbf{z}$ is a vector of numbers drawn from a Gaussian distribution of mean 0 and variance 1, and $\mathbf{A}$ is the Cholesky decomposition of the covariance matrix. After the parameters have been varied in this manner we rerun the fit and record the fit observables.

The resulting distributions of the fit observables are often non-Gaussian so we do not use the standard deviation to quantify the spread in the results. Instead, for the fit values m_i we determine the median value of the fitted points, $\text{median}(m_i) = M$. We then determine the absolute deviation of each point from the median, $(|m_i - M|)$. We finally then determine the median of these deviations, i.e. $\text{median}(|m_i - M|)$. This quantity is more robust to outliers than the standard deviation. It is described in more detail in Ref. [122]. In order to turn the median of the deviations into a 'Gaussian-like' quantity it is multiplied by 1.4826, which is the factor used to scale the quantity obtained for Gaussian distributions [123].

8.4.3.3 Low-mass background lineshape

In order to evaluate the uncertainty associated with the low-mass lineshape, we vary the lower limit of the fit range by ± 50 MeV/c^2 and rerun the fit each time. The magnitude of the variation has been chosen such that the lower peak in the 'double hump' structure at low mass (see Figure 7.5) is either fully included or excluded from the fit. The systematic uncertainty assigned to each observable is the largest difference between the central values obtained using this variation and the default central value.

8.4.3.4 Lineshape scaling factors

The lineshape of the $B^{\pm}\to DK^{\pm}$ peak in the pass slice cannot be determined independently in the fit because of a lack of signal events. Furthermore, there is a large quantity of misidentified $B^{\pm}\to D\pi^{\pm}$ events that impinge upon the signal peak even for a relatively tight bachelor PID cut. A similar situation occurs for the misidentified $B^{\pm}\to DK^{\pm}$ peak in the fail slice.

To obtain the $B^{\pm}\to DK^{\pm}$ lineshape parameters, the fit $B^{\pm}\to D\pi^{\pm}$ parameters are scaled by factors that are determined from fits to Monte Carlo. This leads to a systematic uncertainty which is evaluated by varying each scaling factor by $\pm 1\sigma$ and rerunning the fit. The largest difference between the central values obtained using this variation and the default central value is taken to be the systematic uncertainty. The resulting uncertainty is negligible.

8.4.4 B^-/B^+ production asymmetry

The production asymmetry $A_{\rm prod}$ is taken from another LHCb analysis [121]. This asymmetry is included in the fit as a Gaussian constraint, so the uncertainty on this parameter is included in the uncertainty returned by the fit.

8.4.5 Choice of trigger lines

As described in Section 7.3.2 we have decided to analyse all events that pass the trigger, without discriminating between triggers designed to select hadronic events and those designed to select other decay modes. This method could introduce biases in the central values obtained if significant quantities of non-signal events are retained.

We compare the default central values with those obtained when a more specific trigger configuration is used. In the latter case each event must pass at least one of the following criteria at each stage:

- **L0**: The reconstructed $B^{\pm}$ candidate is TOS[3] with respect to the L0 Hadron line, or[4] TIS with respect to all L0 lines.
- **HLT1**: The reconstructed $B^{\pm}$ candidate is TOS with respect to the HLT 1-track line, or TIS with respect to all HLT1 lines.
- **HLT2**: The reconstructed $B^{\pm}$ candidate must be accepted by at least one of the HLT2 Topological lines.

The complete dataset contains 22.1k events whereas the dataset with the more specific trigger requirements contains 18.0k events.

For each physics observable we determine the difference in central values and take this to be the systematic uncertainty associated with the choice of trigger lines.

A relatively small number of $B^{\pm} \to (K^+K^-)_D K^{\pm}$ events were reconstructed, and the consequently larger statistical uncertainties associated with each physics observable may result in an unrepresentative shift in the central values. This is particularly important for the ratio $\mathcal{B}^{DK}_{\mathcal{CP}}/\mathcal{B}^{D\pi}_{\mathcal{CP}}$. To minimise the impact of limited statistics we determine the uncertainty on $\mathcal{B}^{DK}_{\text{Fav}}/\mathcal{B}^{D\pi}_{\text{Fav}}$ for the decay $B^{\pm} \to (K^{\pm}\pi^{\mp})_D K^{\pm}$, for which a relatively large number of events were reconstructed. We divide this uncertainty by the central value of $\mathcal{B}^{DK}_{\text{Fav}}/\mathcal{B}^{D\pi}_{\text{Fav}}$ to obtain a scaling factor, which is approximately 3%. The central value of $\mathcal{B}^{DK}_{\mathcal{CP}}/\mathcal{B}^{D\pi}_{\mathcal{CP}}$ is multiplied by that factor in order to obtain the uncertainty. For the fit asymmetries, the statistical uncertainty always dominates so we treat each mode individually instead of scaling them relative to $B^{\pm} \to (K^{\pm}\pi^{\mp})_D K^{\pm}$. In this case, we conservatively assign the shift in central values to be the systematic uncertainty.

8.4.6 Conclusions

The most significant sources of systematic uncertainty are the PID calibration procedure, the misID lineshape parameterisation, the low-mass background parameterisation and the choice of trigger lines. The total systematic uncertainty is approximately equal to or less than the statistical uncertainty.

8.5 Final results

In Table 8.5 we list the central values and statistical and systematic uncertainties for each physics observable. Results are shown for a bachelor $\Delta \log \mathcal{L}(K-\pi)$ cut of > 4.

[3]The terms TOS and TIS have been defined in Section 7.3
[4]This is a logical OR.

Quantity	$A^{DK}_{\mathcal{CP}+}$	$A^{D\pi}_{\mathcal{CP}+}$	$A^{DK}_{\rm Fav}$	$A^{K}_{\rm det}$	$\mathcal{B}^{DK}_{\rm Fav}/\mathcal{B}^{D\pi}_{\rm Fav}$	$\mathcal{B}^{DK}_{\mathcal{CP}}/\mathcal{B}^{D\pi}_{\mathcal{CP}}$
Central value	0.06	0.009	−0.109	0.024	0.066	0.093
Statistical uncertainty	0.17	0.042	0.085	0.021	0.005	0.019
PID systematic	0.01	0.001	0.003	0.000	0.003	0.004
MisID lineshape systematic	0.00	0.001	0.005	0.000	0.002	0.002
Low-mass lineshape systematic	0.01	0.002	0.004	0.001	0.001	0.000
Shape scaling systematic	0.00	0.000	0.000	0.000	0.000	0.000
Trigger choice systematic	0.07	0.011	0.017	0.005	0.001	0.001
$DK/D\pi$ correction systematic					0.001	0.002
Total systematic	0.07	0.011	0.019	0.005	0.004	0.005
Total uncertainty	0.19	0.043	0.087	0.021	0.006	0.020

Table 8.5: Central values and statistical and systematic uncertainties for the observables obtained by fitting to $K^{\pm}\pi^{\mp}$ and $K^{+}K^{-}$ with a bachelor $\Delta\log\mathcal{L}(K-\pi)$ cut of 4.

8.5.1 Determination of $R_{\mathcal{CP}+}$

We approximate $R_{\mathcal{CP}+}$ as R_+, which is obtained by dividing $\mathcal{B}^{DK}_{\mathcal{CP}}/\mathcal{B}^{D\pi}_{\mathcal{CP}}$ by $\mathcal{B}^{DK}_{\rm Fav}/\mathcal{B}^{D\pi}_{\rm Fav}$ (see Equation 1.97). We propagate through all statistical and systematic uncertainties in quadrature except for two systematics — the low-mass shape and choice of triggers — that are likely to be correlated between the $\mathcal{CP}$ and Cabibbo-favoured modes. In order to determine the magnitude of the uncertainty on R_+ from these sources we vary the quantities in question and determine the change in the central value of R_+ each time. The change in central value is taken to be the systematic uncertainty. When determining the low-mass systematic the lower fit limit is varied twice; in this case, the largest of the two changes in central value is used as the uncertainty. Following Section 8.4.5, when determining the trigger choice systematic we multiply the central value of $\mathcal{B}^{DK}_{\mathcal{CP}}/\mathcal{B}^{D\pi}_{\mathcal{CP}}$ by 1.03, rather than taking the difference in central values.

There is an additional phenomenological uncertainty due to the approximation made in Equation 1.97. Following Ref. [44] we assign a relative uncertainty of 2.2% to the measured value of $R_{\mathcal{CP}+}$.

We calculate $R_{\mathcal{CP}+} = 1.41 \pm 0.31 \pm 0.13$. Table 8.6 lists each source of uncertainty separately.

8.6 Conclusions

Using the LHCb data taken in 2010 we have made measurements of several key physics observables related to $B^{\pm}\to DK^{\pm}$ decays. In this section we summarise the results and compare them to the values obtained by other experiments. Whenever two uncertainties are reported, the first one is statistical and the second is systematic.

We have measured $\mathcal{B}^{DK}_{\rm Fav}/\mathcal{B}^{D\pi}_{\rm Fav}$ to be $0.066\pm0.005\pm0.004$. The precision on this measurement is competitive with the world average of 0.076 ± 0.006 [11]. In Figure 8.8 we summarise

Quantity	Value
Central value	1.41
Statistical uncertainty	0.31
PID systematic	0.09
MisID lineshape systematic	0.06
Low-mass lineshape systematic	0.02
Shape scaling systematic	0.00
Trigger choice systematic	0.06
Phenomological systematic	0.03
$DK/D\pi$ correction systematic	0.03
Total systematic	0.13
Total uncertainty	0.33

Table 8.6: Central value and statistical and systematic uncertainties on $R_{\mathcal{CP}+}$.

various measurements of this parameter. There is a slight tension between the measurements reported by Belle, BaBar and CLEO; the value we have obtained agrees best with the Belle result.

The ratio $\mathcal{B}^{DK}_{\mathcal{CP}}/\mathcal{B}^{D\pi}_{\mathcal{CP}}$ has been measured as $0.093 \pm 0.019 \pm 0.005$. Measurements of this quantity are summarised in Figure 8.9. The value we have measured is compatible with the world average of 0.086 ± 0.009.

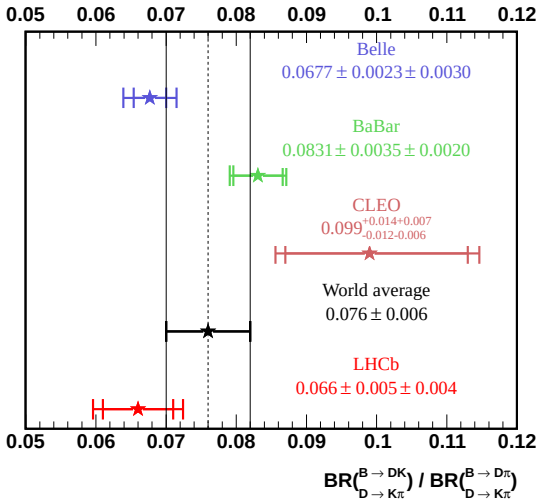

Figure 8.8: Values of $\mathcal{B}^{DK}_{\text{Fav}}/\mathcal{B}^{D\pi}_{\text{Fav}}$ measured by BaBar [124], Belle [125], CLEO [126] and LHCb. The world average is taken from the PDG [11].

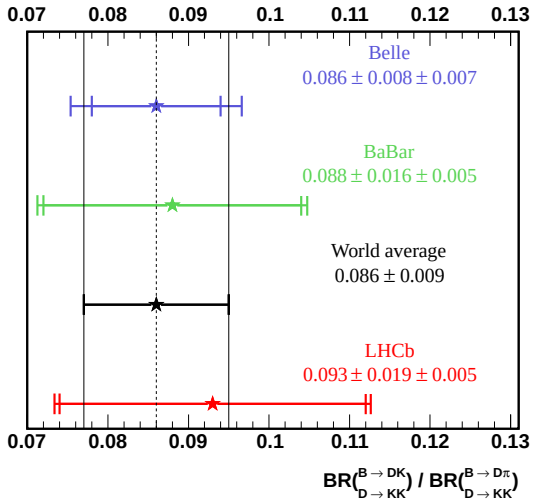

Figure 8.9: Values of $\mathcal{B}^{DK}_{\mathcal{CP}}/\mathcal{B}^{D\pi}_{\mathcal{CP}}$ measured by BaBar [124], Belle [127] and LHCb. The world average is taken from the PDG [11].

The measured value of $A^{DK}_{\mathcal{CP}+}$ is $0.06 \pm 0.17 \pm 0.07$, which is compatible with the world average of 0.24 ± 0.06 [21]. Our measurement is dominated by the statistical uncertainty. We have determined the ratio $R_{\mathcal{CP}+}$ to be $1.41 \pm 0.31 \pm 0.13$, which is again statistically dominated. The world average of this value is 1.18 ± 0.08 [21], which is compatible with our measurement. In Figure 8.10 we summarise various measurements of $A^{DK}_{\mathcal{CP}+}$ and $R_{\mathcal{CP}+}$.

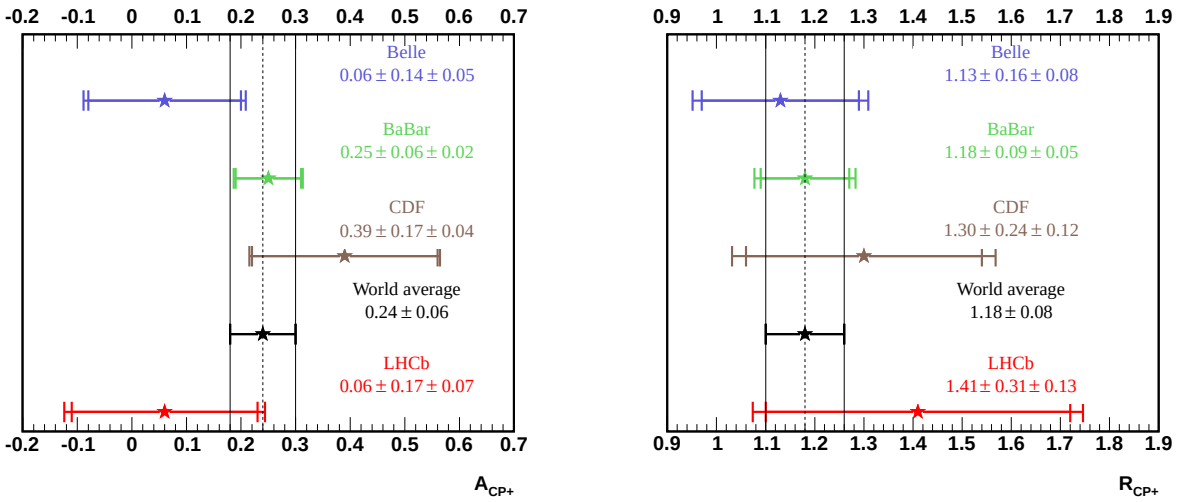

Figure 8.10: Values of $A^{DK}_{\mathcal{CP}+}$ (left) and $R_{\mathcal{CP}+}$ (right) measured by BaBar [44], Belle [127], CDF [128] and LHCb. The world average in each case is taken from Ref. [21].

We have measured $A^{D\pi}_{\mathcal{CP}+}$ to be $0.009 \pm 0.042 \pm 0.011$ and $A^{DK}_{\rm Fav}$ to be $-0.109 \pm 0.085 \pm 0.019$. These measurements are expected to be close to zero because $\mathcal{CP}$ violation is heavily suppressed in both cases. We confirm that the asymmetries are small, although there is a $\sim 1\sigma$ deviation from zero in $A^{DK}_{\rm Fav}$.

There are not enough events in the 2010 dataset to make a measurement of γ, but the values we have obtained are a promising step in the direction of such a measurement. In particular, the quantities $A^{DK}_{\mathcal{CP}+}$ and $R_{\mathcal{CP}+}$ are both dependent upon γ:

$$R_{\mathcal{CP}+} = 1 + (r_B^{DK})^2 + 2r_B^{DK}\cos(\delta_B^{DK})\cos(\gamma), \tag{8.13}$$

$$A^{DK}_{\mathcal{CP}+} = \frac{\pm 2r_B^{DK}\sin(\delta_B^{DK})\sin(\gamma)}{1 + (r_B^{DK})^2 + 2r_B^{DK}\cos(\delta_B^{DK})\cos(\gamma)}. \tag{8.14}$$

It is feasible that LHCb will collect 1 fb^{-1} of data by the end of 2011. If this occurs, the statistical uncertainties on $A^{DK}_{\mathcal{CP}+}$ ($R_{\mathcal{CP}+}$) will drop from 0.17 (0.31) to 0.03 (0.06), which are both significantly more precise than the current world average uncertainties. A precise measurement of 'GLW' decays will thus be possible, which is important to provide constraints in a determination of γ using the ADS/GLW method.

In the study of 2010 data we have not observed the suppressed mode $B^\pm \to (K^\mp\pi^\pm)_D K^\pm$ which is of crucial importance to measuring γ with the ADS approach. However, the suppressed mode has been detected in a study of LHCb data recorded up to mid 2011 [129]. This indicates that a precise measurement of γ will soon be achieved by LHCb.

Chapter 9

Conclusions and outlook

In this thesis we have presented two physics analyses: a determination of the strong-phase difference between D^0 and $\overline{D}^0$ decays to $K^0_S K^+ K^-$, and a measurement of $\mathcal{CP}$-violating parameters in $B^\pm \to D h^\pm$ decays. These analyses are both intermediate steps towards a determination of the CKM angle γ, which is currently one of the principal objectives of flavour physics.

In Chapters 3 and 4 we presented a first measurement of the strong-phase difference between D^0 and $\overline{D}^0$ decays to $K^0_S K^+ K^-$ using 818 pb^{-1} of quantum-correlated $D^0\overline{D}^0$ decays collected by the CLEO-c detector. We have measured the amplitude-weighted cosine and sine of the strong-phase difference in bins across the Dalitz plane. We have determined these parameters for divisions of the Dalitz plane into two, three and four bins of equal strong-phase difference, based on an amplitude model developed by the BaBar collaboration [25]. The results, listed in Tables 4.32 and 4.33, are in good agreement with those predicted using the BaBar model.

In addition, we have used a model-independent method to determine $\mathcal{F}_-$, the fraction of $\mathcal{CP}$-odd events in $D^0 \to K^0_S K^+ K^-$ decays in the kinematic region of the $\phi \to K^+K^-$ resonance. Considering several regions centred on the ϕ invariant mass squared, we find that $\mathcal{F}_-$ is greater than 0.76 at the 90% C.L. In analyses that use $D \to K^0_S \phi$ decays this measurement will be helpful in constraining the size of the systematic uncertainty that is related to the presence of decays that are not $\mathcal{CP}$-odd.

The strong-phase difference results we have obtained can be used in a model-independent measurement of γ using $B^\pm \to (K^0_S K^+ K^-)_D K^\pm$ decays. As described in Chapter 5, we have used simulations to determine the uncertainty on γ related to the CLEO-c results. This uncertainty is between 3.2° and 3.9° depending on the binning of the Dalitz plane. Measurements of γ using this method do not have an uncertainty related to the parameterisation of $D \to K^0_S K^+ K^-$ decays. This is in contrast to model-dependent measurements of γ (see e.g.

Ref. [30]), for which the uncertainties related to the parameterisation are both irreducible and hard to quantify.

LHCb has reconstructed $B^\pm \to (K^0_S\pi^+\pi^-)_D K^\pm$ and $B^\pm \to (K^0_S\pi^+\pi^-)_D \pi^\pm$ decays in the dataset collected in 2010 [120]. The relatively small size of the dataset has precluded the measurement of parameters related to $\mathcal{CP}$ violation with these channels, but this is a positive indication that LHCb will be able to reconstruct the corresponding final states in which the D decays to $K^0_S K^+ K^-$. When LHCb has collected sufficient data to make a measurement of γ using $B^\pm \to (K^0_S K^+ K^-)_D K^\pm$, the CLEO-c measurements that we have presented in this thesis will aid in reducing the uncertainty on γ.

Our results can additionally be used as inputs to the measurement of the time-dependent evolution of the $D \to K^0_S K^+ K^-$ Dalitz plot. Such measurements can be used to constrain charm mixing parameters [25, 130–132]. Current measurements of the charm mixing parameters use models to parameterise the D decay, which introduces significant systematic uncertainties. It is possible to use the strong-phase difference parameters measured in this analysis to make a model-independent measurement of the charm mixing parameters for $D \to K^0_S K^+ K^-$ [133]. As with the measurement of γ, systematic uncertainties related to the model parameterisation are replaced by an uncertainty dominated by the size of the CLEO-c dataset.

In Chapters 7 and 8 we have described the measurement of several observables related to $\mathcal{CP}$ violation in $B^\pm \to (K^\pm\pi^\mp)_D h^\pm$ and $B^\pm \to (K^+K^-)_D h^\pm$ decays using 36.5 pb^{-1} of data collected by the LHCb detector in 2010. We have determined the ratios $\mathcal{B}^{DK}_{\rm Fav}/\mathcal{B}^{D\pi}_{\rm Fav}$ and $\mathcal{B}^{DK}_{\mathcal{CP}}/\mathcal{B}^{D\pi}_{\mathcal{CP}}$ to be $0.066 \pm 0.005 \pm 0.004$ and $0.093 \pm 0.019 \pm 0.005$ respectively. We have measured the asymmetries $A^{DK}_{\mathcal{CP}+}$, $A^{D\pi}_{\mathcal{CP}+}$ and $A^{DK}_{\rm Fav}$ as $0.06 \pm 0.17 \pm 0.07$, $0.009 \pm 0.042 \pm 0.011$, and $-0.109 \pm 0.085 \pm 0.019$ respectively. Finally, we have calculated the ratio $R_{\mathcal{CP}+}$ to be $1.41 \pm 0.31 \pm 0.11$. The measurements we have made are all in agreement with the world average values. In particular, the precision we have obtained on $\mathcal{B}^{DK}_{\rm Fav}/\mathcal{B}^{D\pi}_{\rm Fav}$ is very competitive with the current world average [21].

An extension to the analysis presented in this thesis, which incorporates $B^\pm \to (K^\pm\pi^\mp\pi^+\pi^-)_D h^\pm$ decays [120], has already improved the precision of the results presented here. We anticipate that future measurements of these parameters at LHCb using the data collected in 2011 and beyond will yield world-leading results. A preliminary observation of the suppressed mode $B^\pm \to (K^\mp\pi^\pm)_D K^\pm$ has already been made using data collected in 2011 [129]. LHCb is therefore close to achieving a highly-competitive measurement of γ.

There are many other possible final states whose analyses will yield more information about γ, for example $B^\pm \to D^{*0}(D^0\pi^0/D^0\gamma)K^\pm$ [134] and $B^0 \to D^0 K^{*0}$ [35]. Eventually it will be possible to combine several measurements of γ [135] and obtain a very precise value of this fundamental parameter of nature.

Appendix A

Additional CLEO-c results

A.1 Migration matrices

This section lists the migration matrices for each group of $\mathcal{CP}$ and flavour final states.

A.1.1 Two bins

Equation A.1 shows the migration matrices for $K^0_S K^+ K^-$ against $K^+ K^-$ (left) and $K^0_S K^+ K^-$ against $K^0_S \pi^0$ (right):

$$\begin{pmatrix} 0.950 & 0.021 & 0.000 & 0.000 \\ 0.050 & 0.979 & 0.000 & 0.000 \\ 0.000 & 0.000 & 0.902 & 0.028 \\ 0.000 & 0.000 & 0.098 & 0.972 \end{pmatrix}, \begin{pmatrix} 0.980 & 0.039 & 0.010 & 0.000 \\ 0.013 & 0.961 & 0.000 & 0.000 \\ 0.008 & 0.000 & 0.982 & 0.078 \\ 0.000 & 0.000 & 0.008 & 0.922 \end{pmatrix}. \tag{A.1}$$

Equation A.2 shows the migration matrices for $K^0_S K^+ K^-$ against $K^\pm \pi^\mp$ (left) and $K^0_L K^+ K^-$ against $K^+ K^-$ (right):

$$\begin{pmatrix} 0.966 & 0.030 & 0.008 & 0.000 \\ 0.024 & 0.970 & 0.000 & 0.001 \\ 0.010 & 0.000 & 0.973 & 0.029 \\ 0.000 & 0.000 & 0.019 & 0.971 \end{pmatrix}, \begin{pmatrix} 0.961 & 0.258 & 0.010 & 0.000 \\ 0.028 & 0.742 & 0.000 & 0.000 \\ 0.011 & 0.000 & 0.959 & 0.235 \\ 0.000 & 0.000 & 0.031 & 0.765 \end{pmatrix}. \tag{A.2}$$

Equation A.3 shows the migration matrices for $K^0_L K^+ K^-$ against $K^0_L \pi^0$ (left) and $K^0_L K^+ K^-$ against $K^\pm \pi^\mp$ (right):

$$\begin{pmatrix} 0.895 & 0.149 & 0.003 & 0.000 \\ 0.098 & 0.851 & 0.000 & 0.000 \\ 0.007 & 0.001 & 0.855 & 0.145 \\ 0.000 & 0.000 & 0.142 & 0.855 \end{pmatrix}, \begin{pmatrix} 0.947 & 0.167 & 0.013 & 0.000 \\ 0.040 & 0.833 & 0.000 & 0.002 \\ 0.013 & 0.000 & 0.947 & 0.152 \\ 0.000 & 0.000 & 0.040 & 0.846 \end{pmatrix}. \tag{A.3}$$

A.1.2 Three bins

Equation A.4 shows the migration matrices for $K^0_S K^+ K^-$ against $K^+ K^-$ (left) and $K^0_S K^+ K^-$ against $K^0_S \pi^0$ (right):

$$\begin{pmatrix} 0.958 & 0.015 & 0.010 & 0.000 & 0.000 & 0.000 \\ 0.042 & 0.985 & 0.000 & 0.000 & 0.000 & 0.000 \\ 0.000 & 0.000 & 0.990 & 0.000 & 0.000 & 0.000 \\ 0.000 & 0.000 & 0.000 & 0.948 & 0.013 & 0.000 \\ 0.000 & 0.000 & 0.000 & 0.047 & 0.987 & 0.000 \\ 0.000 & 0.000 & 0.000 & 0.004 & 0.000 & 1.000 \end{pmatrix}, \begin{pmatrix} 0.980 & 0.029 & 0.047 & 0.010 & 0.000 & 0.000 \\ 0.012 & 0.971 & 0.000 & 0.000 & 0.000 & 0.000 \\ 0.000 & 0.000 & 0.953 & 0.000 & 0.000 & 0.000 \\ 0.008 & 0.000 & 0.000 & 0.975 & 0.065 & 0.000 \\ 0.000 & 0.000 & 0.000 & 0.014 & 0.935 & 0.000 \\ 0.000 & 0.000 & 0.000 & 0.001 & 0.000 & 1.000 \end{pmatrix}. \tag{A.4}$$

Equation A.5 shows the migration matrices for $K^0_S K^+ K^-$ against $K^\pm \pi^\mp$ (left) and $K^0_L K^+ K^-$ against $K^+ K^-$ (right):

$$\begin{pmatrix} 0.971 & 0.020 & 0.014 & 0.009 & 0.000 & 0.000 \\ 0.017 & 0.980 & 0.014 & 0.000 & 0.001 & 0.000 \\ 0.001 & 0.000 & 0.973 & 0.000 & 0.000 & 0.000 \\ 0.011 & 0.000 & 0.000 & 0.969 & 0.021 & 0.009 \\ 0.000 & 0.000 & 0.000 & 0.020 & 0.978 & 0.000 \\ 0.000 & 0.000 & 0.000 & 0.002 & 0.000 & 0.991 \end{pmatrix}, \begin{pmatrix} 0.949 & 0.220 & 0.036 & 0.010 & 0.000 & 0.000 \\ 0.037 & 0.772 & 0.012 & 0.000 & 0.000 & 0.000 \\ 0.002 & 0.008 & 0.952 & 0.000 & 0.000 & 0.000 \\ 0.012 & 0.000 & 0.000 & 0.956 & 0.199 & 0.067 \\ 0.000 & 0.000 & 0.000 & 0.033 & 0.794 & 0.013 \\ 0.000 & 0.000 & 0.000 & 0.000 & 0.007 & 0.920 \end{pmatrix}. \tag{A.5}$$

Equation A.6 shows the migration matrices for $K^0_L K^+ K^-$ against $K^0_L \pi^0$ (left) and $K^0_L K^+ K^-$ against $K^\pm \pi^\mp$ (right):

$$\begin{pmatrix} 0.862 & 0.118 & 0.005 & 0.004 & 0.000 & 0.000 \\ 0.113 & 0.881 & 0.005 & 0.000 & 0.000 & 0.000 \\ 0.015 & 0.001 & 0.989 & 0.000 & 0.000 & 0.000 \\ 0.010 & 0.001 & 0.000 & 0.852 & 0.106 & 0.000 \\ 0.000 & 0.000 & 0.000 & 0.139 & 0.894 & 0.010 \\ 0.000 & 0.000 & 0.000 & 0.004 & 0.001 & 0.990 \end{pmatrix}, \begin{pmatrix} 0.945 & 0.132 & 0.011 & 0.014 & 0.000 & 0.000 \\ 0.040 & 0.863 & 0.005 & 0.000 & 0.002 & 0.000 \\ 0.000 & 0.004 & 0.984 & 0.000 & 0.000 & 0.007 \\ 0.014 & 0.000 & 0.000 & 0.941 & 0.126 & 0.017 \\ 0.000 & 0.001 & 0.000 & 0.043 & 0.872 & 0.000 \\ 0.000 & 0.000 & 0.000 & 0.002 & 0.000 & 0.977 \end{pmatrix}. \tag{A.6}$$

A.1.3 Four bins

Equation A.1.3 shows the migration matrices for $K^0_S K^+ K^-$ against $K^+ K^-$ (left) and $K^0_S K^+ K^-$ against $K^0_S \pi^0$ (right):

$$\begin{pmatrix} 0.946 & 0.037 & 0.001 & 0.030 & 0.000 & 0.000 & 0.000 & 0.000 \\ 0.054 & 0.870 & 0.047 & 0.000 & 0.000 & 0.000 & 0.000 & 0.000 \\ 0.000 & 0.093 & 0.952 & 0.000 & 0.000 & 0.000 & 0.000 & 0.000 \\ 0.000 & 0.000 & 0.000 & 0.970 & 0.000 & 0.000 & 0.000 & 0.000 \\ 0.000 & 0.000 & 0.000 & 0.000 & 0.961 & 0.041 & 0.001 & 0.014 \\ 0.000 & 0.000 & 0.000 & 0.000 & 0.039 & 0.878 & 0.051 & 0.000 \\ 0.000 & 0.000 & 0.000 & 0.000 & 0.000 & 0.080 & 0.948 & 0.014 \\ 0.000 & 0.000 & 0.000 & 0.000 & 0.000 & 0.000 & 0.000 & 0.972 \end{pmatrix}, \begin{pmatrix} 0.980 & 0.069 & 0.009 & 0.000 & 0.011 & 0.000 & 0.000 & 0.000 \\ 0.012 & 0.894 & 0.081 & 0.000 & 0.000 & 0.000 & 0.000 & 0.000 \\ 0.000 & 0.037 & 0.901 & 0.000 & 0.000 & 0.000 & 0.000 & 0.000 \\ 0.000 & 0.000 & 0.009 & 1.000 & 0.000 & 0.000 & 0.000 & 0.000 \\ 0.009 & 0.000 & 0.000 & 0.000 & 0.977 & 0.068 & 0.000 & 0.015 \\ 0.000 & 0.000 & 0.000 & 0.000 & 0.012 & 0.881 & 0.071 & 0.000 \\ 0.000 & 0.000 & 0.000 & 0.000 & 0.000 & 0.051 & 0.905 & 0.015 \\ 0.000 & 0.000 & 0.000 & 0.000 & 0.000 & 0.000 & 0.024 & 0.970 \end{pmatrix}. \tag{A.7}$$

Equation A.8 shows the migration matrices for $K^0_S K^+ K^-$ against $K^\pm \pi^\mp$ (left) and $K^0_L K^+ K^-$ against $K^+ K^-$ (right):

$$\begin{pmatrix} 0.969 & 0.031 & 0.002 & 0.000 & 0.010 & 0.000 & 0.000 & 0.000 \\ 0.018 & 0.913 & 0.067 & 0.000 & 0.000 & 0.000 & 0.000 & 0.000 \\ 0.000 & 0.056 & 0.930 & 0.000 & 0.000 & 0.000 & 0.001 & 0.000 \\ 0.001 & 0.000 & 0.001 & 1.000 & 0.000 & 0.000 & 0.000 & 0.000 \\ 0.012 & 0.000 & 0.000 & 0.000 & 0.971 & 0.050 & 0.004 & 0.005 \\ 0.000 & 0.000 & 0.000 & 0.000 & 0.019 & 0.885 & 0.051 & 0.000 \\ 0.000 & 0.000 & 0.000 & 0.000 & 0.001 & 0.065 & 0.942 & 0.000 \\ 0.000 & 0.000 & 0.000 & 0.000 & 0.000 & 0.000 & 0.002 & 0.995 \end{pmatrix}, \begin{pmatrix} 0.943 & 0.249 & 0.058 & 0.048 & 0.011 & 0.000 & 0.000 & 0.000 \\ 0.040 & 0.636 & 0.227 & 0.000 & 0.000 & 0.000 & 0.000 & 0.000 \\ 0.004 & 0.113 & 0.715 & 0.016 & 0.000 & 0.000 & 0.000 & 0.000 \\ 0.001 & 0.002 & 0.000 & 0.935 & 0.000 & 0.000 & 0.000 & 0.000 \\ 0.013 & 0.000 & 0.000 & 0.000 & 0.948 & 0.186 & 0.041 & 0.051 \\ 0.000 & 0.000 & 0.000 & 0.000 & 0.038 & 0.716 & 0.225 & 0.000 \\ 0.000 & 0.000 & 0.000 & 0.000 & 0.002 & 0.098 & 0.734 & 0.000 \\ 0.000 & 0.000 & 0.000 & 0.000 & 0.001 & 0.000 & 0.000 & 0.949 \end{pmatrix}. \tag{A.8}$$

Equation A.9 shows the migration matrices for $K^0_L K^+ K^-$ against $K^0_L \pi^0$ (left) and $K^0_L K^+ K^-$ against $K^\pm \pi^\mp$ (right):

$$\begin{pmatrix} 0.880 & 0.201 & 0.049 & 0.008 & 0.000 & 0.002 & 0.000 & 0.000 \\ 0.092 & 0.665 & 0.203 & 0.000 & 0.000 & 0.000 & 0.000 & 0.000 \\ 0.014 & 0.134 & 0.745 & 0.030 & 0.000 & 0.000 & 0.000 & 0.000 \\ 0.000 & 0.000 & 0.001 & 0.962 & 0.000 & 0.000 & 0.000 & 0.000 \\ 0.007 & 0.000 & 0.001 & 0.000 & 0.870 & 0.180 & 0.044 & 0.022 \\ 0.007 & 0.000 & 0.000 & 0.000 & 0.099 & 0.672 & 0.173 & 0.000 \\ 0.000 & 0.000 & 0.000 & 0.000 & 0.019 & 0.145 & 0.780 & 0.058 \\ 0.000 & 0.000 & 0.000 & 0.000 & 0.012 & 0.000 & 0.003 & 0.920 \end{pmatrix}, \begin{pmatrix} 0.943 & 0.205 & 0.040 & 0.000 & 0.014 & 0.000 & 0.000 & 0.000 \\ 0.037 & 0.681 & 0.201 & 0.000 & 0.000 & 0.001 & 0.000 & 0.000 \\ 0.005 & 0.111 & 0.759 & 0.037 & 0.000 & 0.001 & 0.002 & 0.000 \\ 0.000 & 0.000 & 0.000 & 0.963 & 0.000 & 0.000 & 0.000 & 0.008 \\ 0.015 & 0.001 & 0.000 & 0.000 & 0.928 & 0.239 & 0.044 & 0.011 \\ 0.000 & 0.002 & 0.000 & 0.000 & 0.049 & 0.637 & 0.210 & 0.000 \\ 0.000 & 0.000 & 0.000 & 0.000 & 0.006 & 0.122 & 0.742 & 0.027 \\ 0.000 & 0.000 & 0.000 & 0.000 & 0.003 & 0.000 & 0.003 & 0.955 \end{pmatrix}. \tag{A.9}$$

A.2 Background estimation across the Dalitz plane

In this section we list the quantities used to determine the distributions of backgrounds across the Dalitz plane. The normalised bin areas on the $K^0_S K^+ K^-$ and $K^0_S \pi^+ \pi^-$ Dalitz planes are listed in Tables A.1 and A.2 respectively. Because the bins are symmetric, the areas of the i^{th} and $-i^{\text{th}}$ bins are combined.

Bin	Area		
	$\mathcal{N} = 2$	$\mathcal{N} = 3$	$\mathcal{N} = 4$
1	0.740	0.669	0.601
2	0.260	0.076	0.096
3	N/A	0.255	0.130
4	N/A	N/A	0.173

Table A.1: Normalised bin areas on the $K^0_S K^+ K^-$ Dalitz plane.

Bin i	Area	Bin i	Area
1	0.329	5	0.133
2	0.114	6	0.081
3	0.065	7	0.084
4	0.059	8	0.134

Table A.2: Normalised bin areas on the $K^0_S \pi^+ \pi^-$ Dalitz plane.

The normalised yields of $K^0_{S,L}K^+K^-$ tagged with $K^\pm\pi^\mp$ in MC are shown in Tables A.3–A.5.

Bin i	$K^0_SK^+K^-$	$K^0_LK^+K^-$
1	0.224	0.251
2	0.213	0.204
−1	0.283	0.289
−2	0.281	0.256

Table A.3: The normalised yield of flavour-tagged $K^0_{S,L}K^+K^-$ in each bin of $\Delta\delta_D$ on the $K^0_SK^+K^-$ Dalitz plot: two bins.

Bin i	$K^0_SK^+K^-$	$K^0_LK^+K^-$
1	0.202	0.228
2	0.222	0.212
3	0.013	0.016
−1	0.257	0.264
−2	0.275	0.254
−3	0.031	0.026

Table A.4: The normalised yield of flavour-tagged $K^0_{S,L}K^+K^-$ in each bin of $\Delta\delta_D$ on the $K^0_SK^+K^-$ Dalitz plot: three bins.

Bin i	$K^0_SK^+K^-$	$K^0_LK^+K^-$	Bin i	$K^0_SK^+K^-$	$K^0_LK^+K^-$
1	0.183	0.204	−1	0.227	0.236
2	0.085	0.091	−2	0.090	0.088
3	0.164	0.155	−3	0.218	0.197
4	0.006	0.006	−4	0.028	0.023

Table A.5: The normalised yield of flavour-tagged $K^0_{S,L}K^+K^-$ in each bin of $\Delta\delta_D$ on the $K^0_SK^+K^-$ Dalitz plot: four bins.

A.3 Statistical and systematic correlation matrices

The statistical and systematic correlation matrices for two bins are shown in Tables A.6 and A.7. The statistical and systematic correlation matrices for three bins are shown in

	c_2	s_1	s_2	c'_1	c'_2	s'_1	s'_2
c_1	−1.1	−0.3	−0.3	98.8	−1.1	−0.3	−0.3
c_2		0.3	3.0	−1.1	91.4	0.3	3.0
s_1			7.5	−0.4	0.3	99.4	7.5
s_2				−0.3	2.7	7.5	99.5
c'_1					−1.1	−0.4	−0.3
c'_2						0.3	2.7
s'_1							7.5

Table A.6: Statistical correlation coefficients (%) among $c_i(')$ and $s_i(')$ parameters for two bins.

Tables A.8 and A.9. The statistical and systematic correlation matrices for four bins are shown in Tables A.10 and A.11.

	c_2	s_1	s_2	c'_1	c'_2	s'_1	s'_2
c_1	24.3	6.7	1.5	58.3	20.6	9.0	5.3
c_2		1.6	0.1	22.3	60.7	4.9	5.6
s_1			60.1	4.9	2.3	95.8	52.0
s_2				5.5	4.3	58.9	87.1
c'_1					43.1	16.1	23.1
c'_2						13.5	21.9
s'_1							56.8

Table A.7: Systematic correlation coefficients (%) among $c_i(')$ and $s_i(')$ parameters for two bins.

	c_2	c_3	s_1	s_2	s_3	c'_1	c'_2	c'_3	s'_1	s'_2	s'_3
c_1	0.6	−2.9	−1.3	−0.6	−0.2	97.6	0.6	−2.1	−1.3	−0.6	−0.1
c_2		0.8	1.1	3.2	−0.0	0.6	98.0	0.4	1.1	3.2	−0.0
c_3			−0.3	0.2	2.5	−2.8	0.8	66.4	−0.3	0.2	2.4
s_1				−2.0	6.1	−1.3	1.1	−0.1	99.4	−2.0	5.8
s_2					−3.3	−0.5	3.2	0.1	−1.9	99.9	−3.0
s_3						−0.2	−0.0	2.2	6.1	−3.3	93.7
c'_1							0.6	−2.0	−1.3	−0.5	−0.1
c'_2								0.4	1.1	3.2	−0.0
c'_3									−0.1	0.1	2.2
s'_1										−1.9	5.8
s'_2											−3.0

Table A.8: Statistical correlation coefficients (%) among $c_i(')$ and $s_i(')$ parameters for three bins.

	c_2	c_3	s_1	s_2	s_3	c'_1	c'_2	c'_3	s'_1	s'_2	s'_3
c_1	21.8	6.4	7.2	−2.2	2.4	65.2	19.9	14.5	7.5	0.8	2.4
c_2		11.8	1.2	−15.4	−0.5	13.9	49.9	16.4	1.2	−14.3	−0.8
c_3			−0.5	12.5	−5.5	7.3	10.3	73.5	−0.3	13.3	−6.1
s_1				38.4	8.0	7.4	4.5	−0.1	99.4	37.9	7.9
s_2					7.7	−0.3	−6.1	6.0	38.3	95.6	7.8
s_3						9.9	10.3	2.0	8.4	10.6	96.9
c'_1							41.8	30.7	8.5	10.5	9.8
c'_2								35.6	5.7	5.8	10.1
c'_3									0.8	14.2	1.3
s'_1										38.2	8.3
s'_2											10.7

Table A.9: Systematic correlation coefficients (%) among $c_i(')$ and $s_i(')$ parameters for three bins.

	c_2	c_3	c_4	s_1	s_2	s_3	s_4	c_1'	c_2'	c_3'	c_4'	s_1'	s_2'	s_3'	s_4'
c_1	0.6	−0.2	−2.6	−0.9	0.1	−0.0	0.1	98.2	0.6	−0.2	−1.7	−0.9	0.1	−0.0	0.0
c_2		0.8	−0.1	0.6	1.8	−0.7	0.1	0.6	99.2	0.8	−0.2	0.6	1.8	−0.7	0.1
c_3			−0.1	0.4	−0.3	6.4	0.1	−0.2	0.8	98.0	−0.1	0.4	−0.3	6.4	0.1
c_4				0.6	−0.1	0.1	8.8	−2.5	−0.1	−0.1	63.5	0.6	−0.1	0.1	8.4
s_1					−8.0	8.5	16.0	−0.9	0.6	0.4	0.5	99.7	−8.0	8.5	14.9
s_2						−6.6	−1.3	0.1	1.8	−0.3	−0.1	−7.9	99.9	−6.6	−1.3
s_3							1.5	−0.0	−0.7	6.2	0.0	8.5	−6.6	99.8	1.4
s_4								0.0	0.1	0.1	6.6	15.9	−1.3	1.5	93.2
c_1'									0.6	−0.2	−1.7	−0.9	0.1	−0.0	0.0
c_2'										0.8	−0.2	0.6	1.8	−0.7	0.1
c_3'											−0.1	0.4	−0.3	6.2	0.1
c_4'												0.5	−0.1	0.0	6.4
s_1'													−8.0	8.5	14.8
s_2'														−6.6	−1.3
s_3'															1.4

Table A.10: Statistical correlation coefficients (%) among $c_i(')$ and $s_i(')$ parameters for four bins.

	c_2	c_3	c_4	s_1	s_2	s_3	s_4	c_1'	c_2'	c_3'	c_4'	s_1'	s_2'	s_3'	s_4'
c_1	14.5	19.6	4.3	6.3	−4.0	5.6	2.2	67.7	15.2	19.9	10.9	6.7	−3.1	6.8	4.3
c_2		19.3	6.5	2.2	−7.3	3.7	−1.1	12.4	60.1	17.4	9.6	2.4	−6.7	4.4	0.1
c_3			6.8	10.8	−13.5	24.6	−0.4	18.2	17.8	78.6	12.9	11.2	−12.5	25.6	1.8
c_4				1.3	4.1	1.3	−1.6	8.8	10.6	10.3	80.9	1.7	5.0	2.6	−0.7
s_1					−31.0	71.0	34.7	5.4	3.0	9.4	0.3	99.7	−30.5	70.3	33.2
s_2						−27.8	−0.1	−1.8	−3.3	−9.6	3.9	−30.9	99.2	−27.2	1.9
s_3							13.9	4.3	3.1	19.1	0.7	70.8	−27.5	98.7	12.3
s_4								2.1	0.2	0.4	−6.2	34.6	0.1	13.9	96.7
c_1'									37.3	35.0	23.2	7.1	2.3	10.0	10.9
c_2'										35.5	24.0	4.8	1.0	9.1	9.4
c_3'											23.0	10.8	−6.1	23.7	7.9
c_4'												1.4	6.4	4.2	−2.6
s_1'													−30.2	70.5	33.6
s_2'														−26.1	3.1
s_3'															13.9

Table A.11: Systematic correlation coefficients (%) among $c_i(')$ and $s_i(')$ parameters for four bins.

Appendix B

CLEO-c background acronyms

The tables in this section list the meanings of the acronyms used to represent various CLEO-c backgrounds.

Background	Description
SS/BS	Non-resonant background to the signal-side (SS) final state, or background to both sides (BS).
$K^0_L X$	Background to $K^0_S X$: an event containing $K^0_L X$.
$K^* X$	K^* with other particle(s).
ρX	$\rho(770)$ with other particle(s).

Table B.1: Acronym definitions for fully-reconstructed backgrounds.

Background	Description
SS	Non-resonant background to the signal-side final state.
SS	Non-resonant background to the opposite-side final state.
BS	Non-resonant background to both sides.
$K^0_S X$	Background to $K^0_L X$: an event containing $K^0_S X$.
$K^0_S Y$	Background to $K^0_L X$: any event with a K^0_S *except* $K^0_S X$.
$K^*!\omega$	K^* with other particle(s) that are not ω.
$K^* X$	K^* with other particle(s).
$K^0_L \pi^+\pi^- N\pi^0$	$K^0_L \pi^+\pi^-$ with at least one π^0.
$\pi^+\pi^- N\pi^0$	$\pi^+\pi^-$ with at least one π^0.
$X\ell\nu_\ell$	$\ell\nu_\ell$ with other particle(s).
$K_1 X$	K_1 with other particle(s).

Table B.2: Acronym definitions for partially-reconstructed backgrounds.

Bibliography

[1] CKMFitter group, J. Charles *et al.*, Eur. Phys. J. C **41**, 1 (2005), updated results and plots available at: `http://ckmfitter.in2p3.fr`.
Newest results presented at EPS 2011:
`http://indico.in2p3.fr/contributionDisplay.py?sessionId=2&contribId=392&confId=5116`.

[2] UTFit group, M. Bona *et al.*, JHEP **10**, 81 (2006), see also `www.utfit.org`.

[3] CLEO collaboration, D. M. Asner *et al.*, Phys. Rev. D **78**, 012001 (2008).

[4] CLEO collaboration, J. L. Rosner *et al.*, Phys. Rev. Lett. **100**, 221801 (2008).

[5] CLEO collaboration, N. Lowrey *et al.*, Phys. Rev. D **80**, 031105(R) (2009).

[6] CLEO collaboration, R. A. Briere *et al.*, Phys. Rev. D **80**, 032002 (2009).

[7] CLEO collaboration, J. Libby *et al.*, Phys. Rev. D **82**, 112006 (2010).

[8] P. W. Higgs, Phys. Rev. Lett. **13**, 508 (1964).

[9] F. Halzen and A. D. Martin, *Quarks and Leptons: An Introductory Course in Modern Particle Physics* (John Wiley & Sons, 1984), ISBN 0-471-88741-2.

[10] M. E. Peskin and D. V. Schroeder, *An Introduction to Quantum Field Theory* (Harper-Collins, 1995), ISBN 0-201-50397-2.

[11] Particle Data Group, K. Nakamura *et al.*, J. Phys. G **37**, 075021 (2010).

[12] M. Sozzi, *Discrete Symmetries and CP Violation: From Experiment to Theory* (Oxford University Press, 2008), ISBN 0-199-29666-9.

[13] T. D. Lee and C. N. Yang, Physical Review **104**, 254 (1956).

[14] C. S. Wu *et al.*, Physical Review **105**, 1413 (1957).

[15] J. H. Christenson *et al.*, Phys. Rev. Lett. **13**, 138 (1964).

[16] N. Cabibbo, Phys. Rev. Lett. **10**, 531 (1963).

[17] M. Kobayashi and T. Maskawa, Prog. Theor. Phys. **49**, 652 (1973).

[18] L.-L. Chau and W.-Y. Keung, Phys. Rev. Lett. **53**, 1802 (1984).

[19] A. Buras, M. E. Lautenbacher, and G. Ostermaier, Phys. Rev. D **50**, 3433 (1994).

[20] L. Wolfenstein, Phys. Rev. Lett. **51**, 1945 (1983).

[21] D. Asner *et al.*, `arXiv:hep-ex/1010.1589` (2010),
see also `http://www.slac.stanford.edu/xorg/hfag`.

[22] C. Jarlskog, Phys. Rev. Lett. **55**, 1039 (1985).

[23] M. Goldhaber and J. L. Rosner, Phys. Rev. D **15**, 1254 (1977).

[24] R. Dalitz, Phil. Mag. **44**, 1068 (1953).

[25] BaBar collaboration, P. del Amo Sanchez *et al.*, Phys. Rev. Lett. **105**, 081803 (2010).

[26] S. U. Chung, Phys. Rev. D **48**, 1225 (1993).

[27] J. Blatt and V. Weisskopf, *Theoretical Nuclear Physics* (John Wiley & Sons, 1952), ISBN 0-471-08019-5.

[28] S. M. Flatté, Physics Letters B **63**, 224 (1976).

[29] LHCb collaboration, B. Adeva *et al.*, LHCb-PUB-2009-029 (2010).

[30] BaBar collaboration, P. del Amo Sanchez *et al.*, Phys. Rev. Lett. **105**, 121801 (2010).

[31] Belle collaboration, A. Poluektov *et al.*, Phys. Rev. D **81**, 112002 (2010).

[32] Belle collaboration, I. Adachi *et al.*, BELLE-CONF-1103, `arXiv:hep-ex/1106.4046` (2011).

[33] Y. Grossman, A. Soffer, and Y. Zupan, Phys. Rev. D **72**, 031501 (2005).

[34] M. Patel, LHCb-PUB-2009-011 (2009).

[35] J. Nardulli and S. Ricciardi, LHCb-PUB-2008-038 (2009).

[36] J. Libby, LHCb-PUB-2007-014 (2007).

[37] V. Gibson *et al.*, LHCb-PUB-2007-048 (2007).

[38] K. Akiba *et al.*, LHCb-PUB-2008-031 (2008).

[39] M. Gronau and D. London, Phys. Lett. B **253**, 483 (1991).

[40] M. Gronau and D. Wyler, Phys. Lett. B **265**, 172 (1991).

[41] D. Atwood, I. Dunietz, and A. Soni, Phys. Rev. Lett. **78**, 3257 (1997).

[42] D. Atwood, I. Dunietz, and A. Soni, Phys. Rev. D **63**, 036005 (2001).

[43] D. Atwood and A. Soni, Phys. Rev. D **68**, 033003 (2003).

[44] P. del Amo Sanchez *et al.*, Phys. Rev. D **82**, 072004 (2010).

[45] A. Bondar *et al.*, Eur. Phys. J. C **47**, 347 (2006).

[46] A. Giri, Y. Grossman, A. Soffer, and J. Zupan, Phys. Rev. D **68**, 054018 (2003).

[47] BaBar collaboration, B. Aubert *et al.*, Phys. Rev. Lett. **95**, 121802 (2005).

[48] BaBar collaboration, B. Aubert *et al.*, Phys. Rev. D **78**, 034023 (2008).

[49] A. Poluektov *et al.*, Phys. Rev. D **73**, 112009 (2006).

[50] Belle collaboration, K. Abe *et al.*, Proceedings of Rencontres de Moriond EW 2008 (2008), `arXiv:hep-ex/0803.3375`.

[51] A. Bondar, Proceedings of BINP Special Analysis Meeting on Dalitz Analysis (2002), unpublished.

[52] A. Bondar and B. Poluektov, Proceedings of the CKM2006 workshop, Nagoya, Japan (2007), arXiv:hep-ph/0703267.

[53] A. Bondar *et al.*, Eur. Phys. J. C **55**, 51 (2008).

[54] CLEO collaboration, Q. He *et al.*, Phys. Rev. Lett. **100**, 091801 (2008).

[55] I. I. Bigi and H. Yamamoto, Phys. Lett. B **349**, 363 (1995).

[56] J. L. Rosner, Phys. Rev. D **74**, 057502 (2006).

[57] CLEO collaboration, M. S. Alam *et al.*, Phys. Rev. Lett. **74**, 2885 (1995).

[58] CLEO collaboration, S. Chen *et al.*, Phys. Rev. Lett. **87**, 251807 (2001).

[59] CLEO collaboration, document available at: http://www.lepp.cornell.edu/public/CLEO/spoke/CLEOc/ProjDesc.html.

[60] CLEO collaboration, G. Viehhauser, Nucl. Instrum. Meth. A **462**, 146 (2001).

[61] CLEO collaboration, document available at: http://www.lns.cornell.edu/public/CLNS/1994/CLNS94-1277/CLNS94-1277.html.

[62] CLEO collaboration, D. Peterson *et al.*, Nucl. Instrum. Meth. A **478**, 142 (2002).

[63] CLEO collaboration, D. Peterson, Nucl. Instrum. Meth. A **409**, 204 (1998).

[64] R. E. Kalman, Journal of Basic Engineering **82**, 35 (1960).

[65] CLEO collaboration, M. Artuso *et al.*, Nucl. Instrum. Meth. A **554**, 147 (2005).

[66] CLEO collaboration, E. Blucher *et al.*, Nucl. Instrum. Meth. A **249**, 201 (1986).

[67] C. Grupen and B. Shwartz, *Particle Detectors (2nd ed.)* (Cambridge University Press, 2008), ISBN 0-521-84006-6.

[68] CLEO collaboration, S. Dobbs *et al.*, Phys. Rev. D **76**, 112001 (2007).

[69] http://www.slac.stanford.edu/~lange/EvtGen/.

[70] J. Allison *et al.*, IEEE Transactions on Nuclear Science **53**, 270 (2006).

[71] S. Agostinelli *et al.*, Nuclear Instruments and Methods A **506**, 250 (2003).

[72] B. K. Heltsey, CLEO internal note CBX 06-28.

[73] W. Verkerke and D. Kirkby, (2003), arXiv:physics/0306116v1.

[74] L. Landau, J. Phys. (USSR) **8**, 201 (1944).

[75] G. Cowan, *Statistical Data Analysis* (Oxford Science Publications, 1998), ISBN 0-198-50155-2.

[76] F. James and M. Roos, Comput. Phys. Commun. **10**, 343 (1975).

[77] BES-III collaboration, D. M. Asner *et al.*, International Journal of Modern Physics A **24** (2009), arXiv:hep-ex/0809.1869.

[78] CMS and LHCb collaborations, LHCb-CONF-2011-047 (2011).

[79] LHCb collaboration, R. Aaij *et al.*, Phys. Lett. B **698**, 115 (2011).

[80] LHCb collaboration, A. A. Alves Jr *et al.*, JINST **3**, S08005 (2008).

[81] L. Evans and P. Bryant (eds.), JINST **3**, S08001 (2008).

[82] LHCb collaboration, R. Aaij *et al.*, Phys. Lett. B **694**, 209 (2010).

[83] LHCb collaboration, LHCb-CONF-2010-013 (2010).

[84] LHCb collaboration, CERN-LHCC-98-004 (1998).

[85] LHCb collaboration, CERN-LHCC-2003-030 (2003).

[86] LHCb collaboration, CERN-LHCC-2001-011 (2001).

[87] LHCb collaboration, CERN-LHCC-2000-007 (2000).

[88] LHCb collaboration, CERN-LHCC-2002-029 (2002).

[89] LHCb collaboration, CERN-LHCC-2001-024 (2001).

[90] LHCb collaboration, CERN-LHCC-2000-037 (2000).

[91] LHCb collaboration, CERN-LHCC-2000-036 (2000).

[92] LHCb collaboration, CERN-LHCC-2001-010 (2001).

[93] LHCb collaboration, CERN-LHCC-2003-002 (2003).

[94] LHCb collaboration, CERN-LHCC-2005-0012 (2005).

[95] LHCb collaboration, CERN-LHCC-2003-031 (2003).

[96] V. Gligorov, LHCb-PUB-2011-003 (2011).

[97] M. Williams *et al.*, LHCb-PUB-2011-002 (2011).

[98] LHCb collaboration, CERN-LHCC-2002–011 (2002).

[99] `http://lcg.web.cern.ch/LCG/public/`.

[100] N. Brook *et al.*, Talk from 2003 Computing in High Energy and Nuclear Physics (CHEP03), `arXiv:cs/0306060`.

[101] J. T. Mościcki *et al.*, Comput. Phys. Commun. **180** (2009).

[102] M. Clemencic *et al.*, J. Phys. Conf. Ser. **219**, 042006 (2010).

[103] `http://lhcb-release-area.web.cern.ch/LHCb-release-area/DOC/gauss/`.

[104] T. Sjöstrand, S. Mrenna, and P. Skands, Comput. Phys. Commun. **178**, 852 (2008).

[105] C. Chang, C. Driouichi, P. Eerola, and X. Wu, Comput. Phys. Commun. **159**, 192 (2004).

[106] N. Davidson, T. Przedzinski, and Z. Was, `arXiv:1011.0937v1` (2010).

[107] `http://lhcb-release-area.web.cern.ch/LHCb-release-area/DOC/boole/`.

[108] http://lhcb-release-area.web.cern.ch/LHCb-release-area/DOC/brunel/.

[109] http://lhcb-release-area.web.cern.ch/LHCb-release-area/DOC/davinci/.

[110] I. Antcheva *et al.*, Comput. Phys. Commun. **180**, 2499 (2009), see http://root.cern.ch.

[111] http://lhcb-release-area.web.cern.ch/LHCb-release-area/DOC/moore/.

[112] M. Abramowitz and I. A. Stegun (eds.), *Handbook of Mathematical Functions* (Dover Publications Inc., 1965), ISBN 0-486-61272-4.

[113] K. S. Cranmer, Comput. Phys. Commun. **136**, 198 (2001).

[114] B. Aubert *et al.*, Phys. Rev. D **70**, 112006 (2004).

[115] J. E. Gaiser, *Charmonium Spectroscopy from Radiative Decays of the J/ψ and ψ'*, PhD thesis, SLAC, 1982, SLAC-R-255.

[116] K. Pearson, Phil. Mag. Series 5 **50**, 157 (1900).

[117] https://twiki.cern.ch/twiki/bin/view/LHCb/PIDCalibPackage.

[118] M. Pivk and F. R. L. Diberder, Nucl. Instrum. Meth. A **555**, 356 (2005).

[119] M. Pivk, arXiv:physics/0602023v1 (2006).

[120] LHCb collaboration, LHCb-CONF-2011-031 (2011).

[121] LHCb collaboration, LHCb-CONF-2011-011 (2011).

[122] D. C. Hoaglin, F. Mosteller, and J. W. Tukey, *Understanding Robust and Exploratory Data Analysis* (Wiley Classics, 2000), ISBN 0-471-38491-5.

[123] P. J. Rousseeuw and C. Croux, Journal of the American Statistical Association **88**, 1273 (1993).

[124] BaBar collaboration, B. Aubert *et al.*, Phys. Rev. Lett **92**, 202002 (2004).

[125] Belle collaboration, Y. Horii *et al.*, Phys. Rev. D **78**, 071901 (2008).

[126] CLEO collaboration, A. Bornheim *et al.*, Phys. Rev. D **68**, 052002 (2003).

[127] Belle collaboration, K. Abe *et al.*, Phys. Rev. D **73**, 051106(R) (2006).

[128] CDF collaboration, T. Aaltonen *et al.*, Phys. Rev. D. **81**, 031105(R) (2010).

[129] LHCb collaboration, LHCb-CONF-2011-044 (2011).

[130] CLEO collaboration, D. M. Asner *et al.*, Phys. Rev. D **72**, 012001 (2005).

[131] Belle Collaboration, L. M. Zhang *et al.*, Phys. Rev. Lett. **99**, 131803 (2007).

[132] Belle collaboration, A. Zupanc *et al.*, Phys. Rev. D **80**, 052006 (2009).

[133] A. Bondar, A. Poluektov, and V. Vorobiev, Phys. Rev. D **82**, 034033 (2010).

[134] A. Bondar and T. Gershon, Phys. Rev. D **70**, 091503 (2004).

[135] A. Poluektov, Proceedings of CKM2010 (2011), arXiv:1101.4592v1.